ADVANCES IN

LASER INTERACTION WITH MATTER AND INERTIAL FUSION

Madrid, Spain   3 – 7 June 1996

Editors

G. Velarde

J. M. Martínez-Val

E. Mínguez

J. M. Perlado

Inst. de Fusion Nucl., Univ. Politec. de Madrid

**World Scientific**
Singapore • New Jersey • London • Hong Kong

REPORT DOCUMENTATION PAGE

Public reporting burden for this collection of information is estimated to average 1 hour per response, including the time for reviewing instructions, searching existing data sources, gathering and maintaining the data needed, and completing and reviewing the collection of information. Send comments regarding this burden estimate or any other aspect of this collection of information, including suggestions for reducing this burden to Washington Headquarters Services, Directorate for Information Operations and Reports, 1215 Jefferson Davis Highway, Suite 1204, Arlington, VA 22202-4302, and to the Office of Management and Budget, Paperwork Reduction Project (0704-0188), Washington, DC 20503.

1. AGENCY USE ONLY (Leave blank)	2. REPORT DATE 17 February 1998	3. REPORT TYPE AND DATES COVERED Conference Proceedings

4. TITLE AND SUBTITLE Advances in Laser Interaction with Matter and Inertial Fusion	5. FUNDING NUMBERS F6170896W0098
6. AUTHOR(S) G. Velarde, J.M. Martinez-Val, E. Minguez, and J.M. Peraldo	

7. PERFORMING ORGANIZATION NAME(S) AND ADDRESS(ES) Instituto de Fusion Nuclear Jose Gutierrez Abascal, 2 Mardrid 28006 Spain	8. PERFORMING ORGANIZATION REPORT NUMBER N/A

9. SPONSORING/MONITORING AGENCY NAME(S) AND ADDRESS(ES) EOARD PSC 802 BOX 14 FPO 09499-0200	10. SPONSORING/MONITORING AGENCY REPORT NUMBER CSP 96-1021

11. SUPPLEMENTARY NOTES

12a. DISTRIBUTION/AVAILABILITY STATEMENT Approved for public release; distribution is unlimited.	12b. DISTRIBUTION CODE A

13. ABSTRACT (Maximum 200 words)

The Final Proceedings for 24th European Conference on Laser Interaction with Matter, 3 June 1996 - 7 June 1996

Inertial Confinement Fusion, Hydrodynamic Instabilities, Coronal Interactions, Physics of High-Density Matter, Radiation Transfer, X-Ray Laser, Short-Pulse Interactions, Laser-Driven Experiments, Laser-Driven Reactor Concepts, and Laser Developments.

14. SUBJECT TERMS Nil	15. NUMBER OF PAGES 682
	16. PRICE CODE N/A

17. SECURITY CLASSIFICATION OF REPORT UNCLASSIFIED	18. SECURITY CLASSIFICATION OF THIS PAGE UNCLASSIFIED	19. SECURITY CLASSIFICATION OF ABSTRACT UNCLASSIFIED	20. LIMITATION OF ABSTRACT UL

ESCUELA TÉCNICA SUPERIOR
DE INGENIEROS INDUSTRIALES
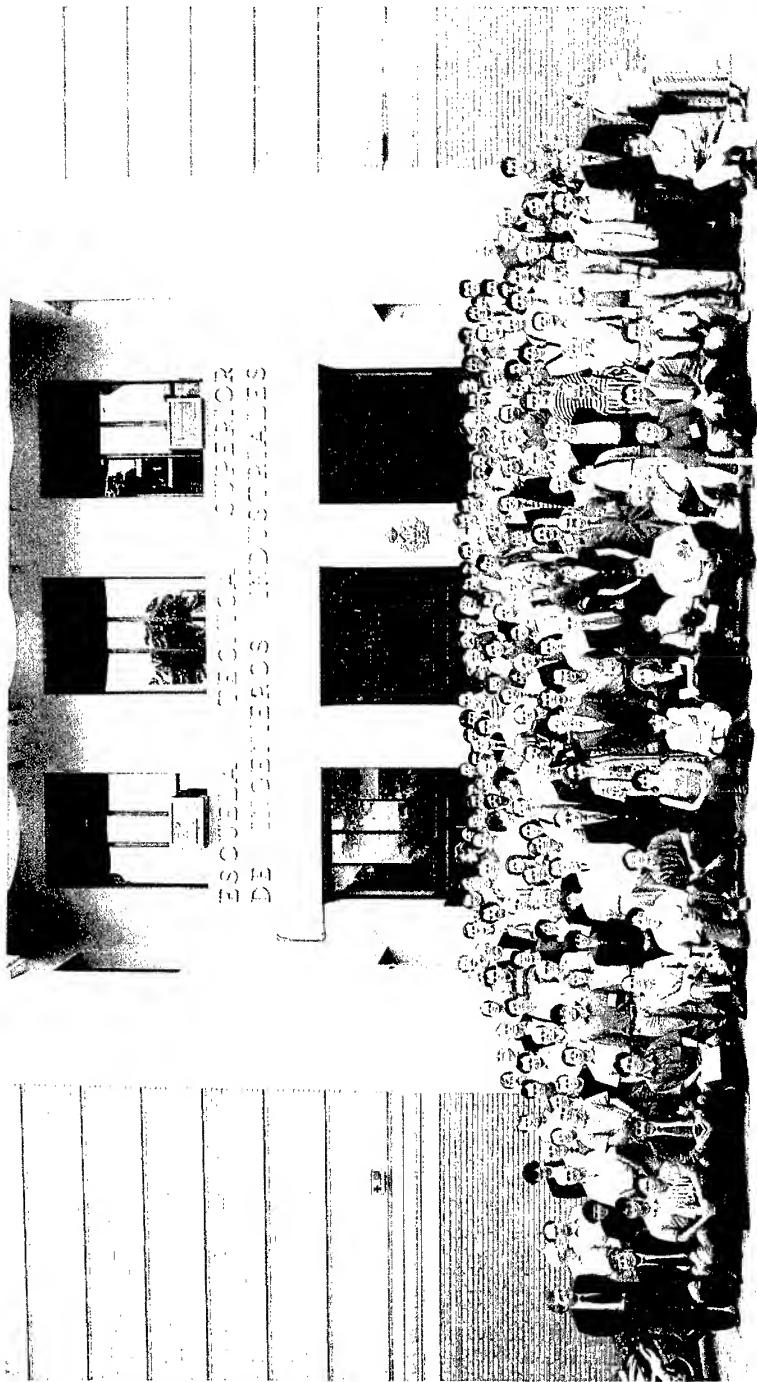
PREFACE

The 24th European Conference on Laser Interaction with Matter (24th ECLIM) was held in Madrid eight years after 19th ECLIM, which was also organised in the same venue by the Institute of Nuclear Fusion.

According to the papers presented at both Conferences, in 8 years our understanding of laser interaction with matter has improved significantly and some new ideas have emerged. However, it seems that more ideas will still be needed before laser-driven fusion can be a reality at a technological level, although it is already a fact at experimental level.

From the papers of our conferences, it can be said that Laser-Fusion is a very open field of research, not dominated by the dogmatism of other fields, where research is only devoted to one type of machine, for instance. In laser-interaction with matter, new contributions and proposals are welcome and it is important to keep the field open to new ideas that can lie outside the mainstream lines of research.

Nevertheless, advancement of Inertial Fusion requires new and more powerful facilities along the pathway that has already been established by the former experimental research in this field. From this viewpoint, it is worth emphasizing the importance of two major programs in France and the USA to build 1-MJ class laser facilities. They will likely attain fusion ignition in routine operation, although they will not specifically be fusion-energy oriented laboratories. Several outstanding papers on both programs can be read in this book. Those facilities will provide unique means to study energy cumulation phenomena in a much higher scale than the level currently available.

In the evolution of Inertial Fusion Research since 19th to 24th ECLIM, to say a period very familiar to the organisers of both conferences, a main change has been observed in international collaboration. It cannot be ignored that a huge fraction of Inertial Fusion research is still under classification, but it is very important to recognize the steps towards declassification. The situation in this context is a similar one to the case of Nuclear Fission Reactors in the fifties. At that time, a clear separation between classified and open research was difficult to define. This fact

explains why the first commercial reactors were fueled with natural uranium. Once classification policies were drawn on more realistic bases, enriched uranium reactors could be built for electricity generation, using to a large extent some of the know-how and technologies previously classified. The nuclear industry was really boosted by such a declassification policy, launched at the United Nations Organization by the USA President D. Eisenhower in his famous program "Atoms for Peace". Inertial Fusion Research seems to be at a similar crossroad, albeit a full similarity does not exist.

As an example of declassification trends, several contributions on indirect drive can be found in this book. Eight years ago, indirect drive was out of the scope of open research, but it has become a standard topic in Inertial Fusion Research, although clearly oriented to the study of physical phenomena relevant for Inertial Fusion Energy scenarios.

This book also contains many contributions on several topics that have been standard in Inertial Fusion for many years. This is the case of Coronal Physics, Hydrodynamics and Numerical Simulation.

It is also worth mentioning the new ideas about uniformization and smoothing of laser beam imprints and other non-uniformities. The field of direct drive can undergo an actual boost from foam-buffered targets and similar proposals to obtain uniform spherical implosions.

There are also new ideas on triggering ignition by different mechanisms and it seems to be that advanced fuels for neutronless fusion could be exploited in Inertial Fusion in a much better way than in other types of confinement.

Another new subject that has stirred a lot of interest among Inertial Fusion researchers is the short-pulse ultra-intense laser interaction. Experimental work and theoretical analysis on this subject are becoming an uprising star.

We must admit that there are some topics not properly covered yet in ECLIM. In our conferences, we have been talking about the same type of lasers for many years and they still dominate the field, without competition from other options. For instance, eight years ago, Free Electron Lasers seemed to be a new tool of our research, but there are no papers on this topic in this book. On the other hand, reactor concepts and target fabrication do not receive too much attention in our conferences. of course, we are still very far away from the technological phase of Laser-Fusion research, but some kind of visionary work is always useful and pleasant.

On the contrary, we must also admit that Diagnostics and Experimental Work occupy an important place in our book and in ECLIM. Although the number of

experimental teams has not increased in eight years, the quality and quantity of the work produced by these laboratories is certainly outstanding. Within this field so dear to ECLIM, prospectives of getting ignition in NIF (the USA) and in *Laser Megajoule* (France) are also paramount. We could then talk of the demonstration of the scientific feasibility of Laser Fusion.

In eight years from now, in 29th or 30th ECLIM, there will be the possibility to see if the new lasers and the contribution of new ideas have been able to demonstrate the feasibility of Laser-Fusion. For us, this is a promising future because Laser-Fusion must be a real option as a 21st century source of energy.

Such a potential has already been assessed by the European Science and Technology Assemby in his Working Party held at Abingdon (UK) on December 1995. This assessment includes a explicit recognition to the soundness and richness of Laser-Fusion research. Papers assembled in this book are an epitome of the highly valuable activities of the Inertial Fusion Research Community.

All the articles included in this Book have followed the current procedure in scientific journals. The Editors want to acknowledge specially the work and time of all the referees.

The Editors want to express their acknowledgement for the Edition of this Book and the success in Organizing 24th ECLIM to: *Direccin General de Investigacin Cientfica y Tecnolgica (DGICYT)* (Spanish Ministery of Education and Culture), *Government of the Community of Madrid* through Secretary of Education and Culture, *Fundacin para el Fomento y la Innovacin Industrial (F^2I^2)*. We wish to thank the *United States Air Force European Office of Aerospace Research and Development* for its contribution to the success of this conference. Finally we want also to thank to the European Union Euroconferences Program for supporting young researchers attending the Conference, and the Direction of the *College of Industrial Engineering (ETSII)*, of the Polytechnical University of Madrid, for their key help in organizing the Conference.

G. Velarde
J. M. Martinez- Val
E. Minguez
J. M. Perlado
Institute on Nuclear Fusion
Polytechnic al University of Madrid.
The Editors / Madrid 1996

CONTENT

xv

5. HIGH DENSITY PHYSICS

7.   LASER DEVELOPMENTS AND X-RAY LASERS

8. SHORT PULSE INTERACTIONS

1.- LASER DRIVEN EXPERIMENTS

Prospect of Laser Fusion

C. Yamanaka

Institute for Laser Technology, Yamadaoka Suita, Osaka 565
Japan

The laser fusion research has been remarkably developed in these 10 years. As for the high temperature demonstration, the LHART experiment got the high neutron yield by using a stagnation free compression. The thin shell target was imploded without mixing the pusher and fuel which could be applied to the volume ignition scheme. This method seems to be very important to avoid the difficulty in the spark ignition scheme due to the instability of implosion.

Concerning the high density demonstration of low isentropic compression, we attained the 1000 times of normal density by using a deutrated plastic shell target of high spherosity and also the uniform irradiation of smoothing laser beams with the random phase system.

The next stage is the ignition demonstration. The 100kJ blue laser will be useful for the low gain experiment in the direct drive case. As for the high gain experiment of the indirect drive scheme, a few MJ drivers such as NIF and Megajoule program are in progress.

A new method for the ignition is proposed to use a petta watt femto second laser which can deliver the energetic electrons into the compressed fuel core to ignite the target. The energy deposition mechanism is a very interesting issue for study which remains in the unknown area.

The ICF program is now preparing for the ignition and burn of fuel. The aim of ICF is to develop the civil energy for the next century. The international collaboration has been highly expected since 1988 by the statement of "Madrid Manifest". We strongly recommend the peaceful application of ICF for the future generation.

1. Introduction

The concept of laser fusion was devised very shortly after the invention of laser. In 1972, the Institute of Laser Engineering, Osaka University was established by the author in accordance with the Edward Teller's special lecture on "New Internal Combustion Engine" for IQEC at Montreal which predicted the implosion fusion. In 1975 we invented the so called indirect drive fusion concept "Cannonball Target" which

became later to be recognized as a same concept of "Hohlraum Target" from Livermore. As well known, ICF research in the US had been veiled for a long time due to the defense classification. In 1988, international members of the ICF research society including the US scientists gathered together at ECLIM to discuss the necessity of freedom in the ICF research and concluded to make a statement "Madrid Manifest" which requested the declassification of the ICF research internationally. After 6 years of halt, the US DOE decided to declassify portions of the program as a part of secretary Hazel O'Leary's openness initiative. Classification impeded the progress by restricting the flow of information and did not allow the ICF work to compete by the open scientific security.

The implosion experiments by GEKKO XII Osaka demonstrated a high temperature compression of DT fuel up to 10keV, neutron yield 10^{13} and a high density compression of CDT hollow shell pellet to reach $1000g/cm^3$ respectively. These results gave us a strong confidence to reach the ignition and burn in near future.

2. Present and Future Prospects

Until now the laser fusion research has been developed as shown in Table 1. As for the high temperature demonstration, the LHART experiment produced the high neutron yield by using a stagnation free compression scheme. The thin shell target was imploded without mixing of thin pusher and fuel which could be applied to the volume ignition. Concerning the high density demonstration of low isentropic compression, we used a deutrated plastic shell target which was prepared under no gravity condition to form an excellent spherosity of the pellet. And also the uniform irradiation of the laser beams was essentially important. In our case, non uniformity was kept below 3%. The beam smoothing technique such as the random phase plate has been fully investigated at ILE as shown in Table 2. The key issue for the high density is the uniform ablation. The famous high compression of 1000 times of normal density could not yet reach the ignition. The neutron yield was 100 times smaller than the expected value. The reason for this was due to the fuel mixing in the final compression stage to reduce the temperature of fuel. The method to overcome this problem is to improve the uniformity of ablation.

In Figure 1, a scenario of the ICF research to the scientific feasibility is indicated. To reduce the mixing, the laser irradiation modes shall be improved by using the larger numbers of beams, the optimized arrangement of beams, the beam smoothing as shown before, the profile

Table 1. Progress of Laser Fusion with GEKKO XII

FY	Achievement	Driver	Pellet & Diagnostics	Theory & Simulation
Interaction and Ablation				
1983	$Y_n=10^{10}$	Completion of GEKKO XII	Glass micro-baloon (GMB)	Hot electron
High Temperature Demonstration (Stagnation free compression)				
1984	High Absorption Complete Ablation	SHG ($\omega \to 2\omega$)	LHART	
1985	$Y_n=10^{12}$			Shock multiplexing
1986	$Y_n=10^{13}$ $T_i=10keV$		Fusion yield calibration	
High Density Demonstration (Low isentropic compression)				
1987		THG ($\omega \to 3\omega$)	CD shell	
1988	$\rho=1000 \times \rho_s$ (main fuel)	Random phase plate	CDT shell	Nonlocal transport
1989			2nd. reaction p knock-on Si activiation	
1990	Fermi degeneracy High density compression			2D, 3D code
Ignition and Burn Demonstration				
1991	Thermal smoothing	Partially coherent light	Cryogenic target	
1992	RT instability R-M instability			a Heating
1993	Impression stability	GEKKO XII	Ultra-fast frame	
1994	Uniform irradiation	Up grade	2D SSD	Ray trace
1995	Hibrid drive		X ray generated	
1996		Additional heating Petta watt laser	Scatter light spectral sifts	2D code ignition

6

control for each beam and the power balance of the beams. As shown in
Table 2, we can keep the absorption nonuniformity better than 1% when
the beam number is 60, the power imbalance is less than 1% and also the
partial coherent laser with the precision RPP is adopted. In these
conditions one will be able to expect the spark ignition judging from the
data of simulation using the α heating to smoothing the turbulence.

A new method to get the ignition is to use a petta watt ignition laser
such as 10^{20}W/cm^2 of a few kJ which may deliver the energetic electrons
into the compressed core to heat the fuel. This new way is now an
intense target of the ICF research. In this case the main compression
laser is enough to have a few 100kJ level. The final stage of the driver
will be a few MJ level for the high gain. As for the pellet gain scaling,
Figure 2 shows the necessary laser energy for the different implosion
velocities by the ILESTA-1D code. According to the ILESTA-2D fuel
simulation for 300kJ ignition experiment of Figure 3, the pellet gain 1
can be attained by the laser absorption uniformity better than 1%.

As well known the growth rate of Rayleigh Taylor instability in the
acceleration phase of implosion can be suppresed by the ablation flow,
however in the dececeration phase the only way to prevent the fuel
mixing is to keep the uniform ablation condition slowing down the
growth of instability. When the ignition starts, the α particle heating in
the compressed fuel will produce the fire polishing to kill the instability.

Table 2. Development of Laser Beam Smoothing Technique

ILE	Laser + RPP (1983) beam segmentation	ASE + RPP (1989) broadband spatial incoherency	ASE + RPP with angular dispersion (1991)	envelope control polarization control multi spherical lens array
NRL	ISI (1983) by echelon	echelon-free ISI (1987)	ASE with complete image relay	envelope control
LLE		1D E-O SSD + RPP (1989)	2D E-O SSD + RPP spectral angular dispersion	60 beams zero correlation mask
LLNL		Noisy SSD + RPP		envelope control Kinoform phase plate
Limeil		Optical fiber smoothing temporal and spatial incoherency by optical fiber		

| Key issue | beam segmentation speckle pattern | → | spatial and temporal incoherency | → | beamlet profile control multi beam irradiation |
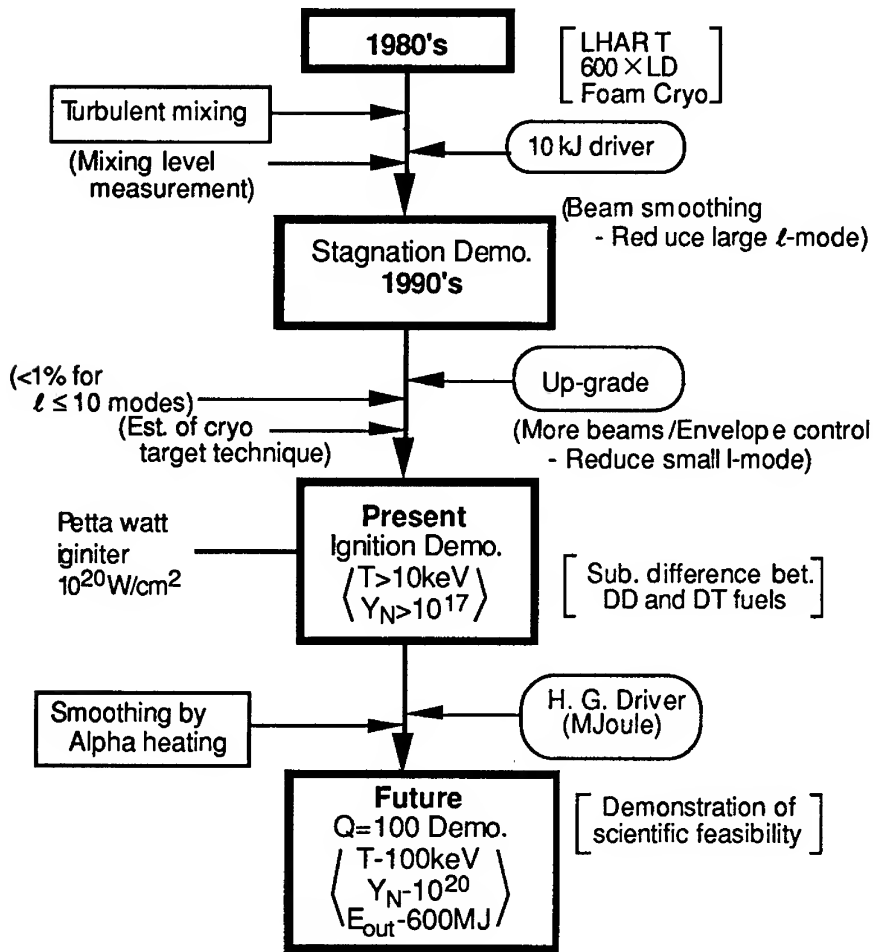
Figure 1. ICF Research Scenario, Osaka

To observe the implosion process precisely the new diagnostics of high resolution framing picture MIXS has been developed at ILE. The obliquely arranged pinholes on the slit of streak camera in soft x ray range can produce the sectors of the images of a compressed core which are computer processed to make a series of core images. The spatial resolution is 15μm, the temporal resolution is 11.7 psec and the frame interval is 8.7 psec. The MIXS can give us the instantaneous behaviors

of the core to analyze the implosion stability. In Figure 4, X ray emission images of the hot spark of the cooled CH shell filled D_2 50 atm + Ar 0.1 atm are irradiated by GEKKO XII, 5.66kJ, green light. The development of novel diagnostics is essentially important in future researches.
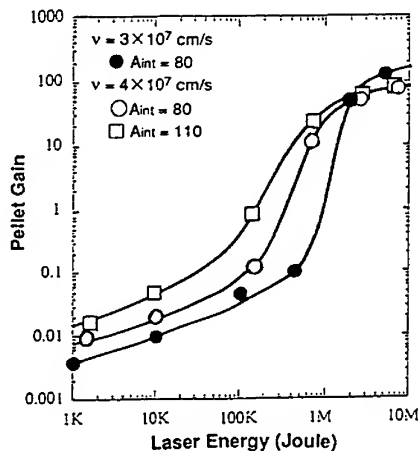
Figure 2. Pellet Gain Scalings
ILESA-1D Code
Inflight Aspect Ratio : A_{int}
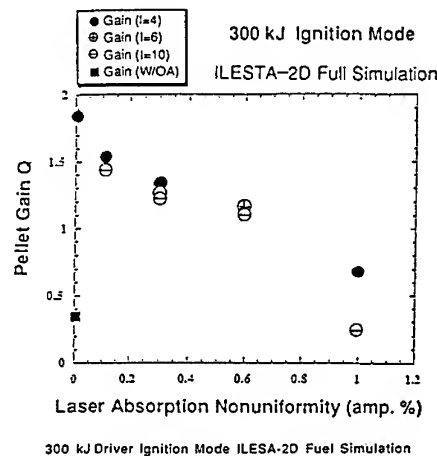
Figure 3. 300 kJ Driver Ignition
Mode ILESA-2D Fuel
Simulation

3. Conclusion

The inertial fusion research is now preparing for the first ignition and burn of fusion target which will be in about 10 years from now with a MJ glass laser by the indirect implosion and or a 300 kJ laser by the direct implosion. In the latter case the additional Peta watt short pulse laser seems very interesting for ignition. Key problems are still symmetry and stability of the implosion which cause the fuel mixing to reduce the temperature of the fuel. The significant progress made in smoothing laser beams as well as the development of high resolution diagnostics gives us a great tool to proceed for ignition and burn. Successful numerical simulation predicts the way to the goal. The volume ignition scheme is also reconsidered to eliminate the fuel mixing by pusher. The energy driver for ignition is considered to be lasers and these for the energy production might be heavy ion accelerators in the longer time scale.

International collaboration has just started to promote the mutual

100 μm
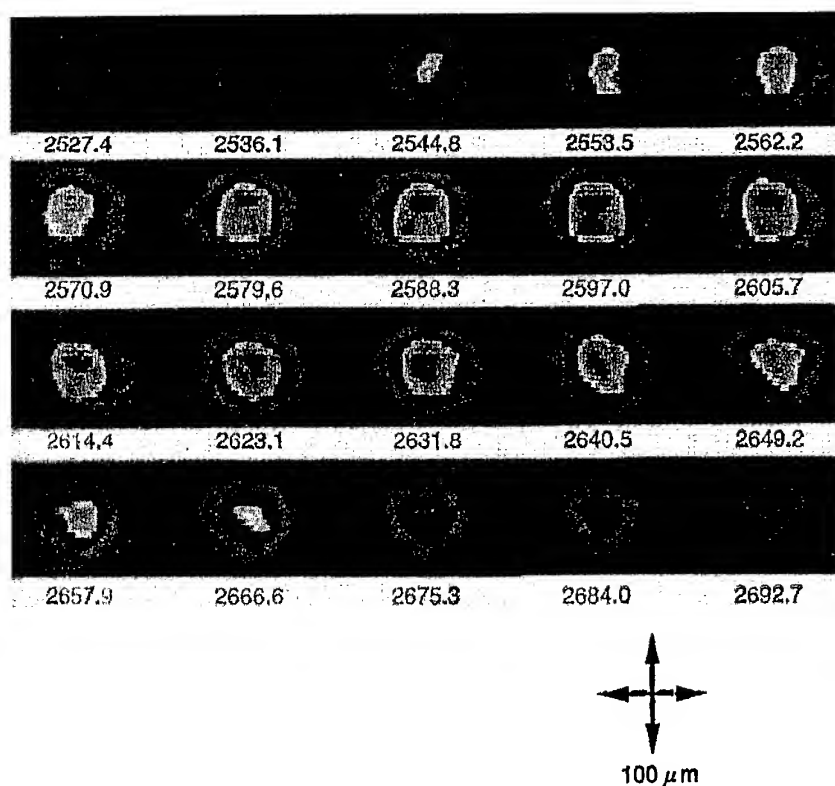
Target: cooled CH shell.diameter=486μm, shell thickness=7.23μm, filled with
   DD=50atm+Ar=0.1atm
Laser: GekkoXII.wave length=0.527μm, pulse duration=1.34nsec, energy=5.66kJ,
   energy imbalance=+9.8/-50% with RPP,
MIXS: temporal resolution=11.7psec, flame interval=8.7psec, spatial
   resolution=15μm, observed spectral range: hv=2.5～4.9keV

Figure 4.   X-ray Framing Camera for Hot Spark — MIX

benefit on ICF research. The declassification steps are to speed up the ICF research.

Applications of inertial confinement fusion include not only civil energy production but also physics at the laser-atom interaction, nuclear matter under extreme conditions, cosmology, special isotope separation, food preservation, hydrogen production and advanced space propulsion. The pursuit of ICF will contribute substantially to overall scientific strength in several areas.

In the international collaboration, the essential advancement in research and the technology development for fusion shall be carried out in the following items,

(1) High-average-power fusion drivers, lasers as well as heavy ion beams

(2) ICF target for power-plant and fueling technology including cryogenic methods

(3) Material for a reactor chamber and the technology of energy conversion

The development of the ICF reactor is essentially important. The material research including target, tritium and structural materials need an intense technology development to realize a fusion power plant by 2025. The international center for integrating a demonstration power plant of ICF shall be considered. No other alternate energy source holds a bright promise than fusion and none has ever presented such formidable scientific and engineering challenges.

References
1. C. Yamanaka : "Present status and future prospects of laser fusion research at Osaka" and "Progress in inertial fusion research" 1st International Symposium on Evaluation of Current Trends in Fusion Research, Washington D. C. 14-18, November (1994).
2. C. Yamanaka, *Introduction to Laser Fusion,* harwood academic publisher (1991).

DIRECT DRIVE LASER FUSION USING KRF LASERS

STEPHEN E. BODNER, YEFIM AGLITSKIY*, JILL P. DAHLBURG,
ALBAN DENIZ*, JOHN G. GARDNER#, THOMAS LEHECKA*, ROBERT
LEHMBERG, EDGAR A. MCLEAN, STEPHEN P. OBENSCHAIN, CARL J.
PAWLEY, LEE S. PHILLIPS#, MARK J. PRONKO, ANDREW J. SCHMITT,
JOHN F. SEELY+, VICTOR SERLIN, JOHN D. SETHIAN, JOHN A.
STAMPER
*Plasma Physics Division, Naval Research Laboratory,
Washington, DC 20375, USA*

The Nike KrF laser began operating in May, 1995. System reliability has been minimally acceptable for routine laser target experiments. The laser nonuniformity in each beam has been measured at 1% rms; this is a major improvement over existing glass lasers that operate at 3rd harmonic. Foil targets have been accelerated with low-mode velocity nonuniformity of less than 1.5%. Initial measurements of the higher-mode laser imprinting and Rayleigh-Taylor growth show that, as expected, more uniform laser beams and smoother targets have less modulation.

1. Nike Laser Performance

The Nike laser was completed and began operation in May 1995. The laser development program had two overall objectives: to demonstrate sufficiently reliable operation of a few-kilojoule KrF laser system, and to utilize the ISI optical smoothing technique (Induced Spatial Incoherence) to produce an ultra-uniform and flat laser profile. Both objectives have been fully met.

The Nike laser has had 240 full power shots on foil targets from May 1995 – May 1996. Typically, the laser has fired 2-4 shots per day, with about 20 shots between routine maintenance, which takes 1-2 days. Although we plan on further laser improvements, the system reliability and durability have been acceptable for routine laser target experiments. On useful shots, the energy in the 56 laser beams has typically been 2.8 ± 0.1 kJ. The ASE is low enough so that it does not ionize the front surface of the target, as diagnosed by a side-on laser shadowgraphy with 6 μm resolution.

The Nike laser beam uniformity has been a spectacular success. A single beam of the laser has a measured nonuniformity of 1% rms in a 4 ns pulse (excluding tilt and curvature) — as predicted by the ISI theoretical model[1]. This is roughly an order of magnitude smoother than existing glass lasers operating in the UV. The

Nike laser now overlaps 40 nearly-independent beams on a flat target; this should lower the laser nonuniformity to well below 1% in the same modal spectrum. We have photographed the soft x-ray emission from the front surface with a cassegrainian multilayer telescope coated for 95 eV x-rays. The measured x-ray spot size was the same as with a single beam, and the x-ray flux nonuniformity was less than 1%, below our diagnostic threshold.

2. Target Experiments

2.1 Flat Foil Acceleration

Our 1995 laser-target experiments measured the low-mode nonuniformity in the pressure drive, thereby demonstrating that Nike can overlap its laser beams and produce a uniform pressure pulse[2].

The first set of experiments diagnosed the uniformity of the shock breakout through plastic foils with an optical streak camera. Over the central 300 μm, the shock breakout is uniform to the resolution of the camera, indicating that the shock velocity is uniform to within 1.5%.

We then measured the uniformity of target acceleration via the double-foil diagnostic: an optical streak camera measures the impact time with a closely-spaced second foil. Within the central 400 μm, the target velocity was uniform to within 2%, peak to valley.

2.2. Initial Measurements of Laser Imprinting and Instability Growth

In early 1996 we implemented additional diagnostics to measure the laser imprinting and resultant Rayleigh-Taylor growth. Typically we use 6 beams for the x-ray backlighter and 6 beams for the x-ray sidelighter, producing 1.86 keV x-rays from a Si target. The x-rays are used with a side-on streak camera, a rear-side pinhole diagnostic with a four-frame camera, and a new spectral imaging diagnostic with a single-frame camera. The spectral imaging diagnostic uses a spherically-bent quartz crystal to image the Si x-rays with a spectral resolution of 0.01 Å. The spatial resolution of this diagnostic was 3 μm with DEF film and 10 μm with an x-ray framing camera. The brightness of the image is comparable to a pinhole. In many ways, this spectral imaging diagnostic is equivalent to a multi-kilovolt x-ray laser.

The high-intensity portion of the laser pulse is 4 ns long at an intensity of 1×10^{14} W/cm^2, preceded by a 3-4 ns long foot pulse typically at 3×10^{12} W/cm^2. The foot and main pulses are chosen so that their shocks arrive near the rear side of the plastic foil at about the same time, thereby keeping the target on a low isentrope. There are two options for the foot of the laser pulse. It can consist of either all 40 of the laser beams, or just one of the laser beams. This allows us to vary the laser beam uniformity in the foot by a factor of ~ 6 (square root of 40) while keeping the other parameters the same.

The targets are flat foils of CH, 30-40 μm thick, with three options on their surface smoothness: (a) smooth targets with roughness in the range of 10-40 Å; (b) randomly roughened targets with a surface smoothness variable from 0.2-2.0 μm; (c) sinusoidal modulations with wavelengths of 30 and 60 μm and amplitudes variable from 0.1-1.0 μm.

Measurements of the foil acceleration with a side-on x-ray streak camera are in agreement within 10% of hydrocode predictions, based upon the measured laser intensity. Measurements of the mass perturbations show that, as one would expect, the target acceleration is more uniform when we use smoother laser beams and/or smoother targets.

We have not yet measured the modulation transfer function for the pinhole camera, or quantitatively compared our measurements with our 2D radiation-hydro computer simulations. However there is some indication that the experiments are showing less growth than the code predictions. Since our 3D computer modeling has been in excellent agreement with the mass imprinting experiments carried out by Imperial College[3], any disagreement between theory and Nike experiments should be subtle. We can identify a few potential weaknesses: limited spatial resolution of our diagnostics; use of a 2D code for inherently 3D nonlinear perturbations; strongly-coupled plasma effects. We hope to resolve these uncertainties in future experiments.

3. Calculations of Laser Imprinting and Mass Perturbations

Optical beam smoothing uses both spatial and temporal incoherence to produce uniform ablation pressures on the target. This smoothing concept was first proposed by Lehmberg and Obenschain[4] of NRL in 1983, and contained two basic assumptions: (a) the distance "d" between the absorption and ablation surfaces must

14

be greater than the wavelength of the laser perturbations λ_p; (b) the hydrodynamic response time τ_h should be much longer that the laser's coherence time τ_c.

The above assumptions are valid except during the initial portion of the laser pulse, when the corona has not yet formed. This exception was first noted by Desselberger et ali[5] and by Emery et al[6]. At the beginning of the laser pulse, before the plasma corona has fully formed, $d < \lambda_p$ and $\tau_h \sim \tau_c$. The temporally fluctuating laser beams can then produce a driven Richtmyer-Meshkov instability that imprints mass modulations on the target. The scientific community is still attempting to fully understand the physics of this mass imprinting. We would like to note here that our 2D calculations predict that the imprinting time (the time during which the mass imprint is created) is approximately 1-3 ns for transverse perturbation wavelengths and pulse shapes appropriate to high gain laser fusion.

For our study we chose the laser pulse shape and target parameters of the Nike experiments; these are typical of the early-time behavior of a high gain pellet. We evaluated the imprinting by two methods. First, the computer model was modified so that the ISI fluctuations are turned off after 0.5, 1.0, or 2.0 ns. We found that the final mass perturbations were similar to the full ISI case only when the ISI was turned off after 2.0 ns. Second, we modified the computer model so that the ISI fluctuations were turned on only after 2.0, 3.5, or 5.0 ns. In all cases there was still mass imprinting, but at a lower value. We conclude that laser imprinting typically lasts a few nanoseconds, and that even if the early-time imprinting could be totally eliminated, one would have to evaluate the lower levels of later-time imprinting.

4. Summary

The Nike reliability and durability are still variable, but acceptable for laser-target experiments. The laser wavelength, the laser beam uniformity, the laser pulse duration, the target smoothness, and target foil thickness are all much closer to high gain ICF conditions than in previous experiments. We have measured the mass perturbations due to the combined Richtmyer-Meshkov imprinting and ablative Rayleigh-Taylor growth, and as expected, laser beams with 0.4% nonuniformity produce a more uniform target acceleration than laser beams with 2.0% nonuniformity (1 ns average). Also, smoother targets have less mass perturbations than rougher targets.

+ Space Science Division, NRL
* Science Applications International Corp., McLean VA

---

[1]T. Lehecka, R. H. Lehmberg, A. V. Deniz, K. A. Gerber, S. P. Obenschain, C. J. Pawley, M. S. Pronko, and C. A. Sullivan, Opt. Comm. **46**, 485 (1995)

[2]S. P. Obenschain, S. E. Bodner, D. Colombant, K. Gerber, R. H. Lehmberg, E. A. McLean, A. N. Mostovych, M. S. Pronko, C. J. Pawley, A. J. Schmitt, J. D. Sethian, V. Serlin, J. A. Stamper, C. A. Sullivan, J. P. Dahlburg, J. H. Gardner, Y. Chan, A. V. Deniz, J. Hardgrove, T. Lehecka, and M. Klapisch ,Phys. Plasmas **3**, 2098 (1996)

[3]R. J. Taylor, J. P. Dahlburg, A. Iwase, J. H. Gardner, D. E. Fyfe, and O Willi, PRL **76**, 1643 (1996)

[4]R. H. Lehmberg and S. P. Obenschain, Opt. Comm **46**, 27 (1983)

[5]M. Desselberger, T. Afshar-rad, F. Khattak, S. Viana, and O. Willi, PRL **68**, 1539 (1992)

[6]M. H. Emery, J. H. Gardner, R. H. Lehmberg, S. P. Obenschain Phys. Fluids B, **3**, 2640 (1992)

THE LLE DIRECT-DRIVE TARGET PHYSICS EXPERIMENTAL PROGRAM: FIRST YEAR OF EXPERIMENTS ON OMEGA

R. L. MCCRORY

Laboratory for Laser Energetics, University of Rochester,
250 East River Rd., Rochester NY 14623

The objective of the ongoing experimental program at the Laboratory for Laser Energetics (LLE) located at the University of Rochester is the validation of high-performance, direct-drive capsule implosions including research in five key physics areas: irradiation uniformity; energy coupling and transport; hydrodynamic stability and subsequent constraints on performance; hot-spot physics; and main-fuel-layer physics. In this paper, LLE's overall direct-drive experimental program plan is summarized. This program includes irradiation uniformity and pulse-shaping enhancements to OMEGA (a 60-beam, 40 kJ, UV laser); planar and spherical hydrodynamic stability experiments; long-scale-length plasma physics experiments; and several spherical implosion campaigns, all leading ultimately to conducting National Ignition Facility (NIF) hydrodynamic-equivalent, 30-kJ cryogenic capsule implosion experiments on OMEGA starting early in the year 2000.

1. Introduction

Recent progress in direct-drive irradiation uniformity coupled with improved multidimensional hydrodynamic simulations has shown that the potential for obtaining ignition and moderate thermonuclear gain on the National Ignition Facility (NIF) exists using direct-drive as well as indirect-drive implosions. The objective of the Laboratory of Laser Energetics' (LLE's) experimental program is the validation of high-performance direct-drive capsule implosions. Associated with this validation is research into five key physics areas: irradiation uniformity; energy coupling and transport; hydrodynamic stability and subsequent constraints on performance; hot-spot physics; and main-fuel-layer physics. In this paper we briefly review LLE's overall direct-drive experimental program plan.

2. LLE Program Plan

The LLE program includes construction of the 60-beam, 40-kJ OMEGA UV ICF facility. This laser met all its specifications and was completed on time within the $61 million budget in May 1995. The system has delivered on-target energy in excess of 37 kJ and is capable of producing up to 45 kJ of UV energy on target.

The five-year experimental plan implemented after construction of OMEGA contains several irradiation-uniformity and pulse-shaping enhancements to the laser as well as a series of experiments in the following areas: planar and spherical hydrodynamic stability experiments; long-scale-length laser plasma interaction experiments; and spherical implosion experiments. The initial experiments con-

ducted on OMEGA included tests of beam focusing, pointing, and irradiation uniformity as well as implosion experiments carried out with polymer and glass capsules filled with deuterium, deuterium-tritium, or deuterium doped with Kr or other gases.

Diagnostics included x-ray imaging, x-ray spectroscopy, neutron diagnostics, and time-resolved imaging. Some of the initial experiments were carried out on glass-shell capsules with diameters up to 1300 μm, glass wall thickness ranging from 2 to 3 μm, and parylene overcoatings up to 2 μm thick. The capsules were filled with up to 20 atm of D^2 or DT gas at room temperature. Up to 32 kJ of UV laser light in pulse widths ranging from 600 to 1000 ns were used to drive these capsules. The capsules were designed to achieve a convergence ratio in the range of 4 to 20, ion temperature in the range of 2 to 15 keV, fuel density in the range of 0.2 to 2 g/cm^3, and neutron yields up to 2×10^{14} (DT) or 10^{12} (D$_2$).

The neutron data are summarized in Fig. 1(a) and produced record yields for ICF experiments. The highest yield recorded in this series was 1.4×10^{14}. This represents a yield efficiency (total thermonuclear energy divided by laser energy) in excess of 1%. Comparison of this data with yield data obtained on the 24-beam OMEGA laser in 1986 shows significant improvement in the agreement between

I1021
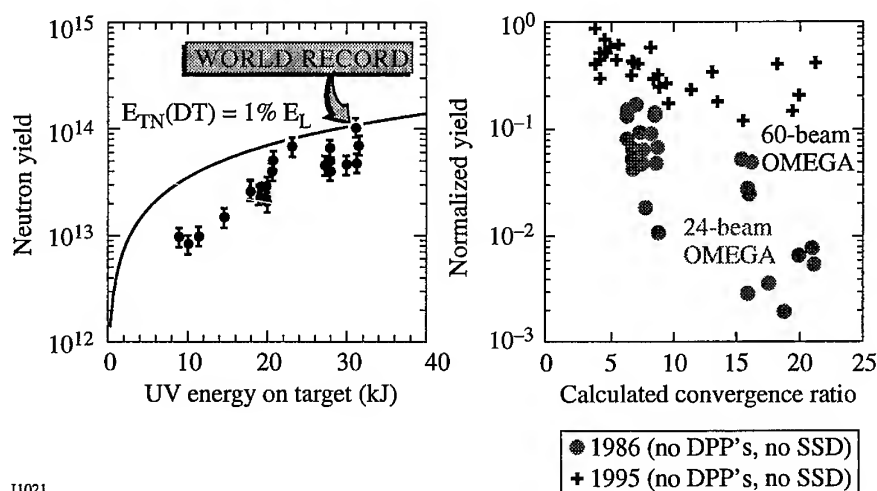
Fig. 1

(a) Neutron yield measured on recent OMEGA 60-beam, 30-kJ implosion experiments producing record yield and yield efficiency. (b) Normalized yield (measured neutron yield divided by calculated clean 1-D yield for the most-recent OMEGA 60-beam experiments (1995) and those from 1.5-kJ, 24-beam experiments carried out in 1986.

18

the experimentally measured yield and that calculated assuming clean one-dimensional performance. This improvement is demonstrated in Fig. 1(b), which compares the normalized yield (measured divided by calculated) versus calculated convergence ratio for the two sets of data.

The significant improvement in performance was accomplished with an increase in beam number and total energy on target but without irradiation uniformity schemes such as distributed phase plates or SSD. Part of the five-year LLE plan, which has already been implemented, is 2-D SSD beam smoothing. This technique for beam smoothing introduces spectral dispersion in two orthogonal directions in the beam using electro-optic phase modulators.[2] The results of this beam-smoothing approach are demonstrated in Fig. 2. In addition to beam smoothing, in accordance with the plan, flexible pulse shaping has also been implemented on OMEGA. In the coming years, these two capabilities will be used to conduct a series of hydrodynamically equivalent capsule experiments to validate NIF capsule performance.

To carry out the hydro-equivalent experiments, cryogenic-fuel-layer capabilities must be implemented on OMEGA. Through a collaboration involving LLNL, LANL, General Atomics (GA), and LLE, the requisite cryogenic capabilities are currently being developed. The cryogenic system ultimately implemented on

5914	5936	5935	5924
$\Delta\lambda_1 = 0$	$\Delta\lambda_1 = 0.6$	$\Delta\lambda_1 = 0.0$	$\Delta\lambda_1 = 0.6$ Å
$\Delta\lambda_2 = 0$	$\Delta\lambda_2 = 0.0$	$\Delta\lambda_2 = 1.5$	$\Delta\lambda_2 = 1.5$ Å
$\sigma_{rms} = 71\%$	$\sigma_{rms} = 31\%$	$\sigma_{rms} = 24\%$	$\sigma_{rms} = 19\%$
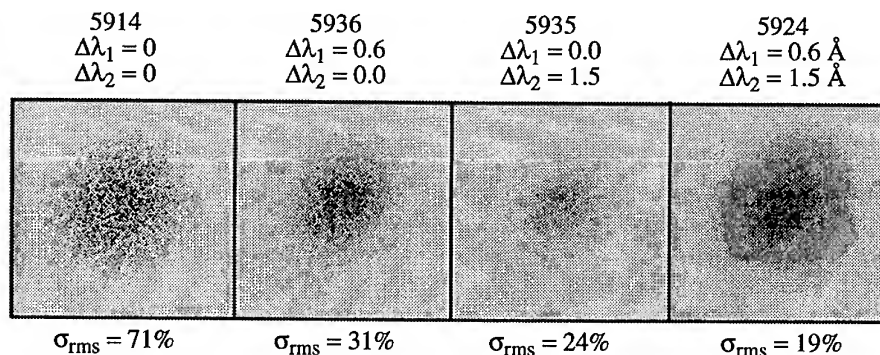
E7874

Fig. 2
Equivalent-target-plane images of one of the OMEGA UV beams at full power showing the improvement in irradiation uniformity with 2-D SSD. Shot 5914 shows the beam imprint with a distributed phase plate only; shot 5936 uses 1-D SSD with modulator #1 set at 0.6 Å; shot 5935 has modulator #2 set at 1.5 Å; and shot 5924 uses both modulators to achieve 2-D SSD. The percentages below the figure represent the rms variation in intensity for each case.

OMEGA will be prototypical of the NIF target-handling system. A schematic of the OMEGA cryogenic target system now being designed for operation in 1999 is shown in Fig. 3. Initial cryogenic target experiments are expected to begin on OMEGA in FY2000.

- Targets can be filled with DT up to 1500-atm pressure.
- Solid layering process will occur outside the chamber, and a fully characterized target will be inserted.
- Liquid layering will probably occur inside the chamber with in situ characterization just before the target is shot.

E7003
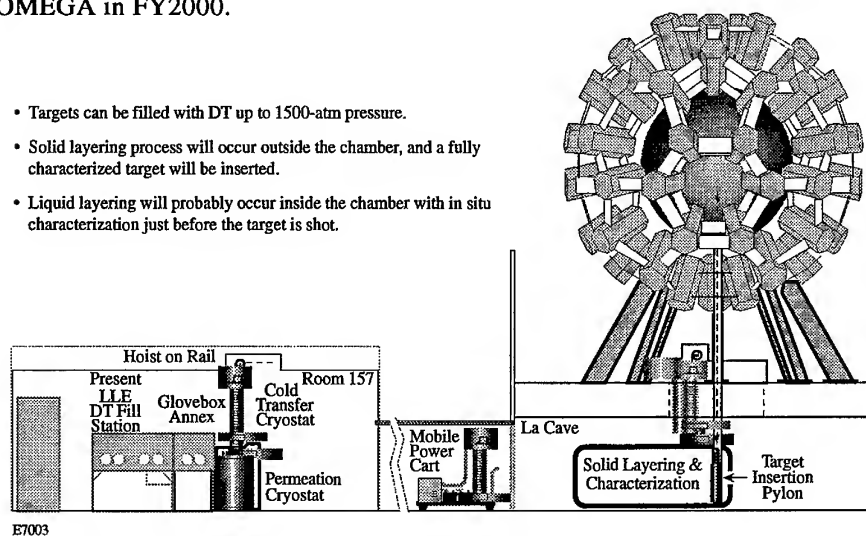
Fig. 3
Schematic of OMEGA cryogenic target system now being designed for operation in 1999.

Acknowledgment

References

1. R. L. McCrory, J. M. Soures, C. P. Verdon, T. R. Boehly, D. K. Bradley, R. S. Craxton, J. A. Delettrez, R. Epstein, P. A. Jaanimagi, S. D. Jacobs, R. L. Keck, J. H. Kelly, T. J. Kessler, H. Kim, J. P. Knauer, R. L. Kremens, S. A. Kumpan, S. A. Letzring, F. J. Marshall, P. W. McKenty, S. F. B. Morse, A. Okishev, W. Seka, R. W. Short, M. D. Skeldon, S. Skupsky, M. Tracy, and B. Yaakobi, "Direct-Drive Laser Fusion Experimental Program at the University of Rochester's Laboratory for Laser Energetics," in *Plasma Physics and Controlled Nuclear Fusion Research 1994* (IAEA, Vienna, 1996), Vol. 3, pp. 33–37.

2. S. Skupsky, R. W. Short, T. Kessler, R. S. Craxton, S. Letzring, and J. M. Soures, J. Appl. Phys. **66**, 3456 (1989).

RECENT PROGRESS OF LASER FUSION RESEARCH AT ILE OSAKA

T. YAMANAKA, K. MIMA, H. AZECHI, H. FUJITA, R. ISHIZAKI, N. JITSUNO,
Y. KATO, Y. KITAGAWA, R. KODAMA, T. KANABE, K. MURAKAMI,
N. MIYANAGA, M. NAKAI, S. NAKAI, K. NISHIHARA, H. NISHIMURA,
K. SHIGEMORI, H. TAKABE, K. A. TANAKA and M. TAKAGI.
Institute of Laser Engineering, Osaka University, Suita, Osaka 565, Japan.

Gekko XII glass laser system has been improved in irradiation uniformity. Power balance control of twelve beams and partially coherent light techniques reduce irradiation nonuniformity less than 1% and 3-4% for spherical mode number l=20-200 and l=1-20, respectively. Growth rate of Rayleigh-Taylor instability, the imprint of the irradiation nonuniformity, the reduction of imprint by x-ray prepulse and rippled shock wave effects are investigated using a partially coherent light. Implosion performances are also investigated using PCL with a fast-rise square pulse preceded by a prepulse to reduce the growth rate of Rayleigh-Taylor instability. The neutron yields is improved due to the suppression of growth rate of the instability.

1 Introduction

The formation of igniter is the key issue of the inertial confinement fusion research after the demonstration of high density compression [1]. In the isobaric implosion the hydrodynamic instability and the resulting fuel-pusher mixing at stagnation phase have to be solved quantitatively in relation with the irradiation nonuniformity and the surface roughness of fuel pellet. ILE Osaka University makes much effort to improve the irradiation uniformity of Gekko XII laser and to understand quantitatively the hydrodynamics instability. And we have also started the fundamental research of the fast igniter. Using the New Gekko XII with high irradiation uniformity we have observed improved implosion performance.

2 Improvement of laser irradiation uniformity

The overall laser irradiation nonuniformity is decided by the single beam factor and the geometrical factor of irradiating laser beams [2]. The power balance between beams has to be taken in to account in the geometrical factor in the actual arrangement. Single beam factor could be controlled using random phase plates and beam smoothing techniques such as the partially coherent light (PCL) [3] and the smoothing by spectral dispersion (SSD) [4] which smears out the speckles temporally. The geometrical factor depends upon the irradiation beam number and their arrangement.

The front end system of PCL is shown in Fig. 3(a) of reference [3], and has

demonstrated that the optical fibers are quite useful for both the coherence control and pulse shaping. The PCL pulse used is the square pulse with the variable duration from 50 ps to 2.2 ns. The beam pattern of the focused PCL on the target plane has the medium mode ($20 \leq l \leq 40$) nonuniformity due to the residual coherence of which coherent time is 3.6 ps. This nonuniformity can be substantially reduced by the angular spectral dispersion. The nonuniformity on the spherical target by 1.6 ns square pulses combined with new random phase plates with hexagonal elements is evaluated using one beam pattern and is shown as functions of spherical mode number and integration time in Fig. 1. The 1.6 ns time integrated nonuniformity σ_{rms} is 1.9% in l=1-120 where main contribution is lower modes of l<20.

New Gekko XII glass laser system is improved system in irradiation nonuniformity by introducing the power balance control instruments and the PCL with SSD. As the beam smoothing techniques have reduced the high-mode ($l \geq 20$) nonuniformity, the power imbalance among the beams that causes the low-mode non-uniformity becomes significant. The calculated absorption non-uniformity of the New Gekko XII is 3-4% with the PCL combined with the improved RPP of 1.85-mm hexagonal element and the power imbalance of 3-5% (rms).

Although the PCL is very useful technique to achieve a high irradiation uniformity, the conversion efficiency to the second harmonics is limited to about 50% in type II KDP crystal even if a rectangular pulse is used. 2D-SSD has been developed to improve the conversion efficiency, which shows 4.7% of irradiation nonuniformity. Combination of PCL for foot pulse and 2-D SSD for main pulse will be introduced to New Gekko XII system.
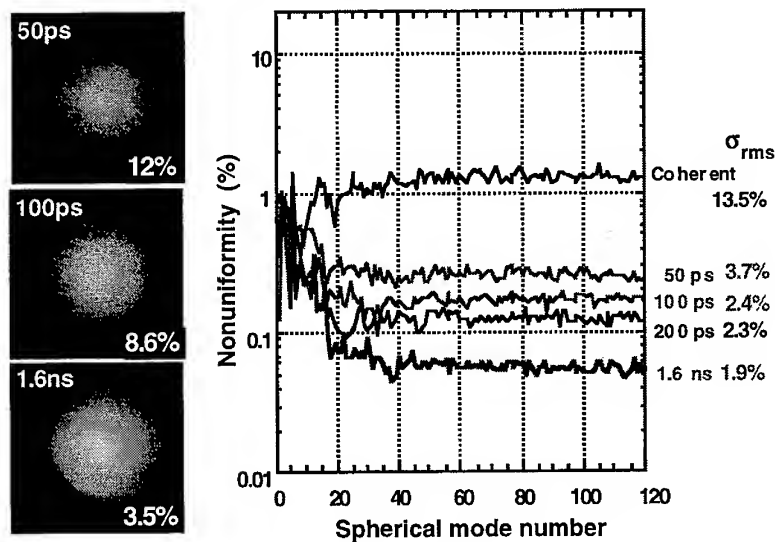
Fig. 1 Temporal change of irradiation uniformity of partially coherent light produced by fiber optics with SSD. One beam pattern and spherical mode expansion on the spherical target. The time in the figure is integration time.

3 Experimental study of hydrodynamic instability

The linear growth rate of R-T instability, the imprint of laser irradiation nonuniformity, the reduction of imprint by x-ray and the propagation of rippled shock wave have been investigated using the 0.53 μm PCL. The pulse shape is 2.2 ns rectangular with 40 ps rise time. The laser irradiation nonuniformity of a beam is 3.5%.

In the measurements of linear growth rate of R-T instability, two pulses, low intensity foot pulse and high intensity main pulse, are used [5]. The foot pulse is 1×10^{13} W/cm^2 in intensity and 1.8 ns in pulse width, which is followed by the main pulse with 1×10^{14} W/cm^2 and either 1.8 or 2.2 ns. The target is 16 μm thick polystyrene foil imposed sinusoidal perturbation of which wavelength is 60 μm. The amplitudes are 0.1, 0.3 and 1 μm. The temporal growth of the perturbation is measured by the x-ray face-on back light method with the 3 μm spatial resolution Advanced Kirkpatrick-Baez (AKB) microscope [6] with streak camera . The x-ray photon energy is 1.1-1.3 keV. The evaluated is the perturbation of areal mass density. The measured growth factor of $(\Delta\rho l / / \Delta\rho l_0)$ is shown in Fig. 2 with the classical one, where $(\Delta\rho l_0)$ is the initial areal mass density. Growth factors of the small initial amplitude cases (0.1 and 0.3 μm) are well fitted to an exponential curve and are scaled as $\Delta\rho l / / \Delta\rho l_0 = 5.1\exp(1.2\times10^{19} t)$. While in the large amplitude case (1 μm), the growth saturates at early stage and switches to nonlinear phase. The measured growth rate $\gamma=1.2\times10^{19}$ /s is about one half of the classical value of $(kg)^{1/2}$ $=2.4\times10^{19}$/s, where k and g are respectively the wave number of initial perturbation and the acceleration which is measured by the side-on x-ray back light method.

The measured growth rate is also compared with the theoretical one with ablative stabilization given by Takabe ($\gamma=0.9(kg)^{1/2}$ - $\beta k v_a$, v_a : ablation velocity in the frame of the accelerated target, β: constant) [7]. Using the values of g and v_a calculated with the ILESTA-1D simulation, the mean growth rate is estimated to be
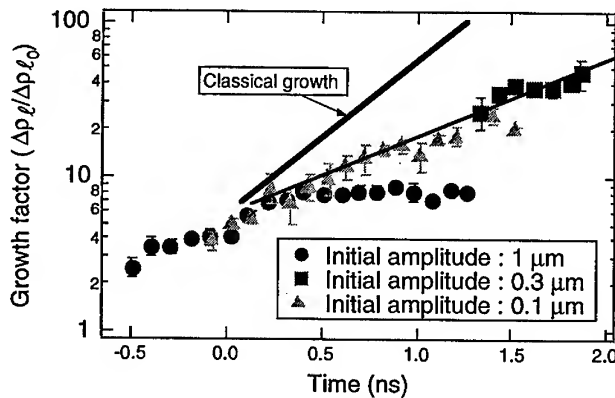
Fig. 2 Growth rate measurement of Rayleigh-Taylor instability. Linear growth of instability is clearly observed due to the small initial perturbation amplitude and uniform laser irradiation. t=0 corresponds to onset time of main pulse.

2×10^9 /s for $\beta = 3$-4, which is still larger than the experimental one. The reason for this discrepancy is under investigation. We tentatively presume that non-local heat transport preheats the target to reduce the density, thereby increasing the ablative velocity.

The initial imprint by laser irradiation nonuniformity is studied with a 16 μm thick polystyrene target by illuminating a quasi sinusoidally modulated low intensity pulse (5×10^{12} W/cm^2) followed by the non-modulated high intensity beam [8]. The modulation intensity $\delta I/I$ is given by a slit mask to be 10% and 40% with spatial wavelength of 100 μm. The amount of the imprint is estimated by interpolating the areal mass density perturbation grown by the irradiation of high intensity beam. The areal mass density perturbation at the onset time of the high intensity beam is 9×10^{-5} and 2×10^{-4} g/cm^2 for $\delta I/I$ = 10% and 40%, respectively. While no imprint is observed for the non-modulated beam.

The reduction of imprint by the uniform preformed plasma is studied in the same way [9]. The preformed plasma is produced by the external x-ray source. The perturbation amplitude of R-T instability is reduced to 60% of that without x-ray pre-irradiation in the case of 40% modulation low intensity pulse irradiation. This reduction factor is discussed with cloudy model in which the reduction factor f is given by $f = \exp(-kD)$ where D is the stand-off distance. For k =630 cm^{-1} (λ=100 μm and D=14 μm, f becomes 0.4 which is close to the experimentally observed value. Here the irradiation x-ray intensity is estimated to be 7×10^{10} W/cm^2 and the stand-off distance given by $C_s \tau$ is 14 μm, where C_s is the sound velocity of x-ray preformed plasma (3.5×10^6 cm/s) and τ is the duration (400 ps). This hybrid method is useful to suppress the initial imprint in direct drive implosion.

The behavior of the ripple shock wave, which gives the areal density perturbation, is also studied using a surface modulated planar target [10, 11]. The phase inversion is observed when the shock traveling distance becomes equal to the perturbation wavelength. The areal density perturbation approaches to be 4 when shock front propagates more than a perturbation wavelength. These results agree well with the theoretical calculation [12].

4 Implosion experiment by New Gekko XII

Plastic shell targets with D$_2$ gas are imploded by irradiating PCL from the New Gekko XII twelve-beam system. Plastic shell is 520-μm in diameter and 8-μm in thickness. The thickness nonuniformity is less than 1% and the surface roughness is 2 nm (rms) for $l \geq 50$. The main square laser pulse with a 0.2 ns prepulse ahead is used. The rise time of both pulses is less than 50 ps. The irradiation nonuniformity is evaluated from the intensity profiles of the x-ray and the second harmonic (λ=0.26 μm) emissions from the gold coated spherical target. The major nonuniformity arises from lower laser energy deposition at the oblique incidence region on the target. The mode-6 nonuniformity due to this factor may amount to 3.5 % in the present configuration. In the experiments the conversion ratio is changed by changing fuel pressure from 30 to 5 atm. The time gap between the prepulse and the main pulse is fixed to be 0.4 ns.

Dependence of the neutron yield ratio (yield in experiment/1D simulation yield) on the convergence ratio (initial fuel radius/ compressed fuel radius in simulation) is shown in Fig. 3 for the different power imbalance among the beams. The neutron yield ratios of the power balanced shots (σ_{rms}) decrease from 0.08 to 0.03 with increasing the convergence ratio from 12 to 16 as shown by closed circles. While when the mode-1 non-uniformity is added by an order of 20%, the neutron yields decrease as shown by closed squares. Although the yield ratio is less than unity, the value of 0.03 for the 16x convergence is significantly higher than our previous results obtained with a single Gaussian pulse PCL irradiation (0.008 for the 7.4x convergence). For comparison the results of the indirect-drive experiments at Lawrence Livermore National Laboratory with the precision NOVA laser facility are also shown by the crosses in Fig. 3.

The neutron yields in the present experiments correspond almost close to those at the second bounce of the shock wave in 1D simulation, while in the single Gaussian pulse irradiation the observed neutron yield corresponds only up to the first bounce of the shock wave in the simulation. These results indicate that the fuel compression and heating continue well during the stagnation phase and the R-T instability is now in better control in comparison to the previous experiments. However the implosion is still away from spherical symmetry. The x-ray emission distribution of the compressed core observed with the AKB microscope (time integrated) and the temporally resolved 2D images shows that the core images are oval and are comprised of localized x-ray emission regions.

The experimental results are compared with the simulation results with mix model [13]. The baseline hydrodynamics is calculated with the ILESTA-1D code. Following processes are taken into account to calculate the fuel-pusher mixing
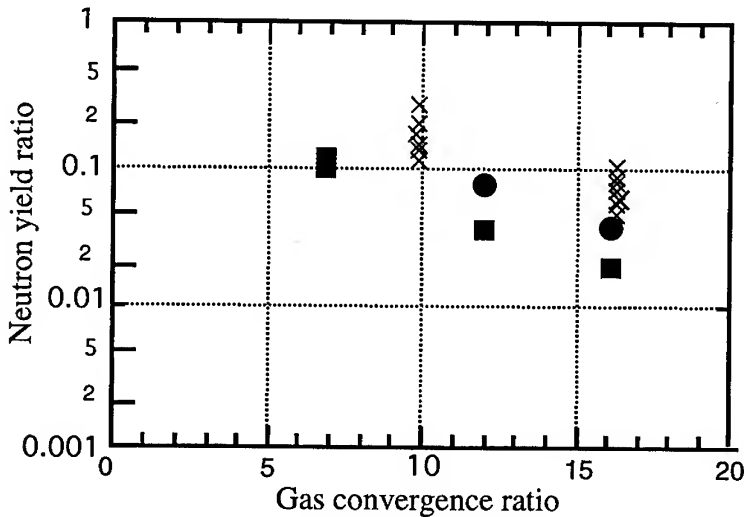
Fig. 3 Neutron yield ratio (N_{exp}/N_{sim}) vs. fuel gas convergence ratio. ●: power balanced shot, ■: imbalanced shot, ✕: indirect drive data after LLNL.

width: R-T instability based on the Takabe formula, the feed through of the perturbation from the outer-to-inner surface of the target, Richtmyer-Meshkov (R-M) and R-T instabilities on the inner surface and the nonlinear saturation based on the Haan's model [14]. In the calculation of neutron yield, the mixing region is so cooled down that the neutron yield is negligible in this region. In the calculation we added 5% and 10 % non-uniformity in each l=1 and 2 mode. These values of low-l non-uniformity correspond approximately to energy imbalance of 10 and 20%, respectively. Even with this exaggerated non-uniformity, the calculated yield with mix model is still higher than the experimental yield. We presume this discrepancy is due to the other low-l non-uniformity arising from the absorption process which is not correctly included in the present model.

5 Summary

The Gekko XII is improved in power balance in twelve beams and intensity profile of each beam by introducing the partially coherent light with SSD as the front-end. The irradiation nonuniformity on the spherical target is 3.5% with new random phase plate with optimized hexagonal element. The hydrodynamic instability is extensively studied in terms of linear growth rate, imprint and rippled shock wave. Partially coherent light square pulse with fast rise time reduces the growth rate of R-T instability. Uniformly preformed plasma shows the suppression of imprint. The neutron yields are also improved by PCL and adding a prepulse prior to the main square pulse. We have started the fundamental research on the fast ignition [15].

References
[1] H. Azechi, et al. 1991 Laser and Particle Beams **9**, 193.
[2] S. Skupsky, et al. 1983 J. Appl. Phys. **5 4** 3662.
[3] N. Miyanaga, et al. 1995 Laser Interaction with Matter, Proceedings of the 23rd European Conference (Inst. Phys. Pub., Bristol] 81.
[4] S. Skupsky, et al. 1989 J. Appl. Phys. **6 6** 3456.
[5] K. Shigemori, et al. 1996 Ann. Progr. Rep. 1995 ILE Osaka Univ. 137.
[6] R. Kodama, et al. 1995 Proc. SPIE **2 5 2 3** 165.
[7] H. Takabe, et al. 1985 Phys.Fluids **2 8** 3676.
[8] M. Nakai, et al. 1996 Ann. Progr. Rep. 1995 ILE Osaka Univ. 141.
[9] H. Shiraga, et al. 1996 Ann. Progr. Rep. 1995 ILE Osaka Univ. 143.
[10]1T. Endo, et al. 1995 Phys. Rev. Lett. **74** 3608.
[10] K. Shigemori, et al. 1996 Ann. Progr. Rep. 1995 ILE Osaka Univ. 133.
[12] K. Nishihara, te al. 1996 24th ECLIM M2-2.
[13] K. Mima, et al. 1996 Phys. Plasmas **3** May.
[14] S.W. Haan 1989 Phys. Rev. **A 3 9** 5812.
[15] R. Kodama, et al 1996 24th ECLIM PP26.

Overview of ISKRA laser fusion activities

G.G. KOCHEMASOV

*Russian Federal Nuclear Center - Institute of Experimental Physics,
607190, Sarov, Prospect Mira 37, Nizhny Novgorod Region, Russia.*

A review of laser fusion investigations will be presented which were performed at VNIIEF on photodissociation iodine laser facilities ISKRA-4 (1 kJ, 0.5 ns, 0.67 μm) and ISKRA-5 (30 kJ, 0.3 ns, 1.315 μm).

1. Introduction

In the RFNC-VNIIEF experimental investigations on laser fusion are conducted during 15 years using laser facilities ISKRA-4 and ISKRA-5. Review of previous efforts it's possible to find in [1,2]. Now Iskra-4 ($\cong$1 TW on the target) is a facility mostly intended for studies on the direct-drive physics, ISKRA-5 ($\cong$30 TW on the target) is a laser for indirect- drive experiments.

In this paper a review of some investigation will be presented which were fulfilled in last two years.

2. Mixing investigations at ISKRA-4 [3]

Two years ago we began experimental investigations of turbulent mixing of thin multilayer foils under laser acceleration. Main idea of these experiments was published in [4,5]. We irradiated the foil consisting of 3 layers: Si (5 μm), Al (2μm) and Au (0.05-0.26 μm). Main laser beam irradiated the Si side, two probe beams irradiated the Au side. One probe beam which was exactly opposite the main beam used for diagnostic purpose. We used additional probe beam as a control one. The pulse duration was 0.8-1.2 ns. Main beam intensity on the foil was $(0.5\text{-}1)\cdot10^{14}$ W/sm^2. We chose the Si-layer thickness so that thermal wave could not reach Al-layer. So Al and Au layers remained relatively cold during acceleration (entropy increasing only due to shock wave and corona x-ray preheat). During laser action on a foil the lighter layer (Al) pushed the heavier layer (Au), so conditions for Rayley-Taylor instability and turbulent mixing realized. We registered the Al line and Au continuum emission from the rear side using x-ray streak-camera. The emission appeared due to heating of the rear side by the probe beams. We chose the conditions in such manner that heating wave could not reach Al layer in the unmixed area against the control beam.

We used random phase plate for beam smoothing. Roughness of Al-Au boundary was less then 0.05 μm, surface roughness of Si layer was (0.1-0.3) μm. Example of x-ray spectrum evolution (near ~1.5 keV) one can possible to see in Fig.1.a for Au layer thickness 0.16 μm. We observed in this case Al line emission
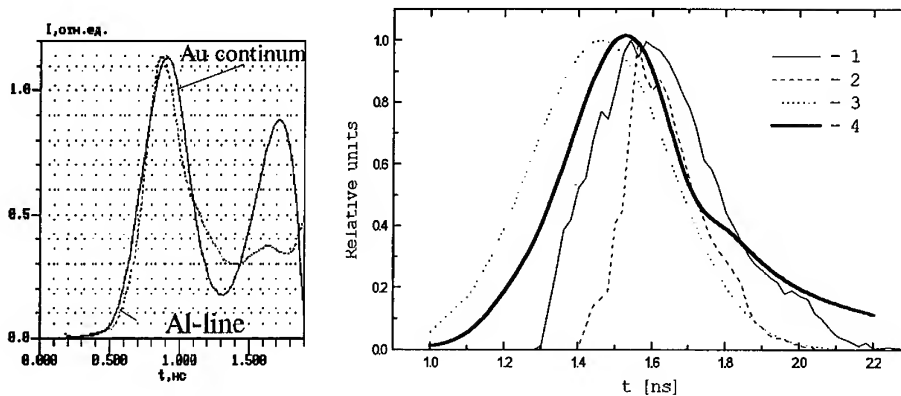
Fig.1. a) Au and Al x-ray from   b) Calculation time dependencies: HeaAl-lines emission rear side
        intensities vs time   of the target on different Au layer thickness (1 - DxAu=0.15 mm; 2-
                                            DxAu=0.3 mm), diagnostic laser pulse - 3, x-ray Au continum - 4

only from diagnostic spot (not from control one).

We could compare the experimental results with SND calculations [6]. For mixing calculations we used highly sophisticated Nikiforov model [7]. The results of calculations for Au layer thicknesses 0.15 μm and 0.3 μm are shown on the Fig.1b. For thin Au layer the time delay of line emission is $\cong$ 50 ps. This value is less than streak camera time resolution in these experiments ($\cong$190 ps). So we obtained qualitative agreement between experiment and calculation. More accurate analysis is now under progress.

3.   Characterization of x-rays in ISKRA-5 spherical hohlraums [8]

For ISKRA-5 the main approach is indirect drive which was discussed in our institute from sixties (A.Sakharov, S.Kormer, N.Popov et al). In this scheme 12 laser beams are injected into the case (hohlraum) through holes. We used mainly spherical hohlraums of (1.3-4) mm diameter with six holes (0.4-0.6) mm in diameter. (See [2] and ref. there). When we placed small spherical capsule in the center of hohlraum we could obtain up to $\cong 10^{10}$ DT neutrons. The DT ion temperature was up to $\cong$3 keV, the velocity of glass shell achieved $3 \cdot 10^7$ cm/s (but with rather high level of entropy). This type of implosions is in a good agreement with 1 D SND calculations. This is due to high level of radiation uniformity. High uniformity is due to the fact that the ratio of hohlraum diameter to capsule diameter is $\cong$7, so all harmonics of irradiation nonuniformity with mode number more than 4 are strongly suppressed. For our relatively long wavelength (1.315 μm) and conditions in hohlraums (for D=2 mm laser beam intensity on the inner surface under the first strike is $3 \cdot 10^{14}$ W/cm^2) absorption of each beam under the first strike

28

is relatively small ($\cong 0.3$), so we obtained the nonzero laser intensity in each point of surface. The level of nonuniformity can be estimated using a simple model. In this model the x-ray emission region is divided into two subregions: hot nonequlibrium laser corona and relatively cold ($\cong(150-200)$ eV) x-ray corona. The emission of laser corona is proportional to the nonuniform absorbed intensity. The temperature of x-ray corona is constant over the inner surface of hohlraum. The results of calculations are presented on the Fig.2.

For accurate calculations of capsule performance it's necessary to know the spectrum of x-rays irradiating a capsule with DT. We performed a series of experiments to investigate

Table 1. Resolution harmonic amplitudes of normal distribution $\overline{I_x}(\theta,\phi)$

j	1	2	3	4	5
at equal channels laser energy	1.3e-4	1.2e-2	1.0e-2	6.0e-3	1.2e-3
channel laser energy imbalance ±10%	4.2e-3	1.8e-2	1.2e-2	6.1e-3	1.2e-3
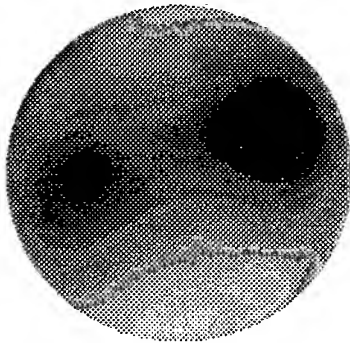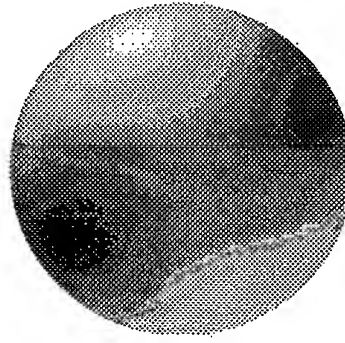
a)   b)

Fig. 2.   X-ray irradiation structure of the central DT capsule obtained in calculation with laser beam channels energy imbalance ±10% at nonuniformity e_{max}=4.7%, $e_{r.m.s.}$=2.3% : a - the front target surface, b - the rear one

this issue. In these experiments we changed the diameters of hohlraums and holes [8]. We measured the x-ray spectrum and compared the relative changes in the spectral emissivity from holes with SND calculations. We could see that SND with average ion model for opacity calculations could reproduce main peculiarities of experimental spectra, but additional experimental and theoretical efforts are necessary for resolving some discrepancies.

4. Fast ion generation [9]

Essential problem for 1 μm wavelength lasers is the generation of hot electrons. Detrimental influence of hot electrons was investigated in many papers. We could estimate the role of hot electrons in the experiments with varying atomic number of material Z on the inner surface of hohlraum (Au, Cd, Cu, Mg). All other conditions were the same for all experiments. We measured x-ray spectrum, neutron yield and other characteristics. When we compared the experimental and calculational x-ray spectrum with different Z hohlraums we could see the similar behavior of these data. But neutron yield for middle Z (Mg) in calculations was less as compared to experimental one. After analyzing these and other data we arrived to conclusion: important part in the energy transfer to the capsule belongs to the fast ions with velocity $\cong (3\text{-}10)\cdot 10^8$ cm/s. We added to SND code semifenomenological model of fast ion generation based on two-temperature rarefaction wave. We calibrated model parameters for the Mg coating case and then calculated the neutron yield for other Z. Tentative conclusion is that in high Z case the influence of fast ions is relatively small (for hohlraum diameter 2 mm, capsule diameter 0.28 μm, pulse duration 0.3 ns, energy ~9 kJ) but for Z and middle this mechanism becomes very substantial.

References

1. A.V.Bessarab et al. Investigations of laser fusion on high power photodissociation iodine lasers ISKRA, in: Physics of high power laser matter interactions, Ed. S.Nakai, G.Miley, World Scientific (1992).
2. G.G.Kochemasov. Laser Fusion Investigations on high power iodine lasers ISKRA, Inst. Phys. Conf. Ser.№140 Section 2, Paper presented at Laser Interact with Matter Conf., Oxford, 19-23 September (1994).
3. V.A.Andronov, S.A.Bel'kov, A.V.Bessarab et al., Turbulent mix investigations of thin multilayers foils under ISKRA-4 laser acceleration, Presented to XXIII Zvenigorod Conference on Plasma Physics and CTF, 19-23 February (1996), Zvenigorod (See also PT-29, 24th ECLIM).
4. A.Raven et al. Phys.Rev.Lett., 47, 1049 (1981).
5. P.A.Holstein et al. Cr.Acad. Sci.Paris, 307, p.211 (1988).
6. S.A.Bel'kov et al, Voprosy atomnoij nauki I techniki Ser.Matematicheskoe modelirovanie fizicheskich processov, vyp.1, 76 (1990).
7. V.A.Andronov et al, Voprosy atomnoj nauki I techniki: Matematicheskoe modelirovanie physicheskich processov, 2, 59, 1994.
8. S.A.Bel'kov, A.V.Bessarab, V.A.Gaydash et al., X-ray generation inside gold spherical hohlraums: ISKRA-5 experimental results and similation, to be presented at 24 ECLIM (PM-66).
9. S.A.Bel'kov, A.V.Bessarab, V.A.Gaydash et al, Analysis of experiments on ISKRA-5 facility with hohlraum covered by materials with different Z, to be presented at 24 ECLIM (H3-5).

LOS ALAMOS HYDRODYNAMIC EXPERIMENTS ON NOVA

R. E. CHRIEN, CRIS W. BARNES, J. B. BECK,
N. M. HOFFMAN, W. W. HSING, G. R. MAGELSSEN,
G. T. SCHAPPERT, D. P. SMITHERMAN
Los Alamos National Laboratory,
MS E526, Los Alamos, NM 87545 USA

Abstract

We are performing experiments to study hydrodynamic perturbation growth in x-ray driven targets to test models used to analyze the stability of ignition targets. We use cylindrical implosions to directly image perturbation growth and "feed-through" to the inner surface in convergent geometry. The implosion trajectories and azimuthal structure of inner and outer marker layers on the cylinder are measured by axial radiography. Perturbation growth of 25 at a convergence ratio of two has been measured on the inner layer, in addition to the effects of hohlraum drive asymmetries, nonlinear mode saturation, mode coupling, and the deceleration phase of the implosion. In other experiments, we are studying the planar analog of instability coupling between the inner surface of a cryogenic ignition capsule and the ablation surface. This instability coupling mechanism provides an important seed for perturbation growth in ignition capsule implosions.

1. Introduction

The Los Alamos inertial confinement fusion (ICF) program is performing experiments to test computational models used to analyze the stability of x-ray-driven capsule implosions, such as capsules for the proposed National Ignition Facility (NIF). The leading capsule design for reaching ignition and moderate gain is cryogenic with a solid deuterium-tritium (DT) shell surrounding a central DT gas region, and surrounded by a plastic ablator [1,2] By carefully controlling the radiation temperature in the hohlraum, the central gas region is heated and compressed to ignition conditions of areal density $\rho R \sim 0.3$ g/cm^2 and ion temperature ~ 10 keV. The fusion burn in the central "hot-spot" then propagates into the colder DT shell, which constitutes the main fuel. Hydrodynamic instabilities, which amplify perturbations at the interface between the hot-spot and the main fuel, pose a major threat to hot-spot ignition by increasing thermal conduction losses from the hot-spot and by reducing the compressional heating and compressed density of the fuel. Computational models [2,3,4] suggest that

NIF capsules will fail to ignite if perturbation amplitude at the gas-fuel interface exceeds $\sim$ 1/3 of the hot-spot radius. Through experiments on the Nova laser at Livermore, we are testing the accuracy of these computational models to predict the most important initial perturbations in the capsule, the growth and nonlinear evolution of hydrodynamic instabilities, and the radial transport of
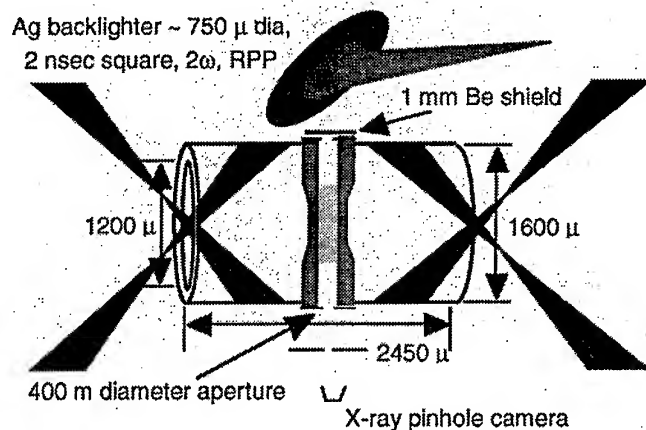
Figure 1.- Experimental configuration for x-ray-driven cylinder implosions. An x-ray backlighter and gated x-ray pinhole camera are used to image the cylinder as it implodes. The cylinder is filled with low-density plastic foam to observe deceleration. The ablator layer is monobromostyrene to increase instability growth and minimize preheat. End effects are reduced by tapering the radial thickness of the cylinder. Parallax effects are avoided by using a short dichlorostyrene radiographic marker layer near the center of the cylinder.

perturbations between different interfaces in the capsule.

2. Cylinder Implosions

Perturbation growth and transport in convergent geometry can be directly observed with cylinder implosions (Fig. 1). This experiment is complementary to planar Rayleigh-Taylor instability measurements,[5] which lack convergent effects, and spherical capsule implosions,[6] in which the perturbation growth on the inner surface is diagnostically inaccessible. An azimuthal perturbation is machined on the outer surface of the cylinder during fabrication. The sequence of gated images (Fig. 2) shows the radial implosion of the marker layer on the inner surface of the cylinder and the appearance of the $m = 10$ perturbation at this surface. Thus the effects of Rayleigh-Taylor instability at the ablation

surface and perturbation transport to the inner surface ("feed-in") are directly observed. Perturbation amplitudes (after feed-in) as high as 25 times the initial amplitude at the outer surface have been observed, well into the nonlinear phase of the instability. Many other effects have been seen, including a P_4 radiation drive asymmetry, mode coupling between the imposed perturbation and drive asymmetry, self-emission from shock convergence on axis, and cylinder stagnation and re-expansion

$t_o + 2.20$ nsec $t_o + 2.26$ nsec $t_o + 2.32$ nsec $t_o + 2.38$ nsec $t_o + 2.45$ nsec $t_o + 2.51$ nsec

$t_o + 2.57$ nsec $t_o + 2.63$ nsec $t_o + 2.70$ nsec $t_o + 2.76$ nsec $t_o + 2.82$ nsec $t_o + 2.88$ nsec
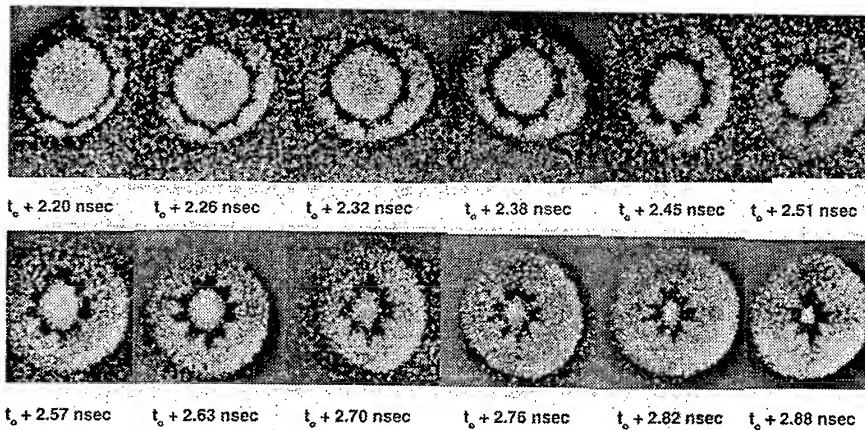
Figure 2.- A sequence of gated pinhole camera images of a cylinder implosion. The dark inner ring is the marker layer. The perturbations are the result of Rayleigh-Taylor instability growth at the ablation surface and perturbation transport to the inner surface of the cylinder.

The implosion trajectories of the ablator and marker layers, in the absence of imposed perturbations, provide a sensitive test of the opacities, equations-of-state, and radiation drive used in the simulations. Experiments are currently in progress to measure the dependence of growth rate and nonlinear saturation on mode number for initially sinusoidal perturbations.

3. Instability Coupling Experiments

Computational modeling[3] suggests that a dangerous seed for instability growth in NIF capsules is the inner surface roughness on the DT ice. It is believed that the first shock to reach this perturbed interface develops a Richtmyer-Meshkov instability. The flow field of this instability transports the perturbation to the ablation surface, where it grows due to the ablative Rayleigh-Taylor instability. The perturbation later couples to the inner surface and grows further during deceleration. For NIF capsules with a plastic ablator, ignition is pre-

dicted to fail for DT ice roughness of $\sim 2\mu$m rms, only 2–3 times greater than the best fabrication capability. Capsules with a beryllium ablator are predicted to be less sensitive to DT ice roughness.[3]

We are performing experiments to test our modeling of instability coupling phenomena. These experiments are very similar to planar Rayleigh-Taylor instability studies,[5] except that the initial perturbation is on the side of the planar package *away* from the x-ray drive. For the first experiments, we used an aluminum ablator to minimize preheat effects. The perturbation was carried by the aluminum or by a thin beryllium layer deposited on the aluminum. The perturbed areal densities were measured by face-on radiography using a 6.7-keV Fe backlighter (Fig. 3). The perturbations are observed to reverse phase, as expected, and are in qualitative agreement with the simulations. In subsequent experiments, we plan to vary the materials to better understand the apparent differences between NIF capsule ablators.
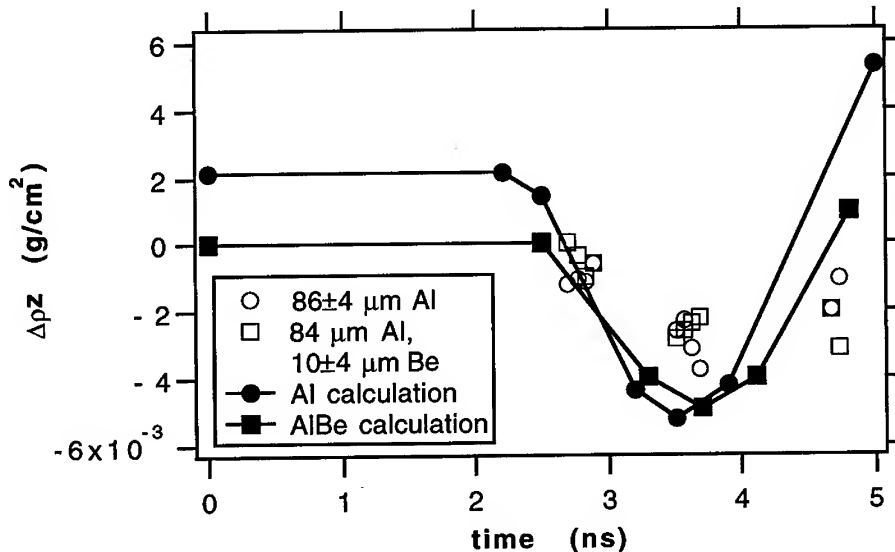
Figure 3.- Measurements and simulations of $\Delta\rho z$ for 50-μm wavelength, 4-μm amplitude initial perturbations on the cold side of an x-ray-driven planar aluminum sample.

1. J. D. Lindl, *Phys. Plasmas* **2**, 3933, (1995).

2. S. W. Haan, et al., *Phys. Plasmas*, **2**, 2480 (1995).

3. W. J. Krauser, et al., *Phys. Plasmas*, **3**, 2084 (1996).

4. N. M. Hoffman, et al., these proceedings.

5. B. A. Remington, et al., *Phys. Fluids*, **5**, 2589 (1993).

6. O. L. Landen, et al., *JQSRT* **54**, 245 (1995).

SIMULATIONS OF SHOCK WAVES PROPAGATION EXPERIMENTS

J.J. HONRUBIA
Instituto de Fusión Nuclear, Universidad Politécnica de Madrid, Spain

R. DEZULIAN, D. BATANI, S. BOSSI
Universitá degli Studi di Milano, Italy

M. KOENIG, A. BENUZZI
LULI, Ecole Polytechnique, France

N. GRANDJOUAN
LPMI, Ecole Polytechnique, France

We have analysed the shock wave propagation experiments performed at LULI and presented at last ECLIM. The targets were aluminium foils with thickness from 5 μm to 25 μm. Simulations were performed with the SARA-1D multigroup radiation code. We have shown a small level of preheating caused by the absorption of x-rays with energies close to the K-edge of aluminium. Several sets of opacities were used to study this effect, including experimental values for cold aluminium. Simulations show a small level of visible emission induced by x-ray preheating before the arrival of the shock.

1. Introduction

Very recently, several shock waves propagation experiments have been done at LULI [1,2] and MPQ [2] by using both direct-drive and indirect-drive schemes. The advantages of the indirect-drive scheme are the uniformity of the illumination and the small importance of preheating effects. The direct-drive scheme has two difficulties related with (1) uniformity of the shock, and (2) the preheating of the foil before the arrival of the shock. However, this scheme has the advantage of the better coupling efficiency than the indirect drive and hence the possibility of creating more intense shocks. The problem of uniformity has been greatly improved by smoothing the laser beams with PZP plates, which produce planar, almost one-dimensional, shock waves [3]. The problem of preheating by high frequency photons produced in the corona region should be studied in order to be sure that the thermodynamic data obtained in experiments are consistent with the density and temperature conditions assumed for the foil. We have analysed the preheating effect in the shock experiments presented at last ECLIM [4] by using the SARA-1D multigroup radiation code [5] and several sets of opacities.

2. Experimental set-up

Three synchronised beams of the second harmonic of neodymium laser directed to a focal spot with a diameter of 400 μm was used. The laser pulse was defined by a maximum intensity close to 10^{14} W/cm^2, and a Gaussian shape with FWHM= 600 ps. The total energy in the target was, roughly, 100 J. The targets were aluminium foils with thickness between 5 and 25 μm. As main diagnostic, an objective coupled to a streak camera imaged the rear side of the foil. Its emission was recorded in the visible range (1-3 eV).

3. Simulation model

The SARA-1D code includes non-LTE multigroup radiation transport coupled with two-temperature hydrodynamic, laser energy deposition by ray-tracing, and SESAME equation of state. Radiation equations take into account the angular dependence of the radiation field by means of the S_n approximation [5].

The opacities and emissivities are computed in line from the populations obtained from a non-LTE average atom (AA) model, in which energy levels depend on the principal quantum number. The line profile is Gaussian with a phenomenological linewidth obtained by comparison with more detailed models [6].

The SARA-1D and the non-LTE opacities used in simulations have been tested with the results presented by Duston et al. [7] about the illumination of an aluminium foil of 8 μm by a Gaussian laser pulse with λ=1.06 μm, 10^{13} W/cm^2, and FWHM=3 ns. A good agreement between both codes was shown.

4. Opacities for cold aluminium

The non-LTE opacities mentioned in last paragraph are used only for the corona region. For the zones of cold aluminium (T<100 eV), two additional set of opacities can be used. The first one is an AA-LTE model with n,l splitting and hydrogenic energy levels and oscillator strengths [6]. The second set has been generated with the SNOP [8] code for high densities and low temperatures ($\geq$1 eV). The comparison between these two opacity sets, the opacities generated with the AA non-LTE (AA-nLTE) model used in the corona, and the experimental opacities reported by Palik [9] is shown in Fig.1 for aluminium at solid density. In this figure, the curves of the opacities obtained from numerical models correspond to 1 eV, and the Palik's opacities corresponds to room temperature. It is worth noting that the SNOP opacity is closer to the Palik's opacity than the AA-LTE and AA-nLTE opacities. This can also be shown by comparing the transmission coefficients for a 25μm foil depicted in Fig. 2, in which we can note that the AA-nLTE and the AA-LTE opacities give higher and lower transmission, respectively, than the Palik's opacities in the energy range close to the K-edge, which is the major responsible of the preheating of the cold aluminium. Then, we have used the SNOP opacities as the reference case to study the preheating effect, and the other two models to see the influence of the opacity model on results. We can see in Fig. 2 that photons coming from the corona with energies higher than 800 eV can go through the foil contributing to the preheating.

5. Results

The influence of radiation transport on the shock arrival time, and the comparison of this time between simulation and experiments are shown in Fig. 3 for different thickness. The arrival times are measured relative to the time at which the pulse reaches the maximum intensity. We can see a good agreement between simulation and experiments and a small influence of radiation transport on arrival times. The difference between arrival times with and without radiation transport is small, but

systematic, increasing slightly with thickness. Then, radiation transport does not affect appreciably the dynamic of the shock. Accordingly, the influence of the opacities used for cold aluminium on arrival times is small, as shown by simulations.

Results indicate that preheating is produced by photons close to the K-edge of aluminium (0.8 - 1.5 keV), and also, to a lesser extent, by photons with higher energies (3 - 4 keV). This result is consistent with the transmission coefficient shown in Fig. 2. The preheating temperature (temperature just before the arrival of the shock) at the rear side of the foil as a function of the thickness is represented in Fig. 4 for the three opacity sets considered for cold aluminium. For thin foils (5 μm), the preheating temperature is lower because the shock arrives earlier and the aluminium has less time to be heated by the photons produced at the corona. For thick foils (25 μm), this temperature decreases again because the spatial attenuation of these photons is more important than longer preheating time. For all the thickness analysed, preheating temperatures go from 0.30 to 0.92 eV, depending on the opacity model used. For the reference case with SNOP opacities, the maximum temperature is, roughly, 0.7 eV. Then, we conclude that the preheating of the cold aluminium before the arrival of the shock wave effectively occurs, increasing slightly the temperature of the foil up to temperatures, at most, of 1 eV. Because of this modest preheating, the zones of the foil close to the rear side slightly expands, inducing a very small delay in the optical emission registered by the streak camera when compared with the case in which no preheating takes place. A measure of this effect can be shown in Fig. 3 by comparing the cases with and without radiation transport.

6. Conclusions
In the simulations carried out, we have seen a significant level of preheating mainly due to photons with energies from 0.8 to 1.5 keV, which are weakly absorbed along the aluminium foil. The preheating temperature of the rear side is between 0.3 and 1 eV, depending on the opacity model used in simulations. This temperature is small enough to have a little influence on shock arrival times. Consequently, the experimental detection of the preheating should be done by analysing the optical signal recorded by the streak camera, and, in particular, by looking at the optical emission previous to the arrival of the shock. We have introduced in simulations the sensitivity of the streak camera as a function of frequency in order to reproduce the signal recorded by the CCD. Results show that the signal of preheating is 3 or 4 order of magnitude under the maximum induced by the shock due to the low sensitivity of the streak for long wavelengths, in such a manner that this signal lies below the detection threshold. New experiments are being designed to measure this effect and to compare with simulations.

References

1. M. Koenig, D. Batani, S. Bossi, M. Temporal, S. Atzeni et al., Phys. Rev. Lett., **74**, 2260 (1995).

2. A. Benuzzi, T. Löwer, M. Koenig, B. Faral, D. Batani, D, Beretta, C. Danson and D. Pepler, Phys. Rev. E, **52**, 2162 (1996).

3. M. Koenig, D. Batani, A. Benuzzi, S. Bossi et al., Phys. Rev. E, **50**, R3314 (1994).

4. M. Koenig, J.M. Boudenne, B. Faral, D. Batani, S. Bossi, A. Benuzzi, S. Atzeni, and M. Temporal, *High Pressure Shock Generation and Propagation in Optically Smoothed Laser-Plasmas*, proceedings of the 23rd ECLIM, Oxford 19th-23rd September, 1994.

5. J.J. Honrubia, J. Quant. Spec. Radiat. Transfer, **49**, 5 (1993).

6. J.J. Honrubia, the average atom LTE (1991) and non-LTE (1993) opacity codes are unpublished. The last one is based in the code CARMEN developed by E. Minguez.

7. D. Duston et al., Phys. Rev. A, **27**, 3 (1983).

8. K. Eidmann, Laser and Particle Beams **12**, 223 (1994).

9. E.D. Palik, Handbook of Optical Constants of Solids, Academic Press (1991).
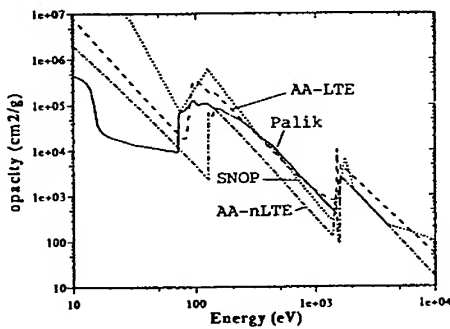
Fig.1- Opacities used for cold aluminium (0.025 eV) at solid density.
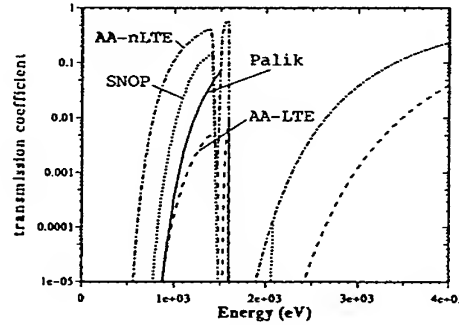
Fig.2- Transmission coeficient of a 25 micron Al foil at solid density and room temperature.
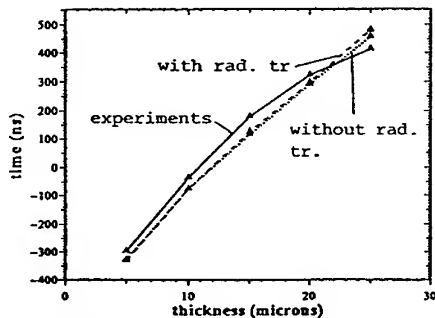
Fig.3- Shock arrival time at the rear side as function of foil thickness.
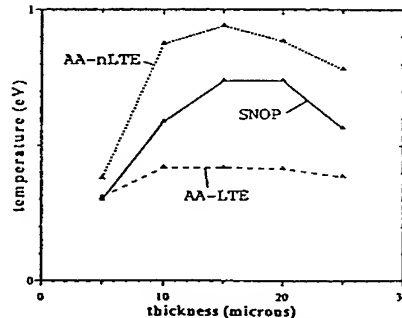
Fig.4- Preheating temperature of the rear side as a function of the foil thickness for different opacity models.

MEASUREMENT OF ELECTRON DENSITY AND LATERAL EXPANSION IN THE COLLISION OF COUNTERSTREAMING LASER-PRODUCED PLASMAS

C. CHENAIS-POPOVICS , F. GILLERON, J.C. GAUTHIER,
Laboratoire pour l'Utilisation des Lasers Intenses, École Polytechnique,
91128 Palaiseau Cedex France

P. SONDHAUß , M. DIRKSMÖLLER , I. USCHMANN , E. FÖRSTER ,
Max-Planck-Arbeitsgruppe "Röntgenoptik", Friedrich-Schiller Universität,
Max-Wien-Platz 1, D07743 Jena, Germany

O. LARROCHE , O. PEYRUSSE
Centre d'Etudes de Limeil-Valenton,
94195 Villeneuve-Saint-Georges Cedex France

As a complement of the study of the collision of laser-exploded thin Al foils where interpenetration as well as electron and ion temperature were measured, electron density and lateral expansion have been determined by X-ray spectroscopy. A new toroidally bent crystal spectrograph with one dimension space resolution recorded the H-like Lyα dielectronic satellites and gave a density in the range 10^{21}-10^{22} cm^{-3}. A flat crystal spectrograph recording the XUV emission in the 4 - 5 nm range provided the lateral dimension of the Al^{8+} to Al^{11+} ions emission.

1. Introduction

The goal of this work was to provide the electron density and the lateral dimensions of the collision of two counter-streaming plasmas created on thin aluminium foils. The measurements of ion and electron temperature obtained from the Doppler boadening of the Al Heβ line were relying on indirect or partial measurements of these parameters.[1] Their direct measurement was important to confirm the non negligible correction factors introduced by Stark broadening which depends on the electron density and reabsorption broadening relying on the lateral size of the plasma.

2. Experimental setup

Two opposite beams of the LULI facility laser ($\lambda = 0.53$ μm, $\tau = 600$ ps) were irradiating 0.8 μm thick Al foils. The exploding foils were colliding in the center of the intertarget space. The distance between the foils was varied between 450 and 1400 μm and the laser intensity from 4 to 6 x 10^{13} W/cm^2 to change the conditions of interpenetration of the plasmas. The beams were focused with f/2.5 lenses and random phase plates to a diameter of 200 μm. Figure 1a shows the geometry of the experiment for which two new spectrographs were mounted.

A quartz (1 0 $\bar{1}$ 0) crystal was toroidally bent to obtain a very high spectral resolution in the range 0.7 nm (theoretical and measured resolving power of 8000 and 7000 respectively) and a high spatial resolution in the transverse direction (5 μm theoretically) which was set parallel to the intertarget axis. The source was set outside the Rowland circle and a film on the Rowland circle as shown in figure 1b. The source was imaged with magnification 0.4 leading to a spatial resolution of 12 μm limited by the densitometer slit. This spectrograph was recording the dielectronic satellites of

the H-like Al 1s-2p (Lyα) line at 0.7 nm, and the electron density was deduced from the satellite line ratios. Although the detector was integrating over time, the density was measured only during the collision due to the short emission time of the Lyα line and its satellites, evaluated around 150 ps from the measurement of the duration of the Heβ line emission .[1]

A flat OHM crystal (Octadecil Hydrogen Maleate) with a large inter-reticular distance (2d=6.33 nm) was space-resolving the XUV emission of the plasma in the range 4 - 5 nm (250 to 310 eV) to measure the size of the emitting region along the foils surface, i.e. across the intertarget axis. The space resolution was limited to 37 μm by the entrance slit. A resolving power of 400 was measured in the range 4.6 - 4.9 nm, to be compared to a calculated resolving power of 1000.[2] The time-integrating detector was a 512*512 back thinned CCD camera filtered with 0.3 μm of aluminium. In spite of a poor homogeneity of the reflection coefficient of this type of organic crystal, Al^{8+} to Al^{11+} lines have been identified.
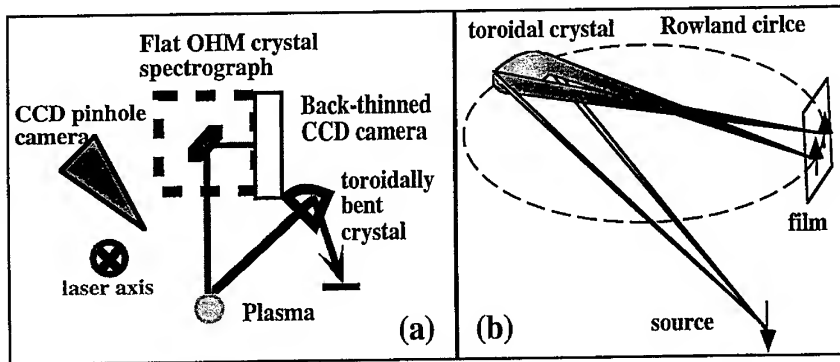
Figure 1 : Experimental setup and mounting of the toroidally bent crystal

3. Electron density measurement

In the range 5 x 10^{20} - 10^{22} cm^{-3}, the ratios of the dielectronic satellites vary with the density. We measured the isolated lines 2p^2 ^{1}D-1s2p ^{1}P and 2s2p ^{1}P$_1$-1s2s ^{1}S$_0$, called hereunder 1 and 3, and the clusters of lines 2p^2 ^{3}P$_{1,2}$-1s2p ^{3}P$_{0,1,2}$ and 2s2p ^{3}P$_{0,1,2}$-1s2s ^{3}S$_1$, called respectively 2a and 2b. The ratios of the integrated lines are compared to the collisional-radiative (CR) model TRANSPEC[3] to get the electron density, the electron temperature being fixed to 800 eV from the previous experimental measurements.[1] As the satellite lines are emitted at high temperature, their emission lasts only around 100 ps. With the CR code FLY[4], we have determined the sensitivity of the measurement on the non-stationarity and on electron temperature. For a density over 2 x 10^{21} cm^{-3}, non-stationary effects are negligible. The variation with the electron temperature between 700 and 1000 eV is of the order of a few percent, lower than the experimental uncertainty. Reabsorption of the

resonance lines and also of the satellite lines could not been neglected as the plasma collision dimension is over 100 μm. So we used a stationary version of TRANSPEC including resonance lines and satellite lines reabsorption to deduce the electron density from the line ratios.

The experimental spectrum has been fitted with four gaussian profiles corresponding to lines 1, 2a, 2b, and 3, and a density value was deduced from each ratio (1/2a, 2a/2b et 3/2a). The electron density is an average of the values obtained from the different line ratios. Figure 2 shows the electron density as a function of the intertarget distance for two different laser intensities 4 and 6 x 10^{13} W/cm^2. The density is in the range 10^{21} - 10^{22} cm^{-3} and decreases slightly with the intertarget distance. The density is also sligthly higher for lower laser intensity. Figure 2 shows also the maximum density in the collision calculated with the eulerian multifluid code MULTIF.[5] The order of magnitude is well reproduced. The code gives a more pronounced variation in function of the intertarget distance than the experimental results. This is probably due to the time-integration of the experimental data.
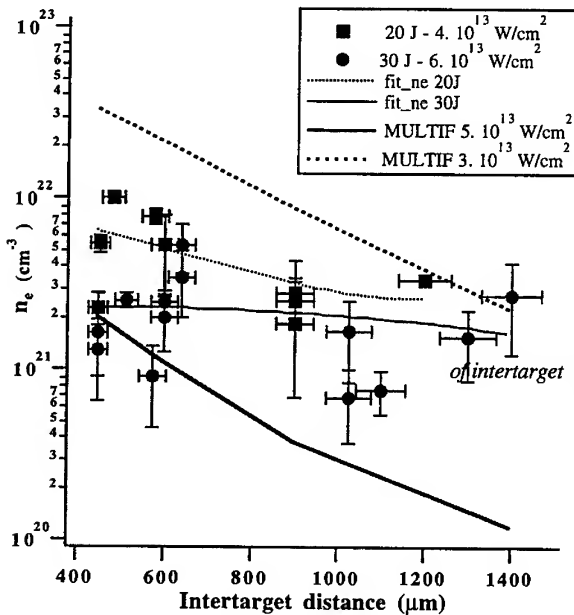
Figure 2 :
Electron density as a function of intertarget distance. Points and thin lines : experiment and polynomial fit ; thick line : MULTIF code .

The variation of the satellite emission as a function of the position along the intertarget axis has been measured in the collision thanks to the 10 μm spatial resolution of the toroidal crystal spectrograph. This has evidenced that the emission is much less localized in the case of large intertarget distance and high laser intensity. This confirms that the collision region spreads more along the intertarget axis when the colliding plasmas interpenetrate each other.

4. Mesurement of the lateral expansion of the collision

The lineouts of figure 3 show the lateral expansion of the emission of aluminium B-like to He-like ions (Al^{8+} à Al^{11+}) measured with the OHM crystal spectrograph. The most ionized species which are emitted during the collision are confined to a 200-300 µm distance. The B-like ions which are emitted in the recombining phase after the collision extend on a larger distance of 900 µm. This measurement confirms the dimensions observed previously on pinhole images and with the monochromatic imaging of the Al Heβ emission.
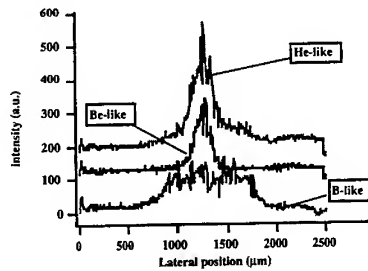
Figure 3 : Lineouts showing the lateral dimension of the emission of different ion species as measured with the OHM crystal spectrograph.

5. Conclusion

The collision of two counter-streaming plasmas is now well understood, in particular the transfer of kinetic to thermal energy and the onset of interpenetration. The comparison of the multispecies code MULTIF with the experiment has given major improvements and this code can be used now for the analysis of the collision of plasmas produced at the front of laser-irradiated targets in conditions closer to ICF conditions.[6]

Acknowledgements

[1] O. Rancu et al, Phys. Rev. Letters 75, 3854 (1995) ;
[2] R. Barnsley et al, Proc. 10th Int. Col. UVX Spectr. Lab. Plasmas, Berkeley, 1992, Cambridge Univ. Press.
[3] O. Peyrusse, Phys. Fluids B4, 2007.
[4]R.W. Lee, B.L. Whitten and R.E. Strout, J. Quant. Spect. Radiat. Transf., 32, 91 (1985).
[5] O. Larroche, Rapport LV/DET/SPI N° DO 571/96, Mars 1996 ; O. Rancu et al, to Phys. Plasmas
[6] P. Renaudin et al, unpublished CEA/CEL-V internal report (1995).

ELECTRON DENSITY MEASUREMENT OF A COLLIDING PLASMA USING SOFT X-RAY LASER INTERFEROMETRY

A. S. WAN, C. A. BACK, T. W. BARBEE, JR, R. CAUBLE, P. CELLIERS,
L. B. DASILVA, S. GLENZER, J. C. MORENO, P. W. RAMBO, G. F. STONE,
J. E. TREBES and F. WEBER

Lawrence Livermore National Laboratory, P. O. Box 808, Livermore CA 94550

We have employed a soft x-ray interferometer, using a Ne-like Y x-ray laser at 155 Å as the probe source, to study interpenetration and stagnation of two colliding laser-produced plasmas. We observed a peaked density profile at the symmetry axis with a wide stagnation region with width of order 100 μm. We compare the measured density profile with density profiles calculated by a fluid radiation hydrodynamic code and a multi-specie fluid code which allows for interpenetration. The measured density profile falls in between the calculated. Using different target materials and irradiation configurations, we can vary the collisionality of the plasma. We hope to use x-ray laser interferometry as a mechanism to validate and benchmark our numerical codes used for the design and analysis of high-energy-density experiments.

1. Introduction

The understanding of the collision and subsequent interaction of counter-streaming high-density plasmas is important for the design of ICF hohlraums.[1] In a typical indirectly-driven vacuum hohlraum, the interaction of the optical laser drive with high-Z inner surfaces generates counter-streaming plasmas which flow unimpeded and collide on the axis of cylindrically-shaped hohlraums. Single-fluid radiation hydrodynamics codes that we typically use to design ICF and other laser-plasma experiments, such as LASNEX,[2] do not allow for plasma interpenetration. Without interpenetration, as the plasmas collide and stagnate, their kinetic energy converts to internal energy, resulting in an unphysically large ion temperature that generates strong shocks propagating away from the axis of symmetry. Furthermore, as the plasma stagnates on the hohlraum axis, the single-fluid codes predict the creation of jets of high-velocity and high-density plasmas that stream toward the capsule located at the center of the hohlraum and can destroy the symmetry of the capsule implosion. Current hohlraum designs for Nova[3-5] and the point design for the National Ignition Facility[1,5,6] employ a low-density fill gas to impede the plasma blowoff.

Past experimental studies of colliding plasmas have primarily focused on laser-produced, low-Z front-illuminated thick targets[7-10] and back-illuminated exploding thin foils[11]. Most of the experiments utilize x-ray spectroscopy and imaging techniques to characterize the plasma parameters.

2. Experimental Setup, Results, and Data Analysis

The recent demonstration of soft x-ray interferometry is a significant step in the measurement of 2-D n_e profiles of high-density, fast-evolving, and large scale length laser-produced plasmas,[12] and allows us to examine the dynamics of colliding plasma in ICF-relevant regimes. We operate at 155 Å, using a Ne-like Y x-ray laser (XRL) as the probe source, which allows us to obtain a two order of magnitude reduction in refraction and

absorption. Two Nova laser beams were used, one to generate the XRL and one to produce the target laser plasma.
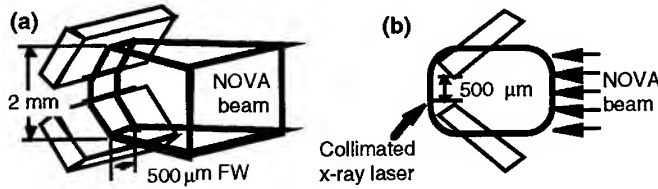
Figure 1: The colliding plasma experimental setup. (a) 3-D view of Nova beam illuminating the 2 Au slabs. (b) side view showing the window of collimated x-ray laser beam which defines the view of the gated detector.

The setup of a colliding plasma experiment is shown in Fig. 1. Two Au slabs are aligned at 45 deg with respect to the symmetry axis. A 500 μm FWHM line-focused laser beam (3×10^{14} W/cm^2 and a 1-ns square pulse) irradiates the slabs, as shown in Fig. 1(a), and generates plasmas blowing toward each other. By varying the geometry, the slab materials, and the intensity of the incident laser, we can change the collisionality of the plasma. At high density and low temperatures, the plasma behaves like a fluid which codes like LASNEX should be able to model accurately. The plasma shifts into a collisionless region with increasing temperature and reduced density where we expect to observe significant plasma interpenetration.

The target was backlit edge-on by the XRL 1.2 ns after the start of the laser pulse. Fig. 1(b) shows this view. In Fig. 2 we show the interferogram of the colliding plasma. Near the symmetry axis of the two slabs we observe significantly large fringe due to the high density of the plasma collision. The visibility is poorer at the right hand edge of the interferogram due to slight mistiming of the gated detector.

At the extreme left and right of the interferogram we can still see the unperturbed fringe pattern where there is no plasma. The beamsplitters were not perfectly flat and that results in one of our experimental uncertainties. We estimate the uncertainty to be of order 0.1 fringe. Another source of the uncertainty is the path length across the target plasma in the direction of the measurement.[13] We assume a uniform plasma with a 500 μm path length, which is the transverse width of the optical laser line focus onto the Au slabs.

One motivation to perform this experiment is to examine the validity of fluid codes in a regime that might deviate from the fluid behavior. Fig. 3 shows a snapshot of a LASNEX-calculated 2-D n_e profile at 1.15 ns. In this calculation we use a multi-group diffusion method to account for radiation. The calculation is symmetric about the horizontal axis.
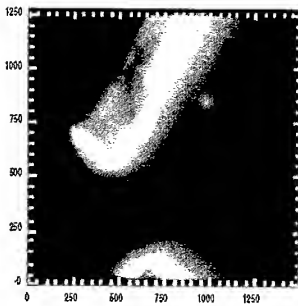
Figure 2: Measured interferogram of the colliding plasma with excellent fringe visibility and strong self emission near the slab surface. Large fringe shifts on-axis is evident due to plasma stagnation.
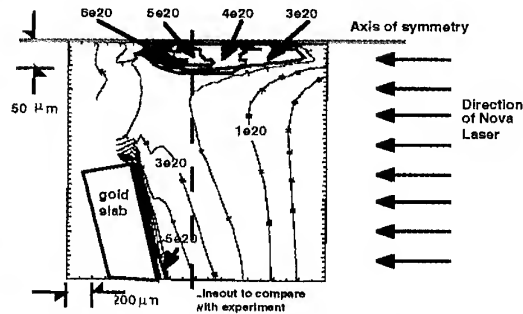
Figure 3: A snapshot of a LASNEX-calculated 2-D n_e profile at a time of 150 ps after optical laser pulse. This time corresponds to the peak of the x-ray laser pulse that served as the gate for our imaging detector used for the experiment.

Neglecting the radiation opacity results in significantly lower plasma temperatures. In the blowoff plasma, T_e is as high as 3 keV. Using the three temperature (T_e, T_i, and T_r, the radiation temperature) approximation, where the radiation is assumed to be optically thin, LASNEX predicts a T_e of order 0.5 keV. The change in the plasma parameters significantly impact the ionization balance and collisionality of the plasma.

As the blowoff plasmas reach the axis, the slowing and stagnation of the counter-streaming single-fluid plasmas results in the conversion of kinetic to internal energy. In this case T_i can reach a unphysically large values exceeding 10^3 keV. The resulting shock waves, whose intensity depends on the collisionality of the plasma, propagate away from the symmetry axis.

Fig. 4 is a plot of 1-D cuts of the measured and calculated 2-D n_e profiles at 250 µm from the slab tip. The position of this line-out is indicated in Fig. 3. We observed a significant density enhancement on-axis due to the collision with the measured n_e (solid line) as high as 6×10^{20} cm^{-3}. The observed stagnation region has a width of order 100 µm. Although LASNEX (dash-dotted line) predicts a comparable stagnation width, the n_e profile peaks at ~ 30 µm off the symmetry axis and is characteristic of the shock heated expansion predicted by LASNEX. In the collisionless n_e will just be the superpositioned density profiles from the two interpenetrating counter-streaming plasmas. The dashed line in Fig. 3 represents a calculated n_e profile of two interpenetrating collisionless plasmas. At the symmetry plane the measured n_e is a factor of 3-4 higher than the n_e value in the collisionless regime. The measured n_e profile falls in between the extrema represented by the two calculated n_e profiles. Incorporating plasma interpenetration in our predictive codes, such as multi-specie fluid codes[14,15] should significantly improve our predictive capability of laser-produced plasmas in a colliding configuration.

3. Summary

We have conducted a set of XRL interferometry experiments to study the collision of
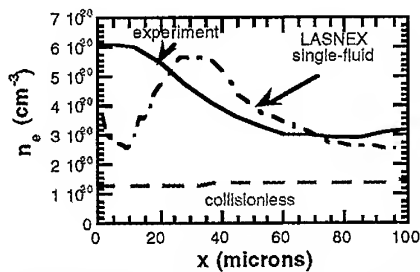
Fig. 4 Comparisons of measured (solid line) and calculated 1-D n_e profiles: LASNEX-calculated single-fluid profile (dashed-dotted line) and profile with a collisionless approximation (dashed line).

high-density, high-temperature plasmas that is of interest to the design of ICF hohlraums. The measured n_e profile peaks at the symmetry plane between the two slabs with a wide stagnation region. The peaked n_e values are a factor of 3-4 larger than the values produced by LASNEX in a collisionless approximation which assumes completely interpenetrating plasmas. Single fluid radiation Lagrangian hydrodynamics codes, such as LASNEX, do not allow for plasma interpenetration and predicts a unphysically large ion temperature and strong shocks propagating from the symmetry plane. The LASNEX-calculated n_e profile, in the signal fluid approximation, shows comparable stagnation width but with n_e profiles peaking off the symmetry plane, which is characteristic of strongly shock-heated, outward propagating plasmas.

Acknowledgments

References

1. S. W. Haan *et al.*, *Phys. Plasmas* **2**, 2480–2487 (1995).
2. G. B. Zimmerman and W. L. Kruer, *Com. Plas. Phys. and Cont. Fusion* **2**, 51 (1975).
3. L. V. Powers *et al.*, *Phys. Plas.* **2**, 2473 (1995); L. V. Powers *et al.*, *Phys. Rev. Lett.* **74**, 2957 (1995).
4. D. H. Kalantar *et al.*, *Phys. Plasmas* **2**, 3161 – 3168 (1995).
5. J. Lindl, *Phys. Plasmas* **2**, 3933 (1995).
6. W. J. Krauser *et al.*, to be published in *Phys. Plasmas*.
7. R. S. Bosch *et al.*, *Phys. Fluids B* **4**, 979 – 987 (1992).
8. R. L. Berger *et al.*, *Phys. Fluids B* **3**, 3 (1991).
9. O. Larroche, *Phys. Fluids B* **5**, 2816 (1993).
10. M. Wilke *et al.*, to appear in "Appl. Laser Plas. Rad. II," SPIE Proc. **2523** (1995).
11. O. Rancu *et al.*, *Phys. Rev. Lett.* **75** 3854-3857 (1995).
12. L. B. Da Silva *et al.*, *Phys. Rev. Lett.* **74**, 3991 (1995).
13. A. S. Wan *et al.*, *J. Optical Society of America B* **13**, 447–453 (1996).
14. P. W. Rambo, J. Denavit, *Phys. Plasmas* **1**, 4050–4060 (1994).
15. P. W. Rambo, R. J. Procassini, *Phys. Plasmas* **2**, 3130–3145 (1995).

INFLUENCE OF THE TARGET ILLUMINATION CHARACTERISTICS ON THE LASER PLASMA EXPANSION INTO A STRONG AXIAL MAGNETIC FIELD

A. KASPERCZUK, R. MIKLASZEWSKI, T. PISARCZYK

Institute of Plasma Physics and Laser Microfusion,
00-908 Warsaw 49, 23 Hery St., Poland

The paper presents results of investigations and the analysis of the behavior of a laser produced plasma in a strong axial magnetic field of the induction 10T. The studied plasma was generated by means of a Nd laser of the energy $5J$ and a pulse duration of about $1ns$. An analysis of the interferometric measurement results allowed to distinguish two characteristic regimes of the plasma expansion: angular and axial. Using 2D MHD computer simulation it was found that these regimes are connected with the character of the target illumination, namely the laser beam spatial intensity distribution in the focal area.

1 Introduction

After careful study of the interferometric data two different regimes of the laser plasma expansion into an external magnetic field were recognized: angular and axial [1]. It was found that plasma expansion into an axial magnetic field as well as a free plasma expansion depends on the laser beam energy distribution in the focus area. Numerical simulation performed using 2D MHD code allowed us to explain these experimentally observed differences in the character of the plasma dynamics.

2 Expansion of the plasma in an axial magnetic field

2.1 Angular expansion

The paper presents results of investigations and analysis performed in an experimental system consisting of a neodymium laser, making it possible to obtain about $10^{14}Wcm^{-2}$ of power density on the target, and a compact one-turn coil for generation of pulse magnetic field of up to $20T$ [1]. The investigations were carried out for the magnetic field lines parallel to the axis of the laser beam illuminating the teflon target. To study the interaction of the laser plasma with the external magnetic field a three-frame interferometry was used [2].

The influence of a magnetic field on the plasma expansion has been investigated for two regimes of the expansion mentioned above. The basic study was carried out for a magnetic field of $B_0 = 10T$. No influence of the magnetic field on the plasma expansion has been found out within the first $5ns$. The dy-

namics as well as spatial distribution of the plasma density were not changed. However, in the comparison with the free expansion essential differences appear after the following $10ns$. The shape of the plasma front changes. A flat front observed in the case $B_0 = 0$ is transformed into a concave one (Fig.1a). It is accompanied
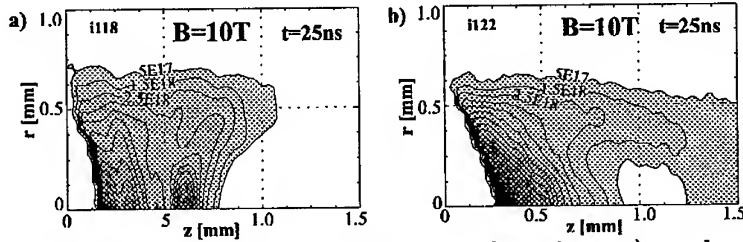
Fig. 1 Isodensitograms of the electron density for the regimes: a) angular and b) axial.

with creation of additional wings of about $0.5mm$ in length in front of the plasma. At the beginning the electron density in these wings does not exceed $10^{18}cm^{-3}$. The axial motion of the bulk plasma is strongly hampered in the central area. The expanding plasma flows around a concave front to the wings leading to significant increase of the plasma concentration in the wings (Fig.1a).

2.2 The axial expansion

Similarly to the case of angular expansion, no differences are observed in the plasma expansion, during the first few nanoseconds as far as the free expansion is concerned. However, after $15ns$ the plasma profile undergoes an essential deformation (Fig.1b). Characteristic wings of low-density plasma appear which are about twice as long as in the case of angular expansion). The central plasma (as in the case of $B_0 = 0$), during the whole time of observation of the phenomenon, has a paraboloidal shape of its front and a maximum electron density about twice higher than in the case of angular expansion, always located on the axis.

3 Numerical modeling of the laser plasma expansion

To understand the behavior of the expanding laser plasma in the external magnetic field a 2D MHD numerical code has been prepared [3]. The code solves a complete set of dissipative MHD equations (two fluid, two temperature) with transport coefficients taken from Braginski [4] completed with the equations describing laser light absorption (via inverse bremsstrahlung).
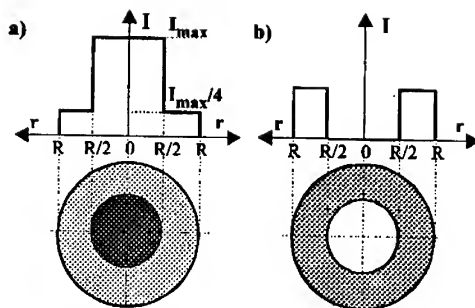
Fig. 2 The spatial distributions of the laser beam intensity in the focal area used in numerical simulations.

The numerical modelling allows us to connect the observed regimes of plasma expansion with the spatial characteristics of the laser beam generating the plasma. We have performed a simulation of the laser plasma expansion into an external magnetic field assuming two different spatial distributions of the laser beam intensity (Fig.2a and b) preserving the total beam energy equal to 5J in 1ns pulse. Unfortunately, we were not able to model the whole processes of laser plasma dynamics in external magnetic field. As it shown in our previous papers [5, 6] the expanding plasma forms an elongated structure with growing longitudinal dimension. Because of limited speed and memory of the computer used (PENTIUM 90) it is not possible to preserve the acceptable accuracy of simulation for such a big area. For the same reason the process of ionization of the target material was not taken into account and it was assumed that the target consists of fully ionized hydrogen. Numerical results presented in the paper are limited to the initial phase of the phenomena (0-1 ns) but nevertheless they allow us to draw some qualitative conclusions explaining the experimentally observed influence of the laser beam intensity distribution on the plasma dynamics.
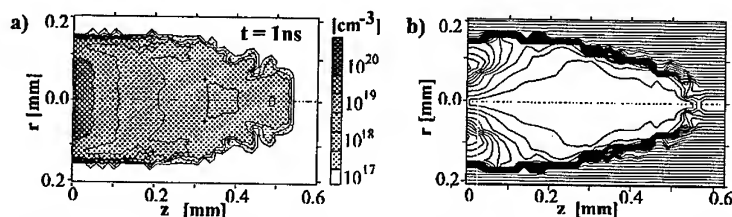
Fig. 3 Results of numerical modeling of the laser plasma expansion into an external magnetic field - angular expansion: a) electron density distribution, b) magnetic field lines. Laser beam intensity distribution as on Fig.2a.

Fig.3 presents the example of results (density distribution and magnetic field lines for t=1ns) obtained for laser beam spatial distributions as on Fig 2a.

From these results one can observe the character of the plasma motion in the magnetic field. The leading part of the hot plasma with $\beta >> 1$ ($\beta =$ plasma pressure/magnetic field pressure) causes the strong distortion of the magnetic field lines. As a result of this process a fieldless cavity is formed and the magnetic field component perpendicular to the axis appears in the area between dense plasma flowing from the target and the cavity. The presence of the perpendicular component of the magnetic field hampers an axial motion of the plasma and a conical plasma flow is observed as a tendency of the plasma to flow around the cavity. The electron density distribution and magnetic field lines presented in Fig.4 was obtained for ring structure of the laser beam (Fig2b). The hot plasma having initially the ring shape expands both inward
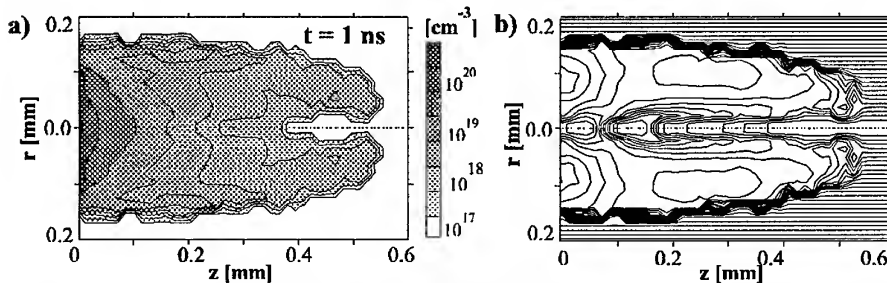
Fig. 4 Results of numerical modeling of the laser plasma expansion into an external magnetic field - axial expansion: a) electron density distribution, b) magnetic field lines. Laser beam intensity distribution as on Fig.2b.

and outward the axis compressing the magnetic field lines on the axis. The fieldless cavity is being formed as well as in the previous case but this time the cavity has ring character. The perpendicular magnetic field in this case is about two times lower than for previous case so its hampering action on the axial flow is much lower. As a result a bulk plasma propagates rather axially although characteristic arms on the plasma density distribution, connected with the flow of the plasma around the cavity is still observed.

4 Conclusions

Numerical simulation performed with the use of the 2D MHD code have shown that the process of mutual interaction of the laser plasma with the magnetic field depends essentially on the character of the target illumination, i.e., the laser-beam intensity distribution in the focal area. Despite of the limitation of the physical model used in the numerical code, the results of simulations gave a qualitative picture of the phenomenon of the laser plasma flow in an axial magnetic field. It was found that the creation of the diamagnetic cavity and the generation of the radial component of the magnetic field during the first few

50

nanoseconds determined the character of the plasma flow observed later, when the plasma pressure is comparable with the magnetic field one. The numerical modeling allowed us to connect the character of the target illumination with the expansion regimes, which can provide a control tool in further efforts aimed at obtaining a plasma structure with desired properties.

References:

[1] A.Kasperczuk and T.Pisarczyk: Physica Scripta vol. 53, (1996), pp.503-507.
[2] T.Pisarczyk at al.: Laser and Particle Beams, vol. 12, No. 3, pp. 549-561,1994.
[3] R.Miklaszewski: Proceedings of the Japan-Central Europe Joint on Workshop Advanced Computing in Engineering, Warsaw 1994, pp.341-344.
[4] S.I.Braginski: "Yavlenija pierenosa v plasmie" in Voprosy Teorii Plasmy, vol.1, Gosatomisdat, Moskva 1963.
[5] Pisarczyk, T. et al., Laser Particle Beams, vol. 10, pp.767 (1992).
[6] Pisarczyk, T. et al., Physica Scripta, vol. 50, pp.72 (1994).

EXPERIMENTAL STUDY INTO THE DYNAMICS
OF PLASMA FORMATION UNDER POWER LASER PULSE
INTERACTION WITH NEAR CRITICAL FOAM MATTER.

S.Yu.GUSKOV, Yu.S.KAS'ANOV[*], M.O.KOSHEVOI, V.B.ROZANOV,
A.A.RUPASOV, A.S.SHIKANOV.

P.N.Lebedev Physical Institute, Moscow, Russia.
[*]*General Physics Institute, Moscow, Russia.*

This work is devoted to an experimental investigation of dynamic processes taking place during the laser beam irradiation of the foam targets made from light elements under the conditions of the electron conductivity thermal wave formation.

1. An interest to the investigation of the laser interaction with low density structured substance is stipulated by an opportunity of heating the plasma up to high temperatures (~1kev) [1,2] with initiation of supersound modes of absorbed energy transport by means of electron or radiation [1,2,3] thermal conductivity processes. The realisation of fast heat transport conditions in plasma is an important point in the solution of the key problem of the inertial fusion: an achievement of homogeneous distribution of absorbed laser energy at the target surface.

2. The experiments on the foam target irradiation have been carried out with "Fenix" laser installation [4]: $\lambda=0.53\mu$m; the pulse duration, $t_L=2.5$ns; the focal spot diameter, $\varnothing\sim15\mu$m; the laser intensity, $I\sim5\cdot10^{14}$W/cm^2. Flat targets with the thickness from 200μm to 800μm, prepared from foam polypropylene (CH)$_x$ with an average density $\rho_a=0.02$gm/cm^3, and cell diameter of $d\sim50\mu$m have been used under normal incidence of the laser beam onto the target surface. The results obtained for the foam matter have been compared to the measurements maid for solid polypropylene targets with the normal density of $\rho_0=1$gm/cm^3.

Typical pin-hole images, obtained under irradiation of the solid a) and foam b),c) targets are presented in Fig. 1. In the case of a solid target a plasma corona with the size of 70-100μm is formed. For the foam matter the plasma is located mainly inside the initial slab borders, and reaches the size of 200-400μm in the direction, perpendicular to the laser beam, and this sufficiently exceeds the diameter of the laser spot. The longitudinal size of the plasma corona, expanding back relatively to the initial border of the foam target, does not exceed ~30μm. Time integrated electron temperature of plasma in both cases, measured by means of absorbers technique, makes ~300-400eV.

The streak camera registration of the plasma selfluminosity region at the wavelength of $\lambda=0.43\pm0.03\mu$m has been carried. The registration angle of 15^0 to the target normal has been used. (Fig. 2). For normal density polypropylene the

diameter of a bright region of plasma at first moment makes about 20μm, and practically corresponds to the laser focal spot diameter. During ~1ns the luminous region increases up to ~100μm, and corresponds to a bright plasma corona arising over the target surface. At 1.5ns the diameter of the bright area begins to decrease, and reaches the size, close to the diameter of the laser spot, and, hereinafter, remains practically constant, and corresponds to the cooling dense plasma located in the crater on the target surface. For the foam polypropylene during the first 1.5ns selfluminosity region size increases from 20μm up to 200μm and remains constant during and after the laser pulse.

The dynamics of plasma formation has been investigated by means of registering the scattered radiation (scattering angles ~90^0 to the axis of the laser beam) in the spectral region near to the laser frequency with spatial and temporal resolution. The streak camera slit was directed along the laser axis. In some of the experiments at a 200μm distance from the rear surface of the target an Al foil has been fixed in order to visualise the moment of the laser radiation penetration through the target. A typical streak picture is presented in Fig.3 (target thickness ~600μm). Strong lateral scattering occurs at the face and the rear surfaces of the target, the intensity of scattering from the internal regions of the slab is notably weaker. Thus, the scattering in the rear surface and Al foil is observed at the beginning of the laser pulse, and is repeated with some time delay, the duration of which changes corresponding to the thickness of the target used.

3. The analysis of the obtained experimental data permits to assume the following scenario of the laser beam interaction with foam matter. The opacity of the foam targets for the laser radiation at initial stage of interaction is, probably, connected with the final duration of the laser pulse front and the existence of plasma formation threshold in polypropylene as well as the availability of weak intensity wings (lower than the threshold of plasma formation) in the aperture of the laser beam. There is one more possible reason for the "opacity" effect in a foam matter with large cell structure ($r_p > r_f$, where r_f -is the focal spot radius, r_p is a cell radius). At the initial stage of interaction the plasma appears in a narrow "absorption channel" with the crossection close to the aperture of the laser beam. As $r_f < r_p$, the primary filling of a cell with plasma takes place up to the density smaller than the average density of the foam. The time t_1, when the plasma density in the laser beam aperture falls to the critical plasma value, may be estimated from the experimental conditions. At the second stage, due to thermal and hydrodynamic energy transport in the lateral direction, the heating and ablation of the cell matter met by the laser beam, takes place, and they are filled in by the plasma with average density of the foam ρ_a during the time t_2. The estimation gives for t_1 and t_2, correspondingly, 0.03ns and 0.2ns. As $t_1 << t_2$, then for given experimental conditions there is possible formation of "the absorption channel" of subrcritical density. Thus, if the condition $\Delta < 2 \cdot r_p \cdot (t_2/t_1) < L$ is true (where Δ-thickness of the target, L-Breamstrahlung absorption length), the target would be transparent for the

laser radiation during: $(\Delta / 2r_p)t_1 \leq t \leq t_2$. The estimation for L and T for the plasma of "the absorption channel" gives: $T \sim 0.5 keV$, $L \sim 1.5 mm$. Then the targets with thicknesses $\Delta < 400\text{-}500\mu m$ could be transparent for the laser radiation at the first nanosecond of the process due to noted mechanism.

At $t \geq t_2$ the plasma density in "the absorption channel" becomes close to an average density of the foam matter, which is greater, than the plasma critical density. The front of the absorption region moves deep into the target body from its face surface with the ablation velocity [5]:

$$\upsilon_{ab} \cong \left(\frac{\rho_{cr}}{\rho_a}\right) \cdot \left[\frac{2(\gamma-1)}{3\gamma-1} \cdot \frac{I}{\rho_{cr}}\right]^{1/3}, t > t_2 \qquad (1)$$

About 1-1.5ns after the beginning of the laser pulse (see Fig.3) the scattering of radiation disappears both from the depth and the surfaces of the foam slab. This confirms that the area of the effective laser radiation scattering is already deep in the target, and is shielded by the plasma of the critical density formed on the "walls" of the channel. The moment of the appearance of the scattering on the back target surface (Fig.3) corresponds to burnthrough time. Basing on a large number of measurements, the value of $(1.5\text{-}3.0) \cdot 10^7 cm/s$ has been obtained for the longitudinal ablation velocity, that corresponds to the mass ablation rate of $(3\text{-}6) \cdot 10^5 gm/cm^2 \cdot s$. The estimation by (1) gives a close result: $\upsilon_{ab} \sim (2\text{-}3) \cdot 10^7 cm/s$.

The energy transfer from "the absorption channel" in the lateral direction is accompanied by volume ablation of the foam matter. This process represents a consecutive evaporation of the wall substance inward the cells with a subsequent transition of the energy of hydrodynamic motion into the thermal one. Thus, due to the thermalization process of the colliding microflows of the matter, the energy of plasma hydrodynamic motion will make a small part of its thermal energy. In a "strong explosion" approximation [6] from indefinitely thin cylindrical source of energy with a variable length $\upsilon_{ab} \cdot t$ for the velocity of lateral volume evaporation wave and for the temperature of plasma at the wave front one can easily to obtain:

$$\upsilon_\perp \cong \left(\frac{3\gamma-1}{\gamma-1}\right)^{1/4} \cdot \left(\upsilon_{ab}\frac{r_f}{t}\frac{\rho_a}{\rho_{cr}}\right)^{1/2}, T \cong \frac{\upsilon_\perp^2}{2B}, t > t_2 \qquad (2)$$

Under discussed experimental conditions the estimation by formula (2) gives for lateral wave velocity the value of $\upsilon_\perp \sim (0.8\text{-}1) \cdot 10^7 cm/s$. Thus, one can obtain the sizes of the heated plasma region in the transverse to the laser beam direction, which are in agreement with the experiments: $R_\perp \sim (200\text{-}300)\mu m$, for $t_L \sim 2.5 ns$.

54

1. Gu s'kov S.Yu., Zmitrenko N.V., Rozanov V.B., JETP, 1995.
2. Kodama R., Tanaka K.A., Nakai M. et.al., Phys.Fluids B 3(3), 1991.
3. Afshar-rad T.,Desselberger M.,Dunne M. et.al., Phys. Rev. Lett., 1994, v.73, N1.
4. Andreev N.V. et.al. JETP 1990, v..98, p.881.
5. Afanas'ev Yu. V., Gus'kov S.Yu., in Nuclear Fusion by Inertial Confinement, ed.
G.Velarde et al. CRC Press. Boca-Ration (1993), p.99.
6. Ze'ldovich B.Ya. and Raizer Yu.P., Physics of Shock Waves and High-
Temperature Hydrodynamic Phenomena (Academic, New York, 1966).
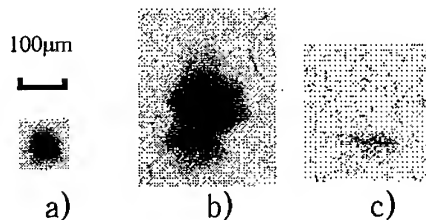
Fig.1. Pinhole images of plasma of: a) solid target, observation angle 45^0 to the normal, b) foam target, 45^0, c)- foam target, 90^0.
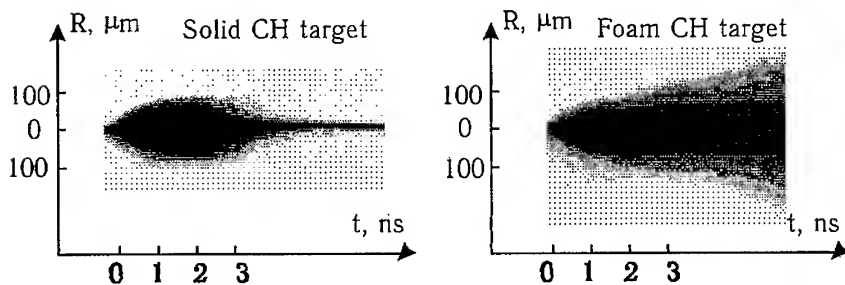
Fig.2. Registration of the hot plasma selfluminosity region with temporal resolution. $\lambda=0.43\mu m$
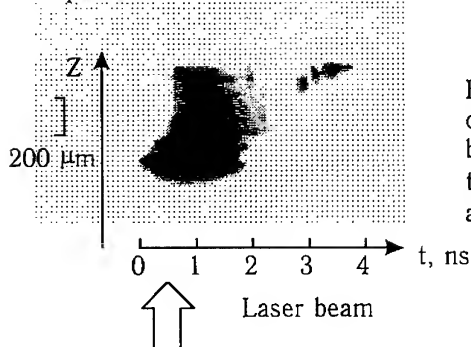
Fig.3. Streak camera picture of laser radiation scattered by foam target plasma at the wavelength of $\lambda=0.53\mu m$ and registration angle 90^0

THE MEASUREMENT OF TWO-DIMENSIONAL TARGET MOVEMENT BY FACE-ON INTERFEROMETRY

E. TAKAHASHI, I. MATSUSHIMA, Y. MATSUMOTO, H. YASHIRO, AND
Y.OWADANO

Electrotechnical Laboratory, AIST, Umezono, Tsukuba, Ibaraki 305, Japan

We have been developing a new diagnostic of target acceleration caused by laser irradiation. The method is interferometry of reflected-light from rear-side of foil target. The interferometric method realizes the measurement of two-dimensional surface movement initiated by laser induced shock wave. Two types of the configuration of interferometer, shearing and folded-wavefront, were adopted. The characteristic structure due to random-phase plate was observed by the shearing interferometry. Two-dimensional absolute target movement was also measured by the folded-wavefront interferometry.

1 Introduction

Uniform target compression is necessary to achieve high gain in laser fusion. To evaluate the uniformity in target acceleration process, various techniques have been applied. X-ray pin-hole images represent the distribution of plasma temperature and density on the target. Areal-mass-density distribution is obtained from X-ray back-light images. X-ray and visible sidelight images measure one-dimensional target acceleration velocity. In this paper, we report the first measurement of two-dimensional movement of foil target rear-surface induced by laser irradiation. This method provides direct information about laser driven shock wave.

2 Experimental Setup

Rear-surface movement is obtained by the measurement of the difference of light paths shown in Fig. 1(a). Phase-difference $\Delta\phi$ is written as [1]

$$\Delta\phi = \frac{2\pi}{\lambda}(s_o - s_i) \cdot d.\qquad(1)$$

Here, d is shift of target surface and s_o, s_i are vectors along the ray of incident and reflect light. Shearing and folded-wavefront [2] interferometer are used to form fringes corresponded to this phase-difference. Shearing interferogram is taken by superimposing two displaced images of same wavefront. We made it by using the optics of Jamin interferometer as shown in Fig. 1(b). The fringes
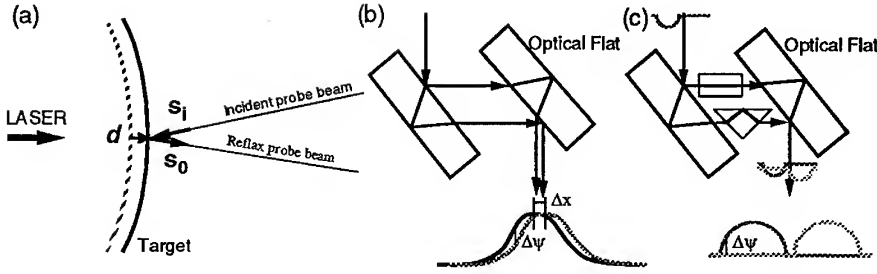
Figure 1: (a) schematic diagram of the change of light path by surface shift (b) shearing interferometer (Jamin type) (c) Folded-wavefront interferometer

of a shearing interferogram are located in constant average wavefront slope over the share distance Δx as follows,

$$\Delta \psi = \frac{\partial \Delta \phi(x,y)}{\partial x} \Delta x, \qquad (2)$$

where $\Delta \psi$ is phase-difference between the two displaced images. Two orthogonal interferograms are required to obtain wavefront since a shearing interferogram gives wavefront slope information only for the direction of shear. [3] On the other hand, folded-wavefront interferogram are made by interfering the wavefront of distorted with reflected wavefront from remained flat surface of the target as reference. (Fig. 1(c)) A prism is inserted into one of the optical paths in the Jamin interferometer and reverses the image by the total reflection. Therefore the interferogram simply represents the wavefront. Spacial resolution ($\sim 20\mu m$) is determined by background fringe spacing and size of the pixel of detector (CCD). The spacial resolution would be improved upto optical limit by magnification of the image and reducing the fringe spacing.
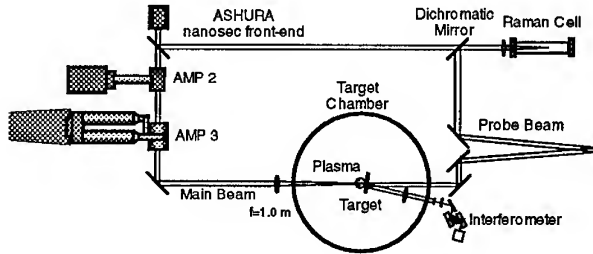
Figure 2: Whole experimental setup
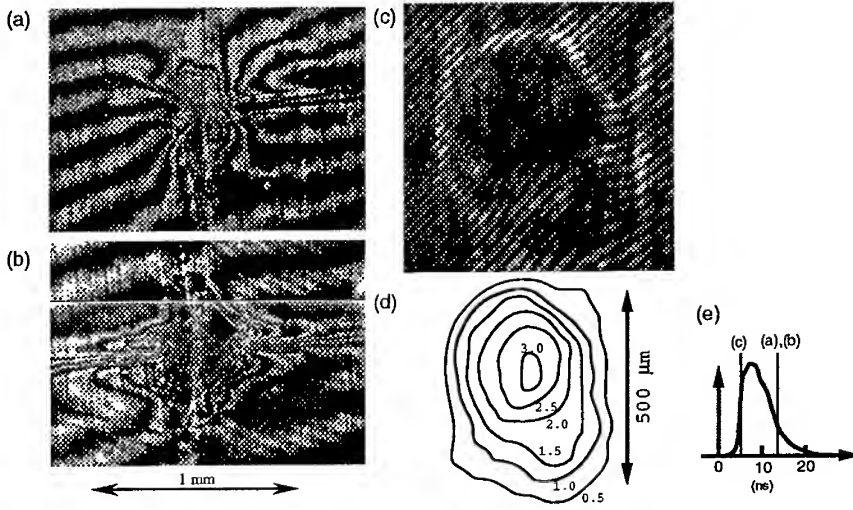
Figure 3: Interferograms (a) shearing without random-phase-plate, (b) shearing with random-phase-plate, (c) folded-wavefront, (d) phase distribution of (c) ,(e) probe injection timing on KrF laser pulse of (a), (b) and (c)

The duration of probe pulse Δt has to satisfy the condition of $v\Delta t < \lambda$ where v is velocity of accelerated target and λ is wavelength of probe beam. Thus less than 200 ps pulse is required for the velocity ranging 1 km/s. A single short probe pulse was generated by backward stimulated Raman scattering in methane and hydrogen gas mixture. [4,5] At the rising edge of the input KrF laser pulse, backward methane-Stokes builds up first. Late build up of forward hydrogen-Stokes component suppresses following backward Stokes spikes which always appears in methane-only-case. The shortest full width half maximum (FWHM) of the backward methane-Stokes pulse was about 67 ps. The schematic diagram of experiment is shown in Fig. 2. The probe pulse is well synchronized with main KrF laser by this configuration. The main KrF laser is directed into the ASHURA laser amplifiers [6] and finally irradiates a target installed in target chamber.

3   Results and Discussion

Obtained shearing interferograms are shown in Fig. 3(a) (direct laser irradiation), (b) (with random-phase plate (RPP) inserted into light path). The size of these interferograms is noted on the bottom of Fig. 3(b). The random-phase

plate for the main beam consists of square pixels of 2 mm. Aluminum foil of 50 μm thickness is used as target. Main KrF laser illumination energy was about 13 J in both (a) and (b). Probe pulse was injected at the time of 6 ns after the peak of main KrF laser having 10 ns duration as shown in Fig. 3(e). Characteristic structure was observed in the interferogram (b). It is caused by higher-harmonics of diffracted light in square random-phase-plate. The interferogram of folded-wavefront is shown in Fig. 3(c) and phase-difference distribution derived from (c) is shown in Fig. 3(d). The size of these is noted on the Fig. 3(d). Main KrF laser energy was about 20 J with RPP. Probe pulse was injected at the time of 2 ns before the peak of main KrF laser. (Fig. 3(e)) The wavefront was obtained by comparing the fringe location with the location taken before the laser shot. The shift of 3 fringe (6π rad) is observed at the center which corresponds to $\sim$ 400 nm movement by the Eq. 1. The light emitted by shock arrival at the rear-surface has been measured by an optical streak camera. [7] Shock wave reaches to the rear-surface at 2 ns before the peak of the KrF pulse for above experimental condition. Therefore shearing interferograms (a), (b) show the image of shock induced uneven surface and folded-wavefront interferogram (c) shows the image just around the time of shock arriving at the rear-surface.

4   Summary

Two-dimensional surface movement initiated by laser irradiation was measured by interferometric method for the first time. Two types of the configuration, shearing and folded-wavefront, were applied. The characteristic structure due to higher-harmonics of diffracted light of random-phase plate was observed by the shearing interferometry. Absolute target movement of $\sim$ 400 nm was measured by the folded-wavefront interferometry.

References

1. C.M.Vest in *Holographic Interferometry* (John Wiley & Sons, 1979).
2. R. Fedosejevs *et al*, *Phys. Rev. Lett.* **39**, 932 (1977).
3. M. P. Rimmer and J. C. Wyant, *Appl. Optics* **14**, 142 (1975).
4. Y. Matsumoto *et al*, *Proc. The Pacific RIM Conf. on Lasers and Electro-Optics* (1995).
5. E. Takahashi *et al*, *Jpn. J. Appl. Phys. Part 2* **34**, 856 (1995).
6. Y. Owadano *et al*, *Laser and Particle Beams* **11**, 347 (1993).
7. K. Koyama *et al*, *Bulletin of The Electrotechnical Laboratory* **56**, 33 (1992) (in Japanese).

MEASUREMENT OF LASER-PLASMA EMISSION IN THE SPECTRAL RANGE FROM THE VUV TO THE X-RAY REGION USING THERMOLUMINESCENT DOSEMETERS

J. KRÁSA, M. FÁRNÍKOVÁ

Institute of Physics, AS CR, 180 40 Prague, Czech Republic

L. RYĆ

Institute of Plasma Physics and Laser Microfusion, 00 908 Warsaw, Poland

We present the use of LiF:Mg,Ti, LiF:Mg,Cu,P and CaF$_2$:Dy dosemeters for measurement of radiation emitted from a laser-produced plasma in a spectral range above ~ 100 eV. For 40 eV radiation a calibration curve of the CaF$_2$:Dy dosemeter is shown.

1 Introduction

Thermoluminescent dosemeters (TLDs) can be used for absolute measurements of X-ray emission from laser-produced plasmas [1-5]. The advantage of the TLDs as detectors of X-ray or soft X-ray radiation from the laser-produced plasma lies in the possibility to detect a very broad-band spectrum of radiation ranging from about 5 eV to tens of MeV. In addition, the TLDs can be easily calibrated, for example, with standard radionuclide sources. The detection of X-ray radiation by TLDs is affected neither by an electrical interference nor by a strong magnetic field. Many TLDs can be used simultaneously in an experiment but only a single readout unit of thermoluminescent responses is needed.

This contribution describes an application of LiF:Mg,Ti (TLD 100), CaF$_2$:Dy (TLD 200) and LiF:Mg,Cu,P (GR 200A) dosemeters for measurement of X-ray radiation from a laser-produced plasma.

2 Experimental details

The dosemeters TLD 100 and GR 200A were discs of 4.5 mm in diameter and 0.85 mm in thickness and TLD 200 were single monocrystals of 3.2 x 3.2 x 0.85 mm^3. The TLDs were calibrated only by the 5.99 keV radiation emitted from a [55]Fe

standard radionuclide source because the sensitivity of the TLDs used does not show a significant dependence on photon energy in the spectral region of interest [2,6,7]. An annealing treatment of two hours at 673 K for TLD 200, one hour at 673 K and subsequently two hours at 373 K for TLD 100, and twenty minutes at 513 K for GR 200A was carried out before each irradiation. The thermoluminescent responses and glow curves (light intensity vs. temperature curve) were recorded by a TLD-871 reader (of Czech manufacture) or a LTM reader (Fimel, France). For TLD 200 it was in the temperature range from 353 to 523 K, for TLD 100 from 343 to 573 K and from 333 to 513 K for GR 200A using mean heating rates of 2.8 K/s, 3.8 K/s and 3 K/s, respectively.

The experiments were performed using both the Nd:glass laser system (λ = 1.06 μm, E_L < 20 J, $\tau \sim$ 1 ns) at the Institute of Plasma Physics and Laser Microfusion, Warsaw and the iodine laser system PERUN (λ = 1.315 μm, E_L < 50 J, τ < 1 ns) at the Institute of Physics, Prague. The experimental set-up was identical for both the experiments. The power density of the focused laser beam on an aluminium target ranged from 10^{13} to $\sim$ 5 x 10^{14} W/cm^2. The distance of the TLDs from the plasma was 175 mm.

3   Experimental results

The comparison of responses of the TLDs to X-ray radiation from the aluminium plasma as well as ^{55}Fe radionuclide permits to determine the ratio of their sensitivities [4], see Table 1. This ratio is relevant only for new dosemeters GR 200A , because they can show an aging indicated by a slight access in the recommended annealing temperature (240 ± 2-5) °C [5,9]. The aging of the TLD 200 as well as the TLD 100 was not encountered in our experiments.

TLD	LiF:Mg,Cu,P (GR 200A)	CaF$_2$:Dy (TLD 200)	LiF:Mg,Ti (TLD 100)
Relative sensitivity	1.0	0.86	0.037

Table 1   Relative X-ray sensitivity of the TLDs

For the detection of plasma radiation in the spectral range above 100 eV the 2 μm thick KG Makrofol foil was used as a filter. Its transmissivity is shown in Fig. 1. The response (TLR) of the TLD 200 dosemeters shielded by the KG Makrofol foil

is compared with the response to the aluminium-plasma radiation filtered additionally by a 300 μm or 1200 μm thick Be foil, see Fig. 2. The ratio of the responses of one of TLD 200 detectors shielded with the Makrofol foil only and the other detector shielded with both the Makrofol foil and the 300 μm thick Be foil ($TLR_{Makrofol}/TLR_{Makrofol+300μBe}$) was about 50. Since it was not possible to verify this value employing another kind of detector having spectral sensitivity over the spectral range of the TLD 200 in this experiment, we recalculated the ratio of the responses from Al spectrum as measured by Chaker et al. [10]. This estimated value is close to the measured values.
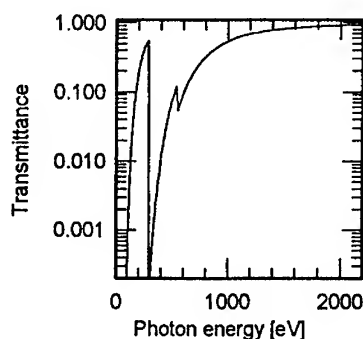
Fig. 1 The transmittance of the 2μm Makrofol foil for photon energy from 30 eV to 2100 eV.
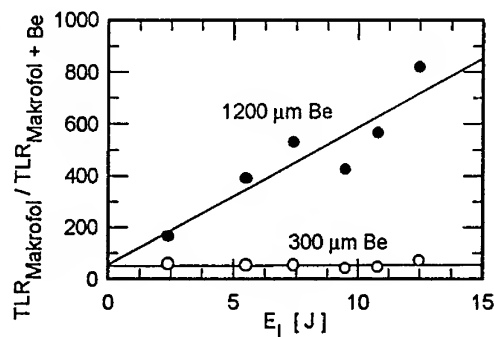
Fig. 2 The ratio of CaF_2:Dy thermoluminescence responses vs. the laser energy focused onto an Al target. One of the dosemeters used was shielded by the 2 μm Makrofol foil and the other one was shielded by the 2 μm Makrofol foil and a 300 μm or 1200 μm Be foil.

The irradiation of CaF_2:Dy dosemeters by 40 eV photons was carried out on the SA23 beam line of the Super-ACO storage ring at LURE-Orsay. This wavelength was selected with regard to the soft X-ray lasing lines corresponding to photon energies from 20 eV to 60 eV [10-12]. All the dosemeters were carefully cleaned before the irradiation. The dependence of TL response on the energy of the 40 eV radiation is shown in Fig. 3 (the Fimel LTM reader was used). It is evident that the saturation of the TL response starts if the incident energy reaches about 25 μJ per dosemeter area.

62
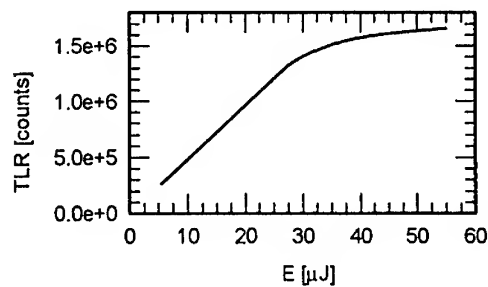
Fig. 3. TL response of TLD 200 to energy of 40 eV radiation.

4 Conclusion

The application of the TLDs for measurement of radiation with broad-band spectrum emitted from a laser-produced plasma is very useful. They may be also used for the measurement of X-ray laser energy.

5 Acknowledgments

[1] Meyer F J, Montry G R and Benn E 1975 *Adv. X-Ray Anal.* **18** 169
[2] Basov N G et al 1990 *Proc. P.N. Lebedev Phys.Inst. (Moscow)* **203** 69
[3] Violet C E 1975 *Adv. X-Ray Anal.* **18** 26
[4] Fárníková M et al 1996 *Nucl. Instr. Meth. Phys. Res.* A **368** 484
[5] Fárníková M, Krása J, Juha L, Ryć L 1996 *J. Phys. D: Appl. Phys.* - in press.
[6] Horowitz Y S and Kalef-Ezra J 1981 *Nucl. Instrum. Meth.* **188** 603
[7] Violet C E 1975 *Adv. X-Ray Anal.* **18** 26
[8] Wang S et al 1986 *Prot. Dosim.* **14** 223
[9] Chaker M et al 1988 *J. Appl. Phys.* **63** 892
[10] Rocca J J et al 1994 *Phys. Rev. Lett.* **73** 2192.
[11] Rus B et al 1994 *J. Opt. Soc. Am.* B **11** 564
[12] Key M H 1992 *"Status of X-ray Laser Research"*, In: Applications of X-ray Lasers (Eds. R. London, D. Matthews, S. Suckewer), CONF-9206170, pp. 1-20.

INTERPRETATION OF SPECTRA OF LASER IRRADIATED ZINC IN THE RANGE FROM 0.6 TO 0.95 nm

J.-F. WYART

Laboratoire Aimé Cotton, Bât. 505, Centre universitaire, 91405 Orsay Cedex, France

C. CHENAIS-POPOVICS, P. RENAUDIN*, T. MIßALLA, J.-C. GAUTHIER

Laboratoire pour l'Utilisation des Lasers Intenses, Ecole Polytechnique, 91128 Palaiseau Cedex, France
*Present address: Centre d'Etudes de Limeil-Valenton, 94195 Villeneuve-Saint-Georges Cedex, France

The main features of a spectrum of zinc irradiated at 2×10^{14} - 10^{15} W/cm^2 laser intensity are analysed in the region 0.6 - 0.95 nm. The strongest emision peaks are attributed to all spectra ranging from lithium-like Zn XXVIII to fluorine-like Zn XXII. The relativistic parametric potential method is used for deriving wavelengths and transition probabilities.

Laser-produced plasmas provide rich X-ray spectra. Their identification is of importance for the physics of ICF and X-ray lasers, of laboratory X-ray sources and of hot astrophysical objects. Zinc X-ray spectra have been measured on the LULI laser facility as a part of systematic investigations in the medium-Z elements from $_{28}$Ni to $_{33}$As. The laser pulse conditions were 600ps duration, 0.53 μm wavelength and 8 to 35 J focused onto 80μm focal spots, leading to irradiations of 2×10^{14} to 10^{15} W/cm^2. Spectra were recorded in the range 0.6 to 0.95 nm by means of two flat crystal spectrometers. Magnesium has been used as a tracer element for wavelength calibration. A preliminary survey of similar spectra obtained for Ni and Cu was presented in [1].

In these conditions of irradiation zinc losses up to 27 electrons and its emission spectrum below 10Å contains characteristic transitions between upper levels having one electron with principal quantum number larger than 2, and lower levels of the ground complex $(2s+2p)^N$. In the literature[2], observed wavelengths longer than 0.7445 nm are compiled for F-like Zn XXII, O-like Zn XXIII and Be-like Zn XXVII, but no experimental data below 70Å are reported neither for the simple spectrum of Li-like Zn XXVIII nor for the most complex spectra excited in these conditions: N-like Zn XXIV, C-like Zn XXV and B-like Zn XXVI.

For all ions involved, the levels with n=2 principal quantum numbers have been accurately determined by Edlén from comparisons along isoelectronic sequences between observed and *ab initio* MCDF transition energies (n=2,Δn=0) in the VUV region [3]. These recommended "experimental" level values are available for checking the accuracy of theoretical models and approximations. We have used the atomic structure codes of HULLAC [4] based on the relativistic parametric potential method [5] for deriving transition energies and probabilities between full complexes

$(2)^N$, i.e. $\quad 2s^2 2p^{N-2} + 2p^N$ and in opposite parity $\quad 2s^1 2p^{N-1}$

$(2)^{N-1}3^1 \quad 2s^2 2p^{N-3}3s^1 + 2s^2 2p^{N-3}3d^1 + 2s^1 2p^{N-2}3p^1 + 2p^{N-1}3s^1$
$\qquad + 2p^{N-1}3d^1 \quad$ and in opposite parity
$\qquad 2s^2 2p^{N-3}3p^1 + 2s^1 2p^{N-2}3s^1 + 2s^1 2p^{N-2}3d^1 + 2p^{N-1}3p^1$

$(2)^{N-1}4^1 \quad$ same as $(2)^{N-1}3^1$ with quantum number 4 instead of 3.

The treatment of full complexes is necessary to take the most important configuration mixing effects into account. A brief account of the main spectral features identified in the present study is reported below, in order of decreasing ionic charge.

Lithium-like zinc Zn XXVIII

Vainshtein and Safronova had derived the energies of n=2 to n=5 levels in the Li-like sequence through krypton [6]. We have determined the same levels with HULLAC. Both calculations are in a good agreement (provided that the $3^2P_{1/2}$ level 12743770 cm^{-1} is considered as a misprint of 12723770, which value makes it fully consistent with the rest of the C IV - Kr XXXIV sequence. Experimental and theoretical wavelengths are compared in Table 1. In absence of Mg lines below 7Å in the spectra, the theoretical wavelength λ 6.1163Å was used as a standard for calibration.

Table 1. The 2-3 and 2-4 transitions of lithium-like Zn XXVIII

λth (Å)	gA (10^{11}s^{-1})	Upper lev (10^3 cm^{-1})	J	Lower lev. (10^3 cm^{-1})	J	λth [6] (Å)	λexp (Å)	Trans
5.8747	242	17022.17	1.5	0.00	0.5	5.8749		4p - 2s
5.8850	123	16992.41	0.5	0.00	0.5	5.8852		4p - 2s
6.0324	449	17041.94	1.5	464.91	0.6	6.0315	6.0354	4d - 2p
6.0700	14	16939.27	0.5	464.91	0.5	6.0695		4s - 2p
6.1170	792	17051.37	2.5	703.53	1.5	6.1163	6.1163	4d - 2p
6.1205	86	17041.94	1.5	703.53	1.5	6.1198		4d - 2p
6.1593	29	16939.27	0.5	703.53	1.5	6.1590	6.1611	4s - 2p
7.8153	537	12795.38	1.5	0.00	0.5	7.8158	7.815	3p - 2s
7.8587	279	12724.70	0.5	0.00	0.5	7.8593	7.8599	3p - 2s
8.0788	1361	12843.03	1.5	464.91	0.5	8.0772	8.0384	3d - 2p
8.2224	2420	12865.38	2.5	703.53	1.5	8.2212	8.2157	3d - 2p
8.2224	265	12843.03	1.5	703.53	1.5	8.2364	8.2295	3d - 2p
8.2435	33	12595.69	0.5	464.91	0.5	8.2419		3s - 2p
8.4089	70	12595.69	0.5	703.53	1.5	8.4077		3s - 2p

Beryllium-like zinc Zn XXVII

This relatively simple two-electron spectrum may be used as a test case for the evaluation of configuration mixing effects by calculating levels with the same set of potential parameters, but different sets of basis states. The total energies of the ground state in different approximations which are compared below show that the *intra*-complex interactions are the most important ones.

Configuration	Total energy (a.u.)	Relative to case a)
a) $2s^2$	-1091.3452	0
b) $2s^2+2p^2 = (2)^2$	-1091.6590	68870
c) $(2)^2+2^14^1$	-1091.6604	69200
d) $(2)^2+2^13^1$	-1091.6636	69880
e) $(2)^2+2^13^1+2^14^1$	-1091.6649	70170
f) $(2)^2+2^13^1+2^14^1+2^15^1+(3)^2$	-1091.6665	70520

The difference in total energies between the isolated complex $(2)^2$ and the most extended basis is 0.0075 a.u.. In the odd parity, the extension of the basis from the *isolated* 2s2p to the 13 odd configurations of $(2)^2+2^1n^1$ (n=3 to 6) adds -0.0109 a.u. to the total energy of 2s2p $^3P_2$ and -0.0452 a.u. for 2s2p $^1P_1$. In the 6Å region, this latter energy corresponds to 0.004Å differences in calculated wavelengths and shows how important the extra-complex interactions may be when a high level of accuracy is required. In all cases the extended bases lead to theoretical energies closer to the experimental levels of Edlén [3]. In Zn XXVII, the transitions which contribute to the strongest emission peaks in the wavelength range 6.0 - 6.4 Å are collected in Table 2 and they were calculated from the 15 configurations of case e).

Boron-like zinc Zn XXVI through fluorine-like Zn XXII

Except for Zn XXII, the transitions 2-4 and 2-3 were calculated independently in these spectra. It is expected that the $(2)^{N}3^1$ complex has upwards repulsive effects on $(2)^{N}4^1$ and downwards effect on $(2)^{N+1}$. Therefore the theoretical wavelengths of 2-4 transitions should be too long in the calculation of the group $(2)^{N+1}+(2)^{N}4^1$ when the $(2)^{N}3^1$ complex is discarded. This is seen for Zn XXVI on the figure 1 where the experimental spectrum compares well with a theoretical tracing shifted by -0.008Å. Most of the lines are blends of unresolved fine structure transitions, and therefore their average wavelengths depend on plasma conditions. A selection of strong lines which characterise the complex spectra of Zn XXVI- XXII is given in Table 2.

In the present work, the wavelength calibration was performed with H-and He lines of Mg and in the lower spectral region with Li-like lines of Zn XXVIII for which theory is presumably accurate. Further observation with Al as a trace element are planned for confirming the present experimental wavelengths. Finally in the comparison of the theoretical and experimental spectra reported in figure 1, a LTE at 100 eV had to be assumed to get a satisfactory agreement. This unexpectedly cold temperature is an incentive to further improvements by means of a collisional-radiative model.

Figure 1 Comparison between the experimental spectrum of zinc and the 2-4 transitions of boron-like Zn XXVI in the assumption of LTE at 100eV
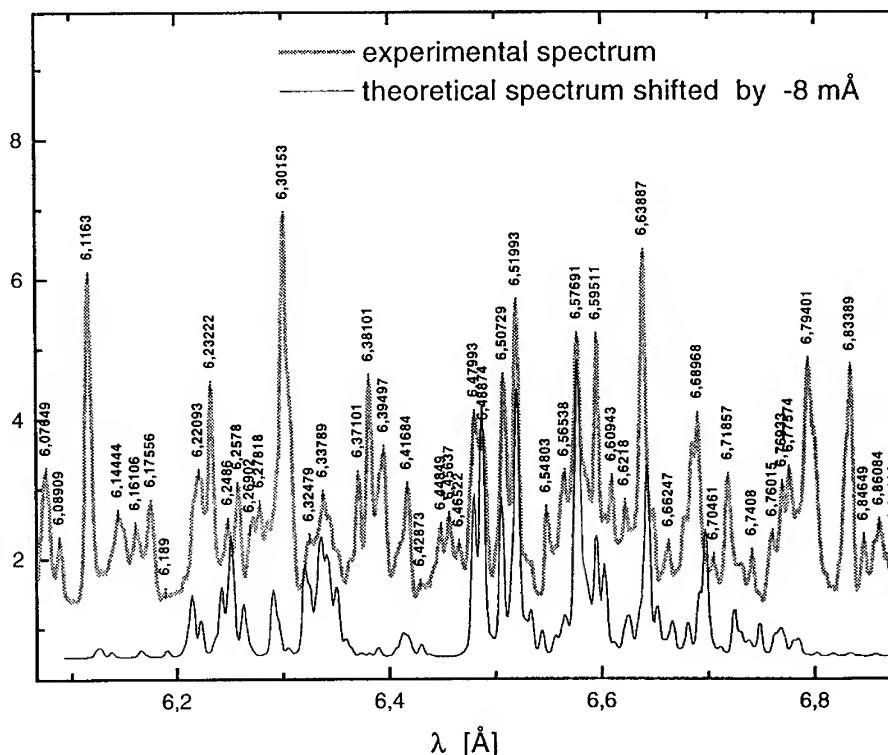
References
[1] C. Chenais-Popovics, J. Racapé, P. Renaudin, J.-C. Gauthier and J.-F. Wyart, Annual Report LULI, 1992. - [2] R.L. Kelly, J. Phys. Chem. Ref. Data, Vol. 16, Suppl. n°1 (1987). - [3] B. Edlén, Physica Scripta 28, 51 (1983); 28, 483 (1983); 30, 135 (1984); 31, 345 (1985); 32, 86 (1985). - [4] M. Klapisch, A. Bar-Shalom and W.H. Goldstein, HULLAC computer codes, unpublished. - [5] E. Luc-Koenig, Physica 62, 393 (1972); M. Klapisch, J.-L. Schwob B.S. Fraenkel and J. Oreg, J. Opt. Soc. Am. 67, 148 (1977) - [6] L.A. Vainshtein and U.I. Safronova, Physica Scripta 31, 519 (1985).

Table 2. The 2-4 transition wavelengths (in Å) of Zn XXVI, Zn XXV, Zn XXIV, Zn XXIII and Zn XXII. The levels (in 10^3 cm^{-1}) of the same parity as the ground state are given under Eb. gA is the transition probability (in 10^{11}s^{-1}) in emission.

λth	gA	Ea	Ja	Eb	Jb	λexp
Beryllium-like Zn XXVII						
6.2352	518	460.71	1.0	16498.66	2.0	6.2322
6.2364	164	460.71	1.0	16495.65	1.0	
6.3036	937	640.54	2.0	16504.55	3.0	6.3015
6.3068	229	17220.68	2.0	1364.84	2.0	
6.3871	1575	17244.64	3.0	1588.15	2.0	6.3810
Boron-like Zn XXVI						
6.4872	237	626.02	1.5	16041.08	0.5	6.4799
6.4877	345	626.02	1.5	16039.76	1.5	
6.4893	270	626.02	1.5	16035.96	2.5	
6.4953	420	15395.69	1.5	0.00	0.5	6.4887
6.4969	583	973.80	1.5	16365.85	2.5	
6.5132	350	511.22	0.5	15864.62	0.5	6.5073
6.5149	421	511.22	0.5	15860.56	1.5	
6.5242	452	1039.76	2.5	16367.24	3.5	6.5199
6.5286	537	718.70	2.5	16035.96	2.5	
6.5296	937	718.70	2.5	16033.68	3.5	
6.5749	411	17245.90	1.5	2036.57	0.5	6.5769
6.5834	348	16996.22	1.5	1806.52	1.5	
6.5839	547	626.02	1.5	15814.51	2.5	
6.5866	737	15403.51	2.5	221.23	1.5	
6.6486	901	1333.25	1.5	16374.10	2.5	6.6389
6.6510	1396	1039.76	2.5	16075.17	3.5	
Carbon-like Zn XXV						
6.7987	511	696.08	2.0	15404.74	1.0	6.7940
6.8005	618	696.08	2.0	15400.93	2.0	
6.8031	411	696.08	2.0	15395.28	3.0	
6.8047	386	14695.72	1.0	0.00	0.0	
6.8397	361	1033.14	1.0	15653.63	2.0	6.8339
6.8403	355	1112.26	3.0	15731.45	4.0	
6.8452	666	1112.26	3.0	15721.09	3.0	
6.8453	534	696.08	2.0	15304.67	3.0	
6.8952	1344	14932.43	3.0	429.66	2.0	6.8849
6.8977	1089	1532.05	2.0	16029.55	3.0	
6.9053	314	14911.31	2.0	429.66	2.0	6.8974
6.9092	621	14692.95	3.0	219.52	2.0	
6.9111	380	16739.14	1.0	2269.68	0.0	

λth	gA	Ea	Ja	Eb	Jb	λexp
Nitrogen-like Zn XXIV						
7.1399	337	1345.76	1.5	15351.50	2.5	7.1366
7.1469	796	14251.65	3.5	259.64	2.5	
7.1499	411	14245.83	2.5	259.64		
7.1564	580	964.56	2.5	14938.01	1.5	7.150w
7.1593	313	13967.77	2.5	0.00	1.5	
7.1613	689	964.56	2.5	14928.59	2.5	
7.1633	563	1390.27	2.5	15350.26	3.5	
7.1660	507	964.56	2.5	14919.31	3.5	
7.2461	1149	14060.22	3.5	259.64	2.5	7.2359
7.2484	588	13983.90	2.5	187.71	1.5	
7.2502	283	14052.32	2.5	259.64	2.5	
7.2606	899	14273.66	2.5	500.72	1.5	7.2525
7.2611	522	14272.65	1.5	500.72	1.5	
7.2622	345	1089.07	1.5	14858.99	2.5	
7.2653	663	1787.19	0.5	15551.16	1.5	
Oxygen-like Zn XXIII						
7.4953	520	13341.75	2.0	0.00	2.0	7.4868
7.4966	341	13446.37	1.0	107.04	0.0	
7.5001	471	13333.18	3.0	0.00	2.0	
7.5078	259	13588.32	2.0	268.83	2.0	7.4932
7.5098	380	13584.80	3.0	268.83	2.0	
7.6283	519	13283.42	2.0	174.28	1.0	7.6219
7.6290	825	13107.88	3.0	0.00	2.0	
7.6291	595	13616.35	1.0	508.58	0.0	
7.6361	804	13364.51	3.0	268.83	2.0	7.6305
7.6381	487	13361.08	2.0	268.83	2.0	
Fluorine-like Zn XXII						
7.8828	255	1371.31	0.5	14057.23	0.5	7.8978
7.8861	231	1371.31	0.5	14051.89	1.5	
7.8875	412	12678.30	2.5	0.00	1.5	
7.8906	362	12673.37	1.5	0.00	1.5	
7.8910	208	12672.62	0.5	0.00	1.5	
7.9455	468	12585.74	2.5	0.00	1.5	7.9531
7.9968	354	12700.92	0.5	195.92	0.5	8.007s
8.0012	454	12694.06	1.5	195.92	0.5	
8.0441	633	12431.46	2.5	0.00	1.5	8.0520
8.0459	319	1371.31	0.5	13799.92	1.5	
8.0472	371	12426.65	1.5	0.00	1.5	

X-RAY SPECTRA OF EXCIMER-LASER-PRODUCED HIGH DENSITY PLASMAS

A.I.MAGUNOV[†], A.FAENOV[†], I.SKOBELEV[†], T.PIKUZ[†], D.BATANI[‡], M.MILANI[‡],
A.CONTI[‡], A.MASINI[‡], M.COSTATO[¶], A.POZZI[¶], E.TURCU[§], R.ALLOT[§], N.LISI[§],
M.KOENIG[‖], A.BENUZZI[‖], F.FLORA[a], T.LETARDI[a], L.PALLADINO[l], A.REALE[l]

† Multicharged Ions Spectra Data Center, VNIIFTRI, Mendeleevo, Russia
‡ Dipartimento di Fisica, Università di Milano, Italy
¶ Dipartimento di Fisica, Università di Modena, Italy
§ Rutherford Appleton Laboratory (U.K.)
‖ LULI, Ecole Polytechnique, France
a CRE ENEA, Frascati, Italy
l Dipartimento di Fisica, Università dell'Aquila, Italy

Time and space-integrated spectra measurements have been performed in plasma produced by 308 nm XeCl ($\tau = 10$ ns) or by 248 nm KrF laser radiation ($\tau = 7$ ps, 16 pulses in train) on CF_2 targets. Theoretical modelling of Lyman and He-like ion resonance series of experimental data shows considerable differences in laser absorption between the two plasmas.

1. Introduction

We describe soft X-ray spectra obtained from teflon targets (CF_2) irradiated with excimer laser radiation. The objective of the experiment was twofold: i) characterise plasma emission in order to prepare an experiment on irradiation of yeast cells in the $h\nu \approx 0.9$ keV range [1]; ii) compare spectra obtained with two different excimer lasers and study how spectra are influenced by plasma properties.

We have used "simple" time and space integrated spectra obtained by a flat crystal spectrometer [2] in cooperation with theoretical modelling. Even if less powerful than spectroscopic methods with high spectral and spatial (or temporal) resolution [3], it can give useful information about features of plasma production.

2. Experimental set-up

Fluorine plasma spectra were obtained with two laser facilities. At Rutherford, the set-up is similar to that described in [4]. The picosecond system has four modules: a) oscillator, b) dye amplifier and frequency conversion, c) multiplexer, d) final double pass KrF amplifier. The multiplexer is a set of mirrors and beam splitters which forms a pulse train by splitting the original pulse in 16 pulses (7 ps each) separated by 2 ns. Final characteristics are: $\lambda = 248$ nm, total energy of train ≈ 300 mJ, repetition frequency a few tents Hz. The beam is focused by a f = 9 cm lens to give an intensity on target $5 \cdot 10^{15}$ W/cm^2.

The laser used in Frascati is a ($10 \times 10 \times 100$ cm^3) discharge pumped XeCl system ($\lambda = 308$ nm) [5]. In this experiment, it was used as an amplifier with PBUR (positive branch unstable resonator) configuration, for the pulse of a Spectra Physics

laser of 10 ns pulse. The energy is 2 J per pulse with a few Hz repetition rate. The beam is focused by a triplet lens to give an intensity on target $\approx (4\text{-}10)\cdot 10^{12}$ W/cm^2.

3. X-ray spectra

The target was a TEFLON (CF$_2$) film (100 μm thickness). X-rays spectra of H-like and He-like fluorine plasma were detected by the same Bragg mini-spectrograph [2], equipped with a RbAP crystal (2d = 26.121 Å), 3 μm Al and 2 μm paralyne filters and Kodak DEF film. Spectra deconvolution took into account film calibration [6], spectrometer geometry and filter transmission. Fig. 1 shows experimental spectra.
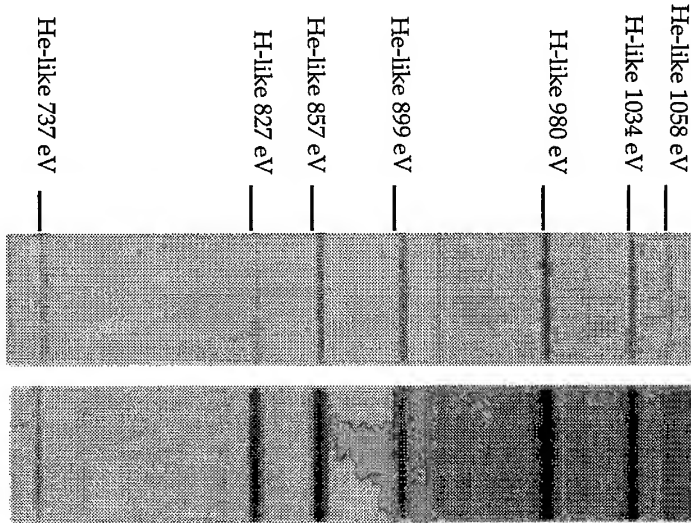
Figure 1. Experimental X-ray spectra from a teflon target obtained in (up) Frascati, (bottom) RAL. Spectra were collected with the same spectrograph: the only difference was in the position of plasma radiation source. F IX and F VIII series are evident.

4. Data interpretation and modelling

We considered that the spectral emission probability may be written as

$$P(E) = (1/4\pi) \iint Q(E,\mathbf{r},t) \exp\left(-\tau(E,\mathbf{n}_E,t)\right) \, d\mathbf{r} \, dt$$

$$\tau(E,\mathbf{n}_E,t) = \int k(E,\rho + \mathbf{n}_E \, s,t) \, ds$$

where E is the photon energy, $\mathbf{n}_E$ is the Bragg angle direction of photons emitted in point $\mathbf{r} = \rho + \mathbf{n}_E \, s$, and τ is the plasma optical thickness. The emissivity $Q(E,\mathbf{r},t)$ and the plasma opacity $k(E,\mathbf{r},t)$ depend on local plasma electron density $n_e(\mathbf{r},t)$,

temperature $T_e(r,t)$ and ion charge abundance. The complete simulation is described in [7]. Here we recall that Q and k are dependent over radiative transition rates, upper and ground level populations, line profile function, and that for our spectra, we must consider the contributions for all the terms of the H-like and He-like line series.

The line profiles can be derived taking into account quasistatic ion microfield Stark broadening, electron elastic collision and Doppler broadening in the form of the Voigt function. We have also assumed an axial symmetry of plasma expansion along the laser beam direction, and have substituted the continuos plasma density profile with a finite sum over uniform plasma layers (each with well defined parameters). In particular we considered six electron densities with $n_e = 2 \cdot 10^{22}$, 10^{22}, $5 \cdot 10^{21}$, $2 \cdot 10^{21}$, 10^{21} and $5 \cdot 10^{20}$ cm^{-3} and varied their size in order to get the best resemblance between theoretical and experimental spectra. The F ion charge abundance was also varied to give correct relative intensities for F IX and F VIII lines. The carbon component was considered as completely stripped. The level populations were calculated in stationary collisional-radiative model and were found to be in thermodynamic equilibrium with continuum for excited states with $n \geq 3$.
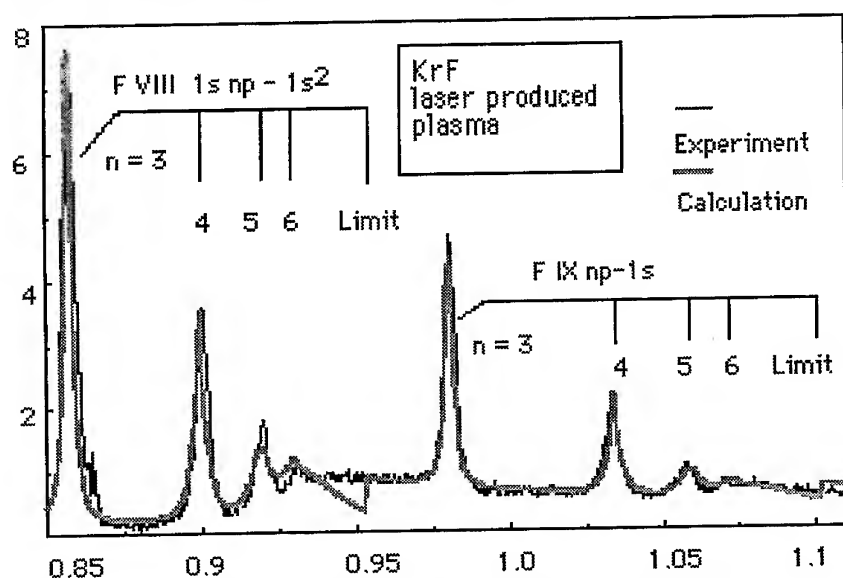
Figure 2. Experimental and theoretical F IX and F VIII spectra emitted from KrF laser-produced plasma. Vertical axis $P(E) \cdot 10^{-9}$, Horizontal axis Photon energy in keV.

4. Results and discussion

Fig.2 shows our experimental and numerical results for the KrF laser-plasma. Simulations show that main contributions to spectra come from regions with an average electron density $n_e = 10^{22}$ cm^{-3} for the case of KrF and $n_e = 3 \cdot 10^{21}$ cm^{-3} for the case of XeCl laser. T_e is less sensitive on the spectra (only through the Debye

screening effect on line shapes and relative intensities through level populations) and cannot be determined with the same accuracy. Anyway it was roughly ≈ 200 eV for in Frascati and ≈ 300 eV for the Rutherford case.

In the case of KrF laser-plasma the critical density is slightly larger ($n_{ec} = 1.8 \cdot 10^{22}$ cm^{-3}). Such a difference could not change sharply the emission spectrum if the mechanisms of plasma formation would be the same. However, the experimental data show considerable differences in these spectra. First of all the $7^1P_1 \rightarrow 1^1S_0$ line disappears in the KrF spectrum and lines with n=6 in H-like and He-like series are much less pronounced then in XeCl case. All lines are broader than would be according to simple scaling of the critical electron density.

These features confirm that in this case the laser radiation is absorbed in plasma layers near critical. Since inverse bremsstrahlung is the dominant absorption mechanism in both cases, the difference is probably due to the different pulse length which in the case of the ps KrF laser does not leave time for the plasma to expand (and reach lower densities) during the laser pulse. Also, according to Mora's model [8], absorption is delocalised if the laser intensity on target is $I_L < I_0$ where

$$I_0 \ (\text{W/cm}^2) = 2 \ 10^{13} \ \lambda^{-5} \ (\mu\text{m}) \ (Z*/3.5)^{-5} \ \tau^{\ 1.5} \ (\text{nsec})$$

and $Z*$ is the average ionisation degree in the plasma. Now, since $Z* \approx 20$ as seen in experimental spectra, $I_L < I_0$ in the Frascati case (and hence absorption takes place at $n_e < n_{ec}$) while $I_L > I_0$ in the Rutherford case (and hence absorption is at $n_e \approx n_{ec}$).

5. Conclusion

Emission spectra of fluorine plasma produced by short wavelength excimer lasers have been measured. The features of resonance series of H-like and He-like ions were used for modelling taking into account different spectral line broadening, population kinetics mechanisms and radiative transfer. The best fitting of theoretical model results and experimental data for XeCl and KrF laser sources shows that differences in time and space integrated spectra are due to different absorption of laser in plasma.

References
[1] D.Batani, M.Milani, E.Turcu et al., Laser and Technology, **5**, 81 (1995).
[2] D.Batani, E.Turcu, G.Tallents, A.Giulietti and L.Palladino, in *Excimer Lasers and Applications III* , T Letardi ed., SPIE **1503** (1991).
[3] B.d'Etal, J.Grumberg et al., *J.Phys.B: At.Mol.Phys.* **20**, 1733 (1987).
[4] E.Turcu, I.Ross, P.Trenda, A.G.Michette, G.Tallents, D.Batani, R.Meldrum et al., in *Applications of Laser Plasma Radiation* SPIE **2015**, 243 (1994).
[5] S.Bollanti, D.Batani et al., *Journal of X-ray Science and Technology* (1995).
[6] P.D.Rockett, C.R.Bird, C.J.Hailey et al., *Appl. Opt.* **24**, 2536 1985
[7] A.Magunov, A.Faenov, D.Batani, E.Turcu et al., sub. to *J.Physics B* (1996).
[8] P.Mora, *Phys.Fluids*, **1503**, 1051 (1982).

PC PROCESSING OF EXPERIMENTAL RESULTS FROM THE THOMSON PARABOLA ION SPECTROMETER WITH IMAGE CONVERTER BASED ON MICROCHANNEL PLATE.

W. MRÓZ

Institute of Optoelectronics, MUT, 01-489 Warsaw 49, 2 Kaliski St., Poland

M. PFEIFER and L. LÁSKA

*Institute of Physics, Academy of Science of the Czech Republic, 180 40 Prague 8,
Na Slovance 2, Czech Republic*

P. PARYS and E. WORYNA

*Institute of Plasma Physics and Laser Microfusion, P. O. Box 49, 00-908 Warsaw,
23 Hery St., Poland*

Possibility of using the Thomson parabola ion spectrometer in investigations of ion emission from high-Z laser created plasma was shown. The results obtained on the tantalum targets are shown: the maximum charge state of ions $z \sim 40$, the maximum ion energy $E_i \sim 2.1$ MeV and the Ta^{35+} ion yield $N = 6.2 \times 10^{11}$ sr^{-1}.

The Thomson parabola ion spectrometer (TS) gives the general view of ionization states and energies of all types of ions of expanding plasma in one laser shot. The advantage of TS has stimulated us to use it in investigations of ion emission from targets with high atomic weights. The construction of the used TS with an image converter based on the microchannel plate (MCP) [1], is based on the configuration with separated electric and magnetic fields. The first measurements of ions from gold, laser created plasma, made by means of this TS were reported in [2]. Images of parabolas were registered on the photographic film, what was not convenient for processing of obtained results. In experiment with the tantalum targets [3], has been shown, that TS may be very useful at the experimental phase, when the optimum experimental conditions are to be founded. The parabolas of light contamination ions, like C^{i+}, have been used as markers of non-separated parabolas from Ta ions with the same charge state-to-mass (z/A) ratio. Obtained results and experience in processing of parabolas enabled us to make the reinterpretation of results form the first experiment. What we have supposed as the overexposition made by dark current of MCP, was the group of high energy, highly charged gold ions.

In this paper we present method of analysis of TS images by means of personal computer (PC) processing. Parabolas analyzed were obtained in an experiment with iodine photodissociation laser system PERUN ($\lambda = 1.315$ μm, $E_L \le 50$ J,

$\tau \sim 350\text{-}500$ ps) [4]. As a targets were used tantalum targets. Processing of registered by Tektronix video camera parabolas was starting from comparison of measured parabolas with ones computed theoretically. Matching of theoretical parabolas with measured, can be made by simultaneous changes of electrostatic and magnetic fields, or one of them. In process of parabolas matching we have changed only the magnetic field, B, because it influences on the parabolas shape is much stronger than the influence of the electrostatic field, E. The equation describing parabolas registered by the TS, known as the equation of Thomson parabolas, can be written in the form :

$$x = \gamma \, ME/z[(B(1+\delta)]^2 \, y^2 \qquad (1)$$

where: x -deflection of ions in direction of E-field, y -deflection of ions in direction perpendicular to the B-field, γ -geometric factor, A/z -mass-to-charge state ratio of registered ions, δ -correction factor.

Correction factor in different shots was changed most often from 0.05 to 0.15. In Fig. 1a parabolas matched to the measured Ta parabolas, from ions with charge states from z = 2 to z = 10 were shown. In spite of the fact, that parabolas of highly charged ions was not separated each from other, we could estimated that parabolas of this group correspond to ions with charge states from $z \sim 18$ up to $z \sim 40$. Knowing, that points of intersection of parabolas with a straight line, x/y = const, that is the line passing the origin of the coordinates, Oxy, corresponds to ions of fixed velocity [1], we can estimate the velocities of the ion group with $z \sim 18\text{-}40$ in the range of $v \sim (0.5\text{-}1.5)\times10^8$ cm/s, what corresponds to ion energies $E_i \sim 280\text{-}2100$ keV (Fig. 1b). Group of fast and highly charged ions consists of three smaller ion groups. The fastest of them, with velocities $v \sim (0.82\text{-}1.5)\times10^8$ cm/s, ($E_i \sim 630\text{-}2100$ keV), consists mainly of ions with charge states from z = 30 up to z = 40. Lowly ionized ions with $z \leq 10$ had velocities $v \leq 3.0\times10^7$ cm/s.

In the experiment with the TS, the ring ion collector (IC), coaxial with the TS has been used. From comparison of IC signal with velocities of different ion groups from the TS, the quantity of highly charged ions can be estimated. Method of estimation of the quantity of ions from ion collector signal was discussed in [5]. Fig. 1c shows the ion collector signal obtained in the same laser shot as the parabolas images. Taking into consideration the fact, that the hydrogen ions registered by the TS in the another laser shots with the Ta targets [3] had the highest velocities, usually $v \geq 3\times10^8$ cm/s, it can be concluded that fastest ions registered by ion collector, with velocities $v \sim (2.7\text{-}5.2)\times10^8$ cm/s are the hydrogen ions.

a)

b)

c)
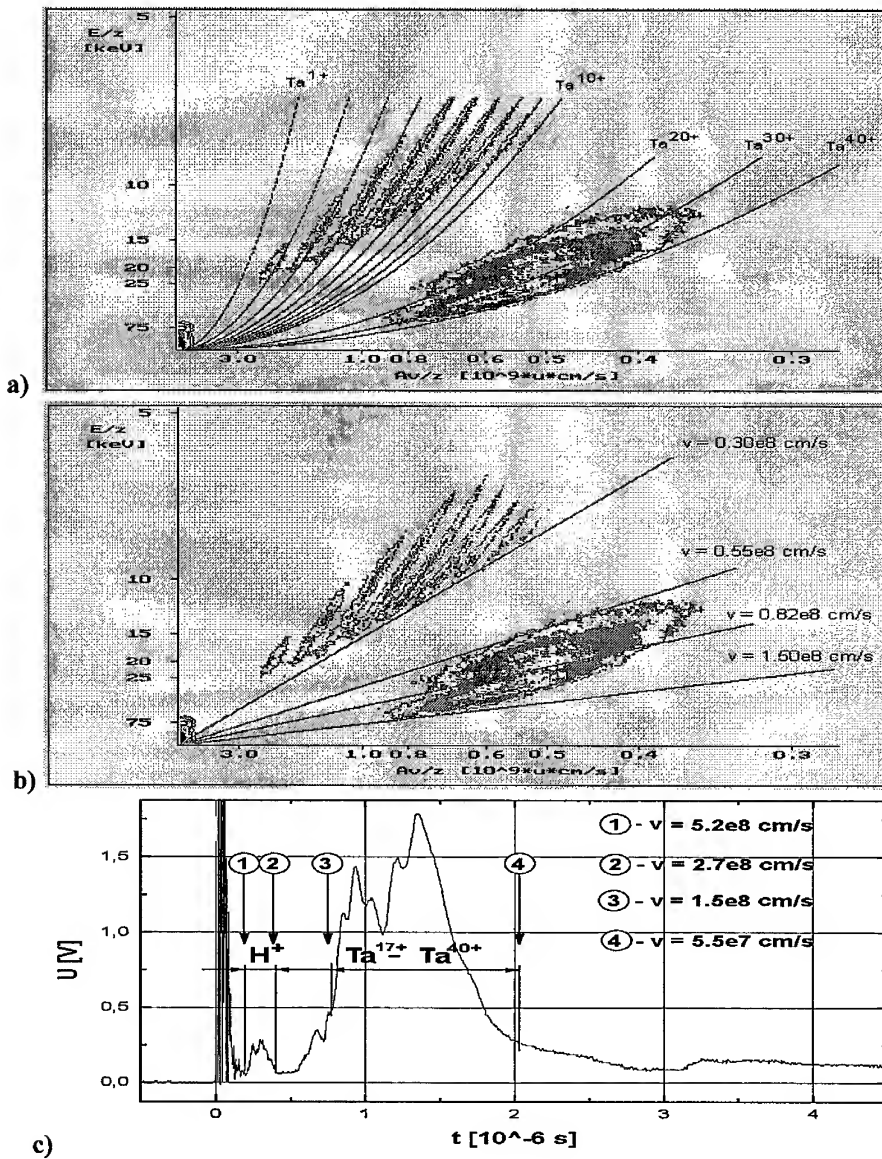
Fig. 1 a) theoretical parabolas matched to the measured, b) velocities of different Ta ion groups,
c) comparison of IC signal with velocities of highly charget Ta ion group.

74

The highest energy of Ta ions, measured in this experiment with an electrostatic ion energy analyzer (IEA), was $E \sim 7,7$ keV [6], what corresponds to velocity of $v \sim 2,9 \times 10^8$ cm/s. These fastest Ta ions are not registered by the TS, because amplification of one MCP amplifier is to low, only $\sim 10^3$-10^4, while amplification of the windowless electron multiplier used in the IEA is of about $\sim 10^8$.

In Fig. 1c the part of IC current corresponding to Ta ions with charge states $z \sim 18$-40 was marked. We have estimated the quantity of ions in this group under assumption that all ion species have the same percentage abundance in the IC current, and that average charge state of ions in this group was $<z> = 29$. This assumption underestimate the quantity of ions with the highest charge states $(z \sim 30$-40), because their percentage abundance is higher than percentage abundance of ions with lower charge states $(z \sim 18$-30) [7]. The secondary ion-electron emission coefficient was taken, equal to average charge state of ions in made estimation. However, this may not be exact because the calibration of ion detectors for multiply charged and high energy ions is necessary, as it follows from measurements made by Fry and Stockli [8]. Under these assumptions we have obtained fluency $N = 0.5 \times 10^8$ cm^{-2} of each ion species, from Ta^{18+}-Ta^{40+}, on the IC located in the distance L=111.5 cm from the target. It is equivalent with the value $N = 6.2 \times 10^{11}$ sr^{-1}. The average ion current compared with the other data [6], by reduction to the distance L = 94 cm, for all ions in this group, was estimated to be about $j = 6$ mA/cm^2.

Acknowledgments

References

[1] Woryna E et al *Laser Particle Beams* -in press
[2] Mróz W et al 1992 *Laser Particle Beams* **18** 689
[3] Mróz W et al 1996 *Rev. Sci. Instrum..* **67** 1272
[4] Chvojka M et al 1992 *Czech. J. Phys.* **42** 899
[5] Woryna E et al *Appl. Phys. Lett.* -in press
[6] Krasa J et al - in this issue
[7] Laska L et al *Czech J. Phys.* -in press
[8] Fry D and Stockli M P *Texas Section of the American Physical Society Conference, Lubbock, Texas,* 1995 -in press.

NANOSECOND TARGET PLASMA UNDER HARMONICS
RADIATION OF THE GIGAWATT ND-GLASS LASER

I.A.BUFETOV, V.B.FEDOROV AND S.B.KRAVTSOV

General Physics Institute of the Russia Academy of Sciences,

Vavilov Street 38, Moscow 117942, Russia

The unknown up-to-date empirical laws, concerning on the nanosecond laser plasma thermodynamic parameters (N,T) in one-dimensional plasma expansion region near the solid target, have been obtained.

'   Plasma heating on Al, Cu- targets was studied under Nd-glass laser harmonics radiation 10 ns- pulses with the sharp (about 1 ns) leading edge of the pulses through the wide range of experimental conditions: radiation wavelengths 1060, 530,   265   nm, laser radiation flux intensity $I=(10^9-10^{13})W/cm^2$, focal spot diameter $d=(0,08-3)$ mm. The targets were in the chamber with residual gas of a low pressure (0.1 Torr). The typical oscillogram of a second-harmonics laser pulse is shown of Fig 1a.
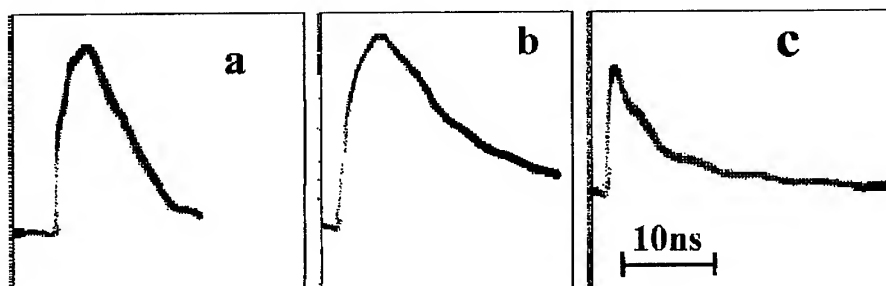
Figure 1. The laser pulse trace (a) and the double charged plasma layer potential traces
$U(t) \approx kT_e(t)/e$, obtained for $d=3.1mm$ (b) and for $d=0.08mm$ (c).

The plasma electron temperature T_e was measured with time resolution not worse than 1ns through the all range of experimental conditions. To determine the values $kT_e \approx eU$ the double charge layer potentials U at the plasma boundary were measured (see Fig.1b,c). The scheme of experiment is shown on Fig.2.
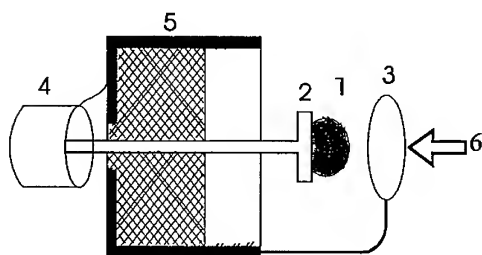
Figure 2. Schematic diagram of the target unit: 1 - laser plasma; 2 - metal target; 3 - probe ring; 4 - 75 Ω cable; 5 - coaxial connector; 6 - direction of propagation of laser radiation.

At the laser flux intensity $I=10^{13}W/cm^2$ X-ray spectroscopy was used to control alternatively the value of T_e for Al and Cu targets.

The measurement results for Al , Cu- targets are following [1]:

T_e, eV
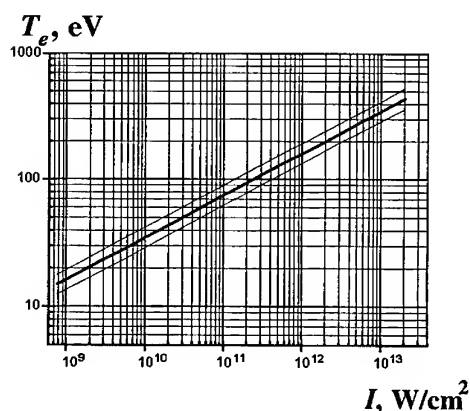
Figure 3. Dependence of the electron temperature of the plasma T_e on the laser radiation intensity. The thin lines are the limits of the expected error in the determination of T_e for the Al and Cu.

I, W/cm^2

The measured maximum plasma electron temperature T_e during the pulse time was reached in the region of one-dimensional plasma expansion near the target. The value T_e was obtained to be independent of the laser radiation wavelength and was governed only by its intensity: $T_e(eV)=(0,016\pm0,002)(I, W/cm^2)^{0,33\pm0,02}$.

The laser plasma pressure $P\sim I^{5/6}$ near the Al-target was measured as well. To find the dependence of a plasma pressure P on intensity of laser radiation I the value of ablative pressure pulse was measured by the ballistic pendulum. The results of measurements are presented on Fig. 4. The ratio between P and I is given by the empirical law $P(bar) = 5.9*10^{-5}*[I, (W/cm^2)]^{0.85\pm0.02}$ and was not depended on radiation wavelength.
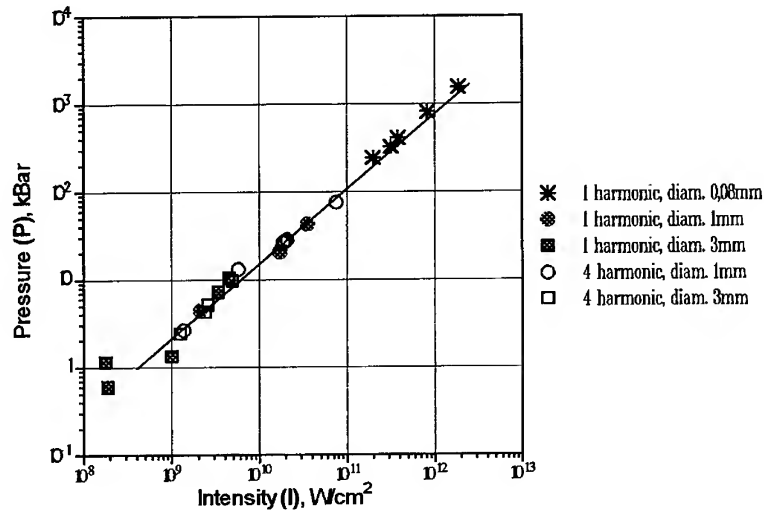
Figure 4. The mean pulse-time value of the laser plasma pressure.

In some previous publications [2,3] there are data on P(I) and $T_e(I)$ through the wide range of $I(W/cm^2)$ or $\alpha I(W/cm^3)$. In [2,3] the data of some original works were summarized. The discrepancy of the results of the reviewed works doesn't permit to find the P(I) and $T_e(I)$ scaling for "one-dimensional" laser plasma such as the one obtained in the present work.

It is possible find density of the Al- plasma. The plasma density, non depending on radiation wavelength (1060 and 265 nm) and being equal to

78

$N(cm^{-3})=N_e+N_i=2,3\times10^{15}(I, W/cm^2)^{0,52}$ in the region of one-dimensional plasma expansion near the target, was found using the (T_e, P) data. One supposed that in these experiments the laser plasma was near ideal one and its ion and electron components were in equilibrium state $T_i=T_e=T$.

To check conditions of ideality and thermal equilibrium of plasma, the time of thermalization of a plasma was calculated $\tau_{ei}\sim10^{-11}$s. It is less than the duration of leading edge of a laser pulse - 10^{-9}s. Through all the investigated range of laser radiation intensity $(10^9\div10^{13})$W/cm^2 the ratio is $\Delta U/T\leq0.1$ (ΔU is the potential energy of plasma) that permits to use the ideal model of plasma.

The Debye size $R_D\sim(1\div3)\times10^{-7}$cm is much shorter than d and the thickness of plasma layer near the target.

Thus, the thermodynamic parameters of "one-dimensional" plasma do not depend on a wavelength of laser radiation $\lambda=(1.06\div0.265\mu)$ and are governed only by its intensity I: $T\sim I^{1/3}$, $P\sim I^{5/6}$, $N\sim I^{1/2}$. This scaling is obtained for the first time.

We think that our results may be interpreted in the frame of the hydrodynamics theory of laser-plasma heating [4]. This problem is now under study.

References:

1. I.A.Bufetov et al. //Quantum Electronics 25 (8), p.794-798 (1995)

2. J.Ready.Effects of high-power laser radiation.AcademicPress,N.Y.London,1971.

3. V.I.Vovchenko et al.// J.Russian Acad.Sci.Physics-Doklady,1994,39,No.9,p.633.

4. Y.V.Afanas'ev et al.,Itogi nauki i tekhniki.,Radiotekhnika,v.17, Moscow, 1978.

INVESTIGATIONS OF PLASMA PRODUCED FROM A HIGH-PRESSURE GAS PUFF TARGET IRRADIATED WITH A NANOSECOND LASER PULSE

A. BARTNIK, H. FIEDOROWICZ, J. KOSTECKI, M. SZCZUREK
Institute of Optoelectronics, Military University of Technology, Warsaw, Poland

V.M. DYAKIN, A.YA. FAENOV, A.I. MAGUNOV, I.YU. SKOBELEV
Multicharged Ions Spectra Data Center, VNIFTRI, Mendeleevo, Moscow region, Russia

A.L. OSTERHELD
Lawrence Livermore National Laboratory, Livermore, CA 94551

This work is devoted to laser interaction with dense and underdense gas puff plasmas. The results of the performed experiment are presented. Three different regimes of the interaction were revealed. The creation of an elongated plasma structure in one of the regimes was shown. Spectra of He-like argon ions and monochromatic images of hot plasma regions are presented.

1 Introduction

A hot and dense plasma can be produced by irradiation of a gas puff target with a nanosecond high-power laser pulse. The plasma emits strong X-ray radiation in 1keV energy range [1]. In this paper we present the investigations of the plasmas produced using high-pressure argon gas puff targets with Nd:glass laser pulses up to 20 J of energy and duration of 1 ns.

2 Experimental setup

The gas puff targets were created by pulsed injection of gas from a high-pressure electromagnetic valve into vacuum. Gas was flowing from the valve through a circular sonic nozzle of 0.5 mm in diameter. The laser beam was focused onto the gas puff target perpendicularly to the flow of gas. The laser spot of about 0.1 mm in diameter was placed symmetrically at the axis of the nozzle. The distance between the center of the laser spot and the nozzle output was changed from about 0.2 mm up to 1.0 mm. The gas backing pressure in the valve was 15 atm. The maximum density of gas in the gas puff target was estimated from the x-ray backlighting measurements. It corresponded to the density of gas under the pressure of about 2 atm in room temperature. The value of the density was varied by changing the time delay between the laser pulse and the opening of the valve, or by increasing the distance between the laser focus spot and the nozzle output.

To study the laser gas puff target interaction the argon plasma parameters were measured using the spectral X-ray diagnostics [2]. Two crystal spectrographs for

two narrow wavelength ranges were used. One of them, containing a spherically bent mica crystal with radius R = 186 mm, working in modified Johann scheme, was adjusted for 3.9 Å to 4.1 Å range. The spectrograph was used to obtain spectra containing the He-like argon resonance line, together with the intercombination and dielectronic satellite lines. The second spectrograph, containing spherically bent mica crystal with radius R = 100 mm, was working in FSSR-1D scheme [3]. This spectrograph enabled to obtain spectra in wavelength range from 3.25 Å to 3.45 Å with one-dimension spatial resolution. To obtain X-ray images of gas puff plasmas a pinhole camera with 30 μm pinhole and 10 μm thick Be filter, or an X-ray microscope [3] were used. The microscope containing spherically bent mica crystal with radius R = 186 mm was adjusted to obtain two-dimensional images of a hot plasma region in two lines $1s2p^1P_1$ - $1s^2$ and $1s2p^3P_1$ - $1s^2$ of He-like argon ions with magnification 1.5 and 2.2 counterpartly.

3 Experimental results

The X-ray spectrum near the $1s3p$ $^2P_1$ - $1s^2$ $^1S_0$ line of the He-like argon is presented in Fig. 1. Spatial size of a hot argon plasma containing He-like ions estimated from such spectra was about 100 μm. The temperature of the hot plasma estimated from relative intensities of the resonance and dielectronic satellite lines was about T_e = 600 eV. The satellite spectrum however is sensitive both to electron plasma temperature and density. So, the spectra obtained in experiment were compared to the spectra calculated using the procedure described in [4]. In our case this method gave N_e = 10^{21} cm^{-3} and T_e = 620 eV for plasma region where He-like argon emission occurs.

resonance   satellite
line   lines
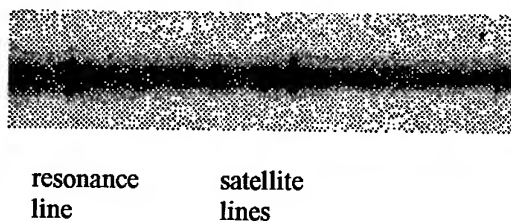
Fig. 1. A spatially resolved spectrum for a plasma structure produced as a result of irradiation of the gas puff argon target with 9 J laser energy.

Typical X-ray images of the plasmas obtained with a pinhole camera are presented in Fig. 2. Three characteristic types of the images were obtained during the experiment. The image presented in Fig. 2a is nearly symmetric according to the plane, perpendicular to the laser beam axis, containing the hottest plasma region. Second type of the image (Fig. 2b) is strongly asymmetric along the axis

and is similar to images of plasmas obtained for a solid target. Third type of images (Fig. 2c) is also asymmetric along the axis, but is different from images obtained for a solid target. One can see a characteristic elongated plasma structure along the axis of laser beam. This structure in different shots was about 300 - 450 mm long and its diameter was about 150 μm.
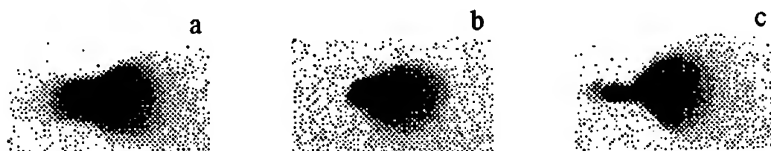
Fig. 2 Typical pinhole images of gas puff plasma.

Some qualitative information on laser energy not absorbed in the plasma we have obtained with a photographic paper placed behind the gas puff target on the laser beam axis. From these measurements it is evident that pinhole images of the second type (Fig. 2b) occur in a case when electron plasma density reaches critical value (the dense plasma case). Pinhole images of the first type (Fig 2a) occur for the underdense plasma. Third type of images occurred in all cases when laser pulse was sufficiently strong and the gas density gradient was large enough.

Spectra with one dimension spatial resolution obtained from the FSSR-1D spectrograph indicate that the radiation coming from $1s3p^1P_1$ - $1s^{2\,1}S_0$ transition in He-like argon was emitted by two hot plasma regions of the size of about 100 μm placed along the axis of laser beam, separated by the distance of about 250-300 μm. To obtain those results the spectrograph was placed in two positions, to have spatial distribution in two perpendicular directions.

A typical two-dimensional image of a hot plasma region in $1s2p^1P_1$ -$1s^2$ line is shown in Fig. 3. The plasma image in this case consists of two spots coming from two intense radiating hot plasma regions. The occurrence of such separate regions together with the presence plasma structure visible on pinhole images are the most important results obtained during the experiment.
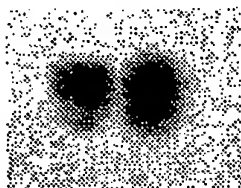
Fig. 3. Plasma image in single line radiation of He-like argon plasma.

82

4 Conclusion

We have presented the preliminary results of the experiment concerning the creation of plasma channel during the interaction of nanosecond laser pulse with gas puff plasma. Parameters of the plasma have been measured. We have roughly defined the conditions of formation of the elongated plasma structure. More detailed analysis of the results will be presented in separate paper.

References

1. H. Fiedorowicz, A. Bartnik, Z. Patron, P. Parys, Appl. Phys. Lett. **62**, 2778 (1993).
2. A. Bartnik, V.M. Dyakin, A.Ya. Faenov, H. Fiedorowicz, J. Kostecki, A.I. Magunov, I.Yu. Skobelev, M. Szczurek, Kwantowaya Elektronika (in press).
3. I.Yu. Skobelev, A.Ya. Faenov, B.A. Brunetkin, V.M. Dyakin, ZETF **107**, 1263 (1996).
4. I.Yu. Skobelev, A.Ya. Faenov, V.M. Dyakin, H. Fiedorowicz, A. Bartnik, M. Szczurek, P. Beiersdorfer, J. Nilsen, A.L. Osterheld, Phys. Rev. E (in press).

MEASUREMENT OF THE IN-FLIGHT PUSHER DENSITY OF AN INDIRECT DRIVE CAPSULE IMPLOSION USING X-RAY BACKLIGHTING

D.H. KALANTAR, S.W. HAAN, B.A. HAMMEL, C.J. KEANE,
O.L. LANDEN, AND D.H. MUNRO
Lawrence Livermore National Laboratory, Livermore, CA 94551

Both the efficiency of an implosion and the growth rate of hydrodynamic instability increase with the aspect ratio of an implosion. In order to study the physics of implosions with high Rayleigh-Taylor growth factors, we use doped ablators which should minimize x-ray preheat and shell decompression, and hence increase in-flight aspect ratio. We use x-ray backlighting techniques to image the indirectly-driven capsules. We record backlit 4.7 keV images of the full capsule throughout the implosion phase with 55 ps and 15 μm resolution. We use these images to measure the in-flight aspect ratios for doped ablators, and we inferred the radial density profile as a function of time by Abel inverting the x-ray transmission profiles.

1   Introduction

In indirectly driven inertial confinement fusion (ICF)[1], a fusion capsule is bathed in soft x-rays created inside a hohlraum. The x-rays ablate the outer surface of the capsule, causing it to implode and compress the fuel. The fuel filled capsules may suffer from preheat due to the x-rays. In order to maintain a low adiabat for the fuel during the implosion, it is necessary to shield the fuel from the x-rays. This is done by introducing dopants that will effectively absorb the x-rays and prevent them from preheating the fuel[2].

The dopant added to the ablator prevents the x-ray drive from preheating the capsule, and as a result, maintains a sharper density gradient and improves both the implosion efficiency and hydrodynamic instability growth[3,4]. To characterize the implosion efficiency and the hydrodynamic instability, we use x-ray backlighting techniques to measure the in-flight areal density of the pusher in an x-ray driven imploding capsule. Previous images of an indirectly driven implosion were used only to provide a measure of the implosion velocity and low-mode distortion[5]. We show large area backlit images that we use to perform radial intensity lineouts and to unfold a radial density profile.

2   X-ray backlit implosions on Nova

We used x-ray backlighting techniques[6] to image an x-ray driven implosion capsule on the Nova laser. The 510 μm diameter plastic capsule consisted of a 3 μm thick polystyrene shell with a 3 μm thick layer of polyvinyl alcohol (PVA), and a 34 μm thick ablator layer coated on the

outside. For some experiments the ablator was doped with germanium to shield the fuel from x-ray preheat.

The capsule was placed at the center of a cylindrical gold hohlraum shown in Figure 1. There were two 650 μm diameter diagnostic access holes in the hohlraum, positioned on opposite sides at the midplane of the hohlraum, and covered with 150 μm thick CH foils. A Ti backlighter disk was positioned approximately 3 mm from the center of the hohlraum, collinear with the capsule and diagnostic holes, and with the diagnostic line of sight for backlit imaging.
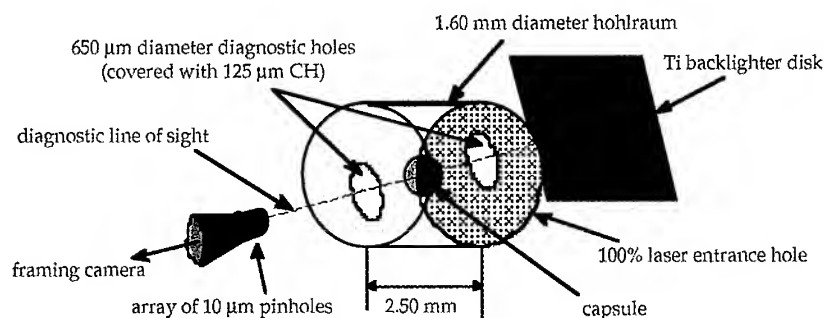
Figure 1: Diagram of the backlighter hohlraum target on Nova.

We used 8 beams of Nova at 0.35 μm to create the x-ray drive in the hohlraum. These beams delivered about 25 kJ in a 2.2 ns pulse with a peak power of about 18 TW. We used two beams at 0.53 μm for the backlighter. These were configured with random phase plates, and focused with a ~700 μm focal spot on the Ti backlighter foil at about 5×10^{14} W/cm2 to generate a large area x-ray backlighter. The laser pulse shape on these two beams was 2 ns square, which gave us a constant intensity of Ti K-shell x-rays. By filtering with 12 μm Ti, the spectrum is nearly monochromatic, principally in 4.7 keV emission from the $1s2p-1s^2$ line of Ti.

We recorded radiograph images of the fusion capsule at various times during the implosion over a range of 3 ns using a gated x-ray framing camera[7,8]. The x-ray camera was configured with 10 μm pinholes at 8X magnification, and it had a gate width of 55 ps.

Figure 2 shows a series of backlit images of implosions using a Ge doped ablator. These images are shown corrected for the diagnostic flat-field and for the spatial emission intensity profile of the x-ray backlighter, which we characterized by imaging the backlighter foil from the back side.
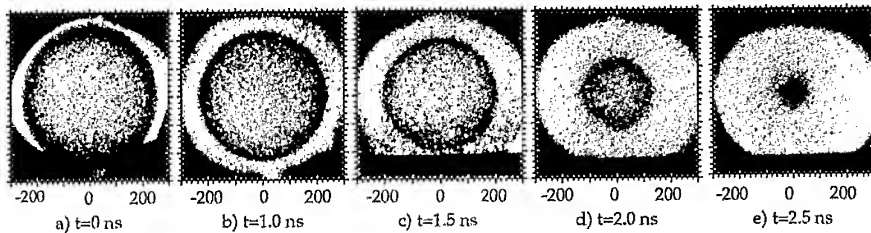
Figure 2: Series of x-ray backlit images of a Ge-doped implosion capsule on Nova. The scales are in microns at the target.

3   In-flight pusher density profile

The images shown in Figure 2 were obtained on two Nova target shots. For each shot, the capsule had an initial outer radius of 255 μm. We performed a radial lineout of each image, averaging in the azimuthal direction. For images where we had a view of unattenuated backlighter around the full azimuth, we averaged around the full 360°. For others where the capsule was partially eclipsed by the diagnostic holes, we were limited to a smaller section of the azimuth.

We performed an Abel inversion of the radial lineouts by assuming that the capsule is spherically symmetric, and that the images are monochromatic. If we then divide the Abel inverted lineouts by the cold opacity for Ge-doped polystyrene, these lineouts represent the density profile of the capsule pusher. They provide a measurement of the radius and the aspect ratio as a function of time.

We plot the radial density profile calculated by Abel inversion for several times in Figure 3. Note that we have smoothed the inverted lineouts at small radius. The azimuthal average smooths the radial lineout at large radius, but we are dominated by the noise statistics and speckle of the backlighter profile at small radius.

We measured the radius of the half maximum density on the outer edge of the Abel-inverted lineouts. This is shown in Figure 4, plotted with the aspect ratio which we calculate as the average radius to the full width at half maximum of the radial density profile for each time. The hohlraum drive temperature is also shown in the graph for timing.

4   Summary

We have used x-ray backlighting techniques to record images of an indirectly driven ICF capsule on Nova. These large area images of the full capsule provide quantitative information about the in-flight pusher

86

density profile as a function of time. This technique may be used to characterize the in-flight aspect ratio of capsules, providing information about the efficiency and hydrodynamic instability of an implosion.
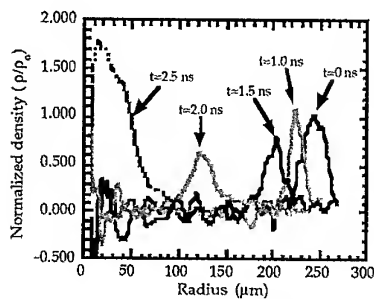
Figure 3: Radial density profiles calculated by Abel inverting radial lineouts of the x-ray transmission through the capsule.
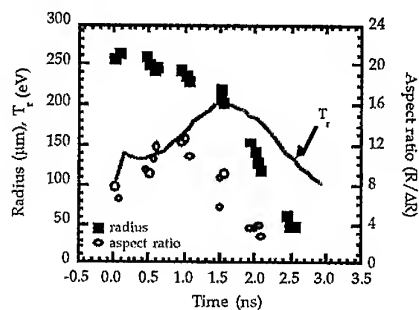
Figure 4: Radius and aspect ratio of the capsule as a function of time. The x-ray drive is overlaid for timing.

Acknowledgments

References

[1] J. Lindl, *Phys.Plasmas* **2**, 3933 (1995).
[2] O. L. Landen *et al*, "Effects of variable x-ray preheat shielding in indirectly-driven implosions", to appear in *Phys. Plasmas*.
[3] O. L. Landen *et al, J. Quant. Spectrosc. Radiat. Transfer* **54**, 245 (1995).
[4] C. Keane *et al, J. Quant. Spectrosc. Radiat. Transfer* **54**, 207 (1995).
[5] M. Katayama *et al, Rev. Sci. Instrum.* **64**, 706 (1993).
[6] S. G. Glendinning *et al*, in *Applications of Laser Plasma Radiation II*, (SPIE, Bellingham, WA, 1995), Vol. 2523, pp. 29-39.
[7] D. K. Bradley *et al, Rev. Sci. Instrum.* **66**, 716 (1995).
[8] P. M. Bell *et al*, in *Ultrahigh and High Speed Photography, Videography, and Photonics '94* (SPIE, Bellingham, WA, 1994), p. 234.

TIME-RESOLVED MEASUREMENTS OF STIMULATED RAMAN SCATTERING IN LASER PRODUCED PLASMA.

E.A.BOLKHOVITINOV, V.Y.BYCHENKOV, M.O.KOSHEVOI, M.V.OSIPOV,
A.A.RUPASOV, A.S.SHIKANOV, V.T.TIKHONCHUK,
A.V.KILPIO[*], N.G.KISELEV[*], D.G.KOCHIEV[*], P.P.PASHININ[*], E.V.SHASHKOV[*],
Y.A.SUCHKOV[*].

Lebedev Physical Institute and [*]General Physics Institute, Moscow, Russia

Abstract. Experimental results of stimulated Raman scattering (SRS) investigation obtained on Nd-glass laser installation are explained on the basis of representations about possibility of plasma profile flat regions formation and their motion. Low and high electron density SRS spectrum cut-off are discussed as well as time-integrated and time-resolved SRS spectrum features.

Experimental results.

In experiments described in publications [1-3] the stimulated Raman scattering (SRS) was studied for massive targets, thin foils and the previously prepared plasma. An intermediate case of laser interaction with target, when a target thickness was greater than, but comparable with the depth of burning-through, was investigated in this report. That is the most interesting case for controlled fusion schemes because it corresponds to the largest coefficient of laser energy conversion into the target kinetic energy.

The SRS in laser produced plasma was studied on a single-channel laser installation "Kamerton" [4]. The plasma was produced by 2.5ns and 30-80J (λ_0=527nm) laser pulse focused onto plane polyethylene targets of 5-12μm thicknesses. The focusing spot dia was ~100μm, the flux density of the heating radiation reached $3*10^{14}$ W/cm^2.

SRS was observed at different angles θ to the heating beam with different spectral resolution $\Delta\lambda$, time resolution Δt and spatial resolution Δx. All the observed SRS spectra for angles observations θ=135^0 and 180^0 and 6 μm foil thickness were located in a wavelength range $\lambda_{min}<\lambda<\lambda_{max}$, where λ_{min}=610-650 nm and λ_{max}=690-750 nm. In accordance with dispersion equations for Raman scattering each wavelength λ is connected with the definite scattering plasma density n:

$$n/n_c=(1-\lambda_0/\lambda)^2 \qquad (1)$$

where n_c - electron critical density, λ_0 – heating radiation wavelength. For instance, the measured values of λ_{min}= 640nm and λ_{max}=725nm correspond to the density
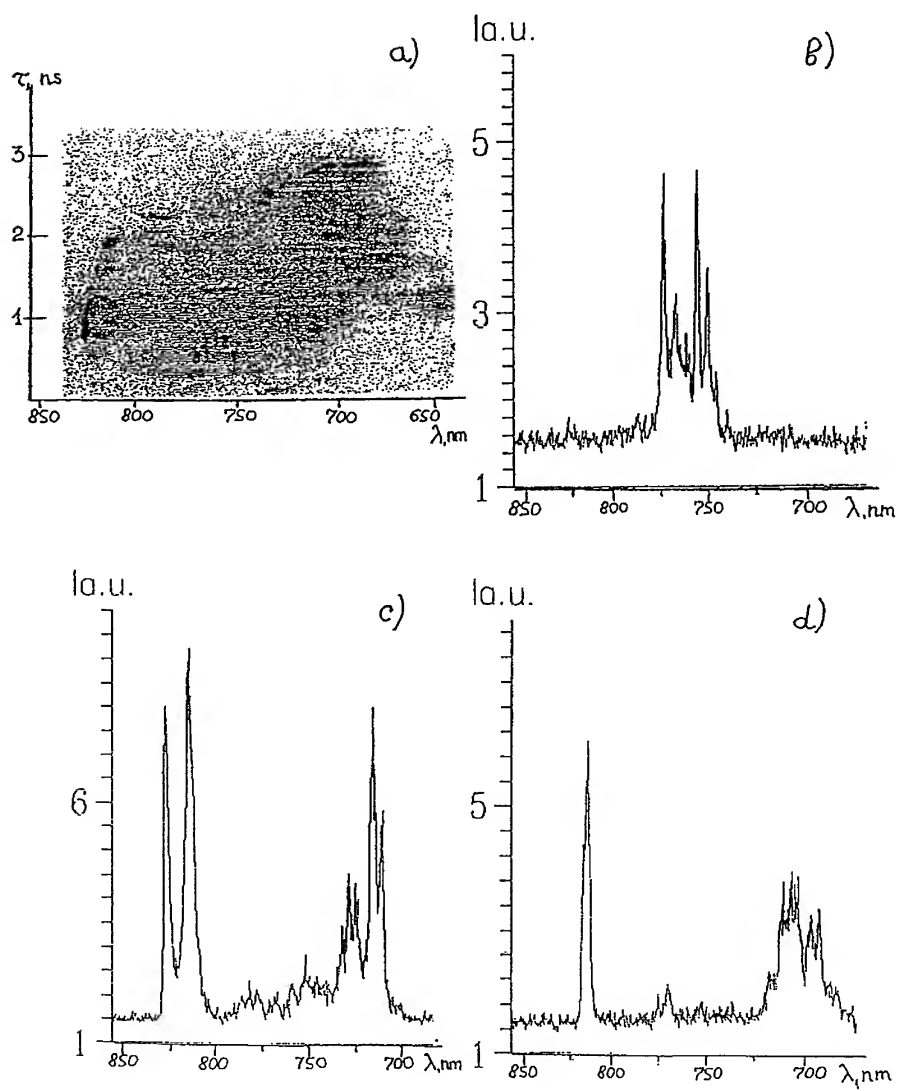
Figure 1 (a) – Time resolved SRS spectra from a thin foil target.
(b),(c),(d) – SRS radiation intensity distributions for time moments
0.5ns, 0.9ns and 1.9ns respectively.

values of n_{min}= 0.030n_c and n_{max}=0.075n_c. Two scales of intensity modulations were observed with distance between peaks $\Delta\lambda$~0.5-1.0nm and 10-20nm. With increase of the foil thickness up to 12μm the SRS intensity decreases, the SRS spectrum is narrowed and shifted to longer wavelengths. At the angle 90^0 to the heating beam no SRS was recorded.

The time-resolved SRS spectra had a complex structure. Typical time-resolved spectrogram is presented on Fig.1a. In the initial part of the laser pulse the SRS radiation of long wavelengths arises and then during laser pulse duration the spectrum is shifted to the shorter wavelengths, i.e. the region of scattering is shifted to the more rare plasma. Therefore the SRS duration at separate wavelength is rather shot (~0.8ns) than the total duration (~2.5ns). There are two types of modulation - temporal (~0.1ns) and spectral (~50nm). Fig.1b-1d present intensity distribution obtained from time-resolved spectrum of Fig.1a for three time moments. For more thick foils the SRS dynamics is changed - the scattered radiation begins simultaneously almost in broad spectral range and there is no the strong dependence of radiation wavelength on time.

Discussions.

The fact of SRS observations suggests that the laser intensity is above the threshold level in the certain density region. Usually the low density (small wavelength) cut-off of the SRS spectrum is related to the rise of the SRS threshold due to the enhanced Landau damping in a low density plasma. Because of the exponential growth of the Landau damping with the wavenumber it is reasonable to consider the inequality

$$k_p r_{De} < 1/3 \qquad (2)$$

as the necessary condition for the SRS (where k_p - plasma wave wavenumber, r_{De} - electron Debay radius). For back scattering $k_p=2k_o$ (k_o - heating radiations wavenumber) and from (2) one can obtain the impression for electron temperature

$$T_e = (m_e c^2/36)*(n_{min}/n_c) \qquad (3)$$

From equations (1) and (3) for a minimum wavelength λ_{min}=630 nm the value of low density cut-off n_{min}=0.025n_c and the evaluation of electron temperature T_e=350eV can be obtained. We can accept this estimate as an overall plasma corona temperature which is valid for the higher densities too. Now about high density cut-off n_{max}, which is equal to 0.09n_c from (1) for λ_{max}=750 nm. It is possible to suggest that this cut-off at electron density n_{max} is also related to the SRS threshold condition. The formula for SRS threshold:

$$v_{e,th}^2 / c^2 = v_{ei}^2 \omega_p / \omega_o^3 + \pi\lambda_o / L_n \qquad (4)$$

where v_e - electron oscillation velocity in laser field exiting SRS instability for $v_e > v_{e,th}$, v_{ei} - electron-ion collision frequency, L_n - electron density scale length.

90

The dissipative SRS threshold (the first item in eq.(4)) is below 10^{13} W/cm^2 for $T_e{\sim}350$eV. However the convective part of the threshold (the second item in (4)) is very large, so that we should assume the inhomogeneity scale length $L_n \sim 3$cm in order to get the necessary threshold intensity about $3*10^{14}$ W/cm^2. This is an unrealistically large length. Meanwhile SRS simulations [5] in the model of homogeneous plasma slab show that the interaction length about 50μm is enough to amplify backscattering signal 400 times above the noise level. Therefore if we assume the existence of one or several local flat regions on the plasma density profile (similar to observed in [6] and supposed also in [7]) it is possible to explain the exiting of SRS for used laser flux density. Such flat region can not stay too long, but the time scale about 10-20 ps is enough to excite SRS and get it into the saturation. Then the flat interaction region can by destroyed (due to the SRS itself or because of hydrodynamic motion of plasma) and appears later in the different place of plasma. This scenario suggests that the instantaneous SRS emission has a very narrow spectral line but it randomly changes its position during the pulse. This may by related to the peak structure of the observed SRS spectra. The motion of flat regions down along the density profile will give the decreasing the SRS radiation wavelength, illustrated by Fig.1b-1d. The high density SRS cut-off we can attribute to steeper gradients in the region $n/n_c{>}0.1$ where a laser beam can not produce flat profiles of the necessary extent. Also the plasma from more thick foil targets has more steep density profile and therefore the possible flat regions should be shorter and generate less SRS that is in accordance with experimental measurements.

References

1. Laser Programm Annual Report - LLNL UCRL, 50021-86, Livermore, (1986).
2. Walsh C.J. et al. *Phys.Rev.Letts*, **53**, p.1445 (1984).
3. Bulatov E.D. et al. *in Proceeding 12st ECLIM*, p.13 (1979).
4. Kilpio A.V., Kiselev N.G., Kochiev D.G. et al. "Interaction of Nd-glass laser second harmonic radiation with plane targets on "Kamerton" installation," *in Proceedings of the 21st ECLIM* , pp.95-98 (1991).
5. Kolber T., Rozmus W., Tikhonchuk V.T., *Phys. Plasmas*, v.**2**(**1**), pp. 256-273 (1995).
6. Zaharenkov Yu.A., Zorev N.N., Krohin O.N., Mikhailov Yu.A., Rupasov A.A., Sklizkov G.V., Shikanov A.S., Pisma v ZhETF, **21**(**9**), pp.557-561 (1975).
7. Seka W. et al. Phys. Fluids 27(8), pp. 2181-2186 (1984)

LASER DRIVEN SHOCK EXPERIMENTS.

A. M. EVANS, S. D. ROTHMAN, P. GRAHAM

AWE Aldermaston Berkshire RG7 4PR

Using a streaked optical breakout diagnostic the uniformity of shocks driven into aluminium witness plates by our standard 1mm hohlraum heated by two 1ns long 500J laser pulses at 532nm are compared with those driven directly by one arm of the AWE HELEN laser at irradiances of 8×10^{14}, 2×10^{14} and 3×10^{13} W/cm^2. The diagnostic technique used in the direct drive case has allowed an evaluation of the HELEN laser spot at varying degrees of defocus to be made. Variations in the measured breakout times across the spot diameter are related to intensity perturbations in the beam. Comparisons are made between the experimentally measured shock break out times and the 1-D NYM simulations for varying laser fluences. The excellent degree of uniformity seen across the drive region from our standard hohlraum has allowed a successful equation-of-state campaign to be fielded[1,2].

1. Indirect Drive.

The standard long pulse HELEN hohlraum is a simple gold cylinder of 1:1 aspect ratio and is heated by two 450J 900ps 532nm laser pulses. The filling holes measure 500μm in diameter and are positioned on the 30 degree line in the curved wall. The cylinder is closed at one end and there is a 600μm diameter diagnostic hole in the other end wall over which an aluminium witness plate is mounted. Two optical streak cameras with orthogonal slits viewed a magnified image of the rear of the witness plate and recorded its brightness as a function of time. Figure 1 shows the standard long pulse Helen hohlraum together with the shock breakout diagnostic.

Long pulse driver

Streak cameras
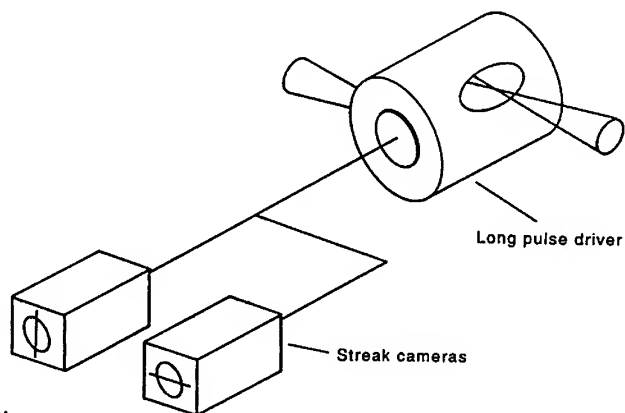
Figure 1.

The beam line was heavily filtered with plates of OG590 filter glass. This together with the cathode response of the camera meant that the spectral window of the diagnostic was between 600 - 750nm. A timing fiducial was provided on the streak records by splitting off a small fraction of the heating beam, frequency converting it and piping it via a fibre optic to the input slit of both cameras. The temporal position of this fiducial marker relative to the peak of the heating beams was established in a dedicated series of shots prior to the main experimental series. Shock planarity for the best shots on a 46μm Al foil as observed by two streak cameras recording the shock breakout from two orthogonal strips ~8μm wide across the witness plate diameter, was measured to be ~$\pm$6 - 12ps over the central 300μm diameter. This corresponds to a drive(pressure) uniformity of <1% in X-Ray flux and confirms initial design predictions. Figure 2 shows a typical streak record from a flat Al witness plate.
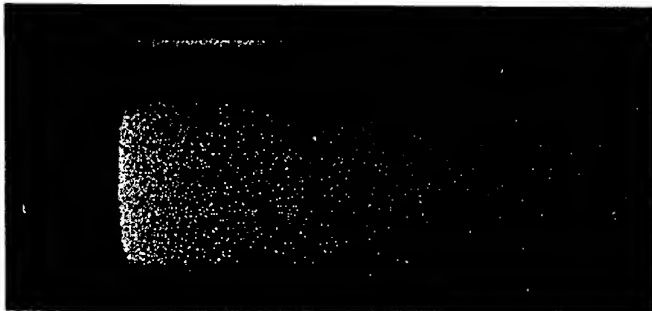
Figure 2.

The timing fiducial can be seen above the breakout record. Some deviations from planarity were seen on some shots and these are attributed to a tilt or kink in the foil relative to the axis of the hohlraum. Shock velocity measurements on stepped and wedged aluminium foils driven by this hohlraum have shown that pressures of up to 10Mbar can be generated[1,2].

2. Direct Drive.

The ratio of the measured fastest and slowest absolute breakout times t_1 and t_2 across the shock front propagated into an aluminium foil by direct drive may be related to the degree of intensity nonuniformity (I_1/I_2) within the laser focal spot.

The peak shock pressure P(MBar) generated by the laser pulse ($\lambda\mu$m, irradiance I in units of 10^{14} W/cm^2) and ignoring 2-D effects can be approximated by[3]:-

$$P \sim 7\,\lambda^{-0.5}\,I^{0.66}$$

with pressure $\qquad$ $P \sim v^2$

$$I \sim v^3 \qquad\qquad \text{taking}$$

for constant thickness $\qquad$ $v \sim t^{-1}$

Hence $\qquad$ $(I_1/I_2) = (t_2/t_1)^3$

Using the same optical diagnostic as above Figure 3 shows typical shock breakout streak records from aluminium witness plates directly driven with a 200ps laser pulse in a 400μm diameter $(8 \times 10^{14}$ and 2×10^{14} W/cm^2) and 800μm diameter $(5 \times 10^{13}$ W/cm^2) spot, also shown is the calculated intensity nonuniformity.

8 X 10^{14} W/cm^2	2 X 10^{14} W/cm^2	3 X 10^{13} W/cm^2
#3795V Intensity Ratio 1.3:1	#3829V Intensity Ratio 1.6:1	#3830V Intensity Ratio 1.5:1
8 X 10^{14} W/cm^2	2 X 10^{14} W/cm^2	3 X 10^{13} W/cm^2
#3795H Intensity Ratio 1.2:1	#3829H Intensity Ratio 1.3:1	#3830H Intensity Ratio 1.5:1
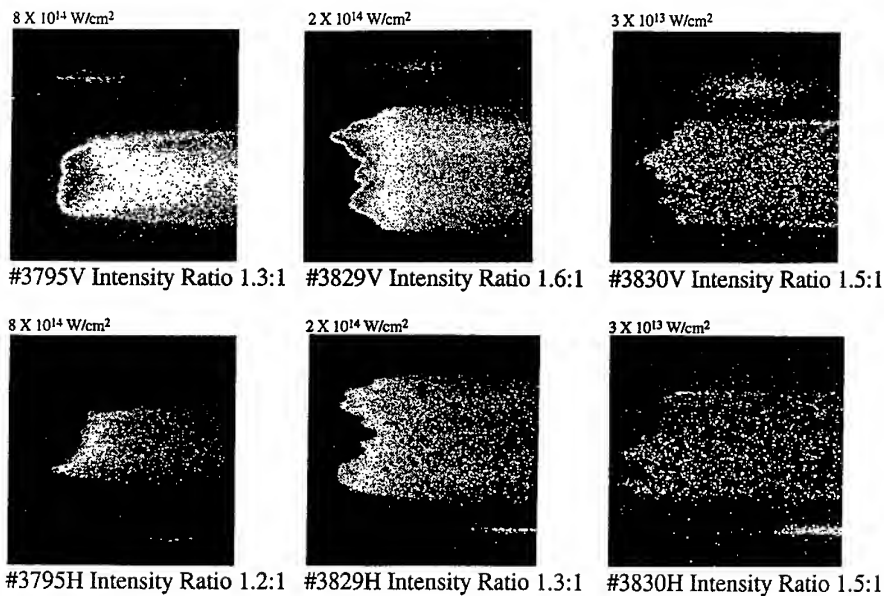
Figure 3.

Figure 4 shows that good agreement was seen between the experimentally determined absolute shock breakout times and their respective 1-D NYM simulations for varying laser fluences. It is suspected however that at the higher intensities 2-D effects are becoming more significant[3].
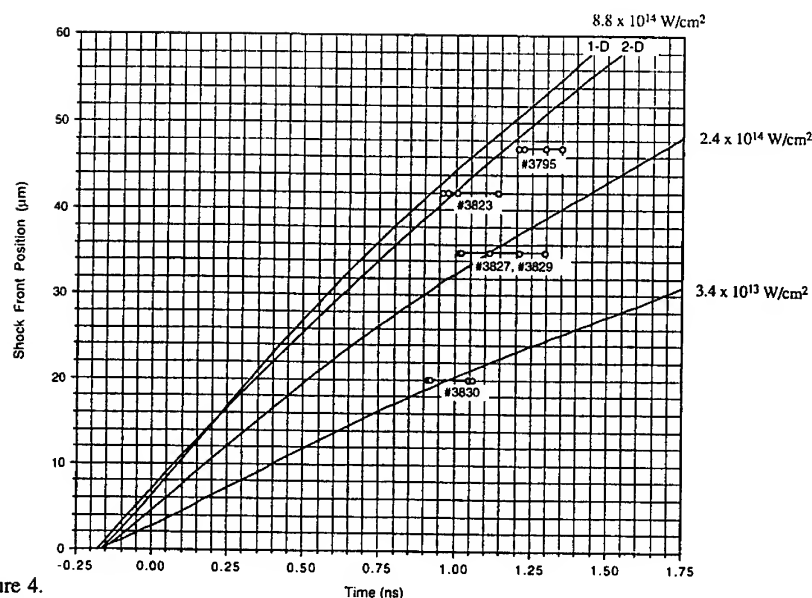
Figure 4.

3. Conclusion

We have demonstrated that indirect drive with our standard hohlraum is capable of producing a shock front with excellent planarity that is ideally suited as the driver for our EOS programme. Data from a recent series of Hugoniot experiments are presented in a companion paper. Shock fronts driven directly however exhibit considerable structure. This structure makes them far from ideal for use in hydro-experiments. However the information gained from shock breakout measurements on directly driven foils has provided valuable information on the intensity profile of our laser beam for varying degrees of defocussing.

Acknowledgment.

Reference

1. A. M. Evans *et al*, Proceedings of the 23rd ECLIM 1994 page 235.
2. A. M. Evans *et al*, Laser and Particle Beams. Vol 14, No. 2 1996.
3. P. C. Thompson, P. D. Roberts, Laser and Particle Beams. 2(1) pp13 - 26 (1984)

DIAGNOSTIC DEVELOPMENT AT LLNL FOR THE NATIONAL IGNITION FACILITY

T. C. SANGSTER, M. D. CABLE, J. D. KILKENNY, R. A. LERCHE,
M. B. NELSON, M. J. MORAN, D. RESS, J. E. TREBES,
R. E. TURNER AND T. W. PHILLIPS*
Lawrence Livermore National Laboratory
L-481, P.O. Box 5508
Livermore, CA USA 94550

ICF implosions at the NIF will produce core plasma temperatures in excess of 10-keV and densities of order 100 g/cm^3. Properties of these plasmas can be measured using a variety of optical, x-ray and nuclear techniques similar to those now in use at facilities such as Nova and Omega. Some of these techniques will be directly applicable on NIF while others, particularly the nuclear-based techniques, will change significantly.

The National Ignition Facility (NIF) will deliver ~1.8 MJ of 0.35-μm light onto mm-scale hohlraum targets with the expectation of controlled thermonuclear ignition and gain (20-MJ yield). Ignition targets will achieve core plasma temperatures in excess of 10-keV and densities of order 100 g/cm^3. Under these conditions, the fusion yield will far surpass (by 4-5 orders of magnitude) the record neutron yields achieved at Nova (4 x 10^{13}) and, more recently, at Omega (10^{14}). However, long before the first ignition experiments occur, a comprehensive set of diagnostic measurements will be required to validate the performance of both the laser and the hohlraum targets. Many of these diagnostics have counterparts at laser facilities such as Nova; however, some will require the development of new techniques and instrumentation.

Apart from the standard laser system diagnostics (pointing, focusing and synchronization), the diagnostics required to validate NIF hohlraum targets fall into two distinct categories – those used to measure the hohlraum temperature and radiation drive spatial symmetry, and those used to characterize the performance of the imploding capsule. The first category of diagnostics will utilize x-ray imaging systems and shock break-out measurements; the second category will rely heavily on nuclear-based techniques and instrumentation. With ignition neutron yields approaching 10^{19}, the challenge will be to develop instrumentation and techniques which are both robust and reliable.

Fuel Areal Density

One of the most critical parameters used to assess both laser and hohlraum performance will be the fuel areal density, <ρR>, at burn time. On Nova, <ρR> is determined by measuring secondary neutron production.[1] This technique is appropriate for modest values of <ρR> (< 0.1 gm/cm^2) but fails at the higher NIF densities (~1.0 g/cm^2) where the range of the primary charged fusion products (p, t, α) is small relative to the size of the fuel core. Indeed, cryogenic d-t ignition capsules require that the primary d-t α's deposit their full kinetic energy in the fuel to initiate and sustain the thermodynamic burn. Consequently, a mechanism for probing the fuel density at burn time is the spectroscopic measurement of tertiary neutrons and protons.

Both tertiary neutrons and protons are produced with energies up to 30 MeV, easily escaping the dense fuel core. The production mechanism for tertiary neutrons (replace the triton with a ^{3}He in reaction 3 for tertiary protons; note too, that the d and t can be interchanged in reactions 2 and 3) proceeds according to the following reactions:

$$d + t \rightarrow \alpha\ (3.5\ \text{MeV}) + n\ (14.1\ \text{MeV}) \tag{1}$$
$$n\ (14.1\ \text{MeV}) + d \rightarrow n^{\cdot} + d^{\cdot}\ (< 12.5\ \text{MeV; elastic scattering}) \tag{2}$$
$$d^{\cdot}\ (< 12.5\ \text{MeV}) + t \rightarrow \alpha + n\ (< 30.8\ \text{MeV}) \tag{3}$$
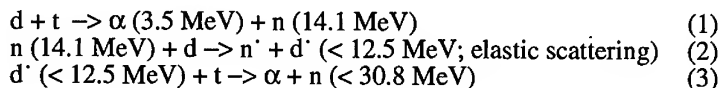
Spectroscopic measurement of these protons and neutrons samples the energy loss of the secondary deuteron in the high density fuel before the tertiary reaction occurs. The shape of the tertiary neutron energy spectrum is then a convolution of the two-body scattering kinematics in 2) with the deuteron fuel core energy loss distribution prior to the fusion in step 3). Figure 1 shows a calculated neutron energy spectrum from a Nova scale hohlraum target. The fuel areal density can be determined from the shape of the spectrum and the absolute yield of tertiary neutrons or protons (approximately proportional to $<\rho R>^2$ for small deutron and triton slowing).

In addition, measuring tertiary proton energy loss (up to 10 MeV) in the fuel further constrains the estimate of total $<\rho R>$. Since the protons sample the fuel density along their flight path, it is possible to estimate implosion asymmetries by comparing proton energy loss along different paths.[2]

A prototype proton spectrometer is currently being developed jointly by LLNL, MIT and LLE for near term tests on both Nova and Omega. The spectrometer will be based on a permanent sector magnet which bends the high energy protons ~30° into an array of CCD detectors placed along the magnet mid-plane. This detector should be implemented on Nova during the summer of 1997. Tertiary neutrons will be measured at NIF using an energy and time-of-flight array similar to LaNSA[3] currently in operation on Nova.

Figure 1. Calculated d-t neutron energy spectrum from a scale-1 hohlraum on Nova. The tertiary neutrons are simply those with a kinetic energy above a threshold of about 17 or 18 MeV (comfortably above the secondary neutron energy).

Imaging

Imaging diagnostics on NIF will include a variety of x-ray pin-hole cameras, gated imagers as well as Wölter and K-B optics. One of the primary difficulties with implementing most of the Nova imaging systems on NIF is the large standoff distance required between the target and pin-hole aperture.

A Wölter optic (such as the 22x microscope on Nova) can be placed a considerable distance from the target. However, the coated optic of a Wölter mirror

is extremely expensive to fabricate using conventional techniques. Therefore, an alternative concept is being pursued at LLNL which is based on replica technology. A precision mandrel is fabricated with the required shape tolerance and surface finish. A multi-layer coating is deposited on the mandrel along with a backing for strength. The optic is then removed from the mandrel in multiple azimuthal sectors yielding a relatively large number (4 - 8) of individual x-ray mirrors. The mandrel can possibly be reused to fabricate additional optics amortizing the high cost of a single mandrel over a large number of relatively inexpensive individual mirrors. With replica technology and advanced coating techniques, it should be possible to manufacture a large number of nearly identical instruments capable of imaging x-rays up to 8 keV (important for the higher density NIF capsules). A prototype mandrel has been designed and work is currently focused on developing methods to recover the shape tolerance once the mirror is removed from the mandrel.

Another promising imaging technology for NIF is based on neutron coded apertures.[4] Neutron imaging will be particularly important for NIF cryogenic targets that achieve a high areal density when imploded and cannot be doped with high-Z gases to enhance x-ray emission. Such targets will be best imaged using neutron emission. A prototype device, the Neutron Penumbral-Aperture Microscope (NPAM) is being developed on Nova. This device consists of a specially shaped gold aperture, a high-precision (30-μm accuracy) alignment system, and a 35,000-element scintillator neutron detector array that incorporates a fiber-optic coupled CCD-camera readout.[5] The prototype device has a potential resolution of 10–15 μm. A number of alternative neutron imaging technologies are also being studied including annular coded-apertures and higher resolution detector strategies.

Burn History

One of the most critical measures of capsule performance will be the burn history (the fusion reaction rate as a function of time). On Nova, neutron-based measurements are made with 25-ps resolution using a scintillator-streak camera combination (NTD[6]) placed a few centimeters from the target. The close target proximity minimizes the influence of the plasma temperature-induced broadening of the neutron energy spectrum. On NIF, close proximity may mean several meters for ignition experiments so any burn history information carried by the neutrons will be completely obscured by the ~10-keV plasma temperature.

Consequently, considerable effort is underway at LLNL to develop a fast instrument sensitive to the direct d-t fusion γ-rays. Such an instrument would be sensitive to the plasma temperature and could be optimally located for the expected yield of each NIF experiment. Two experimental instruments, each based on a two-step conversion process, have recently been fielded on Nova. Each has observed direct γ-ray signals. In one instrument, MOLE (short for Moliere), a thin low-Z layer converts the incoming 16.7 MeV γ's into electron-positron pairs that then emit Cherenkov light in a lucite medium. The light is focused onto a MCP-PMT and the signal is recorded using a 5-GHz oscilloscope. Figure 2 shows data from the MOLE detector using both lead and beryllium converters as well as a "null" spectrum in which the cathode of the PMT is covered. The very low input signal (the fusion d-t γ branching ratio is 5 x 10^{-5} relative to the primary neutron production) compounds background issues. Future work will focus on reducing background sources, most notably, γ conversion in the lucite which is currently relatively unshielded from the target.

98

In a second instrument, electron-positron pairs are created in the high-Z Hevimet nose cone of the NTD. Cherenkov light is produced in a second-stage aerogel foam (the foam provides good background immunity) and recorded with a high-speed streak camera. The challenge for this instrument will be increasing the detector size and efficiency while maintaining temporal resolution.

LLNL will continue to maintain a vigorous program of diagnostic development for the NIF with the primary emphasis on γ-ray based burn history measurements, tertiary neutron and proton spectroscopy and both x-ray and neutron imaging systems.
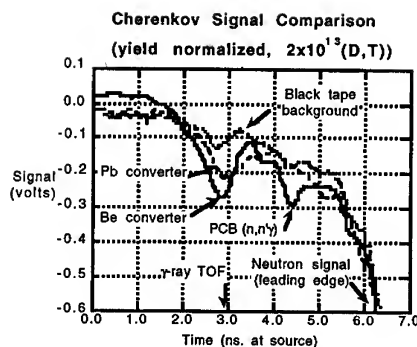
Figure 2. MOLE data from Nova high yield shots using both a lead and beryllium γ-ray converter. The background trace was taken with the PMT covered.

1) M. D. Cable (1994), "Nuclear Measurements of ICF Implosions", in *Laser Plasma Interactions 5: Inertial Confinement Fusion*, edited by M. B. Hooper, Proceedings of the Forty Fifth Scottish Universities Summer School in Physics, St. Andrews, Scotland, 191-208.
2) R. D. Petrasso, C. K. Li, M. D. Cable, S. M. Pollaine, S. W. Haan, T. P Bernat, J. D. Kilkenny, S. Cremer, J. P. Knauer, C. P. Verdon and R. L. Kremens (1996), "Implosion Symmetry and ρR Measurements from Nascent 27-31 MeV Tertiary Protons", submitted to *Physical Review Letters*.
3) M. B. Nelson and M. D. Cable (1992), "LaNSA: A Large Neutron Scintillator Array for Neutron Spectroscopy at Nova", *Review of Scientific Instruments*, **63**(10), 4874-4876.
4) D. Ress, R. A. Lerche, R. J. Ellis, S. M. Lane and K. A. Nugent, "Neutron Imaging of Laser Fusion Targets", *Science*, **241**, 956-958.
5) D. Ress, R. A. Lerche, R. J. Ellis and G. W. Heaton (1995), "High-Sensitivity Scintillating-Fiber Imaging Detector for High Energy Neutrons", *Review of Scientific Instruments*, **66**(10), 4943-4948.
6) R. A. Lerche, D. W. Phillion and G. L. Tietbohl (1995), "25 ps Neutron Detector for Measuring ICF-Target Burn History", *Review of Scientific Instruments*, **66**(1), 933-935.

HIGH-PRECISION MULTICHARGED IONS IONIZATION ENERGY MEASUREMENTS IN LASER-PRODUCED PLASMA

I. SKOBELEV, V. DYAKIN, A. FAENOV, A. MAGUNOV, T. PIKUZ
Multicharged Ions Spectra DC of VNIIFTRI, Mendeleevo, 141570, Russia

T. PISARCZYK, P. PARYS, J. WOLOWSKI, J. MAKOWSKI
Institute of Plasma Physics and Laser Microfusion,
23 Hery St., 00-908 Warsaw 49, Poland

S.A. PIKUZ, V.M. ROMANOVA, T.A. SHELKOVENKO
P.N. Lebedev Physical Institute, 53 Leninsky Pr., Moscow, 117924, Russia

A. OSTERHELD, W. GOLDSTEIN
Lawrence Livermore National Laboratory, Livermore, CA 91550, USA

F. FLORA, P. DI LAZZARO, S. BOLLANTI, N. LISI, T. LETARDI
ENEA, INN. Fis., Frascati (RM), P.O.Box G5, 00011, Italy

A. REALE, L. PALADINO
Dip. Fisica Universita dell'Aquila e INFN, g.c. LNGS, L'Aquila, Italy

D. BATANI, A. MAURI
Dip. Fisica Universita di Milano e INFN, Sezione di Milano, Italy

A. SCAFATI, L. REALE
Lab. Fisica, Instituto Superiore di Sanita a INFN, Sezione Sanita, Rome, Italy

The recombining laser-produced plasma was used to obtain X-ray spectra of He-like Al and Ne-like Ni ions. The wavelengths of high-n resonance lines $n^1P_1 - 1^1S_0$ (n = 6-12) of Al XII were measured with the accuracy (0.3-0.5) mÅ. The wavelengths of nd-2p (n = 5-15), ns-2p (n = 5-8) and np-2s (n = 5,6) transitions in Ni XIX were determined with the accuracy (0.5-1.5) mÅ. The lines were identified by comparison with the results of *ab initio* atomic structure calculations. The values of ionization energy of Al XII ion and the 1-st and 2-nd ionization potentials of Ni XIX ion were deduced from the experimental data and theoretical results.

1 Introduction

The investigation of resonance line series spectra provides valuable tests of *ab initio* atomic structure calculations and gives the methods for plasma diagnostics. High-luminosity focusing spectrograph technique with spatial resolution

[1] allows one to observe resonant transitions from high-n levels of multicharged ions populated *via* recombination in expanded laser-produced plasma [2]. It makes possible to determine ionization energy with the accuracy compared with those in tokamak plasma measurements [3]. The present work uses laser-produced plasma sources to investigate the high-n transitions of the resonant series of He-like Al ions and Ne-like Ni ions and to infer the ground state ionization energies of these ions.

2 Experimental set-up

The measurements with Al plasma were performed at the Nd-glass laser facility at the IPPLM in Warsaw [2]. This laser produces pulses of $\epsilon_0 = 10J$ energy with $\tau_0 = 1ns$ pulse duration. The intensity on the solid aluminum target was $I_0 \approx 10^{13} W/cm^2$. The first set of experiments with Ni plasma we performed at the Nd-glass laser facility at the MISDC [1] ($\epsilon_0 = 10J$, $\tau_0 = 2ns$, $I_0 \approx 10^{14} W/cm^2$). The second set was carried out at the "Hercules" XeCl excimer laser facility at ENEA in Frascati [4] ($\lambda_0 = 308nm$, $\epsilon_0 = 2J$, $\tau_0 = 12ns$, $I_0 \approx 4 \cdot 10^{12} W/cm^2$ and 10 Hz repetition rate). In both cases stepwise targets (nickel and materials provided reference lines) were used.

The X-ray spectra were measured by two FSSR-1D spectrographs [1] containing spherically bent crystals of radius 2R=100 mm and 2R=186 mm. The Kodak DEF x-ray film was placed on the Rowland circle of radius R.

3 Results

The wavelength measurements of the n^1P_1 - 1^1S_0 Al XII lines were carried out in two steps. First, the wavelengths of the transitions with n = 7-10 were measured using Ly_β (6.05291 Å) and Ly_γ (5.73927 Å) Al XIII j-weighted lines as reference lines (see column a of Tab.1). In the second step, the wavelengths

Tab. 1. Spectral lines of He-like ion Al XII

Line	λ_{obs}^a, Å	λ_{obs}^b, Å	λ_{obs}^c, Å	λ_{thr}, Å
$1s12p\ ^1P_1 - 1s^2$		5.98278(50)	5.98271(55)	5.98272
$1s11p\ ^1P_1 - 1s^2$		5.98981(50)	5.99023(55)	5.99019
$1s10p\ ^1P_1 - 1s^2$	6.00035(40)	6.00035(40)	6.00035(40)	6.00003
$1s9p\ ^1P_1 - 1s^2$	6.01314(40)	6.01323(40)	6.01340(40)	6.01340
$1s8p\ ^1P_1 - 1s^2$	6.03255(40)	6.03255(40)	6.03255(40)	6.03217
$1s7p\ ^1P_1 - 1s^2$	6.06007(30)	6.06007(30)	6.06007(30)	6.05976
$1s6p\ ^1P_1 - 1s^2$		6.10281(40)	6.10279(40)	6.10276

of n = 6,9,11,12 lines were measured from spectra calibrated using n = 7,8,10 wavelengths as reference values (see column b of Tab.1). The experimental

precision was of (0.3-0.5) mÅ. The results are in very good agreement with the measurements in X-pinch plasma experiments (column c of Tab.1) and calculated values from relativistic, multiconfiguration parametric potential atomic structure code RELAC [5].

The wavelengths of Ni XIX lines were measured in 4 spectral regions using the reference lines (see Tab.2) and were identified by comparison with the

Tab. 2. Calibration lines for Ni XIX spectra (n is the order of reflection)

Line (Sp. reg.)	Ion	n	λ, Å	Line (Sp. reg.)	Ion	n	λ, Å
$5p - 1s_{1/2}$ (1)	Na XI	2	7.8332	$2^1P_1 - 1^1S$ (3)	Cl XVI	4	4.4443
$4p - 1s_{1/2}$ (1)	Na XI	2	8.0211	$2^3P_1 - 1^1S$ (3)	Cl XVI	4	4.4679
$3p - 1s_{1/2}$ (1,2)	Na XI	2	8.4595	$4^1P_1 - 1^1S$ (3)	Na X	2	8.9827
$7^1P_1 - 1^1S$ (2)	Na X	2	8.6258	4C (4)	Cu XX	2	9.1055
$6^1P_1 - 1^1S$ (2)	Na X	2	8.6863	$2^1P_1 - 1^1S$ (4)	Mg XI	2	9.1681
$5^1P_1 - 1^1S$ (2)	Na X	2	8.7884	$2^3P_1 - 1^1S$ (4)	Mg XI	2	9.2307
$5^1P_1 - 1^1S$ (3)	Na X	2	8.7884	j-satellite (4)	Mg X	2	9.3206

results of RELAC code calculations (see Tab.3). The line designation corresponds to jj-coupling excited states with $J = 1$: nA(B) - $2s_{1/2}^{-1}np_{3/2(1/2)}$, nC - $2p_{1/2}^{-1}nd_{3/2}$, nD(E) - $2p_{3/2}^{-1}nd_{5/2(3/2)}$, and nF(G) - $2p_{1/2(3/2)}^{-1}ns_{1/2}$. The accuracy of wavelength measurements was (0.5-1.2) mÅ for nonblended lines.

Tab. 3. Spectral lines of Ne-like ion Ni XIX (A_{rad} are in units of $10^{10}s^{-1}$)

Line	λ_{obs}, Å	λ_{thr}, Å	A_{rad}	Line	λ_{obs}, Å	λ_{thr}, Å	A_{rad}
6A	8.0136(10)	8.0122	82.17	8C	8.3815(25)	8.3768	134.0
6B	8.0162(10)	8.0153	16.62	9D	8.3815(25)	8.3842	67.90
15C	8.0737(8)	8.0729	12.20	8F	8.4002(7)	8.4007	5.377
14C	8.0930(25)	8.0901	14.78	8D	8.4767(7)	8.4774	148.6
13C	8.1117(10)	8.1115	18.53	7C	8.5136(8)	8.5151	96.33
12C	8.1391(10)	8.1387	24.21	7D	8.6193(8)	8.6180	201.1
11C	8.1753(15)	8.1739	29.72	7G	8.6579(8)	8.6580	4.723
14D	8.1853(25)	8.1850	26.85	6C	8.7381(8)	8.7372	167.3
13D	8.2048(20)	8.2068	37.03	6F	8.7996(8)	8.8002	1.680
10C	8.2172(25)	8.2208	39.23	6D	8.8456(8)	8.8444	295.4
12D	8.2354(10)	8.2347	40.07	6G	8.9132(10)	8.9123	6.920
11D	8.2686(15)	8.2705	59.97	5C	9.1354(12)	9.1339	445.7
9C	8.2835(10)	8.2852	46.70	4B	9.1497(25)	9.1458	151.6
10D	8.3196(10)	8.3184	68.60	5D	9.2487(8)	9.2479	416.3
5A	8.3677(5)	8.3676	119.4	5F	9.2584(5)	9.2582	67.80
5B		8.3731	9.887	5E	9.2662(7)	9.2669	8.207

The results shown in Tab. 1 and 3 can be used to determine the ground state ionization energy of Al and Ni ions. Following [6], the measured wavelengths for the Rydberg series were fit to an expression:

$$1/\lambda_n = E_{ion} - R_Z(Z-1)^2/(n - a - b/n - c/n^2)^2, \quad (1)$$

where E_{ion} is the ground state ionization energy, R_Z is the Rydberg constant for ion with the spectroscopic symbol Z, and a, b and c are fitting parameters.

The value $E_{ion} = 2085.98(10)$ eV obtained from fitting the experimental results for Al XII to Eq.1 agrees well with the theoretical values. The experimental uncertainty is roughly 30% of QED correction [7] and 10% of the electron correlation contribution to the ionization energy. Thus, the present measurements provide a direct test of calculations of these effects contributions.

The fitting procedure of Ni XIX nC and nD series data to Eq.1 gives $E_D^{exp} = 1540.1(5)$ eV, $E_C^{exp} = 1557.1(8)$ eV, and $E_D^{th} = 1539.96$ eV, $E_C^{th} = 1557.82$ eV. The corresponding values of splitting $\Delta E = E_C - E_D$ ($\Delta E^{exp} = 17.0(1.3)$ eV and $\Delta E^{th} = 17.86$ eV) are in conformity with the value 17.85 eV, obtained from direct measurements of the $2p_{1/2}^{-1} - 2p_{3/2}^{-1}$ transition energy in Ni XX [8]. The calculated transition probabilities manifest strong configuration interaction effects, especially for 5C, 8C and 9D lines. We considered the ratio $\alpha = A_{5C}/A_{5D}$. In the single configuration approximation $\alpha_{SC} = 0.65$, while from the values in Tab.3 $\alpha_{CI} = 1.07$ in agreement with $\alpha_{exp} = 1.09$, obtained from measured intensities, *i.e.* if the levels are statistically populated.

4 Conclusions

The use of high-resolution focusing X-ray spectrographs allowed to observe for the first time the high-n lines of resonant series of He-like Al XII (n = 11,12) and Ne-like Ni XIX (n = 8-15) and to determine the wavelengths with the accuracy (0.5-2.5) mÅ. The ground state ionization energies, deduced from these data agree well with the theoretical results and improve significantly previous measurements. Strong electron correlation effects in the intensities of Ni XIX lines have been observed.

References

[1] Skobelev I Yu et al 1995 *JETP* **81** 692.
[2] Dyakin V M et al 1995 *Phys. Scr.* **52** 201.
[3] Rice J E et al 1995 *Phys. Rev. A* **51** 3551.
[4] Flora F et al 1995 *Proc. of SPIE-95, San Diego 12-14 July 1995*, 2523.
[5] Klapisch M et al 1977 *J. Opt. Soc. Am.* **B 61** 148.
[6] Martin W C 1981 *Phys. Scr.* **24** 725.
[7] Indelicato P 1995 *Phys. Rev. A* **51** 1132.
[8] Peacock N J et al 1984 *Phys. Scr.* **T8** 10.

MULTIPLY CHARGED IONS FROM IODINE LASER-PRODUCED PLASMA OF MEDIUM- AND HIGH-Z TARGETS

J. KRÁSA, L. LÁSKA, K. MAŠEK, M. PFEIFER, B. KRÁLIKOVÁ, J. SKÁLA,
P. STRAKA, K. ROHLENA
Institute of Physics, AS CR, 180 40 Prague, Czech Republic

W. MRÓZ
Institute of Optoelectronics, MUT, 01 489 Warsaw, Poland

E. WORYNA, P. PARYS, J. WOŁOWSKI
Institute of Plasma Physics and Laser Microfusion, 00 908 Warsaw, Poland

H. HASEROTH
PS-Division, CERN, 1211 Geneva, Switzerland

A.A. GOLUBEV, B.YU. SHARKOV
*Institute of Theoretical and Experimental Physics, Academy of Sciences,
117 259 Moscow, Russia*

Maximum charge states of ions registered in the far expansion zone from laser produced plasma of Al, Co, Ni, Cu, Ta, W, Pt, Au, Pb and Bi are presented. The ion current density up to above 20 mA/cm^2 at the distance ~ 1 m were measured.

This contribution reports our first experiments with the laser produced plasma of different elements - Co, Ni, W, Pt, Au and Bi - under similar experimental conditions at which the Ta^{50+} ions were obtained [1]. As a driver the iodine laser PERUN [2] at Institute of Physics AS CR, Prague was used (maximum output energy of 50 J, 350 -700 ps pulse duration, conversion to the 2nd (0.657 μm) and 3rd (0.438 μm) harmonics about 50%). The laser beam is focused onto the target either with an aspherical f/2 optics (L) or with a parabolic mirror (M); the diameter of the focal spot is about 100 μm in both cases (the power density ~ 10^{15} W/cm^2). The use of a parabolic mirror with a hole in the center instead of a focusing lens increases the ion extraction twice [3] and makes the ion measurements along the target normal and laser beam axis possible.

The ions were diagnosed applying 1) a Thomson parabola spectrometer (TS) to display a general view of ionization state of expanding plasma and its nature, 2) a cylindrical electrostatic ion energy analyzer (EIA) to determine the distribution of particular charge states and 3) an ion collector (IC) to estimate the ion current density in a far expansion zone [4]. The experiments were performed mainly with laser energy of 22 - 25 J at 350 - 500 ps pulse length. The example of Thomson parabola images is shown in Fig. 1 for Pt.

The promising results from the TS suggest more detail measurements with the EIA. The examples of IC signal and EIA spectra for Pt (E_i/z = 40 keV) is presented in Fig. 2. Two groups of ions (fast and thermal) are seen on IC signal. The obtained results are summarized together with those previous for Al, Cu [5] and Ta [1] in the Tab. 1. The ion current density j is recalculated for the path of flight L = 94 cm. We registered fully stripped Al, or nearly stripped Co and Ni, and ions with the charge state higher than 45+ of heavy elements: Ta, W, Pt, Au, Pb and Bi. It is worth mentioning that moustly the ions with ionization energy below 4 keV (with exception of Ta) were produced in our experimental conditions.

Element	Al	Co	Ni	Cu	Ta	Ta	W	Pt	Au	Pb	Bi
z_{max}	13	25	26	25	55	48	49	50	49	51	51
$E_{i,max}$, MeV	0.35	2.6	2.5		8.8	7.7	4.9	8.5	4.8	5.1	5.1
$<z_{fast}>$		22	20			42	45	40	38	40	40
$<E_{i,fast}>$, MeV		1.9	0.92			2.3	2.0	3.1	3.1	3.3	2.7
j, mA/cm^2		14.2	18.5		12.8	22.8	22.8	12.8	7.0	8.5	10.0
illum. system	L	M	M	L	L	M	M	M	M	M	M

Table 1

In the process of laser-plasma interaction the electron density, the electron temperature and the interaction time are the parameters, which control the ionization state of plasma. The temperature of the plasma as well as the ion energy depend on laser power density [6]. The higher power density focused on a target results in a higher temperature and a faster thermal expansion; non-linear phenomena contribute to the anomalous heating. The suprathermal electrons (or fast ions) are produced with energy proportional to $\sim I^{2/3}$, while the scaling for thermal ions is $\sim I^{4/9}$.

Using the formula for the dependence of T_e on the laser power, average charge state of ions $<z_0>$ in the focal spot and the focal diameter, based on the energy balance of laser absorbed energy and the electron conductivity flux from heated plasma zone [7], the $T_e > 1.5$ keV with average charge state $<z_0> = 40$ can be estimated for our experimental conditions. Another possibility to estimate the electron temperature is given by a mixed model of Busquet [8]. Using it we obtained the temperature $T_e \sim 1.7$ keV (2.4 keV) and the average charge state $<z_0> \sim 50$ for Ta from experimentally given ion energy. This model makes possible to calculate a dependence of average charge state on electron temperature, see Fig. 5.

Explanation of the occurrence of the highly charged ions in a far expansion zone may be based on the presence of the fast and thermal ion groups found in IC signals. Their existence means that the plasma time evolution follows the mechanism of two temperature isothermal expansion [9]. Primarily, a hot electron group with temperature higher than that of thermal group is formed by a collisionless absorption near the critical surface. Escaping the plasma the hot electrons generate electric field which accelerates the ions pulled behind the electrons. The high charge states are guided through the dangerous recombination zone by these hot electrons. This enhances the phenomenon of charge state "freezing" and the ions, originally present in corona, survive.

References

[1] Láska L et al 1996 *Rev. Sci. Instrum.* **67** 950

[2] Chvojka M et al 1992 *Czech. J. Phys.* **42** 899

[3] Woryna E et al 1996 *Appl. Phys. Lett.* - in press

[4] Denus S et al 1977 *J. Tech. Phys..* **18** 25

[5] Mróz W et al 1994 *Rev. Sci. Instrum.* **65** 1272

[6] Gitomer S J et al 1986 *Phys. Fluids* **29** 2679

[7] Roudskoy I V 1993 PhD Thesis, ITEP Moscow

[8] Busquet M 1982 *Phys. Rev.* B25 2302

[9] Wickens L M and Allen J E 1979 *J. Plasma Physics* **22** 167
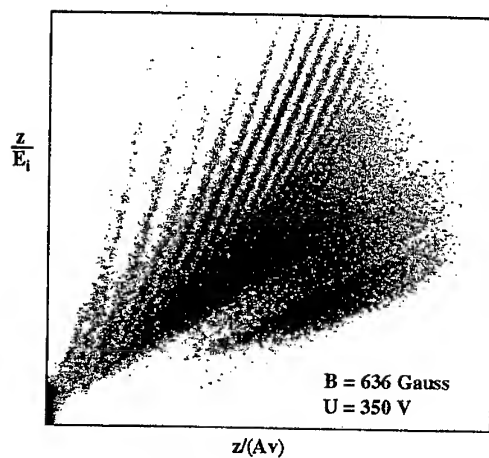
Fig. 1   Thomson parabola picture of Pt plasma.
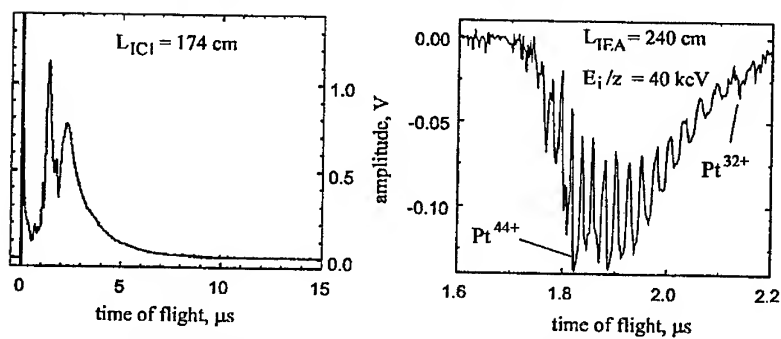
Fig. 2   IC1 signal (left) and IEA spectrum (right) of Pt plasma.
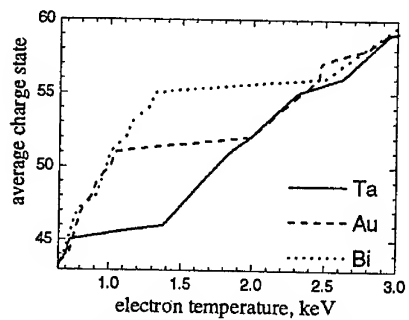
Fig. 3   The dependence of the average charge state of Ta, Au and Bi ions on the electron temperature.

APPLICATION OF INTERFEROMETRIC AND DIAMAGNETIC-PROBE CONTACTLESS METHODS TO INVESTIGATION OF LASER-PRODUCED PLASMA IN STRONG EXTERNAL MAGNETIC FIELD

T. PISARCZYK, A. KASPERCZUK, L. KARPIŃSKI, J. MAKOWSKI,
R. MIKLASZEWSKI, M. PADUCH, K. TOMASZEWSKI, J. WOŁOWSKI,
E. ZIELIŃSKA

Institute of Plasma Physics and Laser Microfusion,
00-908 Warsaw 49, 23 Hery St., Poland

YU.P. ZAKHAROV

Institute of Plasma Physics, RAS, Pr. Lavrentyeva 13/3, 630090,
Novosibirsk, Russia

The paper presents the results of investigations of a laser-produced plasma in a strong transverse magnetic field of 10T in induction, made by means of an interferometer and a magnetic probe. The plasma was generated from a flat teflon target at the laser power density of about $10^{14} W cm^{-2}$. On the basis of interferograms registered in the directions parallel and perpendicular to the magnetic field, a clear asymmetry of the "plasma-blob" for $t \geq 10ns$, caused by an unmagnetized ion Rayleigh-Taylor instability, has been revealed. The analysis of the dB/dt signals from the magnetic probe has confirmed quantitatively the temporal and spatial image of creation of a diamagnetic cavity obtained from the interferometer.

1 Introduction

From the midst of numerous significant physical problems accompanying expansion of a plasma, the following can be treated as fundamental: the process of creation of a diamagnetic cavity and the stability of a plasma filling this cavity. Results of hitherto studies show that the cloud of expanding plasma is usually stopped by the magnetic field B_0 at a distance $R_B \sim B_0^{-2/3}$. The R_B radius approximatelly corresponds to the radius, R_c, of the diamagnetic cavity in which the magnetic field $B = 0$. The created configuration of the plasma is unstable. Some disturbances in the plasma edge area observed, the nature of which is not clear by now. The classical Rayleigh-Taylor (R-T) instabilities induced by the deceleration force require magnetization of ions, whereas the ions in the expanding plasma do not fulfill this requirement [1, 2]. To interpret the development of these disturbances, other kinds of instabilities, taking into account the state of unmagnetization of ions, are proposed, among them the lower-hybrid-drift instability driven primarily by the diamagnetic drift [3] and the unmagnetized ion R-T instability driven by the gravitational drift [4].

2 Experimental set-up

The investigations were carried on in an experimental set-up consisting of a neodymium laser ($E_l \leq 10J$, $\tau \approx 1ns$) and a magnetic-field generator producing a field of induction of up to $20T$ [5]. The desing of a coil producing the magnetic field allowed probing of the plasma both in the longitudinal and transversal directions with respect to the field. To visualize the interaction of the laser-produced plasma with the magnetic field, an automated interferometric system, described in [6], was applied. The measurement of the magnetic-field amplitude and its variations with time was done by means of a "remote" magnetic probe. That method had been applied before for $B_0 \leq 0.5T$ [7]. The primary investigations were performed for flat targets made of teflon at the laser-pulse energy of $5J$ and the magnetic-field induction of $10T$. Due to the lack of axial symmetry of the plasma, caused by the transverse magnetic field, we could not apply the Abel transformation to quantitative processing of the interferograms (the Abel transformation would make it possible to obtain the spatial distributions of the plasma concentration). Thus, the basis for the analysis of the results were phase distributions obtained from the the interferograms. As an external contour of the plasma in the phase distributions,
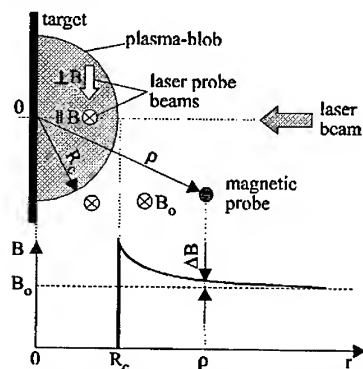
Fig. 1 Geometry of measurement of plasma contour and magnetic field.
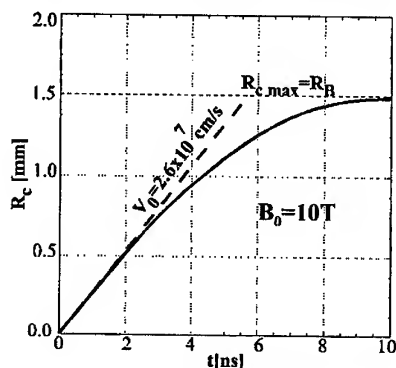
Fig. 2 Dynamics of creation of diamagnetic cavity.

we assumed the equidense corresponding with the phase change equal to 0.4π (the fringe shift 0.2), which corresponds to the electron density of about $5 \cdot 10^{17}cm^{-3}$. The geometry of the measurement of the plasma contour and the magnetic field is presented in Fig.1.

3 Results

In order to investigate the interaction of the laser-produced plasma with the transverse magnetic field, a "remote" magnetic probe placed at a distance

$\rho = 3.5mm$ (Fig.1) was used. Using the Raizer model [8] and considering the measuring geometry, the dimension of the diamagnetic cavity, R_c, was determined from the relation: $R_c(t) = \rho \sqrt[3]{4 \cdot \Delta B(t)/B_0}$, where ΔB is the measured value of the magnetic field, caused by motion of the plasma.

The methodology applied allowed reconstruction of the dynamics of the process of creation of the diamagnetic cavity. Fig.2 presents a typical example of variations in R_c as a function of time. On this basis, we have determined the initial velocity of the plasma front to be $V_0 = 2.6 \cdot 10^7 cm/s$ for $t \leq 3ns$. This velocity corresponds to the velocity of free expansion of the plasma in the initial phase of expansion. With time, for $t > 5ns$, the plasma gets to be clearly decelerated and is stopped after about $10ns$ reaching $R_B = 1.5mm$.
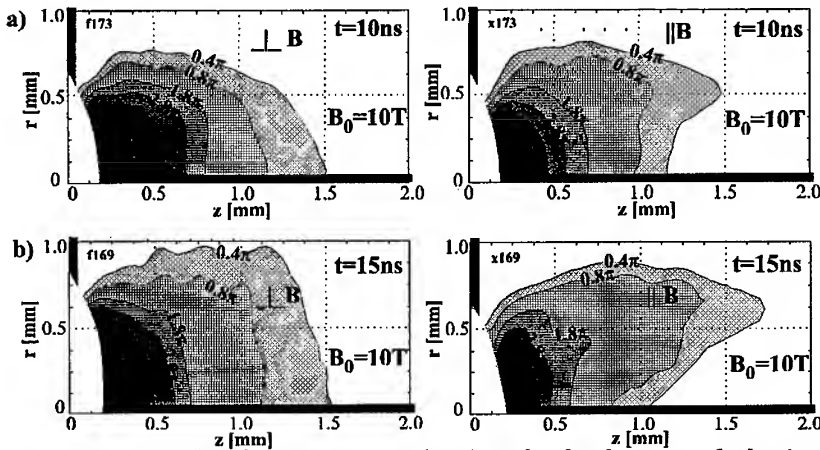
Fig. 3 Changes in the plasma contour related to the development of edge instability ($\perp B$, $\parallel B$ - directions of laser probe beams correspond to Fig.1): a) for $t = 10ns$ i b) for $t = 15ns$.

Interferometric measurements accomplished in this work as well as previous investigations of the dynamics of a plasma in an axial magnetic field in the $5 - 15T$ range [5] show that, in the time $t \leq 5ns$, the magnetic field does not influence expansion of the plasma in practice. After $5ns$, the plasma registered at the level of the electron density $n_e = 5 \cdot 10^{17} cm^{-3}$ reaches the distance $z = 1.2mm$. This means that the initial velocity, V_0, of the plasma amounts $2.4 \cdot 10^7 cm/s$. Due to the fact that this velocity approximatelly equals the initial velocity of the plasma measured by means of the magnetic probe, we assume that the plasma $n_e \leq 5 \cdot 10^{17} cm^{-3}$ is responsible for creation of the diamagnetic cavity. In the further analyses, we will treat the contour $n_e = 5 \cdot 10^{17} cm^{-3}$ as a boundary of the plasma. Observation of the plasma in two mutually

perpendicular directions makes it possible to state that the expanding plasma-blob is characterized by high axial symmetry during this period. At the lack of the magnetic field, the axial symmetry of the plasma is maintained also later. The presence of the magnetic field essentially changes the character of plasma expansion. The plasma, after the period of fast expansion during the first $5ns$, undergoes deceleration and, after about $10ns$ from the beginning of expansion, attains the state of mechanical equilibrium with the magnetic field at a distance of about $1.5mm$ from the target. Already in the phase of deceleration of the plasma, a disturbance in the front of the expanding plasma appears, is distinctly evident at $t = 10ns$ (Fig.3), and enlarges with time. Both the mechanism of generation of this disturbance (the deceleration force) and the flute character of its development (the disturbances develop along the magnetic field lines) indicate that this is a R-T instability. Determining from the interferometric measurements the average deceleration of the plasma-blob, $g_{eff} = 3 \cdot 10^{15} cm/s^2$, and the density length scale, $L_n = 0.05cm$, we can derive the duration of development of the R-T instability: $\tau_{RT} = \sqrt{L_n \cdot g_{eff}} = 4 \cdot 10^{-9}s$. Due to the fact that the Larmor frequency for ions in this duration is estimated to be $\omega = 2 \cdot 10^8 s^{-1}$, the condition necessary for the development of the classical R-T instabilities, $\omega_{ci} \cdot \tau_{RT} \gg 1$, is not satisfied. Moreover, the magnitude of the directed ion Larmor radius, $R_{ld} = V_0 \omega_{ci} = 0.1cm$, proves that the ions are unmagnetized in this phase of plasma expansion. Therefore, in this case, it seems to be more adequate to assume that the reason for the disturbances in the plasma edge is unmagnetized ion R-T instability.

4 Conclusions

It is worth to emphasize that the correspondence of the results of measurements obtained by means of the magnetic probe and the interferometer is very good. This relates to the initial velocity of the plasma, the time of creation of the diamagnetic cavity and its dimensions. This proves the correctness of the methodology applied in the measurements and the analysis of the results obtained with the magnetic probe.

References

[1] Ripin B H et al 1987 *Phys. Rev. Letters* **53** 2299.
[2] Peyser T A et al 1992 *Phys. Fluids* **B4** 2448.
[3] Okada S et al 1981 *Japan Journ. Appl. Phys* **20** 157.
[4] Huba J O et al 1990 *Phys. Fluids* **B2** 1676.
[5] Kasperczuk A and Pisarczyk T 1996 *Physica Scripta* **53** 503.
[6] Pisarczyk T et al 1994 *Laser and Particle Beams* **12** 549.
[7] Zakharov Yu P et al 1986 *Sov. J. Plasma Phys.* **12** 674.
[8] Raizer Yu P 1963 *PMTF* **6** 19.

THE INVESTIGATION OF SPATIAL RESOLUTION OF X-RAY FILMS.

D.A. FEDIN, R.V. FEDORCHUK, M.O. KOSHEVOI, I.V. LUKJANTSEV, A.A. RUPASOV, A.S.SHIKANOV, E. GULLIKSON *.

P.N.Lebedev Physical Institute, Moscow, Russia; *Lawrence Berkeley Laboratory, CA, USA.

Investigations of spatial resolution of widely used x-ray films have been undertaken. A description of experimental methodologies and results are presented. These studies were carried out by using synchrotron radiation. Spatial resolution for Kodak 10106 and RAR2490 films are presented and discussed.

Detectors of the soft x-ray radiation on the basis of x-ray photographic films are widely used in modern physical experiment. The major criterion of the photomaterial quality which gives the ability of a photographic film to reproduce tiny details of the image is the spatial resolution. The resolution is determined by the maximum quantity of the lines transmitted by photomaterial on a length unit which can be resolved under determined conditions of supervision (for example by means of the microdensitometry).

The technique of measurements of the spatial resolution in an optical range of a spectrum is well developed [1,2], however, the works on measurements of photomaterials resolution in the soft x-ray region [3] have individual character, that is connected to the some difficulties inherent to realization of calibration experiments in given area of spectrum. Such difficulty is the strong absorption of soft x-ray radiation in the substance that makes impossible using of the standard masks, made on glass substrates. In the soft x-ray region as a mask need to be used freestanding microstructures which consist of alternated absorbing and transmitting sites of the various sizes.

In the work [3] as a mask linear Fresnel zone plate, made by a photolithography method with the minimum size of 3 μm and maximum one 38 μm was used. Such structure represents sequence of transparent and non transparent regions located on determined law. The contact image of such object on the photomaterial under study was traced using a densitometer with the resolution of 2 μm. However such method has a number of restrictions. In particular, for more exact determination of the spatial resolution value it is necessary, that the densitometer resolution determined by the slit width and the reading step was at least in two or three times less then minimum size of a zone plate. The complexity of such method realisation consists in necessity of use a special microstructure, reasonably difficult of manufacturing and expensive high resolution densitometer.

The method applied in the present work is based on a technique developed to determine the spatial resolution of the photomaterials in the optical range [2] and was applied for the x-ray region by obtaining an x-ray image of a wire mesh mask. This method permits to exclude process of densitometric processing and permits to

use more rough structures as a mask. The mask consists of a mesh of randomly placed freestanding perpendicular gold wires having various widths and thicknesses ranging from 5 to 50 μm. The image was obtained as a contact snapshot of the mask with the film under investigation, using an SR beam passing through a ~100 μm thick *Al* filter as a light source. The spectrum of SR has a intensity sharp recession in the short wave region and a smooth recession in the long wave region. SR spectrum of S-60 accelerator (P.N.Lebedev Institute) has a maximum at λ=14.75 Å for accelerated electron energy E_{max}=630 MeV [4]. Thus, the image was registered by means of x-ray radiation having a wavelength of λ≈5-8 Å.

To evaluate the ability of the films under investigation to record tiny details, a comparison must be made between the image and the actual object. In the present experiments, a diffractometer set-up [5] was used to determine the frequency characteristics of the gold wire mesh mask. This type of diffractometer allows to register the frequency characteristics of a mask and its image on photomaterial to be measured. A comparison of one to the other makes it possible to evaluate the spatial resolution of the films under investigation.

Let on a test object drops a radiation with constant amplitude U. Then modulation of a signal U connected with absorption in object is follows:

$$U(x) = U_0 + \Delta U(x) \qquad (1),$$

where $U(x)$ is a amplitude of total signal behind test object, U_0 is a amplitude of constant component, $\Delta U(x)$ amplitude of useful signal.

As far as in Fourier-plane of the optical scheme the amplitude distribution of an optical signal $Y(x')$ is connected with $U(x)$ through Fourier transform, then

$$Y(\omega) = Y\left(\frac{2\pi \cdot x'}{\lambda \cdot f}\right) = \tilde{F}\left(U_0 + \Delta U(x)\right) = U_0 \cdot \delta\left(\frac{2\pi \cdot x'}{\lambda \cdot f}\right) + \tilde{F}\left(\Delta U(x)\right) \qquad (2),$$

where f is a lens focus and λ is source wavelength. In other words, diffraction picture represents an intensive central peak, connected with the first part in the eq. (1) and diffraction picture at $x'\sim w\neq 0$. The slit filters a certain interval $\Delta x'$, appropriate to a small range of spatial frequencies $w+\Delta w$, hence the photodiode registers a square of spatial harmonic amplitude of corresponding frequency, i.e. have been registered a spectral structure of the object (mask) transmission [5].

We note, however, there is an essential fact of noises existence connected with grain structure of photoemultion, unhomogeneousies of a substrate, gelatine and protective coating. Then the spectrum of the signal includes also a part, connected with this factor

$$\Delta U(x) = \Delta U_0(x) + \Delta U_n(x) \qquad (3),$$

where $\Delta U(x)$ is a useful signal and $\Delta U_n(x)$ is a noise signal. For account of this contribution it is necessary to measure a spectral structure of the noise, i.e. to carry out mentioned above measurements for a film with homogeneousies density. Com-

paring results of such measurements it is possible to judge about received signal ΔU_0 (x) and hence about quality of the mask image.

In Figs. 1 and 2, the results of measuring diffraction intensities of RAR2490 and 10106 films for mask image (curves a) and constant background density (curves b) are presented. Results of the measurements were normalized on a basic signal, obtained in each case integrally for all frequencies without using of the slit. For RAR2490 film (Fig. 1), curves corresponding to the mask's image and the noise spectrum differ in the range of space frequencies $n<0.13\mu m$, and at higher frequencies, these curves practically coincide. Processing of the results it is possible to conclude that the spatial resolution of RAR2490 film is better than 6 μm (167lines/mm), and this is confirmed by the quality of the mask image. In Ref.[3] this value given as a $5\mu m$. The measurements for larger frequencies are impossible, because the smallest detail of the mask restricts its spectrum to $5\mu m$. Using the same methodology, the spatial resolution for 10106 film is estimated to be $30\mu m$ (33lines/mm) (in the region where a useful signal can be discriminated from noise), and thus is worse than that of RAR2490.
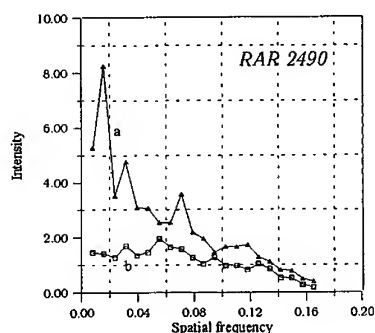
Fig.1
Intensity of diffraction picture, obtained for the mask image registered on RAR2490 film and for film with constant density.
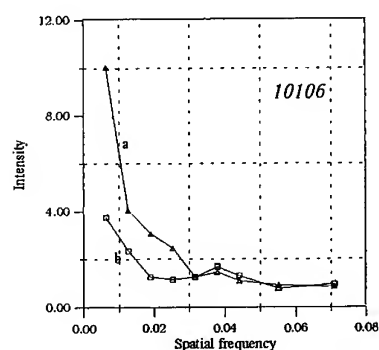
Fig.2.
Intensity of diffraction picture, obtained for the mask image registered on 10106 film and for film with constant density.

The difference between the 10106 film results and those given in Ref.[3], where the spatial resolution is 10 μm, can be explained by the following: the Eastmen Kodak Company does not presently produce such photomaterials and therefore, in the discussed experiments the materials with an overdue time of use have been used. The photographic film development before exhibiting for the back-

ground density determination has shown that the optical background density is $D_{back}>0,5$. If one takes into account that the emulsion layer of this photographic film consists of one layer of AgBr microcrystals, and the maximum density is $D_{max}=1,5$-2 (see, for example, [6]), then, obviously, a significant part of AgBr has been exposed. Whereas, the emulsion layer of a 10106 film has a very dense of the AgBr microcrystals packing (concentration is ~1 [3,6]) and microcrystals touch one another. In that case, when greatly quantity of the exposed AgBr microcrystals (>30%) process of infection development of unexposed microcrystals is rather probable. The similar process was observed on the photographic films Kodak DC-3 and SC-5, intended for UV radiation registration [7]. This effect is invisible for a low background density (for a "new" 10106 film it is $D_{back}=0.05$-0.07) but grows sharply with its increase. On visible just by these effect is explained such low spatial resolution of the 10106 film sample under study.

In conclusion it should be noted, that the discussed method can be successfully used for measuring such important characteristic of the films as the spatial resolution in the soft x-ray spectral range. An elimination from the image processing procedure of the densitometry and appropriate calculations essentially facilitates the obtaining the final result. The only one restriction on the applicability of the method described is connected with the noise of the grain structure of the photographic density, that does not allow to investigate the films having large (~20 μm) thickness of the emulsion layer and high volumetric concentration of AgBr microcrystals.

References

1. A.A.Friesen, A.Kozma, I.F.Adams // Appl.Opt., 1967, v.6, No.5, P.851;
2. P.Hariharan // Appl.Opt., 1970, v.9, No.6, P.1482;
3. B.L. Henke, F.G. Fujivara, M.A. Tester, et.al.// J.Opt.Soc.Am.B, v.1, No.6 , 1984.
4. Yu.M. Alexandrov, M.I. Blagov, A.A. Komar et.al.// Preprint 71, Moscow, FIAN, 1988, (in Russian).
5. L.M.Soroko // Bases of holography and coherent optics, Moscow, Nauka, 1971, (in Russian).
6. Yu.M.Alexandrov, K.Eidman, D.A.Fedin et al. //NIM A308, 1991, P.2536.
7. R.Audron //Int. Konf.Wiss.Phot.Koln, 1956, Darmstadt, 1958, S.279.

TWO DIMENSIONAL EFFECTS IN DENSE PLASMAS CREATED BY COLLIDING FOIL EXPERIMENTS

P. ANGELO, H. DERFOUL, P. GAUTHIER, P. SAUVAN, A. POQUERUSSE,
T. CECCOTTI and E.LEBOUCHER-DALIMIER
Physique Atomique dans les Plasmas Denses, LULI
Ecole Polytechnique, 91128 Palaiseau cedex, France
Université Paris VI, 4 place Jussieu 75252 Paris cedex 05, France

T. SHEPARD, C.BACK
Lawrence Livermore National Laboratory
University of California, USA

M. VOLLBRECHT, I. USCHMANN, E. FÖRSTER
Max Planck Group, Jena University , Germany

We create hot (Te > 200 eV) and dense (Ne > 10^{23}cm^{-3}) plasmas in the colliding zone of two thin foils accelerated by two laser beams of the LULI facilities. Two diagnostics (a space resolved spectroscopy and a 2D monochromatic imaging) are used to drive the efficiency of the compression. We show that a realistic simulation of these experiments must be done by using a code which takes into account the plasma lateral expansion and the foil distorsion. LASNEX code results are in good agreement with experimental results.

1. Introduction

For intermediate coupled plasmas the X-ray emission exhibits satellite-like features [1,2] that have been attributed to new transient emitter structures : the dicenter ions. Recently a molecular emission code has been developed for dense plasmas (Ne>10^{23}cm^{-3}) favourable to the formation of these structures [3]; that is why it is important to design accurate experiments in order to improve this code.

In our first experiments made by irradiation of massive targets [1], the densest zone was rather cold and difficult to access. In the experiments presented here [4], plasmas with the same high density but with a higher electronic temperature have been created by colliding two thin foils with two laser beams. First we report qualitatively on the efficiency of the compression from the diagnostics results, then we present a study of hydrodynamical aspects occuring in colliding foil experiments. The driving simulations of these experiments give initial foil thickness and separation in agreement with the experimental results corresponding to an optimized compression. We show that two dimensional effects are not negligible.

2. Two time integrated emission diagnotics

Two laser beams of the LULI facilities (0.26μm, 25J, 500ps) are focused on two thin Al or CF2 foils initially 100μm separated.

115

The starting point of these experiments is to choose the foil initial thickness and separation in such a way that the remaining matter can collide with a maximum kinetic energy before the end of the pulse. A spectrograph resolves X-ray emission along the collision axis [2]. In fig.1 we give an Al spectrum for conditions leading to a high compression : the lines in the compressed central part are wide and emissive, while in the two coronas they get narrower.

A 2D monochromatic imaging on Lyβ has been implanted in order to measure the inhomogeneities of the emission along both collision axis and transverse direction. The crystal used is a toroidally bent silicon (111) crystal with a bending radius of 150.2mm in the dispersion plane and 139.9mm perpendicular to this plane. The magnification is approximately 8 and the spectral window of the order of $\Delta\lambda/\lambda=2.10^{-2}$. In fig.2a we show an imaging on Al Ly β for the presumed optimized conditions. Numerized microdensitometries along the collision axis and the transverse direction (in the compressed zone) are presented in fig.2b and 2c respectively. From the breakdowns in the emission (fig.2b), we can verify the initial foil distance (100μm). They correspond to a reabsorption in the solid and in the cold dense plasma next to the foils before the collision. The same behavior of the emission (intense core and weak corona emissions) along the laser axis has been simulated ; moreover this simulation reveals that the very intense emission from the central zone occurs mostly after the collision time.

Since 100μm is also the focal spot diameter, one can expect that two dimensional
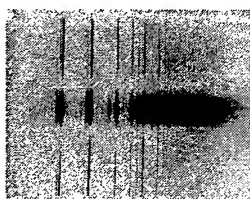
fig.1 Al spectrum for
a high compression
(e=3 μm, d=100 μm)
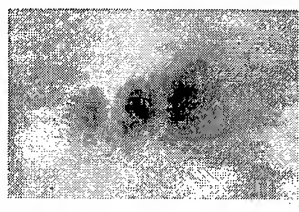
fig.2a monochomatic imaging on
Al Ly β

b

c
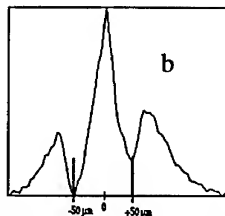
fig.2b emission along collision axis
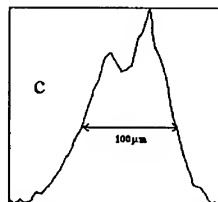
fig.2c emission in transverse
direction

effects be not negligible. However from the transverse emission size (100μm, see fig.2c), we can estimate that the lateral expansion does not make the transverse emission dimension significantly increase with respect to the focal spot size (80 to

100μm). In fact this expansion will be shown to be decisive for the drive of the foil collisions.

3. Lasnex simulations

Focal spot size ($\approx$ 100 μm) joined to foil thickness and separation conditions lead to foil distorsion and absorbed laser energy loss [5], all these defects being caused by plasma lateral expansion [6,7]. As a consequence a realistic numerical prediction for the best initial conditions leading to a "hot matter" compression must be carried out by a code taking into account these two effects (see fig.2 and fig.3). As a matter of fact, the electronic density suggested by a monodimensional simulation is always higher than the two-dimensional result one. Particularly in the colliding zone there could be two orders between the two simulation results. This discrepancy is due to the previously described two-dimensional effects. Moreover for the same initial conditions as in fig.2, fig.3 shows that at the top of the laser pulse, electronic density calculated by a 1D code is higher than the critical density (Nc = 1.6 10^{22} cm^{-3}) contrary to the 2D version prediction. As a consequence at the same time, "2D the electronic temperature" is much higher than "1D temperature", the sub critical plasma being heated by inverse bremsstrahlung. In the two-dimensional simulation, the electronic temperature is high enough for the foils to be pierced by the plasma before the top of the laser pulse [fig.4]. Then electronic density will rapidly decrease in the colliding zone. For this sub critical plasma, the electronic temperature will first increase with incident laser energy, and then rapidly decrease because most of laser energy goes through the plasma and the heating by inverse bremsstrahlung is not very efficient. As a remark, a monodimensional code does not allow the foils to explode and then gives electronic density and temperature corresponding to a completely different physical situation.
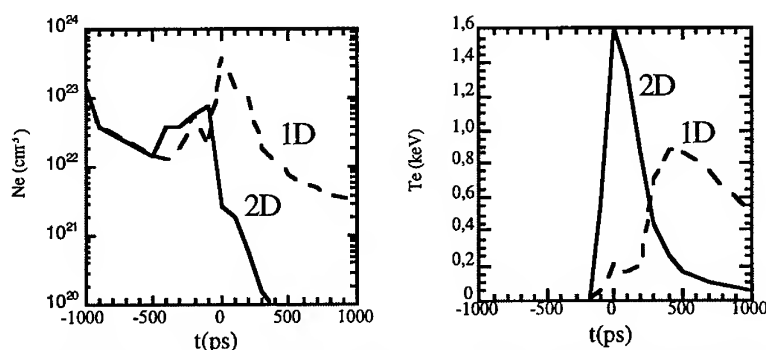
fig.3 Predictions from mono and two-dimensional codes (LASNEX 1D & 2D) versions for the rear face of two CF2 foils (initial thickness 3 μm, initial separation 100μm) irradiated by two laser beams (0.26μm, 16J, 500ps, focal spot diameter 80 μm). 0 ps refers to the top of laser pulse.

118

The simulations of these experiments with LASNEX use the collision symmetry and do the computation in a half space neglecting the possible interpenetration of the two plasmas in the colliding zone (for optimal initial conditions the electron mean free path is much smaller than the density gradient length). We concurrently made several simulations by variing initial thickness and separation of the foils within the previous initial values. LASNEX results [4] show that the CF_2 foil compression is optimized for an initial thickness of 5 μm and an initial separation of 100 μm. These predictions are in very good agreement with experimental results [2,4].
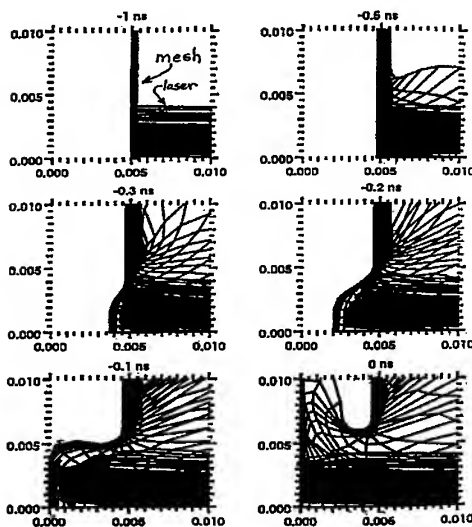
fig.4 LASNEX 2D simulations showing the distorsion in time of a CF2 foil (initial thikness 3 μm, initial separation 100 μm) irradiated by two laser beams (0.26 μm, 16J, 500ps) focused onto 80μm focal spot.s One can also see lateral plasma expansion. The curves correspond to isodensities. 0 ns refers to the top of laser pulse; distances are in cm.

References

[1] E.Leboucher-Dalimier, A.Poquerusse, P.Angelo, Phys.Rev.E, **47** (3), R1467 (1993).
[2] E.Leboucher-Dalimier, P.Angelo, P.Gauthier, A.Poquérusse, AIP, Conference Proceedings 328, Spectral Line Shapes **8** 12th ICSLS, Toronto Canada 1994, ed. by A.D. May, J.R. Drummond, E. Oks.
[3] P.Gauthier, P.Sauvan, P.Angelo, S.Alexiou, E.Leboucher-Dalimier, A.Calisti, B.Talin, 13th ICSLS, Firenze Italia 1996.
[4] P.Angelo, P.Gauthier, A.Poquérusse, H.Derfoul and E.Leboucher-Dalimier, C.Back, T.Shepard, to be submitted.
[5] B.Faral, Phys. Fluids **B2**, 371 (1990).
[6] M.H.Key, Phys. Fluids **26**, 2011 (1983).
[7] F.Cottet et al, LULI report, 133 (1984).

2.- LASER PLASMA INTERACTION

AND

HYDRODYNAMIC INSTABILITIES

HYDRODYNAMIC INSTABILITIES RELATED TO START-UP PROBLEMS

K. NISHIHARA, R. ISHIZAKI, J.G. WOUCHUK

Institute of Laser Engineering, Osaka University,
2-6 Yamada-oka, Suita, Osaka 565, Japan

An analytical model is presented to study hydrodynamic perturbation growth in a start-up phase in laser fusion, namely propagation of a rippled shock driven by laser ablation, a new instability of a uniform contact surface driven by the rippled shock, and the Richtmyer-Meshkov instability of a corrugated contact surface. Those perturbation growths are very important because they seed the Rayleigh-Taylor instability in the subsequent acceleration and stagnation phases. Analytical results agree quite well with experimental data for both the rippled shock propagation and the R-M instability growth.

1 Introduction

To achieve ignition and high gain in inertial confinement fusion, a spherical pellet must implode symmetrically. A laser implosion process can be divided into three phases, start-up, acceleration and stagnation phases. A shock wave driven by the laser ablation propagates through a shell in the start-up phase, and shell acceleration then follows. The ablation surface is Rayleigh-Taylor (RT) unstable in the acceleration phase. Hydrodynamic perturbation growth in the start-up phase seeds the RT instability in the acceleration phase.

An analytical model is developed to study propagation of a rippled shock driven by laser ablation, an instability of a uniform contact surface and the Richtmyer-Meshkov instability of a corrugated contact surface. The model uses the variable transformation introduced by Nikolaev[1] to solve a wave equation and applying suitable boundary conditions depending on the problems, for example, the Rankine-Hugoniot jump condition at the shock front,[1] the Chapman-Jouguet deflagration jump condition at the laser ablation surface,[2] pressure and velocity continuity at the contact surface, and velocity and density continuity at the rarefaction fronts.[3]

2 Rippled shock wave driven by laser ablation

Initial target roughness or nonuniform laser irradiation causes a rippled shock which propagates through a fuel capsule, and results in an areal mass density perturbation. The propagation of the rippled shock is investigated for both cases, initial target roughness and nonuniform laser irradiation. Both oscil-

122

lation period and decay rate of the shock front perturbation agree quite well with experiments.[4] Agreement between theory and experiment is also found in the areal mass density perturbation induced by the rippled shock propagation. We have found the perturbation amplitude of the ablation surface grows with time against the experimental results in which the perturbation does not grow. We also investigate the dependence of the shock front, ablation front and areal mass density perturbation on the laser intensity and laser wavelength, respectively. The generation of the rippled shock and the perturbation growth of the ablation surface are also obtained for the nonuniform laser irradiation case. The normalized shock surface perturbation is found to be $ka/(\delta I/I_0) \sim 0.5$.

3 Instability of a contact surface driven by the rippled shock wave

A new instability of a contact surface is found to be driven by a rippled shock wave.[5] Namely a uniform contact surface becomes unstable when the rippled shock wave passes the surface. We can obtain the theoretical equation of the growth rate in the linear evolution through that we regard the instability as a gravitational instability where the acceleration is induced by the velocity perturbation of the shock front and by the oscillatory damped pressure perturbation behind it. The equation indicates clearly that the growth rate depends on the phase of the oscillating shock at the time when the shock hits the contact surface. The growth rates observed in the simulations using IMPACT-2D [6] agree very well with the theoretical values estimated from the equation when the Atwood number dependence of the growth rates is investigated.

Nonlinear evolution of the instability is also investigated for the large amplitude of the rippled piston, by using IMPACT-2D. The contrast in Fig. 1 indicates the iso-density contour for the Atwood number A = -0.5. A reference frame in the figure is one moving with the piston. As shown in Fig. 1(a) and (b), the mushroom shape of the unstable contact surface appears when the shock hits the uniform contact surface at the phase that the shock front distortion is maximum, while the square shape appears at the phase that the shock front velocity perturbation is maximum. Namely, for both linear and nonlinear cases, the growth rate depends essentially on the phase of the oscillating shock wave at the time when the shock hits the contact surface.

4 Richtmyer-Meshkov instability

Let us consider a plane interface separating two ideal fluids with initial densities ρ_{a0} and ρ_{b0}. The interface is located in the plane $x = 0$ and has an initial corrugation of the form $\psi = \psi_0 \cos ky$, where $k = 2\pi/\lambda$ is the perturbation
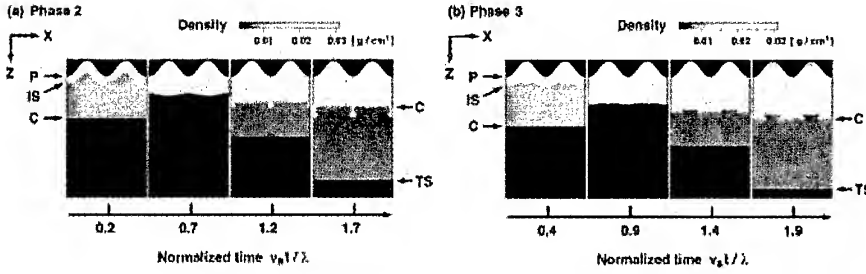
Figure 1: Nonlinear evolution of uniform contact surface instability shown by isodensity contours with contrast for the negative Atwood number of -0.5. P, IS, TS and C correspond to the rippled piston, incident rippled shock, transmitted shock and unstable contact surface.

wavenumber. A shock is coming initially from the right (fluid "b") and hits the interface at $t = 0$. Depending on the fluid properties and on the intensity of the incident shock, another shock or a rarefaction are reflected back in fluid "b" and a shock is transmitted into fluid "a". We consider at first the case in which a shock is reflected at $t = 0+$. It is possible to get the analytic solutions for the perturbations and an approximate formula for the asymptotic interface velocity in the weak incident shock limit:

$$\delta v_i \approx k v_i \frac{\mathcal{R}\psi_{t0} - (1 - \frac{v_1}{v_i})\psi_{r0}}{\mathcal{R} + 1}.$$ (1)

Here, v_1 is the fluid velocity behind the incident shock, v_i is the interface velocity induced by the incident shock, ψ_{t0} and ψ_{r0} are the initial amplitudes of the transmitted and reflected shocks respectively, and $\mathcal{R} = \rho_{af}/\rho_{bf}$ is the ratio of final densities. It is interesting to note that the previous formula can be derived from an impulsive approximation, but taking into account that the transmitted and reflected shocks exert different accelerations, equal to $v_i\delta(t)$ and $(v_i - v_1)\delta(t)$ respectively. We have also studied the time evolution of the areal density between the shock fronts $\left(\mathcal{A}_\rho = \int_{x_t+\psi_t}^{x_r+\psi_r} \rho(x,y,t)dx\right)$. Integrating the wave equation for the pressure perturbations, it is possible to see that:

$$\delta A_\rho \approx (\rho_{af} - \rho_{bf})\delta v_i t + \delta A_\rho^0.$$ (2)

The quantity δA_ρ^0 is an asymptotic shift dependent on shock intensity, that is originated by the entropy disturbances left by the perturbed shocks.

For the rarefaction reflected case we proceed as before, except that to treat the rarefaction zone we follow Yang et al.[3] Now again, in the limit of weak incident shock we can get an approximate formula for the asymptotic
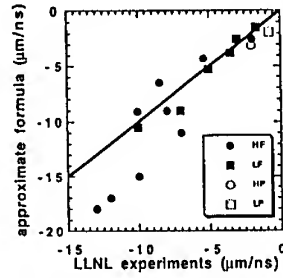
Figure 2: Comparison of experimental results taken from Ref. 7 and the Eq. (3).

interface velocity:

$$
\delta v_i \approx k v_i \frac{\mathcal{R}\psi_{t0} - \left(1 - \frac{v_1}{v_i}\right)\psi_{rt0}}{\mathcal{R} + 1},
\tag{3}
$$

where ψ_{rt0} is the initial amplitude of the rarefaction tail. In Fig. 2 we show a comparison of the predictions of Eq.(3) with recent experimental results.[7] In these experiments, strong shocks were generated by indirect laser irradiation and a rarefaction front was reflected at the contact surface. Fair agreement is observed except for the shortest perturbation wavelengths in which non linear saturation effects should be important since early time. Regarding the mass areal density perturbations, as no entropy is generated inside the rarefaction, the contribution to δA_ρ^0 comes from the transmitted shock in the light fluid.

5 Summary

An analytical model is developed to study propagation of a rippled shock driven by laser ablation (target roughness and nonuniform laser irradiation), a new instability of a uniform contact surface driven by the rippled shock (linear and nonlinear), and the Richtmyer-Meshkov instability (reflected shock and rarefaction). Fairly good agreement is found between theory and experiments.

References

1. Iu. M. Nikolaev, *J. Appl. Math. Mech.* **29**, 785 (1965).
2. H. Takabe *et al.*, *J. Phys. Soc. Jpn.* **45**, 2001 (1978).
3. Y. Yang *et al.*, *Phys. Fluids* **6**, 1856 (1994).
4. T. Endo *et al.*, *Phys. Rev. Lett.* **74**, 3608 (1995).
5. R. Ishizaki *et al.*, *Phys. Rev.* E **53**, (1996) (to be published).
6. H. Sakagami and K. Nishihara, *Phys. Fluids* B **2**, 2715 (1990);
7. G. Dimonte *et al.*, *Phys. Plasmas* **3**, 614 (1996).

Linear Theory of the Ablative Rayleigh-Taylor Instability

R. Betti, V. Goncharov, R.L. McCrory and C.P. Verdon
Laboratory for Laser Energetics, University of Rochester, Rochester NY 14623

The linear stability analysis of accelerated ablation fronts is carried out self-consistently by retaining the effects of finite thermal conductivity, finite-density-gradient scale length (L) and ablative flow. Short-wavelength modes ($kL \ll 1$) are only unstable in ablation fronts with small Froude numbers ($Fr \ll 1$), and their growth rate is reduced by thermal smoothing, finite density gradients, and ablative convection. For $Fr \gg 1$, the growth of long-wavelength modes is reduced by the ablative flow in the overdense and blowoff region.

1   Introduction

In laser-driven inertial confinement fusion (ICF), the accelerating ablation front is unstable to surface perturbations [Rayleigh-Taylor (R-T) instability]. According to the classical treatment of the instability of two superimposed fluids with different densities in a gravitational field g pointing toward the lighter fluid, a small perturbation would grow exponentially in time at the classical rate $\gamma_{cl} = \sqrt{A_T^{cl} k g}$, where A_T^{cl} is the classical Atwood number and k is the mode wave number. However, in ICF, the equilibrium configuration is significantly different from the classical case. The density profile $\rho(x)$ is monotonically decreasing, the density-gradient scale length $L = \left| \rho / (d\rho/dx) \right|$ is finite, and the ablation process produces a mass flow from the heavy to the light fluid.

The equilibrium configuration is characterized by the ablation velocity V_a (ablation ratio per unit area/peak density), the acceleration g, and the typical front thickness L_0. The latter is obtained by balancing the heat flux $\left(-\kappa \nabla T \right) \sim \kappa_a T_a / L_0$ with the internal energy flux at the ablation front $\left[\gamma_h \rho_a T_a V_a / A (\gamma_h - 1) \right]$ leading to $L_0 = \left(1 - \gamma_h^{-1} \right) A \kappa_a / \rho_a V_a$, where $A = m_i / (1 + Z)$ is the average particle mass, γ_h is the ratio of the specific heats, and ρ_a, T_a, κ_a are the density, temperature, and thermal conductivity at the location of the peak density. The thermal conductivity has a power law dependence on the temperature $\left(\kappa \sim T^\nu \right)$ with the power index $\nu \geq 1$. The density-gradient scale length is proportional to L_0, and its minimum value is $L_m = L_0 (\nu + 1)^{\nu+1} / \nu^\nu$.

For a subsonic ablation flow, the isobaric approximation[1] is valid, and the only dimensionless parameters characterizing the equilibrium are the power index for thermal conduction ν and the Froude number $Fr = V_a^2 / g L_0$. In this paper, we summarize the results of the linear stability analysis based on the isobaric model, and we show that the unstable spectrum is strongly dependent on the magnitude of the Froude number.

126

2 Growth Rates

For subsonic ablation flow, the linear stability problem cannot be solved for arbitrary Froude numbers. In the large Froude number limit ($Fr \gg 1$), the stability analysis has been carried out in Refs. 2 and 3 using a boundary layer technique to solve the eigenvalue equation.

The unstable spectrum has a cutoff at wavelengths longer than the front thickness ($k_c L_0 \ll 1$), and the growth rate can be written in the following simple form:[3]

$$\gamma = \sqrt{A_T k g - A_T^2 k^2 V_a V_{b.o.}} - (1 + A_T) k V_a, \tag{1}$$

where $A_T = 1 + O(\epsilon^{1/\nu})$ is an effective Atwood number and $V_{b.o.} = V_a/\mu_0 \, \epsilon^{1/\nu}$ is the blowoff velocity at the distance $(k\nu\mu_0^\nu)^{-1}$ from the ablation front. Here, the parameter $\epsilon \equiv k L_0$ is the dimensionless wave number and μ_0 is a constant defined in Ref. 3. The cutoff wave number k_c is obtained by setting $\gamma = 0$ in Eq. (1). A straightforward calculation yields $k_c L_0 \sim Fr^{-\nu/(\nu-1)}$. Observe that, since $Fr \gg 1$, the cutoff occurs at long wavelengths ($k_c L_0 \ll 1$) and short wavelength modes are stable.

For small Froude numbers ($Fr \ll 1$), short-wavelength modes ($k L_0 \gg 1$) become unstable. Their growth rate is strongly reduced by the finite-density-gradient scale length, thermal diffusion, and the ablative convection. For $1 \ll k L_0 \ll Fr^{-1/3}$, the main stabilizing effects are the finite L and thermal smoothing. The growth rate can be approximated by $\gamma = \sqrt{a(g/L_0) + c_0^2 k^4 D_T^2} - c_0 k^2 D_T$, where $D_T = L_0 V_a \sim A \kappa_a/\rho_a$ is the thermal diffusivity and a, c_0 depend[4] mainly on ν. For $k L_0 \sim Fr^{-1/3}$, the ablative stabilization becomes important and produces the cutoff of the unstable spectrum. The growth rate near the cutoff can be written as $\gamma = c_1 g/(k^2 D_T L_0) - c_2 k V_a$, where c_1 and c_2 depend[4] mainly on ν. Long-wavelength modes[4] are also unstable when $Fr \ll 1$, and their growth rate can be approximated by $\gamma = \sqrt{A_T k g} - b k V_a$, where $b \approx 2$ for $k L_0 \ll Fr^{2/(2-\nu)}$ and $1 < \nu < 2$, and $b = \Gamma(1 + 2/\nu)/\Gamma^2(1 + 1/\nu)$ for any other $k L_0 \ll 1$ [$\Gamma(x)$ is the Gamma function].

3 Determination of ν and L_0

As stated in Sec. II, the applicability of the growth rate formulas requires the determination of the thickness L_0 and the power index for thermal conduction ν. The isobaric model is based on the diffusion approximation for the energy flux ($q = -\kappa(T)\nabla T$, where $\kappa \sim T^\nu$). It is well known that the diffusion approximation represents only a rough description of the radiative energy transport and its validity breaks down for optically thin media. Thus, in order to extend the validity of the isobaric model to configurations with significant radiation energy transport, we determine ν and L_0 by performing an optimum fit of the density profile obtained from

the 1-D simulations including more-sophisticated multigroup radiation transport models. The isobaric density profile obeys the first-order differential equation $L_0(d_x\xi)/\xi^{v+1}(\xi-1) = 1$, where $\xi = \rho/\rho_a$ is the normalized density. The optimum values of v and L_0 approximating the simulation profiles are the ones that minimize the integral

$$I(v, L_0) = \int_{\xi_{min}}^{\xi_{max}} \left\{ \ln\left[L_0(d_x\xi_s)/\xi_s^{v+1}(\xi_s - 1)\right]\right\}^2 d\xi_s, \tag{2}$$

where ξ_s represents the normalized density of the 1-D simulations, and ξ_{min}, ξ_{max} are the minimum and maximum values of the density for which the profile is optimized ($\xi_{min} = 0.01$ and $\xi_{max} = 0.99$ are two possible values). Observe that $I(v, L_0)$ vanishes if the simulation profiles are exactly described by the isobaric model. It follows that the optimum values of v and L_0 satisfy the two linear equations $\partial_v I = \partial_{L_0} I = 0$. One-dimensional simulations of a 120-μm-thick DT planar foil irradiated by a 0.35-μm-wavelength laser with an intensity of 50 TW/cm^2 are fit by isobaric profiles with $v \approx 2.3, L_0 \approx 0.04\,\mu$m, and $Fr \approx 4.5$. An 18-μm CH foil illuminated by the same laser has $v \approx 1$, $L_0 \approx 0.3\,\mu$m, and $Fr \approx 0.03$. Observe the remarkable difference in the values of v, L_0, and Fr between the low-Z material (DT), where electronic heat conduction is dominant, and the higher-Z material (CH), where radiation transport plays an important role in shaping the hydrodynamic profiles.

4 The Simple Fit

The growth rate obtained at small/large Froude numbers and short/long wavelengths (see Sec. II) can be approximated by the simple formula $\gamma^{fit} = \alpha\sqrt{kg} - \beta k V_a$, where α and β are determined by fitting the complicated analytic results of Sec. II for different values of v and Fr. The optimum fit is carried out by minimizing the following integral:

$$J(\alpha, \beta) = \int_{\lambda_c}^{\lambda_{max}} \left(\gamma^{analytic} - \gamma^{fit}\right)^2 d\lambda \tag{3}$$

with respect to α and β $\left(\partial_\alpha J = \partial_\beta J = 0\right)$. Here λ_c is the cutoff wavelength and λ_{max} is an upper limit for the fitting interval ($\lambda_{max} = 50$–$100\,\lambda_c$ are two possible values, and α, β show little sensitivity to the value of λ_{max}). In Figs. 1(a) and 1(b), the parameters α and β are plotted versus the Froude number for different values of v. Observe that α has a weak dependence on v and Fr ($0.8 < \alpha < 1$), and β has a minimum at $Fr \approx 1$. The parameter β increases for large and small Froude numbers, and it is weakly dependent on v for small Fr. These results can be easily applied to the plastic and DT foils of Sec. III. Both targets have similar α's [α(CH) ≈ 0.98 and α(DT) ≈ 0.93]. However, the β for CH is quite larger than for DT [β(CH) ≈ 4.9 and β(DT) ≈ 2.7]. This

TC4187   1(a) Plot of α versus Fr   1(b) Plot of β versus Fr
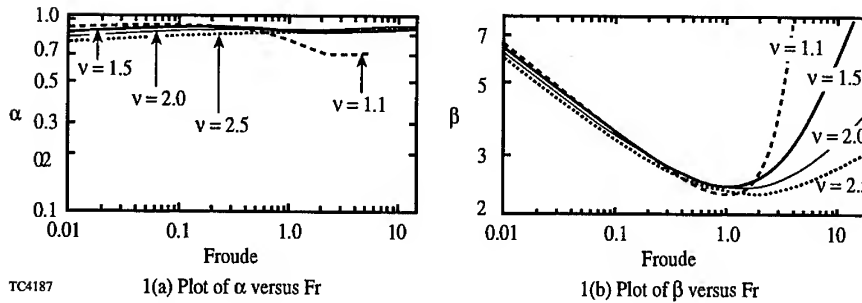
result can be easily explained by noticing that in DT, the ablation velocity is large (about five times larger than plastic) and the density gradient scale length is small (L_m for DT is about four times smaller than for plastic). Thus, the only stabilizing effect in DT is the ablative convection. On the other hand, the ablation-front density profile of plastic targets is smooth. Thus, the stabilizing effects of finite density gradient and thermal smoothing are also important (in addition to the ablative convection). This combination of stabilizing mechanisms results in a larger value of β for CH targets. However, one should not forget that the overall stabilization is represented by the product βV_a, which is larger for DT $\left[\beta V_a(DT)/\beta V_a(CH) \approx 2.5\right]$.

The values of α and β for large Froude numbers are also in good agreement with the numerical results of Takabe et al.,[5] for $\nu = 5/2$.

5   Conclusions

The linear stability analysis of ablation fronts is carried out for subsonic ablation flow. It is found that modes with wavelengths shorter than the density-gradient scale length are stable for large Froude numbers. The analytic growth rate can be approximated by the simple fit $\gamma^{fit} = \alpha\sqrt{kg} - \beta k V_a$, where α and β depend on the power index for thermal conduction ν and the Froude number.

6   Acknowledgment

7   References

1.   H.J. Kull and S. I. Anisimov, Phys. Fluids **29**, 2067 (1986).
2.   J. Sanz, Phys. Rev. E **53**, 4026 (1996).
3.   V. Goncharov, R. Betti, R. L. McCrory, P. Sorotokin, and C. P. Verdon, Phys. Plasmas **3**, 1402 (1996).
4.   V. Goncharov, R. Betti, R. L. McCrory, and C. P. Verdon, "Stability Analysis of Ablation Fronts with Small Froude Numbers", submitted to *Phys. Plasmas* (1996).
5.   H. Takabe, K. Mima, L. Montierth, and R. L. Morse, Phys. Fluids **28**, 3676 (1985).

LASER IMPRINT AND IMPLICATIONS FOR DIRECT DRIVE IGNITION WITH THE NATIONAL IGNITION FACILITY

S. V. WEBER, S. G. GLENDINNING, D. H. KALANTAR, B. A. REMINGTON,
J. E. ROTHENBERG

Lawrence Livermore National Laboratory, Livermore,
CA 94550, USA

M. H. KEY

Rutherford Appleton Laboratory,
Chilton, Didcot, UK

J. P. KNAUER

Laboratory for Laser Energetics, University of Rochester,
Rochester, NY 14627, USA

For direct drive ICF, nonuniformities in laser illumination can seed ripples at the ablation front in a process called imprint. Such nonuniformities will grow during the capsule implosion and can penetrate the capsule shell, impede ignition, or degrade burn. We have simulated imprint for a number of of experiments on the Nova laser. Results are in generally good agreement with experimental data. We have also simulated imprint upon National Ignition Facility (NIF) direct drive ignition capsules. Imprint modulation amplitude comparable to the intrinsic surface finish of ~40 nm is predicted for a laser bandwidth of 0.5 THz. Ablation front modulations experience growth factors up to several thousand, carrying modulation well into the nonlinear regime. Saturation modeling predicts that the shell should remain intact at the time of peak velocity, but penetration at earlier times appears more marginal.

1 Introduction

In direct drive inertial fusion, spatial nonuniformities in the laser intensity create hydrodynamic perturbations in the imprint process. These perturbations grow during the implosions and can degrade performance. Beam smoothing schemes [1,2] introduce spatial and temporal incoherence into the laser beam, giving a strongly modulated speckle pattern at any instant of time. In time average, the modulation smooths out to a large degree. Thermal transport between where the laser energy deposits and the ablation front gives additional smoothing. We have examined the imprint and growth in numerical simulations, and tested the modeling against experiments. Simulations can assess imprint upon ignition capsules such as those planned for the National Ignition Facility (NIF).

2 Numerical Method and Simulations of Experiments

Imprint has been simulated using the computer code, LASNEX. Simulations are two-dimensional with reflecting boundary conditions in the transverse direction, and include multigroup radiation diffusion, electron conduction by flux-limited diffusion with a flux limiter of $f_e = 0.1$, and ray trace laser deposition. The speckle pattern is introduced by adjusting the powers of the rays according to their aim point on the surface of the target.

After some time, the growth history of a perturbation created by laser imprint parallels that of a perturbation originated at the target surface. This fact has been confirmed in Nova imprint experiments [3]. Consequently, we define the "equivalent surface finish" which is the spatial amplitude spectrum which results in the same modulation growth history as some given imprint condition, during the parallel evolution. A related quantity is the "imprint efficiency" which is the ratio of the equivalent surface finish to the intensity modulation amplitude. As long as the hydrodynamic perturbations are linear ($a < 0.1\lambda$), the imprint amplitude should be proportional to the intensity modulation. This quantity tells how smooth the beam must be to obtain a desired level of target smoothness.

Experiments on the Nova laser have measured effects of imprint. Modulations arising in a planar foil accelerated by the laser were diagnosed by x-ray radiography. Imprint of modulations from random phase plates (RPP)[1] and smoothing by spectral dispersion (SSD)[2] for 0.53 μm light at 10^{14} W/cm^2 were examined[3]. The equivalent surface finish decreased from 1.24 μm for RPP illumination to 0.26 μm for SSD with 0.9 THz bandwidth. Imprint of 0.35 μm and 0.53 μm RPP illumination at $1 - 2 \times 10^{13}$ W/cm^2 was compared[4]. The 0.35 μm light generated higher imprint by a factor of $\sim$1.65. Simulations were in approximate agreement with these experiments. Imprint upon 3 μm-thick Si foils was probed with an XUV laser of 15.5 nm wavelength, for 0.35 μm light at 3×10^{12} W/cm^2 [5]. Simulations agreed with the imprinted modulation amplitude for RPP illumination, but predicted a factor of $\sim$3 too little little modulation for SSD with 0.33 THz bandwidth.

3 NIF Capsule Imprint

The dimensions and pulse shape of a NIF ignition capsule design[6] are shown in Figure 1. The capsule is driven with a shaped pulse of 1.5 MJ of 0.35μm light and gives a clean 1-D yield of up to 30 MJ. We have calculated imprint for this capsule a single spatial frequency at a time. We have evaluated imprint in planar geometry, as convergence effects are small during the imprint phase. An

uncorrelated intensity pattern was imposed every laser coherence time. Thus, the laser intensity was take to be a cosine in space direction and white noise in time, with a coherence time of 2 ps, corresponding to the 0.5 THz NIF bandwidth.

Pulse shape, 0.35 μm laser
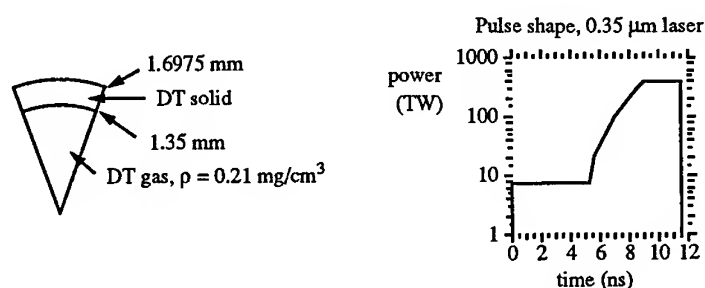
Figure 1. NIF capsule design and pulse shape

We evaluated the imprint efficiency at 2 ns, by which time we expect the imprint is mostly complete. We also used the 2 ns time-average of the white noise intensity modulation as the source amplitude to get the imprint efficiency. The resulting efficiency was about 30 μm for $l < 100$, falling off at higher l from thermal smoothing. Multiplying these imprint efficiencies by the intensity modulation spectrum, we get the equivalent surface finish mode spectrum shown in Figure 2. The total power under this spectrum corresponds to 36 nm rms, compared to 30 nm rms from the surface finish spectrum.
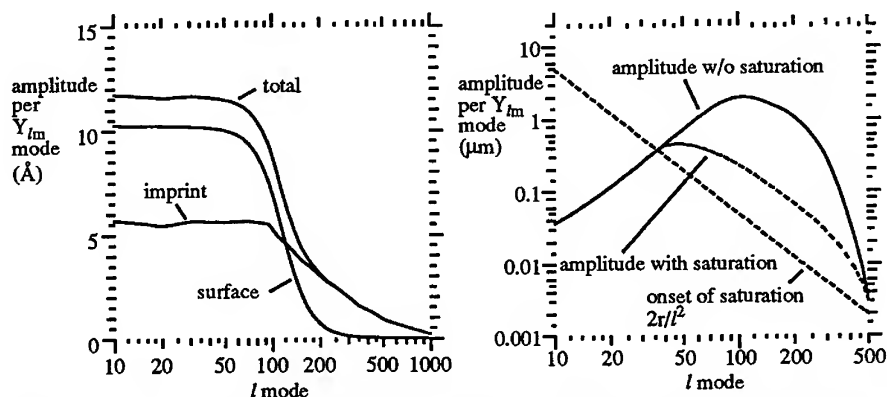
Figure 2. Imprint and surface finish spectra   Figure 3. Modal spectrum at peak velocity

The modulation amplitude during the implosion was evaluated by multiplying the equivalent surface finish by a growth factor spectrum. The effective surface finish used was the quadrature sum of imprint and surface finish, shown by the top curve in Fig. 2. We used the expression for the growth

132

rate[7] $\gamma(k) = \sqrt{\frac{ak}{1+kL}} - 3kv_a$, where the acceleration, $a = 8.5 \times 10^{15} cm/s^2$, the wavenumber, $k = r/l = 0.1cm/l$, the density gradient scale length, $L = 0.5\mu m$, and the ablation velocity, $v_a = 3.4\mu m/ns$. The linear growth factor on the ablation front to the time of peak shell implosion velocity is $GF(k) = e^{\gamma \Delta t}$, where $\Delta t = 4.66ns$ is the acceleration time.

The resulting amplitude spectrum is shown in Figure 3. According to the saturation model of Haan[8], modes enter into nonlinearity when the amplitude exceeds $2r/l$, shown as the dotted line for a radius of 250 μm. The modes above l=30 are nonlinear, substantially so at the peak of the linear spectrum at $l \cong 100$. The dashed curve shows the mode amplitude corrected for saturation. The rms bubble amplitude at peak velocity is 12 μm, well below the shell thickness of 110 μm. 2-D multimode simulations are in progress to test the saturation model and check upon shell viability.

4 Conclusions

Lasnex simulations of imprint are in reasonable agreement with experimental data for several beam smoothing conditions relevant to the performance of ignition capsules. Simulations of imprint upon a specific ignition design indicate that bandwidth of 0.5 THz will be sufficient to yield imprint comparable in effect to an expected intrinsic surface finish of 30 - 40 nm rms. Modulations of this level at the ablation front evolve well into the nonlinear regime. Examination of shell viability to such modulations is still in progress.

Acknowledgments

References

1. Y. Kato *et al.*, *Phys. Rev. Lett.* **53**, 1057 (1984).
2. S. Skupsky *et al.*, *J. Appl. Phys.* **66**, 3456 (1989).
3. S. G. Glendinning *et al.*, *Phys. Rev.* E, in press, 1996.
4. S. G. Glendinning *et al.*, 24th ECLIM, 1996.
5. D. H. Kalantar *et al.*, *Phys. Rev. Lett.* **76**, 3574 (1996).
6. C. P. Verdon, *Bull. Am. Phys. Soc.* **38**, 2010 (1993).
7. J. Lindl, *Phys. Plasmas* **2**, 3933 (1995).
8. S. W. Haan, *Phys. Rev.* A **39**, 5812 (1989).

APPLICATION AND VALIDATION OF DIRECT NUMERICAL SIMULATION FOR ICF IMPLOSION STABILITY ANALYSIS

N.M. HOFFMAN, F.J. SWENSON, W.S. VARNUM, D.C. WILSON, G.R. MAGELSSEN, M.R. CLOVER, W.J. POWERS, J.B. BECK, D.P. SMITHERMAN, CRIS W. BARNES, R.E. CHRIEN, W.W. HSING, G.T. SCHAPPERT

Los Alamos National Laboratory, P. O. Box 1663, Los Alamos, NM 87545, USA

C. K. CHOI

School of Nuclear Engineering, Purdue University, West Lafayette, IN 47027, USA

We have recently been applying a powerful computational tool, direct numerical simulation (DNS), to evaluate the stability of imploding inertial confinement fusion (ICF) capsules designed for the National Ignition Facility. In DNS, we explicitly calculate the evolution of realistic surface perturbations far into their nonlinear regimes, using a 2D Lagrangian radiation-hydrodynamics code. Because the mesh may become greatly distorted during the calculation, requiring frequent application of an automatic rezoner, and because we use a 2D code to represent 3D perturbations whose nonlinear behavior is shape-dependent, we have been seeking to assess the accuracy of DNS in as many regimes as possible. For this purpose, we have conducted experimental campaigns to observe the instability of radiatively driven imploding cylinders, deuterated-shell spherical capsules, and radiatively accelerated flat foils perturbed on the unheated surface ("feedout" experiments). We have compared DNS calculations to data from these experiments, and to theoretical predictions for incompressible Rayleigh-Taylor instability, with satisfactory agreement. Thus we are gradually accumulating confidence in the validity of DNS as applied to ICF.

1 Introduction

Large-memory vector-processor computers have in recent years made it practical to compute the evolution of multimode perturbations in inertial confinement fusion (ICF) capsule implosions throughout the duration of the implosion. Flexible automatic rezoning techniques [1] have enabled the use of 2D Lagrangian radiation-hydrodynamics codes such as LASNEX [2] for this purpose. A typical multimode surface-displacement perturbation, for example, can be followed computationally as it passes from an initial linear stage to an extremely nonlinear late stage, characterized by mode interactions, strong vorticity, and a large departure of the flow field from its unperturbed state. We use the term direct numerical simulation (DNS) to denote the process of

calculating the implosion of capsules and the development of such multimode nonlinear perturbations. [a]

Many DNS calculations have been performed [3,4] to evaluate the stability of capsules designed for the National Ignition Facility (NIF) [5] and similar facilities. DNS has allowed us to: set quantitative limits on the roughness of shell surfaces that is permissible if NIF capsules are to ignite; determine that capsules with expected levels of surface roughness are more sensitive to radiation drive time variations than are idealized 1D capsules; compare the relative hydrodynamic stability of shells with different ablator materials; and demonstrate the coupling of radiation drive asymmetry with surface perturbations.

Because of our increasing reliance on DNS for assessing the stability of NIF capsules, it is crucial that we have confidence in its accuracy. [b] We must try to validate DNS in as many regimes as possible, by comparing the results of DNS to experimental data and exact theoretical solutions, to identify the regimes of validity of the technique. In this article we shall describe briefly several ongoing efforts to carry out such validation, and describe some improvements to the computational technique of DNS.

2 Experimental Comparisons

2.1 Deuterated-shell implosions

An extensive series of experiments has been conducted over several years at Lawrence Livermore National Laboratory's Nova laser, to investigate the growth of perturbations in capsule implosions.[6,7] In the most recent experiments, hundreds of small pits are deliberately introduced into the ablator surface of the capsule during the fabrication process, as a controlled initial perturbation whose subsequent evolution may be diagnosed. We have recently applied DNS to the modeling of one class of perturbed-ablator experiments,

---

[a] In the fluid mechanics community, DNS refers strictly to calculations in which the viscous dissipation scale is resolved. Calculations which do not resolve such a small scale, but instead employ a model of the small-scale flow below the grid resolution, are called large eddy simulations (LES). Our calculations more nearly resemble LES calculations, but use an artificial viscosity instead of a subgrid turbulence model. We prefer to avoid these fine distinctions in the context of ICF, and use the term "DNS" in a loose sense to apply to our simulations.

[b] Accuracy may be compromised by, for example, the severe distortion of the Lagrangian mesh for implosions with relatively large initial perturbations. Typically it is necessary in such situations to perform frequent rezoning of physical quantities to a more nearly orthogonal mesh. Furthermore, accuracy may be compromised by the fact that real perturbations are 3-dimensional, whereas in our calculations we must (so far) represent them as 2-dimensional.

in which the capsule contains hydrogen gas instead of deuterium gas, and a deuterated polystyrene (CD) shell instead of the usual polystyrene.[8] Thus in these implosions the fusion processes occur in the compressed CD shell rather than in the gaseous core, permitting an assessment of thermodynamic processes coupling the core and the shell. DNS has been successful in accounting for the observed variation of neutron yield with imposed surface roughness, including the relatively sudden fall-off in yield due to shell breakup, when the surface roughness exceeds 0.5 μm RMS. The observed width of the neutron spectrum is also explained by Doppler broadening resulting from bulk motion of falling Rayleigh-Taylor (RT) "spikes" of deuterated polystyrene, with velocity of order 10^7 cm/s, during burn.

2.2 Perturbed cylindrical implosions; "feedout" experiment

Two other experiment campaigns of particular value for DNS validation are the cylindrical implosion experiments [9,10] and the "feedout" experiments being performed at Nova. In the former, a cylindrical shell ablator composed of polystyrene and monobromostyrene is fabricated with a single-mode azimuthal surface perturbation (typically $m=10$ or $m=14$). The growth of the perturbation during the x-ray-driven implosion of the cylinder is imaged with an x-ray backlighter. Images of the perturbation have been compared directly with the predictions of DNS, with satisfactory agreement.

The feedout experiment addresses the seeding of ablative Rayleigh-Taylor (ART) instability at the ablation surface of a planar foil by a perturbation initially present on the cold side of the foil. This process is analogous to the seeding of ART by perturbations on the DT ice surface in NIF capsules. In both cases, Richtmyer-Meshkov (RM) instability occurs when a shock traverses the perturbed surface, and the subsequent RM flow field carries a perturbation of all physical variables back to the ablation surface, where the perturbation may be rapidly amplified. Initial experiments show reasonable agreement with computational predictions.

3 Theoretical Comparisons

3.1 Linear phase of incompressible RT instability

We have studied the accuracy of LASNEX calculations of planar incompressible RT instability for small-amplitude perturbations. In this case, the exact growth rate is known from theory. Calculations were performed with large internal energy, so the sound speed c is very high and the flow is nearly incompressible. For a perturbation with wavelength λ and gravity g, the com-

pressibility parameter $M^2 \equiv g\lambda/c^2 \simeq 0.006$. Our study examined the effect of mesh refinement on the accuracy of computed growth rates, for several values of the Atwood number A, where $A \equiv (\rho_2 - \rho_1)/(\rho_2 + \rho_1)$, and ρ_2 and ρ_1 are the densities in the upper and lower fluids, respectively. Calculations were done with $A = 1/3, 5/6$, and $49/51$ and with the number of mesh cells per wavelength N between 10 and 80. Various amounts of linear artificial viscosity were used. We found that for $A \geq 5/6$, the computed linear growth rate was within 5% of the theoretical value provided $N \geq 20$. For smaller Atwood numbers, the convergence with mesh refinement was not so rapid. For $A = 1/3$, it was required that $N \geq 35$ to give a computed growth rate within 5% of theoretical.

3.2 Late-stage bubble rise in incompressible RT instability

After the RT instability becomes nonlinear, the bubble eventually rises with constant velocity V_∞. A simple analysis leads to $V_\infty = \alpha\sqrt{2Ag\lambda/(1 + A)}$, where $0.2 \leq \alpha \leq 0.3$. Layzer [11] found $\alpha \simeq 0.2303$ for a 2D bubble when $A = 1$. We have begun a computational study of the constant-velocity bubble, as a test of the rezoning capability of the code. To date, we have results for $A = 1/3$ and $N = 56$, using several different prescriptions for the extent of rezoning. We find that the bubble velocity approaches within about 5% of the value of V_∞ obtained using Layzer's value of α, at about the time that an extrapolation of the linear-stage bubble velocity reaches this value. The bubble velocity then decreases slightly (for a period of about one time unit $\sqrt{\lambda/2\pi g}$, and then increases slowly again. There is no exact time-dependent theory of the bubble rise for $A < 1$, but the approximate agreement with V_∞ in this case is satisfactory.

4 Improvements to Numerical Technique

We have made progress in understanding the limits of the numerical technique used for DNS, and thereby increased our confidence in its results. Continued experimentation with numerical procedures has led to improvements in the accuracy and efficiency of the rezoning technique. An "anti-bow" capability is being tested, which is an efficient way to identify mesh cells that require rezoning. The use of graded remapping, where various parts of the mesh are allowed to approach farther or nearer the full Brackbill-Saltzman mesh solution, as necessary, has improved accuracy. Mesh refinement studies of full DNS capsule implosion calculations are leading to an understanding of zoning requirements.

We have also identified a surprising effect of mesh "hourglass" oscillations.

Such oscillations are one of the normal numerical modes of a finite-difference mesh, which preserve cell volume even as edge lengths oscillate in a correlated way. Such oscillations do no work on the fluid directly. Nevertheless, we have observed that such oscillations may be triggered by a physical perturbation, whose growth is then enhanced in some way by the presence of the hourglass oscillations, perhaps related to the effect of radiation flux. Thus it is crucial to prevent the occurrence of the hourglass oscillations. We have found several ways of doing so, including refining the radial mesh and rezoning the oscillating cells. Employing an "anti-hourglass" mesh stiffening algorithm may also prove useful.

Acknowledgments

References

1. J. Brackbill and J. Saltzman, *J. Comput. Phys.* **46**, 342 (1982).
2. G.B. Zimmerman and W.L. Kruer, *Comments Plasma Phys.* **2**, 51 (1975).
3. N.M. Hoffman, D.C. Wilson, W.S. Varnum, W.J. Krauser, and B.H. Wilde, to appear in *AIP Conference Proceedings of the 12th International Conference on Laser Interaction and Related Plasma Phenomena*, Osaka, 24-28 April 1995 (American Institute of Physics, Woodbury, NY, in press).
4. W.J. Krauser, N.M. Hoffman, D.C. Wilson, B.H. Wilde, W.S. Varnum, D.B. Harris, F.J. Swenson, P.A. Bradley, S. W. Haan, S.M. Pollaine, A.S. Wan, J.C. Moreno, and P.A. Amendt,*Phys. Plasmas* **3**, 2084 (1996).
5. J.D. Lindl, *Phys. Plasmas* **2**, 3933 (1995).
6. T.R. Dittrich, B.A. Hammel, C.J. Keane, R. McEachern, R.E. Turner, S.W. Haan and L.J. Suter, *Phys. Rev. Lett.* **73**, 2324 (1994).
7. C.J. Keane, G.W. Pollak, R.C. Cook, T.R. Dittrich, B.A. Hammel, O.L. Landen, S.H. Langer, W.K. Levedahl, D.H. Munro, H.A. Scott and G.B. Zimmerman, *J. Quant. Spectrosc. Radiat. Transfer* **54**, 207 (1995).
8. R.E. Chrien, N.M. Hoffman, J.D. Colvin, C.J. Keane, O.L. Landen and B.A. Hammel, submitted to *Phys. Rev. Lett.*
9. W.W. Hsing and N.M. Hoffman, submitted to *Phys. Rev. Lett.*
10. J.B. Beck, Ph.D. thesis, Purdue University (May 1996).
11. D. Layzer, *Astrophys. J.* **122**, 1 (1955).

THE SIMPLEST MODEL WHICH REPRODUCES MAIN RESULTS OF THE MORE SOPHISTICATED RAYLEIGH-TAYLOR SELF-CONSISTENT MODELS IN ICF

A.R. PIRIZ

Consejo Nacional de Investigaciones Científicas y Técnicas (CONICET). Argentina

J. SANZ

E.T.S.I. Aeronáuticos, Universidad Politécnica de Madrid, 28040-Madrid-Spain

The Rayleigh-Taylor instability of a steady ablation front has been studied by means of a simple model based in the sharp boundary approximation. The model includes the effects of thermal conduction behind and across the front and allows for determining the growth rate in terms of the effective density jump r_D. This parameter cannot be self-consistently determined but a good estimation is obtained by means of a corona model. The results are in excellent agreement with more sophisticated theories and numerical calculations.

1. INTRODUCTION

Rayleigh-Taylor instability of an ablation front is one of the main factors which determines the minimum energy for ignition and it is a current matter of extensive studies . Very recently, self-consistent analytical and semi-analytical models based on elaborated mathematical tools have been developed.[1,2] Despite the fact that their results are in excellent agreement with numerical results,[3] the availability of a relatively simple analytical model is of great interest for improving our understanding of the physical process underlying the observed stabilization. Besides, such a model would be more suitable for exploring new regimes of potential interest.

The most simple treatment that we can find in the literature is based on the sharp boundary model.[4] According to this model the ablation front can be taken as a moving surface of zero thickness which is initially at $y=0$ and it separates two homogeneous fluids of densities ρ_1 ($y>0$) and ρ_2 ($y<0$), respectively ($\rho_2>\rho_1$). The heavy fluid is supported against an acceleration g by the lighter one. The main shortcoming of this model is that it requires additional information associated to the flow structure behind the front. Such an information cannot be self-consistently incorporated and it has been usually considered as the main reason for its failure. However, it is a matter of fact that these studies also introduce drastic approximations such as adiabatic perturbations on both sides of the interface, and/or Mach number $M_0=0$ on one or both sides, and/or the thermal flux behind and/or across the front has been neglected. Those assumptions have often led to internal inconsistencies in the model, independently of the extra boundary

condition. Therefore, satisfactory results cannot be expected even assuming that an adequate extra condition is used.

In this paper we present a new version of the sharp boundary model in which the thermal conduction behind and across the front is considered. Besides, we take $M_0 \ll 1$ but not zero, in order to allow for $M_0 \geq \gamma/kc_0$ (γ is the growth rate, k is the perturbation wave number and c_0 is the sound speed). Thus, we get a self-consistent dispersion relation in terms of one unknown. As in the corresponding problem arising when an ablation front is studied by the discontinuity model, such an unknown is the self-consistent density behind the front and it is associated with the characteristic lengths of the ablation process and of the instability.

2. LINEAR STABILITY ANALYSIS

We consider a steady ablation front placed at $y = \xi(x, t)$, with an acceleration $g = g\ e_y$ opposite to the density gradient. Then we perform the stability analysis by assuming that the thickness L_0 of the front we are studying is $kL_0 \ll 1$ and, by linearizing the fluid equations:

$$\frac{\partial \rho}{\partial t} + \nabla.(\rho v) = 0 \ , \qquad \rho\frac{\partial v}{\partial t} + \rho(v.\nabla)v = -\nabla p - \rho g \ , \tag{1}$$

$$\frac{\partial}{\partial t}[\rho(\frac{v^2}{2} + \varepsilon)] + \nabla.[\rho v(\frac{v^2}{2} + \frac{5}{3}\varepsilon) + Q] = \rho v.g \ , \qquad Q = -\kappa_D \nabla\varepsilon, \tag{2}$$

where the fluid has been assumed to be an ideal gas, ρ, v and ε are, respectively, the fluid density, velocity and specific internal energy, and $p = (2/3)\rho\varepsilon$ is the pressure. Then, we assume that every quantity φ evolves in the following form : $\varphi = \varphi_0 + \delta\varphi$, $\delta\varphi \propto \exp(\gamma t + qy + ikx)$, where φ_0 is the unperturbed value, $\delta\varphi \ll \varphi_0$ and q represents the longitudinal wave numbers. Besides, we take $g \ll qc_0^2$, $M_0^2 = v_0^2/c_0^2 \ll 1$, and we assume that perturbations ahead of the front are adiabatic. Furthermore, for simplicity, we consider that thermal conduction is relatively strong behind the front :

$$k\kappa_{D2} / \rho_2 v_2 \ll 1 \ (y < 0) \quad , \quad k\kappa_{D1} / \rho_1 v_1 \gg 1 \ (y > 0) . \tag{3}$$

Then, by solving the linear equations, we find one mode ahead of the front which vanishes at $y \to -\infty$: a sonic mode ($q_{2s} \approx k$). Behind the front we have three modes vanishing at $y \to +\infty$: a sonic mode ($q_{1s} \approx -k$) ; a thermal conduction mode ($q_{1T} \approx -k$), and a vorticity mode ($q_{1v} = -\gamma/v_1$). Every arbitrary small perturbation is a linear combination of those modes and the solutions on both sides of the interface must be matched on the front surface in order to find the dispersion relation $\gamma(k)$. The boundary conditions on the front are obtained by integrating the perturbations of

140

the conservation equations across the moving front with coordinate $\xi(x,t) = \xi_f \exp(\gamma t + ikx)$. Thus, the following boundary conditions are found in the usual manner: [4]

$$\Delta[-\rho_0 \gamma \xi + \rho_0 \delta v_y + v_0 \delta \rho] = 0 , \qquad \Delta[\delta v_x + ik\xi v_0] = 0, \tag{4}$$

$$\Delta[\delta p + v_0^2 \, \delta \rho + 2\rho_0 v_0 \, \delta v_y + \rho_0 g \xi] = 0 , \tag{5}$$

$$\Delta[-(\rho_0 \frac{v_0^2}{2} + \frac{3}{2} p_0)\gamma \xi + \frac{3}{2}\rho_0 v_0^2 \, \delta v_y + \frac{v_0^3}{2} \delta \rho + \frac{3}{2} p_0 \, \delta v_y + \frac{5}{2} v_0 \, \delta p + \delta Q_y] = 0 , \tag{6}$$

where $\Delta[\varphi] = \varphi_2 - \varphi_1$. It is noted that in writing δQ_y we have taken into account that the isotherms move with the front.[1,4] Furthermore, we have $\Delta[\delta Q_y] = -\delta Q_y \approx -k\kappa_{D1} \delta\varepsilon_1$. Since κ_{D1} is strongly dependent on the details of the front structure, it is convenient to write δQ_y in a more suitable way which involves only global properties of the ablation process. Considering that the front behaves as an isotherm, we have : $\delta\varepsilon_1 = -\xi(d\varepsilon / dy)_{y=0}$, $\Delta[\delta Q_y] = k\xi Q_0 \approx k\xi(5/2)p_1 v_1(1 - r_D)$,

where $r_D = \rho_1/\rho_2$ is the self-consistent density jump across the front. From the previous equations we get the growth rate in term of r_D:

$$\gamma = \left[\left(\frac{2kv_2}{1+r_D}\right)^2 - kg\left(\frac{kv_2^2}{gr_D} - A_T\right)\right]^{1/2} - \frac{2kv_2}{1+r_D} , \tag{7}$$

where $A_T = (1 - r_D)/(1 + r_D)$ is the Atwood number. This expression is very similar to the one obtained in Ref.1 and is formally identical to the one obtained by Goncharov et al.[2], provided that r_D is adequately chosen. As we previously mentioned, there is no way to determine r_D self-consistently from the present model and extra information regarding the characteristic lengths of the corona and of the instability has to be introduced. Thus, we assume that r_D is given by the ratio of the peak density ρ_2, reached at the ablation surface, to the density ρ_1 reached at a distance y_1 of the order of k^{-1}. Excellent agreement with numerical results and with self-consistent theory [1-3] is achieved by taking $y_0 = c/k$, with $c=0.4$ to 0.5. On the other hand, we can get an approximate expression for the density profile from a simple corona model ($\kappa_D = \chi \varepsilon^v$, where χ is the coefficient of thermal conduction) :

$$\rho / \rho_2 \approx (vu)^{-1} \ if \ u \ge u_0 \quad ; \quad \rho / \rho_2 \approx (1 + ae^u)^{-1} \ if \ u \le u_0 , \tag{8}$$

where $u = y/L_0$ ($L_0 = 3\kappa_{D2}/5\rho_2 v_2$); $a = \exp(-u_0)(vu_0)^{(1-v)/v}$ and u_0 satisfy the relationship: $vu_0 - (vu_0)^v = 1$. From this equation we get $r_D = \rho_1/\rho_2$ [$\rho_1 = \rho_1(u_1)$, $u_1 = 1/2kL_0$]. In Fig. 1 (dashed line) we have compared the cut-off wave number given by Eqs.(7) and (8) with the numerical results in Ref.3. As we can see, excellent agreement is obtained for $\Gamma \le 1$ to 5 ($\Gamma = gL_0/v_2^2$). This is the regime in which the model hypothesis $kL_0 \ll 1$ holds.

Extensive comparisons of Eqs.(7) and (8) with numerical results can be found in Ref.2. Here, as an example of the potential applications of a so simple

model, we explore the regime $\Gamma \gg 1$. In such a regime kL_0 becomes of the order of 1 and the model hypotheses are not satisfied. In fact, in obtaining Eq.(7) we have neglected terms of the order kL_0. Nevertheless, a good approximation can be obtained by retaining, among those terms, the most physically significant. Numerical results[3] and theory based on the WKB approximation[5] show that for $\Gamma \gg 1$ the lateral transport becomes important. Then, by assuming that this is the most relevant effect arising for $\Gamma \gg 1$, we can retain such a term in Eq.(6) : $\delta Q_x = k \kappa_{D1} \delta \varepsilon_1 (kL_0)$. Therefore, we have:

$$\Delta[\delta Q_y] + \delta Q_x \approx k \xi Q_0 \phi_0 \ , \quad \phi_0 = (1 + kL_0) \ , \tag{9}$$

and the growth rate turns out to be:

$$\gamma = \left[\left(\frac{(1+\phi_0)kv_2}{1+r_D} \right)^2 - kg \left(\frac{2\phi_0 - (1-r_D)}{1+r_D} \frac{kv_2^2}{gr_D} - A_T \right) \right]^{1/2} - \frac{(1+\phi_0)kv_2}{1+r_D} \ . \tag{10}$$

We have represented in Fig.1 the cut-off wave number given by Eq. (10) (solid line) together with the numerical results of Ref.3 and, in Fig.2, we have compared the respective growth rates for $\Gamma=20$ and $\Gamma=100$. As can be seen, the present simple model is in fair agreement with the numerical calculations.
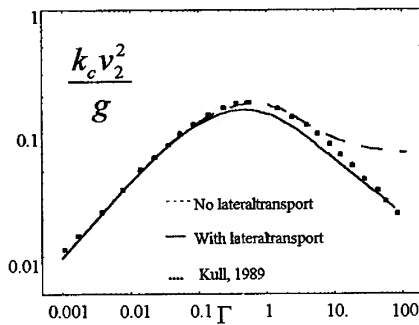
Fig. 1.- Cut-off wave number Vs. the instability parameter Γ for $v=2.5$.
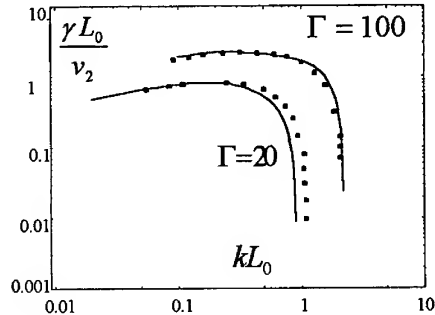
Fig.2.- Instability growth rates for two values of Γ and $v=2.5$.

REFERENCES

[1]J. Sanz, Phys.Rev.Lett., 73, 2700(1994).

[2]V.N. Goncharov, R. Betti, R.L. McCrory, P. Sorotokin, and C.P. Verdon, Phys. Plasmas, 3,1402 (1996). J. Sanz, Phys. Rev. E, 53,4026 (1996).

[3]H.J.Kull,Phys.Fluids B, 1, 170 (1989).

[4]S. Bodner, Phys. Rev. Lett., 33,761 (1974) ; L. Baker, Phys. Fluids, 26,627 (1983).

[5]J.Sanz, L.F. Ibañez, A.R. Piriz, "Linear R-T instability scaling..."This Conference.

PHYSICS OF THE LASER GREEN HOUSE TARGET: REVIEW OF EXPERIMENTAL AND THEORETICAL RESULTS

S.YU.GUS'KOV, V.B.ROZANOV

P.N.Lebedev Physical Institute, Russian Academy of Sciences, 117924 Moscow, Russia, Leninsky , 53

The review of the investigation results on physical processes occurring in the Laser Green House target obtained by research groups from P.N. Lebedev Physics Institute, Institute of General Physics, TRINITI Institute, Institute for Mathematical Modelling is given. The principle of the Green House target operation is based on smoothing of the distribution of absorbed laser energy due to the energy transfer processes under volume absorption of laser radiation in special absorber made of subcritical density matter (foam or matter with a regular internal structure)[1]. Mainly physics of the processes in the Green House target absorber is discussed and the results on high power laser pulse interaction with low density foam, including laser radiation absorption and energy transfer are summarised.

1. One of the approaches to ICF target design is based on smoothing the nonuniformities of the laser beams energy deposition into the target with the help of the plasma phenomena occurring in laser radiation interaction with special absorber . Smoothing process in the Green House target is due to volume absorption of the laser beams and fast energy transfer in a subcritical density absorber (with the density of (1-10) mg / cm³) made of the volume structured matter of light elements. The physics of laser radiation interaction with a foam matter has been much studied now (large number of the experimental results on this subject is presented, for example, in [2]) .

The interaction of high power laser pulse with a subcritical density foam is characterised by several important features. The absorption of a laser beam takes place in the plasma channel which has the length close to that of an inverse bremsstrahlung process. In contrast the laser pulse interaction with a homogeneous media (vs gaseous), the volume absorption of the laser radiation and laser-produced plasma formation in the foam media is accompanied by internal ablation of the matter, when the solid particles are evaporated into the pores under heating by the laser radiation. Such internal ablation process results in a situation when an initial stage of the laser light absorption takes place under conditions of decreasing of geometrical transparency of the foam matter along the direction of the laser beam propagation. The energy transfer process (both in longitudinal and in transverse direction) in the foam matter is accompanied by internal ablation as well. Under this process the collisions of the chaotic hydrodynamic microflows from the neighbour (initially solid) particles leads to thermolization of a plasma, and as a result, to an anomalously prolonged storage of the absorbed laser energy in a thermal component. Under the action of a high power laser pulse (the intensity of 10^{13}- 10^{15} w/cm²) on the subcritical density matter the plasma may be heated up to high temperature (1-5) keV , and, a supersonic electron conductivity wave in the region, where the internal ablation of the

foam has been finished, may be initiated. So, in a foam of light elements the energy transfer wave may be treated as "hydro-thermal" wave ; its front velocity corresponds to the velocity of the internal ablation front, i.e. close to sound velocity , and the temperature distribution behind the front is smoothed by the electron heat conductivity.

2. The wide set of the experiments on studying the physics of high power laser interaction with low density foam was performed in TRINITI Institute (Russia) by I.N. Burdonsky, A.V. Bugrov, V.V.Gavrilov , A.Yu. Gol'tsov , E.V. Zhuzhukalo, N.G.Kovalsky and S.F.Medovshchikov. The experiments were made with Nd laser "Mishen": laser energy, E_L ~100 J, intensity, $I \approx 10^{14}$ W/cm^2, wavelength, $\lambda = 1.06$ μm, pulse duration, $t_L \approx 2.5$ ns, pulse forefront duration, $t_1 \approx 0.3$ ns, and focal spot radius, $r_f \sim 100$ μm. The targets were the plane $(C_{14}H_{18}O_7)_n$ agar foam targets with an average density $\rho_a \approx$ (1-10) mg / cm^3 , the density of the solid particles, $\rho_0 \approx 1$ g/cm^3 and the thickness (along the laser beam axis), $\Delta_a \approx$ (0.1 - 1) mm. The two-layers target: agar foam layer and Al layer of (1-1.5) μm thickness were used also. The X-ray and optical diagnostics techniques were used to study the physics of laser radiation absorption and energy transfer. The basic results obtained for (0.5-1) mm thick targets with of the density 1 and 4 mg/cm^3 are following:

- the duration of the laser radiation absorption region formation is approximately (200-300) ps; the depth of this region along the laser beam axis is about (100-150) μm; during the time of absorption region formation the targets are partially transparent for the laser light; after first(100-300) ps of laser pulse duration the targets become nontransparent for the laser light;

- the velocity of the energy transfer wave inside the targets is approximately (1-2)10^7 cm/s; the size of plasma region along the laser beam axis with the temperature ~ 1keV is ~500 μm for the targets with the density 1 mg/cm^2 , and ~300 μm for the targets with the density 4 mg/cm^3

- the pressure at the rear side of the targets is 1-2 Mbar, and the moment of the appearance of the pressure on the rear side of the targets is approximately 1.5 ns (after the start of laser pulse) for 0.5 mm thick targets and - 2ns for 1 mm thick targets; the velocity of Al layer is (4-8) 10^6 cm/s .

The experimental results may be explained by the effect of internal ablation of the foam matter on the formation of the laser radiation absorption region and by a "hydro-thermal" wave phenomenon. Actually, the internal ablation laser-heated foam particles leads to the drop of a geometrical transparency of foam matter. The length of complete nontransparency is inversely proportional to an average projection of the foam particle square to the laser beam cross section. For the foam with cylindrical particles, such as agar foam, during the internal ablation in the laser beam absorption channel the nontransparency length drops from $L_0 = \pi^2 \cdot \rho_0 \cdot b_0 / 4 \cdot \rho_a$ (b_0 is the initial average radius of the foam particle), corresponding to the initial state of the matter down, to $L_c = L_0(\rho_c / \rho_0)^{1/2}$, corresponding to the particles expansion to the critical

density ρ_c. Then, the absorption region length becomes close to the inverse bremsstrahlung length of the subcritical plasma . In approximation of isothermal expansion of the cylindrical foam particle under the action of the laser pulse forefront (with linear temporal growth of power) the time of nontransparency length drop is equal:

$$t = \left[\left(\frac{L_0}{L(t)}\right)^{1/2} - 1\right]^{1/2} \cdot t_*, \qquad t_* = \left[\frac{24 \cdot \pi^2}{(\gamma - 1)} \cdot \frac{\rho_0 \cdot b_0^3}{k_a \cdot I_m \cdot t_1}\right]^{1/2} \qquad (1)$$

here $I_m = I(t_1)$; k_a is the average absorption coefficient for each of the particles; γ is the adiabatic constant. For the agar foam with a typical size $b_0 \sim 1\ \mu$ the nontransparency length is close to 5 mm for $\rho_a = 1\ mg/cm^3$, and $L_0 \approx 1.25$ mm for $\rho_a = 4\ mg/cm^3$. So, the thicknesses of "Mishen" experiment targets are less than L_0 , and at the initial stage these targets must be partially transparent for the laser light. Assuming $k_a = 0.5$, the expressions (1) give for the moment of transparency stopping of the targets with the thickness, for example, $\Delta_a = 0.5$ mm, the following values: 150 ps for $\rho_a = 1\ mg/cm^3$ and 100 ps for $\rho_a = 4\ mg/cm^3$. According (1), the time during which the inverse bremsstrahlung absorption region length, is established makes $t_c = (\rho_0 / \rho_c)^{1/8} \cdot t_* \approx 250$ ps; the plasma temperature in this region is $T(t_c) \approx k_a \cdot I_m \cdot t_c^2 / t_1 \cdot L_0 \cdot \rho_a \sim 0.5$ keV.

The velocity of spherical "hydro-thermal" wave is close (with accuracy to constant) to one for "high intensity explosion" phenomenon:

$$v_h \cong \left[\left(\frac{3}{5}\right)^3 \cdot \frac{(\gamma - 1) \cdot E_L}{\pi \cdot \rho_a \cdot t_L}\right]^{1/5} \cdot t^{-2/5} \qquad (2)$$

Hence, the moment of time when this wave reaches the rear side of the foam target, and the plasma pressure at this moment are :

$$t_r \cong \left[\left(\frac{3}{5}\right)^2 \cdot \frac{\pi \cdot \rho_a \cdot \Delta_a^5 \cdot t_L}{(\gamma - 1) \cdot E_L}\right]^{1/3}, \qquad P(t_r) \cong \left[\frac{3}{5} \cdot \frac{(\gamma - 1) \cdot E_L \cdot \rho_a^{1/2}}{\pi \cdot \Delta^2 \cdot t_L}\right]^{2/3} \qquad (3)$$

Expressions (3) give the following results for "Mishen" experiments : $t_r \approx 1.3$ ns $P(t_r) \approx 1$ Mbar , and $T(t_r) \sim P(t_r)/\rho_a \approx 2$ keV for the target with $\Delta_a = 0.5$ mm and $\rho_a = 1\ mg/cm^3$; $t_r \approx 2.1$ ns, $P(t_r) \approx 1.6$ Mbar , and $T(t_r) \approx 0.8$ keV for the target with $\Delta_a = 0.5$ mm and $\rho_a = 4\ mg/cm^3$. The velocity of solid layer (with the density ρ_s and thickness Δ_s) will be accelerated by the plasma pressure up to the velocity $v_s \sim [\ P(t_r)/\rho_a]^{1/2} \cdot (\rho_a \Delta_a / \rho_s \Delta_s)$, and this is close to $5 \cdot 10^6$ cm/s for the two-layer target with the parameters $\rho_a = 1 mg/cm^3$, $\Delta_a = 0.5$mm, $\rho_s = 2.7 g/cm^3$ and $\Delta_s = 1.5 \mu m$, while the velocity of "hydro-thermal" wave (2) in foam is $4 \cdot 10^7 cm/s$.

It should be noted, that under experimental conditions of [2], the "hydro-thermal" wave approach (2) gives the energy transfer wave velocity close to that measured in [2] only when the absorbed laser energy is taken to be $0.1E_L$.
3. The experiments on interaction of sharply focused laser beam with a relatively dense foam were performed with Nd glass laser "Feniks"of Institute of General Physics (Russia) by Yu. S. Kas'anov, M. O. Koshevoy, A. A. Rupasov, A. S. Shikanov. The laser parameters are : $E_L \approx 10$ J, $I_m \approx 5 \cdot 10^{14}$ W/cm^2 , $\lambda = 0.53$ μm, $t_L \approx 2.5$ ns, $r_f \sim 7$ μm. The plane $(C H)_n$ polypropylene foam targets with $\rho_a \approx 20$ mg / cm^3 , $\rho_0 \approx 1$ g/cm^3 , $\Delta_a \approx 200 - 1000$ μm and the average size of a pore $r_p \sim (30-50)$ μm were used (so, $\rho_a > \rho_c$ and $r_p >> r_f$). The experiments also showed an effective absorbed laser energy transfer in a large-scale pore foam : the velocity of energy transfer along the laser beam axis v_L $\approx (1-3)$ 10^7 cm/s and in transversal direction $v_t \approx 10^7$ cm/s, were measured.

In contrast to the case of subcritical foam, in the overcritical foam after the internal ablation along the laser beam is finished, the laser light begin to absorb near front surface of a target and later the usual surface ablation process takes place. So, the velocity of the longitudinal energy transfer wave, which is close to the surface ablation front velocity, is the following:

$$v_L \approx \left(\frac{\rho_c}{\rho_a}\right) \cdot \left[\frac{2(\gamma-1)}{3\gamma-1} \cdot \frac{k_a \cdot I_m}{\rho_c}\right]^{1/3}$$

The energy transfer wave in the transversal direction may be described by cylindrical "hydro-thermal" wave with an axial energy source of the length $v_L \cdot t$ and the velocity of such a wave may be written as follows:

$$v_t \approx \left(\frac{3\gamma-1}{\gamma-1}\right)^{1/4} \cdot \left(\frac{\rho_a}{\rho_c} \cdot \frac{r_f}{t} \cdot v_L\right)^{1/2}$$

So, such a model gives the results close to experiment: $v_L \approx 10^7$ cm/s and v_t $\approx 8 \cdot 10^6$ cm/s, and this explains an existence of the energy transfer anisotropy.

Conclusion.

1. The velocity of the energy transfer wave of $(3-5) \cdot 10^7$ cm/s may be reached under the absorption of a high power laser pulse into the subcritical density foam matter. This makes possible to limit the required number of the laser beams for Green House "ignition" target by value 6 - 8.
2 The Green House target design must take into account the existence of the initial stage of the laser light absorption in a low-density foam, when a relatively large length of the transparency of such a matter occurs.

References.

[1] Gus'kov S Yu, Rozanov V B and Zmitrenko N V 1995 JETP **81** 296-305
[2] Koch J A , Estabrok K G , Bauer J D et al Phys. Plasmas 1995 **2** 3820-31

THE COMPUTATIONAL OPTIMIZATION OF INDIRECT-DRIVEN TARGETS FOR IGNITION AND THE ENGINEERING TEST FACILITY.

E.N.AVRORIN, V.A.LYKOV, V.E.CHERNYAKOV, A.N.SHUSHLEBIN,
K.A.MUSTAFIN, V.D.FROLOV, M.Yu.KOZMANOV,
Ya.Z.KANDIEV, A.A.SOFRONOV

Russian Federal Nuclear Center - VNIITF
PO box 245 Snezhinsk (Chelyabinsk-70), 456770, Russia.
E-mail: lyk@nine.ch70.chel.su

The results of 1D-ERA and 2D-TIGR, OMEGA codes calculations of compression and burn of indirect-driven targets for the thermonuclear ignition and Engineering Test Facility are presented. The possibility to obtain high energy yield of $G > 100$ with driver energy of $E_d = 5-10\ MJ$ by using the heavy-ion one-beam accelerator as the main driver and powerful laser for fast ignition of thermonuclear detonation of cylindrical targets is pointed out.

1   Introduction

The progress in experimental and theoretical studies of the indirect-driven targets physics[1] and the development of powerful lasers give hope to achieve the thermonuclear ignition at laser facility NIF and to start working on the projects of various thermonuclear IFC reactors[2,3] The goal of the theoretical research carried out in RFNC- VNIITF is to bring light on the requirements imposed on targets design and laser parameters to obtain the thermonuclear ignition and high energy gain of targets. The results of the 1D-ERA code[4] and the 2D-program complex of the TIGR-3T[5] and OMEGA[6] code calculations of indirect-driven targets are presented below.

2   The results of targets optimization and turbulent mixing obtained by the 1D-ERA code

The simplest type of cryogen shell-target design with the initial shell aspect ratio $A_S = 10 - 20$ and DT-ice layer aspect ratio $A_{DT} = 20 - 50$ was chosen for consideration.

The considered range of $A_S = 10 - 20$ corresponds to the in- flight shell aspect ratio of $A_{inf} = 50-80$, which is limited[7,8] by the achieved technological level of targets fabrication. Such targets do not impose extreme requirements on shape and precision of laser pulse[4].

The results of 1D-ERA code calculations for thermonuclear ignition of targets for a range of hohlraum temperatures $0.3 - 0.4\ keV$ are presented in Table 1 (case A-C). The results of numerical optimization of targets for the ETF performed for a range of black-body radiation temperatures $T_r = 0.20 - 0.35\ keV$ and the glass ablator with inner diameter of $D = 4\ mm$ are presented in Table 1 (case D-F), as well. The linear time dependence of radiation temperature was used in these calculations.

The calculations for case C from Table 1 were performed by the ERA code with account of the turbulent mixing using $k\varepsilon$-model [9] to estimate possible influence of short-wave perturbation development during both shell acceleration and deceleration stages. The growth rate of perturbations with account of ablation stabilization ($\gamma = \sqrt{gk} - \beta k v_a$) with parameter $\beta = 2$ [1,10] was used in the calculations.

The upper limit of outer surface roughness equals to $0.1\ \mu m$ at initial ratio of $k\varepsilon$-model parameters $D_0 = k_0^2/\varepsilon_0 = 0,1\ \mu m^2/ns$ in accordance with performed calculations. The mixing basically takes place at the fuel- glass interface and involves less than 30 % of mass of DT-fuel in this case. The ignition of such target would require the laser type of NIF power.

According to the calculations performed for the ETF type driver the gain could achieve the values of $G_a \approx 100$ for considered targets (cases D-F from Table 1) with the hohlraum temperature linearly rising from the initial value of $50 eV$ up to maximum value of $T_0 \simeq 250 \div 300\ eV$ in time interval of $t_0 = 15 - 20\ ns$, the initial aspect ratio of glass shell $A_0 > 10$ and X-ray energy absorbed by the target of $E_a \simeq 0.5 \div 1.5\ MJ$.

For providing the necessary radiation symmetry in hohlraum design, described in [1], the driver energy of $E_{dr} = (4-6)E_a$ is needed, so the total energy gain could be equal to $G \approx 15 \div 20$. Such value of gain should be obtained for the ETF project considering heavy-ion accelerator as a driver [2] or hybrid thermonuclear reactor [3].

The ratio of DT-fuel mass to ablator mass is $m_f/m_a = 2 - 3\%$ for the designs presented in Table 1 and the ratio of DT-fuel mass to nonablated target mass is about of 20-30 % only, that is why the target gain may be increased in 2-3 times by increasing these ratio. In this case the initial aspect ratio of the layer of DT-fuel will increase up to the value of $A_f = 10 - 20$ and it will need more precise [1] than linear time dependence of temperature T_r, used in our calculations. It is also possible to decrease hohlraum temperatures if the glass ablator is changed to the one with less opacity. It seems reasonable to increase spherical targets gain up to the values of $G = 40 - 60$ at driver energy of $E_{dr} = 5 - 10\ MJ$ if such modifications were made.

Table 1: Simulation parameters and results.

Initial parameters	A	B	C	D	E	F
Target:						
Outer shell radius (mm)	0.32	0.525	1.075	2.1	2.15	2.2
Initial shell aspect ratio	16	21	14	21	14.3	11
Initial shell density (g/cc)	8	6	2.5	2.5	2.5	2.5
D-T thickness (μm)	20	20	20	45	90	90
Hohlraum temperature:						
T_0-max temperature (eV)	390	380	300	250	280	320
t_0-temp. rise time (nsec)	2.5	4	10	18	18	18
Implosion results						
X-ray absorbed energy (MJ)	0.015	0.045	0.140	0.7	1.3	1.7
imploded speed (cm/μs)	35	35	35	32	32	32
Mass ablation (%)	90	90	90	87	87	87
Burning results						
Max. ion temperature (keV)	30	35	40	110	120	130
Mean fuel density (g/cc)	280	230	180	160	150	130
Tritium burn up (%)	15	25	20	36	37	39
Yield (MJ)	0.1	0.8	3.7	60	120	130
Estimated laser parameters						
Energy (MJ)	0.2	0.5	1.4	5	8	10
Power (TW)	500	500	500	–	–	–

3 The two-dimensional TIGR-3T code and OMEGA-3T program complex calculations of compression and burn of indirect-driven target

The 2D-calculations of compression and burn of the target (case C from Table 1) were carried out by the OMEGA-3T program complex that was developed at VNIITF on the base of three- temperature hydrodynamic TIGR-3T code [5] and the OMEGA code [6] that was used for computing thermonuclear reactions kinetics, alpha-particles and neutrons energy transfer.

The results of the TIGR-3T calculations obtained for outer surface perturbations in accordance with the formula $R = R_0 + a_0 \cdot \cos(k\theta)$ and for the initial amplitude: $a_0 = 0.0065, 0.013, 0.026 \mu m$ for parameter: $k = 48, 24, 12$ consequently are presented in Fig. 1-3.
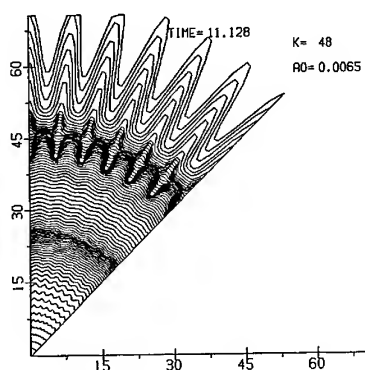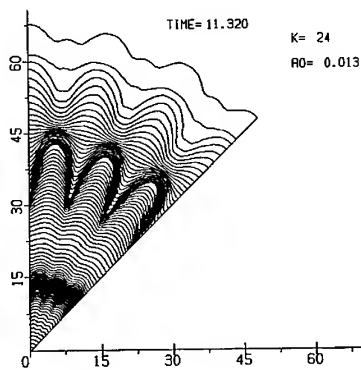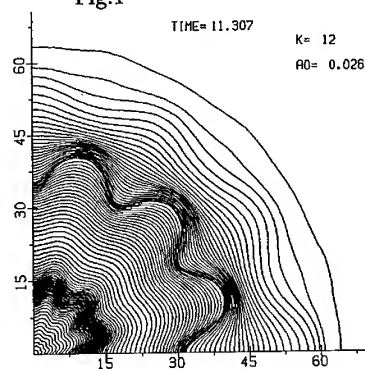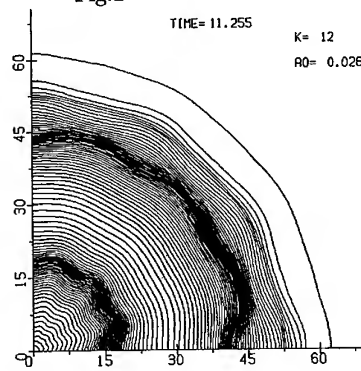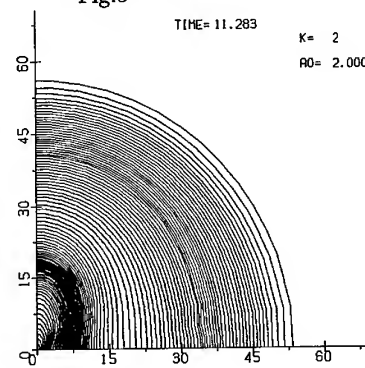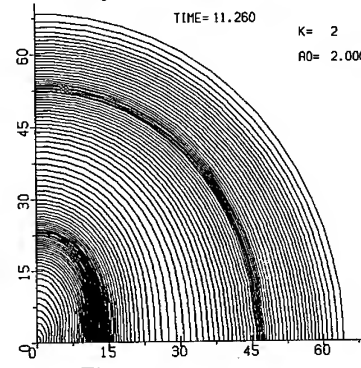
Figures 1-6: The state of target at the moment of maximum compression of DT-fuel obtained by TIGR-3T (Fig.1-3,5) and OMEGA- 3T code (Fig.4,6).

In accordance with performed calculations and results presented in papers [1,7,10], the distinct stabilization of Rayleigh-Taylor instability at ablation front during shell acceleration stage occurs.

During shell deceleration stage the perturbations phase changes and further stabilization of Rayleigh-Taylor instability in DT-fuel volume and at the interface of DT-fuel and glass may happen due to the processes of heat-conductivity and alpha-particles energy transfer, which decreases density gradients [11]. It should be noted that momentum transfer by alpha-particles may also lead to the additional stabilization of Rayleigh-Taylor and Kelvin-Helmgoltz instability [12].

The results of the OMEGA-3T code calculations of thermonuclear burn of target for parameters $a_0 = 0.026 \mu m$ and $k = 12$ are presented in Fig. 4.

The results of the 2D-calculations for perturbations on the inner boundary of DT-ice with parameters: $a_0 = 2\mu m$ and $k = 2$ are presented in Fig. 5 (without burn) and Fig. 6 (with burn).

There were observed no significant changes in tritium burn up in the calculations presented in Fig. 4, 6 to compare 1D-calculations.

4 The computations of radiation homogeniety at target plased in hohlraum

The 2D- and 3D-calculations of radiation transfer in transparent gas approximation for different types of hohlraum designs were performed by the codes developed at RFNC-VNIITF.

The calculations were carried out for the stationary geometry, listed below.

1. Spherical target placed in cylindrical "case" having two entrance holes (LEH) for laser radiation, which heated the inner surface of the "case" [1];

2. Spherical target with two shields placed in cylindrical "case" having two LEH for laser radiation, which heated the outer surface of the shields [1];

3. Spherical target with eight shields placed in spherical "case" having eight LEH for laser radiation, which heated the outer surface of the shields.

The performed optimization of the emplacement of laser irradiated area of the "case" surface in geometry 1 and the emplacement and sizes of shields in geometry 2 points to the possibility to obtain the radiation homogeneity at the spherical target surface better than $dI/I = 6 - 8\%$ (peak-valley ratio) when the albedo of "case" surface equals to $R = 0.8$ and the ratio of "case" to target radii is $R_c/R_t = 3$.

The nonhomogeneity is reduced when the albedo and the number of shields (N) increase approximately as $\delta I/I \sim (1 - R)/N$.

In the hohlraum design using spherical geometry with 8 LEH and shields in cubic symmetry one may obtain the homogeneity of black-body radiation at the spherical target surface better than 2 % (peak-valley ratio) with the ratio of the energy absorbed by the target to the laser energy about of 5 %.

Discussion

The cylinder targets placed into cylindrical case could be used to provide necessary symmetry with one-beam driver for target compression up to 200 g/cc. The shot-pulse laser with the energy of 100 kJ needed for fast ignition of the thermonuclear detonation [6] through such target. The energy gain more than $G > 100$ could be achieved with the driver energy of about 5-10 MJ in this approach as it follows from primary estimations and calculation performed.

Acknowledgments

References

1. J.Lindl, *Physics of Plasma* **2**, 11, 3933,(1995).
2. W.Hogan, R.Bangerter and G.Kulcinski, *Physics Today*, Sept., 42,(1992).
3. L.P.Feoktistov, E.N.Avrorin *et al, Kvantovaja Elektronika*,6,349,(1978).
4. V.A.Lykov, V.E.Chernyakov *et al, Proceedings of 23rd ECLIM Series* **140**, 21, (IOP Publishing,Bristol and Philadelphia, 1995).
5. A.N.Shushlebin, V.D.Frolov and V.A.Lykov *Computation Technology*, **4**, 336,(Novosibirsk,1995).
6. E.N.Avrorin, A.A.Bunatyan, A.D.Gadjiev *et al Phisica Plasmy* ,**10**, 514,(1984).
7. H.Takabe and A.Yamamoto *Phys.Rev.*, **44**, 5142, (1991).
8. V.E.Neuvazhayev *Phys.Rev.E*,**50**, 1394 (1995).
9. V.E.Neuvazhayev and V.G.Yakovlev, *Sbornic VANT, Series:Theoretical and Applied Physics*, 1,28,(Moscow,1988).
10. J.Sanz,*Phys.Rev.Lett.*,**73**,2700, (1994).
11. H.Takabe and T.Ishii,*Jpn.J.Appl.Phys.*, **32**, 5675,(1993).
12. V.A.Lykov,*AIP Conference Proceedings* **318**. *Laser Interaction and Related Plasma Phenomena.*,403, Editor:George H.Miley. (AIP PRESS, NY. 1994).

AFTER-LASER-PULSE K_α EMISSION: SPONTANEOUS MAGNETIC FIELDS IMPRINTED IN FERROMAGNETIC TARGET

A. V. RODE, E. G. GAMALY, AND B. LUTHER-DAVIES
Laser Physics Centre, Research School of Physical Sciences and Engineering,
The Australian National University
Canberra, 0200 ACT, Australia

Abstract

We report the observation of an unusually long sequence of K_α-pulses from planar Fe foil targets irradiated by 180 ps laser pulse at intensities $(0.1-3)\cdot 10^{16}$ W/cm^2. The duration of the K_α emission was up to 5 nanoseconds: approximately 30 times longer than the laser pulse. Our interpretation of these observations is that suprathermal electrons are gradually decelerated as they circulate in the magnetic field imprinted during the laser pulse in the ferromagnetic target material. These results open an opportunity for studies of magnetisation processes in a ferromagnetic at extremely high magnetic field: on the megagauss scale.

1. Introduction

K_α-radiation emitted from a target irradiated by an intense laser beam ($q\lambda^2 \approx 10^{15}$– 10^{17} W·μm^2/cm^2) has been widely investigated both experimentally and theoretically. All of these earlier studies were made for a time interval approximately equal to the laser pulse duration. We present here, for the first time to our knowledge, experimental evidence of pulsations of X-ray K_α-emission from an iron target *after* the laser pulse and lasting a few nanoseconds, i.e. up to 30 times longer than the laser pulse duration. In these experiments the target was irradiated by 180 ps Nd:glass laser pulses at intensities of $(0.1-3)10^{16}$W/cm^2.

In order to explain the K_α-emission after the end of the laser pulse it is necessary to consider forces which might keep the electrons away from the target for some time and later return them to the target. There are at least two which can contribute to this motion: firstly, the force associated with the ambipolar field due to charge separation; and secondly, the Lorentz force associated with the spontaneous magnetic field generated in the plasma during the laser pulse. Generally, these forces exist only during the laser pulse. The ambipolar field allows an electron to return only once, and hence it cannot support this periodic motion. A magnetic field, on the other hand, appears to be a natural reason for periodic motion of a charged particle. In the experiments presented here the target was made of pure iron – a ferromagnetic material. Since it can be magnetised, it can remember,

or implant, the spontaneous magnetic field for a time much longer than the laser pulse duration. The most plausible explanation for the after-laser-pulse K_α pulsation is the revolution of fast electrons around the target in the magnetic field imprinted in the target. The model based on these assumptions allows us to explain reasonably well all of the experimental data.
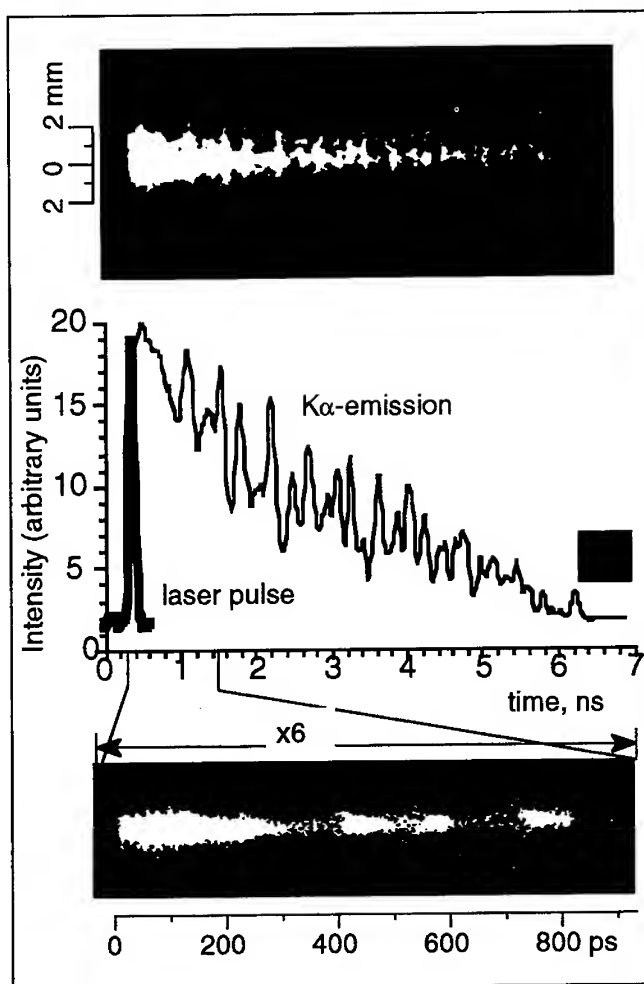
Fig. 1. After-laser-pulse temporal pulsation of K_α emission in the experiments with ferromagnetic target at laser intensity $q = 3 \cdot 10^{16}$ W/cm^2; (a, b) – total length of emission; (c) – K_α "0"-pulse, 1st pulse merged with the "0"-pulse, and the following 2nd, 3rd, and 4th pulses.

2. Experimental conditions

2.1. Target and laser parameters

Plane targets made of pure iron foils were irradiated close to normal incidence by 8-9 J pulses of 180ps duration using a single beam from a Nd:glass laser. The beam was focused using an F=1 aspheric lens to a spot 10-15 μm diameter on the target surface. The on-target laser flux density was $(0.1-3)10^{16}$ W/cm^2.

A cylindrically curved pyrolytic graphite crystal with 35 mm radius of curvature was used in the Von Hamos geometry with x-ray focusing in the direction perpendicular to the dispersion direction to collect and focus the K_α emission onto the input slit of a Hadland Photonics X-Chron streak camera. The focusing efficiency, i.e. the ratio of K_α-photons on the streak camera input slit to a total number of emitted K_α-photons in 4π radians, was about 10^{-5}.

The temporal behaviour of K_α emission was measured using an x-ray streak camera fitted with a caesium-iodide photocathode. Temporal resolution of the system at 6.4 keV was about 15 ps at the time-gate of 500 ps. Typical intensity gain of the streak camera measured on negative film was greater than 1000.

3. Theoretical model

3.1. Major experimental facts and assumptions for the model.

We assume that the pulsations are caused by deceleration of the flux of remnant fast electrons which rotate in a magnetic field *imprinted during the laser pulse* in the cold part of the *ferromagnetic* target where the temperature is lower than Curie temperature for iron ($T_C= 10^3$ °K). The period of rotation in a constant magnetic field is independent of the energy of electrons:

$$T = \frac{2\pi\, m_e c}{e\, B}\,;$$
(1)

where e, m_e are electron charge and mass, c is the speed of light. Thus, the average experimental value for this period $T = 2\cdot10^{-10}$ s corresponds to an imprinted magnetic field of $B = 1.78\cdot10^3$ Gauss (averaged in space and time during the laser pulse).

To calculate a K_α-yield, ie the number of K_α-quanta generated by an electron with kinetic energy E_h as it penetrates through the target. We use a simple model based on energy-loss of electrons given by Bethe-Bloch equation. The average number of K_α pulses observed in the experiments was 16 to 18, and 22 in one experiment. This corresponds to the maximum electron energy of 400–450 keV required to produce the last pulse in the observed K_α-train. Assuming a Maxwellian distribution with temperature $kT_h = 35$ keV, the total number of electrons with energy $E_0 \geq 400$keV in the experiments should be in the order of 10^6.

3.2 Generation of spontaneous magnetic field in laser-produced plasma

There are several mechanisms responsible for the magnetic field generation in a laser-produced plasma. The major mechanisms in the considered conditions might be the resonance absorption (and the influence of the fast electrons generated during this process) along with the thermoelectric currents. The fast electrons may also play an important role in the processes of the magnetic field transport along the target surface. In what follows we will use a conservative estimate of an amplitude of the generated magnetic field based on the thermoelectric currents only:

$$\frac{\partial B}{\partial t} = \frac{c}{e\,n_e}\left(\nabla kT_e \times \nabla n_e\right) \qquad (2)$$

where n_e is plasma electron density. The characteristic size r along the target surface is approximately equal to the focal spot diameter, ie. about the same as d. Now, it is easy to estimate from Eqn. 2 the magnitude of a magnetic field generated during the laser pulse in the experiments:

$$B \cong \frac{c\,t\,kT_e}{e\,n_e\,d^2} \sim 10^7\ Gauss.$$

The plasma plume in the experiments expands only 20 μm during the laser pulse. One can conservatively suggest that the target area affected by either the heat or shock wave cannot exceed the same distance from the centre of a focal spot. For further consideration the target area heated by the laser-produced plasma is taken to be a cylinder with its axis in the focal spot centre and radius 30 μm. At the distances $r > 30$ μm the target should remind cold (below T_C), and consequently could be magnetised if imposed to magnetic field.

4. Conclusions

The spontaneous magnetic field in order of tens MGs and even up to GGs generated in plasma produced by intense laser beam represents a unique opportunity to investigate experimentally such fundamental questions:
- Would it be possible to magnetise the ferromagnetic to the magnetic field comparable or even exceeding the Weiss field in a ferromagnetic?
- What happens to the domain structure in this case?

These and other questions are subject for further investigations of the behaviour of ferromagnetic material in an extremely intense magnetic field generated in laser-produced plasmas created at Pettawatt level of laser power.

IMPRINT REMOVAL BY A PREPULSE PLASMA

B. Králiková J. Krása L. Láska K. Mašek S. Přeučil K. Rohlena
J. Skála A. V. Bessarab[1] S. G. Garanin[1] G. A. Kirillov[1]
Yu. F. Kiryanov[1] G. G. Kochemasov[1] L. V. Lvov[1] A. B. Ryadov[1]
S. A. Sukharev[1] N. A. Suslov[1] A. I. Zaretskiy[1]
Institute of Physics of Czech Acad. Sci., Prague 8, Na Slovance 2,
180 40 Czech Republic
[1]*Russian Federal Nuclear Centre VNIIEF Arzamas-16,*
Nizhniy Novgorod Region, Russian Federation

Abstract

A thermal smoothing of the ablation pressure was demonstrated by driving the main 3ω pulse of an iodine laser through a preformed plasma of a weaker 2ω prepulse.

1   Introduction

In the direct drive experiments an inhomogeneity of the target illumination by laser beams amounting to more than just to a few per cent may lead to an intolerable growth of the Rayleigh-Taylor instability. A smoothing mechanism is built in the plasma itself by the existence of the heat conduction aria beyond the critical surface, where the heat conduction tends to spread any inhomogeneity occurring near the critical surface by the lateral heat transport.

The heat transport mechanism can be controlled by moving the critical surface away from the target, prolonging thus the path of the heat transport. This is effectively achieved either by placing a low density material in front of the target [1] or by a preformed plasma[2], which, however, should not be allowed to push the critical surface too far, as otherwise the laser - target coupling would be critically reduced. A good way how to get out of this difficulty is to use a prepulse of a longer wavelength to form a prepulse plasma

considerably thinner allowing thus the main pulse to penetrate considerably deeper preserving a good part of the coupling.

In the following the experimental investigation of the prepulse effect will be described using pinhole images of the rear side of a thin target illuminated by a spatially inhomogeneous beam.

2 Experimental

To check the prepulse mechanism a series of experiments has been conducted using the iodine laser system Perun at the Institute of Physics in Prague. With a $100\mu m$ focus the system delivers about $10^{15}Wcm^{-2}$ in $400ps$ pulses at $1.315\mu m$. A suitably arranged conversion line using a couple of DKDP crystals allowed for any combination of transformed pulses, their amplitude ratio and time delay. For the purpose of the experiment we chose a weak red 2ω and a blue 3ω main pulse, varying the red spot size and the time delay. A gross scale inhomogeneity was introduced by splitting the beam with a wedge splitter. As a target a 5μ Al foil was used, which observed from the rear side by a pinhole camera visualized the pressure pattern on the ablation surface.

3 Results

The experiment was performed for two different ratios of the power densities in the red and blue pulse for several different time delays. No significant dependence on the power density ratio was observed, but the time delay appears to be a crucial parameter. With the time delay set to zero no significant washing out of the rear side pattern was observed in the pinhole image, fig. 1. However, with a time delay of $0.5ns$ the picture entirely changed, fig. 2. As against fig. 1, where the two focal points are clearly distinguishable on the target rear side, with a time delay of $0.5ns$ in fig. 2 the two foci appear to coalesce.

158
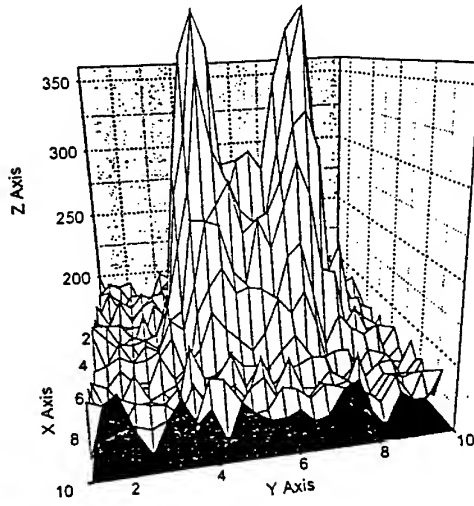
Figure 1: Densitometry of the target rear side. Simultaneous illumination by $2\omega \sim 1.7 \times 10^{13} W cm^{-2}$ and $3\omega \sim 1.4 \times 10^{14} W cm^{-2}$ pulses. 3ω beam is split angularly to form two close foci within a larger 2ω focal spot.
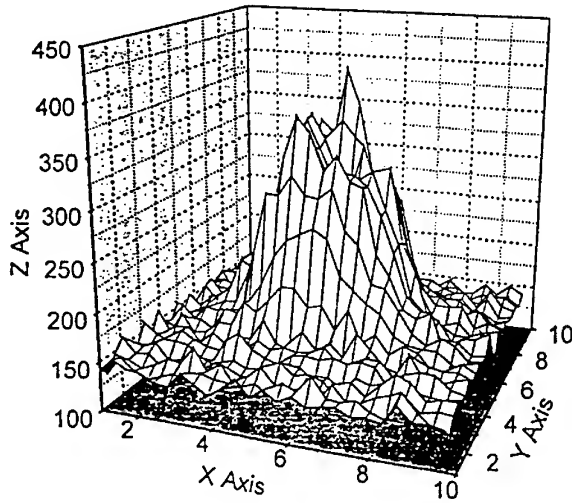
Figure 2: Densitometry of the target rear side. $2\omega \sim 1.1 \times 10^{13} W cm^{-2}$ prepulse, $3\omega \sim 1.4 \times 10^{14} W cm^{-2}$; main pulse time delay $0.5 ns$.

4 Conclusion and discussion

The conclusion about the feasibility of imprint removal by the mechanism of the lateral thermal transport between the critical and ablation surfaces from the behavior of the x-ray image of the target rear side is just an indirect one. A more conclusive evidence could be provided by side-on pictures of the plasma using a backlighting technique. We, however, think that the smearing of the rear side image is not due to some other spurious effect, e.g. by the hot electrons penetrating the target. But even if the thermal smoothing is shown to work in the presence of the red - blue pulse combination a question still remains of the additional entropy introduced into the target volume by the prepulse. A model calculation of a large thermonuclear target hydrodynamics including a neutron yield seems to point to a non negligible rôle of the target preheat in the presence of a prepulse[3].

1. M.Dunne M.Borghesi A.Iwase M.W.Jones R.Taylor
   O.Willy: Phys.Rev.Lett. 75 (1995) 3858
2. B.Králiková J.Krása L.Láska K.Mašek S.Přeučil K.Rohlena
   J.Skála P.Trenda A.V.Bessarab S.G.Garanin G.A.Kirillov:
   Yu.F.Kiryanov G.G.Kochemasov L.V.Lvov A.B.Ryadov
   S.A.Sukharev N.A.Suslov Proc. 23rd ECLIM, *"Laser
   Interaction with Matter"*, Oxford 1994, IOP Conf. Ser. **140**
   p.325
3. I.G.Lebo, V.B.Rozanov, I.V.Popov, V.F.Tishkin, K.Rohlena:
   Results of 2D Numerical Simulation of Subnanosecond
   Iodine Laser Interaction with an Al Foil Target, Proc. Laser
   Optics '93, St.Petersburg, June 1993; also: Preprint FIAN
   No. 38, Moscow 1993; Journal of Russsian Laser Research
   15 (1994) 346

NUMERICAL STUDY OF PHYSICAL EFFECTS ACCOMPANYING GENERATION OF HIGH–CHARGED IONS FROM A PLASMA PRODUCED BY DIFFERENT TYPES OF POWERFUL LASERS

A.E.STEPANOV, K.N.MAKAROV, S.V.HOMENKO, YU.A.SATOV,
V.C.ROERICH

Troitsk Institute for Innovation and Fusion Research, Troitsk, Moscow region,
Russia

The two-dimensional numerical model describing interaction of laser radiation with solid targets was used. The detailed atomic model is incorporated self-consistently in hydrodynamics simulation. Most attention is paid to the analysis of experimental data obtained at TRINITI with CO_2 laser TIR-1. Recombination was found to be essential only for several tens of nanosecond after the laser pulse termination. Results of Ta ions generation by iodine laser radiation at extremely high power density and short pulse duration are presented.

1 Numerical model

For numerical simulation 2D gas-dynamic one-fluid two-temperature model was developed which includes electron heat conduction, electron-ion temperature relaxation and heating by laser light. The electron energy balance equation also includes terms corresponding to ionization and excitation energy of plasma ions. The interaction of laser light with plasma is modeled in the approximation of the geometrical optics by ray-tracing technique. In order to take into account the anomalous absorption effect we have incorporated the semi–empirical model similar to that used in Reference [1].

For description of ion levels population kinetics we use so called "scaled hydrogen-like" atomic model. In the atomic model ground states of all ions are described in detail using correct ionization energies and more reliable elementary processes data. In addition to ground state every ion has several excited levels described by principal quantum number n.

Since total amount of states should not exceed several hundreds we attributed three-body recombination rate calculated from the analytical formula[2] to the level with highest principal quantum number if it is valid. Otherwise, three-body recombination rate was calculated from ionization rate for every level. Dielectronic recombination rate was calculated from the formula[3] corrected for account for finite electron density value[4]. The lead ions atomic model included all ionization stages from neutral to Pb^{40+}. Every ion had 4 hydrogen-like levels, so total number of states incorporated in the model

exceeded 200.

2 Simulation of lead ions production by CO_2 laser

One of experimentally measured values [7] was the charge number of ion producing highest analyzer signal which turned to be close to local average ion charge $\langle z \rangle$. Calculated $\langle z \rangle$ for various values of laser light power density P_0 are plotted on Fig. 1 together with experimental values. It was not possible to
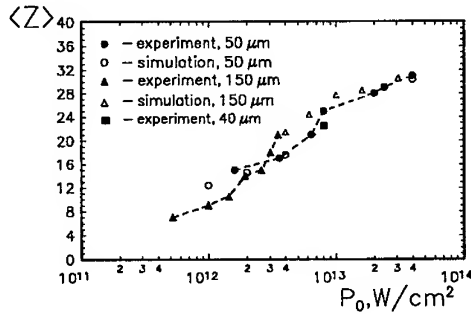
Figure 1: Dependence of $\langle z \rangle$ on laser light power density. Numbers in the legend are focal spot sizes in micrometers

fit experimental values of $\langle z \rangle$ for the whole range of laser power density using single value of electron heat conduction limiting factor f introduced in a usual way. The dependence $f(P_0)$ was derived from fitting the $\langle z \rangle(P_0)$ dependence for the focal spot size 50 μm. Value of f varies from 0.05 for $P_0 = 4 \cdot 10^{13}$ W/cm^2 to 1 for $P_0 = 10^{12}$ W/cm^2. At low laser intensities electron heat conduction trends to classical regime. This dependence was used for simulation of different target materials and focal spot sizes.

Fig. 1 shows close agreement between simulations and experimental data for 150 μm focal spot size. Good agreement was also achieved for a total ion current, total number of particles in different ionization states and for ion velocity spectrum registered after passing through small extraction aperture (direction — normal to the target).

Simulations made in one-dimensional (spherical) geometry reveal right trends but show significant deviations from experimental data.

The fact that the 2D model produces correct results for lead plasma in wide range of laser light power density opens the possibility to use the model

for quantitative predictions.

3 Simulation of Ta plasma created by iodine laser radiation

Parameters of laser (intensity, focal spot size, pulse duration) were taken from[5] as: $P_{max} = 10^{15}$ W/cm², focal spot diameter $= 100$ μm, duration $\tau = 350$ ps (full Gaussian width).

Numerical results also show close agreement with experimental ion spectrum. Calculated value of $\langle z \rangle$ is 39–40, while in experiments[5] was 41–42.

4 Comments on three-body recombination

At distance about 1 meter or more from target surface electron temperature becomes ≤ 1 eV. Three-body recombinational "flow" at such a small temperatures is formed as a result of diffusion of electrons down over highly excited levels due to collisions with free electrons. Under these conditions the recombination coefficient can be evaluated by the Pitaevski formula[2] with very strong temperature dependence of recombination coefficient $- \beta_z \sim T_e^{-9/2}$.

For validity of the Pitaevski formula it is necessary that[6]

$$N_e > N_e^p \equiv 3 \cdot 10^{12} Z^7 \left(\frac{T_e(eV)}{Z^2} \right)^5 \text{cm}^{-3}. \tag{1}$$

If $N_e > N_e^p$ then three-body recombination occurs as a result of diffusion of electrons over highly excited levels, if $N_e < N_e^p$ - after electron capture it relaxes to the ground state through cascade of radiative transitions. For latter regime the temperature dependence of β_z is much weaker than that in formula of Pitaevski.

According to[8] highest principal quantum number of level, above which energy difference between levels becomes smaller than level width, is

$$m = 1.4 \cdot 10^3 Z^{8/15} N_e^{-2/15}. \tag{2}$$

From the Pitaevski theory it follows that major contribution to the recombination rate is produced by recombination on levels with principal quantum number near some n^*. From condition $n^* < m$ the restriction on electron density follows:

$$N_e < N_e^b \equiv 2.16 \cdot 10^{19} \frac{T_e^{15/4}}{Z^{7/2}}. \tag{3}$$
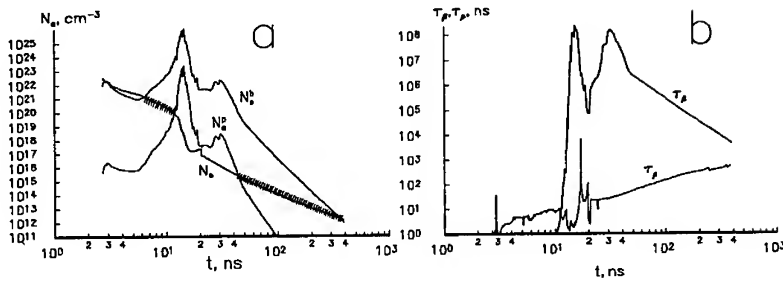
Figure 2: Time history of electron density(a) and characteristic three-body recombination and hydrodynamical times (b)

So, "dangerous" in the sense of decreasing of $\langle z \rangle$ three-body recombination in Pitaevski regime takes place if $N_e^p < N_e < N_e^b$. On Fig. 2a is presented the time history of N_e, N_e^p, N_e^b for a lagrangean cell of a plasma producing the highest value of ion current at 3m distance. Two regions are marked where Pitaevski formula is valid. First region ($t < 10$ ns) corresponds to heating stage and second (45 — 400 ns) — corresponds to rarefaction and cooling. During further rarefaction and cooling role of three-body recombination will decrease because levels on which it could occur are merged to the continuum. On Fig.2b is presented time dependence of characteristic recombination time calculated from Pitaevski formula τ_β and characteristic hydrodynamical time τ_ρ, which corresponds to plasma density changes. It can be easily seen that at the moment of three-body recombination termination $\tau_\beta > \tau_\rho$. This means that in this lagrangean cell three-body recombination is never important.

1. Eder, D. C. 1989, Phys. Fluids B1 **12**, 2462.
2. Pitaevski, L. P. 1962, Sov. J. of Exp. and Theor. Phys., **42**, 1326.
3. Burgess, A. 1964, Astrophys. J., **139**, 776.
4. Zdanov, V. P. 1979, Sov. Plasma Phys., **5**, 572.
5. Láska L. et. al., 1994, Appl. Phys. Lett., **65**, 691.
6. V.I.Derjiev, A.G.Jidkov, S.I.Jakovlenko. Radiation of ions in non–equilibrium dense plasma. EnergoAtomizdat, Moscow, 1986. (in russian)
7. K.N. Makarov, S.V.Homenko,V.K. Roerich, Yu. A. Satov, B.Yu. Sharkov, A.E.Stepanov. Investigation of Highly-Charge Heavy Ion generation in CO_2 Laser-Produced Plasma. 24th ECLIM poster report PM47.
8. K.R.Leng. Astrophysical formulae. Springer-Verlag, 1974.

MEASUREMENTS OF LASER IMPRINT BY XUV RADIOGRAPHY USING AN X-RAY LASER

D. H. KALANTAR, L. B. DASILVA, S. G. GLENDINNING, F. WEBER,
B. A. REMINGTON, S. V. WEBER,
Lawrence Livermore National Laboratory, Livermore, CA, USA

E. WOLFRUM, M. H. KEY, D. NEELY
Rutherford Appleton Laboratory, Chilton, Didcot, Oxon, UK

N. S. KIM, J. S. WARK, J. ZHANG
Clarendon Laboratory, Department of Physics, University of Oxford, Oxford, UK

C. L. S. LEWIS, A. MCPHEE, J. WARWICK
Department of Pure and Applied Physics, Queens University of Belfast, Belfast, UK

A. DEMIR, J. LIN, R. SMITH, G. J. TALLENTS
Department of Physics, University of Essex, Colchester, UK

J. P. KNAUER
Laboratory for Laser Energetics, University of Rochester, Rochester, NY, USA

We have developed a technique for studying the imprint of a laser beam on a thin foil using an x-ray laser as an XUV backlighter and XUV multilayer optics. This technique allows us to measure small fractional variations in the foil thickness due to hydrodynamics imprinted by direct laser irradiation. We present results of imprinted modulation and growth due to a low intensity 0.53 μm drive beam incident on a 2 μm Al foil using a germanium x-ray laser at the Vulcan facility. We present measurements of the modulation due to static RPP, SSD smoothed, and ISI smoothed speckle patterns at 0.53 μm irradiation.

1   Introduction

In direct drive Inertial Confinement Fusion, high intensity laser beams directly irradiate the outside of a hollow spherical capsule that contains a layer of solid fusionable D-T in it inner surface. For ignition scale targets, the laser pulse starts at low intensity 'foot' at 10^{13} W/cm^2 for several nanoseconds before it builds up to more than 10^{15} W/cm^2 during the main drive portion of the pulse. Laser heating of the capsule surface results in an ablation pressure that accelerates the capsule shell radially inward in a spherical implosion. During this acceleration, perturbations due to surface roughness and due to imprint from spatial non-uniformities in the laser irradiation undergo Rayleigh-Taylor growth, potentially severely degrading performance.

We have used an x-ray laser for XUV radiography to characterize the modulations in optical depth of a thin foil due to laser imprint and subsequent Rayleigh-Taylor growth. Preliminary experiments were done using an yttrium x-ray laser backlighter on Nova to characterize the imprint due to 0.35 μm laser irradiation of a 3 μm Si foil[1,2,3]. We have extended these experiments using a Ge x-ray laser backlighter on the Vulcan laser. We characterized the imprint and subsequent Rayleigh-Taylor growth of modulations due to 0.53 μm laser irradiation of a 2 μm thick Al foil at $2\text{-}8\times10^{12}$ W/cm^2. In this paper we describe some results from the experiments conducted at the Vulcan laser facility.

2   XUV Radiography of laser imprint

We generated a Ge J=0-1 x-ray laser at 19.6 nm using six beams of the Vulcan laser. We placed a thin (2 μm) Al foil about 3 cm from the output of the Ge x-ray laser. We then used two multilayer mirrors to image the Al foil in the x-ray laser wavelength onto an XUV sensitive CCD; a 1 m spherical mirror at near normal incidence, and a flat mirror at 45° incidence, as shown in Figure 1. The spherical mirror was placed 53 cm from the Al foil, providing a 16X magnified image of the foil on the CCD, and the 45° angle of incidence planar mirror was used to relay the image onto the CCD and spectrally isolate the image from the thermal background noise.
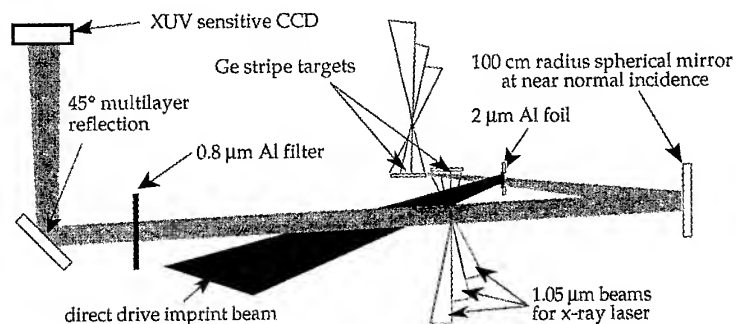
Figure 1: Geometry for the x-ray laser target and XUV imaging system used to measure the modulation in optical depth of a thin Al foil due to direct drive laser imprint.

We used a single Vulcan laser beam with a static random phase plate speckle pattern, SSD smoothed speckle pattern, and ISI smoothed speckle pattern to imprint on the Al foil. We characterized the imprinted modulation as a function of time with the different smoothing schemes.

3. Results and Discussion

In Figure 2, we show optical far field images of the single beam laser focal spot used in these experiments. This figure shows intensity modulation of a) a static RPP speckle pattern, b) a 1-D SSD smoothed speckle pattern, and c) for an ISI smoothed RPP speckle pattern.
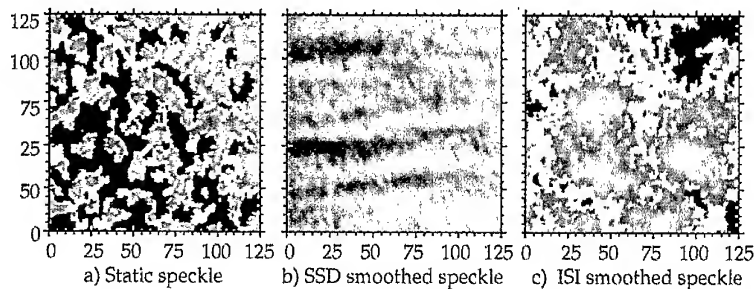
Figure 2: Far field images of the laser focal spot. The scale is in microns at the target.

We irradiated the 2 μm thick Al foils directly by an intensity of 3-8x10^{12} W/cm^2 of 0.53 μm laser light using the three speckle patterns, and we recorded the modulation in optical depth in the foil due to laser imprint and subsequent Rayleigh-Taylor growth using the Ge x-ray laser backlighter. We show XUV radiographs of the modulation in optical depth in the Al foil in Figure 3, recorded at 0.2 ns into the laser pulse.
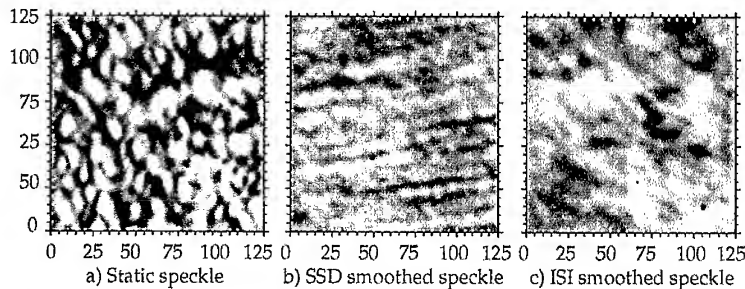
Figure 3: Modulation in optical depth of an Al foil irradiated by a) a static RPP speckle pattern, b) a 1-D SSD smoothed speckle pattern, and c) an ISI smoothed speckle pattern, all at 0.53 μm.

Power spectra for the imprinted modulation measured in these images are shown in Figure 4. The integrated RMS modulations in optical depth we measured from these XUV radiographs were 0.37, 0.17, and 0.20. The RMS measured from undriven Al foil targets was about 0.13. This corresponds to a surface roughness of about 60 nm on the Al foil.

We show the RMS modulation in optical depth as a function of time recorded by XUV radiography in Figure 5. This figure shows that the modulation imprinted due to a static speckle pattern grows faster than for a smoothed speckle pattern. The SSD smoothed case shows a strong reduction in the modulation, but it still grows late in time. The ISI smoothed beam, however, does not show significant growth at any time up to 0.8 ns.
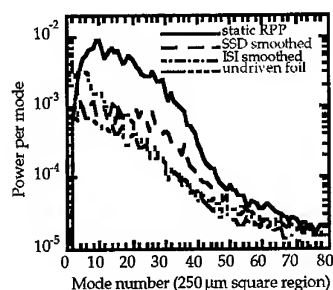
Figure 4: Power per mode calculated from the XUV optical depth modulation measured from the radiograph images shown in Figure 3.
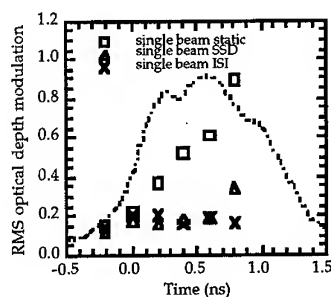
Figure 5: RMS modulation in optical depth in the Al foil as a function of time for the static, SSD smoothed, and ISI smoothed drive beams

4 Summary

We demonstrated measurements of the modulation imprinted by low intensity 0.53 μm irradiation of a thin Al foil using the Ge x-ray laser at the Vulcan laser facility. We measured the imprinted modulation and subsequent Rayleigh-Taylor growth in the foil as a function of time with various laser smoothing schemes.

5 Acknowledgements

References

[1] M. H. Key et al, J. Quant. Spectrosc. Radiat. Transfer **54**, 221 (1995).

2 D. H. Kalantar et al, Rev. Sci. Instrum. **67**, 781 (1996).

[3] D. H. Kalantar et al, Phys Rev. Letters **76**, 3574 (1996).

MEASUREMENT OF SINGLE MODE IMPRINT BY XUV LASER RADIOGRAPHY

E. WOLFRUM, M.H. KEY, D. NEELY, S.J. ROSE
Rutherford Appleton Laboratory, Chilton, Didcot, Oxon OX11 0QX, U.K.

A. DEMIR, J. LIN, R. SMITH, G.J. TALLENTS
Department of Physics, University of Essex, Colchester CO4 3SQ, U.K.

D. KALANTAR, B.A. REMINGTON, S.V. WEBER
Lawrence Livermore National Laboratory, Livermore, CA 94551, USA

N.S. KIM, J. ZHANG
Department of Physics, Clarendon Laboratory, University of Oxford, Parks Road, Oxford, OX1 3PU, U.K.

C.L.S. LEWIS, A. MCPHEE, J. WARWICK
Department of Pure and Applied Physics, Queens University of Belfast, Belfast, BT7 1NN, U.K.

The XUV laser radiography technique has been used to investigate the hydrodynamic response of laser driven targets to single optical modes. A germanium x-ray laser (J=0-1) with wavelength λ=19.6 nm was used as a backlighter. The single mode interference patterns are generated in the focal plane of a lens by double rectangular slit apertures. The two selected uniphase wavefront elements interfere to create single mode perturbations of 15 μm and 30 μm periodicity. The fringe pattern is created under an Airy function envelope, determined by the dimensions of the rectangles and imprinted on 2 μm thick Aluminium foils. The response of the shocked target visible in the radiographs is comprised of a change in opacity due to the compression of the target and thickness perturbations driven by the single mode. A temporal scan of the evolution of the single mode perturbations from shock transit up to 600 ps after shock break out is presented.

1 Introduction

Ignition of thermonuclear burn in directly driven spherical implosions is now a real possibility with megajoule laser facilities planned in the USA and France. A key question determining the robustness of ignition target designs is the level of hydrodynamic perturbations arising from laser speckle and amplified by the Rayleigh Taylor instability. Measurement of hydrodynamic perturbations imprinted on laser driven targets by the smoothed laser speckled patterns envisaged for direct drive has been shown to be possible with high accuracy using XUV laser radiography[1,2,3]. In recent work the germanium J=0-1 XUV laser operating at

19.6 nm has been used in this manner to study imprint on laser driven aluminium foils[4]. Data measured for the continuum of modes present in laser speckle is important for assessing the net effect but does not lend itself easily to investigation of the basic physics of the imprint process. We describe here work in which a single one-dimensional optical mode is generated and imprint due to this single optical mode is measured.

2 Experimental setup

We used a Ne-like germanium x-ray laser[5] as the source for radiographic imaging and an imaging system as described by Kalantar et al.[4]. The single mode interference patterns were generated in the focal plane of a lens by double rectangular slit apertures. The two selected uniphase wavefront elements interfere to create single mode perturbations of 15 μm and 30 μm periodicity. The fringe pattern is created under an Airy function envelope, determined by the dimensions of the rectangles. The scheme for production of single modes together with a computed 2D intensity distribution is shown in figure 1. 2 μm thick Aluminium foils were irradiated with the VULCAN laser (λ = 527 nm) at average irradiances of $2 \cdot 10^{13}$ W/cm^2 where the pulse shape is trapezoidal with a rise time of 200 ps.
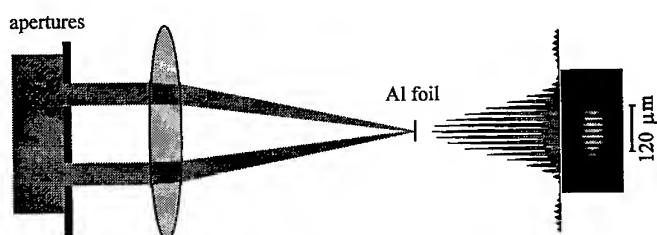
Fig.1: Optical scheme for single mode studies

3 MEDUSA simulation

Modelling was performed with the 1D Lagrangian code MED103. The Sesame equation of state for Al yielded the same results as the corrected Thomas Fermi equation of state. The time of shock breakout is determined by the time at which the shock wave arrives at the last cell. For the given irradiation and pulse shape it has been calculated to be 240 ps after the start of the pulse, i.e. 40 ps into the flat top phase. The total density and hydrodynamic pressure profiles are shown in figure 2 at shock breakout time. The computation also gives the average value of the acceleration a=56.5 μm/ns^2 and the average flow velocity across the ablation front
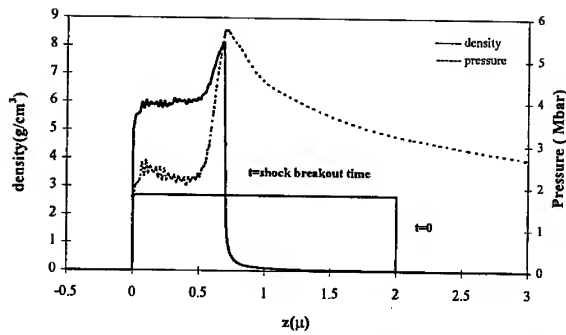
Fig.2: Density and pressure at shock breakout time t=600 ps.
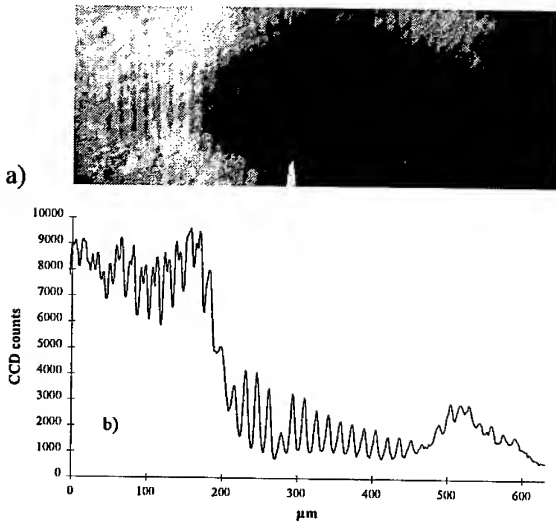
Fig. 3: a) Radiograph of a 2 μm thick Al foil irradiated with single mode fringe pattern of 15 μm periodicity, b) horizontal line profile hereof.

v_a=0.3 μm/ns in the main drive phase. These values have been used with the Takabe formula[5] in the form $\gamma = 0.9(ka)^{1/2} - 3kv_a$, where k is the wave number, to give a rough estimate of the average Rayleigh Taylor growth rate: $\gamma = 4$ μm/ns for 15 μm modes and $\gamma = 2.9$ μm/ns for 30 μm modes.

4 Results

Radiographs were recorded at different times after shock breakout for both modes, 15 μm and 30 μm.

Figure 3 shows a 15 μm mode radiograph together with its horizontal lineout taken 200 ps after shock breakout. The response of the shocked target visible in the radiographs is comprised of a change in opacity due to the compression of the target and thickness perturbations driven by the single mode.

The change in opacity $\Delta\tau_c$, with $\tau_c = \kappa\rho t$, κ the mass absorption coefficient, ρ the density and t the thickness, was evaluated by $\Delta\tau_c = \ln(I/I')$, where I is a linear fit to the radiograph intensities for uncompressed areas and I' the average intensity in the centre of the shocked area. In figure 4 the increase in opacity versus time is plotted, showing a maximum increase by a factor of about 1.65. The calculated shock breakout time appears at 690 ps at this time scale.

171
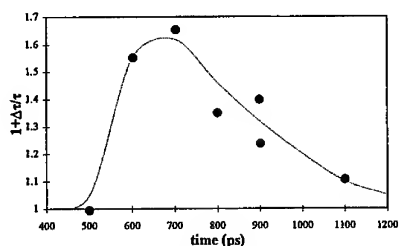
Fig. 4: Relative change in opacity versus time.
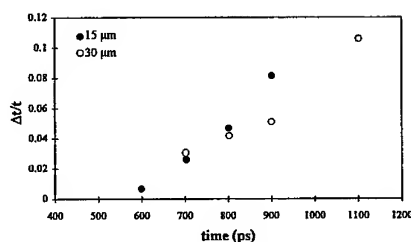
Fig. 5: Single mode fractional rms amplitudes.

The rms amplitudes of the single modes have been derived from the minima and maxima of the fringe pattern in the radiographs, I_{min}, I_{max}:

$$t_{max} - t_{min} = \ln\left(\frac{I_{min}}{I_{max}}\right) * \frac{1}{\kappa\rho} = 2.86\Delta t \qquad (1)$$

where t is the thickness, Δt the rms amplitude of the thickness and the factor 2.86 stems from conversion of maximum amplitude to rms for a sinusoidal curve. In figure 5 the fractional rms amplitudes for both, the 15 µm and 30 µm modes, versus time are shown.

The Rayleigh Taylor growth factors have been used as multipliers on the mode amplitudes of the imprint shown in figure 5 to estimate the amplitude at shock breakout time, resulting in $\Delta t/t$ of 0.03 for both, the 15 µm and 30 µm modes.

Acknowledgements

References

1) M.H. Key et al., J. Quant. Spectrosc. Radiat. Transfer 54, 221 (1995)
2) D.H. Kalantar et al., Rev. Sci. Instr. 67, 781 (1996)
3) D.H. Kalantar et al., Phys. Rev. Lett. 76, 3574 (1996)
4) D.H. Kalantar et al., RAL annual report 1996
5) J. Zhang et al., RAL annual report 1996
6) H.Takabe et al., Phys.Fluids 28, 3676 (1985)

NUMERICAL SIMULATIONS OF 3-D ELECTRON HEAT CONDUCTIVITY WAVES AT LASER BEAMS ABSORPTION IN PLASMA

I.V.POPOV, N.V.ZMITRENKO, V.F.TISHKIN
The Institute of Mathematical Modeling (IMM), 125047, Miusskaya sq. 4a,
Moscow, Russia

S.YU.GUS'KOV, V.B.ROZANOV
Lebedev Physics Institute (FIAN), 117924, Leninsky Pr. 53,
Moscow, Russia

The results of numerical simulations of an electron heat conductivity wave propagation under the action of the laser beam upon a plane target, which consists of layers with different density are presented. The influence of the non-homogeneity of the target matter as well as the dynamics of the formation of a laser beam absorption region are discussed.

1. The problem of the absorption and transport of laser energy in a volume-structured media is an essential one to find the effective conditions to equalize the non-homogeneity of a laser heating.[1] The heat wave of an electron heat conductivity propagation was investigated with a laser beam incidence upon a surface of a plane target which consists if three layer. This problem is studied numerically in this work. In this problem the first and the third layer, which have a sub-critical density $\rho_{1(3)} = 10^{-3} g/cm^3$ were separated by the layer of matter with a density $\rho_2 = 10^{-2} g/cm^3$. The thickness of the first layer is 1000 μm; the second is 100 μm. The substance was a polystyrol $(CH)_n$. In addition the numerical simulations for a homogeneous target were fulfilled, where the density of matter was $\rho = 10^{-3} g/cm^3$. The laser pulse parameteres were closed to experimental ones at "MISHEN" installation in TRINITY. The energy was 60 J, the wavelength was $\lambda = 1.06 \mu m$, the pulse duration was $t_L = 2.5 ns$ and the spot radius was 100 μm. In our simulations the gas dynamic motion is not taken into account.

2. The 3-D heat conductivity equation is considered by means of 3-D numerical code "HEAT-3D". This equation is considered in simple connected region V.

$$\rho C_V \frac{\partial T}{\partial t} = -\text{div}\vec{W} + Q_{\text{LAS}} \qquad (1)$$

where the ρ is the density, C_V is the specific heat, T is the temperature, Q_{LAS} is the source and $\vec{W}$ is the heat flux, which is determined by the equation.

$$\vec{W} = -\kappa \nabla T \tag{2}$$

where κ is the heat conductivity coefficient. At the boundary S of the region V the boundary condition is posed like this

$$\left(-\kappa \frac{\partial T}{\partial \vec{n}}\right)|_S = 0 \tag{3}$$

where $\vec{n}$ is a normal to S.

To construct a discrete modele we replace the initial continuous volume with a discrete grid in a OXY plane. This grid is a manifold of triangles. At the another plane (OZX or OZY) the grid is a quadrangular one. The elementary volume of a grid cell is a prism. Temperature, density and the heat conductivity coefficient are given in the center, but the fluxes are given at the faces (fig. 1). To approximate the equation (1) we suppose that the below
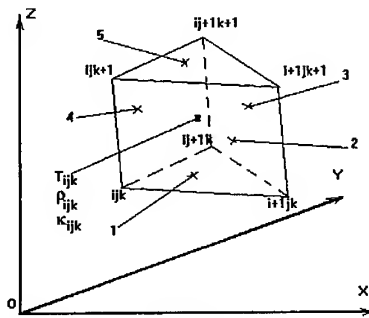
Figure 1.
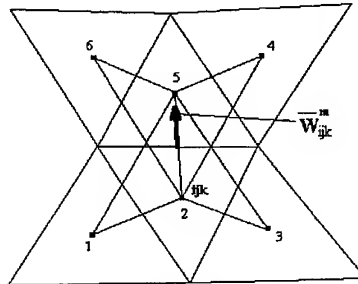
Figure 2.

implicit difference scheme is valid

$$\rho_{ijk} C_{V_{ijk}} \frac{T_{ijk}^{n+1} - T_{ijk}^n}{\Delta t} = -\frac{\sum_{m=1}^{5}(\vec{W}_{ijk}^m, \vec{n}_{ijk}^m) S_{ijk}^m}{V_{ijk}} + Q_{LAS_{ijk}}$$

there n_{ijk}^m are the normals to the corresponding faces $m = 1 \div 5$, S_{ijk}^m are the areas of the corresponding faces $m = 1 \div 5$.

For the equation (2) the flux is determined by means of a six point model (see fig. 2),

$$\vec{W}_{ijk}^m = \left\{WX_{ijk}^m;\ WY_{ijk}^m;\ WZ_{ijk}^m\right\}$$

$$WX_{ijk}^m = \frac{1}{2}(\kappa_2 + \kappa_5) \cdot \frac{\oint_l T^{n+1} dy}{S}; \quad WY_{ijk}^m = \frac{1}{2}(\kappa_2 + \kappa_5) \cdot \frac{\oint_l T^{n+1} dx}{S},$$

where l is the contour with points $1 \div 6$, and S is the area within this contour l. Along OZ axis the flux is determined by the relation

$$WZ_{ijk}^m = \frac{1}{2}\left(\kappa_{ijk} + \kappa_{ijk+1}\right) \frac{T_{ijk+1}^{n+1} - T_{ijk}^{n+1}}{z_{ijk+1} - z_{ijk}}$$

Let us consider the laser flux approximation

$$Q_{LAS_{ijk}} = \frac{I_{ijk+1} - I_{ijk}}{V_{ijk}},$$

where V_{ijk} is the volume of a cell ijk and

$$I_{ijk+1} = I_{ijk} \cdot e^{-K_{LAS_{ijk}}(Z_{ijk+1} - Z_{ijk})},$$

where $K_{LAS_{ijk}}$ is the coefficient of laser absorption in this cell ijk. The initial value of $I_{ijk}(t)$ is determined by the formula

$$I_{ij1}(t) = \frac{P_{LAS}(t)}{\pi R^2} S_{ij1},$$

where the S_{ij1} is area of an upper face, R is the radius of the laser beam spot and $P_{LAS}(t)$ is the power of laser.

3. The results of the simulations.

The spatial distribution of temperatures are shown in fig. 3, at the moment $t = 1\,ns$, for a homogeneous and for a three-layer target respectively. The runs for a homogeneous target show the considerable anysotropy at the heat transfer along the laser beam direction in comparison with a transverse direction. The velocity of a heat wave front along the OZ axis is approximately three times more, than along R direction. It is connected with a considerable influence of the dynamics of the front of the laser beam absorption region on a heat wave front propagation. For instance, at the moment $t = 1\,ns$, the length of a laser energy absorption region is about $800\,\mu m$, and this value corresponds to estimation of a bremsstrahlung length for the given plasma temperature along an absorption channel $(1.3 - 0.5 keV)$. The simulation of a three layers target demonstrates the disacceleration of the electron conductivity heat wave in a layer of a more dense matter. In spite of this fact, the anisotropic effect of a heat transfer is valid, although it is smaller.

Conclusions

1. A numerical code based on nonregular triangle grid to simulate 3-D heat conductivity wave has been created.

2. The simulations, which were fulfilled for the laser-produced plasma of a plane target show the considerable anisotropy of the energy transfer process, which is due to the formation of the laser beam absorption region.

References

1. Gus'kov S.Yu, Zmitrenko N.V, Rozanov V.B, 1995 JETP 81 296 (in English).
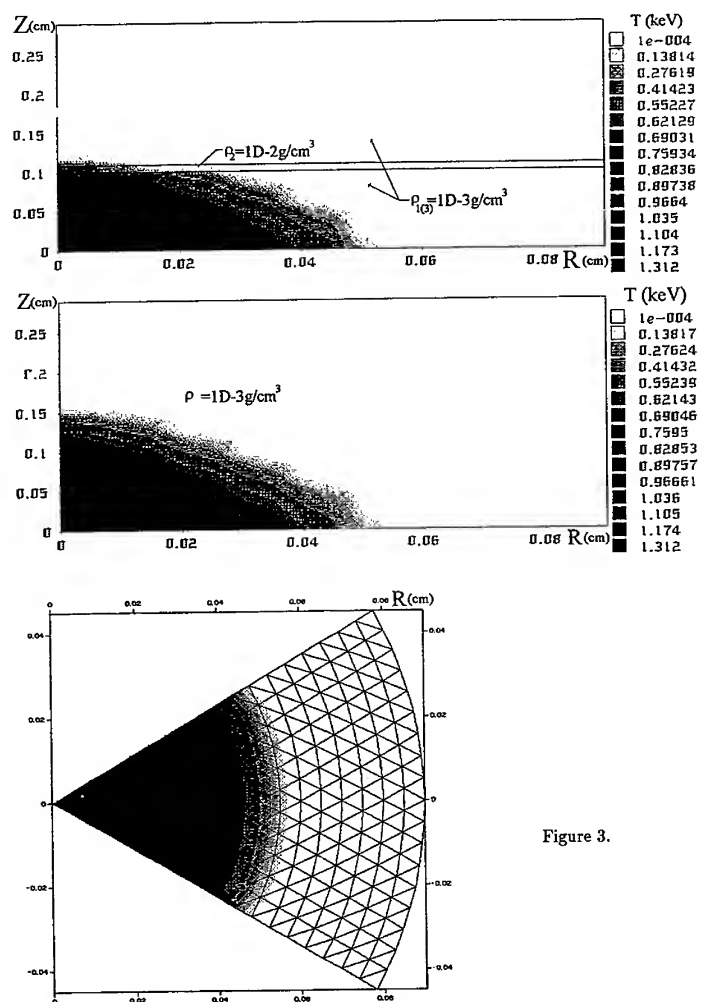
Figure 3.

2D NUMERICAL SIMULATION OF ICF-TARGETS THAT USE RAY-TRACING ALGORITHM

A.B. ISKAKOV, I.V. POPOV, B.F. TISHKIN
The Institute of Mathematical Modeling (IMM),
125047, Miusskaya sq. 4a, Moscow, Russia
I.G. LEBO
Lebedev Physics Institute (FIAN),
117924, Leninskiy Pr. 53, Moscow, Russia

Abstract

Post-processor is designed for simulation of laser beams transportation in plasma of ICF-targets. Post-processor is using together with 2D lagrange code ATLANT and 2D Euler code NUT. The numerical examples of implosion of direct driven targets and "Green-house" targets with allowence for ray-tracing effect of laser beams are presented.

1. Physical and mathematical model.

Calculation were made in the case of axis symmetry. Transportation of beams in plasma is defined by the system of differential equations of geometric-optics [1-2]:

$$\frac{d\bar{r}}{d\tau} = n\bar{s} \ ; \ \frac{dn\bar{s}}{d\tau} = \frac{1}{2}\bar{\nabla}n^2 \ ; \ \frac{dP}{d\tau} = -n\mu P$$

at boundary conditions $P(0) = P_0(\vec{r}_s, t), \vec{s}(0) = \vec{s}_0(\vec{r}_s, t)$, where

$\vec{r}$, radius-vector of the trajectory of ray;

$\vec{s}$, unity vector in the direction of the ray;

P, intensity of the laser;

$n(\vec{r}), \mu(\vec{r})$, functions defining coefficients of refraction and absorption due to the inverse bremsstrahlung mechanism;

$P_0(\vec{r}_s, t), \vec{s}_0(\vec{r}_s, t)$, functions defining on the surface around target $\vec{r}_s \in S$ and time duration of impuls that defines parameters of incident beams.

Particular number of rays successively pass through a set of triangle cells and recieve energy. Inside every cell we locally assume $\bar{\nabla}n^2 = \text{const}$, $\bar{\nabla}(n\mu) = \text{const}$. The previous system may be integrated [2]:

$$n\bar{s}(t) = (n\bar{s})_0 + \frac{1}{2}\bar{\nabla}n^2 t \ ; \ \bar{r}(t) = \bar{r}_0 + \frac{1}{4}(\bar{\nabla}n^2)t^2$$

$$P(t) = P_0 exp\{-(n\mu)_0 t - (\bar{\nabla}(n\mu), (n\bar{s})_0)\frac{t^2}{2} - (\bar{\nabla}(n\mu), \bar{\nabla}n^2)\frac{t^3}{12}\}$$

176

This system is used for every cell.

Algorithm was tested by the well-known analitical solving for incidence s-polarized wave on the plasma layer with the constant gradiend of dielectrical coefficient [3].

2. Direct driven targets.

The shell target compression with allowence for ray-tracing effect and without it (rays pass along radii of target and fully absorbed on the critical surface) were comparised in the case of beams focused in the center of the target. Calculations were made in the 2D lagrange code ATLANT [4, 5]. Parameters of the target and laser pulse are introduced in fig. 1A. In fig. 1B, C results of the calculations $\xi = \xi(t)$ and $\frac{\delta}{R} = \frac{delta}{R}(\xi)$ are represented, where t, time; $\xi = \frac{R_0}{R(t)}$, coefficient of compression; $\frac{\delta}{R}$, relative amplitude of pertrubation of "DT- shell" contact boundary. One can see that the refraction result in the decrease of implosion velocity and the decrease of perturbation growth velocity.

3. "Green-house" targets.

In fig. 2A parameters for compression "Green-house" target are shown [6, 7]. Two contrary pencils of parallel beams enter through the holes on the axis in the outer shell of the "Green- house" target. In fig. 2B the shape of the target in time $t = 1.48ns$ is represented. One can see that to the moment $t \sim 1.5 \div 1.6ns$ work target was destroyed. By this moment neutron yield was $7.6|cdot10^9$.

4. Conclusion.

Ray-tracing effect has appreciable influence on the dynamics of ICF-targets compression. We have developed post-processor allowing to take into account this effect in 2D numerical codes modelling laser target compression.

References.

1. Friedland, L., Bernstein, I.B., *Phys. Rev. A*, v21, N2, 666 (1986).

2. Bolshov, L.A., etc., IAE-4732/16(1988) (in Russian)

3. Ginzburg, V.L., "Propagation of electromagnetic waves in plasma", *Moscow, Nauka*, 297 (1967) (in Russian)

4. Gamaly, E.G., Demchenko, N.N., Lebo, I.G., etc., *Kavantovaja electronica*, 15, N8, 1622 (1988)

5. Lebo, I.G., Popov, I.V., Rozanov. V.B., Tishkin V.F., *Journal of Russian Laser Research*, v15, 136 (1994).

6. Gus'kov, S.Yu., Rozanov, V. B., Zmitrenco, N.V., ZhTEF 108, 548 (1995) (in Russian)

7. Lebo, I.G., Popov, I.V., Rozanov, V.B., Tishkin, V.F., *Kvantovaja electronica*, v22, N12, 1257 (1995) (in Russian)

Direct driven target

Target configuration

DD-gas
1.62 10^{-4}

SiO$_2$ SiO$_2$
2.5   2.5

density (g/sm^3)

247.6   248   250

distance (mkm)

Time impuls profile   Angle impuls profile

Nd-laser
L=1.06 mkm
E=250 Dg

$q(F) = q_d(1+0.25*cos(4F))$

time(ns)   3,6   4,6
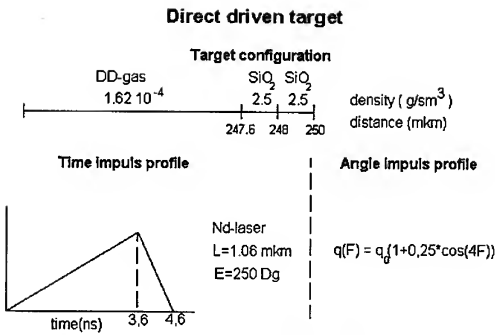
Direct driven target
with allowence for ray-tracing effect

t=4.47ns   R=94mkm
Fig.1a

Refraction influence
on the time of compression

8.00

Coefficient
of compression

6.00

4.00

Without
refraction

2.00

With refraction

Time (ns)

0.00

0.00   1.00   2.00   3.00   4.00   5.00   6.00

Fig.1b

Refraction influence on the regularity of compression

relative
amplitude
of perturbation

0.40

0.30

without
refraction

0.20

with refraction

0.10

coefficient of compression

0.00

0.00   2.00   4.00   6.00   8.00

Fig.1c

"Green-house" target

Configuration of the target

DT-gas	CH	CH	absorber	CH	Cu	density (g/sm^3)
7,16 10^3	1,0	1,0	6,0 10^3	1,0	8,93	

342 346 350   600 622 634 distance (mkm)

Time impulse profile   **Section impulse profile**

L=0.353 mkm
E=6 kDg

1,3   2,6
time (ns)

325

radius (mkm)

FIG.2A

"Green-house" target with allowence for ray-tracing effect

outer shell

rays

inner target

laser beam

Fig.2b

2d Fokker-Planck Simulation for Ablative Rayleigh-Taylor Instability

M.Honda, K.Mima, N.Matsui

Institute of Laser Engineering, Osaka University, Suita, Osaka, 565, Japan

A.Nishiguchi

Osaka Institute of Technology, Asahi-ku, Osaka, 535, Japan

A two-dimensional full Fokker-Planck (FP) simulation code coupled with an ideal fluid equation has been constructed. This code was applied for the direct simulation of ablative Rayleigh-Taylor (RT) instability, which is one of the most crucial issues in symmetrical acceleration of laser-driven implosion. The simulation results show that the preheating of accelerated thin foil target (thickness; $16\,\mu m$) due to nonlocal heat transport causes the depletion of the ablation front density under moderate intensity ($7 \times 10^{13} W/cm^2$) laser irradiation, and significantly suppresses the linear perturbation growth of RT instability by enhancement of the ablation velocity. The concept of the fast laser implosion mode whose isentrope becomes high due to tail electron preheating is also proposed. Our recent 1d-FP simulations in the mode show that the required laser energy for ignition can be reduced to 100kJ or so.

I. Introduction

The preheating due to electron heat transport is one of the most crucial issues in laser driven implosion, because the preheating degrades the compression and might suppress the various macroscopic plasma instabilities. The preheating occurs by the high intensity laser irradiation in the acceleration phase. It is well known in such situation that the Spitzer-Härm (SH) thermal conduction model [1] is not applicable because the thermal electron mean free path is comparable to the scale length of the temperature gradient, so the Fokker-Planck (FP) equation should be numerically solved [2-9]. For the accurate estimation of the preheating by the high energy tail electrons, the FP equation must be coupled with the fluid equations. We made use of the 1d- and 2d-FP fluid code for the investigation of a stable implosion scheme and ablative Rayleigh-Taylor (RT) instability, respectively [8,9].

II. Nonlocal Heat Transport Effects on Rayleigh-Taylor Instability

The RT instabilities mainly occur in two stages of the highly compression processes : the acceleration and deceleration phase of the imploding shell. In this paper, a point of view is only devoted for the former acceleration phase. On the other hand, the nonlocal electron heat transport in an ablative plasma is found to play an important role in the target preheating under moderate to high intensity laser irradiation. The energy spectrum of electron in the corona plasmas typically becomes bi-Maxwellian and the high energy tail electrons cause the significant preheating of cold target. Hence, it is expected that the target expansion by the preheating enhances the ablative stabilization of RT instability and also expected that the properties of the nonlocal heat transport change the numerical factor of ablative stabilization term in Takabe's formula (β) [10].

Our interests are concentrated on the numerical simulation of the RT instability for ablative acceleration of a $16\mu m$ thick planer foil target composed of fully ionized polystyrene (CH : Z=3.5, A=6.5, ρ =1.0 g/cm^3) under moderate peak intensity (7x 10^{13}W/cm^2) laser irradiation, which has the temporal pulse shape of flat top Gaussian with the rise time of 100ps. As soon as the laser light is illuminated on the plane target, the surface is covered with corona plasmas. Ablative RT perturbations imposed at t=500ps are density perturbations of $60\mu m$ wavelength [11]. In the FP case, further, the 2d-FP solver is also turned on at the same time. At 1.0ns, the corona plasmas are heated up to ~ 1keV, and the mass density over the part of target foil are 1.47g/cm^3 (FP) and 1.94g/cm^3 (SH), respectively, so it is found that the target swelling occurs in the FP case significantly even if absorbed laser intensity is moderate level (7x10^{13}W/cm^2).

We have found that the linear perturbation growth of ablative RT instability in the SH simulation is 1.5 times higher than that in the FP simulation and the growth is suppressed dominantly by the preheating of the ablation front by nonlocal electron thermal transport. The linear growth rates of the RT instability in Fig.1 are found to be 1.4ns^{-1} (FP) and 2.1ns^{-1} (SH), respectively whose classical growth rate is $\sqrt{kg}$ =2.6 ns^{-1} , where k=1.0x10^{5}cm/s^2, g=6.7x10^{15}cm/s^2. At 1.5ns, ablation velocities in both cases are v_{abl}=2.7x10^5 cm/s^2 (FP), 2.4x10^{5}cm/s^2 (SH), respectively, so the ablative convection is enhanced in the FP case because of the density lowering of ablation front whose mass ablation rates are almost same in the both cases [9].
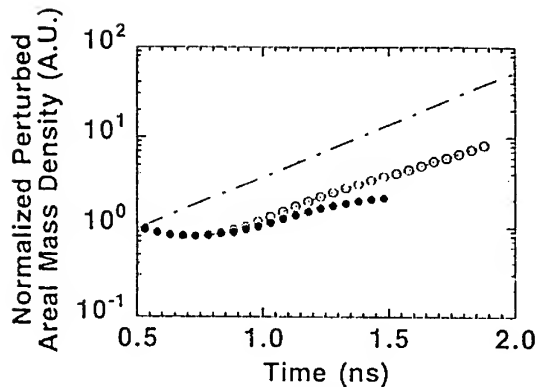
Figure 1 Linear perturbation growth of RT instability. Black and white circles correspond to FP and SH case, respectively. Dashed and dotted line shows the classical RT growth.

III. Fast Stable Implosion as Alternative Scheme

Recently, the concept of the fast laser implosion mode whose isentrope is high because of enhanced preheating and inflight aspect ratio is low, becomes attractive in the laser fusion from the stand point of view of the implosion stability [12,13]. The typical target design and corresponding 100kJ laser conditions in this implosion mode are proposed in Ref.[13]. In this implosion mode, the relatively thick frozen DT shell covered with very thin plastic (polystyrene) CH layer is accelerated up to $5\sim8\times10^7$ cm/s by the high ablation pressure exceeding 100Mbar, and absorbed laser intensity is required to be $10^{15}\sim10^{16}$W/cm^2 at the main pulse peak. Our recent high entropy target design has an advantage over the other hydrodynamic (without additional heating) implosion modes, because this implosion mode is close to the stagnation free-mode. Namely the core structure becomes the isochoric-like around the maximum compression, since the fuel is heated up to the ignition temperature due to the high implosion velocity, and the fluid instabilities on deceleration phase is likely to be eliminated. Hence, the fast implosion mode is essentially a high entropy implosion as a *trade off* for the high ablation pressure and fluid stability.·

The laser energy required for ignition can be also remarkably reduced in the fast implosion mode even if the isentrope is high. We applied the 1d-FP simulation code to investigating this implosion numerically, in order to attain the more detail target design. The laser energy dependencies of neutron yield of thermonuclear DT reaction

are shown in Fig.2. All plots only for FP cases (black circles in Fig.2) are optimized in terms of laser conditions and target parameters. Although, we have not performed the optimization for SH cases (open circles), the gain plots of the SH case are above those of the FP case because of the lower isentrope parameter. Whereas, for "standard" low entropy compression shown by the boldface curve, the ignition and burning condition are satisfied around 1MJ laser energy.
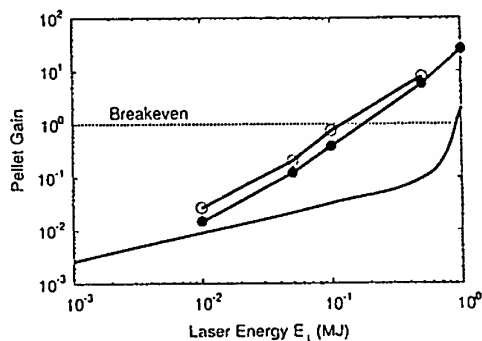
Figure 2 Pellet gain curves for two different implosion schemes. Solid lines with black (FP) and open (SH) circles show the gain curve of fast implosion mode. Boldface curve shows that of "standard" low entropy compression and high gain scheme.

IV. References

[1] L.Spitzer and R.Härm, Phys. Rev. 89, 977 (1953).

[2] A.R.Bell, R.G.Evans, and D.J.Nicholas, Phys. Rev. Lett. 46, 243 (1981).

[3] T.H.Kho, D.J.Bond, and M.G.Haines, Phys. Rev. A28, 3156 (1983).

[4] J.F.Luciani, P.Mora, and J.Virmont, Phys. Rev. Lett. 51, 1664 (1983).

[5] J.R.Albritton, Phys. Rev. Lett. 50, 2078 (1983).

[6] J.P.Matte, et.al., Phys. Rev. Lett. 53, 1461 (1984).

[7] E.M.Epperlein, et.al., Comput. Phys. Comm. 52, 7 (1988).

[8] A.Nishiguchi, et.al., Phys. Fluids B4, 417 (1992).

[9] M.Honda, et.al., (to be submitted).

[10] H.Takabe, et.al., Phys. Fluids 28, 3676 (1985).

[11] M.H.Emery, J.P.Dahlburg, and J.H.Gardner, Phys. Fluids 31, 1007 (1988).

[12] H.Takabe, et.al., Proceedings of IAEA-TCM, Osaka, 15-19, April (1991).

[13] M.Honda, et.al., (to be published in Phys. Plasmas).

ELECTROMAGNETIC INSTABILITIES IN LASER-PRODUCED PLASMAS WITH 3-D PIC CODE

T. OKADA, K. SATOU

Faculty of Technology, Tokyo University of Agriculture and Technology,
2-24-16 Naka-machi, Koganei-shi, Tokyo 184

It is well known that electrons in a velocity distribution with temperature anisotropy cause many kinds of microscopic instabilities. These instabilities give rise to the occurrence of large amplitude magnetic fields. These fields are joined with other physical phenomena and play an important role, *e.g.* in the anomalous thermal flux reduction or in the spherical compression of pellets. In this paper, we will report self-generated intense magnetic fields, which is one of the electromagnetic instabilities caused by temperature anisotropy, with three-dimensional Particle-in-Cell (PIC) code simulation.

1 Introduction

1.1 Temperature anisotropy and instabilities

In laser-plasma interaction of inertial confinement fusion (ICF), it is possible to find temperature anisotropy in electron velocity space between the direction of laser-incidence axis and perpendicular direction to the axis due to anisotropic electron heating by resonance absorption or locally isotropic heating by inverse-bremsstrahlung [1]. Recently, it has been reported that temperature anisotropy in electron distribution function has been observed with X-ray spectrum measurement experiment [2]. They said that this is a first experimental demonstration of temperature anisotropy in laser-produced plasmas. In that paper, two types of temperature anisotropy are observed, *i.e.* strong negative second-order type (equivalent to an oblate distribution) and weaker positive (prolate) type.

These anisotropies cause lots of microscopic instabilities, *e.g.* Alfvén waves. In fact, filamentary structures coupled with intense magnetic fields have been experimentally observed for instance [3] and there have been reports that Weibel-type instabilities [4] have close relation to the occurrence of these strong fields.

It is sure that these intense magnetic fields in the mega-Gauss range should play an important role, for example, in the anomalous electron thermal flux reduction and/or in dynamic behaviours of spherical compression of pellets.

We demonstrate the generation mechanism of Weibel instability using fully electromagnetic and fully relativistic three-dimensional particle simulation, and discus our results and others.

1.2 Weibel-type instabilities

It is well known that there exist many kinds of electromagnetic or electrostatic instabilities in plasmas which have sufficiently deviated velocity distribution from normal Maxwellian. Weibel derived the existence and dispersion relation of this self-generated transverse electromagnetic waves from linearised Boltzmann equation[4].

In many cases, these anisotropies in electron velocity space which give rise to various instabilities are defined between two directions of axis, *i.e.* the direction of beam-incidence axis (let it be x-axis) and other axes. Let us assume that the angular distribution is symmetric about the x-axis, so Weibel instability consists of two modes: the most unstable k_x mode and $k_\perp$ mode. k is the wave vector and k_x mode, $k_\perp$ mode are respectively equivalent to $T_x < T_\perp$ ('pancake-shaped' anisotropy) and $T_x > T_\perp$ ('football-shaped' anisotropy). Each of them have been studied in linear or nonlinear stage, in collisional or non-collisional plasmas, *etc.*.

With the rapid progress of surroundings for ICF, especially laser or large current particle beam technology, various phenomena which have been predicted but not directly observed are revealed by many plasma-interaction experiments. So that, Weibel-type instabilities attract a great deal of attention as a fundamental mechanism of magnetic field generation in plasmas.

2 Three-dimensional PIC code simulation

In order to simulate the generating process of Weibel instability, we performed numerical calculation using electromagnetic PIC (Particle-in-Cell) code simulation. PIC code is one of the typical simulation schemes for performing microscopic instabilities which are directly affected by velocity distribution function.

Our PIC code is fully three-dimensional in both space (x, y, z) and velocity space (v_x, v_y, v_z), fully electromagnetic and fully relativistic. In this code, particle and field quantities are derived from time evolution of closed differential equation system which consists of equations of motion (Newton-Lorentz force) and Maxwell equations (electromagnetic force), and are solved self-consistently.

We chose the x-axis as laser-incidence direction and defined 'pancake-shaped' temperature anisotropy between the direction of x-axis and that perpendicular to it, so we performed k_x mode ($T_x < T_\perp$) simulation. Maxwellian is just as follows:

$$f(v_x, v_\perp) = \frac{n}{(2\pi)^{3/2} u_x u_\perp} \exp\left(-\frac{v_x{}^2}{2u_x{}^2} - \frac{v_\perp{}^2}{2u_\perp{}^2}\right), \qquad (1)$$

where n is the number density and **u** the thermal velocity.

At time-step 'zero', all self-fields are 'zero' and particles, both electrons and ions are 'quietly' loaded into the system with initial velocity distribution (only ions are at a standstill).

3 Discussion

We performed this computer simulation using parameters: time-step $0.1c/\omega_{pe}$, spatial-step $0.2c/\omega_{pe}$, meshes $16 \times 16 \times 16$, electrons 163840, ions 163840, thermal velocity (u_x) $0.05c$ and thermal velocity $(u_\perp)$ $0.25c$, where c is the light speed and ω_{pe} the electron plasma frequency.

Fig. 1 shows the temporal profile of both electric and magnetic fields. Magnetic fields present exponential growth, and reached 8.1MG at the end. On the other hand, electric fields present almost 'zero-growth'. These results are comparable with typical data from recent experiments. But, note that we simulated the 'pure' Weibel instability. In Fig. 2, spatial profiles of current density and induced magnetic field are illustrated. These are local currents in plasmas formed by the temperature anisotropic electron distribution. Two waves have a phase difference of '$\pi/2$'. It indicates that (new) magnetic fields grows under the relation between (old) magnetic field itself and the current. Fig. 3 shows the growing process of same magnetic field, here the field is represented as time-, space-dependent. It shows that self-generated magnetic fields grow up as standing waves.

References

1. M.A. True, *Phys. Fluids* **28**, 2597 (1985).
2. J.C. Kieffer, J.P. Matte *et al.*, *Phys. Rev. Lett.* **68**, 480 (1992).
3. O. Willi, P.T. Rumsby *et al.*, *Opt. Commu.* **41**, 110 (1982).
4. E.S. Weibel, *Phys. Rev. Lett.* **2**, 83 (1959).
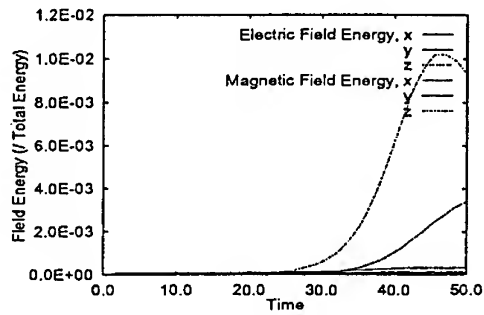
Figure 1: Temporal profile of the fields.
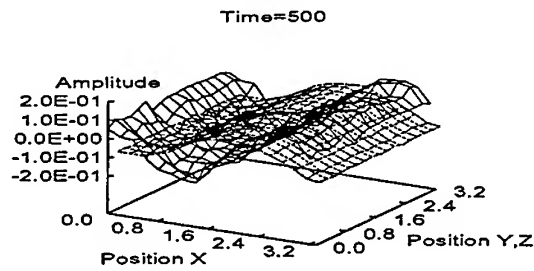
Figure 2: Induced current and magnetic fields.
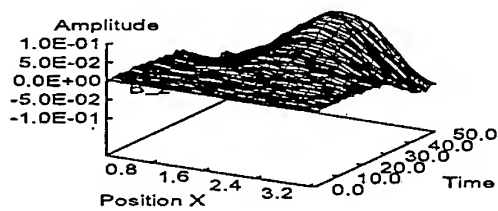
Figure 3: Temporal profile of the induced magnetic field.

THE SHOCK-INDUCED INTENSIFICATION
OF TURBULENT MIXING

S. G. ZAYTSEV, A. N. ALESHIN, E. V. LAZAREVA,
E. I. CHEBOTAREVA, V. V. KRIVETS, S. N. TITOV

The Krzhizhanovsky Power Engineering Institute (ENIN), Leninsky pr.19, Moscow 117071, Russia

The shock wave when passing through a turbulent zone separating gases of different density, intensifies the mixing. This phenomenon was experimentally studied in shock tubes [1]-[4]. Theoretical description of intensification of turbulent mixing was approached by semi-empirical models of turbulence [5]-[7]. The present paper describes studies on the shock-induced intensification of turbulent mixing in shock tubes. Analysis of the data obtained by different methods is given. The data are compared to those obtained by other authors.

1 Experimental design

Experiments were performed in shock tubes. The driven section included a special section with a thin film of given shape which modeled an initial discontinuous interface K_0. We also used an initial continuous interface K_0 obtained by the removal of a sliding plate from the channel prior to experiment. The propagation of incident shock S_{e1a} in gas 1 (on the right of initial interface K_0) resulted in their interaction. This interaction produced the refracted shock wave S_{i1b} propagating in gas 2 (on the left of K_0), the reflected shock S_{i1a} ($\rho_1 < \rho_2$) or the rarefaction wave ($\rho_1 > \rho_2$) propagating in gas 1, and the interface K_{12} separating the shock-compressed flows of gases 1 and 2. We used two types of discontinuous interface. **Version 1.** The initial discontinuous interface K_0 was modeled by a thin planar film placed perpendicularly to the channel axis. The mechanic effect of the incident shock and the following heat effect of the shocked flows resulted in the decay of the film and formation of a mixing zone K_{12}. By the moment of collision of K_{12} with the reflected shock, the mixing zone is assumed to be turbulent. **Version 2.** Initial discontinuous interface K_0 was of 2D sinusoidal shape. K_0 was modeled with a thin film. After the interaction of the incident shock with K_0, we recorded all the stages of the evolution of Richtmyer-Meshkov Instability (RMI) which resulted in

formation of the turbulent mixing zone K_{12} [8]. **Version 3.** The incident shock wave passed through a continuous interface K_0. Unlike for the versions 1 and 2, there was no film to model the interface. In this case, the RMI evolution was qualitatively similar to that for the discontinuous interface [9]. However, the growth rate of the amplitude of K_{12} was lower at initial stages than that for discontinuous interface.

The goal of the present study was to investigate the intensification of the turbulent mixing induced by the passage of the reflected shock S_{e2b} through the mixing zone K_{23} (versions 1, 2, and 3).

2 Results

Version 1. Figure 1 shows a series of Schlieren pictures representing the evolution of the interface K_{12} formed after the passage of the initial shock S_{e1a} through initial interface separating air from helium. Mach number of the S_{e1a} (M_{e1a}) was 1.3, initial pressure p_0 was 0.9 atm. K_0 was modeled by a planar 0.5 μm thick film. Figure 1 shows the process of interaction of S_{e2b} with K_{12}. As seen, the thickness of the mixing zone K_{23} resulted from the collision of K_{12} with S_{e2b} (L_{23}) was larger than the thickness of L_{12}. The values of $\Delta L_{23}/u\Delta t$ which characterize the intensification of turbulent mixing, are given by points 1 in Fig. 4; u is the change in the velocity of the mixing zone caused by the interaction with S_{e2b}. **Version 2.** Figure 2 shows a series of Schlieren pictures demonstrating the RMI evolution for the shock passage from He to Xe through a 2D sinusoidal discontinuous interface at the turbulent stage. The wavelength of initial interface K_0 modeled with 2 μm thick mylar film was 8 mm, the initial amplitude (a_0) was 10 mm (peak to peak). The Mach number of the incident shock was 3.5, the initial pressure (p_0) was 0.5 atm. The values of $\Delta L_{23}/u\Delta t$ for this version are given in Fig. 4 by points 2. **Version 3.** Figure 3 shows a series of Schlieren pictures obtained for the passage of the incident shock wave S_{e2b} from the mixture 0.5 He + 0.5 Ar into He. At the moment of the collision of S_{e2b} with K_{12}, the latter was at the turbulent stage. The values of $\Delta L_{23}(A)/u\Delta t$ for this version are given in Fig. 4 by points 3.

3 Discussion and conclusions

Figure 4 gives a comparison of the $\Delta L_{23}/u\Delta t$ values measured in this study (points 1, 2, and 3), with the data of other authors. Points 5, 6, and 7 are the experimental data obtained in [1, 3, 4], respectively. Note that the data given by the points 1, 5, 6, and 7, were obtained experimentally for the version 1.

Lines 8 determine the probable range of the $\Delta L_{23}/u\Delta t$ value obtained in [5]. The lower of lines 8 coincides with the values obtained in [7]. Significant spread in the experimental data is due to a complexity of the process. The evolution to the turbulent stage develops through the interaction of the large-scale vortex structures. In different runs the vortex structures may be of different scale, and this is a probable cause of the spread observed in the experimental data. Line 4 is the approximation of the data given by points 1. Line 9 is the approximation of the data given by points 2 and those obtained in [3] (for $A > 0$). As seen, the range of the $\Delta L_{23}/u\Delta t$ values is limited by lines 4 and 9, and is far narrower than that determined in [5].

To conclude, we have determined the range of the probable values of the shock-induced intensification of turbulent mixing.

References

[1] V. A. Andronov et al. (1976) Zh. Eksp. Tekh. Fiz., V. 71 (issue 2), 806.

[2] S. G. Zaytsev et al. (1985) Dokl. Akad. Nauk SSSR, V. 283, 94-98.

[3] L. Houas and I. Chemouni. To be published by Phys. Fluids.

[4] M. Vetter and B. Sturtevant. (1995) Shock waves, V. 4, 247-252.

[5] V. E. Neuvazhaev. (1991) Shock Waves (K. Takayama, Ed.), Japan, P. 359.

[6] D. C. Besnard, J.-F. Haas, and R. M. Rauenzahn. (1989) Physica D, 37, 227-247.

[7] Karning O. Mikaelian. (1990) Physics of Fluids A, 2, 592-598.

[8] A. N. Aleshin et al., (1990) Dokl. Akad. Nauk SSSR, 310, 1105-1108.

[9] S. G. Zaytsev, S. N. Titov, and E. I. Chebotareva. (1994) Mekh. Zhid. i Gasa, No. 2, P. 18-26.

Fig. 1.   Fig. 2.   Fig. 3.

Fig. 4. ● - 1, □ - 2, ○ - 3, — - 4, ◇ - 5, △ - 6, + - 7, - - - - 8, —— - 9.
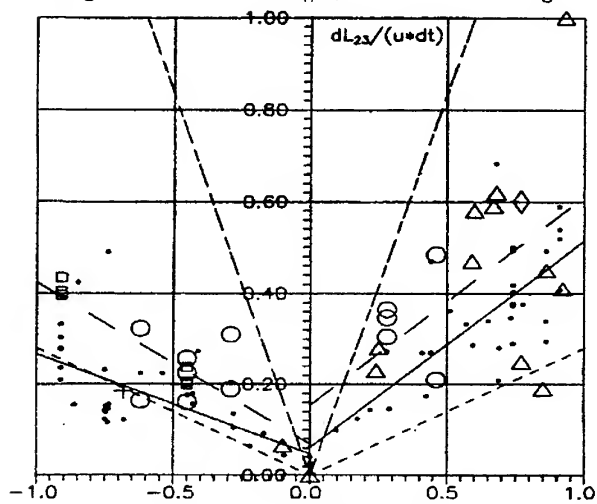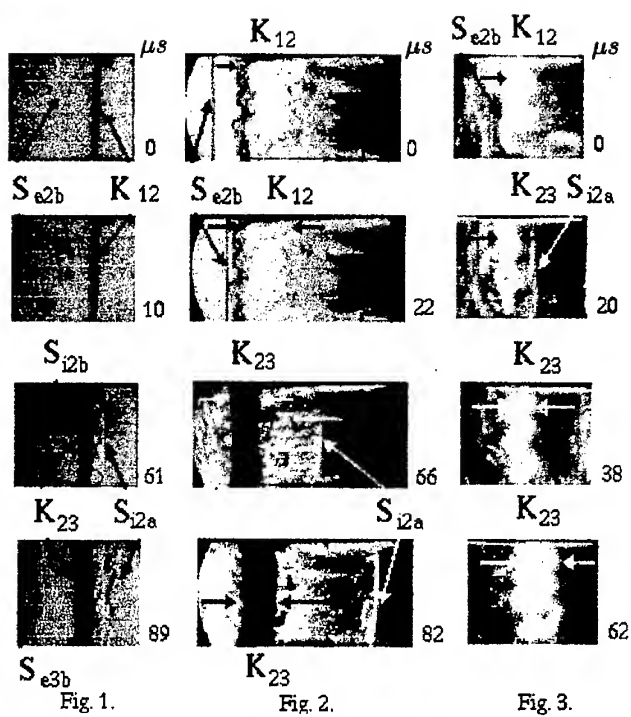
EXPERIMENTAL INVESTIGATION OF THE CLASSICAL RAYLEIGH-TAYLOR INSTABILITY

K. S. BUDIL, B. A. REMINGTON, A. M. RUBENCHIK, M. BERNING[†],
W. M. WOOD-VASEY, K. O. MIKAELIAN AND T. A. PEYSER

Lawrence Livermore National Laboratory, P. O. Box 808,
Livermore, California 94550, USA

The evolution of the Rayleigh-Taylor (RT) instability in a compressible medium has been investigated at an accelerating embedded interface and at the ablation front in a series of experiments on the Nova laser. The x-ray drive generated in a gold hohlraum ablatively accelerated a planar target consisting of a doped plastic pusher backed by a higher density titanium payload with perturbations placed at the plastic-Ti interface. The targets were diagnosed by face-on and side-on radiography. In previous work focusing on single mode perturbations, wavelengths as short as 10 m have been observed to grow strongly at the embedded interface. Here multimode perturbations consisting of either 2, 10 or 20 modes superposed in phase have been investigated.

1 Introduction

One of the critical concerns for inertial confinement fusion is the Rayleigh-Taylor (RT) instability. At an ablation front, growth of short wavelength modes is stabilized. However, short wavelength modes have been shown to grow strongly at an embedded interface.[1] This work examines the growth of perturbations consisting of multiple modes superposed in phase at an embedded interface.

2 Experimental results

The experimental configuration is described in detail elsewhere [1,2] and consists of a planar experimental package mounted across a hole on a 3 mm long by 1.6 mm diameter gold hohlraum. Eight Nova beams at $\lambda = .351$ μm are used to generate a 3.5 or 4.5 ns shaped x-ray drive. The accelerating target is back-illuminated with 6.7 keV He-α x-rays generated by the remaining two Nova beams at $\lambda = .528$ μm, smoothed with 5 mm hexagonal element random phase plates, incident on an iron disk. Images are obtained with a gated x-ray framing camera, the flexible x-ray imager (FXI).[3] Each image is converted to ℓn(exposure) $\propto -$OD $= -\int \rho\kappa dz$, where ρ is density and κ is opacity, and analyzed by Fourier decomposition. The planar experimental packages consisted of a 40 μm thick brominated plastic ablator ($C_{50}H_{47}Br_3, \rho = 1.26$ g/cm^3)

backed by a 15 μm thick Ti payload ($\rho = 4.5$ g/cm^3).

Experimental data are presented for three perturbation profiles. The first profile consisted of a two-mode patttern corresponding to the superposition of $\lambda = 10$ μm and $\lambda = 15$ μm, each with an amplitude of $\eta_o = 1$ μm, superposed in phase. As the growth of these two modes proceeds into the nonlinear regime, defined as when the amplitude to wavelength ratio is no longer small ($k\eta \geq .1$), the two modes couple producing beat modes. The $k_+ = k_{10} + k_{15}$ mode corresponds to a wavelength of $\lambda_+ = 6$ μm which is below the experimental resolution (≈ 8 μm) but the $k_- = k_{10} - k_{15}$ corresponding to a wavelength of $\lambda_- = 30$ μm which is readily diagnosable. Figure 1 shows the amplitude (in ℓn(exposure)) for the 10, 15 and 30 μm modes.
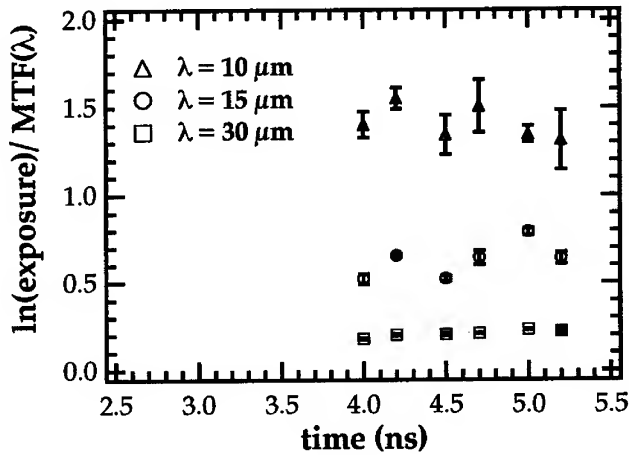
Figure 1: Experimental data and calculations for the growth of $\lambda = 10$ μm and $\lambda = 15$ μm superposed in phase. The growth of the $\lambda_- = 30$ μm beat mode is also shown.

Motivated by the experimental observation that growth of the shortest wavelengths was strongest,[1] the next profile studied was the superposition of two extremely short wavelengths ($\lambda = 4$ and 5 μm), each below the experimental resolution. In this case their growth is diagnosed solely by the appearance and subsequent growth of the $k_- = k_4 - k_5$, $\lambda_- = 20$ μm beat mode. The amplitude of this mode as a function of time is shown in Figure 2. Simulations predict linear growth factors of ≈ 22 and 40 for the 5 and 4 μm modes respectively at $t = 4.5$ ns, when the $\lambda = 20$ μm mode is first observed in the data.

One of the goals of this work is to demonstrate the onset of an *inverse*
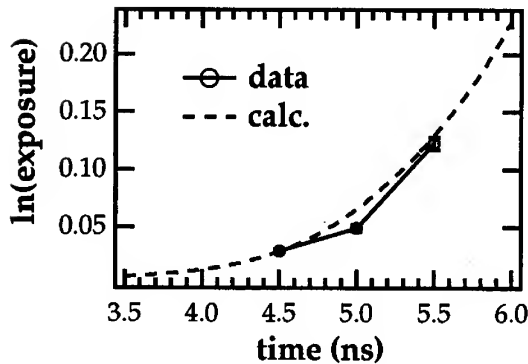
Figure 2: Experimental data and calculation for the growth of the $\lambda_- = 20\,\mu$m beat mode.

cascade in the late nonlinear regime where the mode coupling has proceeded to fill in all mode space and longer wavelength structures are beginning to dominate the flow. A first attempt at an inverse cascade experiment was made by placing a large band of modes, modes 1 through 20 with a fundamental wavelength of $\lambda = 200\,\mu$m, at the embedded interface. The actual perturbation profile used and an image from the "raw" experimental data are shown in Figure 3.

In each case the solid curves represent calculations done using the 1-D radiation hydrodynamics code HYADES[4] to generate the gross foil motion and the time-dependent parameters generated were used in an analytic model to predict perturbation growth in the linear regime, with a correction for the finite layer thickness of the titanium. The nonlinear calculations utilized a model derived using third order perturbation theory[5].

3   Summary

We have investigated the growth of multimode perturbations at an RT-unstable embedded interface. Two-mode initial perturbations showed the appearance of beat modes as their growth proceeded into the nonlinear regime. The growth of two modes which were both below the experimental resolution was diagnosed by the appearance and subsequent growth of the $\lambda_- = 20\,\mu$m beat mode. Targets with a multimode perturbation will allow us to investigate the prediction of an *inverse cascade*, or trend toward longer and longer wavelength structures dominating the flow.
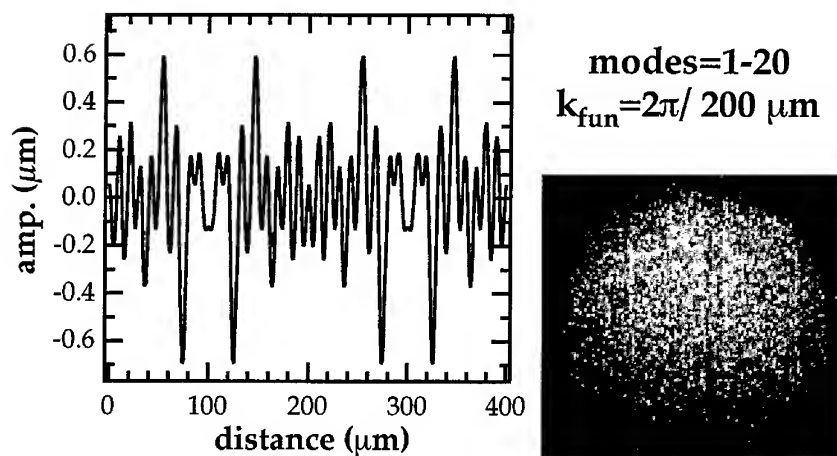
Figure 3: Multimode perturbation consisting of a band of 20 modes (modes 1-20, fundamental $\lambda = 200$ μm) superposed in phase. The experimental image shown was obtained at t = 4.6 ns after the initiation of the laser drive.

Acknowledgments

†Current address the University of Düsseldorf, Düsseldorf, Germany.

References

1. K. S. Budil *et al.*, *Phys. Rev. Lett.* **76**, 4536 (1996).
2. B. A. Remington *et al.*, *Phys. Plasmas* **2**, 241 (1995); K. S. Budil *et al.*, to be submitted to *Phys. Plasmas* (1996).
3. K. S. Budil *et al.*, *Rev. Sci. Instrum.* **67**, 485 (1996).
4. J. T. Larsen and S. M. Lane, *J. Quant. Spect. Rad. Trans.* **51**, 179 (1994).
5. J. W. Jacobs and I. Catton, *J. Fluid Mech.* **187**, 329 (1988); S. W. Haan, *Phys. Fluids* **3**, 2349 (1991).

LINEAR RAYLEIGH-TAYLOR INSTABILITY SCALING APPLICABLE TO TYPICAL TARGET EXPERIMENTS CONDITION

J. SANZ, L.F. IBAÑEZ
E.T.S.I. Aeronáuticos, Universidad Politécnica de Madrid, 28040-Madrid-Spain

A.R. PIRIZ
Consejo Nacional de Investigaciones Científicas y Técnicas (CONICET). Argentina

The Rayleigh-Taylor instability in an ablation front with smooth gradients has been studied by means of an analytical model based in the WKB approximation. The model takes into account the relevant effect of lateral thermal conduction and the results turns out to be in good agreement with the numerical calculations.

1. INTRODUCTION

Stabilization of the Rayleigh-Taylor instability in an ablative expansion can be significantly enhanced by smoothing the density gradient on the ablation front. Gradient effects may be of central importance in determining the instability growth rate γ of a high gain target for inertial confinement fusion. [1] However, relatively few works have been dedicated to this issue. To our knowledge, the most complete study has been performed by Kull, [2] who numerically solved the problem in terms of the instability parameter $\Gamma = \chi_a g / v_a^3$, where $\chi_a = \chi \varepsilon_a^n / \rho_a$ is the thermal conductivity, g is the external acceleration and ρ_a, v_a and ε_a are, respectively, the ablation front density, fluid velocity and specific internal energy. These results show that for sufficiently smooth gradients at the ablation front ($\Gamma \geq 10$), the ablative stabilization becomes strongly affected by the lateral thermal conduction. In such a regime a formula which fits numerical simulations has been proposed,[1] but only a few simulation data have been reported.[3] On the other hand, an analytical model based on the WKB approximation has been presented in Ref.4, but thermal transport which is the relevant effect for $\Gamma \geq 10\text{-}20$ has been neglected. In this paper, we present the first analytical model based on the WKB approximation which takes into account the thermal conduction in an ablation front with smooth gradients.

2. THE ANALYTICAL MODEL

We consider a steady ablation front under the effects of an external acceleration $g = g e_z$ opposite to the density gradient. Such a gradient has a characteristic length $L_0 = \chi_a / v_a$ and we assume small perturbations of wave number k for which the condition $kL_0 \gg 1$ holds. Then, we proceed with the stability analysis by linearizing

the fluid equations and assuming that every perturbation $\delta\varphi$ of a quantity $\varphi(t, x, z)$ is of the form $\delta\varphi(t, x, z) \propto \exp(\gamma t + ikx)$. Thus, after some algebra we get the following equations for the perturbations :

$$\gamma\,\delta\rho + \frac{d}{dz}(\delta\rho v_0 + \rho_0\,\delta v_z) = -ik\rho_0\,\delta v_x \quad , \tag{1}$$

$$\rho_0[\gamma\,\delta v_x + v_0\frac{d}{dz}(\delta v_x)] = -ik\,\delta p \quad , \tag{2}$$

$$\rho_0[\gamma\,\delta v_z + \frac{d}{dz}(v_0\,\delta v_z)] + \delta\rho v_0\frac{dv_0}{dz} = -\frac{d}{dz}(\delta p) + \rho_0 g \quad , \tag{3}$$

$$-ik\,\delta v_x + k^2\frac{\chi_0}{\rho_0}\delta\rho = \frac{d}{dz}[\delta v_z + \frac{d}{dz}(\frac{\chi_0}{\rho_0}\delta\rho)] \quad . \tag{4}$$

These equations can be combined for obtaining a fifth order differential equation for the velocity perturbation δv_z with coefficients depending on the coordinate z. These coefficients involve constants such as the growth rate γ which is the eigenvalue of the system. If this fifth order system has l_1 modes vanishing at $z \to +\infty$ and l_2 modes vanishing at $z \to -\infty$, so that $l_1 + l_2 = 5$, then the dispersion relation $\gamma(k)$ is obtained in the usual way from the condition for the existence of non-trivial solutions. In the WKB approximation the perturbation δv_z is written in the form $\delta v_z \propto \exp\int q\,dz$, where q are the roots of the following fifth order characteristic function:

$$P(u,\gamma,k,z) = (\frac{\gamma}{kv_0} + u)^2 (1 - u^2) + \frac{k\chi_0}{v_0}(\frac{\gamma}{kv_0} + u)(1 - u^2)^2 - G = 0 \quad , \tag{5a}$$

$$G = -\frac{g}{k^2 v_0^2}\frac{d(\ln\rho_0)}{dz} \quad , \qquad u = \frac{q}{k} \quad , \tag{5b}$$

where we have considered that the coefficients of the fifth order differential equations depend weakly on z.

On the other hand, in order to obtain non-trivial solutions, we have to require the existence of two turning points, at $z = z_{1T}$ and $z = z_{2T}$, where the WKB solution breaks :

$$\frac{\partial P}{\partial u} = 0 \quad . \tag{6}$$

In such a case, the dispersion relation arises from the following condition :[5]

$$k\int_{z_{1T}}^{z_{2T}}(q_1 - q_2)\,dz = (2N + 1)\pi \quad ; \quad N = 0, 1, \ldots$$

where q_1 and q_2 are the roots which coalesce at the turning points and Re $q_1 < 0$ and Re $q_2 > 0$ at $|z| \to \infty$. In the limit $k \to \infty$ both turning points coalesce at a point and the following condition is obtained :

$$\frac{\partial P}{\partial z} = 0 . \tag{7}$$

The set of Eqs.(5) to (7) represents the formal solution of the problem. Then, for simplicity and taking into account that $k\chi_0/v_0 \gg 1$, we retain the first term of $P(u,\gamma,k,z)$ only in Eq. (5) and neglect it in Eqs. (6) and (7). In this way, the following solution is found :

$$\frac{\gamma}{kv_0} = \frac{1 - 5u^2}{4u} , \tag{8}$$

$$G = \frac{(1 - u^2)^3}{16u^2}\left(1 + 4u\frac{k\chi_0}{v_0}\right) , \tag{9}$$

$$u^2 = \frac{1 - F(\theta)}{5 - F(\theta)} , \quad F(\theta) = \frac{(2n + 2)\theta - (2n + 3)}{\theta - 1} , \tag{10}$$

where $\theta = \varepsilon/\varepsilon_a$, G is given by Eq.(5b) and we have used a simple corona model for the zero order solution :

$$p_0 = \tfrac{2}{3}\rho_0\varepsilon_0 \approx p_a \quad ; \quad \dot{m} = \rho_0 v_0 \quad ; \quad \chi\varepsilon^n\frac{d\varepsilon}{dz} \approx \frac{5}{3}\dot{m}(\varepsilon - \varepsilon_a) , \tag{11}$$

where p_a is the ablation pressure.

From the previous equations we obtain the dispersion relation $\gamma(k)$ with Γ as a parameter. We have compared the results of the present model with the numerical calculations of Ref. 2 for $\Gamma = 20$ and 100, respectively, in Fig. 1. As can be seen, a good agreement is found despite the fact that, as it was noted in Ref.2, numerical calculations becomes less reliable for $\Gamma \geq 20$.

On the other hand, the model provides the following analytic expression for the cut-off wavenumber k_c :

$$\kappa_c^3\Gamma^2 + \frac{5}{4}\left(\frac{2n + 2}{2n + 3}\right)^n \kappa_c^2\Gamma - 3.5\frac{(2n + 2)^{2n+2}}{(2n + 3)^{2n+3}} = 0 \quad , \quad \kappa_c = \frac{k_c v_a^2}{g} . \tag{12}$$

We have represented in Fig.2 κ_c vs Γ, such as it is given by Eq.(12), together with the numerical results from Ref.2. It is worth to notice that, for relatively large values of Γ, Eq.(12) yields : $\kappa_c = h(n)\Gamma^{-2/3}$, $h(n) \approx 1.5(2n+2)^{(2n+2)/3}/(2n+3)^{(2n+3)/3}$. This expression denotes two interesting facts. First, the asymptotic behaviour of k_c is a power law with the exponent independent of n. Second, k_c is a decreasing function of the exponent n, that is, the opposite tendency observed for $\Gamma \leq 1$.
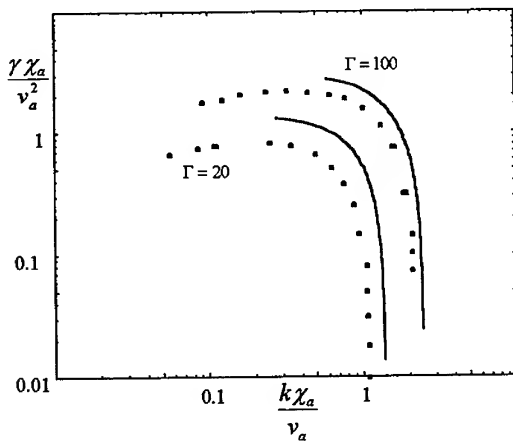
Fig.1 Growth rate instability as a function of the perturbation wave number. Dots represent the numerical calculations of Ref.2 and solid curves are given by the present model
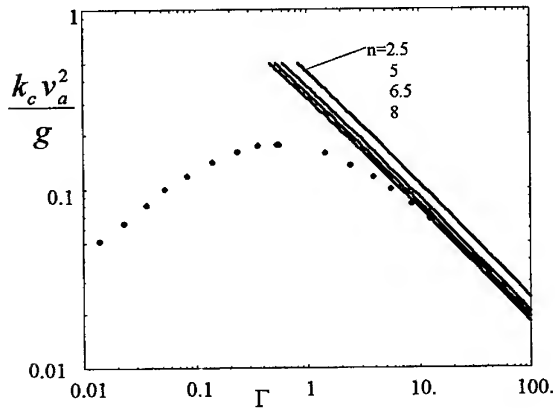
Fig.2 Cut-off wave number as function of Γ. Dots are numerical results from Ref.2

3.CONCLUDING REMARKS

The Rayleigh-Taylor instability in an ablation front with smooth gradients has been described by a model based in the WKB approximation. Lateral thermal transport is found to be significant in determining the growth rate reduction.

REFERENCES
[1]J. Lindl, Phys. Plasmas, 2, 3933 (1995).
[2]H.J. Kull, Phys.Fluids B, 1, 170 (1989).
[3]S.B.Weber et al., Bull. Am. Phys. Soc. 39, 1640 (1994).
[4]A.B. Bud'ko, M.A. Liberman, Phys.Rev.Lett., 2, 178(1992).
[5]H.L.Berk, D. Pfirsch, J. Math. Phys., 21, 2054 (1989).

Investigation of the turbulent mixing on Iskra-4 laser facility

V.A.ANDRONOV, S.A.BEL'KOV, A.V.BESSARAB, **S.G.GARANIN**,
A.A.GORBUNOV, V.N.DERKACH, G.V.DOLGOLEVA, B.N.ILUSHECHKIN,
G.A.KIRILLOV, G.G.KOCHEMASOV, YU.V.KURATOV, V.P.LASARCHUK,
V.A.LEBEDEV, V.M.MURUGOV, L.S.MKHITAR'AN, S.I.PETROV,
A.V.PINEGIN, A.N.RAZIN, N.N.RUKAVISHNICOV, A.V.RYADOV, A.V.SENIK,
N.A.SUSLOV, S.A.SUKHAREV, V.A.TOKAREV, I.N.VORONICH, A.I.ZARETSKY

*Russian Federal Nuclear Center - Institute of Experimental Physics, 607190, Sarov,
Prospect Mira 37, Nizhny Novgorod Region, Russia.*

Experimental investigations results of turbulent mixing of Al and Au thin layers at laser acceleration of plane three- layer targets of Si (4 μm), Al (2 μm) and Au ((0.15-0.3) μm) are presented. The second harmonic radiation from iodine laser Iskra-4 (λ=658 nm) was used in these experiments. Comparison of the experimental results with 1D hydrodynamics code calculations is discussed.

In this report experimental results on investigation of thin Al and Au layers turbulent mixing at acceleration of flat Si-Al-Au targets on Iskra-4 laser facility [1] are presented. The methodical approach of considered experiments was mainly analogous to that offered in [2]. The target Si-Al-Au is irradiated by three laser beams. First high power beam irradiates the target from Si layer side and has intensity of $I_p \approx (0.5-1) \cdot 10^{14}$ Wt/cm^2 (wave length λ=0.66μm, pulse duration $\tau_L \approx$(0.8 - 1.2) ns) (fig.1). The thickness of the Si ($d_{Si} \approx$(4-5)μm) layer is selected
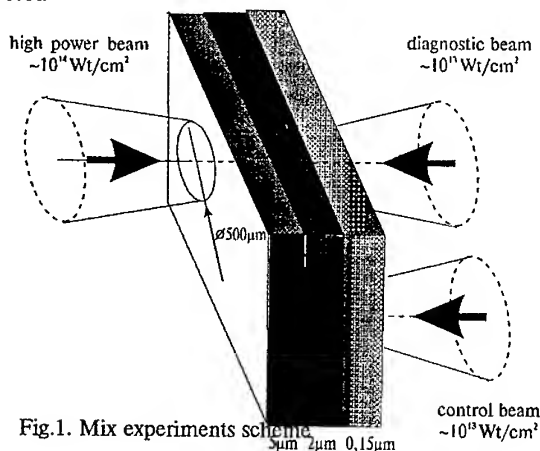
Fig.1. Mix experiments scheme

from a condition that the thermal wave must not reach the Al layer during high power beam action. In this case the layers of aluminum and gold are accelerated in a "cold" conditions (if not to take into account their heating by x-ray radiation of a plasma and shock wave). On the Al-Au boundary the Rayleigh- Taylor instability conditions ($g \cdot \nabla \rho$<0 where g- acceleration, $\nabla \rho$- density gradient) are realized. As a result the mixing zone of the aluminum and gold materials appears.

200

The second diagnostic beam irradiates the target on the gold side with temporal delay of $t_d \approx 0.86$ ns. The intensity of this beam is $I_p \approx 1 \cdot 10^{13}$ Wt/cm^2 (λ=0.66μm, $\tau_L \approx$(0.3 - 0.5) ns). Emission of the Al lines should be observed when the thermal wave created by the action of the diagnostic beam reaches the mixing zone. Variation of the gold layer thickness ($d_{Au} \approx$(0.1-0.3)μm allows basically to estimate the mixing zone dimensions. The possible reason of Al lines emission can be fast "burning through" of a rather thin Au layer due to the presence of "hot" spots in the diagnostic beam transverse distribution. In order to control the presence of this effect the third laser beam (control beam) irradiates a target in undisturbed zone (fig.1). The parameters of the control beam are chosen similar to the diagnostic beam. Time delay between diagnostic and control beam is approximately 0.85ns.

The large scale nonuniformities of all laser beams are smoothed using random phase plate. X-ray diagnostic complex was placed at the rear side of target and consisted of:

- X-ray streak camera with Au cathode and various filters for registration of emission in the spectral region ~1-5 keV with the time resolution of 50 ps;
- X-ray streak camera with CsI cathode and crystal KAP spectrograph for registration of K_α Al line emission (~1.7 keV) with time resolution of 50 ps;
- X-ray streak camera "Agat" for registration of spectra in the region ~0.8-3 keV with the time resolution of 30 ps;
- focusing diffraction grazing incidence spectrograph with the flat registration field for spectral region of ~0.04-0.25 keV, with space resolution of ~200μm;
- survey spectrograph with a flat KAP crystal for the spectral region of 1.4-2.5 keV;
- pinhole camera with space resolution ~30 μm.

In the third series of experiments the Si-Al-Mg target was used in which the instability on Al-Mg boundary was not expected due to the small jump of density. However Al lines have been observed as a result of Mg layer evaporation.

The calculational modelling of flight dynamics of the considered targets was fulfilled using the 1D code SNDP [3] which included the numerical model of turbulent mixing [4]. The following physical processes were taken into account: hydrodynamics, electron and ion thermal conductivity, limited electron heat flux conduction with f=0.1, nonequilibrum spectral diffusion of x-ray radiation, nonequilibrum ionization kinetics of multicomponent plasma.

202
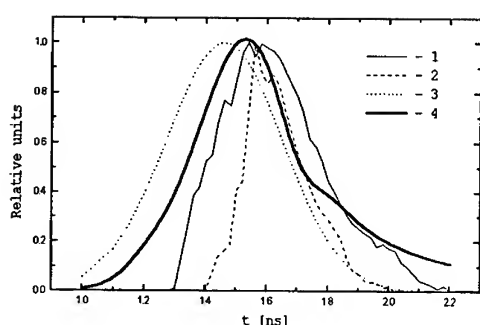
Fig.2. Calculated time dependencies: He_αAl-lines emission from rear side of the target for different Au layer thicknesses (1 - Δx_{Au}=0.15 μm; 2 - Δx_{Au}=0.3 μm), diagnostic laser pulse - 3, x-ray Au continum - 4

On fig.2 calculated temporal dependencies of the Al lines intensity, obtained with gold layer thicknesses equal to 0.15 and 0.3 μm (curves 1 and 2 accordingly) are shown. Here Au continuum intensity is shown also (curve 4). For a thin layer of gold the temporal delay for leading fronts at the level $0.5I_{max}$ between Au continuum spectrum and Al line is small (approximately equal to time resolution of the streak camera- 50 ps). For a thick layer significant delay (about 0.2 ns) is seen.

In the experiment the temporal delay (defined in the same manner) between Au continuum and Al line is absent both for gold layer thickness of 0.15 and is about or somewhat less than 0.1 ns for 0.3 μm (fig.3a,b). At the same time Al lines are not observed under action of a control beam. It testifies that the laser intensity "hot" spots do not burn through a gold layer. Hence Al luminosity under action of a diagnostic beam indicates turbulent mixing of Au and Al layers.

We can suggest that the possible reason of significantly lower temporal delay as compared to calculation in experiment on acceleration of Si-Al-Au targets with the gold layer thickness of 0.3μm is laser irradiation noninfirmities on the target. To verify this hypothesis we plan to carry out experiments on acceleration of the foam-Si-Al-Au targets.

References

1.   1. I.N. Voronich , V.A. Eroshenko, A. I. Zaretsky et al. Izv. AN USSR ser. Phyzicheskaja, 54, 2016 (1990).
2.   2. P.A. Holstein, B. Mayer, M. Rostaing et al. Cr. Acad. Sci. Paris, 307, 211 (1988).
3.   3. S.A. Bel'kov, G.V. Dolgoleva, VANT, ser. Mat. Modelirovanie Fys. Processov, 1, 59 (1992).
4.   4. V.A. Andronov, V.I. Kozlov, V.V. Nikiforov, A.N. Razin, Yu.A. Yudin, VANT, ser. Mat. Modelirovanie Fys. Processov, 2, 95 (1994).

a)

$d_{Si} \sim 4\mu m; d_{Al} \sim 2\mu m; d_{Au} \sim 0.15\mu m$

b) $d_{Si} \sim 4\mu m; d_{Al} \sim 2\mu m; d_{Au} \sim 0.3\mu m$
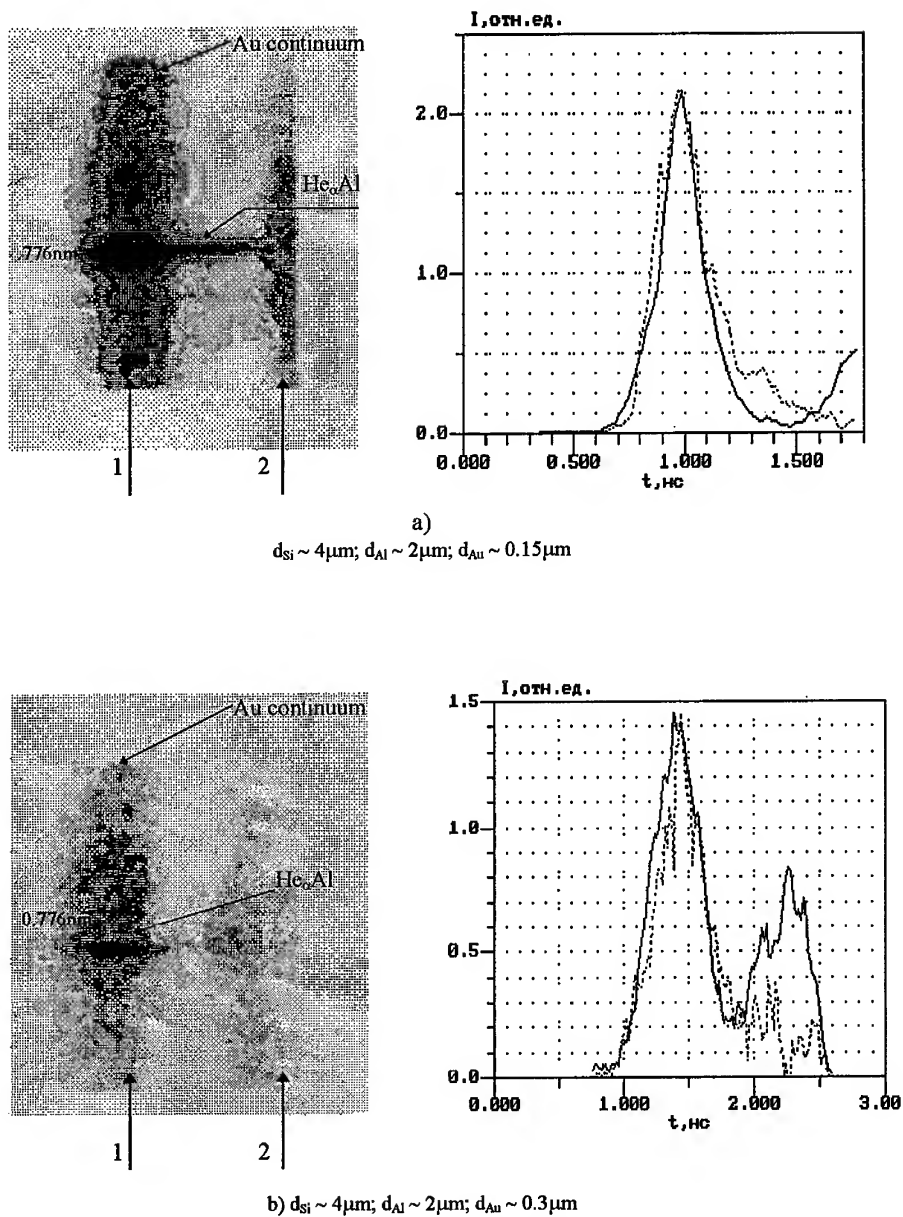
Fig.3. X-ray streak camera with spectrograph registration results

1 - X-ray luminescence due to diagnostic beams   ——————— - Au continuum

2 - X-ray luminescence due to control beams   ------------- - $He_{\alpha}Al$ line

THREE-DIMENSIONAL PARTICLE-IN-CELL SIMULATIONS OF STIMULATED BRILLOUIN SCATTERING

H.X. VU
MS B259
Applied Theoretical and Computational Division
Los Alamos National Laboratory
Los Alamos, NM 87545, USA

HERCULES, a massively parallel three-dimensional hybrid particle-in-cell (PIC) code, implemented on the CRAY-T3D, is based on a physical model where the electrons are modeled as an adiabatic fluid with an arbitrary ratio of specific heats γ, and the electromagnetic field model is based on a temporal Wentzel-Krammers-Brillouin (WKB) approximation. On a CRAY-T3D with 512 processors, the code requires about $0.6\mu s$/particle/time step. The largest problem performed with this code consists of a computational mesh of $4096\times64\times64$ (16 million) cells, and a total of 256 million particles, and corresponds to a plasma volume of $250\mu m \times 64\mu m \times 64\mu m$. We believe HERCULES is the first PIC computational tool capable of simulating low-frequency ion-driven parametric instabilities in a large, three-dimensional plasma volume, and offers a unique opportunity for examining issues that are potentially vital to Inertial Confinement Fusion (ICF), e.g., nonlinear ion kinetic effects and their role in nonlinear saturation mechanisms in three dimensions. A simulation of stimulated Brillouin scattering (SBS) in an f/# 4 diffraction-limited beam

1 Introduction

In Inertial Confinement Fusion (ICF) applications, an external high-frequency monochromatic electromagnetic wave from a laser is employed to irradiate the plasma. The wave, due to its interaction with the plasma, can undergo either electron-driven or ion-driven parametric instabilities, and decay into various combinations of daughter waves [1]. Recent experiments [2–3] and fluid simulations [4–7] indicate that ion-driven parametric instabilities, which affect the propagation of external driving electromagnetic fields, are prevalent in current ICF plasmas of interest. Due to a multitude of spatial and temporal scales that exist in such plasmas and the fact that the external driving electromagnetic field is of high frequency, general-purpose explicit, implicit, and hybrid PIC algorithms are either incapable of simulating the actual physics, or computationally inefficient. In recent works [8–9], HERCULES, a special-purpose three-dimensional hybrid PIC code written for the massively parallel CRAY-T3D platform, was presented in which the electrons are modeled as an adiabatic fluid with an arbitrary ratio of specific heats γ, and the electromagnetic field model is based on a temporal Wentzel-Krammers-Brillouin (WKB)

approximation.

In this paper, we present large-scale three-dimensional PIC simulations of various ion-driven parametric instabilities using HERCULES. In particular, a simulation of stimulated Brillouin scattering (SBS) in an f/# 4 diffraction-limited beam is presented.

2 Physical Model

In the presence of an electromagnetic pump wave of frequency ω_0, the vector potential $\mathbf{A}(\mathbf{x}, t)$ within the plasma can be written as:

$$\mathbf{A}(\mathbf{x}, t) = \frac{1}{2}\left(\mathbf{a}(\mathbf{x}, t)e^{-i\omega_0 t} + \mathbf{a}^*(\mathbf{x}, t)e^{i\omega_0 t}\right) \tag{1}$$

where the temporal envelope $\mathbf{a}(\mathbf{x}, t)$ is complex-valued. The hybrid model, as implemented in HERCULES, treats the electrons as an adiabatic fluid with an arbitrary ratio of specific heats γ. The ions are treated as finite-size particles, allowing ion kinetic effects to be modeled correctly. Because a detailed derivation of the hybrid model can be found elsewhere [8–9], only a summary of the model is given below:

$$i\left(\frac{2\omega_0}{c^2}\right)\frac{\partial \mathbf{a}}{\partial t} + \nabla^2 \mathbf{a} + \frac{1}{c^2}\left[\omega_0^2 - \left(\frac{4\pi e^2 n_e}{m_e} + \sum_i 4\pi e^2 Z_i^2 n_i\right)\right]\mathbf{a} = 0 \tag{2}$$

$$e\phi - \frac{e^2}{4m_e c^2}\mathbf{a}\cdot\mathbf{a}^* - T_{e0}\left(\frac{\gamma}{\gamma - 1}\right)\left(\frac{n_e}{n_{e0}}\right)^{\gamma - 1} = \alpha \tag{3}$$

$$\int \nabla\phi \cdot d\sigma = 0 \tag{4}$$

$$\nabla^2\phi = 4\pi e\left(n_e - \sum_i Z_i n_i\right) \tag{5}$$

$$m_i \frac{d\mathbf{u}_{i\,\mathrm{L}}}{dt} = -eZ_i\nabla\phi - \frac{e^2 Z_i^2}{4m_i c^2}\nabla\left(\mathbf{a}\cdot\mathbf{a}^*\right) \tag{6}$$

$$\frac{d\mathbf{x}_i}{dt} = \mathbf{u}_{i\,\mathrm{L}} \tag{7}$$

Here, $d\sigma$ a surface area element. The particle charges are interpolated onto the computational mesh by means of the tri-quadratic B-spline S,

$$eZ_i n_i(\mathbf{x}, t) = \sum_{p \in i} q_p S\left(\mathbf{x}(t) - \mathbf{x}_p\right) \tag{8}$$

3 SBS in an f/# 4 diffraction-limited beam

Recent experiments in which a nearly diffration-limited laser beam interacts with a plasma to produce filamentation, SBS, self-focusing, and energetic ions, have been reported [10]. Simulations of such experiments using HERCULES, and comparisons with actual experimental data, are ongoing [11]. Here, one such simulation is presented for illustrative purposes.

The plasma consists of protons and carbon ions with $n_H = n_C = n_e/7$, $n_e = 8.9 \times 10^{19} \text{cm}^{-3}$, $T_e = 1\text{keV}$, and $T_H = T_C = 0.5\text{keV}$. The ratio of specific heats γ is taken to be 1. The actual plasma volume is $250\mu\text{m} \times 64\mu\text{m} \times 64\mu\text{m}$, and is simulated using $4096 \times 64 \times 64$ computational cells. The ions are represented by a total of 256 million particles. Here, $\Omega_{pH}\delta t = 0.05$, where Ω_{pH} is the proton plasma frequency. The laser has a vacuum wavelength of $1.06\mu\text{m}$, and is modeled as a diffraction-limited beam with f/# 4 propagating in the $+x$ direction. The diffraction-limited laser intensity $I_0 = 5 \times 10^{15}\text{W/cm}^2$.

Figs. 1 and 2 are color-coded contour plots of the normalized laser intensity (I/I_0), on a plane of symmetry, at times t=0 and t=10.5ps, respectively. Figs. 1 and 2 indicate that there is significant SBS activities, and that the laser beam becomes asymmetric in the laser propagation direction. The laser beam, however, remains symmetric in the transverse directions. Also, the beam tends to disperse wider in the transverse plane. This is in qualitative agreement with the experimental observations [10].
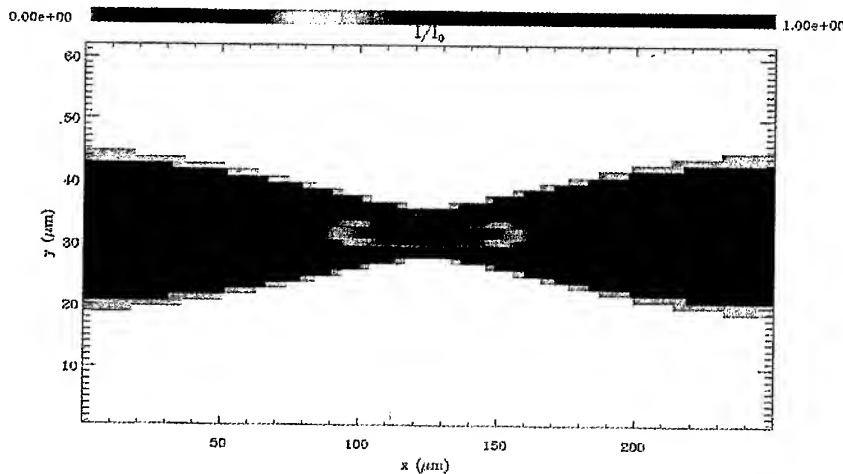
Figure 1: Color-coded contours of I/I_0 on a plane of symmetry at t=0.
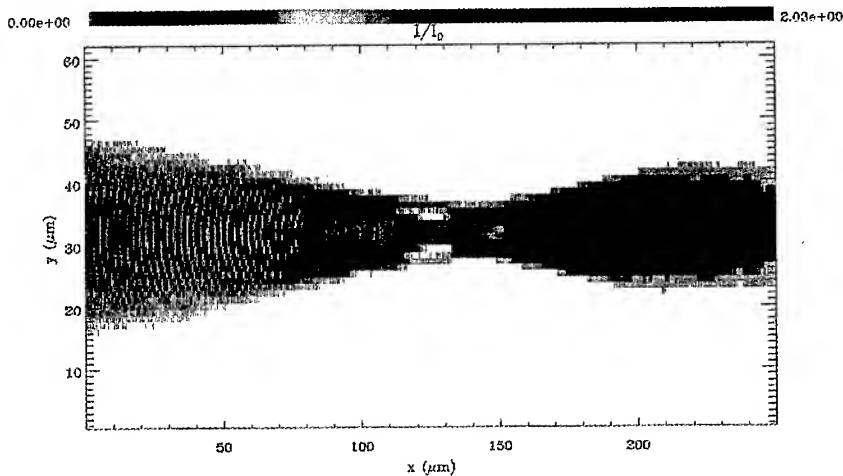
Figure 2: Color-coded contours of I/I$_0$ on a plane of symmetry at t=10.5ps.

Acknowledgments

References

1. W.L. Kruer, *The Physics of Laser Plasma Interactions* (Addison-Wesley, New York, 1988).
2. B.J. MacGowan, *Bull. Am. Phys.* **40**, 1645 (1995).
3. J.D. Moody *et al.*, *Bull. Am. Phys.* **40**, 1824 (1995).
4. H.A. Rose, *Phys. Plasmas* **3**, 1709 (1996).
5. W.L. Kruer, *Bull. Am. Phys.* **40**, 1824 (1995).
6. D.F. Dubois and H.A. Rose, *Bull. Am. Phys.* **40**, 1824 (1995).
7. E.A. Williams and D.E. Hinkle, *Bull. Am. Phys.* **40**, 1824 (1995).
8. H.X. Vu, *J. Comput. Phys.* **124**, 417 (1996).
9. H.X. Vu, "A Massively Parallel Three Dimensional Hybrid Code for Simulating Ion-Driven Parametric Instabilities," *J. Comput. Phys.*, submitted.
10. P.E. Young *et al.*, *Phys. Plasmas* **2**, 2825 (1995).
11. In collaboration with P.E. Young and W.L. Kruer of Lawrence Livermore National Laboratory.

GENERATION AND DIAGNOSTICS OF LASER-PRODUCED PLASMA STREAMS FOR SPACE SIMULATION EXPERIMENTS WITH STRONG MAGNETIC FIELD

J. WOŁOWSKI, L. KARPIŃSKI, P. PARYS, E. WORYNA

Institute of Plasma Physics and Laser Microfusion, 00-908 Warsaw, P.O.Box 49, Poland

Yu. P. ZAKHAROV

Institute of Laser Physics, RAS, Pr. Lavrentyeva 13/3, 630090 Novosibirsk, Russia

The interaction of plasma streams with transverse magnetic field (in the presence or absence of the background plasma) plays the key role in understanding of many processes in the space plasmas. For laboratory simulation of low-Mach-number interaction phenomena in ionospheric and magnetospheric plasmas, we developed a laser-plasma facility at the IPPLM (Warsaw) with a magnetic field of up to 2 T. A Nd:glass laser (1-5 J, 10 ns) is used to production of plasma inside the Helmholtz coils. The primary diagnostics for studying the interaction processes are: ion collectors, Langmuir and magnetic probes, and an electrostatic ion energy analyzer. Preliminary results of measurements show the essential influence of the magnetic field on the propagation of plasma streams in vacuum and in the background gas.

1   Introduction

The properties of the laser-produced plasmas are similar in many aspects to the ones of various kinds of space plasmas. To understand better the low-Mach-number ($M_A \ll 1$) processes of interaction of a plasma cloud with ionospheric and magnetospheric plasmas, we extend the range of the present parameters in the KI-1 experiments [1] ($M_A \gg 1$ for $n' \approx 2 \cdot 10^{13}$ cm^{-3} and $B_0 = 0.1$ T) at the ILP (Novosibirsk, Russia) up to $M_A \ll 1$, $\alpha > 10$, $n' = 10^{12}$ cm^{-3} (α = n/n' - cloud/background density ratio) and $B_0 = 0.5\text{-}2$ T at the reconstructed laser facility at the IPPLM in Warsaw. We hope that the ion magnetization parameter, $\varepsilon_B = R_H/R_B$ (R_H - the ion Larmor radius, R_B - the length of the plasma deceleration by B_0 field), which is the main similarity parameter in simulative experiments, will achieve the value $\varepsilon_B \leq 0.3$. This value corresponds, e.g. , to the conditions in the G-10 release [2] with barium-ion directed Larmor radius $R_H \approx 10$ km and $R_B \approx 30$ km. In such conditions, it is very interesting to simulate the development of high-mode flute instabilities [1] as well as propagation of plasma blobs across the field [3] at the distance higher than R_H and there possible interactions with background media due to Alfven's critical ionization velocity effects.

2 Experimental set-up

An Nd:glass laser with the following parameters: E_L = 1-3 J, $\tau_L \approx$ 10 ns, $I_L \leq$ 10^{11} W/cm², was used in the simulative experiment at the IPPLM, Warsaw. The laser radiation was focused by a lens (f = 136 cm) on a massive, flat plastic targets. The diameter of the focal spot was about 300 μm.

The target was located inside Helmholtz coils generating magnetic field of up to 2 T parallel to the target surface and the inner diameter of the coils was 14 cm. The magnetic field was generated by discharging a capacitor bank through the Helmholtz coils synchronously with the laser pulse.

The main diagnostic techniques used were: ion collectors (IC1-IC4), an cylindrical ion energy analyzer (IEA) [4], a double Langmuir probe (LP) and a magnetic probe (MP) [5]. Two collectors (IC3 and IC4) were located 57.5 cm and 63.0 cm from the target in the plane of the laser beam and the Helmholtz coils axis at the angle of 22.5° and 90° to the laser beam, respectively. The third collector (IC1 or IC2) was located 82 cm or 53.2 cm, respectively, from the target in the plane perpendicular to the above-mentioned one at 45° to the laser beam. The IEA was installed at 45° with respect to the laser beam at the distance of 210.5 cm from the target. The three-turn magnetic probe (MP) with the diameter of 5 mm was positioned at the distance of 5 cm from the target, at the angle of 55° with respect to the laser beam. The LP (with ∅20 μm × 9 mm of collector electrode and optoisolator) was situated near the axis of the Helmholtz coils at the distance of 4.5 cm from the target and at 45° to the laser beam.

Schematic diagram of the experimental set-up is shown in Fig. 1.

3 Preliminary results

The parameters of the laser-produced plasma in the focal spot at B_0 = 0, determined by means of the IEA and the IC1 data, were: the electron temperature $T_e \approx$ 60 eV, the average charge state $<z_0> \approx$ 5, and the percentage plasma composition: C ions - 59%, O ions - 34% , and H^+ - 7%. Simultaneously, the parameters of the ion streams in the ICs' locations were estimated. At the angle of 45° with respect to the laser beam, and at the distance of 82 cm from the target (ion collector IC1), the average ion velocity and ion current density were as follows: v = 1.3×10^7 cm/s and j = 140 mA/cm². The average ion charge state of plasma corresponding to the maximum of IC1 signal is $<z>$ = 1.5. Ion species percentage abundance was as follows: singly charged ions - 81% , twofold - 13.4%, triply - 44% and fourfold - 1.2%. According to collectors and LP data, directly expanding plasma blob carries out an energy of 1 J and has corresponding scales $R_B \approx$ 1.2 cm, $R_H \approx$ 0.4 cm (in a field $B_0 \approx$ 1 T) as well as required value $\varepsilon_B \approx$ 0.3.

Figure 2 shows the influence of the expanding laser-produced plasma on the magnetic field. The maximum disturbance of the magnetic field, $\Delta B \approx 120$ Gauss, was registered by the MP at the external field of $B_0 = 1.2$ T.

The influence of the magnetic field on expansion of the laser-produced plasma in the presence or absence of a background plasma was tested by means of LP (Fig. 3) and ion collectors. In the pressure range 1.5×10^{-5} - 1×10^{-3} mbar, the amplitudes of all-collectors' signals decrease a few times. In the presence of a
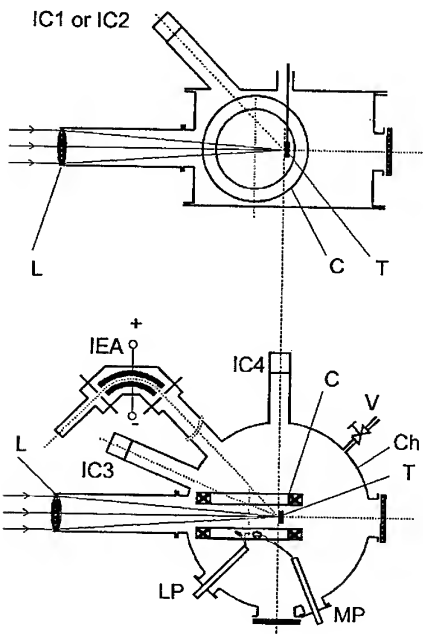
Fig. 1. Experimental arrangement. Top and side views.

- IEA - cylindrical electrostatic ion energy analyzer
- IC1-IC4 - ion collectors
- MP - magnetic probe
- LP - double Langmuir probe
- L - focusing lens
- T - target
- Ch - target chamber
- C - Helmholtz coils
- V - gas inlet valve

Fig. 2. Disturbence of the magnetic field ΔB for different values of B_0.
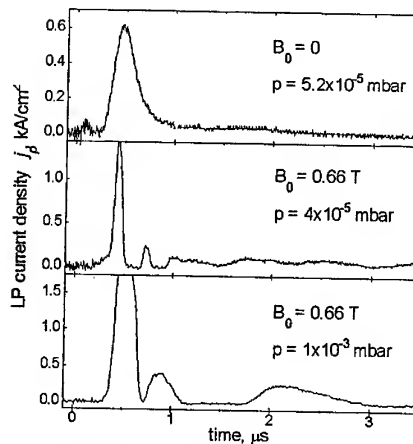
Fig. 3. LP signals measured with and without magnetic field B_0.

magnetic field of $B_0 \approx 1$ T, the collector signals from the IC3 and IC4 have a substructure connected with motion of ion species in the magnetic field. According to IC2 data registered in a far zone, the signal of ions expanding perpendicularly to the axis of Helmholtz coils practically disappears at $B_0 \sim 1$ T.

4 Summary

* The laser-plasma facility for simulation of interaction of ion streams with ionospheric and magnetospheric plasma has been successfully put into operation at the IPPLM, Warsaw.

* Using corpuscular diagnostics, the laser-produced plasma parameters were determined in the laser beam focus and in a far expansion zone.

* Results of preliminary measurements show disturbances in the magnetic field as well as essential influence of the magnetic field on propagation of a laser-produced plasma blob.

5 References

1. Zakharov Yu P, Orishich A M, Ponomarenko A G, 1988 *Laser-Produced Plasma and Simulation of Non-Stationary Space Processes* (Inst. Pure and Appl. Mech.Novosibirsk) - in Russian
2. Huba J D, Bernhardt P A, Lyon J G, 1992 *J. Geophys. Res.* **97A** 11.
3. Zakharov Yu P, Shaikhislamov I F, Eremin A V, 1996 *Book of Abstracts of 11th Int. Conf. High Power Particle Beams*, (10-14 June, Prague) No. P-4-5.
4. Denus S, Farny J, Wereszczyński Z, Wołowski J, Woryna E, 1977 *J.Tech. Phys.* **18** 25.
5. Zakharov Yu P, Orishich A M, Ponomarenko A G, Posukh V G, 1986 *Sov. J. Plasma Phys.* **12** 674.

3.- CORONAL INTERACTIONS

INVESTIGATIONS OF LASER-PRODUCED PLASMA IN POLAND

Z. SKŁADANOWSKI

Institute of Plasma Physics and Laser Microfusion,
00-908 Warsaw 49, 23 Hery St., Poland

Recent investigations of laser-produced plasmas carried out in Poland, partially in collaboration with foreign laboratories, are reported. In particular, the studies of multiply charged ions emitted from high-Z laser-produced plasmas and studies of the influence of strong external magnetic field on properties of the laser-produced plasmas performed at the IPPLM in Warsaw are discussed. The investigations on generation of XUV radiation in the laser-produced plasma performed at the Institute of Optoelectronics of the MUT (IOMUT) in Warsaw are also presented.

1 Introduction

The Institute of Plasma Physics and Laser Microfusion (IPPLM) carries on research works in the field of fundamental plasma physics, laser physics and technology, and pulsed power technology. The main topics of the research activity at the Laser-Produced Plasma Department of the IPPLM are: the properties of high-Z plasmas, the properties of plasma in a magnetic field, and physics and technology of high-power lasers.

The studies of the properties of high-Z laser-produced plasmas comprise: 1) investigations of the anomalous physical processes occurring in such plasmas, 2) optimization of a laser-plasma ion sources (in collaboration with the Inst. of Phys. ASCR in Prague and with the CERN), 3) investigation of X-rays using various measuring methods (in collaboration with the IP ASCR in Prague and with the Res. Inst. for Techn. Phys. in Budapest). The aims of the investigations of laser-produced plasma expanding in a magnetic field are: 1) formation of plasma for effective lasing in the XUV spectral region (in collaboration with the VNIIFTRI in Mendeleevo near Moscow), 2) simulation of the phenomena in space plasmas (in collaboration with the Inst. of Laser Phys. in Novosibirsk). Theoretical modelling as well as works related to the building of a *2-ps2-TW* Nd:glass laser (in collaboration with the Inst. for Laser Phys., St. Petersburg) are also carried on at the IPPLM. Moreover, two high-power Nd:glass lasers (generating nanosecond pulses) are developed and applied in plasma experiments.

The aim of the research works carried on at the IOMUT in Warsaw is to develop an efficient, small-size and debrisless laser-produced x-ray source. Additionally, investigations on highly-charged ions produced with lasers and

laser processing of materials are carried on as well.

2 Investigations of high-Z laser-produced plasmas

The laser-produced plasma can be a convenient and efficient source of ions of all elements. In recent years, on account of the use of the LIS for heavy-ion accelerators, considerable interest has arisen concerning optimization of the LIS in order to obtain the maximum current of highly-charged ions with the required energy range [1].

An Nd:glass laser $(\lambda = 1.06\mu m, t_l \approx 1ns, E_l \leq 1.5J)$ was used to irradiate flat massive high-Z targets (Ta, Pb). For the purpose of thorough investigation of parameters of high-energy ions emitted perpendicularly to the target and coaxially to the laser beam, an aspherical-lens-ellipsoidal-mirror illumination system was applied [2]. Ion collectors (ICs) and a cylindrical ion-energy analyzer (IEA) were used for studying the laser-produced ions. The IEA gave the possibility to distinguish all ionization states at long distances from the target. Basing on the IC signal, the charge carried by the ions as well as the mean ion energy can be derived. The diagram of the experimental arrangement is shown in Fig.1. The ion energy distributions of Ta ions are shown in Fig.2. In the optimum target position (at the focal spot $0.5mm$ inside the target), Ta^{+42} ions $(> 1MeV)$ were registered.
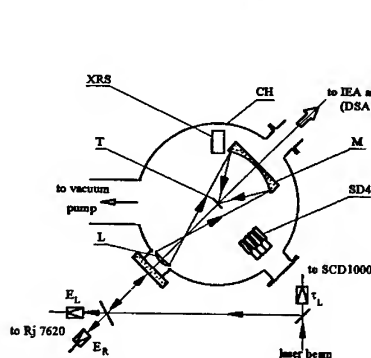
Fig. 1 Experimental set-up   Fig. 2 Experimental results
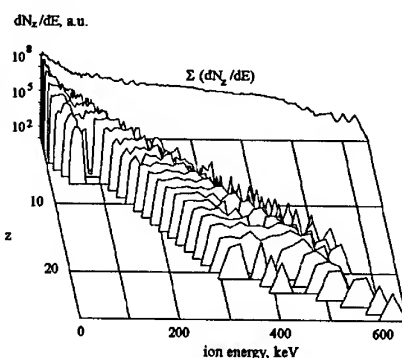
In the common Czech-Polish experiments performed at the IP ASCR in Prague with the use of a photodissociation iodine laser system PERUN $(\lambda = 1.315\mu m,$ $t_l \approx 350 - 650ps, E_l \leq 50J)$, a lens or parabolic-mirror illumination system, and the same ion diagnostics, Ta ions with the charge state higher than 45+ (up to 55+), energy of up to $9MeV$, and the peak current density of about $12.8mA/cm^2$ were found in a far expansion zone $(L = 94cm)$ [3]. Explanation

of these results may be based on the presence of a fast ion group in the collector signals and the charge distribution "freezing" during plasma expansion.

Construction of a laser ion source generating ions of $z = 40$ and energy of $1MeV$ and with the current density of $10mA/cm^2$ seems not to be the physical but the technological problem.

3 Investigations of laser-produced plasma expanding in a magnetic field

This section presents results of investigations and the analysis of the behaviour of a laser-produced plasma in a strong magnetic field both axial and transverse, of 10T in induction. The plasma was generated from a flat teflon target at the laser power density of about $10^{14}Wcm^{-2}$.
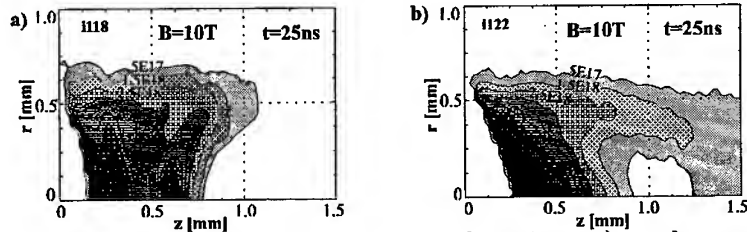
Fig.3 Isodensitograms of the electron density for the regimes: a) angular expansion and b) axial expansion.

The analysis of the results of interferometric measurements performed in a strong axial magnetic field allowed to distinguish two characteristic regimes of plasma expansion: angular and axial (Fig.3) [4]. The 2D MHD simulation [5] allowed to connect these regimes with the character of target illumination, namely the laser beam spatial intensity distribution in the focal area (Fig.4).
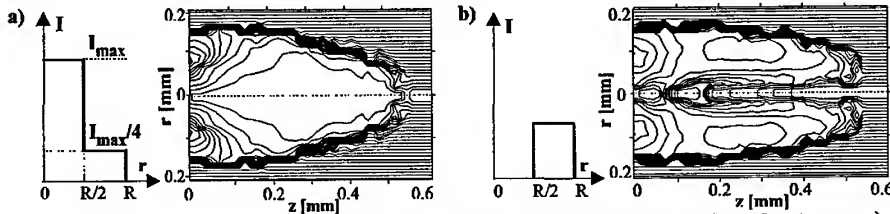
Fig.4 Results of numerical modelling of the magnetic field line distributions: a) angular expansion, b) axial expansion.

It was found that the laser beam having a maximum of its intensity on the axis (Fig.4a) leads to the angular regime of plasma expansion (Fig.3a), whereas the beam with a minimum on the axis (Fig.4b) leads to the axial one (Fig.3b). The results of simulations gave a qualitative picture of the phenomenon of the laser plasma flow in an axial magnetic field. It was found that creation of the

218

diamagnetic cavity and generation of the radial component of the magnetic field during the first few nanoseconds determined the character of the plasma flow observed later, when the plasma pressure was comparable with that of the magnetic field (Fig.4).

Investigations of a laser-produced plasma in a strong transverse magnetic field were made by means of an interferometer and a magnetic probe. On the basis of interferograms registered in the directions parallel and perpendicular to the magnetic field, a clear asymmetry of the "plasma-blob" for $t \geq 10ns$, caused by an unmagnetized ion Rayleigh-Taylor instability, has been revealed. The analysis of the dB/dt signals from the magnetic probe has confirmed quantitatively the temporal and spatial image of creation of a diamagnetic cavity obtained from the interferometer.

4 Studies of laser interaction with gas puff target at the IO MUT

Research at the Institute of Optoelectronics of the MUT in Warsaw in the field of laser-matter interaction includes the following topics: interaction of nanosecond laser pulses with gas puff targets, generation of X-rays from a laser-irradiated gas puff target, creation of an X-ray laser active medium with a gas puff target, characterization of gas puff targets with X-ray back lighting and laser interferometry, and development of a compact high-power Nd:YLF/Nd:glass laser for application to X-ray generation. Plasmas produced from laser-irradiated gas puff targets emit intense X-ray radiation with conversion efficiency that can be higher comparing to solid targets irradiated in similar conditions. This gives potential possibilities to develop an efficient, debrisless laser-produced X-ray source for numerous applications [6]. Investigations on high-resolution X-ray spectroscopy of helium-like argon and neon-like krypton have been performed [7]. The gas puff target approach has been successfully used in X-ray laser experiments. X-ray lasing with neon-like argon at 46.9 nm and nickel-like xenon ions at 10.0 nm has been demonstrated [8]. A new mechanism of the resonant self-photopumping for the neon-like argon X-ray laser has been observed.

References:

[1] H. Haseroth, C.E. Hill, Rev. Sci. Instrum. 67(1966)945-949
[2] P. Parys, J. Wołowski, E. Woryna, J. Farny, W. Mróz, Inst. Phys. Conf. Ser. No 140 Sect. 9(1995)375-378
[3] L. Laska et al., Rev. Sci. Instrum. 67(1966)950-952
[4] A. Kasperczuk and T. Pisarczyk, Physica Scripta 53(1996)503-507
[5] A. Kasperczuk, R. Miklaszewski, T. Pisarczyk, Physica Scripta (in press)
[6] P. Celliers et al., J. Appl. Phys. (in press)
[7] S. Khakhalin et al., Physica Scripta 50(1994)106-109
[8] H. Fiedorowicz, A. Bartnik, Y.Li, P.Lu and E. Fil, Phys. Rev. Lett 76(1996)415

MAGNETIC FIELD SATURATION MECHANISMS
IN LASER-PLASMA INTERACTIONS

M. G. HAINES

Blackett Laboratory, Imperial College, London SW7 2BZ, UK

Abstract

Magnetic fields can be generated in laser-plasma interactions by several mechanisms, in particular the $\nabla T \times \nabla n / ne$ effect, most of which require some transverse non-uniformity. This paper examines the scaling laws for the non-linear growth and saturation mechanisms in various regions. A universal diagram is found in which the magnetic field can be saturated by micro-turbulent processes such as the lower hybrid drift instability at small transverse scale lengths, and by ablative convection at large scale lengths. At the intersection of these regimes, and provided the mean free path exceeds the collisionless skin depth, the magnetic pressure can equal the plasma pressure. At this point the transverse scale length is an ion collisionless skin depth. At lower temperatures classical resistive diffusion limits the magnetic field in the intersecting region, causing $\omega_e \tau_e$, the electron Hall parameter, to be below unity. At the triple point we have $\omega_e \tau_e = 1$ and the mean-free-path equals the electron collisionless skin depth.

1. Introduction

A lack of one dimensional symmetry in laser-matter irradiation can lead to the spontaneous generation of magnetic fields. Locally energised electrons will try to leave the volume; in one dimensional symmetry they are reflected back by an electrostatic field $-\nabla \Phi$, and there is no net current flow.

In two dimensions the return flow is not along the same path and a net current loop is formed thus causing the generation of a magnetic field. By Faraday's law $\partial \underline{B} / \partial t = -\nabla \times \underline{E}$, a back EMF is generated to oppose this change, ie. a $-\partial \underline{A}/\partial t$ term exists in addition to $-\nabla \Phi$. Indeed by employing Ohm's law[1], ie. the generalised fluid equation of motion for electrons,

$$-\underline{E} = \underline{v} \times \underline{B} - \frac{\underline{J} \times \underline{B}}{n_e e} + \frac{\underline{q}_e \times \underline{B}}{\frac{5}{2} p_e} + \frac{\nabla p_e}{n_e e} + \beta \frac{\nabla T}{e} - \eta \underline{J} - \frac{m_e}{n_e e^2} \frac{\partial \underline{J}}{\partial t} + \frac{1}{n_e e}$$

$$\nabla \cdot \left(\underline{\underline{\tau}}_e + n_e m_e \underline{v}_e \underline{v}_e + \langle n_i m_e \underline{\dot{\xi}} \underline{\dot{\xi}} \rangle \right) + \langle \underline{\dot{\xi}} \times \underline{\tilde{B}} \rangle \qquad (1)$$

and by eliminating E in Faraday's law we can arrive at all the sources of $\underline{B}$, the dissipation of $\underline{B}$ and the convection (losses) of $\underline{B}$[2]. Here q_e is the electron heat flux, $\underline{\underline{\tau}}_e$ the traceless stress tensor and $\dot{\underline{\xi}}$ the quiver velocity in the laser fields $\underline{\tilde{E}}$ and $\underline{\tilde{B}}$ given by the high frequency Lorentz force $m_e \ddot{\underline{\xi}} = -e\left(\underline{\tilde{E}} + \dot{\underline{\xi}} \times \underline{\tilde{B}} \right)$. In this paper we will identify under what conditions various loss terms lead to saturation of $\underline{B}$.

2. The source terms

The source term most relevant to long pulse experiments arises from $\nabla p_e / n_e e$ in eq.(1). On taking the curl we arrive at the well known result[3]

$$\frac{\partial \underline{B}}{\partial t} = \frac{\nabla T_e \times \nabla n_e}{n_e e} \qquad (2)$$

showing that if gradients of electron temperature and density are not parallel a spontaneous generation of $\underline{B}$ occurs. Other source terms are the ponderomotive force and the radiation pressure terms[4] (the last two in eq.(1)) and these are particularly important in short pulse laser interactions. Because they create an effective electron pressure or stress tensor we will take the source in eq.(2) as archetypal.

3. Dissipative terms

On balancing the $\nabla p_e / n_e e$ source term with $\eta \underline{J}$ and using Ampère's law we arrive at the first saturation formula

$$B = \frac{\mu_0 k T_e}{e \eta} \cdot \frac{L_\perp}{L_\parallel} \qquad (3)$$

where ∇T_e is $T_e / L_\perp$ and ∇n_e is $n_e / L_\parallel$. This we call *regime 1*, and for a fixed ratio of $L_\perp / L_\parallel$ is independent of the transverse inhomogeneity scale length $L_\perp$.

However, with intense lasers it would be possible for the drift velocity $\underline{J}/n_e e$ to exceed some critical velocity and so trigger anomalous resistivity. If the critical velocity is the ion sound speed, c_s, so that an anomalous resistivity builds up to prevent this being exceeded we find B is now limited via eq.(5) to

$$B = \mu_0 n_e e \left(\frac{ZkT_e}{m_i} \right)^{\frac{1}{2}} L_\perp \qquad (4)$$

This linear dependence on $L_\perp$ will dominate at low $L_\perp$, and we call this *regime 2*. We would expect that lower hybrid drift instabilities would be the dominant turbulence, and take Brackbill et al.'s anomalous collision frequency[5] ν_{LH} in the regime where the electron plasma frequency ω_{pe} exceeds the cyclotron frequency Ω_e,

$$\nu_{LH} = \frac{0.02}{\beta_i} (\Omega_e \Omega_i)^{\frac{1}{2}} \left(\frac{v_d}{v_i} \right)^2 \qquad (5)$$

where $\beta_i = 2\mu_0 n_i m_i v_i^2 / B^2$, $v_d = J/n_e e$ and $v_i^2 = 2kT_i/m_i$, this being found from a fully electromagnetic PIC simulation. Employing this in the resistivity leads to

$$B \propto L_\perp^{1/3} \left(L_\perp / L_\parallel \right)^{1/6} \tag{6}$$

for *regime 2*. An alternative model by Drake et al.[6] employs non-linear mode coupling to electrostatic waves to give a different scaling $B \propto L_\perp^{1/2} \left(L_\perp / L_\parallel \right)^{1/4}$.

4. Convective terms

The ablation velocity $\underline{v}$ is characterised by c_s; thus assuming that the convective $\underline{v} \times \underline{B}$ term balances $\nabla p_e / n_e e$ we find the convective scaling law[7,8]

$$B = \frac{1}{L_\perp} \left(\frac{m_i k T_e}{Z e^2} \right)^{1/2} \tag{7}$$

The $B \propto L_\perp^{-1}$ scaling will dominate at high $L_\perp$, and we call this *regime 3*.

There are two other convective terms, the Hall term which, because $\underline{J}$ has closed loops satisfying $\nabla \cdot \underline{J} = 0$ leads mainly to a redistribution of $\underline{B}$; and the $q_e \times \underline{B}$ term which describes the Nernst convection of magnetic field in a collisional plasma[9] which can lead to amplification at the ablation surface. Non-linear heat flow is characterised by being somewhat greater that $5/2 \, p_e c_s$, and so this convective loss will scale in the same way as eq.(12).

5. The universal diagram for B saturation

The scaling law (4) will intersect (7) at $L_\perp = c/\omega_{pi}$, the ion collisionless skin depth, and at a value of $B = (2\mu_0 p_e)^{1/2}$ ie. $\beta_e = 1$; magnetic and electron plasma pressures are equal. Within a small correction the scaling law also intersects here. This is illustrated in the figure. At the point of intersection the Hall parameter is the ratio of the mean free path to the electron collisionless skin depth

$$\Omega_e \tau_{ei} = \frac{\lambda_{mfp}}{c/\omega_{pe}} \tag{8}$$

In contrast the value of $\Omega_e \tau_{ei}$ in *regime 1* (eq.(3)) is given by

$$\Omega_e \tau_{ei} = \left(\frac{\lambda_{mfp}}{c/\omega_{pe}} \right)^2 \cdot \frac{L_\perp}{L_\parallel} \tag{9}$$

For the condition $L_\perp = L_\parallel$ it follows that for $\Omega_e \tau_{ei} > 1$ case (a), eq.(3) lies above the envelope determined by eqs.(4 or 6 and 7); for $\Omega_e \tau_{ei} = 1$ case (b), a triple intersection point occurs while *regime 1* will actually apply for $\Omega_e \tau_{ei} < 1$ in case (c) when eq.(3)

222

forms part of the envelope. In this region we have $\lambda_{mfp} < c/\omega_{pe}$ and the heat carrying plasma could be unstable to the thermal instability.
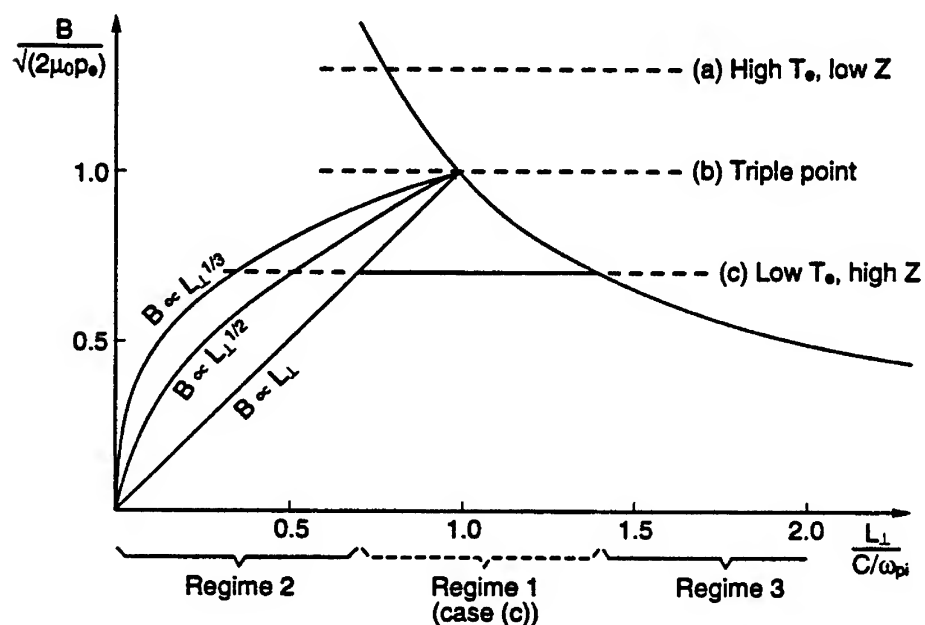
Fig.1. Universal diagram of the saturated magnetic field B versus transverse scale length $L_{\perp}$ (in dimensionless units)

References

[1]   M. G. Haines, *Plasma Phys. & Contr. Fusion* 2 8, 1705 (1986)

[2]   M. G. Haines, *Can. J. Phys.* 6 4, 912 (1986)

[3]   J. A. Stamper, K. Papadopoulos, R. N. Sudan, S. O. Dean, E. H. McLean & J. M. Dawson, *Phys. Rev. Lett.* 2 6, 1012 (1971)

[4]   J. A. Stamper & D. A. Tidman, *Phys. Fluids* 1 6, 2024 (1973)

[5]   J. V. Brackbill, D. W. Forslund, K. B. Quest & D. Winske *Phys. Fluids* 2 7, 2682 (1984)

[6]   J. F. Drake, P. N. Guzdar, A. B. Hassam & J. D. Huba *Phys. Fluids* 2 7,1148 (1984)

[7]   R. S. Craxton & M. G. Haines, *Plasma Phys.* 2 0, 487 (1978)

[8]   C. E. Max, W. M. Manheimer & J. J. Thomson *Phys. Fluids* 2 1, 128 (1978)

[9]   A. Nishiguchi, T. Yabe, M. G. Haines, M. Psimopoulos & H. Takewaki *Phys. Rev. Lett.* 5 3, 262 (1984)

COMPETITION BETWEEN STIMULATED BRILLOUIN
AND RAMAN SCATTERING IN LASER-PRODUCED PLASMAS

C. LABAUNE, H.A. BALDIS, V.T. TIKHONCHUK[*],

E. SCHIFANO, N. RENARD, W. SEKA[**], B.S. BAUER, A. MICHARD

LULI, Ecole Polytechnique and CNRS, 91128 Palaiseau, France
*P. N. Lebedev Physics Institute, Russian Academy of Science, Moscow 117924, Russia.
**Laboratory for Laser Energetics, University of Rochester, USA*

Stimulated Brillouin and Raman scattering have been studied using Thomson scattering of a short wavelength laser beam to measure the temporal evolution of spectral characteristics and location of the ion acoustic and electron plasma waves associated respectively to each of these instabilities. The two types of waves grow over a limited region in the front part of the plasma, but at different times. Location of the waves is partly due to depletion of the pump. As a consequence of the inhibition of Raman by Brillouin during the first part of the laser pulse, the Raman spectra exhibit a gap between 400 and 420 nm.

Stimulated Brillouin scattering (SBS) and stimulated Raman scattering (SRS) are among the most important parametric instabilities in laser-produced plasmas[1,2]. SBS and SRS correspond to the decay of the incident electromagnetic (EM) wave into a scattered EM wave and an ion-acoustic wave (IAW), or an electron-plasma wave (EPW), respectively. Apart from the intrinsic interest of the wave coupling mechanisms, these two instabilities have important implications in inertial confinement fusion (ICF)[3] due to the possible large conversion of laser energy into scattered light affecting ICF drive efficiency and symmetry. A vital aspect of the evolution of the instabilities is their growth in the presence of waves (either IAW or EPW) associated with another instability, or their saturation associated with secondary decays such as the parametric decay of the EPW from SRS.

The first experimental observation of competition between SRS and SBS was reported by Walsh et al[4] who observed a strong correlation between the quenching of SRS plasma waves and the initiation of SBS ion waves. In the same experiment, seeding SBS with a small amount of stimulated backscattered light[5], caused the SRS emission to be completely eliminated. A second experiment has also observed anti correlation between SBS and SRS using one arm of Nova to form the plasma and to pump the instabilities[6]. Numerical simulations have evidenced weakening of SRS by the presence of SBS when including the ion fluctuations in the calculation of the SRS growth[7]. Two of the possible processes which can operate in the competition between the two instabilities are the spoiling of the phase-matching requirement for SRS by the ion waves and pump depletion.

In this paper, we present direct evidence of the temporal and spatial interplay between IAW's associated with SBS, and EPW's associated with SRS. Direct observation

of these waves has been done using Thomson scattering of a short wavelength probe beam. The two types of waves grow in the same region of plasma, but at different times. The EPW's start to grow only when the IAW's have disappeared.

The results presented here are part of the program at the Laboratoire pour l'Utilisation des Lasers Intenses (LULI) to study the physics of parametric instabilities in the context of ICF, using collective Thomson scattering as the key diagnostic[8]. The experiments have been performed using the six-beam laser facility, to produce the interaction between a 1.053 μm pump and a well-characterized preformed plasma. The absolute correlation in time and space of the waves associated with the instabilities has been made possible by a new technique[9] developed for these studies, which permits to multiplex a conventional streak camera, providing simultaneous recordings of the temporal evolution of the Thomson scattered light from the two types of waves on the same detector.

The geometry of the configuration is shown in Figure 1. The 600ps FWHM Gaussian beams were all in the same plane and arrived at the target at different times : two 0.53μm plasma producing beams with peak at t=0, a 0.53μm plasma heating beam at t=1.2 ns, the 0.35μm Thomson scattering probe beam at t=1.48 ns, and the 1.05μm interaction beam at t=1.72 ns. The interaction beam was focused with an f/6 lens through an RPP of 2mm square elements. The combination of the focusing lens and the RPP produces an Airy pattern central maximum with 65% of the total laser energy in a spot diameter of 320 μm. Within this spot, the maximum average intensity is 10^{14}W/cm^2, for an energy of 100J.
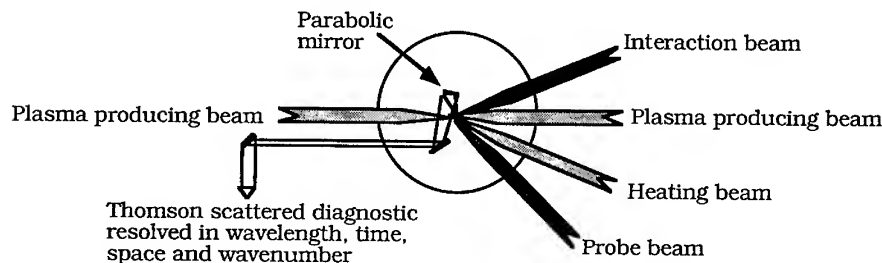
Figure 1 : Experimental set-up

The targets were mass limited free-standing CH foils of 450μm diameter and 1.5μm thickness. At the time of interaction, the plasma had a density profile with an approximately inverse parabolic shape along the laser direction with a scalelength of ~1mm. The maximum electron density evolved from 25% to 8% of critical density (n_c =1.1x10^{21} cm^{-3} is the critical electron density for λ_0=1.05μm light) during the interaction pulse. The electron temperature had been measured using thermal Thomson scattering in the absence of interaction beam, and is ~ 0.5keV at t=1.7ns.

The geometry for Thomson scattering was chosen to observe the scattered light which corresponds to IAW's associated with backscattered SBS and EPW's associated with

backscattered SRS. The Thomson scattering probe was focused with a combination of a lens and an RPP with elongated elements, to form a focal region 100μm by 1mm along the axis of the interaction beam, thus allowing to image the location of the waves over the whole interaction length on the slits of a streak camera. A separate spectrograph-streak camera combination was used to obtain the time resolved spectra of the waves.

Figure 1 shows the time resolved location of IAW's and EPW's along the axis of the interaction beam. The scattered signals are proportional to the square of the density fluctuations $(\delta n/n)_{IAW,EPW}$ associated with the IAW's or EPW's. For both backscatter instabilities the growth is limited to a relatively small region, in the front part of the plasma relative to the interaction beam. The interaction region is smaller than the scale length of the plasma and is not limited by the length of the line focus of the Thomson scattering probe. The interaction region for the IAW's shows, as a function of time, a drift towards the laser side ; the EPW's, on the other hand, drift towards the center of the plasma.
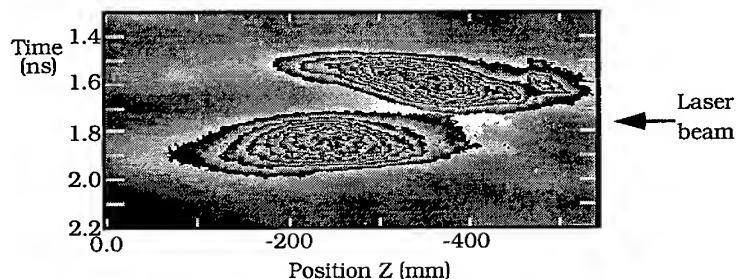
Figure 2 : Location of Thomson scattered light from ion acoustic waves and electron plasma waves, associated with backscattered SBS and SRS respectively, as a function of time.Time is referred to the plasma forming laser pulses, the initial position of the target was at z=0, and the interaction beam arrived from the right. The difference between contours corresponds to a factor of 2 in intensity.

The IAW's and the EPW's exhibit a temporal and a spatial interplay. The onset of the IAW's takes place at the very beginning of the interaction pulse ; the emission lasts around 300ps and is maximum ~100 ps before the peak of the interaction pulse. Simultaneously with the disappearance of the IAW's, one observes a rapid growth in the level of fluctuations associated with EPW's. Further to the temporal interplay between IAW's and EPW's, we observe that the EPW's are located in the same region of plasma where IAW's just disappeared.

The inhibition of EPW's during the first part of the pulse can explain the spectral gap of Raman. Figure 3 shows a time resolved spectrum of Thomson scattered light from electron plasma waves. The component, with wavelength ~ 412 nm, corresponds to the scattering of the probe beam on the electron plasma waves produced by the two plasmon decay instability. The second part of the spectrum starts around the peak of the interaction beam and exhibits wavelengths evolving from 401nm to 372nm. This component lasts ~ 300 ps and corresponds to the scattering of the probe beam on the electron plasma waves produced by backward stimulated Raman scattering. The spectrum

226

of Fig. 3 corresponds to plasma densities evolving between 13% and 4% of the critical density. A large gap between 25% and 13% of critical density, with no Raman emission, is clearly observed.
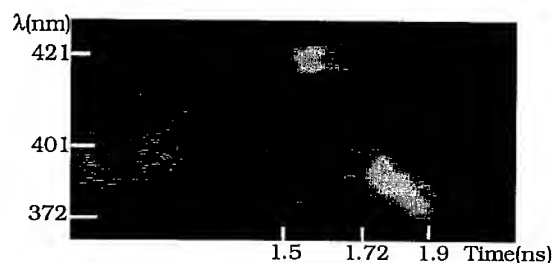
Figure 3 : Time-resolved spectrum of the Thomson scattered ligth from electron plasma waves.

Statiscal theory of SBS and SRS in randomly distributed speckles[10] has been applied to this experiment. This theory predicts fairly well the main observed features. SBS starts first to grow in speckles with intensity around four times average intensity. It dominates SRS because its spatial convective gain is larger in the first half of the interaction pulse. Such SBS-active speckles are in the regime of strong pump depletion which produces a shift of the maximum of density perturbations towards the laser as they follow the intensity distribution. During this period of active SBS, SRS is inhibited because of pump depletion as the two instabilities are sharing the same pump. SRS starts to grow in the second half of the pulse when the SBS gain has been reduced, mainly because of the drop of the electron density. The SRS location in the front part of the plasma corresponds then to the location of the laser intensity distribution which is due to a combination of pump depletion in speckles and absorption of the overall laser beam. In conclusion, the competition between SBS and SRS in randomly distributed speckles can explain the observed temporal and spatial behaviors of SBS and SRS.

[1] W.L. Kruer, *The Physics of Laser Plasma Interactions*. (Addison-Wesley Publishing Company, New York, 1988) p.74-93.

[2] H.A Baldis, E.M. Campbell, and W.L. Kruer, *Physics of Laser Plasmas* (North Holland, Amsterdam, 1991) p.361-434.

[3] J. Lindl, Phys. Plasmas 2, 3933 (1995).

[4] C. J. Walsh , D. M. Villeneuve, and H.A. Baldis, Phys. Rev. Lett. 53, 1445 (1984).

[5] Villeneuve, D. M., H. A. Baldis, and J. Bernard, Phys. Rev. Lett. 59, 1585 (1987).

[6] H.A. Baldis, P.E. Young, R.P. Drake, W.L. Kruer, K. Estabrook, E.A. Williams, T.W. Johnson, Phys. Rev. Lett. 62, 2829 (1989)

[7] H.A. Rose, D.F. DuBois, and B. Bezzerides, Phys. Rev. Lett. 58, 2547 (1987) ; W. Rozmus, R.P. Sharpa, J.C. Samson, and W. Tighe, Phys. Fluids 30, 2181 (1987) ; G. Bonnaud, Laser Part. Beams, 5, 101 (1987).

[8] C. Labaune, H.A. Baldis, N. Renard, E. Schifano, S. Baton, A. Michard, W. Seka, R.E. Bahr, B. Bauer, K. Baker, and K. Estabrook, Phys. Rev. Lett. 75, 248 (1995).

[9] H.A. Baldis and C. Labaune, Rev. Sci. Instr, 67, 451 (1996).

[10] H. A. Rose and D. F. DuBois, Phys. Rev. Lett. 72, 2883 (1994)

STIMULATED BRILLOUIN SCATTERING
UNDER CROSSED BEAMS IRRADIATION

H.A. BALDIS, C. LABAUNE, E. SCHIFANO, N. RENARD, A. MICHARD

LULI, Centre National de la Recherche Scientifique, Ecole Polytechnique,
91128 Palaiseau, France

Using a secondary interaction beam at a reduced intensity, a well defined resonant seeding of ion acoustic waves (IAW) from stimulated Brillouin scattering was observed along the bisecting direction between the two laser beams, as well as a strong reduction of the IAW along off-resonance directions. This is the first experimental evidence that overlapping beams can have a detrimental effect to the growth of SBS, in situations where there is a mismatch between IAW from two independent SBS decay processes.

The characterization and control of stimulated Brillouin scattering (SBS) is an issue of critical importance in inertial confinement fusion (ICF)[1]. Stimulated Brillouin scattering consists of the decay of the incident electromagnetic (EM) wave (ω_0, k_0) into a scattered EM wave (ω_{SBS}, k_{SBS}) and an ion acoustic wave (IAW) (ω_{IAW}, k_{IAW}), where ω and k are the respective frequency and wavevector for each wave. The large size plasma encountered in holhraums can produce levels of scattered light that reduces the energy coupling, as well as modifies the light distribution, affecting the symmetry of capsule implosion[2]. The study of SBS can be further complicated by non linear couplings between the waves associated to multiple interaction beams crossing in the interaction region, situation which occurs near the laser entrance hole of a holhraum.

The problem of crossing laser beams has been addressed recently in the context of energy transfer between beams in theoretical works. These studies show that energy transfer can take place through a parametric process, such as forward stimulated Brillouin scattering, either in the case of illumination with multiple frequencies[3], or by frequency beating between beams with the same frequency[4]. In the present work, we have observed the modification of ion acoustic waves associated with the main interaction beam by ion acoustic waves associated with a secondary laser beam having a much lower intensity and arriving 200ps ahead of the primary beam. These results include the first observation of resonant enhancement of the level of IAW when ion acoustic waves driven by two different beams have common wavevectors and strong reduction of this level when there is a mismatch between IAW from the two independent SBS decay processes. The study was performed using Thomson scattering to measure the IAW associated with SBS, using a short wavelength probe beam. This technique provides the most direct characterization of the waves, including their frequency, wavevector and location. Wavevector resolution permitted to observe the effect of the seed beam along different directions within the interaction region.

The two interaction beams were incident on a preformed plasma. The angle between the two beams was 22,5°. The plasma was produced by two opposite 0.53μm beams, irradiating a mass limited free-standing CH foil of 450μm diameter and 1.5μm thickness, at time t=0 (peak of the pulse). The interaction beams were focused with f/6 lenses through random phase plates (RPP) of 2mm square elements, at time t=1.72ns. The resulting focal spot diameters were 320mm FWHM, with focal depths of 1.5mm. The maximum average intensity in the focal volume of the main interaction beam was $I_{pump}=10^{14}$W/cm^2. At the time of interaction the plasma had a parabolic density profile along the laser axis, with a FWHM of 1mm. The electron density at the peak of the plasma profile evolved from $0.25n_c$ to $0.08n_c$, from the beginning to the end of the interaction beam (where $n_c=1.1\times10^{21}$ cm^{-3} is the critical electron density for $\lambda_0=1.05$μm light). The electron temperature (T_e) of the plasma, obtained by Thomson scattering in the absence of interaction beam, was between 0.4 and 0.5keV.

The Thomson scattering probe beam was at 0.35μm and arrived to the plasma at time t=1.48ns. It was focused with a combination of lens and RPP with elongated elements, to form a focal region 100μm by 1mm along the axis of the interaction beam, allowing to image the location of the waves over the whole interaction region. The probe beam, with aperture f/3, was incident at an angle of 72° with respect to the main interaction axis. Thomson scattered light was collected, with angles between 11° and 47° from the probe axis, with a parabolic mirror and imaged onto streak cameras and spectrometers with secondary spherical mirrors. The parabolic mirror was large enough to collect scattering light from a large range of IAW, using the same probe beam. Other diagnostics included time resolved wavelength spectrum of IAW by Thomson scattering, and time resolved spectra of the SBS light, along the direction of backscatter for the primary beam.

The frequency and wavevector of the IAW produced by SBS depend on the geometry of the SBS decay. If we consider the collection of IAW produced by the two interaction beams, the only waves which will have same wavevector correspond for both cases to sidescattering SBS at 22,5° from the beam axis, in opposite directions, and these waves propagate along the bisecting direction. This direction will be referred to as the resonance direction. All the other waves will present mismatches which depend on the respective geometries of the decays.

Ion acoustic waves traveling along different directions were recorded with temporal and spatial resolution, using masks on the Thomson scattering optics, limiting the collection angle to 5°, and in steps of 5°. Figure 1 shows the temporal evolution of space resolved density fluctuations associated with IAW for two different directions of propagation of the IAW : Fig.1A along the direction of resonance and Fig.1B along the direction of backscatter for the pump beam. Different frames correspond to various reduced intensities of the seed beam, keeping the intensity of the pump beam constant at $I_{pump}=10^{14}$W/cm^2. In the three frames of Fig.2A, only the firt signals in time are related to the IAW.
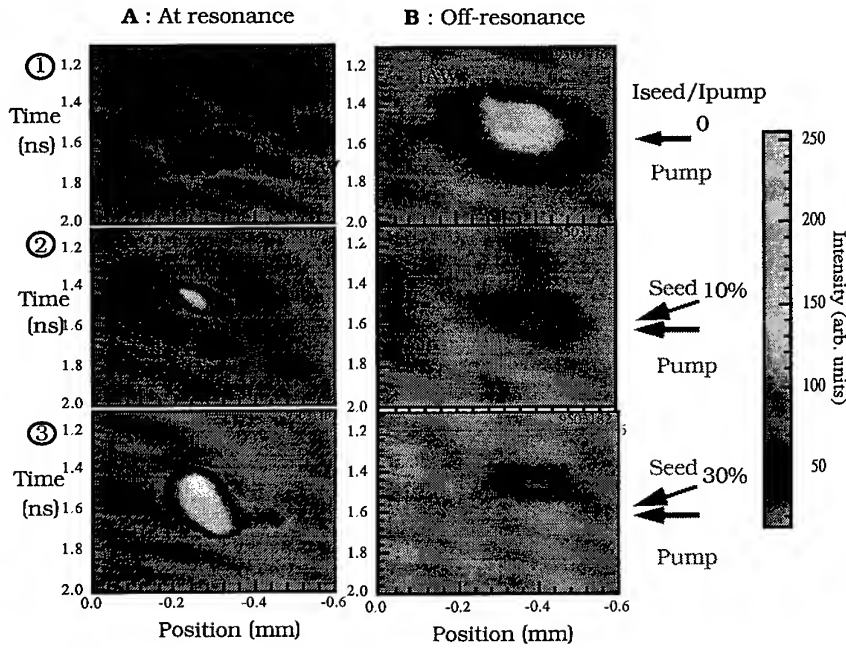
Figure 1 : Temporally resolved location of ion acoustic waves, along the direction of resonance (A), and along the direction of backscatter for the pump beam (B).

Clear enhancement of the IAW level is observed in Fig. 1A as the intensity of the seed beam is increased. All three frames were obtained with the same attenuation on the camera. On the contrary, a strong reduction of the IAW level was observed in Fig. 1B when probing along off-resonance directions. The relative intensities of IAW between the first frame in Fig.1A and Fig.1B are almost the same, but using different attenuations in front of the camera. In agreement with the decreased level of IAW for off-resonance directions, we observed a decrease of the overall SBS reflectivity of the main interaction beam in backward direction in presence of the seed beam, as shown in Fig. 2.

The IAW enhancement observed along the resonant direction is clear evidence of the importance of the initial noise level from which SBS grows. At the onset of the pump beam, the instability starts to grow from ion fluctuations driven by the seed beam, having the right wavevector, rather than from thermal fluctuations. Since enhancement is observed over a very narrow range of angles, the allowable mismatch between the wave numbers of seed and pump IAW has to be small. This result can be connected to the theoretical work addressing the effect of overlapping laser beams on parametric instabilities[5,6], where it was found that the lowest threshold was for collective SBS modes sharing a common daugther wave along the symmetry axis.
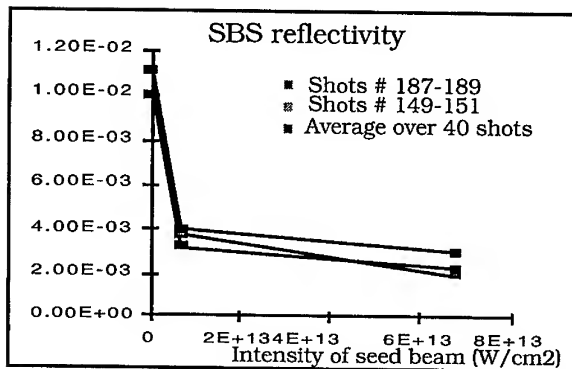
Figure 2 : Modification of the SBS reflectivity as a function of the seed beam intensity.

The reduction of IAW off-resonance is more difficult to explain. This is the first evidence that levels of IAW from SBS can be reduced as a consequence of introducing a second interaction beam. A possible explanation for this effect is the presence of IAW driven by the seed beam, either in backscatter or side scatter, which are seen by the pump beam as long wavelength ion waves. It has been observed in numerical simulations[7] that long wavelength ion fluctuations produce a non-linear inhibition of SBS by introducing an additional damping for the resonant IAW. The evolution of IAW have been studied by Cohen et al.[8] using 2D hybrid code simulations, to allow for sidescattering to interact with backscattered SBS. Their results show that IAW driven by backscatter SBS (a 1D phenomena), saturate and relaxe by 2D effects such as sideways scattering, concurrent with the generation of long wavelength modes.

The results presented here show the sensitivity of stimulated Brillouin scattering to the initial conditions at the point of departure. Low level of ion acoustic fluctuations can either enhance or reduce SBS depending on their spectral characteristics with respect to the ones of the IAW associated with SBS. A detailed characterization of the ion fluctuations and turbulence is then essential, besides the plasma conditions, in order to model the overall evolution of the instability.

[1] W.L Kruer, *The Physics of Laser Plasma Interactions*. 1988, Redwood City, California: Addison-Wesley Publishing Company, Inc.

[2] J. Lindl, Phys. Plasmas 2, 3933 (1995).

[3] W.L. Kruer, S.C. Wilks, B.B. Afeyan, and R.K. Kirkwood, Phys. Plasmas 3, 1 (1996).

[4] V.V. ELiseev, W. Rozmus, V.T. Tikhonchuk, and C.E. Capjack, "Interaction of crossed laser beams with plasmas", submitted for publication

[5] D.F. DuBois, B. Bezzerides, and H.A. Rose, Phys. Fluids B 4, 241 (1992)

[6] D. Pesme, R.L. Berger, E.A. Williams, A. Bourdier, and A. Bortuggo-Lesne, accepted for publication in Phys. Rep.

[7] A. Maximov, W. Rozmus, V.T. Tikhonchuk, D.F. DuBois, and H.A. Rose, Phys. Plasmas 3, 1689 (1996).

[8] B.I Cohen, B.F. Lasinski, A.B. Langdon, and E.A. Williams, "2D Hybrid simulations of ponderomotively driven nonlinear ion waves", Annual meeting of the Division of Plasma Physics, 1995.

HEAT TRANSFER STUDIES IN LASER ILLUMINATED VACUUM INSULATED TARGET: REVERSE ELECTRON CURRENT EFFECTS

D.P. Singh and M. Vaselli
Istituto di Fisica Atomica e Molecolare - C. N. R.,
Via del Giardino 7, 56127 Pisa (ITALY)

The creation of a vacuum gap between the laser absorption surface and the plasma ablation region may be an advantageous approach to retard/prevent the hot electron flow in laser fusion targets. Few electrons escape through the vacuum gap setting up high electric field which inhibits further bulk flow of hot electrons. These electrons cause counterstreaming cold electron current to maintain the charge neutrality condition. The present paper analyses the effects of vacuum insulation and the modified electron velocity distribution due to reverse cold electron current, on the heat transfer from the hot corona to the cold core in laser irradiated spherical pellet in detail.

1. INTRODUCTION

To prevent preheating of the target core, several ways have been suggested in the literature. The creation of a vacuum gap between the laser absorption surface and the plasma ablation region may be an effective approach, which is not only free from mass penalty considerations but also avoids the deleterious plasma heating effects. Some experiments[1] carried out at Los Alamos with two plane thin plastic foils and vacuum insulated spherical pellets concluded a drastic reduction of fast ion flux at vacuum separations > 1mm. Our preliminary calculations[2] also confirmed that a small vacuum gap of few hundred microns in a laser irradiated pellet may reduce the hot electron flux by more than three orders of magnitude. The hot electrons escaping through the vacuum gap may give rise to a counter-streaming flow of cold electrons to maintain the charge neutrality and, hence the electron velocity distribution is modified. The aim of the present paper is to analyse the effects of vacuum insulation and the modified electron velocity distribution, on the heat

231

transfer from the hot corona to the cold dense core in laser irradiated spherical solid target.

2. ELECTRON VELOCITY DISTRIBUTION FUNCTION AND SELF-REGULATION MODEL

It is assumed here that the laser irradiation over the plasma target surface, is spherically symmetric and the plasma flow is radially outward in steady state. The major fraction of the laser energy absorption is considered to occur at the plasma critical layer via collective processes. The hot electron density crossing the vacuum gap (d) is determined by Langmuir[3] as,

$$n_h = \frac{k_B \, T_h n_{cr}}{\left[(k_B \, T_h)^{\frac{1}{2}} + d \left(2 \, \pi \, e \, n_{cr} \right)^{\frac{1}{2}} \right]^2} \qquad (1)$$

where e, k_B, n_{cr} and T_h are the electronic mass, Boltzman constant, plasma critical density and hot electron temperature respectively. Escaping electrons passing through the vacuum layer form a hot electron "halo" around the cold target core, which drives the core compression. Considering that the pellet dimensions are quite lage as compared with the fast electron collisional mean free path, we may follow one dimensional plane flow of the electrons for the electron velocity distribution. Incorporating the condition of zero net current, the expression for energy flux may be written as[4],

$$Q = \frac{1}{2} \, nmv_h^3 \, f \left(\frac{n_h}{n} \right) \ ,$$

$$f \left(\frac{n_h}{n} \right) = \frac{n_h}{4n} \left[1 - \left(\frac{n_h}{n - n_h} \right)^2 \right] \ , \qquad (2)$$

where $f \ (=(n_h/n))$ represents the effective fraction of hot electrons. Assuming that the fast electrons which escaped through the vacuum gap arrived at the internal shell of the plasma target, have a uniform temperature and thermalize with cold electrons with the equipartition time (τ_{eq}), as given by Spitzer[5], the rate of energy loss (power/steradian) of hot electrons may be expressed as[6],

$$S = \frac{3}{2} \frac{k_B}{} \frac{(T_h - T_c)}{\tau_{eq}} \int_{r_e}^{r_c - d} nr^2 \, dr \, , \qquad (3)$$

$$= \frac{3}{2} \frac{k_B}{} \frac{(T_h - T_c) n_{cr} r_c^3}{\tau_{eq}} \left[\ln \frac{(r_c - d)}{r_e} \right]$$

Considering that the width of the plasma ablation region remains of the order of the hot electron mean free path, the self-regulation condition gives

$$\left(\frac{r_c}{r_e}\right)^2 = \frac{1}{\left(1 - \frac{d}{r_c}\right)^2} + \frac{2 \lambda_h}{r_c} \frac{n_h}{n_{cr}} \qquad (4)$$

where $\lambda_h \left[= \left[k_B T \right]^2 / \left[\pi e^4 (Z+1) n_h \ln \Delta \right] \right]$ is the hot electron mean free path calculated at the internal boundary of the vacuum gap. Assuming that the plasma density varies as inverse cube of radius (as predicted in simulations), the total mass of the whole core is,

$$M = \frac{m_i n_{cr} r_c^3}{3} \left[1 + \ln \frac{\rho}{\rho_0} + 3 \ln\left(1 - \frac{d}{r_c}\right) \right] \, , \qquad (5)$$

where (ρ/ρ_0) is the plasma core compression. From Eqs. (3) and (4) the energy balance condition gives the expression of core heating time (τ_c) as,

$$\tau_c = \frac{2}{3} \frac{\left[1 + \ln \frac{\rho}{\rho_0} + 3 \ln\left(1 - \frac{d}{r_c}\right) \right]}{\left[2 \ln\left(1 - \frac{d}{r_c}\right) + \ln\left[\left(\frac{1}{\left(1 - \frac{d}{r_c}\right)^2}\right) + \frac{2 \lambda_h n_h}{r_c \, n_{cr}} \right] \right]} \tau_{eq}, \qquad (6)$$

which reduces to the expression (τ_{co}) of Kidder and Zink[6] without vacuum gap and counterstreaming effects. The numerical calculations have been done for the following set of parameters: $4\pi M = 48 \ \mu g$, $(\rho/\rho_0) = 10^4$, $T = 80 \ KeV$, $Z = 1$, $\lambda = 10.6 \ \mu m$.

3. DISCUSSION OF RESULTS

234

Figure 1 displays the variation of ratio of core-corona coupling in vacuum insulated target to that of the target without insulation and counter-streaming effects. It is obvious that even a small vacuum gap, and counterstreaming effects reduce the coupling of the core with the corona drastically. The existence of a maximum in this curve occurs due to the upperbound in the dependence of hot electron flux on hot electron fraction as seen in expression (2). Other relevant calculations indicate that the dependence of core-corona coupling on laser wavelength and mean electron temperature in the plasma ablation region in principle, remains almost unaffected as seen in previous studies[6].
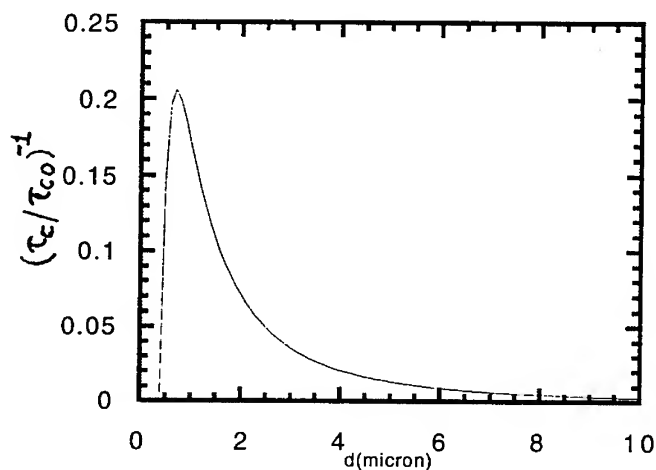
Fig. 1 Plot of relative core-corona coupling versus vacuum gap

REFERENCES:

[1] Lee K. et al., 1979, *Nuclear Fusion* **19**, 1447.
[2] Singh D.P., Deha I. and Vaselli M. 1995 *Laser Interaction with Matter,* Ser. No. **140**. 411.
[3] Langmuir I., 1923, *Phys. Rev.* **21**, 419.
[4] Morse R.L. and Nielson C.W., 1973, Phys. Fluids, **16**, 909.,
[5] Spitzer L. Jr., 1962, *Physics of Fully Ionized Gases,* 2nd Edn. Interscience, New York.
[6] Kidder R. and Zink J. W.,1972, *Nuclear Fusion* **12**, 325.

INVESTIGATION THE STRUCTURE OF SPONTANEOUS ELECTRIC FIELDS IN PLASMA CORONA OF LASER DRIVEN THIN FOILS

I.K. KRASYUK, P.P. PASHININ, A.YU. SEMENOV
General Physics Institute, Russian Academy of Sciences
Vavilov Street 38, Moscow 117942, Russia

This work is devoted to the experimental investigations and analysis of spontaneous electric fields in gas-plasma corona in case of moving shell inside cylindrical channel.

Spontaneous electric and magnetic fields generation is connected with the separation of electric charges in plasma. These fields can affect on physical processes at the interaction of laser radiation with plasma targets corona. The measurement of spontaneous electric fields enables also to evaluate the temperature of laser plasma when it is difficult to use other existent methods. The significant difference given work from other is that developed experimental method allows to obtain the spatial structure of moving electric field, Fig.1.
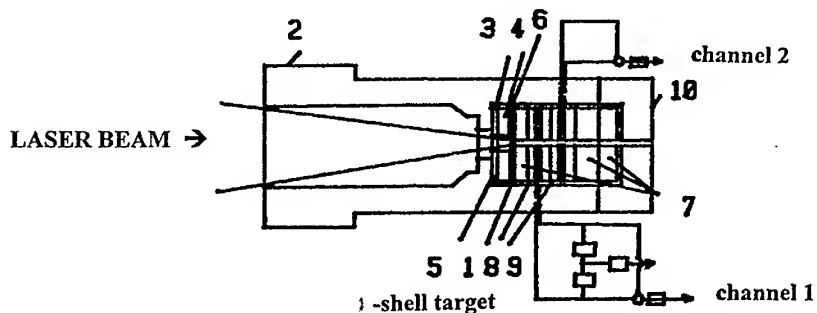
FIGURE 1. Set up of experiment. 1 - target shell, 2 - cylinder, 3-5 and 7 - isolating films, 6 - copper screen, 8-9 - sensors, 10 - lid.

236

Experiments were carry out with Nd-glass laser installation SIRIUS (General Physics Institute). The wave length of laser radiation is 1.06 mkm.

Laser pulse has adjustable shape and duration. For measurements are utilized electrocontact sensors. They represent electrodes by thickness 50 and by width 125 mkm. The electrodes were allocated in the walls of cylindrical target on fixed distance from the input polymer shell of a target. The sensors were protected by special methods from action of electromagnetic disturbances and photoemission.

Analysis showed, that charges multi-layer separation take place in these conditions. Comparison of oscillogramms shows the self-similarity character of the evolution of the spatially- temporal structure of electric field, Fig.2. This fact can be expressed by formulas:

$$\phi(x,t) = [(t - t_0)/(\xi - t_0)]^\alpha \ \phi(L,\xi); \ \alpha = \{1 \text{ for } t<100 \text{ ns}; \ 0 \text{ for } t>100 \text{ ns}\},$$
$$x = (t - t_0)L/(\xi - t_0),$$

where ϕ - potential difference, ξ- self-similar variable, L - sensor allocation, t_0- fixed time moment.
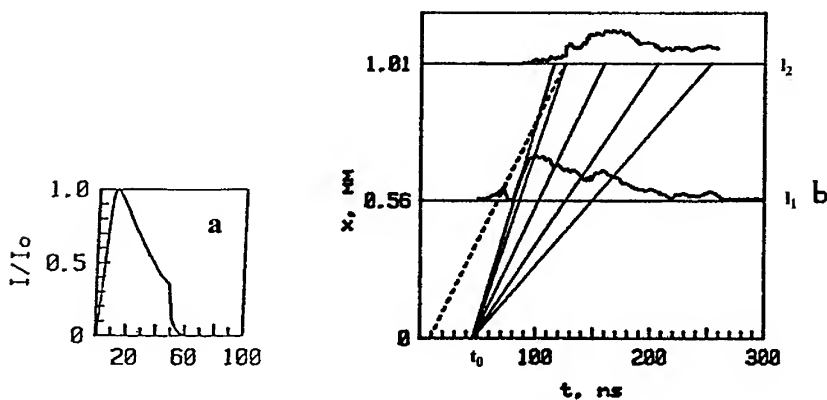
FIGURE 2. Time distribution of electric signal from differently located sensors. The laser pulse is shown also, $I=0.5\bullet10^{11}$ W/cm^2.

This property permits to reconstruct the spatially-temporal structure of electric field, Fig.3.
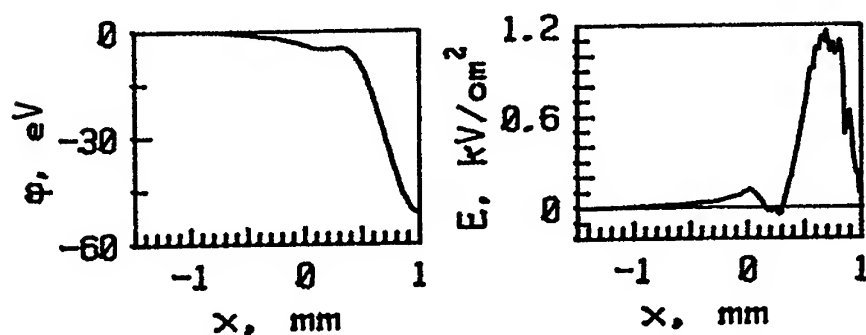
FIGURE 3. Spatially distribution of electric field based on data from Fig.2, t=100 ns. ϕ is the potential difference, E - electric field strength.

Further it is possible to compute the potential difference in investigated plasma and to evaluates effective temperature T: kT=eϕ.

Measurements by means of two-foils X-ray absorbed method confirm these results, Fig. 4.

Obtained oscillogramms shows, that signal polarity is depends on the value of laser intensity. For intensity less than $0.6 \cdot 10^{11}$ W/cm^2 the signals are generally negative. For intensities more than $1.2 \cdot 10^{11}$ W/cm^2 the signal are positive. For intermediate values the signals are bipolar. In case when laser impulse had sinusoidal modulation than the electric signal has symmetrical oscillate structure.

It was detected some special structure of electric field on the signal front (see Fig.2, dotted line) when target was filled with air or another gas. This structure is connected with charge separation on the shock wave front. As known in this case eϕ=kTln(ρ_1/ρ_2), where $\rho_{1,2}$ - plasma densities before and behind shock wave front respectively. The calculated value of the potential difference near shock wave front is equal to 1 eV, (for experiment shown on Fig.2.). And measured value of the potential difference near this shock wave front is equal to 1.75 eV.

238

FIGURE 4. The temperature characteristics of laser plasma. ▷◁- the double layer electric potential measurements, △ - two foils X-ray absorption measurements. Line is in accordance with dependence $kT[eV] = 38 \cdot (I \, [W/cm^2]/10^{11})^{0.45}$.

SUMMARY

Thus, the original experimental method was developed in this work. This method allows to measure a spatial structure of electric field in laser plasma near the moving target shell. Obtained experimental data permit to reconstruct the structure and value of spontaneous magnetic field. This method can be used successfully for estimation of shell plasma temperature inside cylindrical and conical targets for ICF.

INVESTIGATION OF HIGHLY-CHARGED HEAVY ION GENERATION IN CO$_2$ LASER-PRODUCED PLASMA

S.V.HOMENKO,K.N.MAKAROV,V.K.ROERICH,Yu.A.SATOV,
A.E.STEPANOV

*Troitsk Institute for Innovation and Thermonuclear Investigations, Troitsk ,
Moscow region , 142092 Russia*

B.Yu.SHARKOV

Institute for Theoretical and Experimental Physics, Moscow, 117257 Russia

The results of lead ions generation with charge states from Pb^{10+} to Pb^{35+} from laser-heated plasma are presented. CO$_2$ lasers radiation at power density in the range $10^{12} - 6 \cdot 10^{14}$ W/cm^2 were used. Presented work is devoted to establish the scalings of lead ion charge number , ion current , ion pulse duration and average ion velocity vs laser power density . The research was made in the framework of collaboration of TRINITI, ITEP and CERN .

1   Experimental facilities and technique

In the most of research program experiments the single-mode laser generator pumped by an electron beam sustained electrical discharge was used. Temporal shape of the laser pulse was typical for atmospheric pressure CO$_2$ lasers with longitudinal modes self-locking. Envelope curve of a signal consists of the main spike ($\sim$ 35 ns FWHM) and a relatively long ($\sim$ 1 μs) tail which contains about 40–50 % of the total energy that was up to 120 J.

The laser power density estimations were based on diffraction calculations and direct measurements of the far field light distribution. Laser power density P was defined as : $P = 4E'/\pi d_f^2 \tau_p$, where E' is the energy contained in main 35-ns spike of laser pulse in the central diffraction spot; τ_p – FWHM pulse duration; d_f - central focal spot size for level $1/e$.

The full optical scheme of TIR-1 facility [1] was used to form 100-J pulses of 2.5-ns duration.

Using different focal length objective the research covered the range of P:$(10^{12} - 1.5 \cdot 10^{14})$W/cm^2 for τ_p= 35 ns ; $6 \cdot 10^{14}$ W/cm^2 for τ_p= 2.5 ns.

Measurements of ion beam characteristics were carried out in plasma expanding along the normal to the target surface using an electro–static analyzer and ion current collector [1].
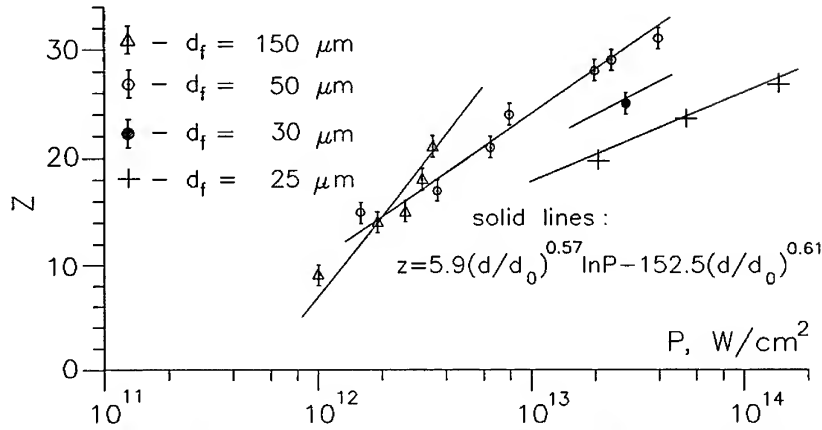
Figure 1: Average charge state number for highly-charged ion group vs power density for different spot diameter.

2 Experimental results

The detailed results of these experiments have been presented in [1] and [2,3]. The characteristic feature of all observed ion spectra for $P = (10^{12} - 4 \cdot 10^{13})$ W/cm^2 is a presence of high charge ion group. The number Z of ion charge state corresponding to a maximum spectrometer signal depends strictly on target power density. It was observed that for $P \geq 10^{12}$ W/cm^2 value of Z is almost equal to average ion charge for high state ion group.

Plasma fluid particle (lagrangian particle) passes through high-temperature near-critical region for few nanosecond. Its ionization state deviates from stationary one at electron densities below $\sim 10^{20}$ cm^{-3}, where characteristic ionization time becomes comparable with time of flight through the hot region. If pulse duration is ≥ 10 ns most particles ionized during heating phase have enough time to pass through hot plasma region and expand so that the recombination is not efficient. The recombination process is discussed more detail in [4]. Experiments with 2.5-ns laser pulses confirmed this conclusion. The experimental data presented below dealt with laser pulse duration $\tau_p = 35$ ns.

The number $\langle Z \rangle$ of ion charge state corresponding to the maximum of spectrometer vs target power density is shown on Fig. 1. The experimental dependency of $\langle Z \rangle$ on the power density within experimental errors can be fitted by the formula

$$\langle Z \rangle = 5.9(d/d_0)^{0.57} \ln P - 152.5(d/d_0)^{0.61}, d_0 = 50\mu m \qquad (1)$$
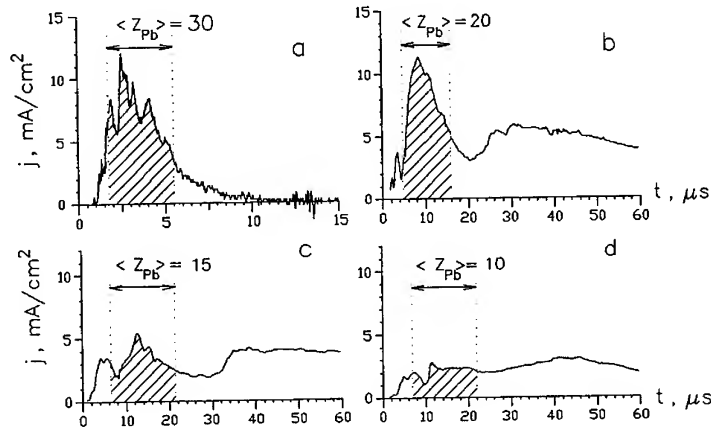
Figure 2: Oscilloscope trace of ion current density at L=1.5m for laser power density : a – $4.5 \cdot 10^{13}$ W/cm^2, b – $4.3 \cdot 10^{12}$ W/cm^2, c – $2 \cdot 10^{12}$ W/cm^2, d – 10^{12} W/cm^2

Ion spectra processing makes it possible to get empirical dependencies of the ion velocity (v) and the ion current pulse duration (τ_i) on the laser power density. The ion pulse duration can be estimated by the formula: $\tau_{i\ 0.5} = 2L\Delta v/(v^2 - \Delta v^2)$, where L is the drift length, Δv is some characteristic half-width of spectrum dependencies dN/dv. The ratio $v/2\Delta v_{0.5}$ remains approximately constant and equals to 1.6 ± 0.5 for the whole power density region.

Obtained experimental scalings are: v [cm/s] $= 9 \cdot P^{0.5}$ [W/cm^2], $\tau_{i\ 0.5}$ [μs] $= 2 \cdot 10^6 P^{-0.43}$ [W/cm^2] L[m]. The typical charge collector signal are shown in Fig. 2.

As follows from ion spectrometer signals, charge collector signals before and after these intervals are related to impurity ions (H, N, O, C) and low charge state Pb ions correspondingly. The latter are generated by laser radiation with low power density ("wings" of focal spot distribution, laser pulse temporal tail).

Additional integration gives the number of particles for a specified time interval. Typically the number of ions corresponding to one charge state $\langle Z \rangle$ was close to 15% from the total number of ions in highly-charged group .

It was found that (for at least 50–150 μm focal spot interval) the ion current density is proportional to the focal spot square and to the laser power density, that is j is proportional to the laser energy $E' \sim d_f^2 P$. Experimental

242

scaling $j(E')$ can be described by the formula

$$j \ [\text{mA/cm}^2] = 1.6 E' \ [\text{J}] L^{-3} \ [\text{m}].$$

(2)

3 Conclusions

1. The ion charge state of the CO_2 laser plasma and ion current density have been investigated for wide range of laser parameters for lead target. The experimental data have allowed to conclude:

   - For effective transformation of laser energy to energy of highly ionized states it has to be used the laser pulse duration longer than 10ns.

   - The average charge state ion number for highly ionized group depends logarithmically on the laser power density for appointed focal spot size and pulse duration (1).

   - The efficiency of the plasma ionization decreases with the focal spot size reduction so that the average charge state number depends on the focal spot diameter approximately as a square root function (1).

   - The ion current density is nearly proportional to the laser pulse energy (2).

2. 2-D model of the coupled hydrodynamics and population kinetics has been developed.

References

1. S.M. Kozochkin et al., Preprint IAE, IAE-5635/7, Moscow, 1993
2. V.,Yu. Bararov et al., Preprint TRINITI-0015-A, Moscow, 1995
3. K.N. Makarov et al., Sov. J. Theor. Exp. Phys. 106, 1649 (1994).
4. A.E. Stepanov, K.N.Makarov, S.V.Homenko, V.K.Roerich, Yu.A. Satov, Numerical study of physical effects accompanying generation of high-charged ions from a plasma produced by different types of powerful laser. 24th ECLIM poster report PH37.

SOLITONS NEAR CRITICAL LAYER IN THE INERTIAL CONFINEMENT FUSION

MIRAMAR BLAZQUEZ, JOSE FELIX

Area de Ingeniería Nuclear. Universidad de Zaragoza. 50015 Zaragoza (Spain).

Cavitons are generated by injecting energy of a high power laser into a quiescent ICF plasma. The data obtained by laser-fusion show a change in the density profile of electrons, caused by ponderomotive force of laser radiation near the critical layer, where $w_p \cong w_o$ being w_p the plasma frequency. We determinate the cavity in the electrons density due to the ponderomotive force. The natural unities are used and the u' variable is the relative velocity of the fluid of electrons. The variation in the density profile of electrons δn_e is function of $|u'|^2$. The absorption mechanism of laser radiation is the inverse bremsstrahlung. The dispersion relation is representative of an inhomogeneous plasma. The non-linear Schrödinger equation is solved as an inverse problem by means of the Inverse Scattering Transform obtaining that the variations of density profile of electrons can be explained as a soliton.. Two pictures of these soliton structures are shown.

I.- Introduction. The non-linear Schrödinger Equation.

Cavitons have been observed in thermonuclear devices and the experiments show structures like the envelope solitons [1]. These structures have been generated by injecting high power laser energy into a quiescent ICF plasmas. The data obtained by laser-fusion, show a change in the density profile of electrons, caused by ponderomotive force of laser radiation near the critical layer, where $w_p \cong w_0$, being w_p the plasma frequency and w_o the laser frequency. The non-linear Schrödinger equation describes aproximately the large-amplitude electron plasma waves. We start the calculations from the linearized equations of force and continuity as well as the Poisson's equation, corresponding to an high frequency electron plasma. The variables t, w, x, u and n correspond to time, frequency, position, fluid velocity and electronic density. These equations are linearized without consider the terms $\vec{u}.\nabla\vec{u}$ and $\nabla(n.\vec{u})$ [2]. We transform to the natural units

$$t' = \omega_p t \ ; \ w' = \frac{\omega}{\omega_p} \ ; \ x' = \frac{x}{\lambda_D} \ ; \ u' = \frac{u}{\sqrt{KT_e/m_e}} \ ; \ \delta n_e' = \frac{\delta n_e}{n_o} \qquad (1)$$

244

being w_p, λ_D and n_o the plasma frequency, Debye length, and non-perturbed electronic density. We drop the prime in x' and t' for simplifiing. At last u' can be written as an especial form of non-linear Schrödinger equation of the form

$$i\left(u'\right)_t = \gamma\left(u'\right)_{xx} + \beta \, u' \left|u'\right|^2 ; \gamma = -\frac{3}{2} ; \beta = -\frac{1}{8} \quad (2) \quad \text{being} \quad \delta n'_e = -\frac{1}{4}\left|u'\right|^2 \quad (3)$$

II.- Solution of the non-linear Schrödinger Equation.

The non-linear Schödinger equation (2) , is solved by means of the Inverse Scattering Transform [3] that is an 2 x 2 eigenvalue problem known as AKNS scheme (Ablovitz, Kaup, Newell and Shabat) [4] . The bounded functions q and r are potentials and ζ is the eigenvalue. We suppose that ζ is invariant in time $(\delta\zeta/\delta t) = 0$. We assume [5], that

$$q = \left(\frac{\beta}{2\gamma}\right)^{1/2} u' \quad (4); \qquad r = -\left(\frac{\beta}{2\gamma}\right)^{1/2}\left(u'\right)^* \quad (5)$$

With (4) and (5) ,and with the change of variable $t'' = (2/3)t$, the differential equation (2) is transformed, and having in mind that t really correspond to t', we obtain

$$iq_{t'} + q_{xx} + 2q|q|^2 = 0 \quad (6)$$

We drop the double prima in time derivation for simplifiing. This equation is the clasical non-linear Schrödinger equation. In accordance with (1) and (3) we obtain $\delta n'_e = -6\,|q|^2$ (7).The eigenvalue ζ correspond to wave vector $\zeta = K = \xi + i\eta$ and we suppose that there is not continous spectrum. There is only one eigenvalue and the eigenvalue is invariant in time. We apply the Marchenko's equation [6].

$$K_1(x,y) + F^*(x,y) \pm \int_x^\infty\int_x^\infty K_1(x,z)F(z+s)F^*(s+y)\,ds\,dz = 0 \quad (8)$$

being $F(x) = -ic\,exp\left(i\zeta x\right)$ (9).We multiply by exp(iζy) both sides of (8) and we operate with $\int_x^\infty exp\left(i\zeta x\right)dy$ obtaining for $q(x)$ and $K_1(x,y)$ the expressions

$$K_1(x,y) = ic^* exp\left[i\zeta^*(x+y)\right]\left\{1 - \frac{|c|^2}{(\zeta-\zeta^*)}exp\left[2i(\zeta-\zeta^*)x\right]\right\}^{-1} \quad (10)$$

$$q(x) = -2K_1(x,x) = -2i\left(c/c^*\right)\eta\ exp\left(-2i\zeta x\right) Sech\ 2(\eta x - \phi) \quad (11), \text{ being}$$

$$\frac{|c|^2}{4\eta^2} = exp(4\phi)\ ;\ c = c_o\ exp\left[-2A_-(\zeta)t\right]\ ;\ A_-(\zeta) = 2i\zeta^2 \quad (12)$$

We obtain the operator $A_-(\zeta)$ having in mind that one solution is obtained by means of the evolution's equation of q with the condition that $|q| \to 0$,in accordance with the compatibility conditions of AKNS scheme . With (10), (11) and (12) we can write (afterwards to put again the prime of x' and t' in the simbology).

$$q(x',t') = 2\eta\ exp\left(-2i\zeta t'\right).exp\left\{2i\left[2(\zeta^2-\eta^2)+\beta_o\right]t'\right\}$$

$$exp\left[-i(\psi_o + \pi/2)\right].exp\left[2\eta x' + 2(-4\xi\eta+\alpha)t'\right] \quad (13)$$

Having in mind the real part only and ($\psi_o = \alpha = \beta_o = x_o' = 0$),the real part of u' can be obtained from (13) as

$$Re(u') = (24)^{1/2}.2\eta\ Sech(2\eta x' + 8\xi\eta t').sin(2\xi x' - 4\xi^2 t') \quad (14)$$

III.- Results and conclusions.

In this work we consider a high frequency ICF electronic plasma and the input data utilized for calculations are the followings : n_o = Electronic density = 1.E31 m^{-3} ; w = Laser frequency = 1.E16 s^{-1} ; KT = 4.0 KeV . With these data input we obtain ξ =1.402804E-2 and η = -8.414776E-2. Numerically $Re(u')$ is given by

$$Re(u') = -0.824476.\ Sech\left(-1.694955E-1.x' + 9.510759E-3.(2/3)t'\ \right)$$

$$sin\left(2.805608E-2\ x' - 7.871436E-4.(2/3)t'\right) \quad (15)$$

showing the tipical structure of an envelope soliton .In another way, the perturbation of electronic density is a soliton . It may be obtained from the expressions (1) and (10), and can be written numerically as

246

$$\delta n_e = -1.699940E30.\left[Sech\left(-1.694955E-1.x' + 9.510759E - 3.(2/3)t'\right)\right]^2 \quad (16)$$

As we can see, there is a negative change δn_e, in the value of n_e, as it has been already observed experimentally. Figures 1 and 2 show in three dimensions detailed pictures of $Re(u')$ and δn_e. The selected limits in natural units are [0,100] for x'' and [0,1000} for t''. The structures, envelope solitons, and solitons, are better obtained at high electronic densities, near n_o =1E31 m^{-3}.

$R_e(u')x\ 0.824476$
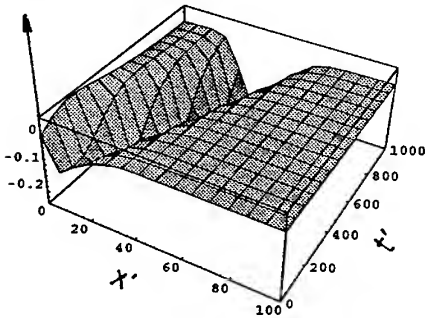
$\delta n_e\ x\ 1.699940E30\ m^{-3}$

Fig.1. $Re(u')$ as a function of x' and t'.
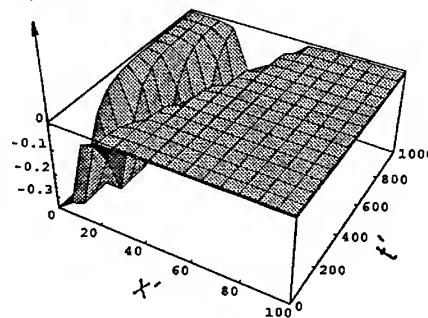
Fig.2. δn_e as a function of x' and t'.

IV.-References.

[1] KARMAKAR,S., DAS, G. C. and IBOHANBI SING, K. H.Plasma Phys. Control. Fusion. Vol. 30. No. 9. pp. 1167-1174. 1988.

[2] CHEN, F. F. " Introduction to Plasma Physics and Controlled Fusion". Ed. Plenum Press. New-York. pp 330-346. 1990.

[3] GHOSH ROY, D. N. "Methods of Inverse Problems in Physics". Ed. C.R.C. Press Inc. Boca Raton. (U.S.A). pp. 313-365. 1991.

[4] ABLOWITZ,M.J. and SEGUR, H. "Solitons and the Inverse Scattering Transform". Ed. Siam. Philadelphia. (U.S.A). pp. 8-42. 1981.

[5] DOOD, R. K., EILBECK, J.C., GIBBON, J.D., MORRIS, H.C. "Solitons and Nonlinear Wave Equations". Ed. Academic Press. London. pp. 495-511. 1982.

[6] [4] Opera. cit. pp. 22-23.

[7] ATZENI, S. Plasma Phys. Control. Fusion.Vol. 24. No.11.pp. 1535-1604. 1987.

ENERGY DEPOSITION AND CONVERSION EFFICIENCY IN A LASER PLASMA X-RAY SOURCE

C. BENEDUCE, A. GIULIETTI, T. CECCOTTI, D. GIULIETTI, A.MACCHI
and R. MILDREN
Istituto di Fisica Atomica e Molecolare, Via del Giardino , 7, 56127 Pisa, Italy

To understand how the energy deposition influences the X-ray emission from a laser produced plasma, we did a systematic investigation of both second harmonic and X-ray emission from Al plasma produced by $3ns$, $1.064\mu m$, laser pulses at 10^{14}W/cm^2. The results show that, though X-ray emission is significantly enhanced by filamentation of the laser light in the corona, the X-ray source keeps homogeneous, suggesting a *smoothing* effect in the energy transport process.

1 Introduction

At temperatures of hundreds eV, typical of laser produced plasma (LPP), the energy emitted in the X-ray region of the spectrum is a relevant percentage of the absorbed laser energy. In the nanosecond pulse regime, most of the laser energy is absorbed in the underdense "coronal" plasma, while most of the X-ray emission is generated in the overdense ($n_e > n_c$) region. Thus the study of energy transport from the underdense to the dense regions of the plasma is relevant to the optimisation of laser produced X-ray sources. Previous experiments[1] suggest that X-ray conversion efficiency is influenced by filamentation instability (FI) of the laser pulse. This hypothesis was also supported by analogies with previous separate measurements on second harmonic (SH) generated by laser plasma filaments[2].

In this work we report on an investigation of both second harmonic and X-ray emission from Al plasma at the irradiance of $10^{14}W/cm^2$. The plasma was created by focusing a 3 *ns* Nd laser pulse on an aluminium target. Time integrated images, streak images and time-resolved spectra of the SH and X-ray emission were captured. Measurements have been recorded for various target positions with respect to the laser beam focus. The electron temperature of the X-ray emitting region had been previously measured[1] to be $T_e \approx 300\ eV$, while in the corona a rather higher temperature can be assumed. The investigated X-ray spectral region was in the range of 1-10 *KeV*.

2 Experimental results

2.1 X-ray and SH yield measurements

The two diagrams of Fig. 1 shows X-ray and SH yields, detected by an X-ray and an optical photodiode respectively, as a function of target position with respect to the laser beam focus. $x = 0$ identifies the position of the focus and x increases in the direction of propagation of the laser beam. The focal position was determined with an uncertainty of $\pm$ 200 μm. Both yields vary when moving the target within $\pm$ 2 *mm* from the beam waist and maxima appear at a positions about 0.5 to 1.0 *mm* either side of the focus. There is a net correlation between the X-rays and SH yields vs the target position.
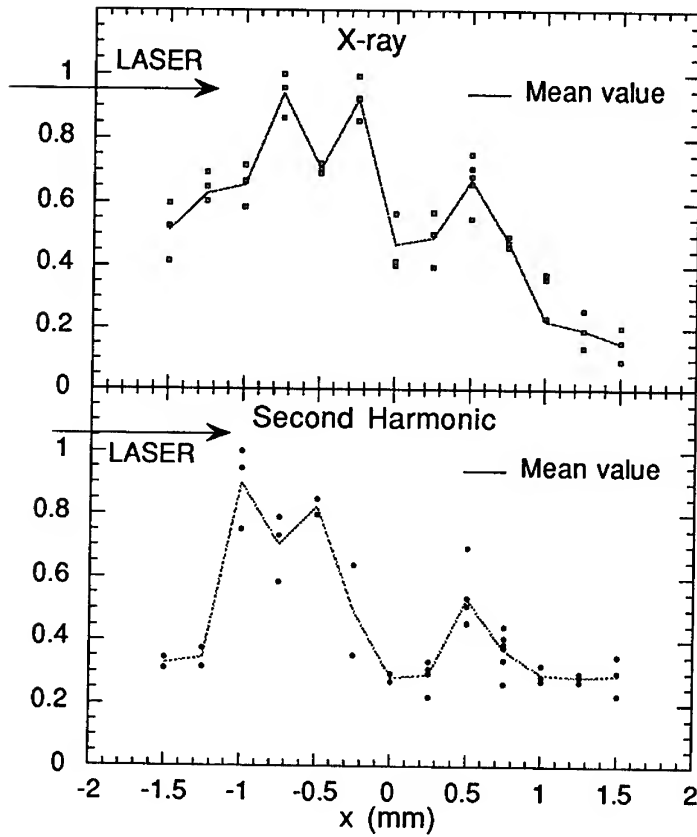
Fig. 1: X-ray (top) and Second Harmonic (bottom) emitted energy vs position of the target with respect to the laser beam focus.

2.2 Localisation of the SH sources

The sources of the SH emission have been localised in two independent ways. First, the plasma has been imaged at a suitable angle in both 2ω and $3\omega/2$ light. This latter harmonic emission is a signature of the $n_c/4$ electron density layer in the plasma[3]. Both time-integrated (with a CCD camera) and time-resolved images (with an optical streak

camera) were obtained. From the comparison of 2ω and $3\omega/2$ images, we observed that the former is emitted from a large plasma region at density below $n_c/4$.

Subsequently time resolved spectroscopy of the SH was performed, by using a spectrometer coupled with the optical streak camera. The time resolved spectra showed that the emitted SH was shifted from the pure $2\omega_0$ frequency, and broadened in comparison with pure frequecy doubling. A typical spectrum is showed in Fig.2. The spectra were interpreted in terms of the theory introduced by Stamper[4] and experimentally proved[5]. According to this theory the generation of appreciable SH emission in filamentary plasmas, requires the existence of either a reflected or a stimulated Brillouin backscattered (SBS) wave within the filament. For backward emitted SH (which is close to our experimental condition) the frequency of the SH field is $\omega_b+\omega_b$, where ω_b is the frequency of the Brillouin backscattered wave. The shift of the SH can be written as:

$$\left(\frac{\Delta\omega}{\omega}\right)_{2\omega_0}=\left(\frac{\Delta\omega}{\omega}\right)_{\omega_0}\approx\frac{2}{c}\left(v_s+v_p\right)$$

were $v_s=1.5\ 10^7\ cm/s$ is the speed of the ion-acoustic wave and v_p is the velocity of the plasma motion. Using this equation, from the spectra we obtain $9.4\ 10^6\ cm/s<v_p<1.9\ 10^7\ cm/s$. We assumed $T_e=500eV$ as a rough estimate of the coronal temperature. From the comparison with the density and velocity profiles obtained from hydrodynamic simulation using the 1-D code MEDUSA, the region of dominant SH emission can be then located at 80 μm from the critical layer, with an electron density from 1.4 to 2.0 $10^{20}\ cm^{-3}$. These values must be considered only as an order-of magnitude estimate because of the crudeness of the 1-D approximation for the plasma motion. However, since the 1-D approximation is likely to overestimate both density and velocity at a given point in space, the reported density values give an upper limit to the density of the 2ω emitting region. Thus we conclude that 2ω emission definitely comes from a region with a density below $n_c/4$, in agreement with the above mentioned result obtained from the comparison of the 2ω and $3\omega/2$ images.
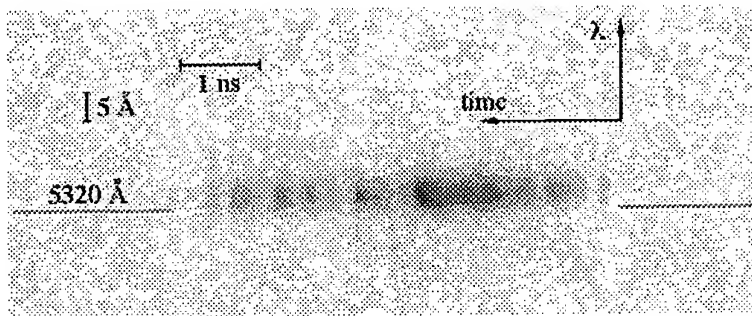
Fig. 2: Time-resolved Second Harmonic spectrum. The line marks the calibrated position for the 5320 Å wanelength.

250

2.3 Intensity distribution

Fig. 3 shows the intensity distribution of:

a) the laser spot without plasma, as obtained by equivalent plane imaging. The measured FWHM spot size was 24 μm, and the intensity distribution in the spot was found to be rather uniform within the resolution of ≈ 4 μm.

b) the SH source imaged close to the backward direction. The SH emission from the corona shows structures with a typical size of 10- 20 μm, which are likely to grow for filamentation instability in a plasma region of T_e=500 eV and n_e=2.0 10^{20} cm^{-3}.

c) the X-ray pin-hole camera image of the plasma, with a resolution of 13 μm. In the limit of the available resolution, the X-ray emitting region looks homogeneous, in spite of the filamentary distribution of SH emission in the corona.
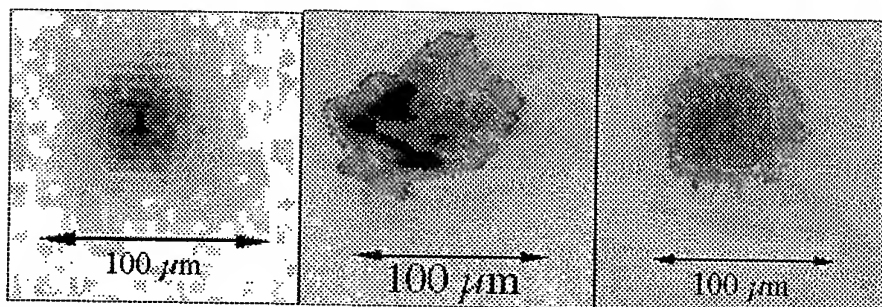
Fig. 3 : Images showing intensity distribution for : the 1.06 μm wavelength laser focal spot (left); the Second Harmonic source (center); the X-ray source (right).

3   Conclusion

Combined measurements of SH and X-ray emission from a laser produced plasma were found to be a very effective tool to study relevant features of energy transport and heating of the dense plasma region. The experimental data show that a filamentary laser energy deposition into the plasma may produce enhanced X-ray emission from the dense region, without degrading the uniformity of the intensity distribution of the X-ray source. There is a clear indication of a *smoothing* effect produced by the energy transport from the corona to the main X-ray emitting layer.

Acknowledgements

References

1. A. Macchi *et al, Il Nuovo Cimento D*, **18**, in press (1996).
2. V. Biancalana *et al, Europhys. Lett.*, **22**, 175 (1993).
3. D.Giulietti *et al, Il Nuovo Cimento D*, **13**, 845 (1991)
4. J. A. Stamper *et al, Phys.Fluids*, **28**, 2563 (1985).
5. A. Giulietti *et al, Phys. Rev. Lett.*, **63**, 524 (1989).

4.- INERTIAL FUSION TARGETS

LASER COMPRESSION AND PARTICLE BEAM IGNITION FOR THE CLEAN PROTON-BORON-11 FUSION

S. ELIEZER[1,2], J.M. MARTINEZ-VAL[1], M. PIERA[1],
G. VELARDE[1], Z. HENIS[2]

[1] *Institute of Nuclear Fusion*
Madrid Polytechnic University, Spain

[2] *Plasma Physics Department, Soreq NRC, Yavne 81800, Israel*

In this paper a solution to the problems of proton-boron fusion is suggested. A mixture of boron-hydrogen target is ignited by a proton beam inducing a nuclear detonation wave expending across a precompressed target. The precompression may be achieved by laser beams. The physical processes involved in this scheme are analyzed.

1   Introduction.

The proton + boron 11 $\rightarrow$ 3α fusion reaction is considered to be the cleanest way for exploiting nuclear energy. However, the very high ignition temperature ($\sim$ 200 keV), the Bremsstrahlung losses and the relative moderate fusion yield per reaction (8.7 MeV), make it very difficult to achieve high energy gain.

For a Magnetic Confinement Fusion reactor using $p -^{11} B$, Dawson[1] concluded that the internal gain (defined as the fusion energy devided by internal energy) can be slightly above one if the produced α particles can be taken away while refueling the system.

For an Inertial Confinement Fusion[2] reactor using $p -^{11} B$, densities of the order of $10^5 g/cm^3$ and spark ($< 10\%$ in mass) temperatures about 200 keV have to be achieved, while the bulk of the matter must reach temperatures smaller than 10 keV. These conditions might impose prohibitive laser (or ion) drive uniformities necessary in order to avoid the hydrodynamic instabilities. An analysis for volume ignition scheme with negative conclusions has also been made[3]. For this approach the extremely high areal density targets would require driver energies in the range of Gigajoules with a potential small gain.

The idea proposed in this paper is based on the creation of a heat detonation wave (energy supplied by α particles) and a heat non-linear wave (by electron

transport, where both waves move with some delay but at the same speed into a precompressed target[4]. These heat waves are induced by a proton beam or proton reach plasmas or jets[5] into a region called "the ignitor", and then they propagate into the "cold" ($\leq$ 1keV) and compressed ($< 10^3 g/cm^3$) boron 11 - proton fuel. It is crucial that the boron to proton number ratio is smaller than 1/3. The heat waves propagate supersonically and thus a large fraction ($> 30\%$) of the boron is burned. If the suitable conditions for propagation are met, the internal energy gain can be as high as 1000, so that an overall (real) gain can be achieved. The most difficult requirement of this approach is the need of a very intense proton beam, acting for a very short time ($\sim 10ps$). New accelerators would be needed for this purpose.

2 Energy balance.

The fusion energy W_f is,

$$W_f\left(\frac{eV}{cm^3.s}\right) = 3.38 \times 10^{-9}\frac{\varepsilon n^2}{(1+\varepsilon)^2}; \varepsilon = \frac{n_B}{n_p}; n = n_B + n_p, \tag{1}$$

The fusion rate was calculated for an ion Maxwellian distribution with a rate $4\times 10^{-16}cm^3.s^{-1}$ and an ion temperature $T_i = 200$ keV. Since in this process the ion temperature is larger than the electron temperature, energy flows from ions to electrons by collisions. The main energy sink is the bremsstrahlung radiation emitted by the electrons. Taking into account relativistic corrections, this term is given by

$$P_B\left(\frac{eV}{cm^3.s}\right) = 9.3 \times 10^{-14}n_e(\sum_i n_i Z_i^2)T_e^{1/2}\left(1 + \frac{2T_e}{m_e c^2}\right) \tag{2}$$

where T_e is in eV, m_e is the electron mass and n_i, Z_i are appropriately the ion densities and their charges.

The ignitor performance is analyzed and simulated by an average energy balance involving the ion and the electron temperature that are governed by the following Eqs.

$$\frac{3}{2}n_e\frac{dT_e}{dt} = P_{ie} - P_B + f\eta W + \eta_p W_p - P_{he} - P_{me} \tag{3}$$

$$\frac{3}{2}n_i\frac{dT_i}{dt} = -P_{ie} + f(1-\eta)W + (1-\eta_p)W_p - P_{mi} \tag{4}$$

where P_{ie} is the ion-electron energy exchange term and P_B is the bremsstrahlung power given by Eq. (2). W_f and W_p are the fusion and the proton power densities accordingly, η and η_p are appropriately the fractions of the fusion α particles and of the proton beam deposited into the electrons, and f is the fraction of fusion born α particles remaining into the ignitor. Our simulations

show that it is possible to start a burning wave with a very high density proton beam, $W_p \sim 5 \times 10^{21} W/cm^2$ with 5 MeV per proton during a pulse duration of about 10 ps. For a 5 mg fusion target with a precompressed density of $1000g/cm^3$ and a beam focus with a radius similar to the α range one needs a 100 kJ proton beam.

3   Time scales for proton-boron 11 fusion.

Successful simulations based on Eqs. (3) and (4) and the following expansion of the heat waves into the precompressed target were performed[4] yielding high gain (~ 1000). In order to understand the transport of the different physical phenomena, it is useful to present a set of time-scales. The following times and precompressed density scaling laws are given for an ion temperature of 200 keV, the minimum ion temperature necessary for this scheme to work. The electron temperature has to be in the domain of 100 keV and the ratio of boron to proton number particle, ϵ, has to be smaller than 1/3, in order for bremsstrahlung cooling not to cut off the fusion. Therefore in our example we take T_e about 100 keV, $\epsilon = 0.2$. The most important scale length in this scheme is the α particle range. For the parameters under consideration $\rho R_\alpha \simeq 1g/cm^2$. The following timescales describe the proton-boron 11 "burning" fusion.

(a) Radiative cooling time of electrons by bremsstrahlung:

$$P_B \tau_{Br} = \frac{3}{2} n_e T_e \rightarrow \tau_{Br} \approx (3.3ps) \left(\frac{10^3 g/cm^3}{\rho} \right) \left(\frac{T_e}{100 keV} \right)^{1/2}$$

(b) Ion cooling time by electron collisions:

$$P_{ie} \tau_{ie} = \frac{3}{2} (n_p + n_B) T_i \rightarrow \tau_{ie} \approx (7.4ps) \left(\frac{10^3 g/cm^3}{\rho} \right) \left(\frac{T_e}{100 keV} \right)^{3/2}$$

In this approximation the cooling time of the system is about 10.7 ps.

(c) Fusion burning time: $\tau_f = (n_p \langle \sigma v \rangle)^{-1} \approx (12ps)/\frac{\rho}{\left(\frac{10^3 g}{cm^3} \right)}$

(d) electron heat wave and α detonation burning wave:

The time defined here is for these waves to travel a distance of the α range R_α. Moreover, in our scheme the heat wave speed U_h equals the detonation burn wave velocity U_{BW}, implying these times to be about 2.5 ps. It must be pointed out that this time scales strongly with electron temperature ($\propto T_e^{5/2}$), however is very weakly dependent on density.

(e) the sound propagation time: $\tau_s = R_\alpha/c_s \approx (2.5ps)(100 keV/T)^{1/2}$

(f) confinement time of the hot plasma:

Solving for hydrodynamic motion of the plasma the following time is derived for a flow velocity U_p, induced by the shock wave implied by pressure gradient. Again the range of α is taken to define $\tau_c = R_\alpha/U_p \approx (4.0ps)(10^3 g/cm^3/\rho)$

From above analysis one can see the importance of bremsstrahlung losses. The heat wave and detonation wave must advance into the next "cold" precompressed fuel before "cooling", therefore in our scheme one needs to precompress the target to not more than $1000g/cm^3$. On the other hand the compression is needed in order to limit the mass of the fuel and thus the total energy output.

4   Conclusions.

The main conclusion drawn from this study is that a fusion-burning wave can be triggered in a proton-boron plasma of optimized isotopic concentration, provided a fraction of this plasma reaches burning conditions by supersonic heating. The highest difficulty to meet this requirement is the need of a very intense beam of charged particles. A second important issue is the need of compressing the plasma before igniting it. Another important issue is the value of the $p^{11}B$ fusion rate $\langle \sigma v \rangle$. We use the value advocated by Dawson[1], however, if this rate is smaller by a factor of 2, then it seems that this clean fusion cannot be achieved.

It must be added that the heat detonation burning of a DT plasma in comparison with a $p^{11}B$ plasma requires less restrictive constrains on the proton beam and on the precompression of the fusion fuel by 2 to 3 orders of magnitude.

References

[1] Dawson, J.M. "CTR using the P-B11 reaction", Plasma Physics Group Report PPG-273, University of California (1976).

[2] Weaver, T., Zimmerman, G. and Woods, L., "Prospects for exotic fuel usage in CTR systems" UCRL-74191 and 74352, Lawrence Livermore Repts. (1973).

[3] Pieruschka, P. et al., *Laser Particle Beams, 10*, 145 (1992).

[4] Martínez-Val, J.M., Eliezer, E., Piera, M. and Velarde, G., *Phys. Lett. A* (1996), in press.

[5] Martínez-Val, J.M. and Piera, M., "Fusion Burning Waves Ignited by Cumulation Jets" (to be published).

Target design for a MJ laser

P.A.Holstein, J.M.Dufour, H.Dumont, J.Giorla,
S.Laffite, Y.Saillard, G.Schurtz, M.Terrier
C.E.A. Limeil
94195 Villeneuve Saint Georges Cedex, **France**

We choose a drive temperature of 4MK to minimize the hydrodynamic instabilities. We have some measurements , a model and some simulations to assess the radiation temperature within 5% which implies ±100TW for the laser. We study some configurations with 2 or 3 rings (using 3 or 4 cones of laser beams)

1. Features of the french MJ laser

Our MJ laser will have 60 beams (60x4 beamlets 40x40cm). Routinely it will deliver 600TW and 1.5MJ and possibly 700TW and 2MJ. 30 beams per hemisphere imply to have 5 or 10 beams per cone because they must be staggered. The laser intensity in the focal spot is supergaussian.

2.Numerical simulations to design targets adapted to a MJ laser

There are three stages in the study:

-a- 1D calculation of the capsule alone to optimize the radiation temperature $Tr(t)$[1].

-b- 2D calculation of the cavity to optimize the symmetry.

-c- 2D calculation of the capsule with geometric perturbations and/or non-uniformity[1]

-a- Optimized drive temperature with 1D code

On table 1 we compare the NIF capsule and the LMJ capsule: they differ mainly by the drive temperature (the DT mass is the same) and the In-flight-aspect-ratio (24 to 36), the convergence ratio are the same ($\approx$40).

table 1	4MK =350eV	NIF 300eV
ext R / abl Thick / DT thick	1000/180/120μ	1110 /160 /80μ
maximum velocity	$4\,10^7$cm/s	$3.9\,10^7$cm/s
gain = Efusion /Elaser	15.7	14.9
total ∫rdr DT g/cm^2	1.7	1.4
In-Flight-Aspect-Ratio	24	36
convergence ratio	38	40
ablated fraction	97%	97%

---

[1] P.A.Holstein and al, "Target design for a MJ laser and connected experiments" Proccedings of SOFE'95 to be published

On the fig 1 the maximum drive temperature obtained in cavity is drawn versus the right parameter which is $E_{las}P_{las}/S_{cav}{}^2$ according to the model: the squares are the measurements done at LLNL by varying the laser power, the circles have been measured with Phebus by varying the sphere diameter (Phebus cylindrical cavity with shields are 20% lower because of the losses due to the shields). The experimental points are in good agreement with the model. The extrapolation between the measurements and the NIF or LMJ (triangles) is only a factor 8 in EP/S^2.
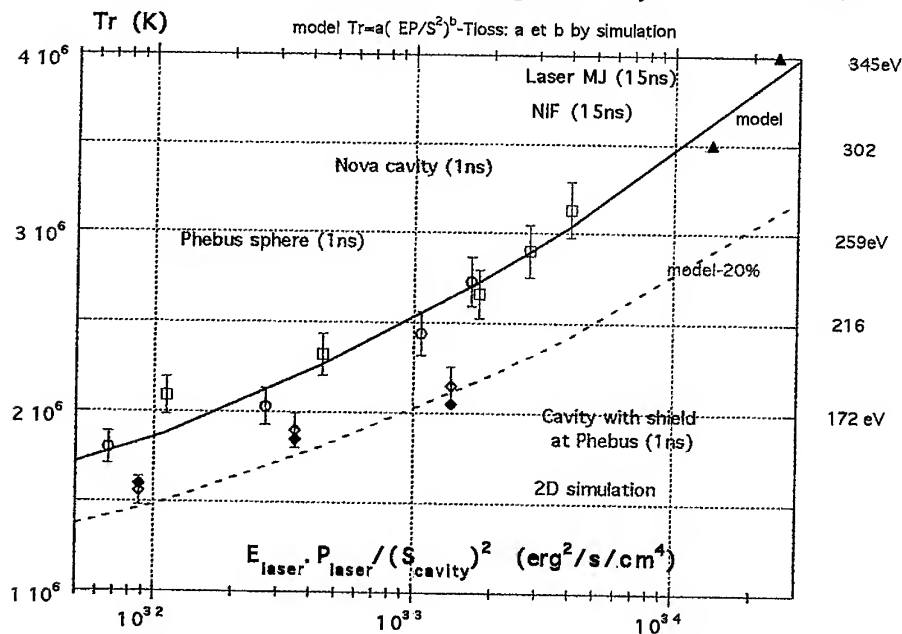
Fig 1   Maximum of radiation temperature in cavity

-b- Cavity simulations

We ran our code FCI2 in 4 configurations by varying the cavity size, the ring number illuminated by the laser cones on the cavity wall and the beam phasing (table 2)

table 2	small cavity	medium cavity	large cavity
L /ø /ø hole	8 /5 /3 mm	9.2 /5.8 /2.9mm	9.5 /5.6 /2.8mm
2 rings	4 cones and beam phasing (BP)		3 cones & BP
3 rings			4 cones & no BP

All the cavities are filled with H+He at 0.8mg/cc and the window is 1μm polyimide as for the NIF.

On fig 2 we can see that all our cavities need the same laser power 600±50TW (at 15.5ns) and the same laser energy 1.65MJ ±0.1 (at 16.5ns) to give the optimised drive temperature: indeed there is some hole closure for the small cavity (the medium and the large ones has the same surface).

The non-uniformities on the flux incident on the capsule are taken near the ablation front and calculated in postprocessing. The spherical Legendre mode 2 has a coefficient given on fig 3: without beam phasing (configuration with 3 rings) it swings from -5% to +5% due to the gold wall expansion leading to the the laser spot motion. With beam phasing (the 3 others configurations with 2 rings) we can keep it between ±2% or better. Of course we can use the beam phasing for the 3-ring configuration in order to lower the mode 2.

The mode 4 depends only on the position of the rings: its coefficient ranges from -3% to 1% following the configuration (fig4)

The modes 6 and 8 are less than 1% (non shown here)

Fig 2 : Laser Power (TW) for different configurations
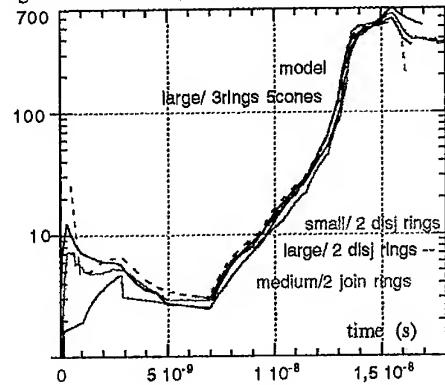
Fig 3 : Spherical mode 2 coeficient
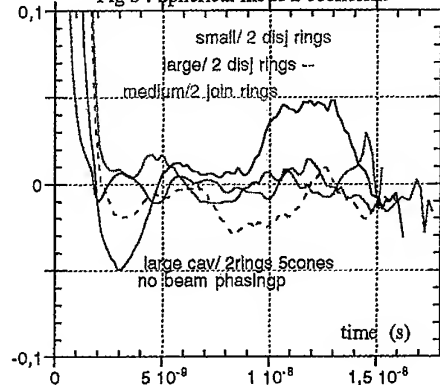
Fig 4 : Spherical mode 4 coefficient
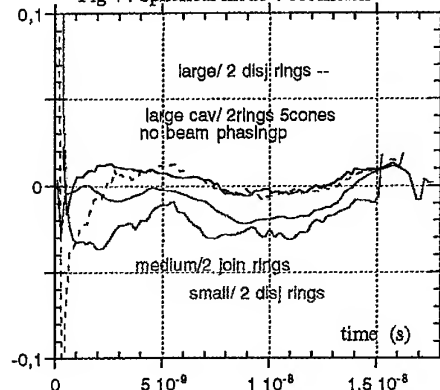
-c- 2D calculation of the capsule with geometric perturbations

The main instability occurs at the ablation front; during the accaleration stage of the implosion the capsule thickness decreases (max of In-flight-aspect-ratio) and the instability may propagate to the DT: according to Takabe's formula we know that the dominant spherical modes at the ablation front are in the range 10 to 50.

We simulate the effect of a single-mode perturbation near the equator of the capsule with FCI2. On fig 5, we draw the amplification of the modes 12, 20, 32 and 40: roughly, they vary from 100 to 1000

It is interesting to notice that some modes change sign before being amplified (here mode 32 and 40), so the growth is delayed. This is due to the transitory regime, before the acceleration of the ablation front.
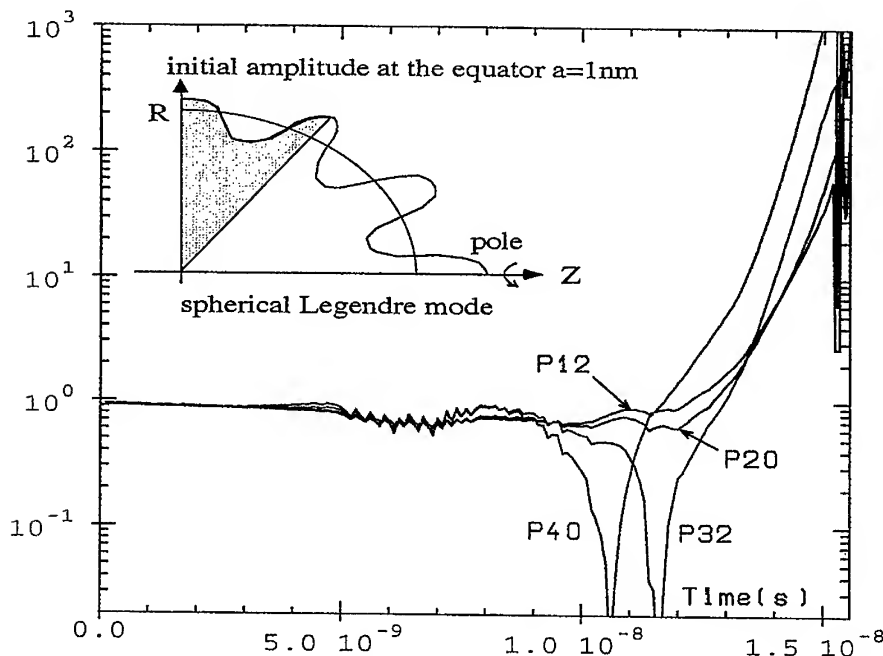
Fig 5   Amplification of the perturbation at the ablation front

In conclusion, the configurations with 2 or 3 rings (using 3 or 4 cones of laser beams) are equivalent in today sate of the simulations, but there are still some uncertainities , particularly for the numerical treatment of the cavity window and of the edges of the holes.

There is a lot of work to do to understand the hydrodynamic instabilities and parametric instabilities in MJ-laser implosion.

LASER FUSION GAINS EVALUATED BY THE SELF SIMILARITY MODEL

H. HORA*, H. AZECHI, Y. KATO, Y. KITAGAWA, M. MURAKAMI,
K. MIMA, S. NAKAI, H. TAKABE, M. YAMANAKA and T. YAMANAKA
Institute of Laser Engineering, Osaka University, Suita Osaka 565, Japan
Perman. Address: Inst. Theoret. Physics, Univ. NSW, Sydney 2033, Austral.

The recent measurements of record DT fusion neutron yields from laser direct drive pellets in Rochester together with measurements at Osaka are compared with the earlier computations of the self similarity model in the range of fusion burn (before volume ignition appears at higher gains). The rather good agreement with the measurements may proof that the conditions of the self similarity model may have been closely fulfilled in the Rochester experiment while the stagnation free ideal adiabatic compression was well proved before at Osaka fulfilling the self similarity solution. It is evaluated under what conditions most optimistic gains may be reached with the present Rochester experiment and the need for megajoule drivers underlined again if one bases the reactor on the uncomplicated concept of volume ignition with ns driver pulses.

1 Introduction

The presently achieved highest fusion gains from laser irradiated glass micro balloons filled with deuterium tritium gas or having this fuel condensed as a layer inside the target sphere, are examined here using the fusion gain calculations based on the self similarity model with an ideal adiabatic compression and expansion (Hora 1970, 1991). The latest result from the experiments of the University of Rochester (Soures 1995) seem to fit this model rather well similar to the results achieved before (Yamanaka et al. 1986; Takabe et al 1988) in both cases applying direct driv.

We apply the model of self similarity volume compression and burn (no ignition yet). This differs strongly from the later aim to produce a hot spot uniform density [Kidder-Bodner isochoric model, Kidder (1976)] or the even more complex isobaric model (Meyer-ter-Vehn 1982; Storm et al 1988). Contrary to these hot spot models, the extension of the self similarity model with inclusion of alpha reheat and of partial re-absorption of bremsstrahlung led to the scheme of volume ignition (Hora t al. 1978; Basko 1990; Lackner et al 1994; Martinez-Val et al 1994, Atzeni 1995) however at laser pulse energies about 10 times higher than the present esperiment (Soures 1995).

2 Fusion Gains from the Self Similarity Model

The first obvious connection of the recent measurements of the laser fusion gains to the volume burn self similarity solution can be seen from Fig. 1.
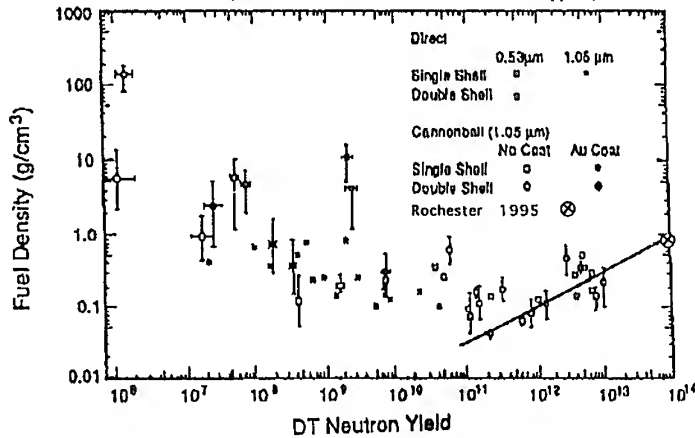
Fig. 1 Measured densities and DT neutron yields from Livermore and Osaka with a line suggesting the iso-thermal condition for the Osaka results which arrives accurately at the recent Rochester result

The line drawn in the diagram was published before (Hora 1991) expecting higher neutron gains from the Osaka measurements contrary to the expected decrease. The line corresponds to isothermal conditions with a quadratic neutron increase on the density. It is remarkable that the recent result of the Laboratory for Laser Energetic of the University of Rochester (Soures 1995) with 10^{14} neutrons measured for a density of 1 g/cm^3 just fits this predicted line.

3 Volume Burn Parameters

A more detailed evaluation of the measurements is given in Fig. 2 [see Hora, 1991) Fig. 13.6]. In this case the fusion core gain G refers to

(1) G = (fusion energy)/E_0 = $(E_0/E_{BE})^{1/3}(n_0/n_s)^{2/3}$ = const $n_0 R$

where E_0 is the energy which is spread uniformly into the DT fuel which has a uniform temperature and initial density n_0 from where on the fusion plasma is expanding adiabatically. while producing fusion energy following all the time steps of the self similarity model. This core gain G differs from the total gain G_{tot} where the hydroefficiency η is included. If the uniform volume of the fuel $V_0 = [4\pi/3]R^3$ with a fuel radius R has an initial density n_0 of compression in multiples of the solid state n_s then one can calculate the gain G as function of E_0 with V_0 as

parameter. The result in the diagram of Fig 2 are the dashed parabolas for gains less than G=8. Parabolas for the same n_0 have an asymptotic fully drawn line which are straight for gains below 8. The lines are bent for higher gains what is an expression of volume ignition (Hora et al 1978;1991). From the lines one arrives at the formula (1) with the break even energy E_{BE} (equal 6 MJ for DT) and the solid state density n_0 published in 1970 and algebraically identical with Kidder's (1975) nR-values. The lines correspond for G less than 8 to an optimum plasma temperature of 17 keV.
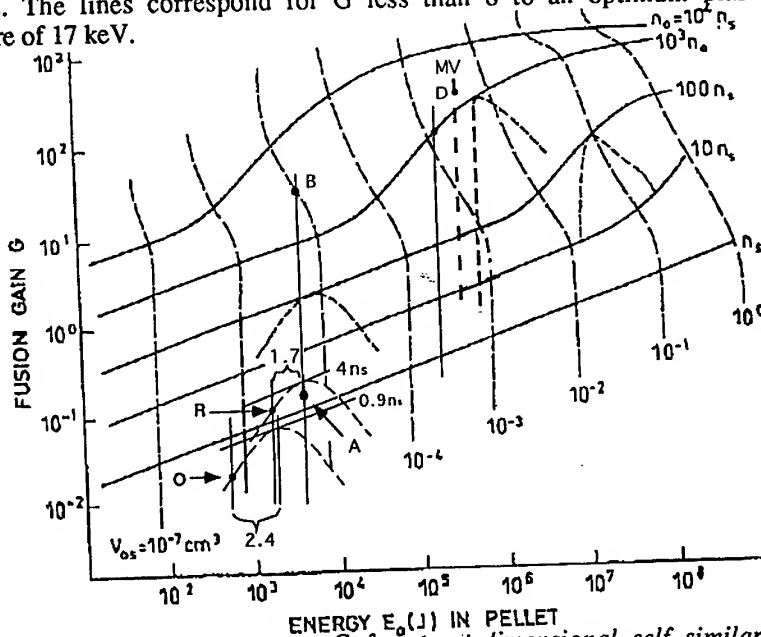
Fig. 2 *Optimised core fusion gains G for the 3-dimensional self similarity hydrodynamics (Hora 1991) with volume ignition for G above 8 and fusion burn (quenching) at lower gains. The Rochester (R) and Osaka (O) measurements fully agree with these results.*

Soures (1995) measured n_0=4 and 30 kJ laser energy for 10^{14} neutrons. E_0=2.1kJ assuming the usual hydroefficiency of 7%. This result is point R with a core gain of 14%. This experimental value has to be fit by a parabola with the line of n_0=4n_s as tangent. The factor 1.7 corresponds to a plasma temperature 1.7 times less than the optimum value of 17 keV, The resulting 10 keV are in a surprising agreement with the measurement of 10 keV though the self similarity model is very crude and simplifying. However it is three dimensional.

The same evaluation can be done for the Osaka Measurement (Takabe et al 1988) with 10^{13} neutrons (Fig.1) and o.9 time solid state density: Point O in Fig. 2. We arrive then at a temperature 7.1 keV as measured.

264

4 Estimation of highest possible Gains and the Fast ignitor

If the Rochester laser should come to volume ignition [by factor 2 below spark ignition: Basco(1990), Lackner et al (1994)], one sees from Fig. 2 that the conditions have to be lifted from A to B (3000 n_s, initial temperature 11 keV, total gain $G_{tot} = 3$ at $\eta = 10\%$). It is evident that ignition is much easier with NIF lasers (vertical lines between initial volumes of solid state between 10^{-4} to 10^{-3} cm^3 where total gains of 80 can be reached at 3000 n_s and total input energy of 1.7 MJ (Martinez-Val et al 1994) Point MV in Fig. 2.

If the driver energy should go down to the 100 kJ range, on can achieve this only by reducing the ablations losses, e.g. by the fast ignitor (Tabak et al 1995) where the main energy is brought into the pellet with nearly no loss by the ps-100 kJ laser pulses after the pellet had to be compressed to few thousand times the solid state and few 100 eV temperature by a usual 50 kJ ns pulse.

Since the range of the energetic particles from the assumed short range stopping area of the ps pulse is very large it may not be possible to reach the spark ignition conditions. We estimated that the range may in the best way spread the energy of the ps laser pulse to the whole compressed plasma and heat it uniformly to the ideal 3 keV temperature for a volume ignition which then can be followed along the scheme of Fig. 2. Preliminary estimations result then indeed in values of 10 MJ gains of fusion energy with a little more than 150 kJ total laser energy. But if this would not be achieved technologically, what is available technology is the classically designed uncomplicated volume ignition with ns-MJ driving taking into account the high ablation losses. This conservative solution is at least at hand and proved by the Centurion-Halite measurements. The half meter liquid or ceramic pebble blanket immediately in front of the pellet is an easy solution without the problem of wall erosion for the reactor with hydrodynamically softened and 1000 times (than chemically) reduced shocks of the controlled explosion.

Atzeni, S., 1995, Jpn. J. Appl. Phys. 34, 1980
Basco, M.M., 1990, Nuclear Fusion 30, 2443
Hora, H. 1970, *Laser Interaction and Realted Plasma Phenomena*, H. Schwarz et al eds, (Plenum, New York) Vol. 1, p. 365 and 427
Hora, H., and Ray R., 1978, Zeitschr. f. Naturforsch. 33A, 890
Hora, H., *Plasmas at High Temperature and Density* (Srpinger, Heidelberg)
Kidder, R.E., 1976, Nucl Fusion 16, 405
Lackner, K.S., Colgate, S.A., Johnson, N.I., Kirkpatrick, R., Menikoll, R., and Petschek, A.G., 1994, Laser Interaction and Related Plasma Phenomena, G.H. Miley ed., AIP Conf. Proceed., No. 318 (Am. Inst. Phys. p. 356
Martinez.Val, J.-M., Eliezer, S., and Piera, M., 1994, Laser and Particle Beams 12, 681
Meyer-ter-Vehn, 1982, Nucl. Fusion 22, 561
Soures, J.M., 1995, Bull. Am. Phys. Soc., 40, 1694
Storm, A., Lindl, J., Campbell, E.M., Bernat, T.P., Coleman, L.W., Emmet, J.L., Hogan, W.J., Horst, Y.T., Krupke, W.F., and Lowdermilk, W.H., 1988, Livermore LLNL Report 47312
Tabak, M., Hammer, J., Glinsky, M.E., Krue, W.L., Wilks, S.C., Woodworth, J., Campbell, E.M, Parry, M.D., and Mason, R.J., 1994, Phys. Plasma 1, 1626
Takabe, H., Yamanaka, M., Mima, K., Yamanaka, C., Azechi, H., Myianaga, N., Nakatsuka, M., Yabe, T., Sasaki, T., Yoshida, K., Nishihara, K., Kato, Y., Izawa, Y., Yamanaka, T., and Nakai, S., 1988, Phys. Fluids 31, 2884
Yamanaka, C., and Nakai, S., 1986, Nature 319, 757

INTERACTION EXPERIMENT WITH ISI SMOOTHED BEAMS ON THE ABC FACILITY

A. CARUSO, C.STRANGIO, P.L.ANDREOLI, G.CRISTOFARI, A. DATTOLA, P. MACI.
Associazione EURATOM- ENEA sulla Fusione, C.R. Frascati
Via E.Fermi, 27, 00044 Frascati (Italy)

In this paper we present experiments performed with the ABC facility, in the framework of Inertial Fusion Physics and Technology Group entrusted task, to maintain a critical evaluation capability on energy oriented ICF, in the context of the ENEA-EURATOM association.
Specifically we discuss the studies on laser ablatively accelerated thin foils and on the smoothing effects induced by coupling a beam integrator to the focusing lenses. A comparison with experiments performed in the same regimes without this additional optical system will be described, as well as normalisation, based on the experimental results, of some theoretical models included in our 2D (COBI3) and 1D (COMO3) codes.

1 Introduction

The ABC facility was built for ICF energy oriented studies. It includes a two beams neodymium glass laser (driven by a 0.15 THz bandwidth glass oscillator), an appropriate focusing optics (a smoothing system being available), diagnostics and a small area for target preparation. The Neodymium glass laser powering the facility is characterised by:

- maximum power density: 3×10^{15} W/cm^2 (by F/1 optics);
- minimum spot size: 40 μm;
- FWHM duration (fig.1):   3 ns;
- operating wavelength: 1.054 μm;
- optional: 2ω conversion.

The two laser beams are focused on the target throughout two (holed) aspherical F/1 lenses (focal length = 10 cm) placed inside the vacuum chamber. A suitably designed array1 composed by random thickness lenses (beam integrator) may be

easily coupled to (or removed from) each F/1 lens for near field ISI smoothing, see Fig 2. As shown in the same figure, the interaction experiments have been performed with circularly polarised light.
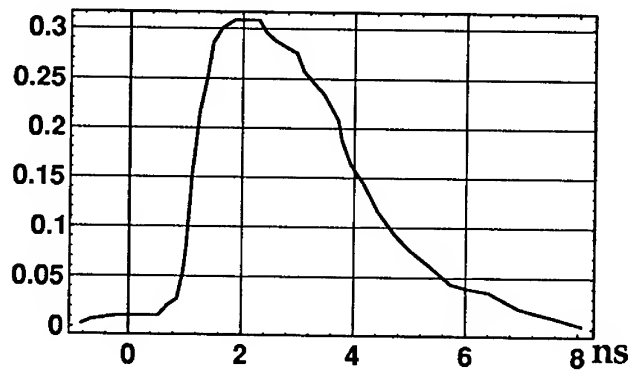
Figure 1: Power time dependence of the ABC laser pulses
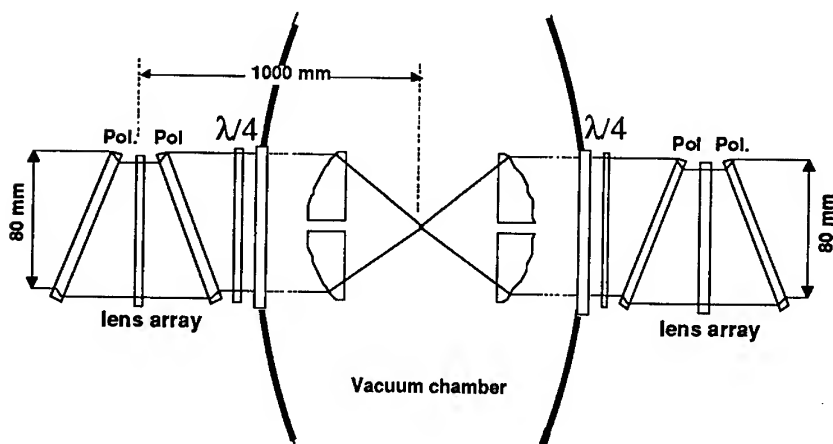
Figure 2: The final transport optics on the ABC facility. Two lens arrays can be inserted outside the vacuum chamber to produce ISI smoothing.

Without smoothing technique applied, the standard focusing optics generates spots with a 6% flat top peak-to valley modulations (Fig. 3).
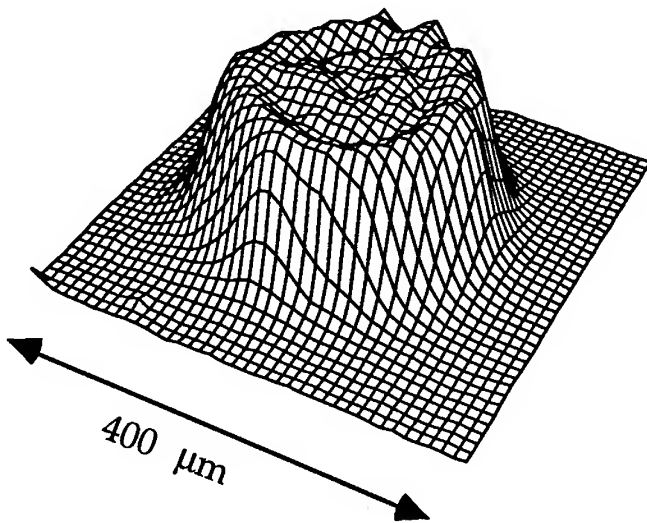
Figure 3: Intensity distribution profile in the focal region without smoothing system as measured in operative conditions.

By coupling the beam integrator to the standard focusing lenses, a rather smooth distribution near the focal plane (Fig. 4) has been found by measurements performed in operative conditions.
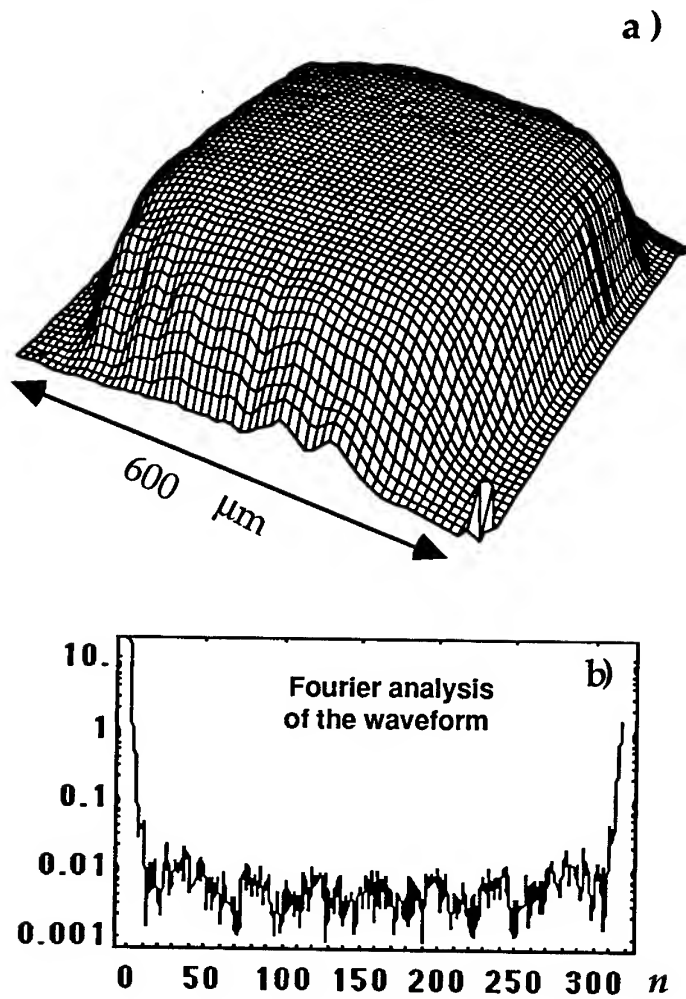
Figure 4: Energy distribution profile in the focal region with smoothing system inserted (a). The relative space mode intensity distribution for a middle profile section (b).

The studies we shall discuss in the following are essentially based on time resolved optical diagnostics and time resolved X-ray imaging, both aligned for side views according to the general lay-out displayed in Fig.5.
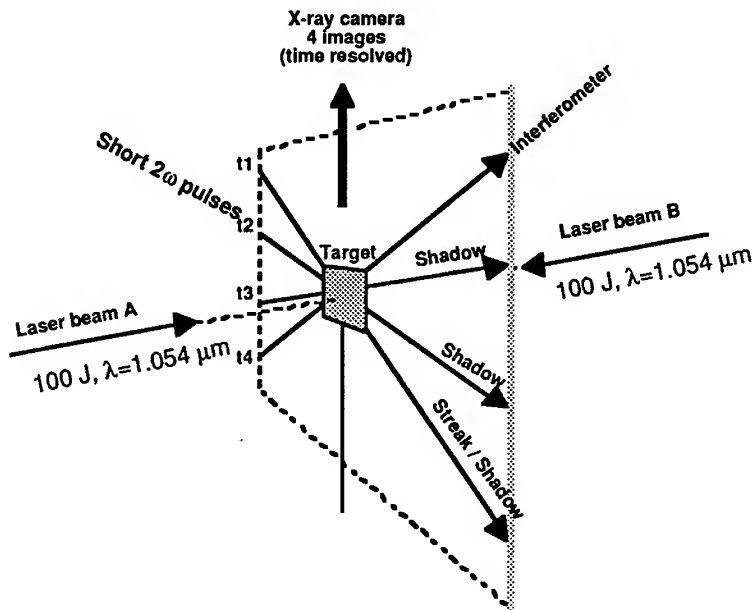
Figure 5: General lay-out of diagnostics and irradiation geometry.

Four 2ω low energy short pulses (FWHM$\approx$ 300 ps) are synchronised with the laser driving pulse and are available in the same shot, to probe the irradiated target at different times (between $t \approx$ -1 ns and $t \approx$ +15 ns.). These pulses are independently processed according to the diagnostic set-up on each line and sent to form images on four cameras.

The image processing optics is flexible enough to render techniques such as Schlieren, dark field shadowgraphy and interferometry, possible through simple changes in the optics. In the same shot, at different instants referred to the laser target interaction, are also taken four X-ray frames by a 2D time gated imaging system (Fig. 6).
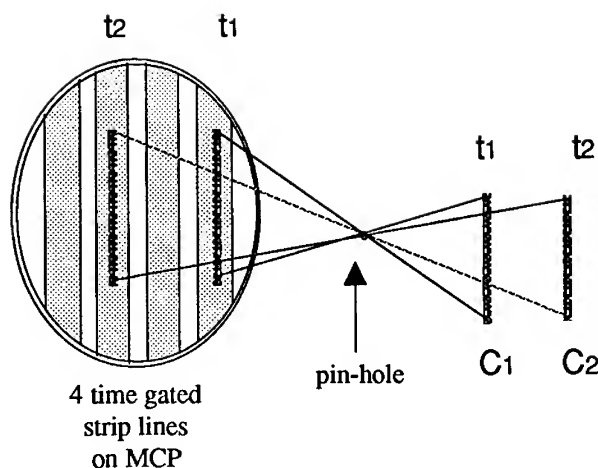
Figure 6: Time resolved X-ray imaging for the dense phase evolution. A target passing from the configuration C1 at time t1 to the configuration C2 at time C2, is imaged trough a single pin-hole on the time gated strip lines.

The experiments have been performed by using as targets on-stalk mounted thin SiO_2 square foils (700x700x4mm) of very high optical surface quality.

2 Experimental results

In fig. 7 it is shown the optical interferometry of a thin SiO_2 foil irradiated through the focusing lenses without beam integrator. In this situation, in spite of the 6% modulation on the illumination profile flat top, we have observed smooth dense phase displacement.

This feature is maintained for a quite long time (up to $\approx$ 15 ns).
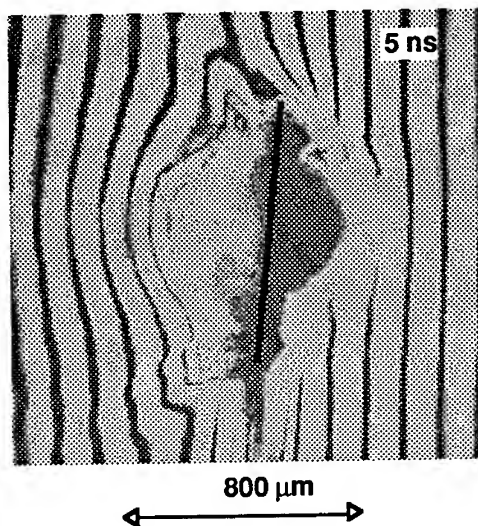
Figure 7: Time resolved interferogram showing the dense phase displacement and the corona structure for a target accelerated with the laser pulse and focusing conditions represented in figures 1 and 3. The time delay is taken from the beginning of the high power ramp of figure 1. The straight line represents the initial target position.

In the explored regimes the corona X-ray emission remain intense enough to be useful for the 2D time resolved imaging assembly for about 1.5 ns. With this constraint, to take X-ray images of the dense phase motion, with delays greater than this time, we have operated (with proper delay respect to the driving beam A) the laser beam B (Fig.5) to produce a secondary X-ray source on the rear side of the displaced dense phase.

With this method, especially advantageous because it provides a fiducial for the initial target position, we have obtained results (Fig.8) in very good agreement with the optical diagnostics observations.

With the beam integrator inserted dense phase displacements have been observed that are quite planar. The resulting corona structure is also very smooth and reproducible as clearly shown by optical diagnostics. This scenario has been confirmed by X-ray images, showing thin foils accelerated over 100÷200 μm, and still maintaining a flat and smooth structure (Fig.9).

272
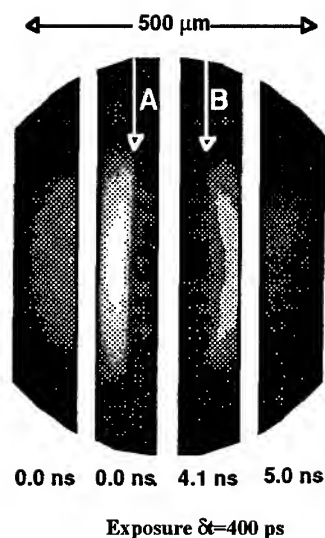
Figure 8: Time resolved X-ray imaging showing the dense phase displacement for a target accelerated with the laser pulse laser pulse and focusing conditions described in figures 1 and figure 3. The arrow A indicates the initial target position, the arrow B corresponds to the dense phase displacement.

The results obtained in these experiments have been also used to check and normalise theoretical models, e. g., for a simple electronic heat diffusion description based on a flux limiter, which is included in our numerical codes (2D-COBI3 and 1D-COMO3) [2].

Fig. 10 shows, as an example, the sensitivity of the theoretical dense phase profile to the value of the flux limiter. Comparison with the experimental dense phase displacement profile allows the selection of the proper value.
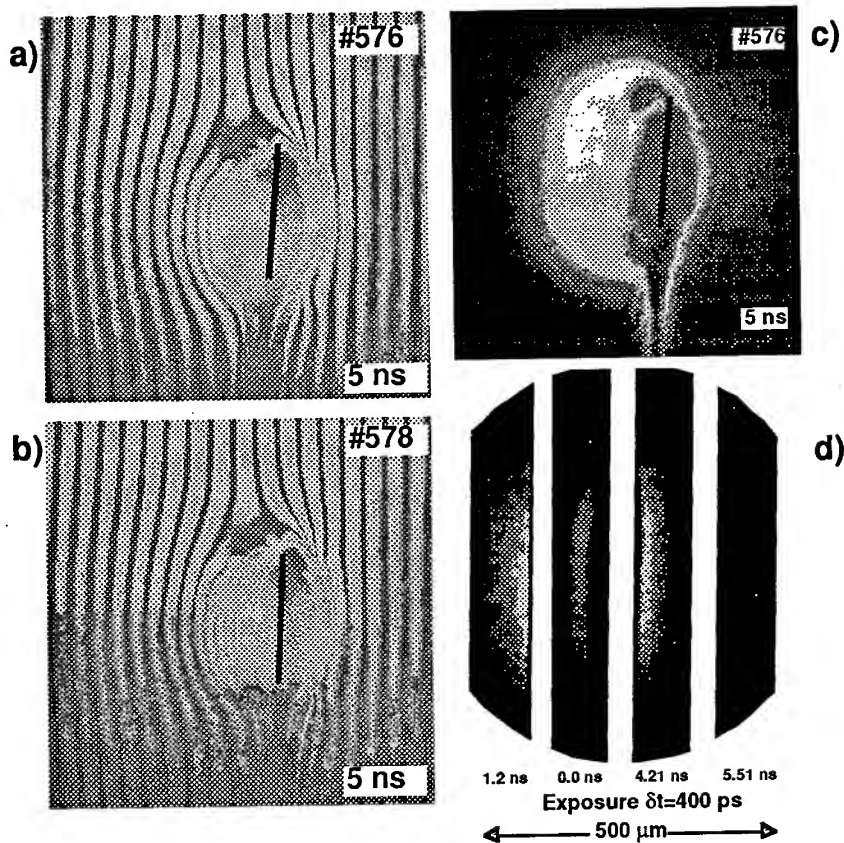
Figure 9: Optical and X-ray imaging for a target accelerated with the laser pulse and focusing conditions described in figure 1 and figure 4. The interferograms a), b) show the shot reproducibility as well as the smooth corona structure confirmed by the dark field shadowgraphy displayed in c). The X-ray frames show the target planar displacement starting from the initial position at t=0.0 ns to that reached at t=4.21ns. The straight lines represent the initial target position.

274
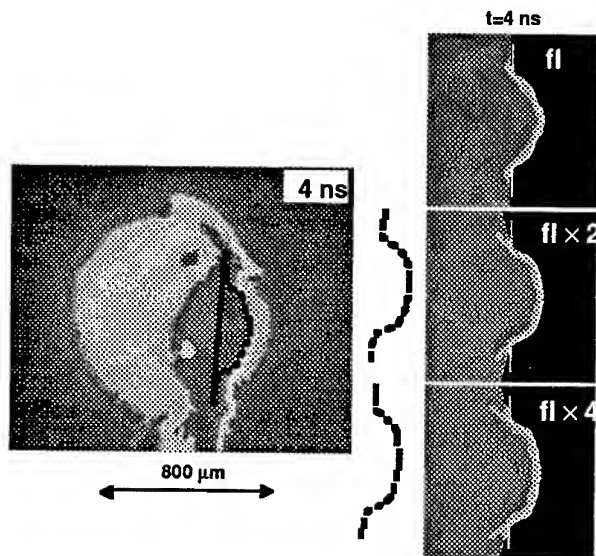
Figure 10: Dense phase displacement as predicted by code COBI3 for three different values of the flux limiter. These simulations have been performed for the laser pulse and the focusing conditions described in figure 1 and figure 3. Only for a value fl the shape agrees with the profiles experimentally observed. The straight line represents the initial target position.

References

1. C. Strangio and A. Caruso, Laser and Particle Beams, **8**, 135 (1990).
2. The mentioned numerical simulations performed with code COBI3 and COMO3 of Inertial Fusion Physics and Technology Group at ENEA Frascati, have been made by V.A.Pais.

IGNITION CONDITIONS AND FUEL ENERGY GAIN OF SPARK-IGNITED AND VOLUME-IGNITED ICF TARGETS

S. ATZENI, M.L. CIAMPI,[a] A.R. PIRIZ [b]

Associazione EURATOM-ENEA sulla Fusione, C.R.E. Frascati
C.P. 65, 00044 Frascati (Rome), Italy

The fuel gain of compressed DT microspheres, with initial conditions of relevance to different ICF approaches, is computed by 1-D radiation-hydrodynamic simulations. The formation of the central hot spot at collapse of an imploding shell and the velocity scaling of the energy threshold for the achievement of central ignition are discussed. Pulse requirements for fast-ignitors are also studied by 2-D simulations.

1 Introduction

Studies on the achievement of ignition in ICF targets rely on complex numerical simulations,[1] also at our laboratory we addressed some symmetry issues by 2-D simulations,[2] and other aspects of ignition energetics by 1-D radiation hydrodynamics studies.[3] Nevertheless, simple model problems, isolating a few basic processes, can still provide guidance to current target research. In this paper we first summarize the main results of recent work comparing the burn performance of compressed fuel configurations relevant to different ignition schemes. Next, with reference to central ignition in a collapsing shell, we discuss spark formation and the velocity scaling of the ignition energy threshold. Finally, we study the pulse requirements for the recently proposed fast-ignitor scheme,[4] in which the ignition spark is created close to the surface of an already compressed fuel. Preliminary results are also presented of a study on (pure) deuterium burning fast-ignitors.

2 Fuel energy gain of compressed DT microspheres

A systematic study [5] has been performed by 1-D radiation hydrodynamic simulations of the burn of compressed fuel assemblies, with radius r_c, initially at rest, and with the following initial conditions (i.c.): a) isobaric i.c., with a central hot spot, surrounded by denser, cold fuel; b) isochoric i.c., with a central hot spot in a homogeneous fuel; c) homogeneous density and temperature. Case a) is relevant to the standard, central ignition approach to ICF, case b) to fast-ignitors, case c) to volume ignition. In all cases we consider step

---

[a]ENEA-SIF fellow
[b]Permanent affiliation: CONICET, Argentina

profiles and denote with r_0, ρ_0 and T_0, the radius, density and temperature of the hot region. In cases a) and b) the isentrope parameter, α, is introduced, as usual,[6,7] to characterize the status of the cold fuel. Burn performance is measured by the fuel gain G_F (the ratio of the fusion yield to the compressed assembly initial energy E).

For centrally ignited targets, the limiting gains $G_F^*(E, \alpha)$, that is the maximum gains that can be achieved by fuel assemblies with internal energy E and bulk isentrope α, are fitted by

$$G_F^{*\text{isobaric}} = 5600 \left(\hat{E}\alpha^{-3}\right)^{0.3}, \tag{1}$$

$$G_F^{*\text{isochoric}} = 19200 \left(\hat{E}\alpha^{-3}\right)^{0.4}, \tag{2}$$

where $\hat{E} = E/(1 \text{ MJ})$. The scalings with E and α are just those predicted by well known analytic models,[6,7] notice that the advantage of isochoric over isobaric configurations is found smaller than previously anticipated,[6,7] due to the more restrictive ignition condition for the isochoric case. Indeed, pressure inbalance between spark and bulk fuel results in large mechanical energy loss, so that the optimal ignition point is ($\rho_0 r_0 = 0.5$ g/cm^2 ; $T_0 = 12$ keV), to be compared with ($\rho_0 r_0 = 0.4$ g/cm^2 ; $T_0 = 5$ keV) or ($\rho_0 r_0 = 0.2$ g/cm^2 ; $T_0 = 8$ keV) which apply to isobaric i.c.

It is also found that the isobaric model,[6,7] using the burn fraction formula $f = \rho R/(\rho R + H_B)$ with a constant value of H_B, is inaccurate when r_0/r_c becomes substantially larger than value corresponding to limiting gain, and typically, for $r_0/r_c > 0.6$.[5]

For volume ignited targets (for which no scaling laws were previously published), we find that for fuel masses in the range 0.1–100 mg, the limiting gain is well approximated by

$$G_F^{*\text{vol.ign.}} = 1000\hat{E}^{0.16} \tag{3}$$

The comparison of Eqs. (1), (2), and (3) confirms that if a spark can be created without raising the entropy of the bulk fuel too much, spark ignition has a considerable advantage over volume ignition.

3 Central ignition by shell implosion

In the standard approach to ICF, the ignition configuration is created at the collapse of a shell, which implodes with velocity v_i. Straightforward use of the isobaric model[6] leads to estimating the fuel energy required for ignition

as $E \propto (T_0 \rho_0 r_0)^3 \alpha^3 v_i^{-10}$. In fact, the ignition conditions do depend on v_i and α, and the configuration is not strictly isobaric. An improved evaluation can be performed by a model, whose details are given elsewhere,[8] describing the process of spark formation at collapse, and also considering more realistic profiles.[9] Such profiles exhibit a transition layer (with $r_0 \leq r \leq r_h$) between the hot spot, where α is very large, and the cold fuel, where α is low and uniform; the density gradually rises in the transition region, peaks at $r = r_h$ and decreases again for $r > r_h$. It was shown [9] that in such a case a relevant parameter is $H_h = \int_0^{r_h} \rho dr$, and that the energy required for ignition is $E \propto H_h^3 \alpha^3 v_i^{-4}$. In the model the shell is considered to stagnate isentropically, except in a central region of the fuel where the balance is dominated by heating by compressional work and cooling by thermal conduction and radiation losses; a relationship can then be found between H_h, the peak temperature T_m and v_i (approximately, $T_m \propto H_h^{6/25} v_i^{26/25}$). A velocity $v_i > 2 \times 10^7$ cm/s is required to overcome conductive losses and to reach $T_m \geq 5$ keV, so that alpha-particle heating becomes significant. As the shell comes close to rest, fusion alpha particles must replace compressional work as the heating mechanism, and this leads to an ignition condition of the form $(\overline{\sigma v})_m T_m^{-3} H_h > v_i S$, where S is a weakly varying function depending on details of the target and pulse design, and $\overline{\sigma v}$ is the reaction rate. Inserting the proper expression for T_m, one then gets an ignition condition in the approximate form $H_h > g(v_i)$; the function g takes a minimum $H_{min} = 0.8$ g/cm^2 at $v_i \approx 4 \times 10^7$cm/s. For $3 \times 10^7 \leq v_i \leq 4 \times 10^7$cm/s, the ignition boundary is defined by $H_h \propto v^{-a}$, with $a = 0$–0.4.

The ignition energy then scales as $E \propto v^{-(4+3a)}$, which is in reasonble agreement with the v_i^{-5} dependence found by 1-D implosion simulations,[1] and also with hohlarum target studies performed at our laboratory.[3] Also notice that 1-D simulations [3] show that ignition is only achieved if the global $\rho R \geq 1$ g/cm^2, which is roughly consistent with the above requirement on H_h.

4 Pulse parameters for fast ignition

The pulse parameters (energy E_p, power P, and flux Φ) for fast ignition can be roughly estimated by using the ignition conditions for isochoric i.c. (Sec.2) and evaluating the spark mass as $m \approx (4\pi/3)\rho_0 r_0^3$, the pulse duration as $t \approx r_0/c_s$, (c_s: sound speed) and taking the beam radius equal to the spark radius. One thus gets $t \approx 40/\hat{\rho}$ ps, and energy $E_p \geq 72/\hat{\rho}^2$ kJ, where $\hat{\rho} = \rho/(100\text{g/cm}^3)$. For a better evaluation we have performed 2-D simulations, considering a DT sphere or cylinder at high density, ρ, heated by fast particles with range at 10 keV comparable to the hot spot diameter (this exploits an idea first presented by Caruso[10]). For $50 \leq \rho \leq 1000$ g/cm^3 the required pulse parameters

turn out to be fitted, to within 12%, by

$$E_p = 140\,\hat{\rho}^{-1.85} \text{ kJ} \tag{4}$$

$$P = 2.9 \times 10^{15}\,\hat{\rho}^{-1} \text{ W} \tag{5}$$

$$\Phi = 2.4 \times 10^{19}\,\hat{\rho}^{0.90} \text{ W/cm}^2 \tag{6}$$

We have also begun a study on fast-ignitors burning pure deuterium fuels. The work is in progress, but a few preliminary comments can already be made here. First, given the high value of the burn parameter, densities about 10^4 times the solid density are required to achieve significant burn with a fuel mass of interest to ICF. In addition, from the relevant ignition condition ($\rho_0 r_0 \geq$ 8 g/cm^2 at $T_0 \approx 25$ keV) it follows that igniting pure deuterium requires, at a given density, about 10^4 more energy than igniting DT. However, in a deuterium-based economy one can still exploit the tritium (and the ^{3}He) bred in the targets and left unburnt.[12] E.g. one can conceive targets with DT hot spot and pure-D bulk fuel. We have tested [11] that a sufficiently large amount of DT, ignited by a pulse satisfying Eqs. (4)–(6), can drive the burn of a large, very dense deuterium pellet. Whether this is still feasible in a target where the tritium mass (concentrated in the spark) is only about 1–2% of the total (spark and bulk) deuterium mass can only be answered by simulations with accurate neutron transport. Simulations with diffusion of all charged fusion products and knocked-on deuterons, but with local interaction of 2.45 MeV neutrons and neglect of 14 MeV neutrons, indicate that this could be marginally possible.

References

1. J.D. Lindl, *Phys. Plasmas* **2**, 3933 (1995), and refs therein.
2. S. Atzeni, *Europhys. Lett.* **11**, 639 (1990); *Laser Part. Beams* **9**, 233 (1991).
3. S. Atzeni and M. Temporal, to appear in *Fusion Eng. Design*
4. M. Tabak *et al.*, *Phys. Plasmas* **1**, 1626 (1994).
5. S. Atzeni, *Jpn. J. Appl. Phys.* **34**, 1980 (1995).
6. J. Meyer-ter-Vehn, *Nucl. Fusion* **22**, 561 (1982).
7. M. Rosen and J.D. Lindl, LLNL, rep. UCRL 50021-83 (1984) p. 3-5.
8. A.R. Piriz, to appear in *Nucl. Fusion*.
9. A.R. Piriz and J.G. Wouchuk, *Nucl. Fusion* **34**, 191 (1994).
10. A. Caruso and V.A. Pais, to appear in *Nucl. Fusion*.
11. S. Atzeni and M.L. Ciampi, to be published.
12. M. Ragheb *et al. J. Fusion Energy* **4**, 339 (1985).

The Different Approaches To The Laser Target Design For Fusion-Fission Reactor

N.G.Basov, L.P.Feoktistov, I.G.Lebo, V.B.Rozanov
The Lebedev Physics Institute (FIAN), Moscow 117924, Leninsky Pr.
53, Russia
V.F.Tishkin
The Institute of Mathematical Modelling (IMM), Moscow 125047,
Miusskaya sq.4, Russia

1. Introduction

It is necessary to reach large gains in laser target (G) to get useful
energy in a fusion reactor. Using the fission blanket in reactor allows
one to increase the energy gain. In [1] it was suggested to use a
two-cascade hybrid reactor scheme, allowing one to reach gain in
fission blanket more than 1000. As a result it will be possible to use
laser target with $G \sim 0.1 - 1$ in such type of a reactor.

In order to achieve $G \sim 0.1 - 1$ in direct-driven target it is necessary to
irradiate the shell pellet uniformity by laser pulse with energy $\sim$
100-200 kJ. But it demands to use a lot of laser beams around target
to provide with spherical symmetry of laser irradiation. Large surface
"will be lost" for fission blanket.

It is necessary to use about an five-ten times more laser energy to get
"ignition" in indirect driven target.

In [2] it was suggested the new target design, named "Greenhouse
target". It is very important problem to compensate the negative
influence of holes on compression symmetry. It was suggested in [3] to
use the target with "relief" to compensate this effect. This target
design is studied now.

In [4] we discussed two types of target designs for such reactor - 1)
target with inner laser energy input and 2) high aspect ratio target for
long time laser pulse. As follows from 1D simulations, one can achieve
$G \sim 0.1$. But there are very complicated problems - short pulse ($\tau \leq$
0.1 ns in first case), the stable implosion (in second case),
non-onedimensional geometry.

We continue here to study the other approaches to the laser target
design for hybrid reactor.

The numerical simulation were made by using Lagrange code
"ATLANT" [5].

2. Conic Target.

It is easier to reach 10% and more of the pump energy conversion into the laser emission by making use a laser facilities with pulse duration of 100 ns. This would allow one to close to energy cycle at G ~0.1, when the gain of the blanket is over 1000.

Fig.1a presents the scheme of a two-cascade cryogenic conic target. The acceleration of the external gold shell has been modeled by 1D simulations. It is assumed that the cone walls do not influence the shell acceleration at this stage. The stage of the shell deceleration has been described with the help of the model given in [6,7]. The model assumes that the temperature and density of the DT-fuel and the shell are constant in space, and change with the time. The cone wall, as a whole, moves under the fuel pressure with the velocity $\sqrt{\frac{2P}{(\gamma+1)\rho}}$, where P is the pressure in fuel; ρ , the wall density; γ , the adiabatic constant in the wall.

Main results.

1) To reach the neutron yield of $10^{15} - 10^{16}$ the mass of the fuel should be ~ 500 μg and the external shell velocity more than 400 km/s;

2) the cones should have the radius $R \sim 1$ cm, and the targets should have the aspect ratio $As \sim 500 - 1000$. The laser pulse must be of the energy of ~ 1-2 MJ, and the pulse wavelength must be 0.27 μm. The radiation intensity must grow with the time toward the end of the pulse. In this case 75% of the energy should be deposited into the plasma during 25% of the pulse duration (total pulse duration is 60-80 ns); 3) The fuel temperature and neutron yield may be increased, if one uses a two-side irradiation of the target illustrated in Fig.1b (double conic target). Such target design makes it possible to use two laser beams of the same power, and this will allow one to increase the fuel temperature due to the collision of the shock waves in the apex of the cone.

It is possible to use other scheme. The second laser pulse must be more powerful and short ($t \leq 0.1$ ns) but it may be of smaller energy. It should be introduced into the DT-plasma just at the moment when the fuel accelerated by long laser pulse reaches the apex of the cone; 4) the problem of the acceleration of such high-aspect targets in the cones, the stability of their implosion, as well as the problem of the wall influence require additional investigation.

3. Spherical Shells And Conic Targets Under "Exploding Pusher" Regime Destined For CO_2 - Laser.

We have made 1D numerical simulations (in 2T and 3T physical models) of the gold (DT-fuel filled) shell compression in the regime of the "exploding pusher". At laser intensities of $\sim 10^{14} - 10^{15} W/cm^2$ the temperature of the hot electrons is $\sim 40 - 100$ keV (see [8]), the free path in gold $\sim 10 \mu m$. The multi-layers (polyethylene - gold - DT-ice) spherical targets. Outer radius $R_1 \sim 900 - 1200$, μm, mass of shell $M_{Au} \sim 2 - 3 mg$, M_{DT}, mass of fuel, $= 600$ μg, E, the absorbed laser energy, ~ 300 kJ E_{em}, emanated X-ray energy from surface, ~ 40 kJ, Main results.

1) It is shown that one can reach the neutron yield of $10^{15} - 10^{16}$ at the absorbed energy of 300 kJ, and instanteneous energy deposition under "Exploding pusher" regime. The calculations assumed an instanteneous and homogeneous (over the mass) energy release in plasma due to the energy trasfer by hot electrons. Spectral distribution of the electrons energy is not taken into account; 2) the creation of the layered targets with different density of the layers (e.g. polyethylene - Au - DT-liquid) will enable one to increase the neutron yield at a fixed absorbed energy; 3) one of the target possible designs may be the "exploding cone", when the radiation comes to the fuel through the holes (Fig. 2b). The problem of the longwave radiation absorption efficiency, the mechanism of the energy transport in plasma will be considered.

Short Conclusion.

The possibility to use in the fusion-fission reactor the targets with the gain less than 1 significantly extends the range of the lasers and target designs. There appears a possibility to turn to low-compressed targets (for example, conic targets) and longwave laser or the shortwave lasers with long pulse duration. The choice of the target design depends mainly on what gain coefficient may be attained in a two-cascade reactor.

References.

1. Feoktistov L.P. Matematicheskoe modelirovanie, (1995),.27,N3,p.41 (in Russian)

2. Gus'kov S.Yu., Rozanov V.B., Zmitrenko N.V. ZhTEF, (1995),108, p.548

3. Lebo I.G., Popov I.V., Rozanov V.B., Tishkin V.F. Kvantovaja elektronika,(1995),v.22 (in Russian)

4. Lebo I.G.,Rozanov V.B.,Feoktistov L.P.Tishkin V.F. Large-Scale Laser Target Design. Alternative Approaches. Laser Interaction and Related Plasma Phenomena. (Osaka,Japan,April 24-28,1995)

5. Lebo I.G., Popov I.V., Rozanov V.B., Tishkin V.F. Journal of Russian Laser Research, (1994),v.15,p.136

6. Taran M.D., Tishkin V.F., Favorski A.P., Feoktistov L.P., Preprint of Keldish Appl.Math.Institute,N127,Moscow-1980 (in Russian)

7. Gamaly E.G., Lebo I.G., Rozanov V.B. Preprint FIAN N97, Moscow-1981 (in Russian)

8. ICF Quarterly Report, Lawrence Livermore National Laboratory, April-June 1994,v.4,N3
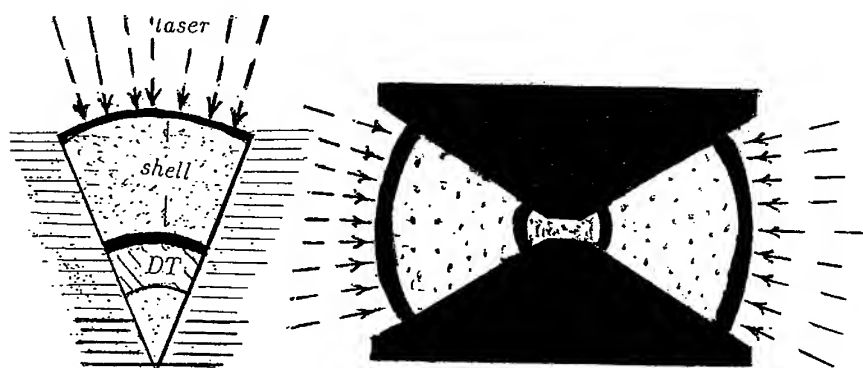
Fig.1 a) Two-cascade conic target; b) Double-side conic target
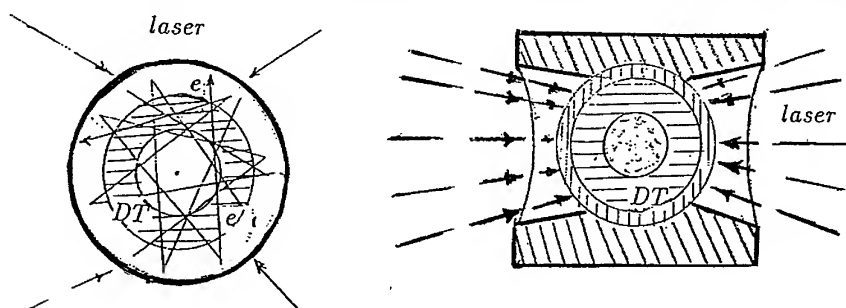
Fig.2 "Exploding pusher" spherical (a) and conic (b) targets

SUPERSONIC CUMULATION JETS PRODUCED IN LASER-DRIVEN HOLLOW-CHARGES

J.M. MARTINEZ-VAL, P.M. VELARDE, M. PIERA
Institute of Nuclear Fusion, E.T.S.I.I.
Madrid Polytechnic University, Spain

Conical liners imploded under the action of chemical explosives
are currently used in jet-forming hollow charges. Those jets do not
need to reach supersonic speeds for current practical applications.
However, new possibilities could be taken into account in the case
of supersonic jets. For instance, they could be used to ignite fusion
burning waves in fusionable pellets. Moreover, they could be ap-
plied to the study of new physical situations characterized by very
high energy densities and pressures in very small volumes.

Cumulation jet principles

A standard hollow-charge corresponds to an empty cone made inside a block
of chemical explosive. This empty space is lined with a metalic coating thick
enough to generate a massive jet and thin enough to reach high collapsing speed
under the action of the detonation wave created by the chemical explosion.

An alternative to the standard hollow charge is depcited in figure 1, where
a conical foil (of Al, iron, Au or any solid material) is illuminated either by
a laser beam (direct drive) or by the thermal radiation field created inside a
hohlraum illuminated by a laser (indirect drive). The cone walls can reach
supersonic collapsing speeds, as it usually happens in Inertial Fusion Targets.

Chemical explosives detonated around conical liners [1-9] are currently used
(since the Second World War) as armor-piercing weapons. The detonation
wave compresses the metal liner inwards and generates a ultrafast jet (or cu-
mulation jet, see figure 2) that can penetrate a thick metallic shielding.

Jet speeds of the order of 3 km/s have been routinely achieved for alu-
minum liners, which implies an energy density ρv_j^2 of $2.5 \times 10^{13} J/m^3$ (which is
equivalent to 250 Mbar of Pressure when the momentum conservation law is
written to analyze the impact of such a jet. As the plastic strength of a metal

is about $5 \times 10^8 N/m^2 (5kbars)$, it means that the jet can easily produce the plastic deformation of any metal, i.e., it can penetrate it.

Figure 2(a) represents the collision in the laboratory frame of reference. Figure 2(b) shows the same collision in a reference frame fixed to the collision point. As a a symmetric collision is assumed, the lower plate is subsituted by a perfectly rigid plane (in the conical case, this line would be the cone axis).

If Bernouilli equation is applied around this point, and we consider $P_p = P_j$ (and both of them much smaller than $\frac{1}{2}\rho w^2$) we can also assume (for incompressible fluids) $\rho_j = \rho_p$. Thus

$$w_j = w_p = \frac{v_p}{tan\alpha} \qquad (1)$$

Hence, the jet speed is

$$v_j = v_c + w_j = v_p \left(\frac{1}{tan\alpha} + \frac{1}{sin\alpha} \right) \qquad (2)$$

It must be pointed out that at a very small conical angel α, the jet speed becomes exceedingly large. However, the assumption of incompressible fluids is no longer valid in this case [5-7]. First of all, it must be noted that w_p becomes very large as α decreases, and the fluid plate speed (in the collision reference frame) will be supersonical. In that case, shock waves will appear and the fluid will be compressible.

On the other hand, it is easy to show that the jet mass tends to zero as α does. (Hence, the jet becomes useless). If we call m_p the plate mass (per unit length) and m_j is the jet mass and m_s is the slug mass, conservation equations of mass and horizontal component of the momentum give

$$m_j = m_p sin^2(\alpha/2) \qquad (3)$$

However, if we also compute the energy conversion efficiency (from plate kinetic energy into jet kinetic energy) it is found

$$n_j = \frac{m_j v_j^2}{m_p v_p^2} = cos^2\left(\frac{\alpha}{2}\right) \qquad (4)$$

Nevertheless, when $\alpha = 0$ we have a head-on collision and the former picture is not valid. Moreover, it has already been said that the plates will act as a compressible fluid once the relative speed w_p becomes supersonical. In laser-driven conical liners this would be the case, and the analysis has to be modified accordingly.

Early after the War it was already theoretically postulated [5] that the collapse of metal plates in a hollow charge would be jetless if the semi-angle α

was below a critical value that depends on the collapsing velocity of the plates v_p.

Some authors [2,4] make calculations for conical liners with the same equations of the planar case, although a different collision speed w_p can be assumed for different sections of the cone (in general w_p is considered to be decreasing and so is the jet speed in many experiments [3,4]. Nevertheless, with a suitable detonation wave geometry, w_p can be tailored as an increasing function of time). In any case, jets coming from supersonic collapses seem to be non-cohesive [6,7], and the radius of the jet increases as the standoff does.

Our preliminary analysis of conical liners indicate that the critical value of the cone half-angle (below which a jet is not formed) is smaller than the value predicted by the planar theory. In the jetless case, a standing shock is attached to the collision apex (that moves at v_c speed in the laboratory frame). In the shock, the liner density jumps from its nominal density to a higher density. If m stands for the ratio of densities ($m > 1$) it can be seen that the pressure behind the shock scales almost as m^2. This jump has to be compatible with the material Hugoniot and with the mass conservation principle. In a cone, as the liner flows to the collision apex, the flow cross section is not constant, because it goes to zero (theoretical limit) as the radius does. Hence, the jump in density has to be larger to accomodate the incoming flux, than in the planar case. Hence, for the planar critical angle, a conical hollow-charge has to produce a jet (under the same boundary conditions).
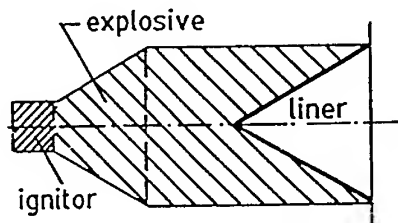
Fig. 1.-   A standard hollow-charge
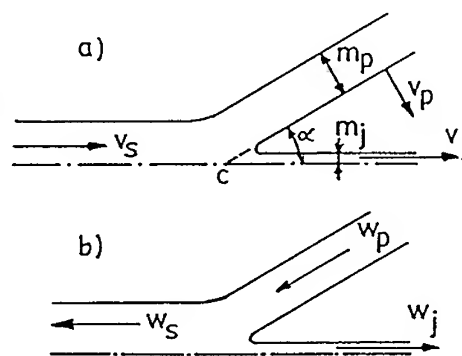
Fig. 2.-   Hydrodynamic equations in the laboratory frame (a) and in the collision point frame (b)

Such a jet could be used to trigger a fusion burning wave inside a fusionable pellet. For that purpose, it is important to increase the jet cross section up to a value close to the range of the fusion product charged-particles. Of course, the specific kinetic energy or the jet has to be large enough to heat supesonically the ignitor region of the pellet, that must have a size of R^3, where R is the range of the fusion product charged particles that reheat the plasma and sustain the fusion wave propagation.

For the DT reaction in a pellet at nominal density $(0.2g/cm^3)$ both the ignitor mass and the jet energy have to be very large, 145 mg and 620 MJ. However, if the DT pellet is previously compressed to $10g/cm^3$, the ignitor mass is only 60 μg and the jet energy 240 kJ, because both magnitudes scale as ρ^{-2}. In all the cases, the jet speed has to be higher than $5 \times 10^8 cm/s$. If a velocity multiplication factor of 10 is achieved in the hollow-charge collapse, it would require a collapsing speed of the liner of $5 \times 10^7 cm/s$, which can be produced by laser-driven ablation.

References

1. G. Birkhoff, D.P. Mac Dougall, E.M. Pugh and G. Taylor. *J. App. Phys.*, **19**, 563 (1948).

2. E.M. Pugh, R.J. Eichelberger and N. Rostoker. *J. Appl. Phys.*, **23**, 532 (1952).

3. R.J. Eichelberger and E.M. Pugh. *J. Appl. Phys.*,**23**,537 (1952).

4. W.S. Koski, F.A. Lucy, R.G. Shreffler and F.J. Willig. *J. Appl. Phys.*,**23**, 1300 (1952).

5. J.M. Walsh, R.G. Shreffler and F.J. Willig. *J. Appl. Phys.*, **24**, 349 (1953).

6. G.R. Cowan and A.H. Holtzman. *J. Appl. Phys.*, **34**, 928 (1963).

7. P.C. Chou, J. Carleone and R.R. Karpp. *J. Appl. Phys.*, **47**, 2975 (1976).

8. V. Ya. Ternovoi. "Jet formation in plasma compression in acute-angle geometry". Translated from Zhurnal Prikladnoi Mekhaniki i Tekhnicheskio Fiziki, no. 5, pp 68-73, Sept.-Oct. 1984, Plenum Pub. Co. (1985) UDC-533.082.5.

9. E. Zababakhin and I. Zababakhin. "Unlimited Cumulation Phenomena", Chapter 1, Nauka Publishers, Moscow (1990).

10. J.M. Martinez-Val, M. Piera. "Fusion burning waves ignited by cumulation jets". Submitted to *Fusion Technology*, (1996).

FORMING AND SMOOTHING D$_2$ AND HD LAYERS FOR ICF
BY INFRA-RED HEATING

G. COLLINS[1], D. BITTNER[2], E. MONSLER[2], D. TISZAUER[1], and M. FEIT

[1] *Lawrence Livermore National Laboratory, University of California,*
Livermore, CA 94551

[2] *W. J. Schafer Associates, Inc.*
Livermore, CA 94550

We describe a technique to form and smooth uniform solid D$_2$, HD or D-T layers for inertial confinement fusion targets. Pumping the infra-red (IR) collisionally induced vibration-rotation band generates a bulk heating of the solid. Shadowgraphs reveal that this bulk heating quickly redistributes the solid into a relatively uniform layer depending on the IR intensity profile. Measured redistribution time constants are used to determine the conversion efficiency of IR light into bulk heating. Phase shifting interferometry reveals that the surface roughness decreases with increasing IR heating.

1. Introduction

Smooth and uniform 50 to 300 μm thick deuterium-tritium (D-T) layers on the interiors of 1 to 3 mm diameter spherical capsules are required for ignitable inertial confinement fusion (ICF) targets for the National Ignition Facility (NIF).[1] To form these layers, D-T is initially frozen to an anisotropic multicrystalline solid inside a capsule. The tritium decay heat generation in solid D-T, Q_{DT} = 0.05 W/cm^3, causes the thicker regions of the solid to have a higher temperature and thus a higher vapor pressure. This results in a redistribution of the solid until the inner D-T surface is isothermal. For an isothermal spherical capsule a D-T layer will be a uniform spherical shell.[2] The time constant for this redistribution (when no ^{3}He is present) is τ_0= lρ/Q$_{DT}$= 23 minutes, where l is the latent heat (J/mole), and ρ is the density (moles/cm^3). The surface continues smoothing until the thermal energy associated with material redistribution, is comparable to the surface energy gained in having to form a higher energy viscinal surface.[3] The surface structure of a multicrystalline D-T film is a function of the D-T bulk heating rate and the distribution of crystallite sizes and orientations which are determined by the initial nucleation and growth.[4]

Because there was no redistribution mechanism for non-tritiated solids and since the bulk heating rate (and thus the redistribution rate and surface roughness) for D-T is fixed, we have developed a technique to generate bulk heating in any hydrogen isotope or mixture. Pumping the infra-red (IR) collision induced vibration-rotation band generates a bulk heating of the solid, Q_{IR}. We have measured redistribution rates, (and thus Q_{IR}) in HD up to ten times higher than the D-T value. These values are limited only by the laser used in these experiments and vibrational relaxation time measurements suggest Q_{IR} can be ~1000

287

288

Q_{DT}.[5] This enables us to control the surface roughness for any hydrogen layer by infra-red heating. Phase shifting interferometry measurements show the surface roughness decreases with increasing infra-red heating to values well below the NIF specification.

2. Experimental setup

Figure 1 shows a sketch of the experimental setup. The sample cell consists of a 6 mm sapphire cube containing a 5 mm O.D. cylindrical hole. The hole is sealed by a sapphire window at the bottom and an infrasil window at the top of the cell. A hydrogen fill tube is glued into a 381 μm O.D. hole in the side of the sapphire cube. The cell is thermally and mechanically attached to the cold tip of a helium flow cryostat. An F- center laser generates the IR light. Two rotating diffusers remove spatial coherence in the beam, leaving a maximum speckle average of 0.1% with a coherence modulation factor 1/e distance of ~ 7μm.[6] The resultant beam has a Gaussian wavefront with a 5° divergence.
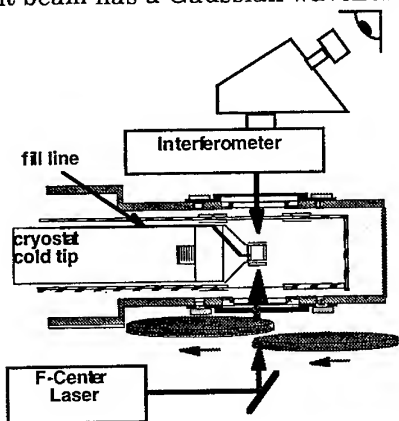
Fig. 1. The surface structure is controlled by a smoothed IR beam and measured by phase shifting interferometry. The IR beam is smoothed by two rotating diffusers.

3. Experimental results

To determine the conversion efficiency of IR light into Q_{IR}, we measured the redistribution time constant. Fig. 2 shows Q_{IR} versus incident flux for HD.[7]
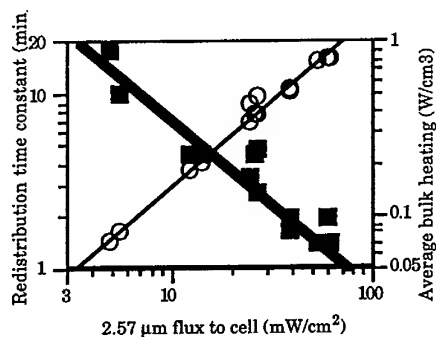
Fig. 2. Measured (dark squares) and calculated (bold line) redistribution time constants and the average heat generation rate (open circles and thin line) versus incident flux for HD.

IR illumination exhibits dramatic influence and control of the hydrogen layer profile. Figure 3 shows optical path depth interferograms of an HD layer illuminated with IR without any beam smoothing and after the beam is smoothed with two rotating diffusers. These results show that we can either modulate the hydrogen layer profile for advanced target designs or smooth the layer profile for high yield NIF targets. The bull's eye fringe pattern results from the Gaussian curvature in the smoothed IR beam.
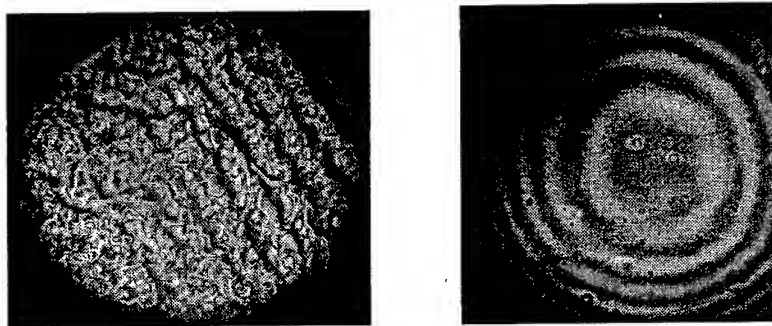
Fig. 3. Optical path depth interferograms of HD layers formed by ~ 50 mW of non-smoothed (left) and smoothed (right) 2.57 μm radiation.

Hydrogen surfaces are smoothed both by surface heat and bulk heat. Figure 4a shows the surface roughness rms versus Q_{IR} after removing the layer curvature. The Gaussian IR wavefront causes the Gaussian curvature in the layer. The length scale for these rms measurements is 3mm. The surface roughness decreases with increasing Q_{IR} to values well below the NIF specification. The solid line in Fig. 4a shows a best fit to surfaces smoothed by a surface heat flux. The ability to smooth an interface with either bulk heat or surface heat flux is proportional to the increase in surface temperature with

increasing layer thickness, $\delta T/\delta h$, where h is the layer thickness. For bulk heat $\delta T/\delta h \sim Qh/\kappa$, and for surface heat $\delta T/\delta h \sim F/\kappa$, where κ is the thermal conductivity of the solid and F is the surface heat flux. We plot the surface heat flux data in Fig. 4a by setting $F = Q_{IR}$ h.[3]
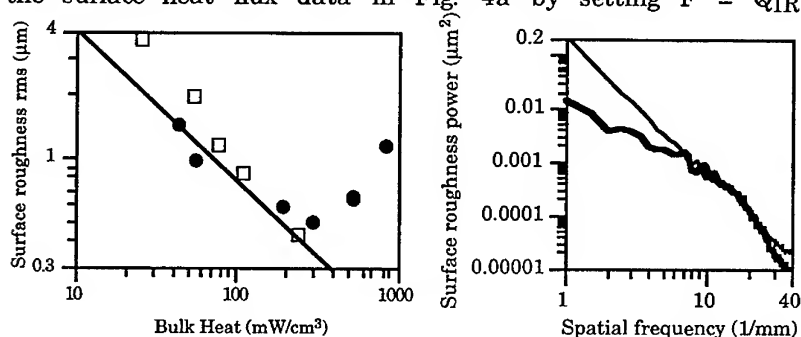
Fig. 4 (a) Surface roughness rms versus bulk heat for HD, 60 μm thick at 16 K,(open squares) and 100 μm thick at 16.4 K (dark circles). The bold line shows the surface roughness rms from surface heat flux experiments. (b) Surface roughness power spectra for 60 μm HD with 100 (thin) and 235 (thick) mW/cm^3

Finally in Figure 4b we show surface roughness power spectra for two smoothed HD layers. Bulk heating smoothes the low frequency components most effectively. Modeling shows that the efficiency of smoothing surface roughness, $\sim\delta T/\delta h$, decreases with spatial wavelength as

$$\frac{\partial T}{\partial h} \approx \frac{Q_{IR}h}{\kappa\sqrt{1+(2\pi h/\lambda)^2}}.$$

4. Conclusion

We have developed a technique to redistribute and smooth hydrogen (D_2, HD, D-T etc.) layers for ICF by pumping the rotation-vibration absorption bands of the solid. With this technique we can form modulated layer profiles for advanced target designs or smoothed layer profiles for high yield ignition targets on NIF.

[1]J. Lindl, Phys. of Plasmas, V2, N11:3933-4024 (1995). E. M. Campbell, J. C. Browne, Science 271 130-132 (1996).

[2]R. J. Simms, and R. B. Jacobs, J. Vac. Sci. Technol. A 6 (3), 1885 (1988); J. K. Hoffer and L. R. Foreman, Phys. Rev. Lett. 60, 1310 (1988); T. P. Bernat, E. R. Mapoles, and J. J. Sanchez, ICF Quarterly 1, 57 (1991).

[3]G. W. Collins, E. R. Mapoles, J. Sanchez, R. Bell, W. Unites, J. Hoffer, L. Forman, and J. Simpson, "Solid Hydrogen Surfaces," ICF Quarterly 3, 81 (1993).

[4]Solids Far From Equilibrium edited by C. Godreche, (Cambridge University Press., Cambridge, 1992). In this paper we ignore effects from ^{3}He born in the solid. The effects of ^{3}He cannot be ignored in DT layers which have aged for longer than ~ a day.

[5]C. Y. Kuo, R. J. Kerl, N. D. Patel, and C. K. N. Patel, Phys. Rev. Lett. 53, 2575 (1984).

[6]Partlo et al. J. Vac. Sci Tech. B 9 3126 (1991).

[7]In the redistribution experiments the HD was IR illuminated from the top.

Reducing Deuterium-Tritium Ice Roughness by Electrical Heating of the Saturated Vapor*

E. R. MAPOLES
Lawrence Livermore National Laboratory
L-481, PO Box 5508
Livermore, CA USA 94550

J. D. SATER, E. MONSLER
W. J. Schafer Assoc., Inc.
303 Lindbergh Ave.
Livermore, CA USA 94550

J. PIPES
Allied Signal Incorporated
2021 Las Positas Court
Livermore, CA USA 94550

High gain targets for inertial confinement fusion (ICF) contain a layer of deuterium-tritium (DT) ice which surrounds a volume of DT gas in thermal equilibrium with the solid. The roughness of the cryogenic fuel layer inside of ICF targets is one of the sources of imperfections which cause implosions to deviate from perfect one dimensional performance. Experiments at Lawrence Livermore National Laboratory have shown that applying a heat flux across the inner surface of a hydrogen layer such as that inside of an ICF target reduces the intrinsic roughness of the surface. We have developed a technique to generate this heat flux by applying an electric field to the DT vapor in the center of these shells. This vapor has a small but significant conductivity due to ionization caused by beta decay of tritium in the vapor and the solid. We describe here experiments using a 1.15 Ghz cavity to apply an electric field to frozen DT inside of a sapphire test cell. The cell and cavity geometry allows visual observation of the frozen layers.

All high gain target designs for inertial confinement fusion employ uniform layers of condensed DT to achieve efficient ignition of the fuel. Various routes to the formation of these layers within target shells have been investigated[1], and the most promising method relies on the radioactive self heating of condensed DT to redistribute the solid along the isotherms in the structure containing the fuel[2,3,4]. The resulting roughness of the ice surface has been characterized optically and been found to be in the range of 1 - 1.5 μm rms for cylindrical layers approximately 100 μm thick and 2 mm in diameter. It is desirable to decrease this roughness to reduce the effects of mix during the implosion of an ICF capsule and increase the drive flexibility available to experimental designers.

Electrical Conductivity of DT

The electrical properties of DT gas are only roughly known but measurements have been made by Souers[5,6]. This data may be used to estimate the free electron density in the DT gas to be 4 x 10^{13}/m^3 at 20 K in 100 mole/m^3 density DT. However, these measurements were done on the gas alone without the additional

radiation load of the surrounding DT solid found in an ICF target. Souers[7] estimates the fraction of beta particle energy escaping from a surface layer of hydrogen of areal density 1.4 moles/m^2 as 0.11. This is about five times the beta energy generated in the vapor of an ICF target. Since the free electrons are only about one percent of the charged particles in the gas[5,6], their recombination rate is approximately independent of density and we can estimate the free electron density in the gas as 2 x 10^{14}/m^3. The electron mobility can be estimated from electron mobilities measured in 76.8 K D$_2$ gas[8] and from ref. 7. For a field of 5.0 x 10^4 V/m and a density of 100 moles/m^3 these give μ_e=0.1 m^2/V-s.

A high gain NIF target has a DT ice layer approximately 2.2 mm in diameter and 0.1 mm thick. This surrounds a gas volume of V=4.2 x 10^{-9} m^3 with an inner ice surface area of S=1.26 x 10^{-5} m^2. The power coupled into this gas volume is:

$$P=e\,\mu_e\,n_e\,E^2\,V,$$

where E is the root mean squared electric field and e is the electron charge. To reach a heat flux equivalent to the bulk heat produced by DT requires P=SqL=63 μWatts, where q is the bulk heating rate of DT or about 0.05 Watts/m^3, and the ice thickness, L is 100 μm. The corresponding field is E=6.9 x 10^4 V/m. Given the electron mobility above and the interior diameter of 2 mm, the electron transit time through the DT gas space is 0.3 μsec. In order to avoid the loss of electron mobility as they drift into the DT ice we choose to work at a frequency much higher than this. The desired field can be generated using a resonant cavity with reasonable rf power. For practical reasons concerning the size of the cavity, we choose to apply the field at about 1 Ghz.

Sample Cell

In order to facilitate the imaging of the DT ice our sample cell is roughly cylindrical with flat windows sealing the ends. The portion of the sample cell inside of the rf field was made entirely from sapphire parts. A 5 mm diameter sapphire rod has a 3 mm hole bored through the center perpendicular to the rod axis. Flats are ground on either side of the 3 mm hole to provide a flat surface on which windows are epoxied. A sapphire ring 3 mm in diameter and 1 mm wide with a 2 mm inner diameter is positioned in the center of the 3 mm bore and epoxied in place. The inner edges of this ring are beveled to provide a 500 μm wide surface on the inside of the ring. Then the ends of the 3 mm bore are sealed with sapphire windows. A 100 μm hole in the top of the cell provides access for the DT gas. The function of the ring is to provide a surface on which to image the DT ice which is not vignetted by the outside edge of the 3 mm bore. The assembled sapphire cell is epoxied to a sapphire tube which holds it in the center of the microwave cavity.

Data collection and Analysis

The roughness of the DT ice surface is characterized optically. A long range microscope looks through windows in the cryostat and the cavity, and is focused on the ring centered in the sapphire cell. Images are taken with a Photometrics camera using a Kodak KAF-1400 CCD array , and downloaded to a personal computer for

analysis. Images are saved using a 1024 x1024 subarray of pixels on the CCD. Each 6 μm pixel at the CCD corresponds with 2.15 μm at the focal plane.

Raw images such as that shown in figure 1 have a bright central region which makes a transition to a dark outer region where the ice surface blocks the light. Analysis of the images consists of locating the center of the transition from light to dark as a function of angle. This is done by initially guessing the coordinates of the center of the bright region and sampling the image along radial lines emanating from the center estimate. Image intensity along the radial line is estimated at one pixel increments using a bilinear interpolation scheme. The resulting linear array of intensities is scanned to find the point of maximum derivative in intensity as an initial estimate of the location of the edge. The linear data is then fit to an error function using a Levenberg-Marquardt method allowing the center, height, baseline, and width of the fit function to vary. This procedure is repeated as a function of angle to produce an array of edge radii versus angle. The center is recalculated and the entire procedure in repeated until the center estimates converge. At this point the roughness of the surface is computed by calculating the root mean square fluctuation of the edge estimates from their average, and a power spectrum of the surface fluctuations can be calculated in the usual way.
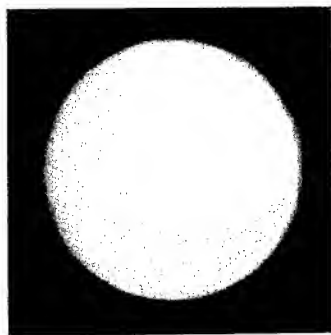
Figure 1. Image of DT ice
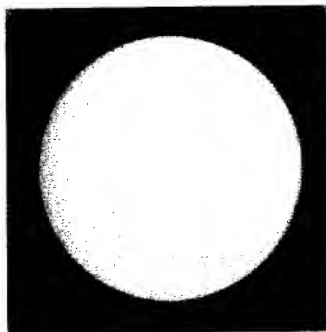
Figure 2. DT ice after E Field smoothing

Experimental Results

Application of the rf field results in a rapid decrease in the apparent roughness of the DT ice in the cell. Figure 2 shows the surface resulting after applying 350 mWatts (6.0×10^4 V/m) of rf power to the cavity for 300 secs. The rms roughness of the surface was initially 2.6 μm and the final rms is 0.8 μm. The initial roughness is exaggerated due to the roughness of ice on the front window. The final roughness includes contributions at low frequencies which are due to anisotropy in the electric field inside the sapphire cell. Sapphire has a dielectric constant of about 10 so the complex shape of this cell produces variations of the field in the interior of the cell. This effect is much reduced in the plastic shells used for ICF targets.

In order to evaluate the coupling of the electric field to the gas we measure the rate at which freshly frozen liquid in the cell forms a uniform layer as a function of rf power into the cavity. At each rf power value we allow the ice to evolve into a uniform layer, photographing the layer in the cell at a constant rate. Each photo is

294

analyzed as described above and the fourier transform of the surface fluctuations is computed. The decay of the second harmonic is plotted for each power and fit to an exponential decay. The layering rate at that power is then taken as the time constant of the exponential. These fit results are plotted in figure 3 as a function of rf power into the cavity. Since heat flux through the surface is proportional to the square of the electric field which is proportional to the power into the cavity, we find that the layering rate is proportional to the power into the cavity.
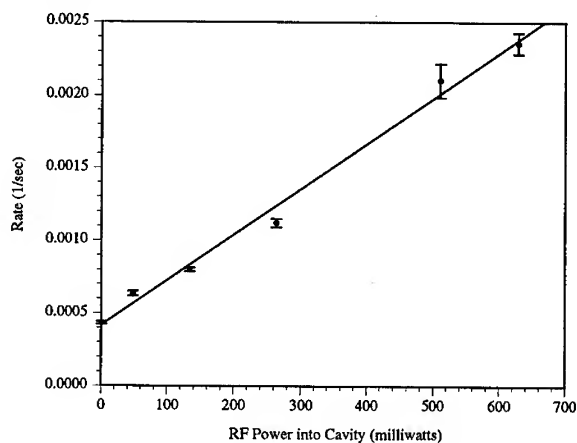
Figure 3. Layering rate versus rf power into the cavity

The improved surface finish and the increase in the layer rate to a value about six times the natural beta layering rate confirm that the electric field couples sufficiently strongly to the DT to provide a useful technique for modifying DT surface roughness.

1) K. Kim, L. C. Mok, M. J. Erlenborn, and T. P. Bernat, "Non contact thermal gradient method for fabrication of uniform cryogenic inertial fusion target," *J. Vac. Sci. Technol.* A. Vol. 1 no. 2, page 1196. (1985)

2) J. R. Miler, Los Alamos Scientific Laboratory Report LA-6245-PR, Dec. 1975, p. 82; *Methods and Apparatus for Producing Cryogenic Inertially Driven Fusion Targets*, U. S. Patent 4,292,340 (Jan. 1987)

3) A. J. Martin, R. J. Simms, and D. L. Musinski, KMS Fusion, Inc. Report No. 1348 (1985, unpublished); A. J. Martin, R. J. Simms, and R. B. Jacobs, *J. Vac. Sci. Technol.* A **6** (3), 1885. (1988)

4) J. K. Hoffer and L. R. Foreman, *Phys. Rev. Lett.* **60**, 1310 (1988).

5) P. Clark Souers, E. M. Fearon, and R. T. Tsugawa, *Cryogenics* **21**, 667 (1981).

6) P. Clark Souers, E. M. Fearon, and R. T. Tsugawa, *J. Vac. Sci. Technol.* A **3** (1), 29 (1985).

7) P. Clark Souers, *Hydrogen Properties for Fusion Energy*, (University of California Press, Berkeley, 1986) pg. 216

8) A. G. Robertson, *Aust. J. Phys.* **24** 445 (1971).

CRYOTARGET FACTORY FOR INERTIAL FUSION ENERGY: DEVELOPMENT OF THE INITIAL TECHNOLOGICAL AND OPERATIONAL BASE

E.R. KORESHEVA, I.E. OSIPOV, I.V. ALEKSANDROVA,
I.A. NIKITENKO, S.M. TOLOKONNIKOV, V.S. BUSHUEV

P.N. Lebedev Physical Institute,

Leninskiy Prospect 53, 117924, Moscow, Russia

Abstract

This report presented at the 24th ECLIM considers some results obtained at LPI in the scope of cryotarget formation and delivery as well as our near-term program aimed to adapt the created science and technical base to the experiments on a MJ-class laser facility.

Although the cryolayer formation inside a non-suspended target followed by the target injection is the unconventional method for current experiments in inertial confinement fusion (ICF), nevertheless it is the only way which is possible for application in a future reactor. Furthermore, it is much promising for cryotarget formation and its delivery in ICF on upgraded facilities with the laser capability of 30-kJ-2 MJ. At present such method and the associated technologies progress at LPI [1- 4].

The system for cryotarget formation and injection created at LPI can work as follows:

- to inject spherical targets inside the solid angle from 1 to 6 mrad for 50% of the events;

- to synthronize the injected target and the laser beam arrival at the given point of the research chamber;

- to exclude in principle the idle laser shot in ICF experiments;

- to operate in a single-step/or repetitive regimes of target delivery;

- to cool fuel-filled glass microsphere from 300K to 4.2K (cooling speed $\sim$ 1000K/s) and to fabricate inside it a solid cryogenic layer up to 15-μm-thick studied (from H_2, D_2 or their mixture) having the stable characteristics of quality in 87% of the events.

The created system is useful in the following parts of the ICF researches:

296

- for target delivery inside the research chamber of cryostat (Fig. 1), inside the simulation chamber (Fig. 2), inside the target chamber of the multibeam ICF facility (Fig. 3);

- for cryotarget technology development (Aleksandrova et al. Rept. at 24th ECLIM, Madrid, June 3-6 1996);

- for the investigations of the cryotarget life-time in the conditions close to ICF experiments, for study of target trajectory correction and synchronization (Fig. 4);

- for ICF experiments with cryogenic targets and for study of the influence of cryolayer morphology on the implosion results;

- for state-of-the-matter-equation experimental study;

- for the scientific researches of the structure-sensitive properties of hydrogen isotopes enclosed inside the volume of a microsphere (Fig. 5).

The developed system and the associated technologies are of initial base for the development of a cryotarget factory to supply the burn area with fuel synchronously with driver pulses arrival. Fig. 6 shows a principal scheme of the design of a cryotarget factory for single-shot laser experiments. This device is able to operate in a closed of fuel-filling $\rightarrow$ layering $\rightarrow$ delivery and can be improved for target delivery in the repetition rate regime of 1-10 Hz.

Our near-term goal is to adapt the existing modules of the system to the experiments on a MJ-class laser facility. In the frame of this goal two issues are of most importance. These are the creation of a special system to fill the polymer capsules with highly pressurized gas fuel (up to 1000 atm at 300 K) and to transport them into the layering module without mechanical rupture; and the improvement of the existing fall-and-strike technique to obtain thick cryogenic layers (up to 50-100 μm; layer material is D_2 or $D_2 + H_2$ mixture modeling, in our case, the behaviour of DT fuel) on the inside surface of a spherical polymer shells.

LPI starts to work under these issues.

References

[1] I.V. Aleksandrova, E.R. Koresheva, I.E. Osipov, *J. Moscow Phys. Soc. 1994*, v4 N2 p.81, N3 p.183;

[2] FROM TARGET SUSPENSION TO CRYOTARGET FACTORY. Crytarget Group presentations, 1992-1995. Preprint LPI N39 1995, 165p.

[3] E.R. Koresheva, Yu.A. Merkuliev, A.I. Nikitenko et al. *Laser and Particle Beams* 1988, v6 pt.2 p.245; S.M. Tolokonnikov, V.S. Bushuev, A.I. Nikitenko. *Fusion Technol.* 1995, v28 p.1787;

[4] I.V. Aleksandrova, E.R. Koresheva, I.V. Osipov, L.V. Panina. *Laser and Particle Beams* 1995, v13 N4 p.539.

Fig.1
Cryotarget injection inside the research chamber of cryostat at 4.2K
(glass capsule of 400μm-diam., average thickness of solid hydrogen (35% J=1) is 6.8 μm,
filling pressure of ~115 atm).

0   40msec   80msec

cryostat

Fig.2
Target injection inside the simulation vacuum chamber at 300K.
(a)high-speed video recording (500 fr/s); (b) photographs of the trecks of
the injected targets; (c)high-speed filming (1200 fr/s)

(b)

Fr.1

(a)   Fr.4   2 mm   (c)

Fig.3
The alignement of the injectors inside multibeam ICF chamber.

gravitational
injector

electromagnetic
injectors

laser beam

298

Fig.4
Operation of the module for sinchronization between the injected target and the laser beam arrival at the laser focus.
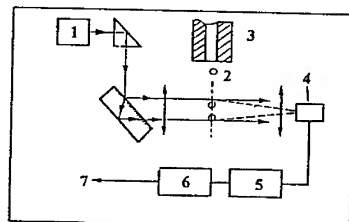
1- He-Ne laser; 2- target; 3- nozzle of injector; 4- photodiod;
5- amplifier-formation; 6- time-delay; 7- laser trigger.

Fig.5
Crystallization of quasi-amorphous solid H_2 (35% J=1) at target heating. (Frame 1: 4.2K, 1 mtorr; 1-cryolayer after speed cooling inside the vertical channel, 2-empty shell, 3-polycrystalline layer after the equilibrium cooling)

T=4.2K   T=7.7K
Frame1   Frame 2
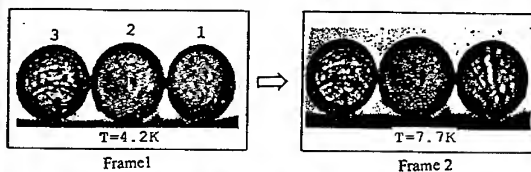
The process of polycrystalline cryolayer homogenization at 4.2K
(H_2,75% J=1,average thickness of 8μm ,glass shell)

| 0 | 16s | 105s | 165s | 196s | 608s |
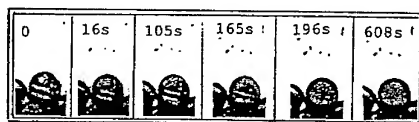
Fig.6
Cryotarget factory design for single-shot ICF experiments (made in team-work with the Rutherford Appleton Laboratory, UK).
(a) Principal design; (b)Disassembled model.
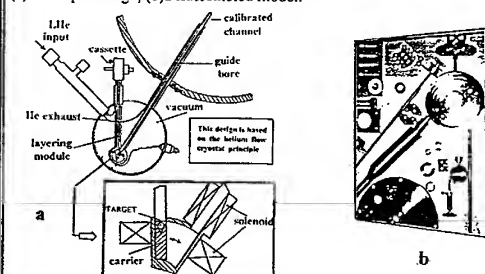
CRYOGENIC FUEL LAYERING RELYING ON A BULK HOMOGENISATION OF STRUCTURE

I.V. ALEKSANDROVA, E.R. KORESHEVA, I.E. OSIPOV

P.N. Lebedev Institute

Leninsky Prospect 53

Moscow 117924, Russia

Abstract

Laboratory Inertial Confinement Fusion (ICF) has embarked on a new stage of research which provides an opportunity to produce pure fusion ignition and burn by using high-energy laser systems and appropriate-scale targets. The ignition and high-gain target design requires a condensed uniform layer of fuel on the inside surface of a spherical polymer shell. In addition, to reach the goal of laboratory micro-fusion following a well-known scenario in plasma physics, a cryogenic layer must have the quality of surface finishes better than 0.5 μn. In this report, we discuss in some detail our recent and current activities in the area of cryogenic target fabrication.

1 Introduction.

Our approach to the issue is based on the development of structure-sensitive methods resulting in the bulk homogenisation of fuel. Guided by general rules of crystallography, they also take into account the peculiarities inherent in the hydrogen isotopes as quantum molecular solids. These methods allow one either to form quasi-amorphous layers by fast inverse sublimation of the vapour onto the target wall (Fall and Strike Technique - FST), either to convert crystalline layers into a homogeneous state within $\sim 150 - 600$ seconds due to low-temperature phonon-modulation of structure (Impact Load Technique - ILT) [1-4].

The FST keeps the rapid cooling of initially the gas-filled target by its strikes (repeated many times) with cold wall of the layering channel during its downward fall. Each gas-filled target comes to the top part o the layering channel from the target supply system through a special guidance unit. This allows to place the target in such a trajectory when strikes- initiated heat losses become sufficient in order to maintain high cooling rates ($V_c > 1000 K/s$ and in the process $V_s \sim 20 \mu n/s$), that, finally, is the crucial factor of amorphization.

Thus, the target motion inside the channel is carried out in a stick-slip fashion. Among strikes the target rotates randomly, which supports the uniform layer formation. In addition, high-frequency oscillations of the target wall arising due to strikes favours amorphization. The layered target leaves the channel through the outlet nozzle by means of which it is injected into the research chamber. The FST was studied for H_2, D_2 and $50 : 50 H_2 - D_2$ cryolayers in the range from $1.5\mu n$ to $15\mu n$. The principle of ILT was demonstrated for frozen $n - H_2$ having initially a coarse crystalline structure. All the cryolayers were between $3.9\mu n$ and $25\mu n$ thick at 4.2 K.

An unique feature of these experiments is the target injection into the research chamber (containing a target trap called "target-in-basket" support) that has no analogue in the world's practice. This is precisely the condition which in many respects has defined a successful course of research.

2   Experimental results.

The study is designed to generate different regimes of layering channel operation for testing and benchmarking the conditions that are applied to thick-layers formation. The experimental arrangement is shown in Fig. 1 which also shows the primary experimental apparatus: two tuneable-temperature cryostats. These are KG-14 and UTREX-1-RTA with operational temperature 4.2-300 K and 4.2-80 K, respectively. Tiny resistance sensors made of doped single crystal semiconductors control the temperature along the layering channel to an accuracy of 0.01 K at 5 K and of 0.1 K at 250 K [2,4]. In the experiments we use glass microspheres filled with hydrogen with a different $J = 1$ concentration.

2.1   Temperature profiling

We have examined the feasible area of temperature profiling in terms of structure variations at layering. Two extreme regimes were found: (a) amorphous and (b) crystalline layer formation (see Fig. 2,3). Fig. 2 demonstrates the target injection with amorphous hydrogen ($[J = 1] = 75\%$) layer into the research chamber ($P \sim 0.1 mTorr, T = 4.2K$). The three upper images show sequential video frames, 40 msec apart. The next image shows the frame 3 with 2.5 x magnification, 40 min apart. The last image shows amorphous- to-crystalline layer conversion at heating. We have also found that there is a possibility to elevate the thermal layer stability by lowering a $J = 1$ concentration in hydrogen (see E.R. Koresheva at el. Rept. at 24th ECLIM, Madrid, June 3-6 1996). Fig. 3 demonstrates that temperature profiling along the channel leaves a perpectible imprint on the layering process; actually, we have obtained crystalline structure instead of homogeneous one. Does it mean that crystalline solid layering is a misnomer? This is not necessarily so, if taking into account the potentials which the ILT opens in structural reorganisation of hydrogens.

We can consider the crystalline layer formation as the first stage of cryogenic solid layering, i.e., symmetrization, followed by the second one-homogenisation. Therefore, going to thick fuel layers we have the following options: (1) clear FST and (2) FST &ILT. It should be noted that ILT operation is highly sensitive to $J = 1$ concentration [4].

2.2 Angular-distribution point.

This regime results in the decreasing of strikes amount during the layering. At sufficiently narrow distribution, a hot target, i.e., a gas-filled one is injected into the cold ($T = 4.2K$) research chamber. In this case it is readily seen that after target landing there occurs a hydrogen drop inside the shell, then it moves to the shell bottom, wets its inner surface, and freezes (see Fig. 4).

3 Conclusion.

Let us compare Fig. 2,3 and 4. Evidently, that the phase state of the layer after target injection is quite different, i.e., we can govern the layering process during the FST. This area of our researches will be considerably extended in the future. Prominence will be given some other parameters such as: layering channel geometry (diameter, length, profile), special-purpose coatings deposited on its inner wall to promote not only thermal conductivity increasing but also its levelling over the layer, FST in electromagnetic field and etc. Nevertheless, the "database" information obtained in the experiments discussed here has a key value for the development of simulation code of layering channel operation.
References

References

[1] Aleksandrova, I.V., Koresheva, E.R., Osipov, I.E. Preprint LPI N57, pt. 1,2, 1992, 49p.; K. Moscow Phys. Soc. v3 N2 pp. 85-100, (1993).

[2] Aleksandrova, I.V., Koresheva, E.R., Osipov, I.E. J. Moscow Phys. Soc. v4, N2 p. 81-127, N3 pp.183-242, (1994).

[3] Aleksandrova, I.V., Koresheva, E.R., Osipov, I.E., Panina, L.V. Laser Part. Beams v13 N4 pp.539-557, (1995).

[4] Aleksandrova, I.V., Koresheva, E.R., Osipov, I.E. FROM TARGET SUS-PENSION TO CRYOTARGET FACTORY. Preprint LPI N39, 165 p. (1995).

302
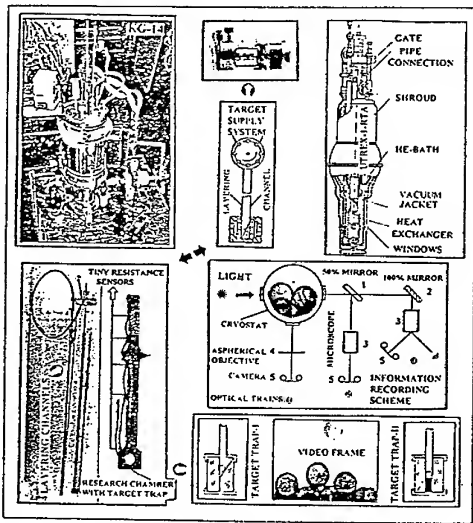
Fig.1 Experimental arrangement.
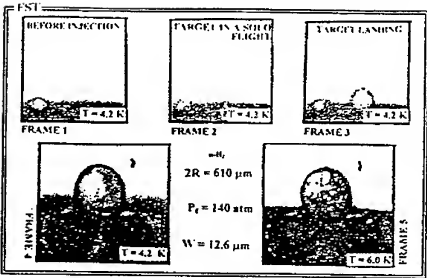
Fig.2 Amorphous solid layering inside the channel.

Fig.3 Crystalline solid layering inside the channel.
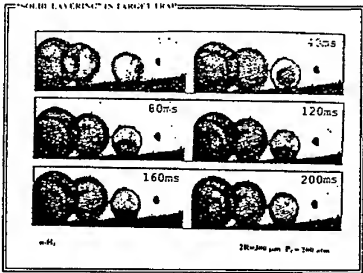
Fig.4 Hot target injection.
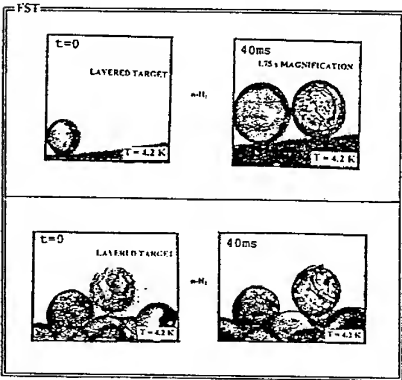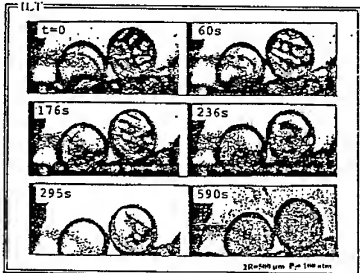
Fig.5 Structural reorganization of crystalline hydrogen (|J=1|=75%) at 4.2K.

The Laser Target Design And Problems of Hydrodynamic Instability

I.G.LEBO, V.B.ROZANOV,
The Lebedev Physics Institute (FIAN), Moscow 117924, Leninsky Pr. 53, Russia

V.F.TISHKIN
The Institute of Mathematical Modelling (IMM), Moscow 125047, Miusskaya sq.4, Russia

V.V.DEMCHENKO
Moscow Institute of Physics and Technology (MFTI), Dolgoprudny,Moscow Region,141700,Russia

The direct driven targets make it possible to reach the gain of about a unity , the laser energy being 100-300 kJ. However, due to the hydrodynamic instability, the neutron yield in modern laser fusion experiments differ by 10^2 times as compared to the prediction obtained from 1D simulations.

Basing on 2D simulations we have been studying the methods against hydrodynamic instability in the large scale laser targets. We have considered three approaches:

1) the use of a symmetrizing laser prepulse;

2) the symmetrizing X-ray prepulse

3) thermal equalization and hydrodynamic compensation in "laser green house" target

The calculations have been made with the use of 2D Lagrange code "ATLANT" and 2D Euler code "FAKEL"

1. Symmetrizing Prepulse.

As shown in [1-4], the symmetrizing prepulse allows one to reduce the growth velocity of the target perturbations. However, the prepulse increases the preheating of the DT-fuel and reduces its compression. The 2D calculations presented in [4] have shown that the prepulse with the wavelength three times as much as the wavelength of the primary heating pulse makes it possible to reduce the heating and increase the compression of the fuel, as well as to reduce the velocity of the of the perturbation growth at the "shell-fuel" contact boundary.

There is a chance of creating a symmetrizing prepulse with the help of an X-ray. In this case the working target should have a thin gold shell. In such a target, as shown in [5], a significant part of the absorbed laser energy is transformed into the X-ray centrally directed radiation.

The calculations have been performed by using three-temperature Lagrangian code ATLANT in 2D spherical geometry (the constants, r,θ,t). The code description is given in [6]. We have chosen the following target design: a polyethylene shell (the radius, R_0= 0.123 cm, and the mass M_s =0.775 mg) with a M_{DT} = 0.366 mg DT-ice layer frozen onto the inner surface of the target. The temporal dependendence of the laser pulse presents a triangle with the time moments t_0 =0 ns and t_2 =5.1 ns at the base, and t_1 = 5 ns at the apex. The absorbed laser energy made 202 kJ at the wavelength λ=0.353 μm. The calculations have been made in two- and three-temperature approximations. In the first case the neutron yield reached $Y_N = 4*10^{16}$, and the compression degree made $\xi = R_0/R_m$ =25.7 (R_0, R_m are the initial and minimal value of the "shell-fuel" contact boundary radius). In the second case: $Y_N = 10^{16}$, and ξ=22.4 . The compression of the discussed target, irradiated with no prepulse, has been calculated in three-temperature approximation (variant 1). In variant 2 the energy of the main heating pulse is 180 kJ, and the prepulse energy at the wavelength λ=0.35 μm is 22 kJ. The prepulse temporal shape presents an isosceles triangle with the base duration of 1 ns. In variant 3 the prepulse has the same parameters as in variant 2, but the wavelength is λ =1.06 μm. Figure 1 illustrates temporal dependence of the compression in variants 1,2,3 (1D cases). For modeling an X-ray prepulse at the shell external boundary the radiation flux is given. Note that the radiative temperature T_X increases up to the time moment t_2 =0.5 ns, and at t_3=1.5 ns drops to 0. The shell compression depends on the radiative temperature. At maximal T_X^{max} = 200 eV (this corresponds to the prepulse energy of $E_X \approx$ 12-13 kJ) the target has been completely heated. At T_X^{max} = 120 eV ($E_X \approx$ = 1-2 kJ) only the external layer of the target has been heated. Figure 2 shows temporal dependence of the fuel compression for the discussed variants 4,5. The perturbations of the shell external boundary have been taken in the form $R_{pert} = R_0 + \alpha * \Delta *cos(n * \theta)$ where R_{pert} and R_0 are the perturbed and unperturbed external boundaries; Δ, the shell thickness; α, n the perturbation amplitude and harmonic number. Figure 3 illustrates the dependence of the internal boundary perturbation (δ/R) (δ - the amplitude of perturbation, R- current radius of contact boundary -"fuel-shell") on the degree of compression for $n = 20$ and α=0.05 for the variants 1 and 5 (2D case). we could not complete the calculation of

the variant 1 (2D) because the grid was destroyed. (Note that for $\alpha =$ 0.01 the perturbations growth is rather slow. This calculation was made completly. The shape of the compressed zone does not significantly differ from spherical).

2. Symmetrizing low-dense coatings. "Laser Green House" target.

In [7], using the 2D simulations, we have studied a possibility of reducing the influence of the target irradiation inhomogeneities on the contact boundary perturbation growth rate with the help of low-dense (supercritical density) coatings. The result is negative. In [8] it was proposed a so-called "Laser Green House" target. The laser radiation is introduced into a low-dense matter through the holes in the external cavity, and is absorbed there. Here the temperature in the absorber turns to be much higher than that in the corona of the direct-driven target. Small scale perturbations are suppressed due to thermal smoothing.In [9] it was proposed to make a profiled working target in order to compensate the influence of the holes. Figure 4 shows the results obtained with the help of the code "ATLANT". The target has a leaden external shell with the 0.1506 mm radius and 6 μm thickness. Inside the external shell there is a polyethylene working target (the radius, 910 μm; the thickness, 20 μm) with a 10 μm thick frozen DT layer. The low-density absorber has dinsity $1 mg/cm^3$. We have performed the modeling of the target irradiation through 6 holes (2 holes on the axis and 4 holes on the "equator"). Figure 5 shows the perturbation amplitude growth for the internal "nonprofiled" (variant 1) and "profiled" working target (variant 2 and 3) with amplitudes $\alpha =$ 0.55, 0.8. Figure 6 illustrates the neutron yield. Variant 1: 1D calculation; variant 2: "nonprofiled" working target; variant 3: "profiled" working target. One can see that the use of the "profiled" target makes it possible to come close to the results obtained from 1D calculation (for details see [9]). The calculations made with ATLANT code do not take into account the influence of the holes. In order to study this effect there has been developed a 2D Euler code FAKEL. The physical models used in ATLANT and FAKEL codes are identical. The target and the laser pulse parameters are the same as shown above. In the external cavity the holes have been made near the "pole" (the angle $0 \leq \theta \leq 20°$) and the equator (the angle, $60° \leq \theta \leq 120°$). To avoid the re-radiation from the lead we have put a

10 *mum* thick polyethylene layer onto the internal surface. The working target has been destroyed up to the time moment t = 2.2 ns. Figure 7 shows the density isolines at t=2 ns. A comparison of the perturbation growth rates obtained with "ATLANT" and "FAKEL" codes is also presented in this figure. One can see that in the second case the perturbatios grow faster.

References

1. Bokov N.N., Bunatyan A.A. et al. PMTF, N 40, 20 (1982) (in Russian).

2. Gamaly E.G., Lebo I.G. et al. Laser and Particle Beams, 8, 398 (1990).

3. Mashek K,...,Garanin S, et al. XXIII ECLIM (Oxford,1994)

4. Lebo I.G., Rohlina K. et al. Quantum Electronics, 26(1), (1996).

5. Eliezer S., Hourubia J., Velarde G. Phys.Lett. A, 166, 249 (1992).

6. Lebo I.G., Popov I.V. et al. Journal of Russian Laser Research, 15, N2, 136 (1994).

7. Lebo I.G., Rozanov V.B., Tishkin V.F. Laser and Particle Beams, 12, N3, 361 (1994).

8. Gus'kov S.Yu., Zmitrenko N.V., Rozanov V.B. ZhETF, 108, 548 (1995) (in Russian).

9. Lebo I.G., Popov I.V. et al. Quantum Electronics 25(1), 1220 (1995).
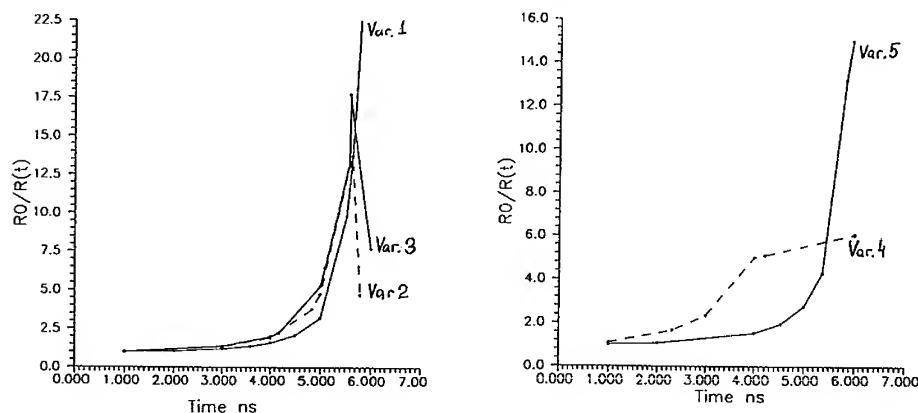
Fig.1 The convergent ratio as a function of time for the cases of laser symmetrizing prepulse (a) and X-ray prepulse (b)
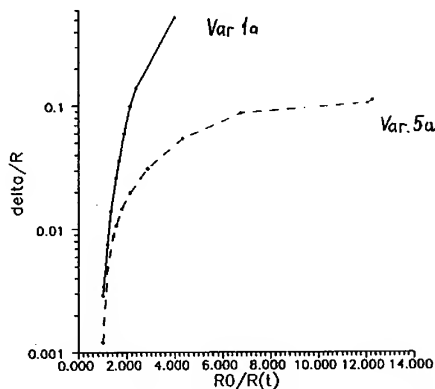
Fig.2 The development of perturbation of contact boundary
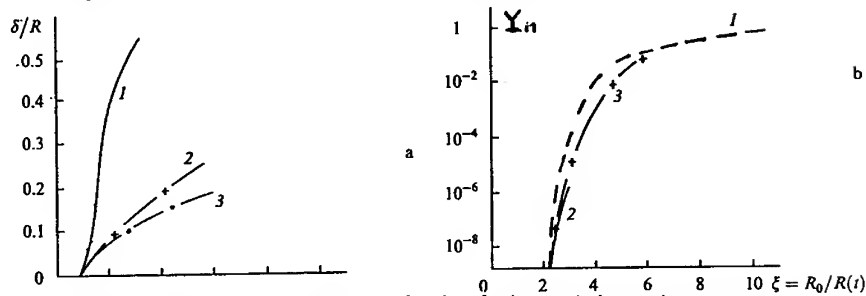
Fig.3 Results of "ATLANT"-code simulation. a) dependence of the
amplitude of perturbations at shell-fuel boundary on the convergent
ratio, b) dependendences of the neutron yield on the convercent ratio.
Dashed line - 1D simulation.
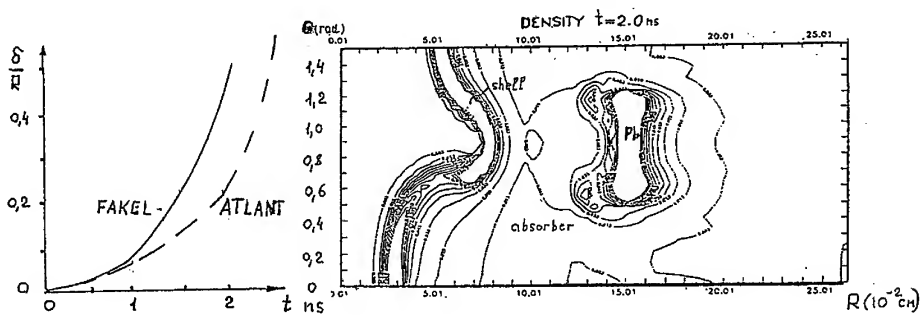
Fig.4 Results of "FAKEL"-code simulation, a) dependence of the
amplitude of perturbations on time, b) izolines of density of
"Greenhouse" target at the moment t=2 ns

"RELATIVISTIC RADIATION EFFECT IN VOLUME IGNITION AND THE RETROGRADE H-B REACTION"

G.Kasotakis[1], E.T.Sarris[1,2], E.Kakoulidis[2], Chr.Scheffel[3], J.Torne[3], S.Eliezer[4], R.Höpfl[3], H.Hora[3], J.M.Martinez-Val[4], M.Piera[4],

European Network "High Energy Density in Matter"
[1] National Observatory of Athens, Greece
[2] Demokritos University of Thrace, Greece
[3] Anwenderzentrum, Regensburg, Germany
[4] DENIM Polytechnic University of Madrid, Spain

ABSTRACT

The gain, fuel depletion and ignition temperature in inertial confinement fusion have been calculated on the basis of the self similarity volume ignition model, which includes alpha reheat and the classical Bremsstrahlung emission and re-absorption. Pellets of DT or HB are spherically and symmetrically irradiated by intensive laser beams. The photon's energy is mostly absorbed by a thin outer shell of the pellet, which rapidly explodes, while the rest of the pellet undergoes subsequently implosion and after that explosion. In this work we study in detail the corrections to the above calculations of the gain, fuel depletion and ignition temperature due to the inclusion of relativistic Bremsstrahlung effects. It is shown that these effects can be important for advanced fusion fuels at high temperatures. We have analyzed the earlier reported retrograde behaviour of the H-B reaction and can explain it by the extremely low Debye length of the used collective stopping power model.

1. Introduction

From historical point of view the Self - Similarity Model was introduced in Astrophysics by Milne in 1933 for the explanation of the expansion of the Universe. Use of this model in ICF was reported in 1963 by Basov and Krokhin, and in 1964 by Dawson and Hora. The recent development of this model, which we use, is based on modifications introduced by H. Hora and oriented towards the volume ignition. The main assumptions used by the Self-Similarity/Volume Ignition Model (Hora version) can be summarised as follows given that we start our calculations from the instant that the fuel is fully compressed and starts to expand,

1) Spherical and symmetrical target irradiation by very intense laser and the target expansion becomes in the vacuum.
2) A linear velocity profile is valid during the expansion.
3) During the expansion, adiabatic transfer of thermal to kinetic energy occurs.
4) A box like approximation of the ionic density Gauss distribution is used.
5) The instant pressure and temperature values can be assumed spatially constant, during each very little expansion step, at which we refresh the variables, while the temperature is reduced adiabatically with the time.

Emission and re-absorption (reheat) of the non-relativistic and relativistic Bremsstrahlung, alpha reheat and depletion of the nuclear fuel are taken into account. By using modern cross-section data, it is found that fusion occurs even at approximately 1KeV kinetic plasma temperature (Kasotakis 1989). Finally, calculations of the energy gain, ionic depletion and ignition temperature have been done, for DT and HB fuel. Parallel scheme exist for ion beams models (Martinez-Val 1994).

## 2.	Bremsstrahlung emission and re-absorption

The initial calculations on the emission and re-absorption of the non-relativistic Bremsstrahlung have been done for electron temperature less than 30 keV. According to Maxon the relativistic correction can be expressed in the form of the multiplication coefficient $\{1 + \dfrac{2T_e}{m_e c^2}\}$ (Maxon 1972) where T_e is the electron temperature in eV. By combined this coefficient to our classical Bremsstrahlung formulation (Glasstone 1960), we obtain the following result ($T_e > 30$keV):

$$P_{br} = 9.3 \times 10^{-14} n_e^2 \overline{Z} T_e^{1/2} \left\{ 1 + \frac{2T_e}{m_e c^2} \right\} , \text{ cgs units, } T_e \text{ in } {}^\circ\text{Kelvin}$$

For the case of relativistic Bremsstrahlung re-absorption, the term Λ^* or Λ of the Coulombs logarithm ($\ln\Lambda^*$ or $\ln\Lambda$) and the collision frequency v_{ei}, are modified as follows (Kasotakis PhD Thesis, DUTH 1994):

$$\Lambda^* = \frac{3(m_0 c^2)^{3/2}}{2\pi^{1/2} Z e^3 n_e^{1/2}} (\gamma - 1)^{3/2} \qquad \text{where} \qquad \gamma = (1-\beta^2)^{-1/2}$$

$$\Lambda = \frac{3}{2\pi^{1/2} Z e^3} \left(\frac{K^3 T^3}{n_e} \right)^{1/2} \qquad \text{(remains as it was by Hora 1991)}$$

$$v_{ei} = \begin{cases} \dfrac{Z\pi^{3/2} e^4 n_e}{2^{5/2} m_0^2 c^3} \dfrac{3}{(\gamma^2 - 1)} \ln\Lambda^* & \text{if } I_B \gg I_r \\[4mm] \dfrac{Z\pi^{3/2} e^4 n_e}{2\ m_0^{1/2}} \dfrac{1}{(\gamma^2 - 1)^{3/2}} \ln\Lambda & \text{if } I_B \ll I_r \end{cases}$$

where I_B represents the Bremsstrahlung intensity and $\quad I_r = \dfrac{3 m_0 \omega^2 c^3}{8\pi e^2}$

## 3.	Retrograde in H-B Fusion Gains

When calculating the fusion gains for the H-B reaction (50-50) from the volume ignition point of view under the non-relativistic radiation assumption (resulting in slightly different gains than reported here) it was found that the initial plasma temperature was reduced from about 200keV to 23keV if densities $10^5 n_s$ were used, because of the strong alpha reheat and the reabsorption of the bremsstrahlung on our fully detailed computations showed. This is the basis that with initial energy E_0 (deposited by the laser in the compressed) of up to 100MJ, and drivers with ›50% efficiency, the very clean energy generation is possible (Hora 1991). In these calculations an anomaly was observed that an increase of the

310

plasma density did not always result in the initially expected increase of gain but in a decrease (retrograde behaviour, Stening et al 1992).

A more detailed result including the relativistic radiation effect is given in fig 1 Our analysis arrived at the following explanation of the retrograde behaviour. At all our usual computations of the volume ignition we used the collective model of the stopping power (Hora et al 1972) where flowing down of the alphas (or other changed nuclear reaction products) is due to interaction with the whole Debye sphere. This collective stopping power model was introduced by Gabor (1953) on the basis of the Debye-Milner theory and results in much shorter stopping length than binary interaction with electrons. In our case of H-B, the extremely high densities reduce the Debye length in such low values that the stopping power changes into binary interaction at certain values seen by the retrograde behaviour.

4. Conclusions

The volume ignition self similarity model in inertial confinement fusion on DT (50-50) targets, taking into account alpha reheat, ionic depletion and bremsstrahlung re-absorption, it is found that the final energy gain is increased by up to 4% if we calculate the re-absorption of relativistic bremsstrahlung, for $T_e \! > \! 30 keV$, instead of the classical one (Fig. 2 and 3). By using HB (50-50) targets, a retrograde behaviour is found.
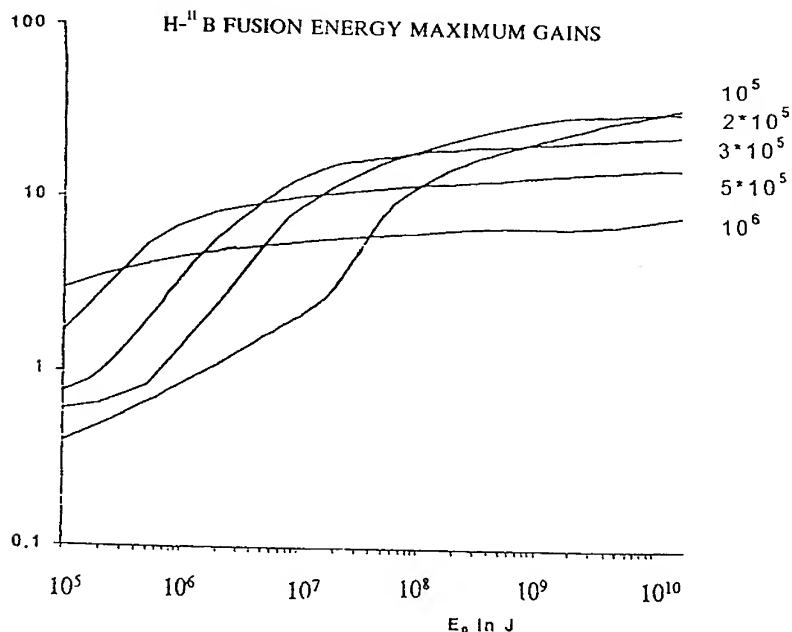
Fig. 1. Core Fusion Gain G at volume ignition of HB depending on the input energy E_0 at various densities (as multiples of the solid state density n_s) as parameter.

Laser Fusion Fuel : DT 50-50
cont. line : Relativistic Bremsstrahlung correction case (KTe>30keV)
dashed line : Nonrelativistic Bremsstrahlung case
target volume range : from 1E-7 cm3 to 10 cm3
Initial ion density range : from 1,000 to 100,000 times the solid state density
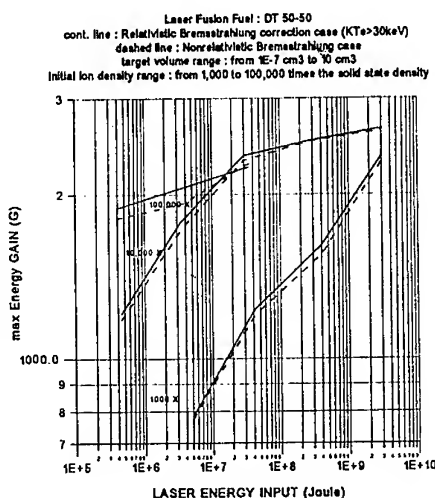
Fig. 2 Details from the relativistic and non-relativistic energy gain comparisons. The 3 cases (initial plasma density from 1000 to 100000 times the solid state density) show that for kinetic temperatures more than 30keV, the relativistic bremsstrahlung reabsorbtion contributes to a continue energy gain increase.

Laser Fusion Fuel : DT 50-50
target volume range : from 1E-7 cm3 to 10 cm3
Initial ion density range : from 1 X to 100,000 X the solid state density
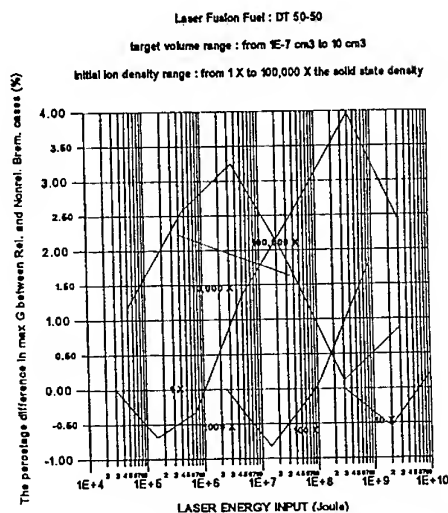
Fig. 3 The differences at the energy gain between the relativistic and non-relativistic bremsstrahlung emission and reabsorbtion cases which, in initial plasma density, range between 1X and 100000X the solid state density. A kind of antagonistic competition between bremsstrahlung and stopping power occurs.

REFERENCES

Basov , N. G., and O. N. Krokhin, 3rd International Quantum Elect. Conf., Paris, 1963, P. Grivet and N. Bloemberger ed., Dunod, Paris, vol. 2, p. 1373, 1964.

Gabor , D. Proc. Roy. Soc. London, A213, 73, 1953.

Glasstone , Samuel and Ralph H. Lovberg, "Controlled Thermo-nuclear Reactions. An Introduction to Theory and Experiment", ed. D. Van Nostrand Company Inc., Princeton, New Jersey, 1960.

Hora , H., Inst. Plasma Phys. Garching, Rept. 6/23, 1964.

Hora , H. D. Pfirsch, Laser Inter. and Related plasma Phenomena, v.2, p.515, 1972.

Hora , H., P. S. Ray, "Increased Nuclear Fusion Yields of Confined DT Plasma due to Reheat", Z. Naturforsch. 33a, 890-894, 1978.

Hora , H., "Plasmas at High Temperature and Density. Applications and Implications of Laser Plasma Interaction", Springer - Verlag, Berlin, Heidelberg, 1991.

Kasotakis , G., L. Cicchitelli, H. Hora, R. Stening, "Volume Ignition in Pellet Fusion", Nuclear Instruments and Methods in Physics Research, A278, p. 110-113, Elsevier Science Publishers B. V., North Holland, Amsterdam, 1989.

Kasotakis , G., Ph.D. Thesis, Demokritos University of Thrace (DUTH), Greece, 1994.

Martinez-Val , J.M., S. Eliezer, M. Piera, "Volume Ignition Targets for Heavy-Ion Inertial Fusion" Laser Particles Beams, vol. 12, No 4, pp. 681-717, 1994.

Maxon , M.,S., Phys. Rev., A5, 1630, 1972.

Milne , E. A., Z. Astrophys., 6, 1, 1933.

Stening , Robert J., Rasol Khoda - Bakhsh, Peter Pieruschka, Gregory Kasotakis, Edgar Kuhn, George H. Miley, and Heinrich Hora, "Volume Ignition for Inertial Confinement Fusion", Laser Interaction and Related Plasma Phenomena, vol.10, p. 347, ed. G. H. Miley, H. Hora, Plenum Press, New York, 1992.

NUMERICAL INVESTIGATION OF COMPRESSION OF DEUTERIUM IN CONICAL TARGETS BY CIRCULAR CUMULATIVE JETS [a]

A.A. CHARAKHCH'YAN

Computing Center RAS, Russia 117967, Moscow GSP-1, ul. Vavilova 40

This paper continues a numerical investigation of circular cumulative jets collapsing on to the axis of symmetry in conical targets. [1,2] The investigation has been initiated by the experiment [3] which is exceptional among other similar ones in the very low velocity (5.4 km/s) of a striker. Unfortunately, the experiment [3] was not continued after 1980 and was not repeated somewhere else. Nevertheless, the considered way to compress deuterium in conical targets has novelty and merits further investigation even if the experiment [3] has been erroneous.

In this paper two new problems are considered in the framework of the equations of gas dynamics with the equations of state from [4] for metals. We use second-order-accurate difference schemes on a moving regular grid with explicit identification of interfaces as certain grid-lines. An information about check computations on different grids is omitted.

1 On Stability of Circular Cumulative Jets

The problem to be considered is as follows. An aluminum striker impinges on a lead target with conical cavity filled by gaseous deuterium and put down an aluminum cover. The problem parameters correspond to the experiment. [3]

Fig. 1 shows the interfaces between the substances at two instants of time (a: a circular cumulative jet of aluminum arises near the cone boundary; b: it collapses on to the axis of symmetry). The problem of flow stability for axisymmetric perturbations of the aluminum-deuterium interface is considered.

Let r be the radial coordinate, z be the axial one reckoned from the vertex of the cone. The initial position of the non-disturbed aluminum-deuterium interface is defined as $z = z_0$ for $0 \leq r \leq r_0$, where r_0, z_0 are the coordinates of the intersection point between the interface and the cone. The perturbed initial position of the interface takes the form

$$z = z_0[1 + d\sin(m\pi r/r_0)] \qquad \text{for } 0 \leq r \leq r_0. \qquad (1)$$
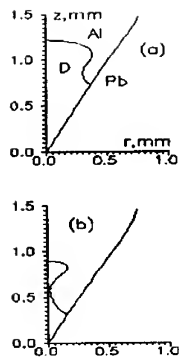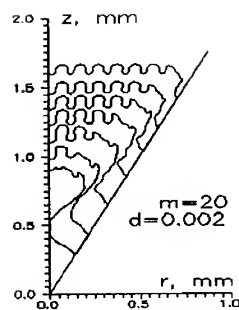
Figure 1

Figure 2

The striker initiates a shock wave into the cover of the target. When the shock wave reaches the aluminum-deuterium interface, Richtmyer-Meshkov's instability begins. First the perturbation changes its sign ('hills' become 'hollows', and on the contrary). Then the amplitude grows linearly in time with following transition to a non-linear stage.

A later evolution of the perturbation is shown in Fig. 2 for $d = 0.002$, $m = 20$. The positions of the interface for a set of time instants are presented. The cumulative jet is formed during the evolution of the instability at the greater part of the interface. Small oscillations with the amplitude decreasing in time remain at the boundary of the jet as a trace of the instability. When the jet collapses, its boundary becomes smooth. Although we have not performed the computation for $m > 20$, it seems improbable that a critical value of m exists beginning from which oscillations will penetrate into the cumulative jet and increase in amplitude.

Mechanism of terminating oscillations near the cumulative jet is as follows. Apart from the heading shock wave considered above, another shock wave propagates in aluminum from the cone boundary to the axis of symmetry and increases pressure behind itself, which causes an additional acceleration of the interface from aluminum to deuterium. As a result, the perturbation changes its sign once more. The amplitude of the oscillations falls, but the oscillations of opposite sign have no time to begin because the corresponding section of the interface bends and becomes the boundary of the jet.

As time goes on, more and more part of the interface becomes the boundary of the cumulative jet. When the jet collapses, the shock wave in aluminum also reaches the axis of symmetry. As a result, the interface becomes rather smooth even near the axis of symmetry.

2 High-Velocity Impact of Thin Foils

The problem to be considered (see Fig.3) simulates an experiment performed at the same time as[3] and published in[5]. Thin (30μ) aluminum foils with the initial velocity 18 km/s compressed deuterium in cone targets with two values of the cone angle $\theta = 30°$ and $60°$. In the case of the first target the neutron yield was rather high while it appreciably fell for the second target.
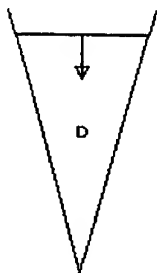
Figure 3
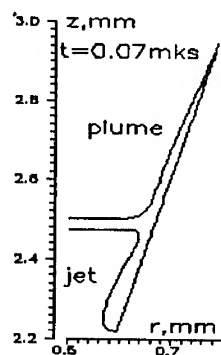
Figure 4
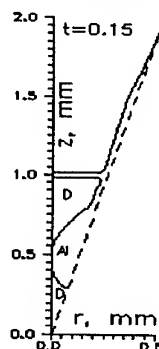
Figure 5

First we present numerical results for $\theta = 30^\delta$. Fig. 4 shows the boundary of the foil at a certain time instant. The circular cumulative jet overtakes the central part of the foil while "a plume" of the aluminum remains on the target boundary behind the central part. The reason of the both tongues is a high peak of pressure in the central part of the foil near the cone boundary. The pressure in this region remains almost unchanged with time because a disturbance will not penetrate deeply into the foil owing to its small thickness.

Consider the stage of the collapse of the cumulative jet. The foil boundary at the corresponding time instant is shown in Fig. 5. The flow in a vicinity of the jet is analogous with the case of a thick striker considered in[1,2]. Refer to high-velocity jets (100 – 150 km/s) of deuterium along the axis of symmetry. Following[1,2], point to a certain analogy between the deuterium high-velocity jet penetrating into a much more calm deuterium and a beam of heavy-water-clusters bombarding a deuterated target with the velocity of about 100 km/s in the experiment.[6]

We will now consider the case of $\theta = 60°$. As one would expect, the cumulative phenomena become more strong. Nevertheless, an examination of the computed distribution of the foil material in phase offers a quite plausible explanation of an appreciable fall of the neutron yield in the experiment. Most of the cumulative jet for $\theta = 60°$ is in the state of transition from liquid to

vapour. Most likely, that sort of jet is destroyed because of the cavitation when regions with vapour bubbles are generated within a liquid. Unlike the case of $\theta = 60°$, most of the jet for $\theta = 30°$ remains in solid state, which prevents the cavitation.

Conclusions

The circular cumulative jet arising in the experiment [3] is stable for the axisymmetric perturbation of the aluminum-deuterium interface. Evolution of Richtmyer-Meshkov's instability at another part of the interface turns out to be considerably suppressed.

In the case of another experimental run when thin foils are used as compressing pistons for the targets with the cone angle 30°, the circular cumulative jet also arises and collapses on to the axis of symmetry. In the case of the cone angle 60° the jet is destroyed because of the cavitation, which explains a fall of the neutron yield in the experiment.

The author hopes that the results of this paper together with the results from [1,2] will stimulate a new experimental investigation of the cumulative compression in conical targets.

Acknowledgments

References

1. A.A. Charakhch'yan, Comput. Maths Math. Phys. **33**, 683 (1993).
2. A.A. Charakhch'yan, Pril. Mekhan. i Tekhnich. Fiz. (J. Appl. Mechan. Technical Phys.) , No. 4, 22 (1994).
3. S.I.Anisimov *et al*, Pis'ma v Zh. Eksper. Teor. Fiz. (JETP Letters) **31**, No.1, 67 (1980).
4. A.V.Bushman *et al*, Thermophysics and Dynamics of Intensive Pulsed Actions (Institute on Chemical Physics USSR AS, Chernogolovka, 1988).
5. V.I.Vovchenko *et al*, in Proc. of IOFAN, Vol. 36, 5–82 (Nauka, Moscow, 1992).
6. R.J. Beuler *et al*, *Phys. Rev. Lett.* **63**, 1292 (1989).

PHYSICAL PROCESSES IN CONICAL TARGETS FOR ICF

I.K. KRASYUK, P.P. PASHININ, A.M.PROKHOROV, A.YU. SEMENOV
General Physics Institute, Russian Academy of Sciences
Vavilov Street 38, Moscow 117942, Russia

V.F.FORTOV
High Energy Density Research Center, Russian Academy of Sciences
Izhorskaya street 13/19, Moscow 127412, Russia

Communication is devoted to the review of results obtained at the experimental measurements and theoretical analysis of physical processes in conical targets, filled gaseous deuterium, for inertial confinement fusion (ICF).

It was shown, that the compression and heating of deuterium up to thermonuclear temperatures take place at laser [1] and explosive [2] interaction with conical targets. Such target is a one of the kinds of targets for inertial confinement fusion - ICF.

Conical target represents a cavity of conical shape in lead closed with thin shell and filled deuterium (Fig.1a). Investigation were done with cone angle 30° and 60°. Targets had the diameter of input hole equal 2 mm. Polymer films $[C_{10}O_4H_8]_n$ by thickness 1, 3 and 5 mkm were used as shells. Nd-glass laser installation SIRIUS (General Physics Institute) with the wave length 1.06 mkm ensured power up to 80 J at the duration of laser pulse 22 ns.

It was established, that shell target velocity is described by model of reactive movement with high accuracy. It was shown, that the shell of target is converted to the cloud of evaporated matter with density significantly less, than initial one, on the first stage of interaction with laser radiation. The velocity of leading part of the shell, moving into the target, arising up to 10^7 cm/s. Calorimetric measurements showed, that about 15% from the full energy of laser radiation fall into the target. Only 10% from this energy transforms into kinetic energy of the shell. The part of laser radiation penetrating through the target shell is dependent on the type of shell and does not exceed 1.5%.

The measurements of neutron yield depending on the conditions of experiences were carried out for the diagnostic of deuterium plasma within target. There were varied the angle of target, initial gas pressure and laser power. The most registered
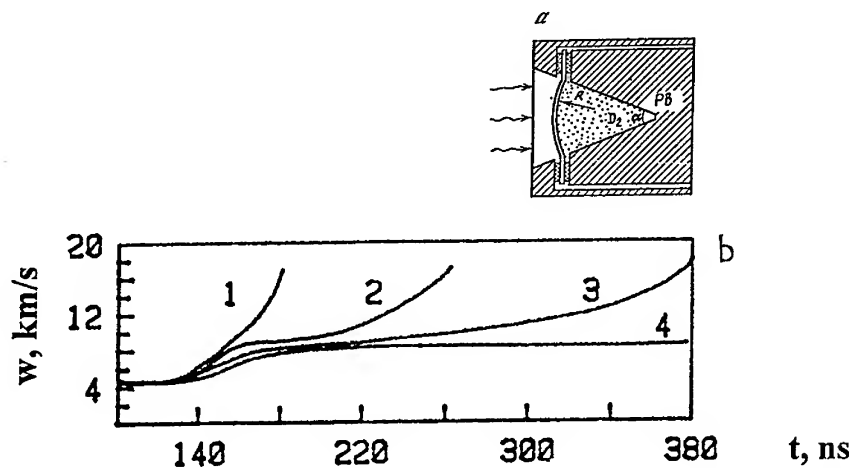
FIGURE 1. Conical target (a) and cumulative velocity increasing of aluminium liner inside lead cone (b). $\alpha = 52°$ (1), $36°$ (2), $28°$ (3) and $0°$ (4)

value of neutron yield in these conical targets was up to $4 \bullet 10^4$ neutrons per shot. The analysis of these measurements showed, that in the context of done hypothesis (i.e. the heated plasma energy is proportional to full laser energy E_{las}) it occurs the specified functional dependence of neutron yield from initial conditions [3]-[4]. This important result give ability to estimate the effective deuterium temperature in the process of interaction: $kT[keV] = 22.5 \bullet (E_{las} [J]/m_o [mg])$, m_o- deuterium mass. Evaluations show the interval of kT variation from 3 to 20 keV. Moreover, it occurs, that not above 16% of all D_2-gas mass is heated up to thermonuclear temperatures.

For the initiation of thermonuclear fusion in conical targets are used also linear driver system based on usage of chemical explosive. This approach permits to study and to optimize the targets for ICF. This method make possible to investigate the "clear" hydrodynamics, without the consideration of the multi aspect processes of interaction electron and laser beams with plasma. The main result of these experiments can be stated as follows. Neutron yield of 10^6 neutrons was measured for liner velocity 5.6 km/s and 10^7 - for 18 km/s. In last one is was used the additional layer cumulative system.

318

2D computational modeling based on equations of hydrodynamics with wide-range real equations of state for lead (the body of target) and for aluminum (shell) lead to specific picture of processes in these conical targets. On the first stage of process arises the acceleration of the target shell by laser radiation or by linear explosive driver system. At the interaction of moving shell with target walls there are the cumulative effects carrying into increasing of velocity of leading part of the shell, see Fig.1b. The D_2 plasma heating up to thermonuclear temperatures is the result of interaction of the shock waves with spherical top of cone [5], Fig.2. (Radius of cone top is equal to 7.5 - 10 mkm and depends on technique of the making.)
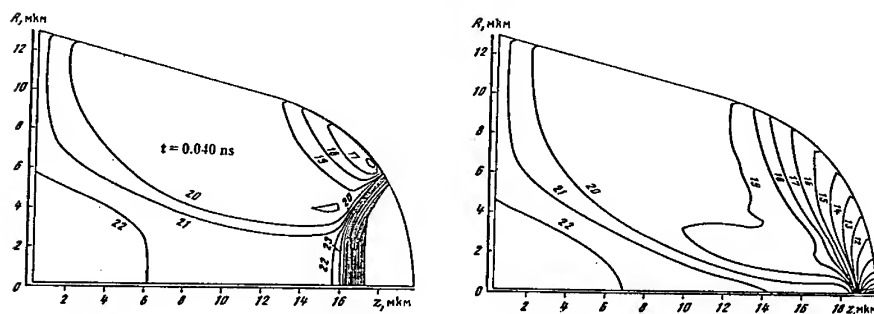
FIGURE 2. Compression of the deuterium gas in spherical top of a cone [5]. Collapse parameters, t = 0.047 ns, P(max) = 14 Mbar, r(max) = $2 \cdot 10^{-3}$ g/cm^3, T(max)= 7.1 keV. Isobaric lines- lg(Pn [Mbar])= - 0.1n +lg12.6.

Apropos, the calculated value of temperature (7.1 keV) was found almost equal to mentioned above statistical estimation (6.1 keV). Process is finished by the expansion of lead in the region of cone top.

SUMMARY

Such conical targets are interesting for the initiation and ignition of thermonuclear fusion in laboratory conditions with the usage of drivers with moderate energetic characteristics.

REFERENCES

[1] V.I.Vovchenko et al. Generation of thermonuclear neutrons by laser action on a conical target //*Pis'ma Zh.Eksp.Teor.Fiz.* 1977. **26.** No. 9. P.476-477.

[2] S.I.Anisimov et al. Generation of neutrons a result of explosive initiation of the DD reactions in conical targets //*Pis'ma Zh.Eksp.Teor.Fiz.* 1980. **31.** No. 1. P.67-70.

[3] I.K.Krasyuk, P.P.Pashinin, A.Yu.Semenov. New similarity relations based on the statistical analysis of laser thermonuclear fusion experiments //*J. Russian Acad. Sci. Physics-Doklady.* 1994. **39.** No. 5. P.330-332.

[4] I.K.Krasyuk, P.P.Pashinin, A.Yu.Semenov. New scaling based on statistical analysis of laser fusion experiments //*Laser Physics.* 1994. **4.** No. 3. P.532-537.

[5] A.I.Marchenko, V.V.Urban. Modeling of two-dimensional shock waves cumulation in conical target. In: "Investigation of physical processes in planar and conical targets". Moscow: Nauka. 1992. Proc. IOFAN, **36.** P.112-124.

ASSESSMENT OF FIRST WALL DAMAGE FROM TARGET X-RAY EMISSION AND SCATTERED LASER LIGHT FOR THE NATIONAL IGNITION FACILITY

M. TOBIN, A. ANDERSON, A. BURNHAM, AND T. BERNAT*
Lawrence Livermore National Laboratory
L-481, P.O. Box 5508
Livermore, CA USA 94550

Predictions for NIF ICF target x-ray emission are presented. Validation experiments confirm the key features of the x-ray emissions and their effects on the NIF chamber B_4C first wall. Predictions of a possible first wall 0.35-μm laser irradiation compared to more experimental results conducted to determine B_4C response all suggest B_4C is an acceptable first wall material.

The National Ignition Facility (NIF) will consist of a 1.8 MJ, 0.35 μm laser with 192 independent beamlets, a ~ 50-fold increase in laser energy over the Nova facility located at Lawrence Livermore National Laboratory (LLNL). The main pulse length will be ~ 4-5 ns. Beams are transported into the chamber in 2×2 groups and further in cones, of ~ 27° and ~ 53° oriented around each pole of the sphere, supporting the baseline inertial confinement fusion (ICF) indirect drive approach to ignition. The maximum routine yield will be 20 MJ, a ~ 300-fold increase in non-neutron emissions over current Nova experiments. NIF will be designed to eventually conduct as many as fifty 20-MJ shots in one year, in addition to shots of lower yield and no yield. The annual yield will be bounded by 1200 MJ.

Part of the criteria for setting the radius for the NIF chamber is the smallest value that results in acceptable x-ray damage to a first wall for a 20-MJ yield. Acceptable damage is partially defined as, at best, no material being evolved for a 20-MJ shot, or as a minimum, evolving less material from the first wall surface than is introduced by the target itself. Emitted material will deposit on the final optical surface, a fused silica debris shield, and contribute to beam obscuration, posing potentially significant but as yet unquantified maintenance concerns. Elimination or minimization of the first wall contribution may alleviate some of these concerns.

NIF First Wall X-ray and Laser Irradiation Threats

The baseline NIF ICF target we consider is a 1-cm long, 0.6-cm diameter, 0.3-cm laser entrance hole (LEH) and 30-μm thick Au wall. Accurate knowledge of the x-ray emission from NIF targets is critical to our study of first wall response. A series of 1-D LASNEX calculations have been performed that predict the x-ray emissions for yields ranging from 100 kJ to 20 MJ.

The x-ray output of the target is partitioned into two components in the LASNEX runs. First is the radiation 'leak source' that simulates LEH x-ray losses. The other part is the radiation flux on the outside surface of the gold for transmission through and emission by the gold hohlraum wall. Time history plots of each component were examined to determine the time interval for emission of 10% to 90% of the total energy. Shapes of spectral curves for each radiation were fit to blackbody (color) temperatures (BBT) to give one- or two-BBT fits for LEH emission and wall radiation. For calculation of fluences within the chamber, the assumed angular distributions were isotropic emission for wall radiation and

Lambertian distribution (cosine law) for x rays emitted from the LEH. Table 1 shows the results for laser energy on a disk, and yields of 100 kJ and 20 MJ.

Table 1. Predicted NIF ICF target x-ray emissions. Nova equivalent fluences are based on matching B_4C melt depths (or peak surface temperature if no melt occurs).

Yield (MJ)	Laser Energy (MJ)	X-ray Yield (MJ)	BBT (eV)	Pulse 10-90% (ns)	Peak NIF 1st Wall Fluence (J/cm^2)	Nova Equiv. Fluence (J/cm^2)
(disk)	1.50	1.05	200	3	0.66	0.76
0.1	1.80	1.08			0.56	0.33
		0.70	255	10	0.44	
		0.23	52	61	0.07	
		0.15	12	61	0.05	
20.0	1.80	4.94			2.61	1.85
		2.30	400	13	1.44	
		1.05	207	13	0.66	
		1.38	81	67	0.44	
		0.21	15	67	0.07	

A curve-fitting technique was used to approximate the x-ray output pulses obtained from the 1-D LASNEX simulations. The form of the curve fit is a double exponential, which is well suited to describing the x-ray pulse shapes. The rapid "turn on" of the LEH and wall emissions can be captured, as can the slow decay. The decay in the LEH x rays comes from the gradual hole closure and the cooling of the hohlraum interior. The wall emission decays with its temperature as energy is lost radiatively and as the material expands into the vacuum.

LASNEX is typically used to predict conditions inside the hohlraum in the time before and during the thermonuclear burn. The accuracy of LASNEX predictions of the x-ray emission from the exterior of the hohlraum wall was confirmed with two experiments on the Nova laser facility.[1] The total x-ray emission (including late time) from the thin wall (30 μm) of a gold hohlraum was measured with the Dante diagnostic[2] and compared to a LASNEX simulation. The timing of peak emission, rate of decay of emissions, and effective blackbody spectra agreed well.

NIF will be configured to allow the implementation of direct drive ICF experiments by designing into the facility the ability to create symmetrical target irradiation. This would be done during an extended maintenance period by changing up to half of the beamlet paths from indirect drive irradiation cone angles to near equatorial ports. Direct drive targets are fully illuminated by each beam. As the target implodes, significant amounts of incident laser light can be refracted to the chamber wall, presenting the possibility of unacceptable material removal.

Testing of candidate first wall materials to predicted x-ray fluences was done using x-ray emission from Nova hohlraum targets. Due to differences between the predicted NIF x-ray threat and the x-ray environments available on Nova (~ 220 eV spectrum and 2 ns pulse), an equivalent NIF fluence for Nova irradiation conditions had to be considered in interpreting results. For example, we predict that a Nova fluence of 1.85 J/cm^2 produces the same melt depth in B_4C as the predicted 20-MJ x-ray output shown in Table 1. We believe that the dominant material response is spall of partially melted material so that matching melt depths is appropriate. This experimental approach constitutes an overtest, since the shorter pulse on Nova

322

induces a greater peak stress in the material. Quantifying the degree of overtest is an area of ongoing investigation and provides a degree of conservatism to our results and conclusions.

Predictions of the laser first wall irradiation using LASNEX were performed by Weber of LLNL. The direct drive target chosen for analysis had a radius of 1.695 mm and was irradiated with a 1.6-MJ continuous laser pulse, with about 200 kJ in a foot pulse of 5.5 ns and the remainder in a 6-ns main pulse. The non-absorbed laser energy fraction becomes a few percent at ~ 7.5 ns resulting in a first wall laser pulse duration of ~ 4 ns. Results suggest that up to 40% of 1.6 MJ incident light can be directed toward the first wall. The peak fluence on the chamber wall is < 0.3 J/cm^2.

First Wall Responses to X-rays and Laser Irradiation

Boron carbide had the least material removed in Nova x-ray exposure experiments, as shown in Figure 1. Most samples show thermal stress cracking, and all materials show surface roughening above about 1.0 J/cm^2. Multple exposures cause additional roughness and the appearance of angular pits in the surface. The pits seem to be locations where small sections of thermally shocked material has been flaked off or popped out by the additional thermal loading. The models for predicting this ablation mechanism, including brittle crack nucleation/growth and statistical methods for the pop-out of isolated flakes, are being developed.
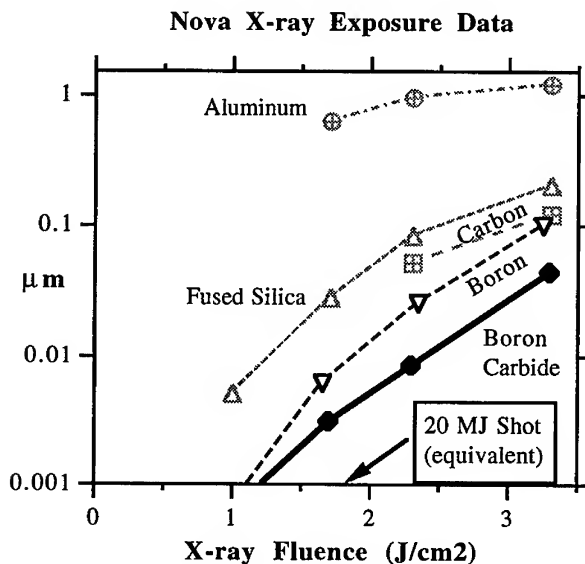
Figure 1. Estimated removal depths as a function of x-ray fluence for Nova experiments.

The small amount of B$_4$C that is removed by x-rays is likely caused by thermal crazing and spalling of small particulates. The degree of crazing and spalling

depends on the fluence and source of the B_4C. At 1 J/cm^2, corresponding to NIF disk and low-yield ignition shots, no crazing or spalling is present, but there is some evidence of surface melting. At 1.6 J/cm^2, corresponding to a 15 MJ yield, slight crazing appears after one shot on a polished surface, and a few percent of the surface spalls to a depth of about 0.35 μm on subsequent shots. At 2.3 J/cm^2, corresponding to a 30 MJ yield, substantial crazing occurs, and a higher surface covage of 0.5 μm pits are formed by spallation.

For 350-nm light irradiation of 2.4 ns, the threshold for significant B_4C surface melting is between 0.5 and 1 J/cm^2, and higher fluences induce thermal crazing of the surface similar to that observed for x-rays. The fluence damage threshold varies with pulse length. Thermal conduction and two-photon effects predict a $t^{0.5}$ dependence, but observed dependence is weaker. The primary mechanism for material removal at ≤ 1 J/cm^2 appears to be particulate spallation. Most of the spalled particules are < 5 μm. The onset of vaporization is ~ 1.5 J/cm^2, which would result in a thin absorbing film on the final optic and must be avoided for NIF.

Laser light is attenuated exponentially as it is absorbed in material, as long as the intensity is below a threshold for plasma formation at the target surface. The linear absorption coefficient decreases roughly exponentially with wavelength from 31 μm^{-1} to 3.9 μm^{-1} over the range of 350 to 1050 nm. That the observed damage threshold is several times higher for 1.053 μm light than 0.35 μm light is consistent with the smaller absorption coefficient. Results suggest the NIF first wall 3ω fluence is half the spall fluence and 1/4th the incipient vaporization fluence. These results suggest a diffraction grating that distributes unconverted NIF laser light uniformly to the first wall (0.7 J/cm^2 of 1,2, and 3ω), would be a superior solution to the wedged focus lens/absorbing glass first wall solution currently proposed.

Optics that had collected particulate debris from the laser-irradiated samples were subsequently tested for damage threshold at 0.35 μm. The 3ω light tends to clean B_4C particulates from the optic and provide some number of useful high fluence shots before the onset of severe damage. An optic with a clean damage threshold of 15 J/cm^2 that received particulate contamination survived 100 shots at 9 J/cm^2 with no damage and 3–5 shots at 13 J/cm^2 with acceptable damage. The average fluence for a NIF 1.8 MJ shot is ~ 7.5 J/cm^2. A similar optic having a 6-nm thick-film of B_4C formed from vaporization of the B_4C target at 1.5 J/cm^2 of 3ω light had a damage threshold of only 1 J/cm^2, indicating that fluences where B_4C vaporizes must be avoided.

Experimental results of both laser and x-ray irradiation indicate B_4C may be an acceptable first wall material for the 5-m radius NIF chamber.

1) Anderson, A., and R. Turner (March 7, 1996), *Benchmark Experiment for Nova Hohlraum X-Ray Emission*. Lawrence Livermore National Laboratory, Livermore, California, Internal Memo L-21623-01.

2) Kornblum, H., R. Kauffman, and J. Smith (1986), "Measurement of 0.1–3 keV X Rays From Laser Plasmas," *Review of Scientific Instruments*, **57**(8), 2179-2181.

A COMPARATIVE ANALYSIS OF THE ELECTRON HEAT CONDUCTIVITY AND RADIATION TRANSFER IN DIRECT AND ICF TARGETS.

N.V. ZMITRENKO

Institute of Mathematical Modeling, Russian Academy of Sciences,
4 Miusskaya Sq., 125047, Moscow, Russia

S.Yu. Gus'kov

P.N. Lebedev Institute of Physics, Russian Academy of Sciences,
53 Leninsky Pr., 117924, Moscow, Russia

We have analysed the typical physics situations which occur in the "laser greenhouse" targets [1] and in the indirect driven ICF targets. In the first case the role of radiation processes in non-considerable one. The sizes of capsule under break-even conditions are approximately the same both for direct and indirect scheme. So, we obtain the similar ablation processes (with a considerable role of gas dynamic motions) and similar scaling of ablative pressure upon an absorbed power.

1. "Laser Greenhouse" target analysis

It is typical for a break-even design, that the electron heat conduction fluxes which produce an ablative pressure are about a few *TWt* or 20 - 40% of a laser power. The corresponding intensity is about 2×10^{14} *Wt/cm²*. The radiation flux is approximately in one hundred times less. A radius of a such kind of a capsule is about 1000 *μm*, an aspect ratio is belonged to the range of 10 - 200.

It is essentially, that an electron temperature in a foam absorber of a "laser greenhouse" target and in an ablation region is about 2 - 4 *kev*. It means, that the ablative velocity is comparatively high (about 5 - 10 *μm/ns*). So, the "laser greenhouse" can be more stable, than the traditional direct drive scheme due, particularly, this reason.

The hot region in a "laser greenhouse" target has a low density (about 2×10^{-2} *g/ccm)*. It means, that the optical thickness of a foam and an evaporated ablator matter is very small (less, than 10^{-6}).

This condition provides an approximation of a bulk emission for a radiation. In addition, the radiation flux is about 1 - 2 % of a laser power. The rate of energy losses due to the radiation is very small in comparison with a laser energy deposition.

We have investigated the heat wave, which evaporated an ablator of a capsule. It is essentially, that this heat wave is belonged to a second type. If we do not take into account a gas dynamic motion, we shall obtain a wrong estimation of a hot region size. The alternative regime can be occur with laser intensity more than 10^{15} *TWt/cm²*.

Because the role of a radiation is not considerable the simulations within three-temperature or spectral radiation transport approximation give the same values of a compression and a neutron yield, that the bulk emission one.

2. Indirect targets

Let us consider the various capsules with radius about 1000 *μm* = 0,1 *cm* like in a "laser greenhouse" break-even design. So, we can speak not about intensity *W*, but flux $H = r^2W$. In addition, we can use a subscription W_e for an electron heat conductivity fluxes and W_r for a radiation ones.

Then we can use an universal scaling for an ablation pressure in a form

$$p_a \cong 30H^{2/3} Mbar,$$

where *H* is *TWt*.

If we consider the "laser greenhouse" target, $H = H_e$ is approximately 30 % of a laser flux. If we consider the indirect target, $H = H_r = r^2W_r = r^2\sigma T_r^4$. So, the ablative pressure about 1 Mb is corresponded to radiation temperature $T_r \cong 50eV$.

In the last case the capsule will be compressed for 50 - 100 ns. These conditions correspond a long time action of the low temperature radiation. We've simulated the such targets with an ablator of polystyrol (CH) or berillium (Be). The high values of a compression ratio $(C_r \approx 10 \div 50)$ were obtained. This case

326

corresponds $H_r \approx 10^{-2}\,TWt$ or the value, which occurs in "laser greenhouse" targets for radiation fluxes.

Another case should be corresponded to a radiation flux of a 2 - 4 TWt range, like an electron heat conductivity flux in a "laser greenhouse" target. These conditions correspond a radiation temperature of about 300 eV. It is typical for various indirect driven scheme for a break-even design.

Appendix

References

1. S.Yu. Gus'kov, N.V. Zmitrenko and V.B. Rozanov, *JETP* **81(2)**, 296 (1995).

5.- HIGH DENSITY PHYSICS

LASER-PLASMA RESEARCH AT LULI :
AN OVIERVIEW

H.A. Baldis, F. Amiranoff, C. Chenais-Popovics, J.C. Gauthier, M. Koenig,
C. Labaune, E. Leboucher-Dalimier, D. Pesme, A. Migus

Laboratoire pour l'Utilisation des Lasers Intenses (LULI), CNRS UMR 100
Ecole Polytechnique, 91128 Palaiseau Cedex, France

LULI plays a key role as a major laser facility for France and Europe. We will review some highlights of research programs carried on by LULI during the past year, as well as the present program of upgrade "Jouvence du LULI". Areas of research we will discuss include laser acceleration of particles and interaction physics in conditions of interest to ICF, such as parametric instabilities, atomic physics in high density plasmas, shocks and equations of state, and collision of plasmas. Part of the ongoing project of upgrade is to bring on line an ultra high intensity short pulse, synchronised with the main laser system.

1 - Introduction

The Laboratoire pour l'Utilisation des Laser Intenses (LULI) is a CNRS research laboratory at Ecole Polytechnique, and one of the leading European's major laser facilities for research on high intensity interaction with matter. Principal areas of research include parametric instabilities and equation of state studies in the context of Inertial Confinement Fusion (ICF), X-ray lasers and applications, atomic physics, particle acceleration with the aid of laser fields, and basic laser-plasma physics and applications.

The LULI facility consists of a glass laser system delivering 6 beams with a total energy of about 600 J in a 0.6 ns pulses, and a newly developed facility with chirped pulse amplification of a subpicosecond pulse with a few tens of terawatt capability. Five experimental rooms complete the facility, allowing different experimental configurations.

Apart from serving a large community of French and European research groups, LULI has a strong group of in-house research programs. Some recent research highlights will be presented in the following sections.

2 - Parametric instabilities in the context of ICF (C.Labaune et al.)

Using the six-beam facility, an extensive program on the study of parametric instabilities in the context of Inertial Confinement Fusion (ICF) has been carried out. The studies have been focused on stimulated Brillouin and Raman scattering which are among the most important parametric instabilities in laser-produced

330

plasmas. The results have been obtained using a 1.05μm wavelength as a pump interacting with a well-characterised pre-formed plasma, and Thomson scattering as the key diagnostic[1].

Direct observation of the location of ion-acoustic waves (IAWs) in the front part of the plasma explains for the first time the stimulated Brillouin Scattering (SBS) spectra in backward and in side directions. This is shown in Fig. 1 in the case of back-scattering. The region of SBS activity is rather limited and the location depends on the SBS geometry[2].
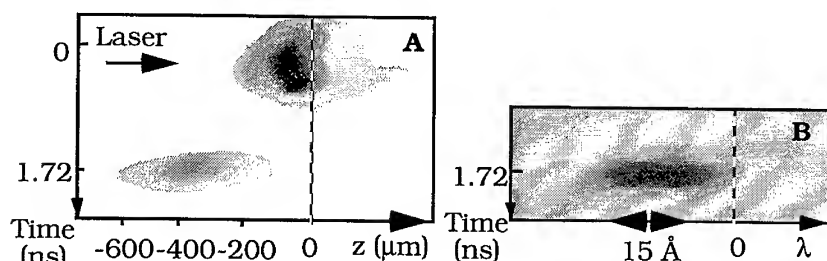
Figure 1 : A) Location of the ion acoustic waves associated with backward SBS as a function of time. The early signal corresponds to plasma emission during pre-forming beams. The late signal corresponds to Thomson scattered light from IAWs during the interaction. B) Time-resolved spectrum of the back-scattered light..

Temporal and spatial interplay between IAWs associated with stimulated Brillouin scattering (SBS) and electron plasma waves (EPW) associated with stimulated Raman scattering (SRS) has been observed in conditions of interest to ICF. Although these waves grow over the same well localised region of plasma, they are never observed to be present at the same time. Raman starts only in the second part of the laser pulse when SBS has disappeared, mainly because of the reduction of electron density due to plasma expansion. The dominance of SBS over SRS may have important implications in the interpretation of results from multiple beams configurations, such as in the interior of holhraums.

The sensitivity of stimulated Brillouin scattering to the initial conditions has been studied using two interaction beams. Results include the first observation of resonant behaviour when ion acoustic waves driven by two different beams have a common wave-vector, and the first evidence that overlapping beams can have a detrimental effect to the growth of SBS in situations where there is a wave-vector mismatch between IAWs from two independent SBS decay processes.

3 - High pressure generation and EOS studies (M. Koenig et al)

The study of the Equation of State (EOS) of matter in high pressure conditions (above 10 Mbar) is a subject of great interest for several fields of modern physics. In particular, it is important in the context of ICF research and astrophysics. In the

past, EOS measurements in the tens of Mbar domain could be performed only by nuclear explosions. Nowadays it is possible to reach very high pressures in laboratory by using powerful pulsed laser-generated shock waves in solid material.

Flatness of the shock fronts and low preheating in the material ahead of the shock waves are essential to obtain accurate measurements of EOS. Owing to the moderate energy available at LULI, we favoured the direct drive approach with optically smoothed laser beams using Phase Zone Plates (PZP). It allowed the production of a flat-top intensity distribution of laser light in the focal spot and hence of flat shock fronts[3] . We also paid attention on time history of the target rear side emissivity which gives information about the preheating effects. Once high quality shocks are obtained, it becomes possible to measure shock parameters precisely . In order to perform EOS measurements, we adopted the impedance-matching technique which makes it possible to achieve a relative determination of one EOS point of one material by taking the EOS of the other one as a reference. As a first step we applied this technique to aluminium and gold (Fig. 2) whose EOS are known in this range of pressures in order to test the overall precision of the method. The error bars have been determined considering all the sources of errors in the measurement of the shock velocity: uncertainties in the step thicknesses ($\pm$ 0.03 μm), the shock breakout time ($\pm$ 5 ps) and the streak camera sweep speed .
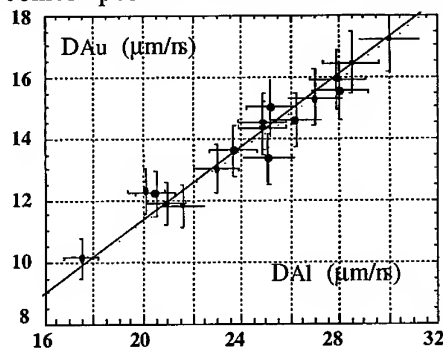
Figure 2. Experiments with aluminium-gold targets. The shock velocity in gold is plotted versus the shock velocity in aluminium. Error bars are 4.5% and 6% for aluminium and gold respectively. The solid line represents the theoretical SESAME data.

With this experiment, we have shown the possibility of obtaining quantitative measurements of EOS assuming known a reference material[4]. But one would be interested to have an absolute determination of EOS when the impedance matching technique cannot be applied. Therefore it is necessary to measure a second parameter such as fluid velocity or temperature. We have recently performed some experiments to infer shock temperature by measuring the so-called "color temperature". The principle consists of recording the target rear face emissivity on the same streak camera in two different visible spectral windows. The ratio between the two spectral intensities, assuming blackbody emission, gives an equivalent temperature "color temperature" T_c of the plasma. This temperature is different from the shock temperature T_s because of the rear face unloading in the vacuum. Taking into account such an expansion by simulations or simple self-similar solutions, we have shown that T_s can be deduced within twenty percent of accuracy. This technique can only be applied for a certain range of shock temperatures (typically $\leq$ 10 eV) where the blackbody emission in the visible is around its maximum.

4 - Atomic physics in hot plasmas (C. Chenais-Popovics et al)

The experimental activity of the group of Atomic Physics of Hot Plasmas has been centred on the study of the collision of counter-streaming intermediate-Z plasmas and the evidence of the stagnating to interpenetrating regimes. This is of interest for indirect drive ICF since plasma collisions inside the hohlraum could perturb the implosion. Experiments and simulations have been performed in a simple geometry where two opposite laser beams of the LULI facility ($\lambda = 0.53$ μm, $\tau = 600$ ps, $I = 3\text{-}9\text{x}10^{13}$ W/cm^2) were focused on two 0.8 μm thick Al or Mg foils separated by a distance of 450 to 1200 μm. The conditions in the collision were varied by changing the laser intensity and the inter target distance. Inter-penetrating of the plasmas and ion temperature in the collision have been measured, as well as electron temperature.[5] The experiment has been completed by a measurement of the electron density in the collision region and the lateral spread of the plasma (see paper W 1-4).
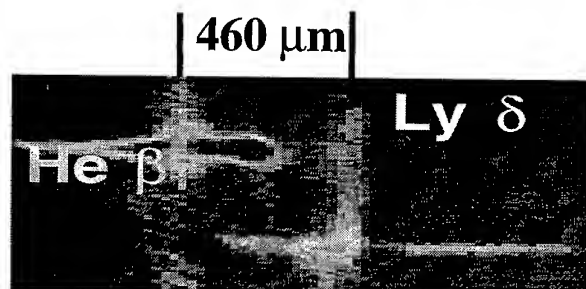
Figure 3 Measurement of inter-penetrating.: spectrum obtained for a laser intensity of 6x 10^{13} W/cm^2, and an inter target distance of 460 μm.

An ion temperature of 10 keV has been measured. Figure 3 shows a spectrally resolved image which has evidenced the inter-penetrating of the plasmas, by the presence of aluminium and magnesium X-ray emission in the same region. Comparison of the experiments with simulations done with a 1.5-D multi-fluid eulerian code explains clearly the transition between stagnating and interpenetrating plasmas by the difference in density and relative velocity of the plasmas. Details will be found in paper W1-4 of this conference, and in a coming publication.

Opacity measurements and calculations have been started recently in the Atomic Physics group. Collaborative experiments have been performed with MPQ (Garching, Germany) in which the absorption of an Al foil has led to electron temperature measurements in complement of measurements done in the XUV range (see paper PM24). Average atom calculations of opacities with n-l splitting in the atomic structure have been performed and can be used in non-Local-Thermodynamic-Equilibrium (see paper PM23).

5 - Atomic physics in dense plasmas (E.Leboucher-Dalimier et al)

Recent experiments have produced data for understanding the radiative properties of strongly coupled plasmas. These experiments gave some evidence of the existence of quasi-molecular emission (satellites) and forbidden transitions [6,7]. We create hot (Te>200eV) and dense (Ne>10^{23}cm^{-3}) plasmas of moderate Z elements (Al, F) by colliding two thin foils accelerated by two laser beams (λ=.263 µm, E=25J, τ=500ps). The densest and most emissive plasmas have been created for very weak initial thickness (a few microns) and initial foil separations quite similar to the focal spot diameter. These values are in agreement with hydrodynamic simulations (1-D1/2 FILM and 2-D LASNEX (collaboration with T. Shepard, Lawrence Livermore Laboratory)) taking into account two-dimensional effects. These effects, deleterious for the compression, have been exhibited and measured thanks to two independent diagnostics: spectroscopy with a space resolution perpendicular to the collision axis and monochromatic 2-D imaging (collaboration with E. Förster, University of Jena). Recently beam smoothing techniques have been implemented (RPP and PZP plates) in order to enhance the overdense plasma X-Ray emission (collaboration with A. Giulietti, University of Pisa, and C. Danson, Rutherford Appleton Laboratory).

Using Molecular Dynamics simulations (collaboration with A. Calisti, University of Marseille) we showed that the plasma conditions are favourable to a quasi-molecular approach: the probability density for ions to be mutual Nearest Neighbours (NN) and to be Next Nearest Neighbour (NNN) reveal well separated maxima. Moreover, correlation parameters in the range $1 < \Gamma < 2$
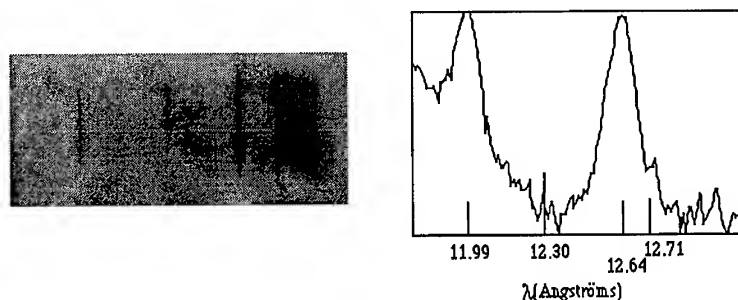
Figure 4: Fluor Lyβ line and its molecular satellite at 12.71Å. The molecular satellite occurring at 12.765Å is not resolved from helium like dielectronic satellites.

have been deduced from our experimental results exhibiting molecular satellite-like features on the red wing of the Fluor Lyβ profile (Fig.4). Thus an exact calculation of the (NN) interaction and a molecular emission code taking into account plasma perturbation have been developed. The code gives access, for moderate Z, to the equipotentials for the dicenter embedded in the plasma, to the molecular transition

334

energies and to the dipolar matrix elements. The molecular satellite features (Fig.4) remain even if space and time integrations are involved : this possibility comes from the fact that the molecular satellite positions do not evolve significantly with density and temperature.

6 - Electron Acceleration (F. Amiranoff et al)

a - Beat Wave

A program on the production of intense electric fields in plasmas by beat-wave and on the acceleration of relativistic electrons in these fields has been recently completed [8]. In this scheme the beating of two laser pulses with frequencies whose difference is close to the plasma frequency resonantly excites an electron plasma wave with a relativistic phase velocity. Electrons injected in this plasma wave with a velocity close to the speed of light will then be accelerated over long distances and gain a very large energy.

In the experiment performed at LULI, we used two pulses 65 mm in diameter at 1.053 μm (90ps, 12J) and 1.0642 μm (200ps, 4J) focused with a 1.5 m focal length doublet in deuterium at the resonant pressure corresponding to a fully ionised plasma with an electron density close to $1.12 \cdot 10^{17}$ cm^{-3}. A relativistic electron beam is injected in the plasma along the laser axis and the accelerated electrons are measured with a magnetic spectrograph. Figure 5 summarises the results. The higher the injection energy, the longer the electrons stay in phase with the accelerating part of the wave. The maximum energy gain is close to 1.4 MeV for electrons with an initial total energy of 3.3 MeV. A comparison with a simple acceleration model indicates a maximum field of 0.7 GV/m and a characteristic accelerating distance of 2.8 mm. This is in agreement with previous results indicating that in our case, the plasma wave is saturated by modulational instability at a level close to 1 GV/m.
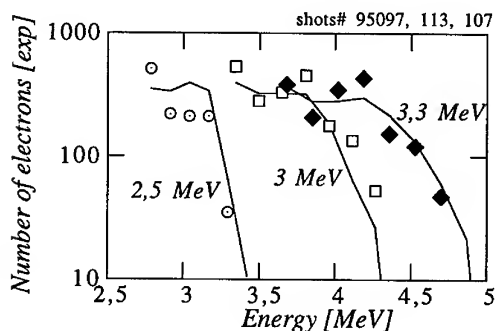
Figure 5 :Best spectra of accelerated electrons for three injection energies. The lines are the spectra calculated with a simple model assuming a maximum field of 0.7 GV/m and an accelerating distance (FWHM) of 2.8 mm.

b - Radial Wakefield

Another mechanism which produces relativistic plasma waves is the laser wakefield. A short laser pulse pushes the electrons of the plasma once forward and once backward. The electrons then freely oscillate at the plasma frequency in the wake of the laser pulse, thus generating a large space-charge electric field.

This density oscillation has been directly measured for the first time by a two pulse frequency-domain interferometry technique [9]. The laser pulse (120 fs FWHM at 0.8 μm and 30 mJ) is focused in helium at low pressures (0.5 - 3 mbar). As the pulse is much longer than the focal spot diameter (11 μm at 1/e in intensity) the electron density perturbation is mainly radial. The next figure shows the radial profile of the density perturbation and its time evolution on axis. These results are in very good agreement with numerical calculations and show very large density perturbations of the order of 100%. The longitudinal regime, relevant to the acceleration of charged particles, will be reached with a more powerful laser.
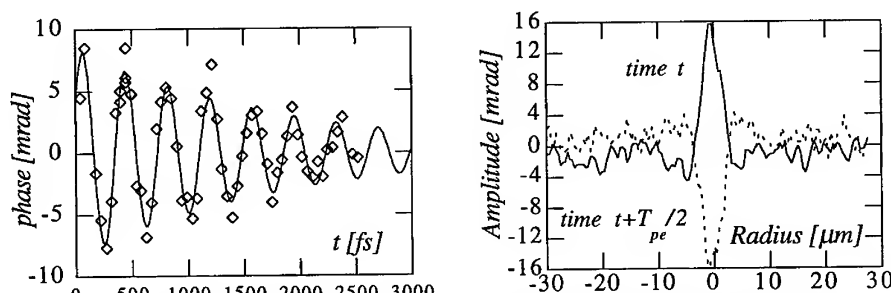
Figure 6 :Electron density perturbation in the wake of the laser pulse in 2.2 mbar of He.
Amplitude as function of time (left) and as function of radius (right). T_{pe} is the plasma period.

References

[1] C. Labaune, H.A. Baldis, N. Renard, E. Schifano, S. Baton, A. Michard, W. Seka, R.E. Bahr, B. Bauer, K. Baker, and K. Estabrook, Phys. Rev. Lett. **75**, 248 (1995).

[2] C. Labaune, H.A. Baldis, E. Schifano, B. Bauer, A. Michard, N. Renard, W. Seka, J.D. Moody, K.G. Estabrook, Phys. Rev. Lett **76**, 3727 (1996).

[3] M. Koenig et al., Phys. Rev. E, **50** , R3314, (1994).

[4] M. Koenig et al., Phys. Rev. Lett., **74** , 2260 (1995).

[5] O. Rancu et al, Phys. Rev. Letters **75**, 3854 (1995).

[6] E. Leboucher-Dalimier, P. Angelo, H. Derfoul, P. Gauthier, A.Poquérusse, AIP **8**,122 (1995).

[7] E. Leboucher-Dalimier, A. Poquérusse, P. Angelo, Phys.Rev. E **47**, R1467 (1993).

[8] F. Amiranoff *et al.*, Phys. Rev. Lett. **74**, 5223 (1995) ; F. Amiranoff et al., to be published in IEEE Transactions on Plasma Science, and references therein.

[9] J.R. Marquès *et al.*, Phys. Rev. Lett. **76**, 3566 (1996), and references therein.

HIGH QUALITY SHOCK GENERATION AND EOS STUDIES IN THE MULTIMEGABAR REGIME

A.BENUZZI[†], Th.LÖWER[¶], M.KOENIG[†], D.BATANI[‡], D.BERETTA[‡], S.BOSSI[‡], T.HALL[§], J.KRISHNAN[†]

† LULI, Ecole Polytechnique, 91128 Palaiseau, France
‡ Dipartimento di Fisica, Università di Milano, Italy
¶ Max Planck Institut fur Quantenoptik, Garching, Germany
§ University of Essex(U.K.)

High quality shock waves with direct and indirect laser drive were generated. We used Phase Zone Plate smoothing technique in the case of direct drive and thermal X-rays from laser heated cavities in the case of indirect drive. The possibility of producing homogenous, steady shock waves without significant preheating effects with both methods has been proved. By using such shocks, copper EOS measurements have been performed up to 40 Mbar, which was previously obtained only with nuclear explosions.

1. Introduction

EOS experiments with shock waves are based on Hugoniot-Rankine relations which depend on u, ρ, p and E i.e. the fluid velocity, the mass density, the pressure and the specific internal energy of the material. Being a system of 3 equations with 5 unknowns, they allow one point on the EOS of the material to be found once two parameters are experimentally measured.
Now, although it has been known for many years that lasers could produce shocks with pressures up to 100 Mbar [1], there has always been reluctance from the EOS community to use them as a quantitative tool in high pressure physics. This was due to the "bad" quality of the shocks as for flatness of the fronts, constant shock velocities and the problem of preheating caused by hot electrons or hard X-rays.

In recent experiments, we showed the possibility of creating spatially very uniform shocks in solids with negligible preheating by using two different methods. The first one consists in producing shocks by direct laser drive with optically smoothed beams [2] (see fig. 1.a); the second one uses thermal X-rays from laser heated cavities to generate shocks ("indirect" drive [3]). Here the beam is focused into a small cavity through an entrance hole and an isotropic X-ray radiation is created whose temperature depends upon the cavity size and the laser power (see fig. 1.b).
For the generation of intense shocks, direct drive allows higher pressures for the same incident laser energy, since no energy is lost in the intermediate step of X-ray conversion. Indeed the shock pressures (in Mbar) are of the order of [4]

$$P_{dir} \approx 8.6 \ (I_L/10^{14})^{2/3} \ \lambda^{-2/3}$$

$$P_{ind} \approx 44 \ (I_c/10^{14})^{10/13} \ \tau_L^{-3/26}$$

in direct and indirect drive respectively. Here I_c is the primary X-ray flux on the cavity wall, I_L the laser intensity on target (both in W/cm^2), τ_L is the laser pulse duration (in ns), λ is the laser wavelength (in μm). Hence in order to reach the same

pressure, for typical laser and cavity parameters, the laser pulse energy required with the indirect method is a factor ≥ 3 bigger than needed with direct drive.
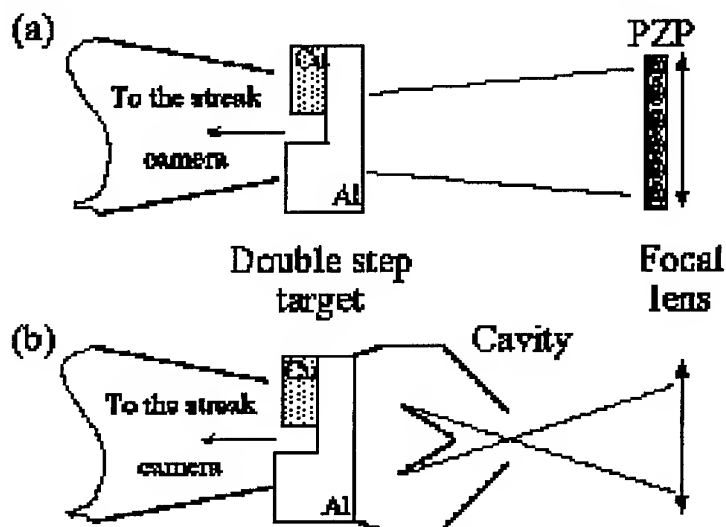
Figure 1: Schematic arrangements of the two experimental set-ups. Double step targets were used to measure the shock velocities in the two materials shot by shot with a visible streak camera. (a) Direct drive configuration. The laser beam, smoothed with a PZP, was focused onto the target. (b) Indirect drive configuration. The laser beam was focused in the cavity whose geometry was designed to avoid preheating.

Anyway, considering shock quality, the indirect drive approach has always been considered the best since it could assure a better irradiation uniformity and hence produce smoother and more planar shock waves. On the other side, in indirect drive, X-ray preheating was the main problem, due to the very high X-ray flux produced inside the heated cavity. To this respect we have shown that, by optimising the shape of the cavity, it is possible to drastically reduce the preheating.

Direct drive experiments were instead mainly affected by the uniformity problem which is connected to the laser intensity distribution in the focal spot (not flat but, in first approximation, gaussian and with many speckles or hot spots). This allowed relatively uniform irradiation to be achieved only using very large focal spots and using targets with dimension smaller than the focal spot radius. This is of course very inefficient and requires very high energy lasers.

In our direct drive experiment we have used the Phase Zone Plates beam smoothing technique [5]. PZPs are made of a Fresnel lens array, each with a random dephasing of 0 or π to break the laser beam spatial coherence and give smoothing effects like in Random Phase Plates. But unlike RPPs, they allow a top-hat intensity distribution to be obtained in the focal spot. As a result, 2D effects are almost completely eliminated (around the centre of the focal spot) and high quality flat shock waves are generated. This also allows high pressures (10 - 50 Mbar) to be reached with relatively small lasers (≈ 100 J).

2. Experimental technique

The experiments were performed using the ASTERIX iodine laser of the MPQ and at the LULI Laboratory, Ecole Polytechnique, at laser intensities $I_L \leq 2\ 10^{14}\ W/cm^2$. In particular in Garching the high laser energy per pulse allowed experiments to be performed with both the direct and the indirect method.

The diagnostic used to detect the shock emergence was the same in the two configurations, i.e. detection of emissivity, in the visible region, of the target rear face, illuminated on the other side by the laser beam. The arrival of the shock causes a sudden variation in temperature and hence in emissivity. A photographic objective imaged the rear face onto the slit of a visible streak camera in order to record such variations in time. Shock velocity can be determined with high precision by measuring the shock emergence time from the base and from the step of the target.

In the indirect laser drive configuration we used a 1 mm size gold cavity and measured a temperature radiation in the range of 100-150 eV. Our cavity has been designed not only to reach such high temperatures, but also to minimise the preheating of the target, produced by direct primary X-rays. Here, a shield with a conical shape has been constructed so that the laser irradiated area and the shocked material are not in direct view of each other, as shown in fig. 1.b.

Finally, instead of measuring 2 parameters in order to determine the EOS, in our experiment we have used the impedance-matching technique with two-step, two-material targets. Here a "relative" EOS point of one "unknown" material can be obtained if the EOS of a "reference" material is assumed to be well known. In our case, the target is made of a base of aluminium (chosen as reference material), which supports two steps, one of aluminium and the other one of the material to be investigated. This target geometry allows the shock velocities to be experimentally determined in the two materials on the same laser shot. By knowing the aluminium EOS and using the laws of shock transmission at the interface between the two materials (the impedance-matching conditions) we could then find the unknown EOS points. , We have recently proved the reliability of this method, used in the past in nuclear experiments, in laser driven shock experiments [6].

4. Results

The technique has been applied to perform relative copper EOS measurements in the 10 - 40 Mbar pressure range. Our results are presented on the (P,U) plane, as usual when the impedance-matching technique is used. Fig. 2 shows all the copper experimental points obtained up to now. These points are compared with the SESAME EOS. The copper EOS is well defined for pressures below 5 Mbar thanks to measurements performed with gas-guns or chemical explosions. The interesting region, where there are few data, is beyond 10 Mbar. Our data are displayed in this region together with those by Trunin [7] and Rothman et al. [8], which were obtained using nuclear explosions and indirect drive respectively. Data are also compared with the SESAME EOS (developed at Los Alamos [9]).
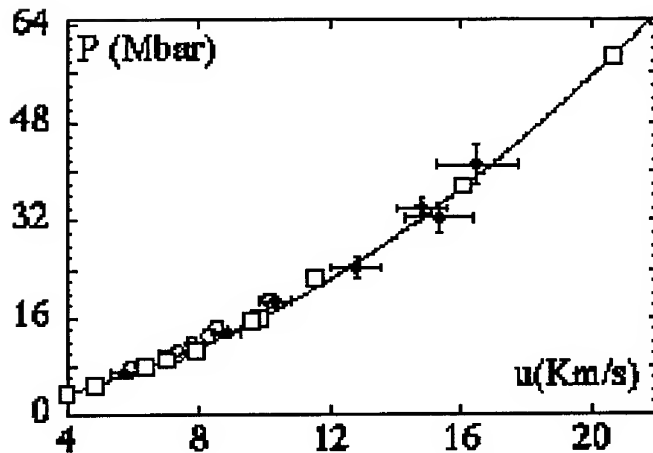
Figure 2. Copper shock pressure P, vs fluid velocity U. Experimental data are compared with the SESAME tables (continuous line). ♦ : our points obtained with direct and indirect drive; □ : Trunin et al. [12] with underground nuclear explosions; O : Rothman et al. [13] points obtained with indirect drive..

Comparing our results with those of ref. [8] we see that higher pressures (up to 40 Mbar) have been reached because we also used the direct drive configuration which has a higher efficiency. A quantitative example of the difference between the two configurations, can be seen by comparing our results obtained at LULI with those obtained in Garching with the indirect drive. In the first case, pressures in aluminium of 10 Mbar were produced with a laser energy on the target of 70 J using direct drive, while with the indirect drive, 250 J were needed to reach the same pressure.

The error bars of our points have been determined considering all the sources of errors in the measurement of shock velocity, i.e. uncertainties in step thicknesses, shock breakthrough time, streak camera sweep speed. Copper EOS points were determined with a precision better than ± 8% which can be easily improved.
The method which has been developed can now be used to measure EOS points of other materials such as carbon or iron, of interest in astrophysics, and doped plastics or low density foams of interest in ICF.

References

[1] F. Cottet et al., Appl. Phys. Lett. 47, 678 (1985).
[2] M.Koenig, D.Batani et al., Phys. Rev. E 50, R3314 (1994).
[3] Th.Löwer, R.Sigel et al., Phys.Rev.Lett. 72, 3186 (1994).
[4] J.Lindl, Phys. Plasma, 2, n.11 (1995).
[5] R.M.Stevenson, C.Danson, I.Ross et al., Optics Letters 19, 363 (1994).
[6] M.Koenig, D.Batani et al., Phys. Rev. Lett. 74, 2260 (1995).
[7] R.F.Trunin, Phys. Uspekhi, 37, 1123-1145 (1994)
[8] S.D.Rothman et al., Proc. APS Topical Conf. on Shock Waves, Seattle (1995)
[9] SESAME Report on the Los Alamos Equation-of-State library, Report No. LALP-83-4 (T4 Group LANL, Los Alamos, 1983).

SEARCH FOR PLASMA SHIFTS IN HIGHER TRANSITION LINES OF ALUMINUM LYMAN SERIES

O. RENNER, E. KROUSKÝ

Institute of Physics, Academy of Sciences CR, 18040 Prague, Czech Republic

D. SALZMANN

Soreq Nuclear Research Centre, 81800 Yavneh, Israel

P. SONDHAUSS, E. FÖRSTER

Research Unit X-ray Optics of the Max-Planck-Gesellschaft, 07743 Jena, Germany

A. DJAOUI

Rutherford Appleton Laboratory, Didcot, Oxon OX11 0QX, United Kingdom

K. EIDMANN

Max-Planck-Institut für Quantenoptik, 85740 Garching, Germany

Spatially resolved spectra of hydrogenic aluminum emitted from a laser-produced plasma were studied using a vertical-geometry Johann spectrometer. The red shifts observed for Lyman series members γ, δ and ε were related to plasma densities via numerical simulation of the experiment. The shifts increase with ion density and the upper principal number of the transition, in accordance with predictions of the ion sphere model.

1 Introduction

The shift in the wavelength of spectral lines due to free electrons in dense and hot plasma[1] (the so-called plasma polarization shift, PPS) belongs to one of the most controversial topics of atomic and plasma physics. The theoretical approaches to line shift predictions and the results of some experimental investigations performed hitherto are partly contradictory. While the theoretical and experimental results of line shifts of H and He$^+$ start to converge, the only successful experiments with higher-Z material were reported by Jamelot *et al.*[2] and Leng *et al.*[3] who observed a strong red asymmetry and a measurable shift of the Li Ly$_\alpha$ and C Ly$_\gamma$ lines. Several experiments carried out for high-Z ions provided questionable results or could not show measurable line shifts.

The aim of the reported experiments was to obtain high-precision spectroscopic data for Lyman series of aluminum which could be used as a benchmark for different theoretical models of the line shifts.

2 Theoretical background

At temperatures typical for our experiment, the red shifts predicted for higher Lyman transitions by using an uniform electron-gas ion sphere model (ISM) are comparable with results of the quantum-mechanical impact theory. [4] Within the framework of the ISM, the formula for the line shift of the spectral lines is

$$\Delta h\nu = \frac{2\pi}{3}\bar{Z}e^2 n_i (r_f^2 - r_i^2), \tag{1}$$

where $\bar{Z}$ is the average ion charge, n_i is the ion density, and $r_{i(f)}^2 = \langle i(f)|r^2|i(f)\rangle$ is the mean square radius of the initial (final) electronic states. For hydrogenic states $r_{nl}^2 = a_0^2 n^2/2Z^2 \cdot [5n^2 + 1 - 3l(l+1)]$. The resulting formula for the Lyman $np \to 1s$ transitions in hydrogen-like ions is given by

$$\Delta h\nu(np \to 1s) = -4.223 \cdot 10^{-3}\text{eV}\frac{\bar{Z}}{Z^2}\left(\frac{n_i}{10^{21}\text{cm}^{-3}}\right)\left\{5n^2(n^2-1)-6\right\}. \tag{2}$$

This formula suggests that at ion densities $(1-2)\cdot 10^{21}$ cm^{-3} which correspond to the conditions of our experiment, measurable line shifts well above the experimental error can be expected for Al Lyman series members γ and higher.

3 Experimental

The experiment was performed at the MPQ iodine laser system ASTERIX. The scheme of experimental setup is shown in Fig. 1.
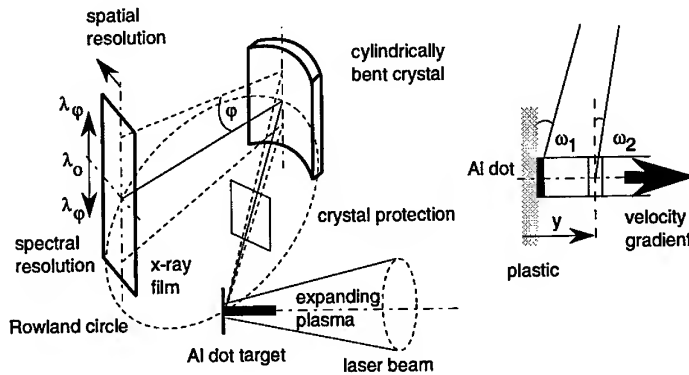
FIG. 1: Experimental arrangement (left) and a schematic diagram of the plasma observation close to the target surface (right).

The laser beam containing an energy of 170 J of frequency-tripled radiation

$(0.44 \, \mu m)$ in a pulse length of 0.4 ns was focussed to a diameter of 250 μm and irradiated an aluminum microdot with dimension of $100 \times 100 \times 1 \, \mu m^3$ deposited on plastic 10 μm thick. According to the 2D code POLLUX simulation,[5] the constrained flow plasma retained the quasi one-dimensional character up to a distance of at least 200 μm from the target surface.

The profiles and positions of the spectral lines Al $Ly_{\gamma-\varepsilon}$ were measured by using the vertical-geometry Johann spectrometer[6] with a cylindrically bent crystal of quartz. The instrument was set to observe the plasma at angle of emission 2° to the target surface and to provide 1D spatial resolution better than 10 μm along the plasma column. The spectra were recorded in single shots on x-ray film. The line positions were measured relatively to the reference wavelengths defined at the distance of 200 μm from the target; their tabulated values were corrected for the PPS and motional Doppler shifts due to variable angle of observation ω along the plasma column (see Fig. 1) and the plasma parameters predicted by the simulations.

The best fit of the spatially resolved spectral lines was provided with the symmetric Gaussian profiles. The line postitions were related to ion densities via the numerical simulation carried out by means of the 1D hydrodynamics code MEDUSA.[7] The computations suggest that the spatially-resolved emission from each point y can be ascribed to a rather narrow range of the plasma parameters (density, temperature, ion charge and velocity). These parameters were averaged over all timesteps by using the emission rate as weighing factor. The validity of this approach was confirmed by comparing the widths of the measured and synthetic spectral line profiles.[8]

4   Results and discussion

The experimental results obtained for members γ, δ and ε of the Al Lyman series are shown in Fig. 2a; for clarity, most of the error bars are suppressed. The observed energy shifts are generally small, approximately 8-10% of the spectral line width (FWHM), but well above the experimental uncertainties. In accordance with the theory, the spectral line energies decrease with the growing ion density and the upper principal quantum number of the transition.

The quantitative comparison of the theoretical and experimental results is provided in Fig. 2b. In view of the very high accuracy required for these measurements, the agreement between the theoretically predicted and observed red shifts is very good. The behaviour of the observed red shifts, i.e. their increase with the growing ion density and with transitions from the higher excited states, indicates that we have observed the real plasma polarization shifts, and not phenomena induced by combined effects of the plasma gradients

and opacities. To confirm unequivocally this interpretation, experiments at higher density plasmas would be required.
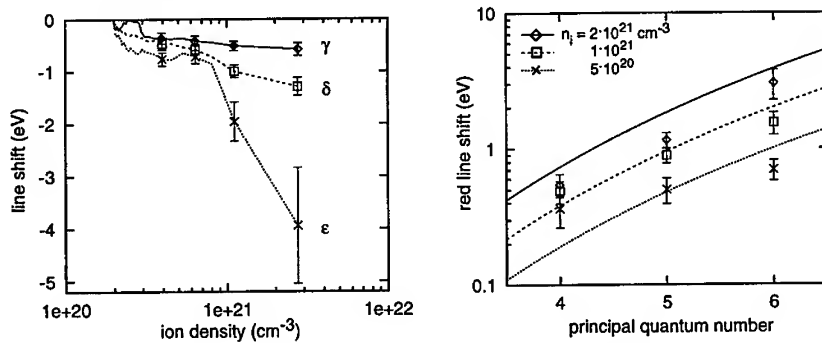
FIG. 2: (a) The experimentally observed shifts of the spectral lines Ly_γ - Ly_ϵ as a function of the plasma ion density. (b) The comparison of the observed (points) and theoretically predicted shifts (lines) for three ion densities n_i.

In conclusion, we report the high precision measurements of the line shifts in a hot, dense plasma. The combination of the dot target geometry producing the constrained flow plasma and of high resolution and efficiency provided by the novel high-dispersion x-ray spectrometer, were paramount to the success of this experiment. The red shifts observed agree well with the PPS predictions inferred from the simple ion sphere model.

Acknowledgments

References

1. H.R. Griem, J. de Physique **49**, C1-293 (1988).
2. G. Jamelot *et al*, J. Quant. Spectrosc. Rad. Trans. **44**, 71 (1990).
3. Y. Leng *et al*, Phys. Rev. E **52**, 4328 (1995).
4. H. Nguyen *et al*, Phys. Rev. A **33**, 1279 (1986).
5. G.J. Pert, J. Comput. Phys. **43**, 111 (1981).
6. O. Renner, T. Mißalla and E. Förster, Proc. SPIE **2523**, 155 (1995).
7. A. Djaoui and S.J. Rose, J. Phys. B **25**, 2745 (1992).
8. O. Renner *et al*, Phys. Rev. Lett. (submitted).

PROGRESS IN SHOCK HUGONIOT MEASUREMENTS USING THE 1TW HELEN LASER.

A.M. EVANS, P. GRAHAM, S.D. ROTHMAN, B.R. THOMAS.
AWE Aldermaston, Reading, Berks, RG7 4PR, U.K.

Use of laser heated hohlraums to generate quantitative high pressure shock Hugoniot data continues to look promising. Although more work is required we have now assembled a body of data from copper in the 10-20Mbar regime that is consistent with that derived from nuclear driven experiments. Application of the technique to a brominated plastic demonstrates the need further to control preheat from the hohlraum. Calculations suggest that a 100TW class laser could support 100Mbar EOS measurements in 100μm samples.

1. Introduction.

A knowledge of the equation of state (EOS) of a wide variety of materials is essential to the design and analysis of ICF hohlraums, capsule implosions and associated physics studies. Fundamental to this is the principal shock Hugoniot. Conventional techniques such as gas-guns[1] and chemical explosives[2] are limited to pressures of a few Mbar, above this the only data comes from nuclear driven experiments performed by the US and USSR[3-6]. Laser driven shocks have typically offered considerably lower accuracy, however in a series of experiments reported at the 23rd ECLIM[7] we demonstrated accuracies approaching 2% in shock velocity from impedance match techniques using the drive from a gold hohlraum heated by the 1TW HELEN laser.

2. Experimental Results.

In reference 7 it was concluded that the greatest uncertainty and source of error lay in target fabrication and target metrology. With this caveat, the data from impedance match experiments using aluminium-copper targets show good consistency, but with a tendency for the derived copper Hugoniot to be a little harder than that inferred from the existing data and represented by the SESAME 3332 EOS.

A further series of aluminium-copper impedance match experiments has been performed. Targets were produced at AWE by vapour deposition and included the aluminium ablator and gold preheat shield combination. Step height metrology by means of a Zygo New View white-light interferometer rather than the laser scanning microscope used previously: this enabled us to determine the 8-10μm steps to better

344

than 1%. Surface finish was about 100nm, a factor 2 worse than in the earlier targets. The streak records show rise times for the optical signal from shock breakout to be correspondingly slower. The improved accuracy in step height characterisation is thus balanced by an increased error in shock transit times resulting in no change to the estimated error in shock velocity and emphasises the need for greater control in fabricating these thin targets.

The data from both series of HELEN laser shots are included in the pressure-particle velocity plot of figure 1. The latest experiments form a self-consistent set which appears rather softer than the earlier laser experiments. Differences include: thickness of the gold preheat layer - $2.7\pm0.3\mu m$ against $3\pm0.3\mu m$ in the earlier shots, metrology method, streak camera calibration and data analysis code. To date none of these has been identified as a root cause of the discrepancy between the two sets of data. Although encouraged by the general agreement of our data with that obtained from nuclear driven experiments more work investigating these systematics is required before we can truly rely on our Hugoniot measurements.
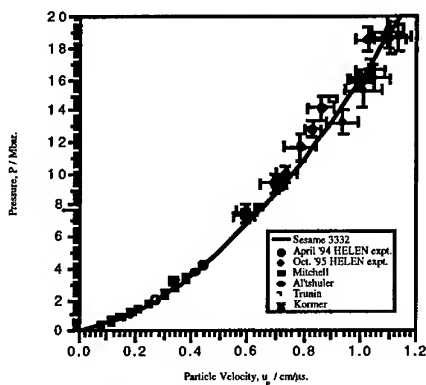
Figure 1. Pressure vs particle velocity for copper principal Hugoniot..
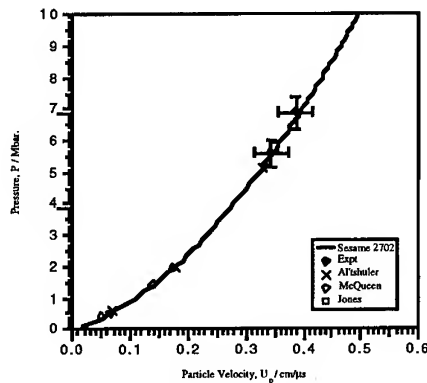
Figure 2. Pressure vs particle velocity for gold principal Hugoniot..

We have applied the technique to two materials of direct interest to ICF. For gold the much lower shock velocity necessitates thinner steps, $5-6\mu m$, to match transit times to the $10\mu m$ aluminium with a corresponding loss of accuracy in step height characterisation. Also, the increased separation of the gold and aluminium Hugoniots in the pressure-particle velocity plane enhances errors due to uncertainties in the aluminium standard EOS. However, the two HELEN shots at around 6Mb are shown in figure 2 and show excellent agreement with the data of Al'tshuler[8] and Jones[9].

346
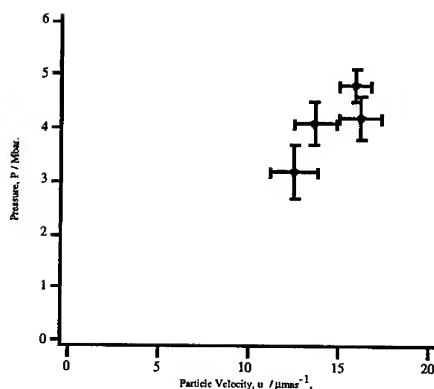
Figure 3. Pressure vs particle velocity for brominated plastic principal Hugoniot..

Recently attention has turned to the brominated plastic used in the LLNL Rayleigh-Taylor instability experiments[10]. The target bases were produced at AWE and steps of brominated plastic were attached at LLNL by hot pressing. Some targets were given a flash of aluminium to modify the shock breakout signal. Large-scale height variations in the brominated plastic were caused by delamination or entrapment of particles between the plastic step and aluminium base. The targets with the aluminium flash coating show clean shock breakout signals although the rise time is up to 40ps. With no aluminium coating there is evidence of some preheat in the brominated plastic due to absorption of M-band emission from the gold hohlraum. We deduce errors in shock velocity from these experiments to be much larger than for the copper and gold shots, of order 5-10%. The results are shown in figure 3. Further work is required to eliminate the preheat.

Conclusions.

Our studies to date have convinced us that accurate Hugoniot data can be obtained from hohlraum driven samples at pressures in excess of those currently available to other laboratory techniques. Although further work is required, useful data at ~10Mb can be obtained from TW class systems while calculations suggest that the next generation of 100TW lasers should enable us to address the 100Mb regime in much larger samples, permitting the targets to be machined from bulk material rather than vapour deposited.

Acknowledgements.

References.

1. W.J. Nellis *et al*, *Phys. rev. Lett.* **60**, 1414 (1988).
2. L.V. Al'Tshuler *et al*, *Sov. Phys. JETP* **11**, 573 (1960).
3. A.C. Mitchell *et al*, *J. Appl. Phys.* **69**, 2981 (1991).
4. S.B. Kormer *et al*, *Sov. Phys. JETP* **15**, 477 (1962).
5. L.V. Al'Tshuler *et al*, *Sov. Phys. JETP* **15**, 65 (1962).
6. R.F. Trunin *et al*, *Sov. Phys. JETP* **29**, 630 (1969).
7. A.M. Evans *et al*, in *Laser Interaction with Matter*, ed. S.J. Rose (Inst. of Physics Publishing, Bristol & Philadelphia, 1994).
8. L.V. Al'Tshuler *et al*, *Sov. Phys. JETP* **7**, 614 (1958).
9. A.H. Jones *et al*, *J. Appl. Phys.* **37**, 3493 (1966).
10. B.A. Remington *et al*, *Phys. Plasmas* **2**, 241 (1995).

Lyapunov Exponent and Diffusion Coefficient in Coulomb Many Body Systems

Y.Ueshima, K.Nishihara
Institute of Laser Engineering, Osaka University, Suita ,Osaka 565 Japan.

D.M.Barnett and T.Tajima
Fusion Studies, University of Texas at Austin, Austin, Texas 78712 U.S.A.

H.Furukawa
Institute for Laser Technology, Suita ,Osaka 565 Japan.

The largest Lyapunov exponents are measured in one component plasmas with the use of a three dimensional particle code SCOPE [K.Nishihara, Kakuyugo Kenkyu 66,253(1991)]. Different scaling laws for the Lyapunov exponent are found for the dilute gas, dense liquid and solid plasmas. We explain qualitatively the simulation result in liquid and solid states on the analogy of a rigid body particle system and a weakly nonlinear lattice system, respectively. In the dilute gas state, an analytical model is developed for the Lyapunov exponent, and a relation between the largest Lyapunov exponent and the dielectric response function is found. The relation is expected to be applicable for a non-equilibrium system.

1. Introduction

Recently, there has been a great deal of research efforts devoted to finding relations between a Lyapunov exponent and macroscopic statistical quantities [1~6]. The Lyapunov exponent is the rate at which knowledge of an initial state in 6N phase space is lost, and a mechanical quantity which can be defined even for a strongly non-equilibrium system. Present statistical mechanics cannot treat dissipative processes in such a non-equilibrium system. The Lyapunov exponent is expected to give a new tool to explore dissipative processes. In previous works [1~3], systems that are determined only by short range forces and/or small degrees of freedom were considered. In such systems, the Lyapunov exponent is expected to be proportional to the collision frequency. In this paper, we consider a Coulomb many body system whose dynamics is determined by long range forces. Therefore, the Lyapunov exponent in the Coulomb many body system is expected to be different from that in short range force systems. Since the dielectric response function determines macroscopic dissipation in a Coulomb many body system, we conjecture that the Lyapunov exponents must be related to the dielectric response function. Thus, we will present an analytical model which gives a relation between the Lyapunov exponent and the dielectric response function.

A one component plasma is characterized only by the Coulomb coupling constant, $\Gamma \equiv e^2/aT$, where a, e and T are, respectively, the particle sphere radius, charge of particle and temperature in energy units ; the particle sphere radius a is related with the number density n in the form, $1/n \equiv 4\pi a^3/3$. In the case of $\Gamma \ll 1$, the plasma can be regarded as an ideal (dilute) plasma. On the other

hand, provided $\Gamma \geq 1$, the plasma should be regarded as a dense plasma, and then the particle correlation cannot be neglected.

2. Simulation result

Figure 1 shows the dependence of the Lyapunov exponents on the Coulomb coupling constant Γ, which is obtained by molecular dynamics simulations using the three dimensional particle code SCOPE [7]. The Lyapunov exponents in Fig.(1) are worked out by time-averaging the instantaneous expansion rates with respect to a separation distance between two adjacent trajectories in a 6N phase space by the rescaling method [5].
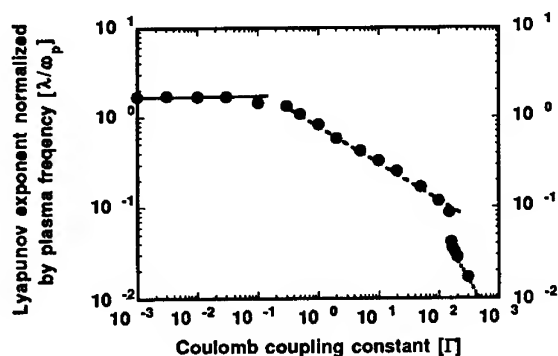
Figure 1   Simulation result of dependence of the Lyapunov exponents normalized by the plasma frequency on the Coulomb coupling constant. Solid, broken and dashed lines are obtained by a least squares method with the observed data in the dilute, liquid and solid plasmas, respectively.

The Lyapunov exponent normalized by the plasma frequency, $\omega_p \equiv \sqrt{4\pi n e^2 / m}$, (m is the particle mass) are represented by the closed circles. It is found that the Lyapunov exponent normalized by the plasma frequency, $1/\omega_p$, is independent of Γ for $\Gamma < 0.05$, proportional to $\Gamma^{-2/5}$ for $1 < \Gamma < 150$, and to $\Gamma^{-6/5}$ for $\Gamma > 170$. These states correspond to the dilute gas, dense liquid and solid plasmas, respectively. In the dilute gas state, the magnitude of the Lyapunov exponent is also found to be of the same order as the plasma frequency in this range, which is very large compared with the collision frequency for such dilute plasmas. The large jump of the Lyapunov exponent at $\Gamma \sim 170$ corresponds to the phase transition from liquid to solid state [8]. The Lyapunov exponent depends on the thermal mechanical states and thus it may be related to macroscopic quantity, such as dielectric constant.

3. Model for the Lyapunov exponent

For the liquid plasma, the repulsive force between two particles is so large that a particle can not get into the ion sphere of other particles. This fact indicates that the liquid plasma may be treat as a rigid body particle system. In the system, the Lyapunov exponent is estimated from the mean relative velocity, $V_0 = 4\sqrt{1/\pi}\,v_{th}$, the mean free path $l = 4a^3/(3R^2)$, and an amplification factor of the separation distance between two adjacent trajectories in a collision [1]. In the rigid body particle system, the Lyapunov exponent is then estimated as :

$$\lambda \sim \frac{V_0}{\ell} \ln\left[\frac{\ell}{2R} + 1\right] = 3\sqrt{\frac{1}{\pi}}\,\frac{v_{th}R^2}{a^3}\ln\left[\frac{2}{3}\left(\frac{a}{R}\right)^3 + 1\right] \tag{1}$$

where R represents the radius of a rigid body particle. The nearest distance between two particles is the same order as the ion sphere radius, independently of the Coulomb coupling constant. Then, the Lyapunov exponent normalized by (v_{th}/a) becomes of the order of one, and it almost becomes independent of the Coulomb coupling constant. The estimated value agrees roughly with the simulation result, $\lambda/(v_{th}/a) \sim 1.4\Gamma^{0.11}$,where $(v_{th}/a) = \omega_p/\sqrt{3\Gamma}$.

For the solid plasma, every particle is oscillating around a lattice point because it does not diffuse in the position coordinates space. The rigid body particle model can not be applied for the solid model, but the analogy of a nonlinear lattice system can be used. Then, the trajectory instability can be caused by lattice vibration as a nonlinear lattice. In a harmonic lattice, the amplitude of lattice vibration is proportional to the square root of the kinetic energy of a particle and its oscillation period, $2\pi/\omega_p$, does not depend on its amplitude. If nonlinearity of the lattice is small, it is expected that the growth rate of the trajectory instability is proportional to the square of the amplitude of the lattice vibration [2]. As a result, the Lyapunov exponent normalized by the plasma frequency is proportional to the kinetic energy, that is, Γ^{-1}. This estimation is also in good agreement with the simulation result: $\lambda/\omega_p \sim \Gamma^{-1.1}$.

For the dilute plasma, the observed fact cannot be explained by these models. So, an analytical model [6] is developed for the N-body largest Lyapunov exponent. The largest Lyapunov exponent in 6N phase space is determined as the maximum eigen-values of a matrix **T** for long time limit, which is a time advance operator on a perturbation of the 6N phase space trajectory.

$$\dot{\delta} \equiv \begin{pmatrix} \dot{\delta p} \\ \dot{\delta q} \end{pmatrix} = T(\Lambda)\delta \tag{2}$$

The treatment of Van Kanpen [9] is adopted to solve Eq.(2). Assuming that many body particle correlations can be neglected and the system is isotropic, the matrix

is then reduced to 2x2 elements. After the elements are averaged by a momentum distribution function, the largest Lyapunov exponent is obtained as the maximum eigen-values of the matrix as follows :

$$\frac{\lambda}{\omega_p} = \left\{ \frac{a^3}{18\pi^2\omega_p^4} \int_0^\infty dk \int_0^\infty d\tau \frac{k^2 \left\{ \int_{-\infty}^\infty d\omega \, \text{Re}[\varepsilon(k,\omega)-1] e^{-i\omega\tau} \right\}^2}{\tau} \right.$$

$$\left. + \frac{2\lambda_D^2 a^3}{3^2\pi^2} \int_0^\infty dk \int_{-\infty}^\infty d\omega \frac{k^4 \, \text{Im}[\varepsilon(k,\omega)] \text{Re}[\varepsilon(k,\omega)-1]}{\omega |\varepsilon(k,\omega)|^2} \right\}^{\frac{1}{2}}$$

(3)

where $\varepsilon(k,\omega)$ is the dielectric response function. The relation is expected to be applicable for a non-equilibrium system. In thermal equilibrium, the model shows that the Lyapunov exponent of one component dilute plasmas is the same order as the plasma frequency and independent of the Coulomb coupling constant. These results agree fairy well with the simulation result for one component dilute plasmas.

4. Summary

By three dimensional particle simulations, three different scaling laws for the Lyapunov exponent were found for the dilute gas, dense liquid and solid plasmas. The scaling laws in liquid and solid states were explained qualitatively on the analogy of a rigid body particle system and a weakly nonlinear lattice system, respectively. In the dilute gas state, the analytical model was developed for the Lyapunov exponent, and the relation, Eq.(3), between the largest Lyapunov exponent and the dielectric response function was found. The relation is expected to be applicable for a non-equilibrium system.

5.References

1.   N.S.Krylov, Works on the Foundations of Statistical Physics
        Prinsceton University, Princeton, New Jersey (1979).
2.   M.Pettini and M.Landolfi, Phys.Rev.A 41, 768 (1990).
3.   S.Chandhuri et al. Phys.Rev.E. 47, 311 (1993).
4.   D.M.Barnett et al. Phys.Rev.Lett. 76, 1812 (1996).
5.   Y.Ueshima et al. submitted to Phys.Rev.E.
6.   Y.Ueshima et al. submitted to Phys.Rev.Lett.
7.   K.Nishihara, Kakuyugo Kenkyu 66, 253 (1991).
8   J.P.Hansen, Phys.Rev.A 8, 3096 (1973).
9.   N.G.van.Kampen, Stochastic Processes in Physics and Chemistry,
        North-Holland Physics Publishing, Amsterdam (1983).

ABSORPTION AND EMISSION COEFFICIENTS CONSISTENT WITH RADIATION

V.G. NOVIKOV, A.D. SOLOMYANNAYA

Keldysh Institute of Applied Mathematics, Miusskaya pl., 4, Moscow, 125047, Russia

A simple interpolation model for calculating the spectral characteristics of non-LTE plasma consistent with radiation field is developed. The comparison of straightforward calculations and interpolation results for several intermediate intensities of radiation have been carried out for gold plasmas. The computation time is comparatively small that is very important for high-Z materials with very complicated spectrum.

In the radiation transfer equation $\frac{1}{c}\frac{\partial I_\omega}{\partial t} + (\vec{\Omega}\nabla)I_\omega = j(\omega, I_\omega) - \kappa(\omega, I_\omega) \cdot I_\omega$ the absorption coefficient $\kappa = \kappa(\omega, I_\omega)$ and emissivity $j = j(\omega, I_\omega)$ are defined by the local properties of matter with electron temperature T, density ρ and local intensity of radiation I_ω (ω is the photon energy). To determine the matter properties it is required to solve the system of kinetics equations that connects populations with the processes proceeding in plasma. The simplest approximation is the approximation of average atom [1]

$$\frac{dN_\nu}{dt} = (1 - \frac{N_\nu}{g_\nu})S_\nu - N_\nu L_\nu, \tag{1}$$

where N_ν is the average population and g_ν is the degeneracy of the level ν, S_ν is the summary rate of processes increasing the population of level ν whilst L_ν is the summary rate of processes which depopulates the level ν:

$$S_\nu = \sum_{\mu<\nu} N_\mu(\alpha_{\mu\nu}^{abs} + \alpha_{\mu\nu}^{ex}) + Z_0(\alpha_\nu^{ph-r} + \alpha_\nu^{3-b} + \alpha_\nu^{d-r}) + \sum_{\mu>\nu} N_\mu(\alpha_{\mu\nu}^{em} + \alpha_{\mu\nu}^{dex}),$$

$$L_\nu = \sum_{\mu<\nu}(1 - \frac{N_\mu}{g_\mu})(\alpha_{\nu\mu}^{em} + \alpha_{\nu\mu}^{dex}) + \alpha_\nu^{ph-i} + \alpha_\nu^i + \sum_{\mu>\nu}(1 - \frac{N_\mu}{g_\mu})(\alpha_{\nu\mu}^{abs} + \alpha_{\nu\mu}^{ex}).$$

All rates are in $1/c$, $\alpha_{\nu\mu}^{ex}$ is the rate of excitation $\nu \to \mu$, $\alpha_{\mu\nu}^{dex}$ is the rate of de-excitation $\mu \to \nu$, α_ν^i is the rate of electron-impact ionization from level ν, α_ν^{3-b} is the rate of three-body recombination to level ν, α_ν^{ph-i} is the rate of photoionization from level ν, α_ν^{ph-r} is the rate of photorecombination to level ν, $\alpha_{\nu\mu}^{em}$ is the radiative rate of emission in lines $\nu \to \mu$, $\alpha_{\mu\nu}^{abs}$ is the radiative rate of absorption in lines $\mu \to \nu$, α_ν^{d-r} is the rate of dielectronic

recombination to level ν, Z_0 is the mean ion charge. For rates the Born-Coulomb approximation[2] was used. The system (1) is being solved with the help of hydrogenic approximations for energy levels and wave functions[3]. After the solving of system (1) in steady state approximation (i.e. for time t such as $dN/dt \approx 0$) the calculations of absorption coefficient $\kappa(\omega)$ and emissivity $j(\omega)$ are made according to the HFS model[4,5].

Condition of equilibrium in quasistationary case ($\frac{dN}{dt} = 0$) between the main groups of states a and b in assumption that $N_a/g_a \leq 1$ and $N_b/g_b \ll 1$ gives that approximately the dependence of populations N_ν on radiation I_ω is possible to present either linear (when considering radiation) or as inverse to linear (when considering absorption)[6]: $N \approx A + B \cdot \eta$, or $N \approx \frac{C}{A+B\cdot\xi}$, where the values A, B, C do not depend on I_ω, and parameters ξ and η are proportional to I_ω. According to these formulas we assume that under the conditions of arbitrary intensity of radiation I_ω the degree of ionization Z_0 is determined by $Z_0 = Z_0^{(1)}/ \left[1 + \xi \left(Z_0^{(1)}/Z_0^{(2)} - 1\right)\right]$, or $Z_0 = Z_0^{(1)} + \eta(Z_0^{(2)} - Z_0^{(1)})$, where $Z_0^{(1)}$ and $Z_0^{(2)}$ are average degrees of ionization for transparent and dense plasma respectively. Here the index "(1)" labels the results of calculation for transparent plasma (then $\xi = 0$, $\eta = 0$), and index "(2)" is for the results of calculation for dense equilibrium plasmas ($\xi = 1$, $\eta = 1$). For calculation of the coefficient ξ the following formula is obtained

$$\xi = \int \frac{\kappa I_\omega}{\omega^3} d\omega / \int \frac{\kappa I_\omega^{(2)}}{\omega^3} d\omega. \tag{2}$$

The value ξ characterizes not only the intensity of radiation in plasma but also consistency of this radiation with absorption spectrum. As Z_0 does not depend on which of the processes (radiation or absorption) we consider, the following equality should be fulfilled: $Z_0(\xi) = Z_0(\eta)$ so

$$\eta = \frac{Z_0(\xi) - Z_0^{(1)}}{Z_0^{(2)} - Z_0^{(1)}}. \tag{3}$$

The interpolation formulas for k and j obtained by using similar way describe only average values, however they do not describe the shifts of lines and edges due to a change of the mean ion charge. It is possible to modify them to take the shifts into account by using the appropriate scale factor.

The position of the main lines and edges of photoionization shall be described with the help of scale factor $\lambda = Z_0^\alpha$, where the degree α is determined by practical consideration (as it has appeared to be the most suitable $\alpha(\omega) = \exp -(\omega/\theta - 3)^2$).

354

The final interpolation formulas with the corresponding scale shift have the form

$$\kappa(\omega, I_\omega) = \frac{\kappa^{(1)}\left(\frac{\lambda_1}{\lambda}\omega\right)}{1 + \xi\left[\kappa^{(1)}\left(\frac{\lambda_1}{\lambda}\omega\right)/\kappa^{(2)}\left(\frac{\lambda_2}{\lambda}\omega\right) - 1\right]}, \tag{4}$$

$$j(\omega, I_\omega) = j^{(1)}\left(\frac{\lambda_1}{\lambda}\omega\right) + \eta\left[j^{(2)}\left(\frac{\lambda_1}{\lambda}\omega\right) - j^{(1)}\left(\frac{\lambda_2}{\lambda}\omega\right)\right], \tag{5}$$

where $\lambda_1 = (Z_0^{(1)})^{\alpha(\omega/\theta)}$, $\lambda_2 = (Z_0^{(2)})^{\alpha(\omega/\theta)}$, and ξ and η are determined by formulas (2) and (3).

Thus, having previously prepared tables on T, ρ and ω for $\kappa^{(1)}$, $\kappa^{(2)}$, $j^{(1)}$, $j^{(2)}$, $Z_0^{(1)}$ and $Z_0^{(2)}$ it is possible to obtain the emissivities and absorption coefficients under arbitrary conditions in plasma. As parameters ξ and η depend on state of plasma, its space distribution and intensity of radiation, then during the solution of radiation transfer equation the consistency of average degree of ionization (i.e. average populations) with intensity of local radiation is being fulfilled.

The results of calculations for gold at temperature T=200 eV and density $\rho = 0.01$ g/cm^3 are presented in Table 1 and in Fig.1-2. The calculations were carried out with $I_\omega = 0.5\rho\omega^3\exp(-\omega/T_r)/[1 - \exp(-\omega/T_r)]$ TWt/(cm^3 eV steradian), where the temperature of radiation $T_r = \beta T$.

References

1. D.E.Post, R.V.Jensen, C.B.Tarter et al., At.Data Nucl.Data Tables, v.20, p.397, 1977.
2. W.Lotz *Electron-impact ionization cross-sections for atoms up to $Z-108$*, Ztschr.Phys., v.232, p.101, 1970.
3. A.F.Nikiforov, V.G.Novikov, A.D.Solomyannaya, *Analytical wave functions in self-consistent field models for high-temperature plasma*, Laser and Particle Beams, 1996 [to be published].
4. R.D.Cowan, *The theory of atomic structure and spectra*, Berkeley University of California press, USA, 1981, 731p.
5. V.G.Novikov, A.F.Nikiforov, V.V.Valko, *Photon absorption coefficients by Dirac-Fock-Slater model and their comparison with results of semiempirical methods*, Teplofizika Vysokikh Temperatur (High Temperature), v.31, p.881, 1993 [in Russian].
6. G.A.Vergunova, V.G.Novikov, V.B.Rozanov, *Simulation of emission and absorption spectra of the laser produced plasma* Preprint No 20 of the Lebedev Physical Institute, 1992 [in Russian].

Table 1: Mean values of the ion charge Z_0, Rosseland opacity k_R, Planck opacity k_P, total emissivity $J = 4\pi \int j(\omega) d\omega$ of gold at temperature $T = 200$ eV and density $\rho = 0.01$ g/cm^3 for transparent ($\beta = 0$), LTE plasma ($\beta = 1$) and intermediate case ($\beta = 0.5$).

		$\beta = 0$	$\beta = 1$	$\beta = 0.5$	
				calculation	interpolation
Z_0		25.12	38.53	27.77	27.42
k_P,	cm^2/g	$2.857 \cdot 10^3$	$6.553 \cdot 10^3$	$5.870 \cdot 10^3$	$4.248 \cdot 10^3$
k_R,	cm^2/g	$1.014 \cdot 10^3$	$2.786 \cdot 10^3$	$2.656 \cdot 10^3$	$2.339 \cdot 10^3$
J,	TWt/cm^3	$9.92 \cdot 10^3$	$1.359 \cdot 10^4$	$6.85 \cdot 10^3$	$9.74 \cdot 10^3$
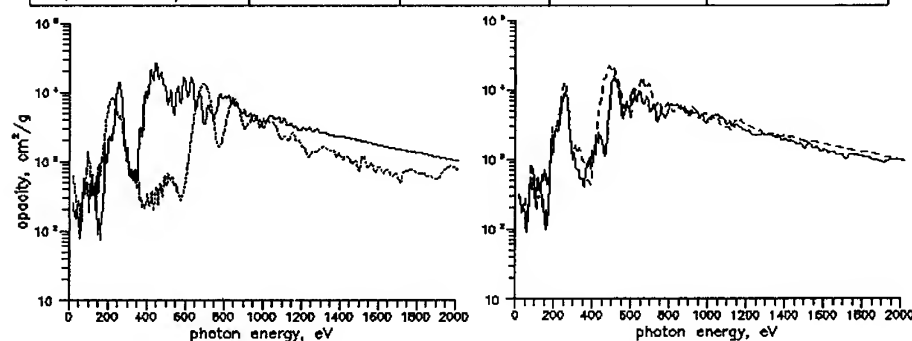
Figure 1: Opacity for gold at $T = 200$ eV, $\rho = 0.01$ g/cm^3. Left: LTE plasma ($\beta = 1$, solid line) and transparent plasma ($\beta = 0$, dashed line). Right: $\beta = 0.5$ (solid line — calculation, dashed line — interpolation).
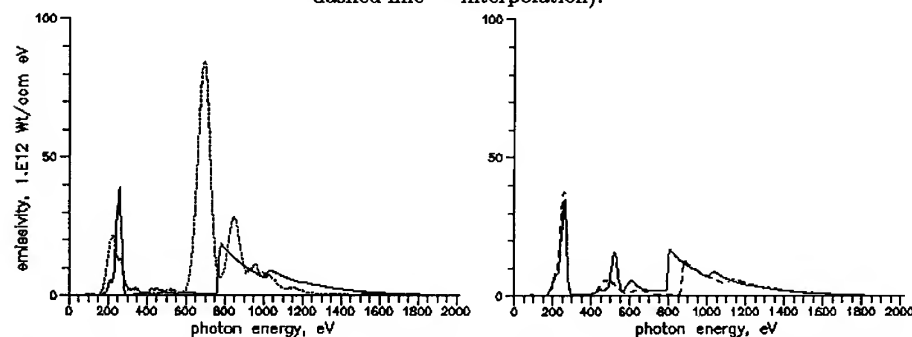
Figure 2: Emissivity for gold at $T = 200$ eV, $\rho = 0.01$ g/cm^3. Left: LTE plasma ($\beta = 1$, solid line) and transparent plasma ($\beta = 0$, dashed line). Right: $\beta = 0.5$ (solid line — calculation, dashed line — interpolation).

STATISTICAL TREATMENT OF THE SPECTRAL PROPERTIES OF PLASMAS IN LOCAL THERMODYNAMICAL EQUILIBRIUM USING A SCREENED HYDROGENIC MODEL

G. FAUSSURIER, C. BLANCARD, and A. DECOSTER

Commissariat à l'Energie Atomique
Centre d'Etudes de Limeil-Valenton
94195 Villeneuve Saint-Georges Cedex, France

ABSTRACT. A technique using both the screened hydrogenic average atom model and methods of classical statistical mechanics is presented. It allows a fast estimation of the configuration distribution around the average atom one and, in consequence, a rapid evaluation of spectral opacities of Local Thermodynamical Equilibrium (LTE) highly charged ion plasmas.

1. INTRODUCTION

The knowledge of radiative opacities is very important in astrophysics or laboratory plasma physics because an essential contribution to the energy transport in hot dense plasmas comes from radiation. Methods of varying degrees of complexity have been used for opacity calculations, such as Detailed Configuration Accounting (DCA) or Detailed Term Accounting (DTA). In practice, due to the huge number of photoabsorption lines, these methods prove to be very complex and computer time consuming[1-4].

During a typical plasma simulation, radiation effects may be significant and modify the hydrodynamic behavior of the medium. It is then essential to know the opacity when the information is needed, or in others words, in-line. As an explicit configuration accounting is infeasible for time reasons, one must resort to use cruder but simpler methods. At the present time, for media in LTE, the solution combines the screened hydrogenic average atom notion[5-9] and the classical theory of fluctuations[10-11]. As a result, each bound-bound or bound-free average atom one-electron transition is statistically broadened: the quality of the average atom spectrum is naturally enriched without explicitly splitting an average atom one-electron transition in many components as in DCA or DTA methods[12-13].

2. STATISTICAL BROADENING OF RADIATIVE TRANSITIONS

Consider a one-electron transition between two configurations α and β. The LTE photoabsorption bound-bound opacity $\overline{\kappa^{bb}}$, at photon energy $h\nu$ and without the correction due to stimulated emission, is equal to[13]:
$$\overline{\kappa^{bb}}(h\nu) = \frac{6.61\ 10^7}{A} \sum_{\substack{\alpha,\beta \\ E(\alpha)<E(\beta)}} \mathcal{P}(\alpha)\ f_{\alpha,\beta}\ \Psi_{\alpha,\beta}(h\nu)\ ,\ \text{where}\ \mathcal{P}(\alpha)\ \text{is the proba-}$$
bility of the initial configuration, A the atomic number of the element, $f_{\alpha,\beta}$ the oscillator strength of the transition and $\Psi_{\alpha,\beta}$ the line profile[14]. Introducing the chemical potential μ, the populations $[P_k(\alpha)]$ of the K_{Max} bound subshells of the ion with configuration α, and its energy $E(\alpha)$, $\mathcal{P}(\alpha)$ is proportional to:
$$[\prod_{k=1}^{K_{Max}} C_{D_k}^{P_k(\alpha)}]\ \exp\{-\beta[E(\alpha) - \mu \sum_{k=1}^{K_{Max}} P_k(\alpha)]\}.\ \text{For simplicity,}\ \Psi_{\alpha,\beta}\ \text{is chosen to}$$
be a Dirac distribution centered at the energy $\Delta E_{k,k'}(\alpha)$ of the transition $k \to k'$ ($3p \to 3d$ for example). Since LTE conditions are assumed, only configurations close to the average atom one notably contribute to $\overline{\kappa^{bb}}$. Hence, due to the Boltzmann factor, the oscillator strength $f_{k,k'}(\alpha)$ may be substituted by the average atom one $\tilde{f}_{k,k'}$ and $\overline{\kappa^{bb}}$ is equal to: $\overline{\kappa^{bb}}(h\nu) = \frac{6.61\ 10^7}{A} \sum_{k \to k'} \tilde{f}_{k,k'} \sum_{\alpha} \mathcal{P}(\alpha)\ \delta(h\nu - \Delta E_{k,k'}(\alpha))$.
At this point, it is particularly attractive to use the classical theory of fluctuations[10] which is justified when the lines overlap. Their original discrete splitting tends to be smeared to produce a quasi-continuous broadening. Of course, each individual line is broadened by the various well-known mechanisms[14] which accentuate the former quasi-continuous broadening whose origin comes only from statistics (hence the name of statistical broadening for this phenomenon[15-16]). The calculation proceeds as follows. Electronic populations are allowed to vary continuously: the discrete summation becomes a multidimensional integral. In the frame of the screened hydrogenic average atom model (the method can be also applied to any average atom model), $\mathcal{P}(\alpha)$ may be approximated by a Gaussian probability density[11]. Expressing the transition energy $\Delta E_{k,k'}[(P_k)]$ as a first-order Taylor expansion in occupation numbers around the average atom configuration and introducing the variance of the transition energy $\sigma_{k,k'}^2$,[12] $\overline{\kappa^{bb}}(h\nu)$ reduces to:

$$\overline{\kappa^{bb}}(h\nu) = \frac{6.61\ 10^7}{A} \sum_{k \to k'} \tilde{f}_{k \to k'}\ \int du\ \delta(h\nu - \overline{\Delta E}_{k,k'} - u)\ \frac{e^{-\frac{u^2}{2\sigma_{k,k'}^2}}}{\sqrt{2\pi\sigma_{k,k'}^2}}.\ \text{In summary,}$$

the initial summation which can contain a large number of configurations finally involves a limited number of terms. When the line profile is taken into account, the convolution product cannot always be calculated analytically. One notes that a similar expression is obtained for bound-free one-electron transitions. With a judicious choice of $\mathcal{P}(\alpha)$, the splitting in integer charge states can be included too[13].

358

3. RESULTS

Photoabsorption spectra obtained with More's Screened Hydrogenic Model[6,7] (MSHM) and the New Screened Hydrogenic Model[13] (NSHM) are compared to a spectrum calculated with the more sophisticated opacity code OPAP[17] (figure 1). A LTE iron plasma $(T = 25$ eV, $\rho = 8 \ 10^{-3} \text{g/cm}^3)$ has been chosen.
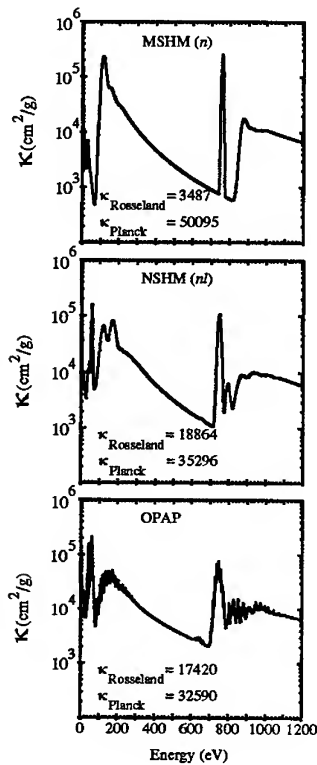
Figure 1. Photoabsorption spectra of a LTE iron plasma $(T = 25$ eV, $\rho = 8 \ 10^{-3} \text{g/cm}^3)$: MSHM, NSHM, and OPAP (see text).

The first difference between MSHM and NSHM is the peak around 60 eV which is due to the $\Delta n = 0$ transition $3p \rightarrow 3d$. This line contributes to fill the gap in this frequency domain[1,18]. Moreover, important features appear in the NSHM spectrum which is qualitatively quite close to the OPAP one. Regarding the values of opacity coefficients, the agreement is now quantitative. For Planck opacity, the method of calculation of the oscillator strengths leads, for the NSHM, to a correct value of $35296 \text{ cm}^2/\text{g}$ because sum rules are respected and bound-bound and bound-free parts of the spectrum are linked by continuity[13]. In MSHM, only continuity is used: sum rules may be violated because the threshold amplitudes are estimated using semi-classical results[19]. As for Rosseland opacity, both ℓ-splitting and the statistical broadening of lines explain the accurate value of $18864 \text{ cm}^2/\text{g}$. It is known that line profiles have to be well described in a region near four times the temperature (100 eV here), hence the importance of the last parameter, and a description of the atomic physics as good as one can imagine , hence the importance of the former parameter $(3p \rightarrow 3d$ transition). The gap at low frequency is filled, which raises Rosseland opacity by a factor five (from 3487 to $18864 \text{ cm}^2/\text{g}$).

4. CONCLUSION

The screened hydrogenic average atom model with ℓ-splitting and a statistical treatment of radiative transitions based on the classical theory of fluctuations are necessary to obtain good estimation of spectral opacities. This method can be implemented in an atomic physics package of a hydrodynamic code for fast calculations.

REFERENCES

[1] F. J. Rogers and C. A. Iglesias 1992 *Astrophys. J. Suppl. Ser.* **79** 507.

[2] C. Bauche-Arnoult, J. Bauche, and M. Klapisch 1979 *Phys. Rev.* **A20** 2424.

[3] M. J. Seaton 1987 *J. Phys. B* **20** 6363.

[4] A. Bar-Shalom, J. Oreg, W. H. Goldstein, D. Shvarts, and A. Zigler 1989 *Phys. Rev.* **A40** 3183.

[5] H. Mayer 1947 *Report LA-647*, Los Alamos Scientific Laboratory (Los Alamos N. M.).

[6] G. B. Zimmerman and R. M. More 1980 *J. Quant. Spectrosc. Radiat. Transfer* **23** 517.

[7] R. M. More 1982 *J. Quant. Spectrosc. Radiat. Transfer* **27** 345.

[8] G. D. Tsakiris and K. Eidmann 1987 *J. Quant. Spectrosc. Radiat. Transfer* **38** 353.

[9] A. Rickert and J. Meyer-Ter-Vehn 1990 *Laser and Particle Beams* **8** 715.

[10] L. Landau et E. Lifchitz 1985 *Mécanique Statistique* (Mir, Moscou).

[11] F. Perrot 1988 *Physica* **A150** 357.

[12] S. Bayle 1991 *Thèse de l'Université Paris XI* (France).

[13] G. Faussurier 1996 *Thèse de l'Ecole Polytechnique* (France).

[14] M. R. Griem 1977 *Spectral Line Broadening by Plasmas* (Academic Press, New York).

[15] D. Shalitin, J. Stein, and A. Ron 1984 *Phys. Rev.* **A29** 2789.

[16] T. Błeński and B. Cichocki 1990 *Phys. Rev.* **A41** 69.

[17] Code OPAP *unpublished* (Limeil, France).

[18] L. B. Da Silva, B. J. Mac Gowan, D. R. Kania, B. A. Hammel, C. A. Back, E. Hsieh, R. Doyas, C. A. Iglesias, F. J. Rogers, and R. W. Lee 1992 *Phys. Rev. Lett.* **69** 438.

[19] R. M. More 1986 *Plasmas processes in non-ideal plasmas* in *Proceedings of the 29th Scottish Universities Summer School in Physics — Laser Plasma Interactions.* (IOP, Bristol).

Inverse Bremsstrahlung absorption:
degeneracy and solid/liquid corrections

S. Jacquemot, A. Decoster, and L. Bonnet
Commissariat à l'Energie Atomique
Centre d'Etudes de Limeil-Valenton
94195 Villeneuve Saint-Georges Cedex, France

ABSTRACT. A model for the complex conductivity from kinetic theory is described. The collision operator only includes the contribution from electron-ion scattering, and the electron degeneracy effects are taken into account by using a Fermi-Dirac distribution. The plasma and solid/liquid phases are considered through adequate velocity-dependent electron-ion collision frequency formulas. The derived Inverse Bremsstrahlung absorption coefficient and permittivity apply to most useful temperatures and densities and are expressed in computationally "simple" analytical forms which generalize both usual ac and classical plasma expressions.

1. MOTIVATIONS

The description of Inverse Bremsstrahlung energy deposition in ns pulse experiments requires the knowledge of an absorption coefficient K_{abs}. Current ICF codes use the Johnston-Dawson formula [1], assuming a Maxwellian classical (hot and underdense) plasma and a High Frequency laser. These conditions are not met during the first 100 ps of an interaction, when the state of matter changes from solid/liquid to cold and overdense (degenerate) plasma. Improvements (degeneracy and different phases effects) are then needed. Accounting for high density leads also to question the HF assumption. Furthermore, in ps regime, the necessary resolution of the Helmholtz wave equation (ElectroMagnetic solver) involves the use of a complex conductivity σ, generally obtained through the generalization of a d.c. expression to nonzero frequencies [2]. This "Drude" extrapolation unfortunately fails at HF limit and has to be revised. Besides, when the geometric optics approximation becomes valid again, attention must be paid to link the two theories together.

2. ELECTRON KINETIC EQUATION AND TRANSPORT COEFFICIENTS

If the electron distribution function f differs only sligthly from its equilibrium form f_0 [$f = f_0 + \delta f$], the kinetic equation $\frac{\partial f}{\partial t} + \mathbf{v} \cdot \frac{\partial f}{\partial \mathbf{r}} - \frac{e}{m} \left(\mathbf{E} + \frac{\mathbf{v}}{c} \times \mathbf{B} \right) \cdot \frac{\partial f}{\partial \mathbf{v}} = \frac{\partial f}{\partial t} \rfloor_{coll}$

for a spatially uniform but periodically varying electric field ($E \propto \exp(-i\omega t)$) and no magnetic field can be written: $-i\omega\delta f - \frac{e}{m}E \cdot \frac{\partial f_0}{\partial v} + \nu_{ei}(v)\delta f = 0$, assuming $\frac{\partial f}{\partial t}\rfloor_{coll} = -\nu_{ei}(v)\delta f$ (relaxation-time approximation). Contributions from electron-electron and electron-neutral scattering are thereby neglected.

Electron degeneracy is taken into account by using a Fermi-Dirac distribution function $f_0 = 2\left(\frac{m}{2\pi\hbar}\right)^3 / \left[1 + \exp\left(-\eta + mv^2/2T_e\right)\right]$.

The permittivity $\epsilon \equiv 1 + i4\pi\sigma/\omega$ is derived from the relation between electric field and current density ($\sigma E = j = -e\int v\delta f d^3v$); averaging over v directions, $\epsilon = 1 + \frac{16\pi^2 e^2}{3m\omega^2}\int \frac{v^3\partial f_0/\partial v dv}{1 + i\nu_{ei}(v)/\omega}$. The Inverse Bremsstrahlung absorption coefficient is then $K_{abs} = \frac{\omega}{c}\frac{Im\epsilon}{Re\sqrt{\epsilon}}$.

3. ELECTRON-ION COLLISION FREQUENCY

The calculation of the permittivity is based upon a velocity-dependent electron-ion frequency $\nu_{ei}(v)$. Following Lee and More [3], two distinct states of matter are described. In plasmas, Coulomb scattering is simply considered. The frequency exhibits then an $1/v^3$ dependence: $\nu_{ei}^{pl}(v) = n_i\frac{4\pi e^4 Z_i^2 \ln\Lambda_{BI}}{m^2 v^3}$, where the Coulomb logarithm $\ln\Lambda_{BI}$ accounts for Debye-Hückel screening, electron degeneracy, and strong ion coupling. In solids or liquids, the Ziman theory allows to introduce a constant mean free path $L^{sl} = R_0 \max(1, 50T_m/T_i)$ leading to a frequency $\nu_{ei}^{sl}(v) = v/L^{sl}$ directly proportional to v. A mean collision frequency $\overline{\nu_{ei}} = \frac{1}{3}\sqrt{2/\pi}\,\nu_{ei}(v_{th})$ at thermal velocity ($v_{th} = \sqrt{T_e/m}$) is moreover defined, which reproduces the well-known formula for plasmas [4].

4. OVERALL FORMULATION

A reduced complex conductivity $\tilde{\sigma} = \frac{3}{2}F_{1/2}(\eta)\frac{m\omega}{n_e e^2}\sigma$ is actually modeled. It appears to be easily parametrized with only two independent variables: $\chi = \omega/\overline{\nu_{ei}}$ and $\eta = \mu/T_e$. The analytical form

$$\tilde{\sigma} = \frac{\chi}{\alpha_1(\eta, \chi) + \beta_1(\eta, \chi)\chi^2} + i\frac{\chi^2}{\alpha_2(\eta, \chi) + \beta_2(\eta, \chi)\chi^2}$$

is then found to accurately reproduce (to within 16%) results from numerical integrations over a wide range of these parameters.

Notations: $Z^* \equiv$ mean ionization, $Z_i = \max(1, Z^*) \equiv$ ionic charge, $n_{i(e)} \equiv$ ion (electron) density [$n_e = Z_i n_i$], $T_{e(i)} \equiv$ electronic (ionic) temperature, $\eta = \mu/T_e \equiv$ reduced chemical potential, $R_0 \equiv$ interatomic distance, and $T_m \equiv$ melting temperature [5].

362

For solids and liquids, $\alpha_1 = 3\sqrt{\pi}/F_0$, $\alpha_2 = 18\pi/F_{-\frac{1}{2}}$, $\beta_1 = 1/[6\sqrt{\pi}F_1]$, and $\beta_2 = \frac{2}{3}/F_{\frac{1}{2}}$, while for plasmas $1/\alpha_1 = 2\sqrt{\pi}F_2\left[\left(1+\frac{3\pi}{32\alpha_\perp}\right) + \left(1-\frac{3\pi}{32\alpha_\perp}\right)f_\infty^9\right]$, $\frac{16}{\pi}F_{\frac{7}{2}}\alpha_2 = \left(1+\frac{70\alpha_\perp^2}{\pi\alpha_\wedge}\right) + \left(1-\frac{70\alpha_\perp^2}{\pi\alpha_\wedge}\right)f_\infty^{0.99}$, $3F_{\frac{1}{2}}\beta_2 = (1+\alpha_\wedge)+(1-\alpha_\wedge)f_\infty^{0.99}$, and $\beta_1 = \frac{2}{3\sqrt{\pi}}F_0\left[\left(1+\frac{\alpha_\wedge^2}{\alpha_\perp}\right)+\left(1-\frac{\alpha_\wedge^2}{\alpha_\perp}\right)f_\infty^9\right]$.

This formulation has been in fact derived from judicious interpolations (hence "smoothing" functions $f_\infty^p = \ln\left[\left(1+\frac{p}{10}e^\eta\right)/\left(1+\frac{p}{10}e^{\eta-2}\right)\right] - 1$) between exactly-integrated expressions obtained at high frequency limit ($\omega \gg \overline{\nu_{ei}}$ where, for classical plasmas, the usual [1] expression for K_{abs} can be reconstructed), low frequency limit ($\omega \ll \overline{\nu_{ei}}$ where the Lee-More [3] plasma d.c. conductivity is recovered), for a fully degenerate medium ($\eta \to +\infty$) and a classical one ($\eta \to -\infty$, for which Lorentz plasma calculations [6] have been used through the $\alpha_\perp$ and $\alpha_\wedge$ rational expressions). For a smooth interpolation of solid/liquid and plasma formulae, $\epsilon = 1 - \frac{n_e}{n_c} + 1/\left[\frac{1}{\epsilon^{sl}-\left(1-\frac{n_e}{n_c}\right)} + \frac{1}{\epsilon^{pl}-\left(1-\frac{n_e}{n_c}\right)}\right]$ is finally assumed. It must be pointed out that the deduced absorption coefficient, instead of the usual one (proportional to $1/\sqrt{1-n_e/n_c}$), do not present any divergence at critical density.

5. ILLUSTRATION

To quantify the degeneracy and multiphase effects, hydrodynamical conditions (electronic temperature and density) are required. Fig. 1 shows results for a $0.35\,\mu$m wavelength laser on gold: $n_e = 0.9\,n_c$, 10^{-2}eV $\leq T_e = T_i \leq 10^5$eV .
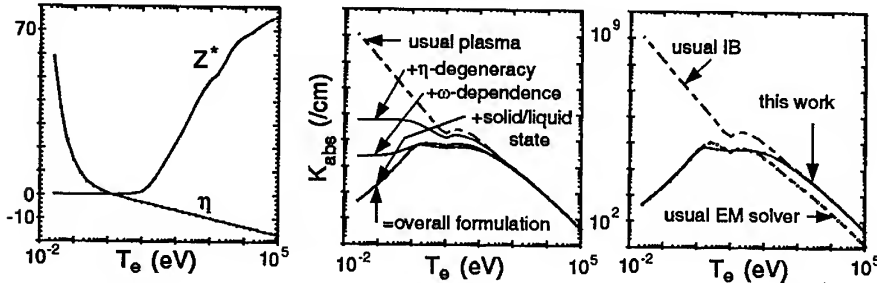
Fig. 1. NOHEL mean ionization Z^* and reduced chemical potential η versus electronic temperature T_e (eV) (left) – influence of the different improvements on the absorption coefficient K_{abs} (/cm) (center and right).

$F_p = \int\limits_0^{+\infty} t^p/[1+e^{t-\eta}]\,dt \equiv$ Fermi-Dirac integral, $\alpha_\perp = 1 - \frac{4.73\chi+9.17}{\chi^2+13.8\chi+13.0}$, and $\alpha_\wedge = 1 + \frac{2.53\chi+1330}{(\chi^3+1180\chi^2+21900\chi+3540)^{8/9}}$ [6], $n_c = \frac{m}{4\pi e^2}\omega^2 \equiv$ critical density.

Mean ionizations and chemical potentials are provided by a non-LTE screened hydrogenic average ion model (NOHEL).

The classical [1] IB coefficient is obviously much too high at low temperatures (6 orders of magnitude), correctly accounting for degeneracy being the predominant reduction factor. The laser energy deposition was consequently drastically overestimated at the beginning of an interaction. At the opposite, the Drude model [2] result is 5 times too low leading to an absorption default during a coronal expansion. It is also important to notice that a highly charged plasma such as gold appears to be classical only for temperatures exceeding 100 eV.

The energy of a photon being here $\hbar\omega = 3.5\,\mathrm{eV}$, the plasma Coulomb logarithm becomes erroneous and should be replaced [7] by a free-free Gaunt factor at low temperatures ($T_e \lesssim \hbar\omega$). This effect has not been yet included in the model (it would moreover have no influence in the present example, the matter under such conditions being solid/liquid). In the comparisons above, the induced emission correction factor to the absorption $[1 - \exp(-\hbar\omega/T_e)]$ is not included either.

6. CONCLUSION

The implementation in a hydrodynamical code of these analytical formulas leads to *consistent* ns and ps laser energy deposition simulations. It should also imply – by correctly treating the real (solid/liquid or degenerate plasma) state of the medium – a noticeable decrease of the absorption level during the first 100 ps of a nominal ICF experiment, affecting – for example – the temporal profile of the X-ray conversion efficiency.

REFERENCES

[1] T.W. Johnston and J.M. Dawson 1973 *Phys. Fluids* **16**, 722.

[2] W.E. Alley 1992 *LLNL Annual Report* **UCRL-LR-105820-92**, 160

[3] Y.T. Lee and R.M. More 1984 *Phys. Fluids* **27**, 1273.

[4] I.P. Shkarofsky, T.W. Johnston, and M.P. Bachynski 1966 *The particle kinetics of plasmas* (Addison Welsey, Reading).

[5] R.M. More *et al.* 1988 *Phys. Fluids* **31**, 3059.

[6] E.M. Epperlein and M.G. Haines 1986 *Phys. Fluids* **29**, 1029.

[7] D.G. Hummer 1988 *Ap. J.* **327**, 477

ELECTRON CONDUCTION OPACITY OF STRONGLY COUPLED PLASMAS

A. H. KHALFAOUI, D. BENNACEUR

Laboratoire Interaction Laser-Matière, CDTA, 2 Bd. Frantz Fanon, BP 399
Alger-gare 16000, Algeria

Abstract. Plasmas produced by heavy ion beams as well as laser driven indirect ICF target physics in a hohlraum- capsule system have attracted considerable attention recently. The study of the transport phenomena of these media, in their extreme conditions, still require some important refinements. For that, electron conduction opacity of highly degenerate weakly coupled electrons and strongly coupled semi- classical ions is treated by a quantum collective approach. The e-e collisions contribute to the thermal conductivity calculation in the intermediate coupling regime; showing thereby, that the extensively used Lorentz gas approximation cannot be justified for both plasma of ICF physics and of astrophysical interest. The present results are compared to existing theories on electron conduction in dense plasmas.

1 Introduction

The wide range of temperature and density spanned by astrophysical plasmas has significant overlap with conditions attainable using high-power laser facilities. This latter provides an opportunity to create, control and characterize plasma in the laboratory that describe conditions in some of the most important cosmological systems.

One of the main parameters which is sought with accuracy, in connection with radiation transport, is the opacity of the plasma thus produced. It is a key parameter in the knowledge of the quantitative energy transfer efficiency to the target.

With temperature relatively low and density high enough, the radiant energy density and the radiation pressure are negligibly small in comparison with energy and pressure of the plasma.

However the radiant energy may become comparable to the energy of the plasma at very high temperatures. And hence the conductive opacity of the plasma should be known with the best accuracy taking into account the main plasma nonidealities.

The nonidealities considered to affect thermal transport are the inelastic scattering, the quantum and finite temperature effect and electron-electron (e-e) interactions [1]. This latter effect considered more recently [2] may contribute unequally to the relaxation times of the electrical and thermal conductivities.

Another formalism has been developed to calculate thermal resistivities for dense plasma through solution of quantum-mechanical transport equation for the electrons [3,4].

To evaluate correctly the impact of the nonidealities on transport coefficients, a unification scheme of both treatments of short- and long- range Coulomb collisions

would be a more comprehensive approach.

For that, the Bloch transport theory [5] is extended here and applied to very high density plasma with concepts similar to those used for solids and liquid metals.

The properties of these systems can be solely described by elementary excitations that are quasiparticles obeying Bose-Einstein statistics.

The formalism of the present model used to solve the quantum Boltzmann-Bloch equation has been reported elsewhere [2].

Herein these results are now completed and applied to quantify an important property of dense plasma: the conductive opacity.

2 Conductive opacity

The conductive opacity is given by [6]:

$$\chi_C = 4acT^3 / 3\rho\lambda \qquad (1)$$

where c is the speed of light, a the radiation constant and ρ the plasma mass density.

The temperature T and the electron thermal conductivity λ are related through the thermal energy $\vec{Q}$ carried by electrons in a temperature gradient and defined by the Fourier law as:

$$\vec{Q} = -\lambda\vec{\nabla}T \qquad (2)$$

The total opacity of the medium χ is also due to the radiative opacity χ_r such as ($\chi = (\chi_C^{-1} + \chi_r^{-1})^{-1}$). The present work deals only with χ_C for which λ in equation (2) will be explicitly calculated through a quantum model.

3. Thermal conduction in quantum plasmas

In order to calculate χ_C in equation (1), the thermal conductivity λ has to be defined through a quantum collective approach.

In this approach, the collision term of the Boltzmann equation has to satisfy the maximum entropy production, this is achieved by using a method proposed by Kohler [7], when the integral equation is reduced to a variational principle. In this model, the electrons being considered as waves absorbing and emitting plasma waves (plasmons and ion sound waves), relaxing the perturbed electron distribution function in the process.

This calculation procedure allows the obtaintment of a perturbed electron distribution function which will be used to calculate the generalized forces relating the current density $\vec{J}$ and the rate of flow of heat $\vec{Q}$ through a gradient of

temperature $\vec{\nabla}T$ and an electric field $\vec{E}$ present in the plasma.

In such a way, all the transport coefficients are systematically defined and in particular the thermal conductivity λ.

Moreover, the thermal conductivity is obtained from both types of interactions e-e and e-i through Mathiessen rule such as $1/\lambda = \Sigma_s\ 1/\lambda_{es}$, $s = e,i$.

4 Results and discussion

4.1. e-e interaction effects

To evaluate the net impact of the e-e interactions, the quantity:

$$\Delta\lambda = \lambda\ /\ \lambda_{ei}\ , \tag{8}$$

is introduced to indicate the relative reduction in the thermal conductivity and hence the increase in the opacity. Here λ_{ei} is the thermal conductivity which still include the nonideality effects inherent to the present model such as inelastic scattering, quantum and finite temperature effects, but no e-e collisions, i.e., in the Lorentz gas approximation.

This is achieved by assuming in the collision process only the interaction of the electrons with the ion sound waves.

In table I, values of $\Delta\lambda$ are reported for hydrogen plasma over a wide range of densities ($r_s = a_e\ /a_o$, $a_e = (3/4\pi n)^{1/3}$, a_o is the Bohr radius) and the intermediate coupling regime ($1< \Gamma \leq 10$). In general e-e collisions may reduce λ by up to 50% and such a result is in good agreement with the model developed in ref. [6].

Γ	1	2	3	4	5	7
r_s=0.9	0.460	0.460	0.550	0.756	0.934	1
=0.5	0.460	0.460	0.818	0.934	0.991	1
=0.1	0.756	1	1	1	1	1

Table I: $\Delta\lambda$ as function of Γ and r_s .

4.2 Conductive opacity comparisons

In figures 1 and 2 are shown conductive opacities χ_P as given by equations (1) and (3). They are compared to several existing theories for helium and carbon over a wide range of densities.

The contribution to the thermal conduction of the present model are the nonideality

effects to which is sensitive to conductive opacity. The most important contribution in this range of densities and temperatures is the e-e collisions.

Such an effect is itself a sensitive function of the degree of degeneracy θ ($\theta = k_B T/E_F$, E_F is the Fermi energy) and the coupling parameter Γ of the plasma ($\Gamma = (Ze)^2/a_i k_B T$, $a_i = (3Z/4\pi n)^{1/3}$). All details on the physics involved in these comparisons are reported in ref. [8]
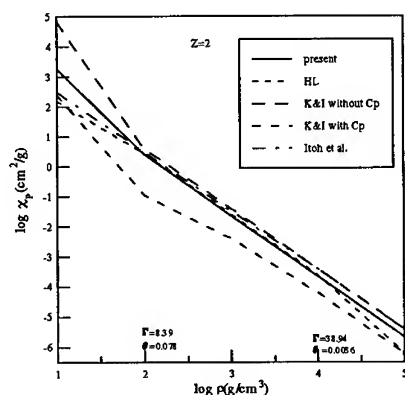
Fig. 1
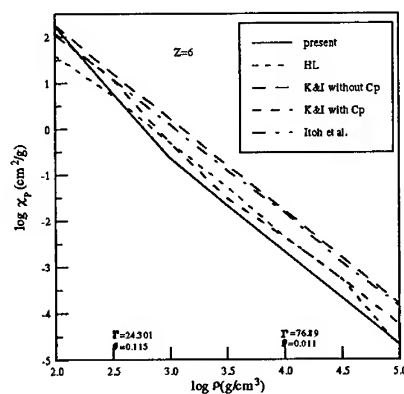
Fig. 2

Figs. 1,2: In these figures are seen conductive opacities for Helium at $T=10^{5.5}$ °K and Carbon at $T=10^6$ °K respectively where HL is from ref. [6], K&I from ref. [4] and Itoh et al ref. [9].

References

[1] Leger, D., and Deutsch, C. 1992, Phys. Fluids B4, 3162.

[2] Khalfaoui, A. H., and Bennaceur D. 1994, Phys. Plasmas 1, 2026.

[3] Tanaka, S., Yan, X. Z., and Ichimaru, S. 1990, Phys. Rev. A 41, 5616.

[4] Kitamura, H., and Ichimaru, S. 1995, Phys. Rev. E 51, 6004.

[5] Shaw, L. J., and Ziman, J. M. 1963, Sol. Stat. Phys. Vol. 15 (N.Y.: Academic).

[6] Hubbard, W. B., and Lampe, M. 1969, Astrophys. J. Supp. 18, 297.

[7] Kohler, M. 1949, Z. Phys. 125, 679.

[8] Khalfaoui, A. H., and Bennaceur D. 1997, Astrophys. J. 468.

[9] Itoh, N.and Kohyama, Y. 1993, Astrophys. J. 804, 268.

INVESTIGATION OF THE DYNAMIC FRACTURE PROCESS AT ULTRAHIGH STRAIN RATE CAUSED BY LASER-INDUCED SHOCK WAVES IN SOLID TARGETS

V.I. VOVCHENKO, I.K. KRASYUK, P.P. PASHININ, A.YU. SEMENOV

General Physics Institute, Russian Academy of Sciences
Vavilov Street 38, Moscow 117942, Russia

This work consists of three main parts. In the first part dependence of amplitude of ablation pressure from intensity of laser radiation in a specified range is experimentally investigated. In the second part measurements of spall strength of a researched material from deformation rate up to $3 \cdot 10^7 \, s^{-1}$ are performed. In the third part measurements of mechanical work, expended on separation of spall layer, are carried out.

In the present work results of research of some characteristics of destruction process of metal targets are presented at large rates of deformation, Fig. 1. In experiments Nd-glass laser installation with a length of a wave of radiation 1.06 μm was used. The laser pulses had the form, closed to triangular, with a duration of a pulse on the foot from 10 up to 80 ns. The laser radiation was focused on the target in a spot with diameter 1–1.2 mm. The targets in the majority of cases
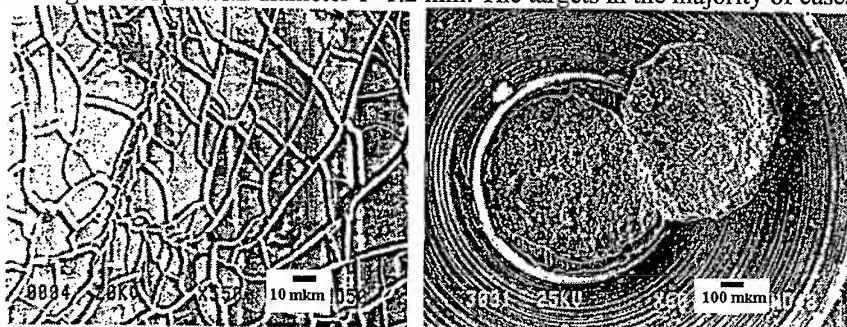
FIGURE 1. The results of the laser-induced spallation process. Development of crystal structure on back surface of the target is showed on the left hand. Separation of a spall layer is showed on the right hand.

had thickness from 230 up to 400 μm. These are made of the aluminum alloy AMg6M. As has appeared in these conditions spallation process arose at laser radiation intensity in a range 10^{10}–10^{12} W/cm^2. The researches are based on joint application experimental methods and methods of numerical modeling.

The results of the first part of this work are shown on Fig. 2. For definition of ablative pressure below-listed methods, designated on drawing by (a-d) are used.
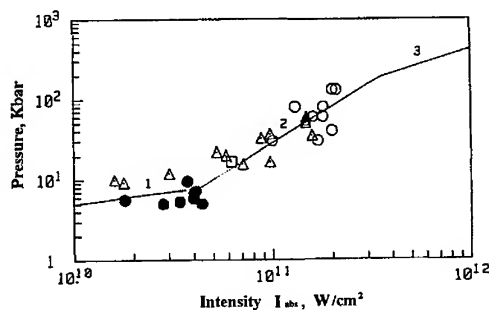
FIGURE 2. Experimental dependence of ablative pressure P_a versus intensity of absorbed laser radiation I_{abs}., ○ - a, ● - b, △ - c, □ - d.

(a) The method is based on measurement the propagation time of shock waves in aluminum targets.

(b) The method is based on registration the profile of laser acceleration of aluminum foils with the using of VISAR type velocity interferometer.

(c) The method is based on discrete registration the characteristics of deceleration polymer foils by thickness from 5 up to 12 μm in a cylindrical channel, filled in by air or xenon.

(d) The method is based on continuous registration with the using of Doppler effect of polymer foils laser acceleration (foil thicknesses from 1 to 5 μm) in a deuterium filled conic channel. The processing of received experimental data by method of least squares results in a relation

$$P_a(\text{kbar}) = (28\pm3)\bullet(I_{abs}[\text{W/cm}^2]/10^{11})^{1.5\pm0.2}$$

Here P_a is the ablation pressure, I_{abs} is the intensity of absorbed laser radiation. On Fig. 2 this relation is shown by curve 2. There is the concurrence with data of paper [1] in the interval 10^{10}–$4\cdot10^{10}$ W/cm^2 (curve 1 on Fig. 2). Curve 3 was received in paper [2]. All these experimental data permit to construct wide-range dependence ablation pressure from laser intensity up to 10^{15} W/cm^2 [3].

In the second part of work spall layer thickness is measured in each experience. Then the value of material deformation rate and the value of the maximum strain (negative) pressure were calculated in a spall plane by using numerical modeling method [6]. For this purpose a special numerical code is developed on the basis of equations of hydrodynamics in view of the real equation of state for the researched material and opportunity of the description of rarefaction waves with negative pressure. The results of research are shown on Fig. 3. In some cases the specified values were determined by a conventional method with use of a free surface velocity profile structure with VISAR. The analysis shows that these data

370

complement each other and characterize the spallation phenomenon more complete. Some differencies of the data on Fig.3 may be caused with variation the structure of Al-targets used by different authors, see also [9].
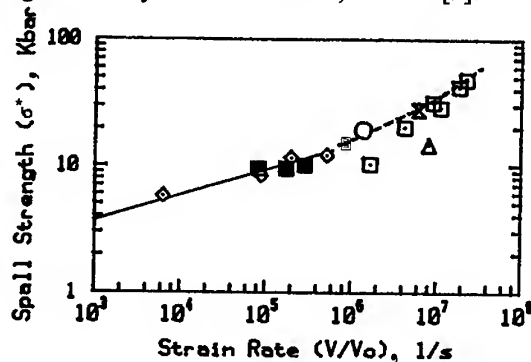
FIGURE 3. Experimental dependence of the spall strength versus the strain rate: (□) new laser data, (Δ) D.L.Paisley et al [4], (▤) E.Moshe et al [8], (▷◁) light ion beam data of H.Bachman et al [5], (◊,■) explosive data of G.I.Kanel et al. data [6], (O) based on L.Tollier et al data [7].

In the third part of the present work measurements of spall layer velocity are perform by means of the electrocontact method. On the basis of these measurements, the kinetic energies values of separated layers were determined. Kinetic energies of aluminum plates glued on a back surface of a target (artificial spall layer) were measured by similar way. The thickness of these layers corresponded to thickness of the real spall layers. The difference between kinetic energies of real and artificial layers was accepted as the value of the fracture work. It occurs that measured values of fracture work of the spall layer is considerably less than it in the case of explosive experiments. The results of these measurements are shown on Fig. 4. It is obviously that sharp decrease of destruction work occurs for a investigated material at deformation rate $10^6 \, s^{-1}$. This result is received for the first time and its explanation requires further researches.

In addition, influence of the target form on some characteristics of the spallation phenomenon was investigated. In these experiments simple and stepped targets were used. For qualitative understanding of spallation phenomena two-dimensional numerical modeling was carried out. Results of modeling show that conditions for spallation occur on the layer periphery, and then, they will be realized and in a frontal plane of the target.
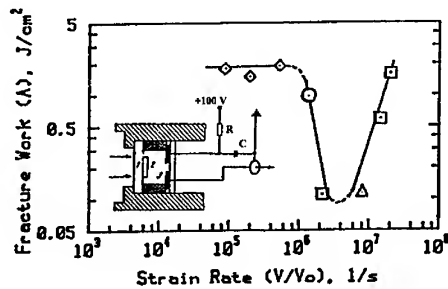
FIGURE 4. The measuring dependence of the fracture work from the strain rate. The marking is the same as on Fig 3. Experimental set up is shown on the left hand. 1- target shell, 2 - artificial spall layer, 3 - electrocontact sensors.

SUMMARY

For aluminum alloy AMg6M the following results were obtained.

-the value of spall strength was studied for the strain rate up to $3 \cdot 10^7 \text{ s}^{-1}$;

-it was found that the value of fracture work at separation of the spall layer significantly decreases when the strain rate is equal to 10^6 s^{-1}.

[1] Combis P., Cazalis B., David J. et al. Low-fluence laser-target coupling //*Laser and Particle Beams*. 1991. **9**. No. 2. P.403–420.

[2] Dahamani F., Kerdia T. Measurements and laser-wavelength dependence of mass-ablation rate and ablation pressure in planar layered targets //*Ibid*. No. 3. P.769–778.

[3] Vovchenko V.I. et al. "Wide-range dependence of ablation pressure on laser radiation intensity //*J. Russian Acad. Sci. Physics-Doklady*. 1994. **39**. No.9. P.633-634.

[4] Paisley D.L., Wames R.H., Kopp R.A. Laser/driven flat impacts to 100 GPa with sub-nanosecond pulse duration for material property studies. "Shock compression of condensed matter". 1992. Elsevier Science Publishers. B.V. P.825-828

[5] Bachman H. et al. Target experiments with light-ion beams at KALIF: measurements of the dynamic strength and spallation threshold of metals at high strain rates. Paper #PB-43 at: BAMS'92- 9th Int. Conf. on High-Power Particle Beams, Washington DC, May 1992.

[6] Kanel G.I., Fortov V.E. Mechanical properties of condensed matter by intensive pulse interaction //*Advances in Mechanics*. 1987. **10**. No.3. P.3-82.

[7] Tollier L. et al. Interaction laser-matiere a bas et moyen flux (1 a 300 GW/cm^2)-mesures de pression d'ablation et application a l'etude de lendommagement de materiaux. LULI Rapport Scientifique. 1993. P.98-110.

[8] E.Moshe et al. Development of an optically recording velocity interferometer system for laser induced shock waves measurements //*Apll. Phys. Lett*. 1996. **69** No.10. P.1379-1381.

[9] V.E.Fortov et al. Spallation of metals under laser irradiation //*J.Appl.Phys*. 1991. **70**. No.8. P.4524-4531.

MULTIPHOTON IONIZATION DRIVEN BY A SEQUENCE OF TWO LASER PULSES

ZOHAR HENIS
Plasma Physics, Soreq NRC,
Yavne 81800, Israel

Abstract

Multiphoton ionization of a two-level model atom excited by a sequence of two laser pulses is considered. It is found that the ionization probability oscillates as a function of the delay between the two pulses. An increase in the ionization probability of more than an order of magnitude occurs when the two pulses are separated by a time of the order of the duration of each pulse. As the laser peak intensity increases the maximum ionization signal shifts towards higher delays.

Introduction.

The interplay of exitation and ionization of atoms irradiated by short pulse high intensity lasers has been a of much interest lately motivated by the results of the recent experiments[1-6] of irradiation of noble gases with high power short pulses lasers. These experiments showed that significant amounts of ionization and residual excited-state occured simulatenously. These findings raised some controversy since according to the original shell model[7-10] multiphoton ionization (MP) is a resonant process induced by an excited state that is Stark shifted into resonance without itself becoming populated. An alternative model[1] sugests that MP is a two step process: the intermediate state is brought into resonance with the laser and real population is transferred to the excited state. Subsequently, this excited state ionize by single photon absorption later in the pulse. These studies show that the final state of atoms irradiated by short laser pulses is sensitive to the time history of the laser pulse. Oscillations in the ionization signal were studied[15-19] as a funcion of the peak intensity of a single laser pulse, showing that both resonant and nonresonant population transfer to the upper state play an important role in the MP process.

The purpose of this work is to present a model of coherent excitation of a two state system by a sequence of two identical pulses. The first pulse excites part of the population from the ground state to the excited state. The two states interact again during the second pulse. During the time between the two pulses the two states acquire different phases due to their different energies. The difference in phase is dependent on the time delay between the two pulses. Therefore after the second pulse, the population in each state and the ionization probability will exibit a modulation as a function of the delay between the two pulses. The atomic and laser parameters, such as the strength of the coupling between the

two states, the rate of decay into the continuum of the upper state, the Stark shift, the peak intensity, the pulse duration and the laser wavelength determine the details of the above modulation. The model considered here consists of two bound states with a parametric description of the intensity dependent level shifts and the decay rate of the resonance exitation. The ionization probability is calculated from direct integration of the Schroedinger equation. Modulations in the ionization signal are found as a function of the delay between the two pulses and the peak intensity. Single peak or multiple oscillations are found in the ionization probability as a function of the delay between the two pulses. At these peaks it is found that the interaction is dominated by nonresonant exitation.

The model.

The equations determining the time evolution of the amplitudes of the two states are given by[11]

$$\frac{dc0}{dt} = -iVe^{-i\Delta t} \quad ; \quad \frac{dcl}{dt} = -iVe^{i\Delta t}c0 - (\Gamma + i\Delta)cl \tag{1}$$

$c0(t)$ and $cl(t)$ are the complex probability amplitudes of the ground and the excited states, V is the effective Rabi frequency, describing a process in which the atom undergoes a transition from the ground state to the excited state by absorption of n photons, $V(t) = V_n \cdot |E(t)|^n$, V_n is the dipole coupling strength. $\Gamma(t) = \Gamma_0 \cdot |E(t)|^2$ is the ionization cross section of the upper state, E is the electric field of the laser. $\Delta(t) = \Delta_0 + \alpha \cdot E(t)^2$, Δ_0 is the zero field detuning of the exited state from the ground state dressed by n photons, i.e. $\Delta_0 = E_t - E_0 - nh\omega \cdot E_t$ and E_0 are the energies of the two states. α is the ac Stark coefficient. We assume that the excited state shifts by an amount equal to the pondermotive energy $U_p = e^2/(4m\omega^2)$ as the excited state approaches the ionization threshold. The field is taken to be classical, linearly polarized and a double Gaussian pulse is assumed:

$$E(t) = E_0 \cdot e^{-t2/\tau 2}L \cdot cos(\omega t) + E_0 \cdot e^{-(t-\tau)2/\tau 2}L \cdot cos(\omega(t-\tau)) \tag{2}$$

E_0 is the poeak electric field, the intensity full width at half maximum (FWHM) is $\tau(2ln2)^{1/2}$, $h\omega$ is the laser photon energy and τ is the delay between the two pulses.

The probability of ionization $P(t) = 1 - c0(t)^2 - cl(t)^2$ is studied as a function of the delay time between the two pulses for several values of the laser peak intensity. Eqs. 1 were integrated numerically from $-t_0 t o t_0 + \tau$, with the initial conditions $c0(-t_0) = 1$ and $cl(-t_0) = 0$, using the Matlab ode45 routine.

Numerical results.

The parameters corresponding to the exitation of the state 4f in xenon irradiated by 100 fs, 620 nm pulses are used in the calculations. This state is separated by 11.26 eV from the ground state and it is near resonant by 6 photons. Using atomic units: $\Delta_0 = 0.0265, \tau = 3539, \Gamma_0 = 0.3, \Omega_n = 385000, \omega =$

0.0734. E was varied from 0.02 a.u. to 0.035, corresponding to intensities from $1.4.10^{13} to 4.29.10^{13}$. The intensity required to bring the excited state in resonance with the laser is $2.10^{13} W/cm^2$.

Fig. 1 shows the asymptotic value of P(t) as a function of the delay τ (in units of the single pulse duration) between the two pulses for different values of the peak field E_0. Several features are seen:
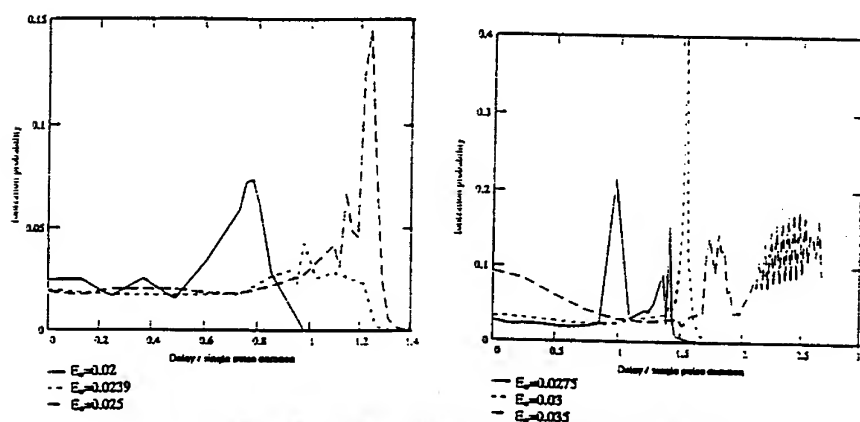
Fig.1 The ionization probability as a function of the delay between the pulses

For the range of intensities studied here the ionization probability is larger when the two pulses are separated than when they are overlapped. The increase in the ionization probability can reach more than an order of magnitude, depending on the peak field value. The maximum value of P obtained here was an order of magnitude, depending on the peak field value. The maximum value of P obtained here correspond to $E_0 = 0.03$. Several behaviours of P as a function of τ are seen, depending on the intensity.

For the higher intensities in the range considered here, P first decreases as a function of τ, then increases and oscillates. For lower intensities, P does not change with the delay τ then more than one peak or oscillations are seen. As the peak field value E_0 increases the peak (or peaks) of the ionization shift towards higher values of the delay between the pulses.

Different time histories of the populations of the two levels P0(t) and P8t) occur, depending on the laser field E_0 and the time delay between the two pulses. Fig. 2 shows an example when the two pulses are overlapped, $\tau = 0, E_0 = 0.03$. As the intensity in the pulse raises, the upper state is brought into resonance. The upper state population has a resonant component as shown by the rapid oscillations and also a slowly varying non resonant component as shown by the rapid oscillations and also a slowly varying non resonant component originating from adiabatic following of the dressed states[18]. The behaviour of the populations of the two levels is completly different at the peak of the

ionization probability as a function of the delay between the two pulses. Fig. 3 displays this case. No oscillations occur in this case. The population of the upper state increases to a maximal value and then decreses during the falling time of the second pulse.

Different shapes of the modulation in the ionization probability are obtained, depending on the laser intensity and the delay between the two pulses. Single peak or multiple oscillations are found in the ionization probability as a function of the delay between the pulses. At these peaks in the ionization probability no rapid Rabi oscillations occur, indicating that the interaction is dominated by nonresonant exitation.

Conclusions.

It was shown that a large modulation in the multiphoton ionization probability can be obtained with a double short pulse laser exitation. In a simple two-level system the ionization can be enhanced by at least an order of magnitude when the two pulses are separated by a time of the order of the duration of each pulse.

Aknowledgment

1. M.P. de Boer & H.G. Muller, *Phys. Rev. Lett.* 68, 2727 (1992).
2. G.N. Gibson, R.R. Freeman & T.J. McIllrath, *Phys. Rev. Lett.* 69, 1904 (1992).
3. J.C. Story, D. I. Duncan & T.F. Gallangher, *Phys. Rev. Lett.* 70, 3012 (1993).
4. R.B. Vrijen et al. & L.D. Noordam, *Phys. Rev. Lett,* 70, 3016 (1993).
5. M.P. de Boer, L.D. Noordam & H.G. Muller, *Phys. Rev. A*, 47, R45 (1993).
6. R.R. Jones, D.W. Schumacher & P.H. Bucksbaum, *Phys. Rev. A* 47, R49 (1993).
7. R.R. Freeman et al., *Phys. Rev. Lett* 59, 1092 (1987).
8. R.R. Freeman P.H. Bucksbaum, . *J. Phys. B* 24, 325 (1991).
9. G.N. Gibson, R.R. Freeman & T.J. McIlrath, *Phys. Rev. Lett.* 69, 1904 (1992).
10. T.J. McIlrath et al. *Phys. Rev. A* 40, 2270 (1989).
11. M. Protopapas & P.L. Knight, *J. Phys. B: At. Mol. Opt. Phys* 28, 4459 (1995).
12. R.R. Jones et al., *Phys. Rev. Lett.* 71, 2575 (1993).
13. R.R. Jones et al., *J. Phys. B: At. Mol. Opt.* 28, L405 (1995).
14. A. Wojcik & R. Parzynski, *Phys. Rev. A* 51, 4787 (1995).
15. R.R. Jones, *Phys. Rev. Lett.* 74, 1091 (1995).
16. H.P. Breuer, K. Dietz & M. Holthaus, *Z. Phys. D* 10, 13 (1988).
17. M. Dorr, R.M. Potviegle & R. Shakeshaft, *J. Opt. Soc. Am. B* 7, 433 (1990).

376

18. X. Tang, A. Lyras & P. Lambropoulos, *J. Opt. Soc. Am B* **7**, 456 (1990).
19. G. Gibson et al., *Phys. Rev. A* **49**, 3870 (1994).
20. M. Edwarks & C.W. Clark, *J. Opt. Soc. Am. B* **13**, 101 (1996).
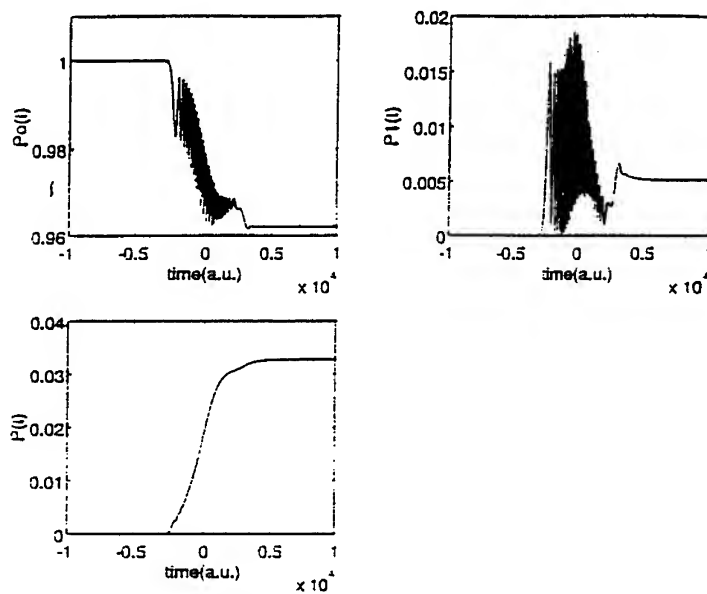
Fig.2 The population of the two levels P0(t), P1(t) and the ionization probability P(t) for $E_0 = 0.03$, $\tau = 0$
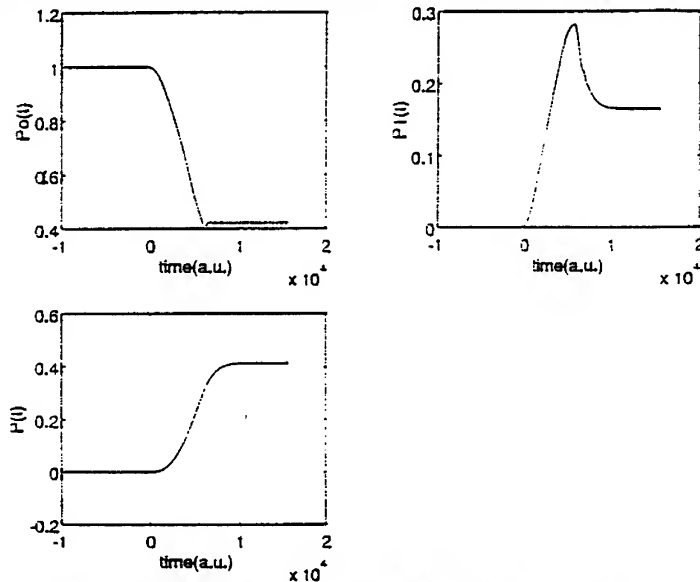
Fig.3 The population of the two levels P0(t), P1(t) and the ionization probability P(t) for $E_0 = 0.03$, $\tau = 1.53$

THE ROLE OF ELECTROMAGNETIC FORCES IN THE STATE EQUATION OF LASER PLASMA CREATED BY SUPER INTENSE RADIATION

A.N.STARODUB, V.V.IVANOV, A.K.KNYAZEV, A.V.KOUTSENKO,
A.A.MATZVEIKO, YU.A.MIKHAILOV, V.P.OSETROV, A.I.POPOV, and
G.V.SKLIZKOV.

Laser Plasma Laboratory, P.N.Lebedev Physical Institute, Leninsky Prospect 53, Moscow 117924, Russia

Abstract. *The results of the experiments with plasma heated by laser radiation pulses of ns- and ps- duration and flux densities in the range 10^{13}-10^{15} W/cm^2 are reported. The fast electrons with maximum energy up to 380 keV have been observed. The energy of macroscopic electromagnetic fields was measured at the level of 10% of absorbed laser energy. The experiments with laser irradiated thin foils showed the sharp decrease of the laser energy passed through a foil with the increase of the foil thickness and the passed pulse length changes.*

The recent experiments in P.N.Lebedev Physical Institute on high energy electron generation in laser plasma [1-3] opened a new look on the problem.

The generation of electrons with the energy many times more than the energy of thermalized electrons in laser plasma is extremely interesting phenomenon both for fundamental research of laser-plasma interaction [4,5] and for practical applications of laser plasma [6-9]. For example, fast electron generation in laser plasma can have negative or positive role in laser fusion. In the schemes of hydrodynamic compression of a target even very small amount of high energy electrons can decrease compression ratio [6,7]. In the scheme of laser fusion called "fast ignition" [8,9] the energy transport by them into the ignition region is one of the most important factors of the success.

The experiments have been carried out in Laser Plasma Lab. at the laser installation "PICO". *Al* massive and foil targets were used. The principal experimental scheme is presented in Fig.1 The flux density was varied from 10^{13} W/cm^2 to 5×10^{14} W/cm^2. The two nano- and picosecond *Nd*-lasers were used. The pressure of residual gas (air) in target chamber was varied in
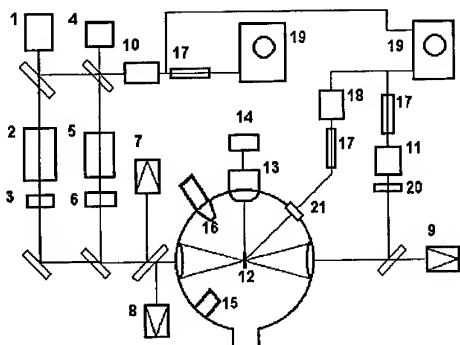
377

the range 10^{-2} - 6×10^{-6} Torr. The laser pulse duration was 2 ns and 5 ps. The laser energy in ns- regime was changed from 2J to 20J. In ps- regime the energy of single pulse was changed in the range 40 mJ-240 mJ. The laser radiation divergence was 2α = $(5\div8)\times10^{-4}$ rad; the energy contrast ratio was K_E= 10^3-10^5. The laser spectral range was $\delta\lambda$=30A for ns- and $\delta\lambda$=7A for ps- laser.

The detailed description of experimental method and equipment for measurements of high energy electron generation in laser plasma are presented in [1]. The maximum energy of fast electrons measured in these experiments was E_{max} = 380 ± 50 keV in ns- and E_{max} = 30 ± 5 keV for ps- regime. In the case of ns-regime the typical electron current pulse duration was 3×10^{-9} s. The averaged value of electron current is 8kA. At the same time the current related to the electron energy more than E_{max} equals about 12A. The assessment of electron current and current density gives up to 0.5 MA and 10^9 A/cm^2 for ps-regime.
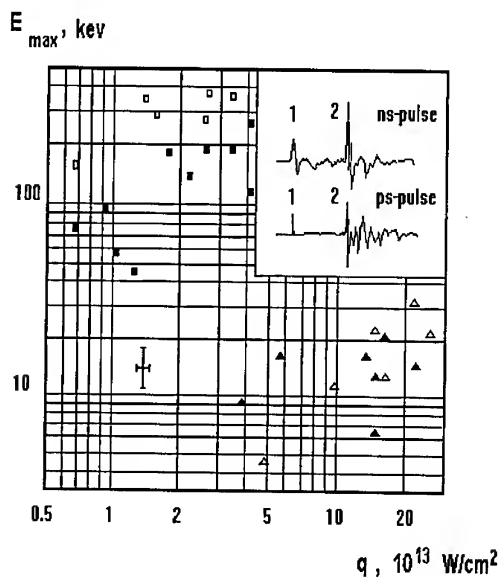
Fig.2 presents the experimental results of maximum electron energy dependence on laser radiaton flux density for ns- ($\square$) and ps- ($\triangle$) regimes and for different values of gas pressure in the chamber p_1 = 10^{-2} Torr ($\square\triangle$) and p_2 = 10^{-5} Torr($\square\triangle$). One can see rather strong depen-dence of maxi-mum electron energy on flux density and gas pressure. The measured difference between maximum electron energy for ps- and ns- pulses may be connected with difference in energy contrast ratio (10 times less for picosecond pulses) or with principally different mechanisms of generation. In the corner of Fig.2 the typical oscillograms of laser pulse (1) and high energy electron current pulse (2) are presented. The magnitudes of positive electron current pulses (2) correspond to 320 keV (ns-pulse) and 30 keV (ps-pulse).

One of the most interesting and important result of the experiments reported consists in the fact that the energy of macroscopic electromagnetic fields in plasma has been observed of the level of 10% of absorbed laser energy. This result have given the evidence that even at rather moderate laser radiation flux densities on the target the energy of macroscopic electromagnetic field in plasma may be comparable with gas-kinetic or thermal radiation energy. It's necessary to note that the energy required to acieve the ionization observed in the experiment is in the range 50-70% of absorbed energy. Thus at least at flux densities more than 10^{14} W/cm^2 it is necessary to consider terms related to macroscopic currents and ponderomotive forces, when a particular state equation is used.

Possible way to correct a state equation may consists in taking into account the additional term like $H^2/8\pi$. In the frames of semiempirical model the internal energy ε can be written with this correction as $\varepsilon(\rho,T) = \varepsilon_c(\rho) + \varepsilon_T^{(e)}(\rho,T) + \varepsilon_T^{(i)}(\rho,T) + \varepsilon_{EM}$, where the first three terms in the right sides describe elastic properties of cold matter, and electrons state and ions motion; and the last term corresponds to electromagnetic energy related to the charge separation. For electrons in hot plasma for ideal Bolzman gas of free electrons approximation: $\varepsilon_T = k/m_p M_{eff} \left(3/2\, ZT_e + I \right)$, where Z- is effective ion charge, I - energy of ionisation, m_p and M_{eff} - proton and ion mass, and $H^2/8\pi$ - energy density of electromagnetic field. For calculations it's nessesary to find the derivation $\dfrac{\partial \varepsilon_T}{\partial T_e} = \dfrac{k}{m_p M_{eff}} \left(\dfrac{3}{2} Z + \dfrac{3}{2} \dfrac{\partial Z}{\partial T_e} T_e + \dfrac{\partial I}{\partial T_e} \right) + \dfrac{H}{4\pi} \dfrac{\partial H}{\partial T_e}$ [10] .

E$_t$, mj
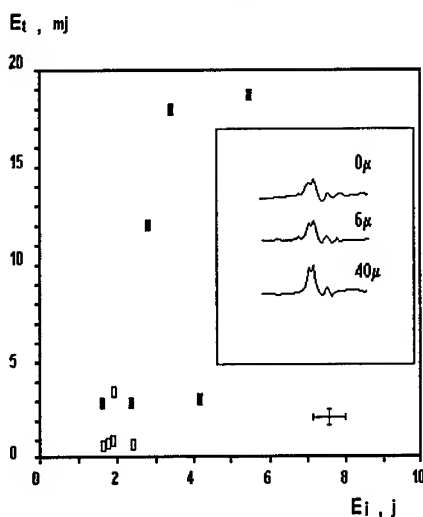
The second group of the experiments described is devoted to the energy balance of laser radiation interaction with thin foils. The calorimetric and time-resolved measurements of laser radiation fallen on the target surface, and scattered and reflected from the target, and passed through a foil has been done at the same shot (see Fig.1).

Fig.3 gives the dependence of laser radiation energy passed

380

through the target on incident energy for different thicknesses of a foil. One can see the sharp dependence of the transmitted energy on foil thickness. The picture in the corner of Fig.3 presents typical oscillograms of laser pulse passed through Al foils of different thickness. The delay of the begining of laser pulse is connected with variation of foil thickness. More thick foil results in higher delay of laser pulse and more absorption of laser radiation.

Interpretation of these results can be understood from consideration of heat propagation in target plasma. For nonlinear heat wave with the coefficient χ dependence on temperature like $\chi = aT^n$ the heat equation is written as :

$\frac{\partial T}{\partial t} = a \frac{\partial}{\partial x} T^n \frac{\partial T}{\partial x}$. For thin foils and typical radiation conditions the model of automodel heat wave from the instantaneous flat sourse can be used.

In this case for parameter $\xi = \dfrac{x}{\left(aE^n t\right)^{\frac{1}{n+2}}}$ the solution can be find [11] as :

$$T = \left(E^2 / at\right)^{\frac{1}{n+2}} f(\xi) \; ; \; f(\xi) = \left[\frac{n}{2(n+2)}\left(\xi_0^2 - \xi^2\right)\right]^{\frac{1}{n}} ;$$

From this solution it's possible to find formulas for front propagation x_f and velocity: $x_f = \xi_0\left(aE^n t\right)^{\frac{1}{n+2}}$, $\dfrac{dx_f}{dt} = \xi_0\left(aE^n\right)^{\frac{1}{n+2}} t^{\frac{1}{n+2}-1}$. This model for $n=5$ ($\xi=0,77$) gives an agreement with experimental results reported here.

Fig.1. The principal scheme of experiment. 1-picosecond master oscillator; 2-laser amplification stages; 3-optical isolator; 4-nanosecond master oscillator; 5-laser amplification stages; 6-optical isolator; 7,8,9-calorimeters; 10,11-fast photodiods; 12- target; 13,14-target position sistem; 15-X-Ray spectrometer; 16-multichanel X-Ray microscope; 17- coaxial line; 18,21-sistem of fast electrons registration; 19-oscilloscopes; 20-optical filter.

Fig.2. Experimental dependence of maximum electron energy (E_{max} on laser flux density (q) for ns- ($\square$) and ps ($\triangle$) regimes and for different residual gas pressure 10^{-2} Torr ($\square\triangle$) and 10^{-5} Torr ($\square\triangle$).

Fig.3. Experimental dependence of laser energy (E_t) passed through the foil on incident laser energy (E_i) for different foil target thicknesses 40 μ ($\square$) and 6 μ ($\square$) for ns-pulse at residual gas pressure 10^{-2} Torr. The error bars correspond to instrumental deviations.

REFERENCES

[1] V.V.Ivanov, et.al. Instruments and Experimental Techniques, **38**, 4 , 2, 497 (1995). [2] V.V.Ivanov et.al. Proc.12th Intern. Conf. on Laser Interaction and Related Plasma Phenomena. Osaka, Japan (1995). [3] V.V.Ivanov et.al. JETP, **109**, 4, 12 (1996). [4] C.S.Liu, M.N.Rosenbluth. Phys. Fluids, **19**, 967 (1976). [5] A.Simon et.al.Phys. Fluids, **26**, 3107 (1983). [6] J.Nuckolls et.al. Nature, **239**, 139 (1972). [7] .G.Basov et.al. Trudy FIAN,**170**, 3 (1986). [8] N.G.Basov et.al. Journ. of Sov. Laser Research, **13**, 5, 396 (1992). [9] M.D.Perry, G.Morou. Science, **264**, 917 (1994). [10] A.V.Bushman, V.E.Fortov. Uspehi Fizicheskih Nayk, **40**, 2, 177 (1983). [11] G.L.Barenblatt, Prikladnaya Matematika I Mechanika, 16, 67 (1952).

INSTABILITY OF STRONG SHOCK WAVES IN METALS

I. Rutkevich, E. Zaretsky, M. Mond
Pearlstone Center for Aeronautical Engineering Studies,
Department of Mechanical Engineering, Ben-Gurion University,
Beer-Sheva, Israel

An equation of state satisfying a given empirical law for the Hugoniot adiabatic has been obtained and employed for calculating the criterion of spontaneous emission of sound and vortex waves from shocks in metals. It has been found that in some metals sufficiently strong shocks may become unstable with respect to spontaneous emission.

1 Introduction

Generation of high-density plasma by strong shocks propagating in condensed matter is important for various applications, including the problem of inertial confinement fusion [1]. Since the first theoretical studies of laser - target interactions it has been recognized that hydrodynamic and plasma instabilities, first of all, the Rayleigh - Taylor instability, may lead to serious limitations on inertial fusion [1,2]. Possible instabilities of shock waves propagating in a cold material, such as a solid DT target or a heavy metal layer (in the case of structured targets) were not the subject of special consideration. The problem of corrugation instability of a shock front was first addressed by Dyakov [3] and Kontorovich [4]. The criteria of shock instability are given in literature in terms of the function $p = p_H(\rho)$ connecting the pressure $p = p_2$ and the density $\rho = \rho_2$ of the shock-compressed material along the Hugoniot adiabatic (HA) and in terms of the Mach number of the flow behind the shock wave in the frame of reference where the shock is at rest: $M_2 = (D - U)/c_2$, where c_2 and U are the sound velocity and the particle velocity behind the shock, D is the shock velocity [5]. For shock waves in solids the experimental Hugoniot adiabatic (HA) is commonly presented as a relationship between D and U. For most metals $D(U)$ is a linear function [6]. The main purpose of this paper is to obtain the equation of state (EOS) that is consistent with a given HA, allow calculating the sound velocity c_2 along the HA and testing the criterion for the spontaneous emission (SE) of acoustic and vortex waves from the shock front.

2 Equation of State

When an experimental dependence $D(U)$ is known, two out of the three Rankine-Hugoniot relations representing the conservation of mass and mo-

mentum allow determining the Hugoniot adiabatic in the plane of variables (ρ_2, p_2)[7]. The problem considered below is formulated as follows: For a given form of the HA find the EOS determining the pressure p as a function of ρ and T. The model that is adopted here is an EOS that is the sum of three terms that describe the contribution of the cold elastic pressure as well as the thermal atomic and electronic pressures to the total pressure. The lattice and electronic Grüneisen parameters connect the atomic and electronic pressures terms to the respective contribution to the internal energy. The electronic Grüneisen parameter is chosen to be 2/3 which is adequate for both the degenerate electronic gas that satisfies the Fermi-Dirac statistics and for the fully ionized plasma behind strong shocks. The EOS is then determined by the solution of a system of equations that is obtained from the Slater-Landau model[7-9], which provides a relationship between the lattice Grüneisen and the cold pressure, and from the relationship between the latters that is determined by the known internal energy along the HA. Once the solution is obtained the EOS may be used in order to calculate the isentropic sound velocity. Numerical calculations were carried out for a straight HA given by $D = c_0 + SU$.

3 The Criterion for SE

When a planar shock propagates in a uniform cold material with the constant velocity $\mathbf{W} = -D\mathbf{e}_x$, it is convenient to consider its interaction with small perturbations in the frame of reference K , which moves with the same velocity $\mathbf{W}$. In this frame the shock is at rest and its front can be specified as $x = 0$. In this case, a cold medium in the domain $x < 0$, i.e. ahead of the shock, moves with supersonic velocity $\mathbf{V}_1 = D\mathbf{e}_x$, while the compressed medium behind the shock ($x > 0$) moves with subsonic velocity $\mathbf{V}_2 = (D - U)\mathbf{e}_x$. In the subsonic domain $x > 0$ the two-dimensional perturbations in the form $exp[i(k_x x + k_y y - \omega t)]$ can describe various types of linear waves. When an incident upstream acoustic wave reaches the shock front, both a downstream acoustic wave and an entropy-vortex wave moving away from the shock are generated. Since $k_y \neq 0$, the initially planar shock front undergoes sinusoidal corrugation [5]. Such a shock emits waves spontaneously if the non-trivial solutions with real frequency ω for the reflected downstream acoustic and entropy-vortex waves exist in the absence of an upstream acoustic wave. The criterion for SE is [4]

$$h_c(\bar{\rho}, M_2) < h < 1 + 2M_2, \quad h = -V_2{}^2 \left(\frac{d\rho_2}{dp_2} \right)_H \qquad (1)$$

where

$$M_2 = \frac{V_2}{c_2} < 1, \quad h_c = \frac{1 - M_2{}^2(\bar{\rho}_2 + 1)}{1 + M_2{}^2(\bar{\rho}_2 - 1)}, \quad \bar{\rho}_2 = \frac{\rho_2}{\rho_1}$$

Here h_c is the critical value of the Dyakov parameter h determining the threshold for SE.

4 Results

Numerical calculation of the lattice Grüneisen parameter and the cold elastic pressure for several metals allowed us to calculate the sound velocity behind the shock. The calculated dependence of the sound velocity along the HA for aluminum is in good agreement with experimental results presented in [8]. As a result, the critical parameter h_c has been calculated and the Kontorovich criterion for SE (1) has been tested. It was found that SE from shock fronts may occur in metals, for which the slope S of the straight-line HA is less than 1.4 (for example, in aluminum where $S = 1.35$ and in molybdenum where $S = 1.26$). The threshold for SE in aluminum corresponds to the degree of compression ρ_2/ρ_1, which is close to 2.5. Although such strong degrees of compression in these materials were achieved behind shock waves produced by underground nuclear explosions [10], a purposeful experimental search for possible instabilities associated with SE was not carried out.

It should be noted that the thermodynamic model which neglects the electronic contributions to the total energy and to the total pressure always predicts the occurrence of SE for sufficiently strong shocks [11]. Taking account of the thermal pressure and the thermal energy of free electrons may have stabilizing effect for metals with relatively large values of the parameter S (such as copper, for which $S = 1.5$ and lead, for which $S = 1.57$). The difference in qualitative behaviour of the parameter h_c for molybdenum and lead is seen in the figure. The electronic contributions were found to be important also for density dependence of the lattice Grüneisen parameter. Taking into account the electronic contributions to the total pressure increases the values of the lattice Grüneisen parameter. Employing alternative models instead of the Slater-Landau model (such as the Dugdale-MacDonald model [8]) may lead to a noticable changes in the Grüneisen parameter. However, these changes have weak influence on the threshold for SE.

384
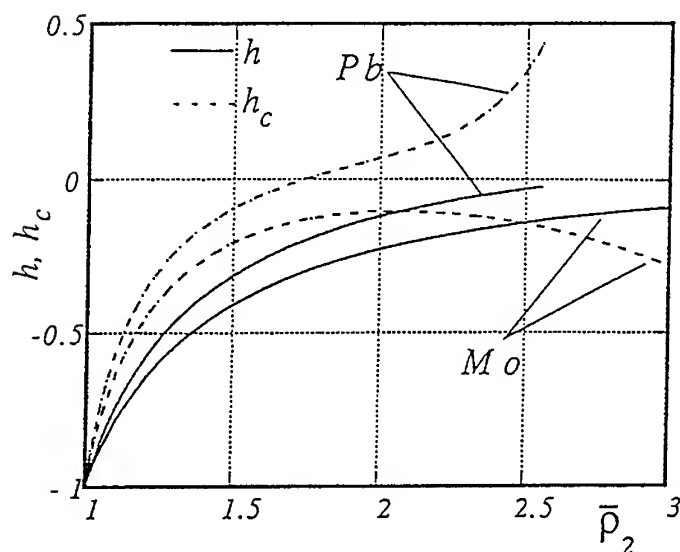
Behavior of h and h_c along the Hugoniot
adiabatics for Molybdenum and Lead

References

1. K.A Brueckner and S. Jorna in *Laser Driven Fusion*, (KMS Fusion Inc., Ann Arbor, Michigan, 1973).
2. J.D. Kilkenny *et al.*, Phys. Plasmas 1, 1379 (1994).
3. S.P. Dyakov, Zh. Eksp. Teor. Fiz. 27, 288 (1954).
4. V.M. Kontorovich, Sov. Phys. JETP 6, 1179 (1957).
5. L.D. Landau and E.M. Lifshitz in *Fluid Mechanics*, (Pergamon Press, 1987).
6. A.C. Mitchell and W.J Nellis, J. Appl. Phys. 52, 3363 (1981).
7. I.B. Zel'dovich and Y.P. Raizer in *Physics of Shock Waves and High-Temperature Hydrodynamic Phenomena*, (Academic Press, 1966).
8. L.V. Al'tshuler, Sov. Phys. Uspekhi 8, 52 (1965).
9. S. Eliezer, A. Ghatak and H. Hora in *An Introduction to Equation of State*, (Cambridge University Press, 1986).
10. C.E. Ragan III, Phys. Rev. A29, 1391 (1984).
11. I. Rutkevich, E. Zaretsky and M. Mond, J. de Physique IV C8, 728 (1994).

ANALYTICAL POTENTIALS INCLUDING TEMPERATURE AND DENSYTY EFFECTS FOR CALCULATION OF PLASMA OPTICAL PROPERTIES

J.M. GIL†‡, P. MARTEL†‡, J.G. RUBIANO†, R. RODRIGUEZ†, E. MINGUEZ‡, and L. DORESTE†‡

(†)Department of Physics, Universidad de las Palmas de Gran Canaria, 35080 Las Palmas de Gran Canaria, Spain. (‡)Institute of Nuclear Fusion, Universidad Politécnica de Madrid, José Gutiérrez Abascal 2, 28006 Madrid, Spain.

Two non isolated analytical potentials obtained from an isolated atomic parametric potential are presented. Level energies, transition energies and oscillator strengths of several ions at different conditions of temperature and density calculated by using both potentials are showed and discussed. Opacities for iron plasmas at several condition of temperature an density obtained making use of these potentials are compared with those obtained by means of the isolated potential.

1 Introduction

A method to generate an analytical potential including temperature and density effects has been developped and used to obtain a non isolated analytical potential by assuming the linearized Debye-Hückel approximation for modelling the plasma density [1]. This potential was generated starting from an isolated atomic parametric potential [2] whose parameters were fitted to a self-consistent potential. In this paper we present another non isolated analytical potential generated by using the same methodology above metioned but assuming the ion-sphere approximation instead of the linearized Debye-Hückel one. The same isolated atomic parametric potential [2] has been used in this procedure.

Level energies, transition energies and oscillator strengths of several ions at different temperature and density conditions calculated by using both non isolated analytical potentials and the above mentioned isolated potential are compared.

In a previous work [3] we used the isolated parametric potential to calculate plasma opacities, obtaining results very closed to those calculated by means of a detailed opacity model (JIMENA-DCA code) [4]. This model was tested with other procedures during the Third Opacity Workshop [5]. Furthermore, we showed how the parametric potential allows to make detailed calculation of opacities with a considerable economy of computation time. Following a similar procedure bound-bound crossections and mean opacities are calculated, now using the non isolated analytical potentials for iron plasma.

386

2 Non isolated analytical potentials

For an ion with nuclear charge Z, and N electrons into a plasma of density $\rho_p(r)$, an effective analytical potential was generated [1] under the linearized Debye-Hückel approximation and considering a potential for the optical electron equal to $\frac{1}{r}$. It is

$$U_{eff}^I(r) = -\frac{1}{r}\left\{ \left[Z^* + a^2(N-1)C\right]e^{-ar} + (N-1)\left[1 - a^2\chi(r)\right]e^{-a_1 r} + 1 \right\}$$

(1)

$$C = \frac{2a_1 a_2}{\left(a_1^2 - a^2\right)^2} - \frac{1}{a_1^2 - a^2} \quad and \quad \chi(r) = C + a_2\left(\frac{1}{a^2} + \frac{1}{a_1^2 - a^2}\right)r$$

for $N < 12$ ($a_2 = 0$ for $4 \le N \le 7$) and if $N \ge 12$

$$U_{eff}^I(r) = -\frac{1}{r}\left\{ \left[Z^* + \frac{1}{2}a(N-1)\eta(0)\right]e^{-ar} \right.$$

(2)

$$\left. + (N-1)\left[e^{-a_1 r^{a_3}} - \frac{1}{2}a\eta(r)\right] + 1 \right\}$$

being $\eta(r) = \int_0^\infty e^{-a|s-r|}e^{-a_1 s^{a_3}}ds$, $Z^* = Z - N$ and a the inverse Debye radius. Parameters (a_1, a_2, a_3) of the isolated potential [2], were obtained for the ground states from He-like to U-like ions. This potential is given by

$$U_0(r) = -\frac{1}{r}\left\{ (N-1)\Phi(r) + Z^* + 1 \right\}$$

(3)

$$\Phi(r) = \begin{cases} e^{-a_1 r^{a_3}} & if \ N \ge 12 \\ (1 - a_2 r)e^{-a_1 r} & if \ 8 \le N \le 11 \ or \ N = 2,3 \\ e^{-a_1 r} & if \ 4 \le N \le 7 \end{cases}$$

(4)

Following the same procedure and if we assume now that: (i) $\rho_p(r) = \frac{Z^*}{\frac{4}{3}\pi R_0^3}$ (i.e. the ion-sphere approximation with radius R_0), and (ii) $-rU_{eff}(r)$ trend to Z in the origen and to 0 in $r = R_0$. This yield

$$U_{eff}^{II}(r) = U_0(r) + U_0(R_0) + \frac{Z^*}{2R_0}\left\{ 1 - \left(\frac{r}{R_0}\right)^2 \right\}$$

(5)

3 Results and discussion

For an ion at a given density and temperature, the level energies and orbital functions are obtained for each nlj-subshell by solving the Dirac equation with both analytical potentials given by Eqs. (1)-(2) and (5). In order to have a reference to compare we have followed the same procedure using the isolated analytical potential given by Eqs. (3)-(4). These results have been used to generate the transition energies ($\Delta E_{if} = |E_i - E_f|$) and the oscillator strength, f_{if}, by mean of the dipolar electric approximation. Here E_i and E_f are the level energies of the initial (nlj) and final $(n'l'j')$ states. In the following paragraphs we discuss the temperature and density effects by means of the parameter b which represent the inverse Debye radius a and the inverse ion-sphere radius $1/R_0$.

As may be expected, for a given ion the energy levels calculated by both potentials ($U_{eff}^{I}(r)$ and $U_{eff}^{II}(r)$) increase as the parameter b rises, i.e. are shifted toward the continous. Therefore, the level shift, δE_i, (i.e. $E_i - E_i^0$, being E_i and E_i^0 the non isolated and isolated values of the i level energies) and the relative shift to the isolated energy level (i.e. $\frac{\delta E_i}{E_i^0}$)will show a similar behaviour. These increases are larger for the ion-sphere model than for the Debye-Hückel one. Hence, for a given value of b, when the principal quantum number, n, rises, the level shifts obtained by both potentials decrease, and the relative shifts increases. We also observe a monotonic increment or decrement as the orbital quantum number, l, increases for each atomic shell.

When we analyze the dependence on the number of electrons N and on the atomic number Z we find that for a given value of b and for each isoelectronic sequence, when Z rises, the level shifts obtained increases, and the relative shifts decrease. Fixing Z and b the level shifts obtained by both potentials decrease as the electron number, N, rises.

We have use these potentials to calculate transition energies and oscillator strenghts, finding the following behaviours. In transitions between states with different principal quantum number, $(n' > n)$ the transition energy decreases. This behaviour can be explained taking into account that the level shifts decrease as the principal quantum number increases and therefore, the transition energy shifts, δE_{if}, (i.e. $\Delta E_{if} - \Delta E_{if}^0$) are negative. If transitions take place between states with the same principal quantum number, the transition energy can increase or decrease depending on the value of the orbital quantum number, l. We should note that for small values of b the Debye-Hückel potential provides, for these quantities, larger values than those supplied by the Ion-sphere potential. This behaviour changes for a given value of b. Similar behaviour has been detected for the oscillator strenghts.

388

Table 1: Rosseland (K_{R0}, K_R^I, K_R^{II}) and Planck (K_{P0}, K_P^I, K_P^{II}) mean opacities calculated with the isolated potential(Eqs. 3-4) and with (1)-(2) and (5) in cm^2/g.

Case	K_{R0}	K_R^I	K_R^{II}	K_{P0}	K_P^I	K_P^{II}
a	2.04×10^4	2.07×10^4	2.07×10^4	5.31×10^4	5.31×10^4	5.31×10^4
b	2.61×10^4	2.82×10^4	2.85×10^4	4.46×10^4	4.66×10^4	4.67×10^4
c	1.82×10^3	5.56×10^3	2.40×10^3	6.89×10^3	1.61×10^4	6.92×10^4
d	1.45	1.57	1.51	1.06×10^2	1.07×10^2	1.02×10^2

The bound-bound cross sections and the Planck and Rosseland mean opacities are calculated following the methodology described by Martel et al.[3] but using $U_{eff}^I(r)$ and $U_{eff}^{II}(r)$ instead of the isolated analytical potential given by Eqs. (3) and (4). Calculation were realized for several cases of iron plasma, mainly those cases already included in previous reference [3], such as:a) and b) at 20 eV temperature and densities of 10^{-3} g cm^{-3} and 10^{-2} g cm^{-3}, respectively,c) at 200 eV and 7.86 g cm^{-3}, and d) at 1000 eV and 1 g cm^{-3}. The calculations performed using non isolated potentials show that the line transitions are shifted, and the relative minimum are arisen, in relation to the result obtained from the isolated potential. The shift of peaks could be explained from the behaviour of δE_i, as it was discussed above. In most cases under study, we observe an increment in the values of mean opacities calculated by using the non isolated potential in relation to the isolated values (Table 1).

In this work we show how to use a non isolated potential yields to differences for opacities results with respet to the isolated case which depends on the plasma density model assumed. We think that these potentials could be very useful for detailed opacities calculation in high Z plasmas.

References

1. J.M. Gil, P. Martel, F.H. Ruano, J.G. Rubiano, E. Mínguez, and L. Doreste, to be submited to *JQSRT* , ().
2. P. Martel, L. Doreste, E. Mínguez, and J.M. Gil , *JQSRT* **54**, 621 (1995).
3. P. Martel, J.M. Gil, R. Rodríguez, E. Mínguez, and L. Doreste accepted for publication in *Laser Particle Beams* , (1996).
4. E. Mínguez and R. Falquina *Laser Particle Beams* **10**, 651 (1992).
5. A. Rickert, K. Eidmann, J. Meyer-Ter-Vehn, F.J.D. Serduke, and C.A. Iglesias, Editors, "Third International Opacity Workshop and Code Comparison Study", Max Planck Intitute für Quantenoptik Report, MPQ-204, August 1995.

NON LTE OPACITY CALCULATIONS WITH N-L SPLITTING FOR RADIATIVE HYDRODYNAMICS CODES

A.MIRONE, F.GILLERON, C.CHENAIS POPOVICS, H.MERDJI, J.C.GAUTHIER
LULI, Laboratoire pour l'Utilisation des Lasers Intenses, Ecole Polytechnique,
91128 Palaiseau Cedex France

We present a new method for calculating opacities in a non LTE plasma, based on modelling of the one-electron atomic potential. In this model the collisional-radiative equations of an average ion are solved and the resulting screened charges are used to reconstruct the one-electron atomic potential. The degeneration in the angular momentum number is removed calculating Average Ion wave functions, oscillator strengths and Slater's integrals by quantum mechanics in the reconstructed potential. A detailed configuration accounting is done, using binomial distribution and first order perturbation theory. Our method, compared to previous hydrogenic ion calculations, gives improved values of plasma opacities, especially in the XUV range where the $\Delta n=0$ transitions play an important role.

1 Introduction

In the interaction of high power lasers with a high or mean Z target, an important role is played by the conversion layer. In this layer radiative cooling competes with heating by electron heat conduction from the critical density layer and microreversibility is broken. In order to describe correctly this NLTE region we must consider both radiative and collisional phenomena at once. The usual approach to solve efficiently the collisional-radiative equations is within the framework of the Hydrogenic Averaged Ion with Screened Charges. Such a model is numerically very convenient but, if applied to opacities modelling, it fails to describe some important spectral features, especially the $\Delta n=0$ transitions, which play a significant role in the soft X-rays range.

We show in this work how to reconstitute, on the basis of the screened charges values, some important spectral features which, in the original model, are not taken into account.

2 Some basic notions

The ions in a plasma can exhibit a large range of electronic excited states. The simplest method to describe an ion state is considering mono-particle electron bound states. In this theoretical frame each electronic configuration is specified by a different way to distribute the electrons over the bound states. For high or mean Z elements, even this simple approach gives a considerable number of different

configurations. In order to further simplify the computational task, one calculates just one ion : the most representative one, the Average Ion. The Average Ion is defined by the occupation probabilities of its bound states.

The detailed configurations are then taken into account, after calculation of the Average Ion, by first order perturbation theory. Neglecting wave functions relaxation, the detailed configuration properties are written as simple functions of occupation numbers and Average Ion Slater's integrals.

The Average Ion occupation probabilities are calculated self-consistently with energies, wave-functions and the external environment. At LTE one needs to know just temperature and chemical potential.

In our NLTE calculation, we solve the collisional-radiative equations for the Screened Charges Ion [1,2]. This ion-model is numerically very convenient. In this model the electron energy depends only on the principal quantum number n and on a screened charge Q_n defined by :

$$Q_n = Z - \sum_j S_{nj} 2n^2 p_n . \qquad (1)$$

where Z is the nuclear charge and p_n the occupation probability of shell states. The factors S_{nj} are empirical screening constants [3]. The screening by free electrons and the energy broadening into bands for the outermost electrons are also accounted in the complete treatment. Expressing electron energies and oscillator strengths by simple hydrogenic formulas, the screened charges model can conveniently be applied to the resolution of collisional radiative equations.

3 Reconstruction of the one-electron potential

The screened charges model, thank to its analytical simplicity, is numerically very convenient for the solution of the set of collisional-radiative equations, but it is yet too simple to match some important radiative properties. In order to improve the opacities calculation we propose a method to reconstruct the one-electron potential.

Our driving idea is that the electric field depends on Q_n as :

$$-\frac{dV}{dr}(r_n) = \frac{(Q_n - 4\pi r_n^3 \rho / 3)}{r_n^2} \qquad (2)$$

where ρ is the free electrons density. A potential V satisfying the above equation is easily found by a piecewise Thomas-Fermi method. The potential V is univocally determined by the above conditions and, within each interval $[r_i, r_{i+1}]$ by the Poisson's equation :

$$\Delta V = \frac{\sqrt{2}}{\pi^2} F(V,T,\mu_i) \qquad (3)$$

where F is the Fermi-Dirac integral and μ_i is the chemical potential in $[r_i, r_{i+1}]$ which is function of i (we are NLTE) and whose corresponding V satisfies equation 2.

The Reconstructed Potential Method gives energies and matrix elements but not occupation probabilities. As the screened charges model makes no distinction between states having the same n, we face now the problem of assigning to each state nl, resulting from potential reconstruction, its occupation probability. We assume that the populations of the states of a given shell n, are at thermodynamic equilibrium respect to each other. This is a reasonable assumption for the plasmas that we usually study where electronic collision play an important role in the $\Delta n = 0$ transitions. A similar hypothesis can be found in the literature [4] (l mixing). Calling p_n and E_n the occupation probability and energy respectively for the shell n in the Screened Charges model, we can define a chemical potential μ_n satisfying:

$$P_n = \frac{1}{1 + e^{(E_n - \mu_n)/T}} \qquad (4)$$

where T is the electronic temperature. The occupation probabilities in the reconstructed ion are calculated by replacing in the above equation the energies E_n with the E_{nl} of the reconstructed model. One could question why this procedure and not another one. The important point in this procedure is that an LTE Screened Charges Ion gives an LTE Reconstructed Potential Atom. This is a very important point if we want that our opacity and emissivity joins smoothly LTE at high densities.

4 Results

We show opacities calculations for Germanium at T=60 eV and $\rho = 10^{-2} g/cm^3$. The calculations were made, for the graph in figure 1, by solving the collisional-radiative equations for a screened charges ion and applying hydrogenic formulas for the oscillator strength and Slater's Integral and, for the graph in figure 2, by fitting the atomic potential to the screened charges and proceeding as explained in this work. The $\Delta n = 0$ transitions are taken into account by the reconstructed potential model. They are very important in the soft x-rays range. The pick width for the transition (n=2 ;n=3) varies notably between the two models. The reason is that, in the new model, the better knowledge of wave functions brings improved values for the Slater's Integrals.

392
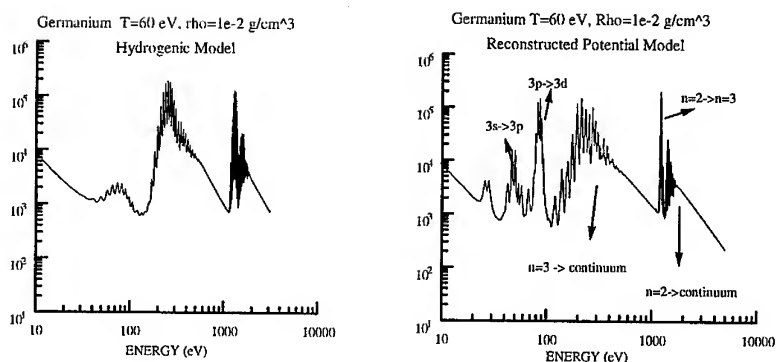
Figure 1 : opacities by the hydrogenic model.   Figure 2 : opacities by the reconstructed potential

5 Conclusion

In the proposed model the degeneration in the angular momentum number is removed by reconstructing the one-electron potential. Dipolar matrix elements and Slater Integrals are calculated from Average Ion wave functions and have improved value with respect to hydrogenic formula, especially for the orbitals close to the ion core. This improvement in Slater's integrals results in more accurate line shapes which is very important for Rosseland opacities. The correct treatment of $\Delta n=0$ transitions allows to generate opacity tables for the simulation of soft X-rays radiative transfer.

6 Aknowledgment

7 References

[1] Lokke and Grassberger, « Model XSN » Report UCRL-52276. (LLNL, 1977)
[2] R.M. More, « Physics of Dense Plasmas », Report UCRL-84991 (LLNL,1981)
[3] G.B. Zimmerman and R.M. More, JQSRT 23, 517 (1980)
[4] M. Busquet, J.P. Raucourt, J.C. Gauthier, « Atomic Populations Kinetics with Global Transition Rates », JQSRT 54, 81 (1995)

OPACITY AND TEMPERATURE MEASUREMENTS IN THE KEV RANGE OF AN X-RAY HEATED AL FOIL

H. MERDJI*, G. WINHART, K EIDMANN
Max Planck Institut für Quantenoptik, D-85740 Garching, Germany
*Actually at LULI, CNRS , Ecole Polytechnique, 91128 Palaiseau cedex France.

C. CHENAIS-POPOVICS, A. MIRONE, J.C. GAUTHIER
LULI, CNRS, Ecole Polytechnique, 91128 Palaiseau cedex France.

The absorption of a radiatively heated aluminium plasma have been spatially and spectrally measured in different experimental conditions. An absorption model based on LTE ion populations and atomic data calculated with the RELAC code is used to fit the data and gives the temperatures for each experimental case. Temperature and density deduced from radiative hydrodynamic modelling with the 1D code MULTI are compared to these results.

1 - Introduction

Many problems in astrophysic(1) or in inertial confinement fusion plasmas (2) depend on the understanding of the radiative properties of hot dense plasmas. The determination of x-ray opacities is essential for the modelisation of such plasmas. Experimental datas in homogeneous temperature and density conditions are needed to validate opacity models.

Measurements have been done in the photon energy range of 70 to 280 eV for aluminium, iron and holmium at the MPQ (3). We present here complementary measurements of aluminium in the keV range. The transmission of an X-ray probe beam through an Al plasma was spatially and spectrally resolved. The absorption structures are very sensitive to electron temperature which can be deduced from the measurements if an estimation of the density is known. An absorption model based on local thermodynamic equilibrium (LTE) ion populations and atomic data calculated with the RELAC code [4] is used to fit the data. The electron temperature is deduced for the different experimental cases. Temperature and density are also inferred from radiative hydrodynamic modelling with the 1D code MULTI [5]. .

2 - Experiment

Figure 1 shows the experimental geometry of this experiment. A spherical gold hohlraum is heated by the main beam of the iodine laser ASTERIX IV (160J /400 ps at 0.440µm or 500J /400ps at 1.344µm wavelength). We have used 1.7 mm and 3 mm hohlraums in different irradiation configuration. An aluminium foil (1100Å, 550Å) glued on one half of the two diagnostic holes of the cavity was radiatively heated by the hohlraum X-ray emission. Each sides of the sample foil was coated with a carbon layer (500Å) to limit the foil expansion and to get a more uniform density in the sample. The thickness of the sample is chosen to obtain an optical depth close to unity in the spectral range of the 1s-2p Al transitions around 0.8 nm. This set-up provides a uniform heating of the sample which stays in LTE and allows quantitative transmission measurements for several temperature and density conditions. The aluminium sample is probed by using the technique of point projection spectroscopy. A backlighter beam is created by focusing a second laser beam (50J, 400ps, ω) with a fixed delay to the main beam

394
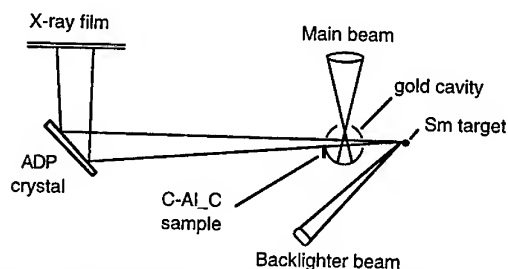
FIG. 1. Schematic drawing of experiment. The sample is glued on one half of the two diagnostic holes, so that the emission of the samarium spectrum and the spectrum transmitted through the Al sample are simultaneously measured with an ADP crystal spectrograph.

(600 and 800ps) onto a samarium target (Sm, Z=62). The material of the backlighter target has been chosen in order to get enough emission in the probed spectral range. The backlighter has a pulse duration of 400 ps. In the analysis of the data,

the variation of the sample parameters during the probing time was taken into account.

The spectrum in the wavelength 7.9 - 8.4 Å was recorded on Kodak DEF film by an ADP crystal spectrograph. A wavelength resolution of 1 eV was achieved and the spatial resolution was about 100 μm. As the samarium spectrum is very sensitive to laser conditions, simultaneous measurement of the backlighter spectrum and the transmitted spectrum through the Al plasma insured quantitative measurement of the Al absorption structures.

3 - Analysis

MULTI 1-D hydrodynamic simulations were use to study the heating of the aluminium sample. The radiative heating of the sample by the gold cavity emission was supposed to be a Planckian x-ray drive. These simulations shown in figure 2 give a first estimate of the temperature and density of the aluminium plasma during the measurement for different Planckian temperatures of the cavity. The temperature and the density are spatially uniform and are quite stable during the probe time (the temperature varies less than 25 % and the density less than 12%).
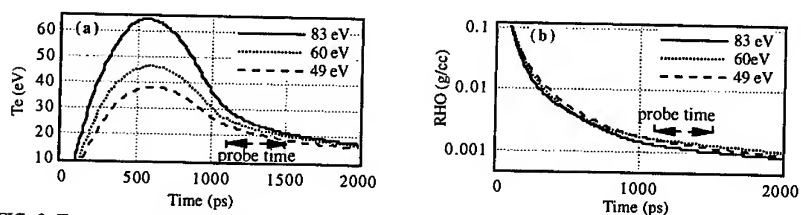
FIG. 2. Temporal evolution of the electronic temperature (a) and the matter density of the absorbing plasma for different Planckian drive temperatures (83, 60 and 49 eV).

The transmission of the heated foil at the photon energy hν is given by :

$$T(\nu) = I / I_0 (\nu) = \exp (-\sigma(\nu,\rho,T) \, \rho\Delta x) \ ,$$

where Δx is the plasma depth, ρ the sample density and $\sigma(\nu,\rho,T)$ is the absorption coefficient. We have used the RELAC code to analyse the experiment by fitting the experimental absorption

spectrum. The absorption structures are inferred from atomic data calculated by RELAC coupled to an LTE calculation of the population at a fixed temperature and density. Natural, Doppler and instrumental broadening have been included for each absorption line. The ionic balance depends strongly on the electron temperature so that a change of a few eV of the foil temperature can be easily detected in the absorption spectrum. It is shown that the absorption structures are less sensitive to the sample density. A temperature variation of about 30 % changes significatively the absorption spectrum.

In figure 3 is presented the comparison of experimental and theoretical absorption spectra of the aluminium plasma in two experimental cases. The experimental wavelength scale was corrected for the crystal dispersion. The film density was converted to intensity (photon/μm^2). Film fog and overlying emission spectrum are subtracted from the same film record. In the calculation of the theoretical spectrum the temporal variation of the plasma temperature is taken into account by fitting to the experiment the linear combination of two absorption spectra at two different temperatures (ref. 6).
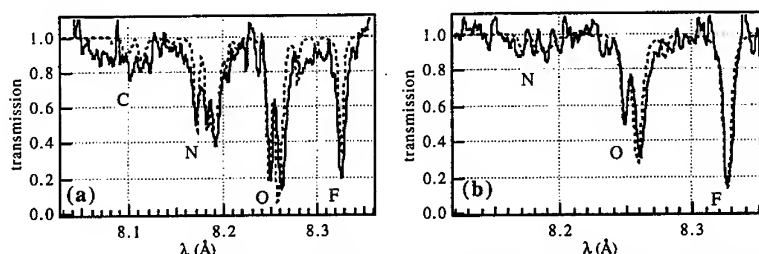
FIG. 3. Comparison of experimental (solid lines) and theoretical (dotted lines) absorption for an aluminium plasma of 0.01 g/cc density. (a) 3mm hohlraum heated with 150 joules at 3ω. (b) 3mm hohlraum heated with 95 joules at 3ω.

The lines shapes of the specific ionic species and the ratio between the absorption lines and are well reproduced by the simulations. No wavelength shift was introduced to obtain the agreement between theory and experiment. The transitions of the different ions are referred by their isoelectronic series (F, O, N, C). The evolution of the absorption with the laser energy appears clearly : in the first case (fig. 3a), the absorption features corresponding to ions from F-like to C-like indicate a higher temperature of the absorbing plasma than in the second case (fig. 3b) where the F-like absorption is dominant. The simulated spectrum gives the best agreement for the following combinations 50% $Te=21\ eV$ + 50%$Te=26\ eV$ in the first case and 50% $Te=16\ eV$ + 50% $Te=20\ eV$ for the second one obtained for a total density of 0.01 g/cc.

The MULTI results give a temperature between 20 and 28 eV for the first case and between 17 and 24 eV for the second one. The total density was found to be 0.002 g/cc for the two cases. Using this density instead of 0.01 g/cc, the fit of theoretical to experimental spectra would yield 30 % lower temperatures.

In table 1 is presented the results of the simulations in different experimental cases. In the case c where the aluminium foil is thinner the absorption was less saturated than in the first case. The

ionic species having the strongest oscillator strength are more absorbing in a thinner plasma. When the plasma is thicker the absorption on the transitions with strong oscillator strength are getting saturated while the other transition are absorbing more. The electronic temperatures deduced from the comparison with RELAC are on the same order in the two cases and the density is two times lower.

	cavity	energy	Al	delay	RELAC Te	RHO
a	3 mm	150J, 3ω	1100Å	900 ps	50% 21 eV + 50% 26 eV	0.01 g/cc
b	3 mm	95 J, 3ω	1100Å	900 ps	50% 16 eV + 50% 20 eV	0.01 g/cc
c	3 mm	150J, 3ω	550Å	900 ps	50% 22 eV + 50% 27 eV	0.005 g/cc
d	1.7 mm	150J, 3ω	1100Å	900 ps	60% 26 eV + 40% 32 eV	0.01 g/cc
e	3 mm	150J, 3ω	1100Å	600 ps	50% 24 eV + 50% 29 eV	0.01 g/cc
f	3 mm	440J, ω	1100Å	600 ps	60% 23 eV + 40% 33 eV	0.01 g/cc

TABLE 1 : Results of the simulations in different experimental cases.

The temperatures deduced for the case (d) (26 and 32 eV), show that for a smaller hohlraum we get a higher temperature in the aluminium plasma. This was confirmed by the MULTI simulations. The case (e) shows that with a shorter delay (600ps), the plasma was effectively probed at a higher plasma temperature. The comparison between the last case (f) and the precedent demonstrates that the heating of the cavity is more efficient at shorter wavelength as the same temperature is obtained for an energy 3 times smaller at 3ω than at ω.

4 - Conclusion

From quantitative absorption measurements we have determined the ionic state and the temperature of an LTE aluminium plasma. As the absorption is very sensitive to the temperature, the fit of the experiment to the simulated absorption spectrum using two temperatures in a very narrow range shows the accuracy of the results.

The temperature deduced from radiative hydrodynamic modelling with the 1D code MULTI is well estimated for each case. However it was obtained by fixing the density five times higher than the code value to obtain the temperature inferred from our measurement.

(1) E. Storm, Journal of Fusion Energie 7, 131 (1988).
(2) F. J. Rogers and C. A. Iglesias, Science 263, 50 (1994).
(3) G. Winhart et al, J. Quant. Spectrosc. Radiat. Transfer Vol. 54, 437 (1995) ; Phys. Rev. E 53, R1332 (1996).
(4) E. Luc-Koenig, Physica Scripta 62, 393 (1972); M. Klapish, J.L. Schwob, B.S.Fraenkel and J. Oreg, J. Opt. Soc. Am. 67, 148 (1977).
(5) R. Ramis, R. F.F. Schmalz, and J. Meyer-ter-Vehn, Comput. Phys. Commun. 49, 475 (1988).
6) A. Bar-Shalom, J. Oreg, J. F. Seely, U. Feldman, C. M. Brown, B. A. Hammel, R. W. Lee, C. A. Back, Phys. Rev. E 52, 6686 (1995)

INTERACTION OF ULTRA-HIGH-POWER LASER BEAMS WITH OVERDENSE PLASMAS

A.V. IVLEV, M.G. CADJAN, M.F. IVANOV,
High Energy Density Research Center, IVTAN, Moscow, Russia

Results of numerical simulation of ultra-high-power laser beams interaction with overdense plasma is presented. Calculations was carried out using 2- and 2.5D PIC relativistic code. A number of new results has obtained; the most interesting result is a plasma surface instability under influence of a strong plain EM wave. A nonlinear theory is developed that describes a nature of revealed effect.

At the present time an interest to the research of ultra-high-power laser beams interaction with plasmas is increasing. Really, at absorption of radiation having intensity $10^{18}W/cm^2$ and higher by condensed matter electrons of created plasma become highly relativistic. It causes the essential change of ion density profile, which already can not be considered as motionless. So, when irradiating plasma becomes relativistic a number of new and very interesting effects appear that strongly changes character of the radiation-plasma interaction compared with non-relativistic case.

Above all, on relativistic plasmas a spatial dispersion effect becomes significant not only in case of electron-plasma wave interaction but as well in case of electron-transverse electromagnetic (EM) wave interaction. It considerably increases a radiation absorption processes. Apart from that, in plasmas under action of ultra-high-power radiation the processes of a parametric decay instabilities develop rapidly because of increments of this processes are proportional to the root of EM radiation intensity.

We would like to present the results of numerical analysis of basic physical mechanisms providing the EM radiation penetration and absorption in overdense plasma. For modeling of the plasma kinetics the Particle-in-Cell (PIC) 2- and 2.5D relativistic code with taking into account ion mobility was used. The electron/ion mass ratio is: $m_e/m_i = 1/1836$. The simulations were carried out for the rectangular region that is congruent with xy plane. The dimensions of area: $L_x = 36c/\omega_0$, $L_y = 32c/\omega_0$, where ω_0 is radiation frequency. Initially plasma temperature had varied from 4KeV to 10 KeV and borrowed area $10c/\omega_0 \leq x \leq L_x$; initial plasma density $n = 4n_{cr}$, so unperturbed plasma frequency $\omega_p = 2\omega_0$. Cases of the normal (as to axis x) incidence of laser radiation having either $p-$ polarization (when the electric field vector $\mathbf{E}$ lies into xy plane) or $s-$ polarization ($\mathbf{E}$ vector is perpendicular to xy plane) was considered. The intensity of external radiation is $I \propto I_{max} \cdot \exp[-(y - 0.5L_x)^2/D^2] \cdot (1 - \exp[-t/\tau])^2$, where $D = 12c/\omega_0$

$(1/D = 0$ for the case of plane EM wave), $\tau = 50\omega_0^{-1}$. The intensity value $I_{max} = 10^{19} W/cm^2$, so the corresponding electric field is high enough to cause the electron quiver velocity to become highly relativistic ($|eE|/(m\omega_0 c) \simeq 3$).

We have obtained a number of new results that are absent in analogous works [1,2]. Some of this results are (a) excitation of high-frequency EM harmonics in the plasma boundary layer, (b) generation of long-living quasistatic electron vorticities and, the most interesting effect- (c) a plasma surface instability. Let's consider in detail the last effect. For $s-$ polarization on the late stage of the development of the plasma boundary dynamics the local density maximums arise on the plasma surface. Then the "cell" structure is forming on the plasma surface. The cell structure rise on the density gradient was found in [1], however this phenomenon is observed in absence of the density gradient too. It is caused by plasma boundary instability in powerful EM radiation. As it was shown in [3] this instability has another origin and mechanisms of development despite of the exterior similarity with Rayleigh-Taylor instability.

For complete investigation of nature of the found effect the calculations of the plain EM wave (intensity does not depend on transverse $y-$ coordinate) interaction with the overdense plasma surface were carried out. For $p-$ polarization external radiation pushes a plasma boundary uniformly and any periodical structure does not form. For $s-$ polarization formation of periodical structure near the plasma surface is clearly seen. Then it transforms into the nonlinear standing wave on the plasma surface. In the course of time plasma perturbations grow, keeping initial spatial period. So, the obvious picture of instability developing on the plasma surface in the $s-$ polarization case but lacking in the $p-$ polarization case has obtained (Fig. 1).

Described effect has the following nature. At compression of plasma by external radiation the layer with depressed density occurs near its surface, where dielectric permittivity $\varepsilon > 0$. In this layer of transparent plasma the development of a parametric decay instability of external EM wave caused by strong plasma modulation takes place. This instability is accompanied by exciting of the couple (ω_1, k_1) and (ω_2, k_2) of arbitrary waves. This waves are connected with initial EM wave (ω_0, k_0) by energy and momentum conservation equations: $\omega_0 = \omega_1 + \omega_2$, $k_0 = k_1 + k_2$ (k, ω are wave number and frequency of considered wave correspondently). High-frequency pressure of excited waves evokes a quasistatic plasma density perturbation. Transverse plasma perturbation causes a self-focusing effect of external EM radiation. Using Maxwell equations and well-known nonlinear relation between plasma dielectric permittivity $\varepsilon^{(0)}(E_a)$ and high-frequent electric field E_a one can obtain an equation analogous to the self-focusing equation [4]:

$$ik_0(\partial_x + \tfrac{1}{u}\partial_t)E_a + \tfrac{1}{2}\nabla_\perp^2 E_a + \eta(|E_a|^2 - |E_{a0}|^2)E_a = -\tfrac{\omega_0^2}{2c^2}E_a \sum_q a_q \cos(qy + \varphi_q)$$
(*)

$\nabla_{\perp}^2 = \partial_y^2 + \partial_z^2$, $k_0^2 = (\omega_0/c)^2 \varepsilon^{(0)}(\mathbf{E}_{a0})$, $\mathbf{E}_{a0} = const$ is unperturbed electric field, $u = (dk_0/d\omega_0)^{-1}$ is a group wave velocity, $\eta = (e^2/8m\omega_0^2 T)[1 - \varepsilon^{(0)}(\mathbf{E}_{a0})]\, k_0^2$. Right-hand term corresponds to periodical plasma perturbation caused by excited waves.

It worth to note that Eq.(*) is obtained by decomposition on the small parameter $\mathbf{E}_a - \mathbf{E}_{a0}$ (not the $\mathbf{E}_{a0}$, as usual). Therefore, to correct use of (*) there is no necessity to be a field $\mathbf{E}_{a0}$ small. Linearizing Eq.(*) it's easy to show that it allows the solution

$$\mathbf{E}_a = \mathbf{E}_{a0} + \sum_q \delta \mathbf{E}_q(y, t) \tag{1}$$

$\delta \mathbf{E}_q \sim \exp\{i(\gamma t + qy + \varphi_q)\} + \text{c.c.}$ and term $\delta \mathbf{E}_q$ does not depend on x. For $s-$ polarization ($\mathbf{E}_{a0}$ is perpendicular to $xy-$ plane) by substituting (1) in (*) we can obtain an expression for γ

$$\gamma(q) = \pm \frac{qc}{2k_0} \sqrt{q^2 - 4\eta |\mathbf{E}_{a0}|^2} \tag{2}$$

As $\eta > 0$ then γ value becomes complex in the case $q^2 < 4\eta |\mathbf{E}_{a0}|^2$. So $\delta \mathbf{E}_q$ increases exponentially in the course of time.

As it seen from (2), at $q = q_{max} = 2\eta |\mathbf{E}_{a0}|^2$ increment $|\gamma(q)|$ attains of maximum, which is equal to

$$|\gamma(q_{max})| = |\mathbf{E}_{a0}|^2 \eta \frac{c}{k_0} \tag{3}$$

So, for $s-$ polarization the perturbations having spatial period q_{max}^{-1} along $y-$ axis will increase more rapidly.

For $p-$ polarization vector $\mathbf{E}_{a0}$ is parallel to $y-$ axis and perturbations of electric field $\mathbf{E}_{a0}$ lie in $xy-$ plain. Therefore, term $\frac{1}{2}\nabla_{\perp}^2 \mathbf{E}_a$ in (*) will be absent. So, for $p-$ polarization, instead to $s-$ polarization case there is no selective amplification of the field perturbation having the certain spatial period q_{max}^{-1}.

Basing on the presented results, we can make the next conclusions. The interaction of ultra-high-power laser beams with plasmas causes a number of new physical effects that were neglected for less intensities. The plasma surface instability in the field of a plain EM wave is an obvious demonstration of such a statement. One-dimensional initially problem has lost 1D geometry during relatively short (about $100\, \omega_0^{-1}$ s) period. So, we can conclude that any problem which is similar to discussed above cannot be considered as 1D anyhow.

400
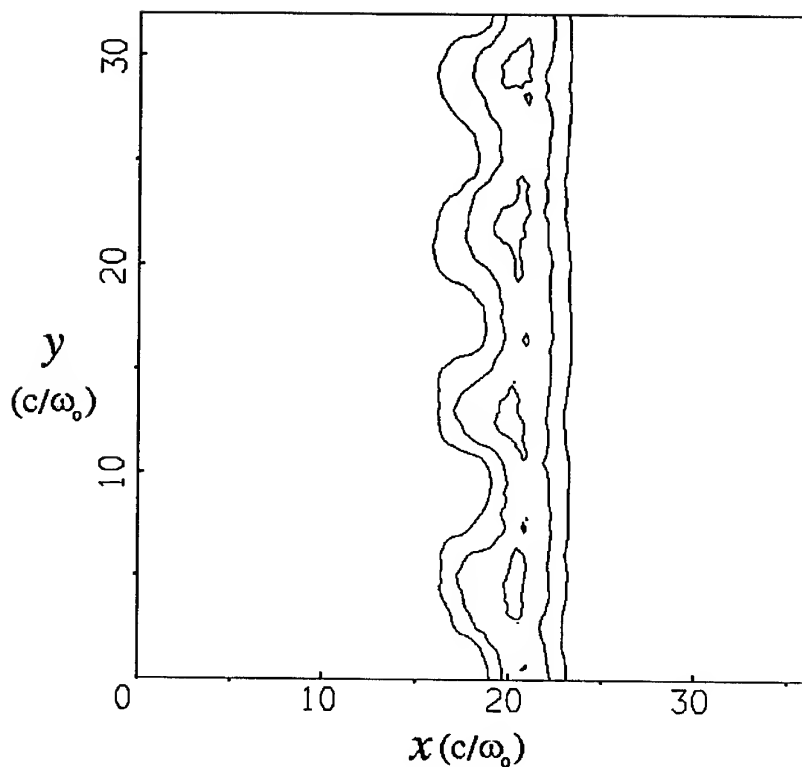
Figure 1. The contours of ion density at late (b: $\omega_0 t = 400$) stages of the evolution of instability. Parameters: s-polarization, plane EM wave, $I = 3 \cdot 10^{18}$ W/cm^2, sharp plasma boundary initially is located at $10\, c/\omega_0$.

References

[1] Wilks S.C., Kruer W.L., Tabak M. and Langdon A.B. *Phys.Rev.Lett.*, **96**, 1383, (1982)

[2] Batishev O.V., Karas' V.I., Levchenko V.D., Sigov Yu.S. *Fizika plazmi*, **20**, 654, (1994)

[3] Ivanov M.F., Ivlev A.V., Cadjan M.G. (Submitted to Physical Lett.)

[4] Landau L.D., Lifshits E.M. *Elektrodinamika sploshnyh sred*, Hauka, Moskva, (1993)

HIGH DENSITY EFFECTS ON TRANSPORT COEFFICIENTS IN CONDUCTION AND ABLATION ZONES IN LASER PLASMAS

H.DERFOUL
Physique Atomique dans les Plasmas Denses, LULI-Université ParisVI. Ecole Polytechnique, 91128 Palaiseau Cedex France
Université Paris VI, 4 place Jussieu 75252 Paris cedex 05 France

New analytic formulas for the electron thermal and electrical conductivities which take into account for the physical effects of electron degeneracy and plasma oscillations in unmagnetized dense plasmas are derived. For nondegenerate ideal plasmas, the resulting formulas obtained are in good agreement with Spitzer-Härm (SH) conductivities. However, for degenerate nonideal plasmas, the conductivities obtained are reduced compared to those predicted by (SH) formulas and their analytical forms show a great similarity with those of low temperature metals.

The Spitzer-Härm (SH) formulas [1] for the electrical and thermal conductivities of fully ionized gases are still widely used as a basis for comparison with experimental data. These formulas are based on a solution of the Boltzmann equation under the assumption of Maxwellian distribution function and binary collisions due to shielded Coulomb potential with a Debye length. However, their application to dense plasmas at solid density in nonideal regime, such those produced by focusing an intense laser beam on solid target [2], give erroneous results [3,4]. By nonideal plasma we define a plasma in the temperature-electron density regime (T,n) where the electron-ion coupling parameter Γ_{ei} (ratio of mean Coulomb interaction to thermal energies) is closer or greater than unity. In this regime the Debye length $\lambda_D \approx \Gamma_{ei}^{-1/2} n^{-1/3}$ becomes of the order of (or smaller than) the mean interparticle distance $\approx n^{-1/3}$ and, therefore, it loses its physical meaning as shielding length and upper impact parameter. Moreover, the binary collisions lose their additive character as electron density increases and the particles interact through the mean self-consistent field and generate, by their collective motion plasma waves. In this respect, collective effects are more important than single effects and the (SH) model remains incapable to describe correlated dense plasmas.

In order to extend the (SH) formulas to dense plasmas produced by laser, we solve the Boltzmann equation in the relaxation time approximation [5] and under the assumption of stationary state and equilibrium Fermi-Dirac (FD) distribution function. Thus we have :

$$v \frac{\partial f}{\partial z} - \frac{eE}{m} \frac{\partial f}{\partial v} = -\frac{f - f_0}{\tau} \tag{1}$$

and

$$f_0 = \frac{1}{1 + e^{\varepsilon - \mu/kT}}, \tag{2}$$

where f=f(z,v,t) is the electron distribution function involving in time t and space-velocity (z,v), v is the electron velocity, e is the electron charge, m is the electron mass, E is the electric field, τ is the electron relaxation time, f_0 is the equilibrium Fermi-Dirac (FD) distribution function, ε is the kinetic energy, μ is the chemical potential and k is the Boltzmann constant.

402

In the following, we consider a nonrelativistic dense plasma ($n \leq 10^{24} cm^{-3}$) without magnetic field formed by electrons neutralized by a background of ions. Due to the large ratio of ion mass to electron mass, the ions are assumed at rest and nondegenerate. For ideal plasma, the variation of the electron motion is caused by binary collisions with plasma particles (electron-ion scattering). However, for nonideal plasma, the collective effects are more important than the single effect : the electron motion is strongly affected by the longitudinal plasma waves (plasmons) which are thermally excited. Therefore, we consider that the wave-particle interaction gives an additive contribution to the collisional frequency. We choose to define the electron relaxation time the following formula :

$$\tau = \frac{\tau_c \tau_w}{\tau_c + \tau_w} \tag{3}$$

with

$$\tau_c = \frac{3m^{1/2}(kT)^{3/2}(1+e^{-\beta})F_{1/2}}{2\sqrt{2}\pi Z^* ne^4 \ln\Lambda} \quad \text{and} \quad \tau_w = \frac{5\pi\hbar^3}{2^4 m \, Z^* e^4} , \tag{4}$$

where $\beta = \mu/kT$, Z^* is the ionic charge, $F_{1/2}$ is the (FD) integral, $\ln\Lambda$ is the Coulomb logarithm and $\hbar$ is the Planck constant divided by 2π. Herein τ_c is the electron collision time due to binary collisions [4] and τ_w is the electron relaxation time due to the scattering of the electron by plasmons [6].

To calculate the transport coefficients in a plasma, we adopt the classical perturbation method where the electron distribution function is given by the first two terms of its expansion in Legendre polynomials :

$$f = f_0 + f_1 cos(\theta) \quad / \quad f_1 << f_0 , \tag{5}$$

where θ is the angle between v and direction of z (also the direction of E).
By substituting Eq.(5) in Eq.(1), we obtain to first order approximation the electron perturbation function f_1 :

$$f_1 = \tau v \frac{\partial f_0}{\partial \varepsilon} \left[\left(\frac{\varepsilon - \mu}{T} + \frac{\partial \mu}{\partial T} \right) \frac{\partial T}{\partial z} + eE \right]. \tag{6}$$

By assuming a spherical Fermi surface, the electronic heat flux, denoted q_e, and the current density, denoted j_e, are given by :

$$q_e = \frac{1}{3} \left(\frac{2}{m} \right)^{1/2} \int_0^\infty \varepsilon^{3/2} D(\varepsilon) f_1(\varepsilon) d\varepsilon, \tag{7}$$

$$j_e = -\frac{1}{3} e \left(\frac{2}{m} \right)^{1/2} \int_0^\infty \varepsilon^{1/2} D(\varepsilon) f_1(\varepsilon) d\varepsilon, \tag{8}$$

with $\quad D(\varepsilon) = \frac{3n\varepsilon^{1/2}}{2\varepsilon_F^{3/2}} , \tag{9}$

where ε_F is the Fermi energy.

The electron thermal conductivity is defined as the ratio of q_e to ∇T for the situation in which the charge neutrality is preserved i.e. $j_e = 0$. This last condition gives :

$$f_1 = \left(\frac{2}{m}\right)^{1/2} k\,\tau\varepsilon^{1/2} \frac{\partial f_0}{\partial \varepsilon}\left[\frac{\varepsilon}{kT} - \frac{5}{3}\alpha(T)\right]\frac{\partial T}{\partial z}, \qquad (10)$$

where $\quad \alpha(T) = \left(\int_0^\infty \varepsilon^{3/2} f_0(\varepsilon)d\varepsilon\right) \Big/ kT\left(\int_0^\infty \varepsilon^{1/2} f_0(\varepsilon)d\varepsilon\right). \qquad (11)$

Then it follows from Eq.(6-9) and Eq.(10) that the thermal conductivity becomes

$$K_e = \frac{nk(kT)}{m\Theta^{3/2}}\tau\left(I_{7/2} - \frac{5}{3}\alpha(T)I_{5/2}\right), \qquad (12)$$

with $\quad \Theta = \frac{\varepsilon_F}{kT}, \quad I_\sigma = \frac{\partial F_\sigma(\beta)}{\partial \beta}, \quad F_\sigma(\beta) = \int_0^\infty dx \frac{x^\sigma}{\left(1 + e^{x-\beta}\right)}, \quad x = \frac{\varepsilon}{kT}. \qquad (13)$

On the other hand, the electron electrical conductivity is defined as the ratio of j_e to E when $\nabla T = 0$ in Eq.(6). This yields :

$$\sigma_e = \frac{ne^2\tau}{m\Theta^{3/2}}I_{3/2}. \qquad (14)$$

The physical meaning and the validity of above results Eq.(12) and Eq.(14) will be discussed in the following by considering two opposite limits of plasmas.

Case of nondegenerate ideal plasma ($\Theta \ll 1$)

For ideal plasmas, characterized by high temperature and relatively low density, the chemical potential is negative :

$$\mu = kT\,ln\left(\frac{4}{3\sqrt{\pi}}\Theta^{3/2}\right). \qquad (15)$$

Therefore, the (FD) integral is given by [7] :

$$F_\sigma(\beta) \cong \Gamma(\sigma + 1)e^\beta, \qquad (16)$$

where $\Gamma(\sigma + 1)$ is the gamma function.

Under these considerations, Eq.(3) and Eq.(11) become respectively to

$$\tau \cong \tau_c = \frac{3}{4}\frac{m^{1/2}(kT)^{3/2}}{\sqrt{2\pi}Z^* ne^4\, ln\,\Lambda} \quad \text{and} \quad \alpha(T) = \frac{3}{2}. \qquad (17)$$

Thus Eq.(12) and Eq.(14) lead to the reduced following forms which are the well-known (SH) conductivities :

$$K_e = \frac{15}{8\sqrt{2\pi}}\frac{k(kT)^{5/2}}{m^{1/2}Z^* e^4\, ln\,\Lambda} \quad \text{and} \quad \sigma_e = \frac{3}{4\sqrt{2\pi}}\frac{(kT)^{3/2}}{m^{1/2}Z^* e^2\, ln\,\Lambda}. \qquad (18)$$

404

Case of degenerate nonideal plasma ($\Theta \gg 1$)

For degenerate nonideal plasmas the chemical potential μ is given by the Fermi energy. Then the (FD) integral is given by :

$$F_\sigma(\beta) \cong \frac{\beta^{\sigma+1}}{\sigma+1}\left\{1+\sigma(\sigma+1)\frac{\pi^2}{6}\frac{1}{\beta^2}\right\}. \tag{19}$$

Hence Eq.(3) and Eq.(11) become :

$$\tau \cong \tau_w = \frac{5}{2^4}\frac{\pi\hbar^3}{mZ^*e^4} \quad \text{and} \quad \alpha(T) = \frac{3}{5}\beta\left(1-\frac{\pi^2}{2}\frac{1}{\beta^2}\right) \tag{20}$$

Under these considerations, Eq.(12) and Eq.(14) lead to

$$K_e = \frac{\pi^2}{3}\frac{nk^2T}{m}\tau_w \quad \text{and} \quad \sigma_e = \frac{ne^2}{m}\tau_w. \tag{21}$$

According to Eqs.(21), the thermal conductivity K_e is both linear function of electron density and temperature whereas the electrical conductivity σ_e is a linear function of density only. These conductivities are reduced compared to those predicted by (SH) formulas (which exhibit divergence behaviour for small λ_D) and their resulting analytical forms show a great similarity with those of low temperature metals. Therefore, we conclude that the plasma undergoes a phase transition into lattice phase at high density and low temperature.

In summary, the solving of the modified Boltzmann equation permit us to derive more complete (SH) formulas that can be applied both to ideal and nonideal plasmas. This analytic approach may be achieved if the theory of wave-particle interaction in nonideal plasmas is developed and the physical effects of spatial inhomogeneities in a plasma are taken into account.

References

[1] Cohen R., Spitzer L. and Routely P., 1950 Phys. Rev. **80**, 230; Spitzer L. and Härm R., 1953 Phys. Rev. **89**, 977

[2] Angelo P., Gauthier P., Brisard M., Poquérusse A., Leboucher-Dalimier E. and Shepard T., 1995 LULI Report

[3] Larsen J.T. and Lane S.M., 1994 JQSRT **15**, 179

[4] More R.M., 1991 Physics of Laser Plasma (Rubenchik A. and Witkowski S., North-Holland)

[5] Krall N.A. and Trivelpiece A.W., 1973 Principle of Plasma Physics (McGraw Hill, New york)

[6] Haug A., 1972 Theoretical Solid State Physics (Pergamon Press, Hungary); Khalfaoui A., 1984 IEEE Trans.Plasma Sci. **12**, 179

[7] Ichimaru S., 1993 Reviews of Modern Physics **65**, 255

TRANSPORT COEFICIENTS AND DIELECTRIC PERMITTIVITY OF STRONGLY COUPLED NONEQUILIBRIUM PLASMAS

M.M. BASKO

Max-Planck-Institut für Quantenoptik, D-85748 Garching, Germany

A practical model is proposed for evaluating the thermal and electrical (both direct current and frequency-dependent) conductivities of matter under the conditions ranging from those in metals at room temperature to hot thermonuclear plasmas. The model can be applied to simulate the optical properties of solids compressed in strong shocks and/or irradiated by ultrashort laser pulses.

Theoretical interpretation of many experiments, where the surface of a solid is either irradiated by an ultrashort laser pulse or heated by an emerging multi-megabar shock front, requires a practical method for evaluating the transport coefficients and frequency-dependent dielectric permittivity of strongly coupled non-equilibrium ($T_e \neq T_i$) plasmas. Here we propose a model which, similar to that of Lee and More[1], uses the approximation of the Lorentz plasma and incorporates the effects of strong ion-ion coupling. The model is based on the assumption that one can distinguish between the free and bound electrons, and it is free electrons which determine the heat and charge transport and the dielectric properties.

1   General formulae

For the Lorentz plasma, the linearized Boltzmann equation for the distribution function of free electrons can be solved in the approximation of velocity dependent collision frequency[2]. If the Fermi-Dirac function $f_0(\mathbf{p})$ (normalized to the electron number density n_e) is used as the equilibrium distribution, then the effects of Fermi degeneracy are properly accounted for (here $\mathbf{p} = m\mathbf{v}$ and $\epsilon = \frac{1}{2}mv^2$ are, respectively, the momentum and the energy of a free electron). The dielectric permittivity at a frequency ω is given by the integral[2]

$$\varepsilon(\omega) = 1 + 4\pi e^2 \int \frac{v^2}{3} \frac{(1 - i\,\nu_{ei}/\omega)}{\omega^2 + \nu_{ei}^2} \frac{\partial f_0}{\partial \epsilon}\, d^3\mathbf{p}. \tag{1}$$

Electrical (dc) and heat conductivities due to the electron-ion (e-i) collisions are given by similar expressions[2], which can be found also in Ref.[1].

As was shown explicitly by Brysk[3], the rate of energy exchange between the ions and the Fermi-Dirac electrons in weakly coupled plasmas is determined

by the mean [averaged with $v^2(\partial f_0/\partial \epsilon)$] e-i collison frequency $\langle \nu_{ei} \rangle$,

$$\rho \frac{d\epsilon_i}{dt} = -\rho \frac{d\epsilon_e}{dt} = 3 \frac{m}{m_i} n_e \langle \nu_{ei} \rangle (T_e - T_i). \tag{2}$$

(ϵ_i and ϵ_e are, respectively, the specific internal energies of ions and electrons, m_i is the ion mass). We assume that Eq. (2) is valid in a more general case, including the limit of strong ion-ion coupling.

2 Collision frequency and the effect of ion-ion correlations

The velocity-dependent rate of Coulomb e-i collisins in the Debye limit of weakly coupled plasmas is given by[2]

$$\nu_{ei} = n_i v \sigma_{tr,ei} = \frac{4\pi n_i z_i^2 e^4}{m^2 v^3} \ln \Lambda_{ei}, \tag{3}$$

where

$$\Lambda_{ei} = \ln \frac{2mv}{\hbar/D_{ei}}, \quad D_{ei}^{-2} = D_e^{-2} + \frac{4\pi n_i z_i^2 e^2}{T_i}, \quad D_e^{-2} = \frac{4\pi n_e e^2}{[T_e^2 + (\frac{2}{3}\epsilon_F)^2]^{1/2}}, \tag{4}$$

and $\epsilon_F = \frac{1}{2}mv_F^2$ is the Fermi energy. To describe the limit of strongly coupled plasmas, we note that the Coulomb divergence in the transport cross-section for the e-i scattering does not occur when the ion-ion correlations are taken into account. This indicates that the limit of strong ion-ion coupling could be included by modifying appropriately the Coulomb logarithm in Eq. (3).

Above the Debye temperature, the transport cross-section for the e-i scattering in a crystal lattice can be evaluated as the Born cross-section[4]

$$\sigma_{tr,ei} \propto \frac{z_i^2 e^4 \xi^2}{\hbar^2 v^2} \tag{5}$$

for scattering on a dipole potential $U(r) = z_i e \xi / r^2$, where $\xi^2 \propto T_i/(n_i z_i^2 e^2)$ is the mean square displacement of a lattice ion from its equilibrium position under the assumption that the free electrons form a uniform background of compensating negative charge. From Eqs. (5) and (3) we see that one can describe the limit of strong coupling by assuming $\ln \Lambda_{ei} \propto \Lambda_{ei}^2$ when $\Lambda_{ei} < 1$ and $T_i \lesssim [T_e^2 + (\frac{2}{3}\epsilon_F)^2]^{1/2}$. The numerical factor here is determined by the details of the phonon spectrum of a given crystal, which is beyond the scope of our consideration. We match two opposite asymptotical forms of the Coulomb logarithm by adopting a simple interpolation formula

$$\nu_{ei} = \frac{4\pi n_i z_i^2 e^4}{m^2 v^3} \ln \left(1 + \frac{\Lambda_{ei}}{1 + g_{ei}/\Lambda_{ei}} \right). \tag{6}$$
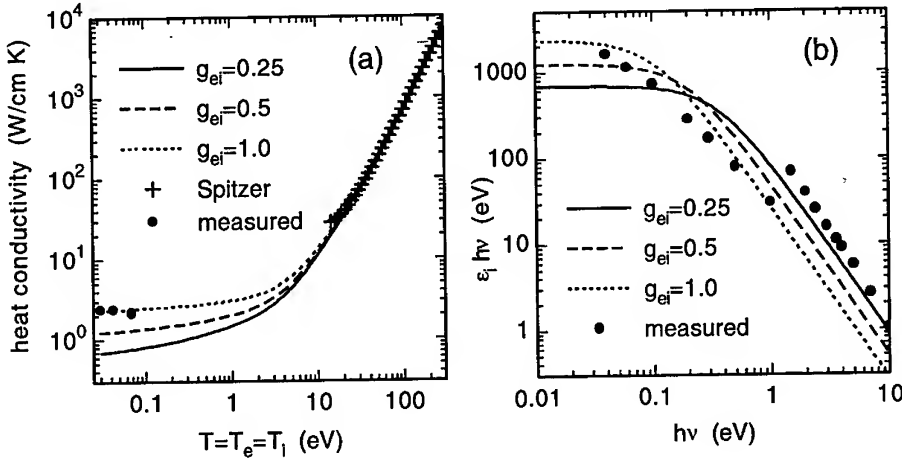
Figure 1: (a) Temperature dependence of the heat conductivity of Al at normal density. (b) Imaginary part of the dielectric permittivity of Al at normal conditions as a function of the photon energy $h\nu = \hbar\omega$. The 'ionization degree' is fixed at $z_i = 3$.

Equation (6), combined with the Eq. (4), constitutes the main new element of the present model. It provides a smooth transition from the limit of a weakly coupled plasma ($\Lambda_{ei} \gg 1$) to the limit of metals at room temperature ($\Lambda_{ei} < 1, T_i > T_{Debye}$) and has one free parameter g_{ei}. The value of g_{ei} does not affect the limit of weak coupling but can be chosen to fit the experimental conductivity and optical properties of a particular solid at room temperature, when $T_i = T_e \ll \epsilon_F$ and the e-i mean free path $l_{ei} = v_F/\nu_{ei} = g_{ei}(\hbar^2 v_F^2/4e^2)T_i^{-1}$. As an example, consider aluminum. Its measured values of the heat and electrical conductivities are quite accurately reproduced by $g_{ei} = 1.1$ (with $z_i = 3$ and $n_e = n_i z_i$; see Fig. 1a). On the other hand, the experimental values of $\varepsilon(\omega)$ for the visual light are in good agreement with $g_{ei} = 0.27$ and $z_i = 3$ (see Fig. 1b). In practice, an intermediate value of $g_{ei} \simeq 0.5$ can be assumed.

3 Contribution of the e-e collisions to the heat conductivity

The e-e collisions make a dominant contribution to the heat conductivity of non-degenerate low-Z weakly coupled plasmas and still play a significant role in moderately degenerate plasmas[5]. We take them into account by using the Matthiessen rule

$$\kappa_e = (\kappa_{ei}^{-1} + \kappa_{ee}^{-1})^{-1} \qquad (7)$$
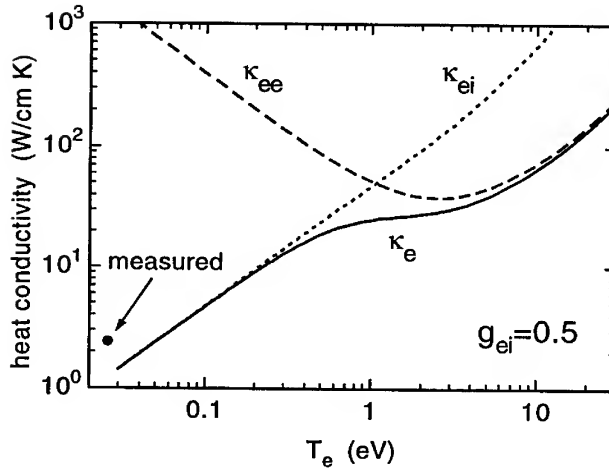
Figure 2: Contribution of the e-e collisions to the heat conductivity of Al as a function of the electron temperature T_e for constant values of $T_i = 300\text{K}$ and $z_i = 3$.

and adopting the following interpolation to the calculations by Lampe[5]:

$$\kappa_{ee}^{-1} = \frac{72}{5\pi^3}\frac{e^4}{T_e^2 v_F}\left[1+\left(\frac{T_e}{6\epsilon_F}\right)^2\right]^{-1/4}\frac{2}{3}\ln\left(1+\frac{\Lambda_{ee}^{3/2}}{1+0.12\Lambda_{ee}^{3/2}}\right), \quad (8)$$

$$\Lambda_{ee} = \frac{D_e}{\hbar}\frac{\sqrt{2mT_e}}{[1+(9\pi\epsilon_F/64T_e)^2]^{1/4}}. \quad (9)$$

Note that Λ_{ee} can be less than 1. Figure 2 illustrates the role of the e-e collisions in the heat conductivity of Al under strongly non-equilibrium conditions, when ions remain cold and electrons are heated to temperatures of $T_e \simeq 1\text{--}10$ eV.

References

1. Y.T. Lee and R.M. More, Phys. Fluids **27**, 1273 (1984).
2. E.M. Lifshitz and L.P. Pitaevskii, *Physical Kinetics* (Pergamon Press, Oxford, 1981).
3. H. Brysk, Plasma Physics **16**, 927 (1974).
4. D.G. Yakovlev and V.A. Urpin, Sov. Astron. **24**, 303 (1980).
5. M. Lampe, Phys. Rev. **170**, 306 (1968).

DETERMINATION OF THE COLOUR TEMPERATURE IN HIGH QUALITY SHOCKS

D.BATANI [1], S.BOSSI, [1] T.A.HALL [2], M.MAHDIEH [2], M.KOENIG [3], J.KRISHNAN [3], A.BENUZZI [3], TH.LÖWER [4]

[1] *University of Milan, Dept. of Physics, via Celoria 16, 20133 Milan, Italy*
[2] *University of Essex, Dept. of Physics, Wivenhoe Park, S04 3SQ Colchester, UK*
[3] *Laboratoire LULI, Ecole Polytechnique, 91128 Palaiseau, France*
[4] *Max Plank Institut fur Quantenoptik, Garching, Munich, Germany*

Measurements of the colour temperature in Aluminium laser shocked targets are presented. The colour temperature is calculated from e.m. emission in two different spectral channels by assuming a black body spectrum. We also measured the shock velocity in order to compare the real temperature obtained from the SESAME EOS with such colour temperature.

Introduction

The knowledge of the Equations of State (EOS) of strongly compressed materials is very important in Astrophysics[1] and in the framework of Inertial Confinement Fusion (ICF)[2]. The only way to compress materials to pressures in the multimegabar domain is by dynamic shocks whose propagation is regulated by the Hugoniot-Rankine relations[3].

Here we present some preliminary results on a method to measure the "colour temperature" in laser produced shocks. Simultaneously, we measured the shock velocity D_s, which can be used to deduce the real shock temperature if the EOS of the material is known. For this reason we used Aluminium targets which have a well known EOS in the investigated range of pressures (≤ 10 Mbars).

In the experiment the shock wave is generated by focusing an intense laser beam on a single-step Al target (the use of such targets allows a direct determination of the shock velocity shot by shot[4]). When the shock arrives on the target rear face, it produces an increase of the e.m. emission. This is recorded in two spectral regions by splitting the image of the target rear face onto the slit of a visible streak camera and filtering them with different coloured filters. Two time-space resolved images of the shock breakthrough in two channels of emission ("red" and "blue)" are then obtained. If a blackbody emission is assumed, the ratio between these spectral intensities gives an equivalent temperature T* (called "colour temperature"). This would be the true temperature of the radiating body if it emits as a blackbody, while, in a general case, T* is only an approximation of the real temperature.

In the experiment, direct drive approach with Phased Zone Plates has been used. With this optical smoothing technique it is possible to obtain a flat top intensity profile in the focal spot[4]. Planar shock fronts are then produced allowing precise measurements of shock parameters.

Experimental set-up

The target was irradiated with a $\lambda=0.53$ μm laser pulse gaussian in time with a FWHM ≈ 600 ps and focused by an $f/6$ lens ($f=50$ cm). A Phased Zone Plate (PZP) was placed just after the lens to produce a flat top profile with a FWHM ≈ 350 μm and a flat region of ≈ 200 μm. Spatially averaged intensities up to $3 \ 10^{13}$ W/cm^2 were then obtained on the target surface. An optical system made of an objective (Olympus 50 mm, 1/1.2) a field lens and a final lens was used to image the target

410

rear face onto the slit of a visible streak camera. A biprism allowed the image to be splitted into two and each was filtered by using two different coloured filters.

Results

Fig.1 shows the result obtained with a stepped target made of a 9 μm base and a 4 μm step of Aluminium. A shock velocity $D_S \approx 20$ μm/ns (Km/s) has been measured which corresponds to a pressure $P_S \approx 6$ Mbar according to SESAME EOS[5].

205 ps

blue image   red image
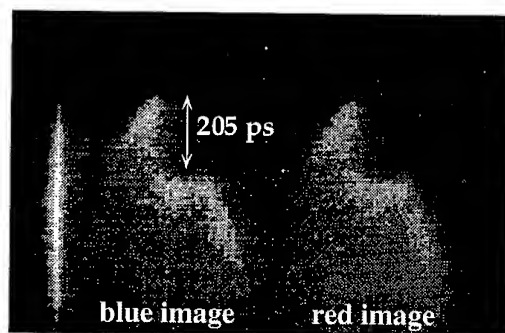
Fig.1: Streak camera image of a stepped target made of a 9 μm base + 4 μm step of Aluminium. As shown, the shock takes 205 ps to travel in the step. On the left side of the image the fiducial signal is recorded.

Concerning the determination of T*, fig.2 shows the emissivities in the two spectral regions as a function of time. Both channels show a very sharp peak of emission followed by a slow decay due to plasma expansion after shock breakout. It has been shown that such emissivity profiles indicate negligible preheating effects due to hard X-rays which in our case could be produced in the plasma corona[6].
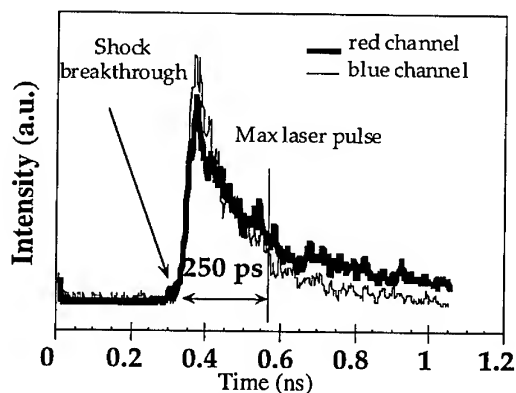
Fig.2: Intensity profile as a function of time in the two channel of emission. As in the case of unpreheated targets, this profile shows a pronounced peak with a fast decay.

Once the intensity in both channels is recorded, the value of the ratio I_{red}/I_{blue} can be calculated and, keeping into account the sensitivities of the filters and of the streak camera, it corresponds to a given value of the colour temperature (see fig.3).
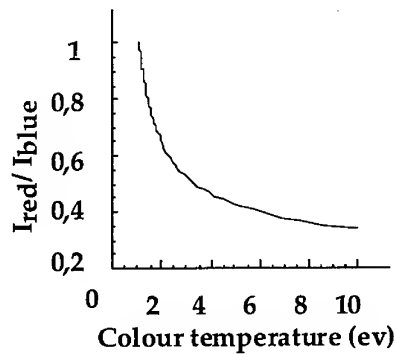
Fig.3: Plot of the colour temperature T*, as a function of the ratio between the intensities I_{red}/I_{blue} in the two spectral channels.

The colour temperature T*, corresponding to the data in fig. 1 and fig. 2, is plotted in fig.4. As expected, there is a temporal correspondence between the maximal temperature and the maximal emission in both channels. A value T* ≈ 2.5 eV has been measured at shock arrival while, according to SESAME tables, with the measured shock velocity, the expected shock temperature is $T_S = 3.5$ eV.
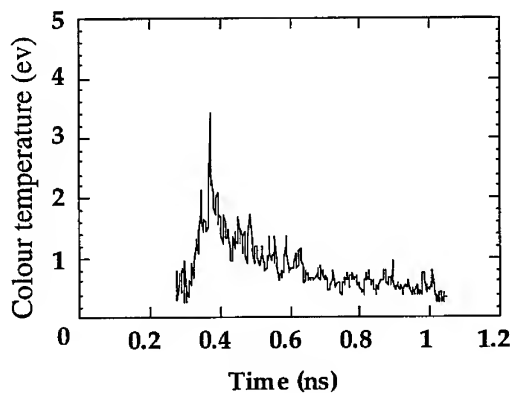
Fig.4: Colour temperature as a function of time for the intensity profiles of fig.2. The maximal temperature corresponds in time with the maximal emission.

There are two possible causes for such discrepancy. First, due to fast plasma expansion, our temporal resolution (± 5 ps has been achieved) could be not enough to resolve the shock breakthrough. Indeed some preliminary works[7] have shown that the first flash of light from the target rear side lasts only for a few ps. Hence

412

our data should be coupled to a model of expansion in order to extrapolate the value of T* at shock breakthrough from its values at later times.

Second, T* and T_S, at shock arrival, may be very different due to the effect of plasma opacities which causes both absorption of light in the plasma and emission different from a blackbody. In this case the knowledge of plasma opacities in the visible region is needed.

Conclusions

With the use of an optically smoothed laser beam we have been able to produce high quality shock waves with measured velocities of the order of $D_S \approx 20$ μm/ns i.e. a shock temperature $T_S = 3.5$ eV according to SESAME tables. On the other hand, through the "two images" optical diagnostics, we have measured a colour temperature $T* \approx 2.5$ eV. Investigation are going on about the interpretation of such differences by taking into account plasma opacities and plasma expansion.

Acknowledgements

References:

[1] Ross M. & Nellis W.J. 1982 in *Shock waves in condensed matter -1981* Nellis W.J., Seaman I., Graham R.A. Eds. (American Institute of Physics, New York).

[2] Nuckolls S J., Wood L., Thiessen A , Zimmerman G. 1972 *Nature*, **239**, 139.

[3] Zeldovich Ya. B. & Raizer Yu. P. 1966 *Physics of Shock Waves and High Temperature Hydrodynamic Phenomena* (Academic Press, New York and London).

[4] Koenig M., Faral B., Boudenne J.M., Batani D., Bossi S., Benuzzi A. 1994 *Phys. Rev. E* **50**, R3314.

[5] Holian, K.S. 1984 (editor) *T-4 Handbook of Material Properties Data Bases: Vol. 1c, Equations of State*, Los Alamos National Laboratory, Report LANL No. LA-10160-MS, UC-34 (unpublished).

[6] Löwer Th., Sigel R., Eidmann K., Foldes I.B., Huller S. et al. 1994 *Phys.Rev.Lett.* **72**, 3186.

[7] Huller S., J. Meyer Ter Vehn, Th. Löwer and R. Sigel, GSI-94 *Annual Report*.

TWO-CENTER FORMATION AND EMISSION
IN HOT DENSE PLASMAS

P. GAUTHIER, P. SAUVAN, P. ANGELO S. ALEXIOU, E. LEBOUCHER-DALIMIER
Physique Atomique dans les Plasmas Denses, LULI
Ecole Polytechnique, 91128 Palaiseau cedex, France
Université Paris VI, 4 place Jussieu 75252 Paris cedex 05, France

A. CALISTI, B. TALIN
PIIM, Université de Provence , Marseille, France

We show that transient ionic molecule can be found in hot and dense moderately coupled plasma ($\Gamma \sim 1$-2). For such plasmas a molecular emission code is proposed for hydrogenic lines and not to low Z emitter. This code gives coherent results with experimental F Lyβ spectra.

Introduction

Theoretical studies in dense plasmas ($Ne > 10^{23} cm^{-3}$) take into account possible configurations where several ions approach each other to the extent that the usual spherical symmetry around each ion is distorted or destroyed. For cold (Te $\sim$ 10eV) dense highly correlated plasmas the importance of treating quantum mechanically the free electron component in Molecular Dynamics simulations has been probed [1 to 4]. In the intermediate regime $\Gamma \sim 1$ to 2, i.e. for hot (Te > 200eV) dense plasmas, the electron component acts through a screening of the ionic interactions in the standard classical Molecular Dynamics simulations. In this last regime it can be shown that a dicenter formation may occur. Different approaches can describe a dicenter emission : the cylindrical model [5] and the quasimolecular model [6]. It is the last one we have chosen to follow. This choice has been guided by our experimental results obtained under $\Gamma \sim 2$ conditions : fluorine Lyman β red wing exhibits satellite-like features that cannot be identified to helium-like dielectronic satellites [7].
In this paper we first show that our plasma conditions are propitious to a dicenter formation and then we develop an atomic physics model within a quasimolecular approach which gives spectral characteristics leading to a relevant interpretation of our experimetal results.

1. Experimental results

Emissive dense fluorine plasmas have been created by colliding thin CF_2 foil experiments with two laser beams. The foil thickness (5μm) and initial distance (100μm) have been optimized thanks to 2D hydrodynamics simulations for a good drive of the emissive compression. The two LULI laser beams were operating at $\lambda_L = 0.263\mu$m with a pulse duration τ=500ps. The laser intensities on the focal spots ($\varnothing$100μm) were $\sim 2.10^{14}$W.cm^{-2}. The space and spectral resolved X-ray emission

414

around F^{8+} Lyβ and Lyγ spectral domain were recorded thanks to PABURCE spectrograph with improved characteristics (spectral resolution = 2000, entrance slit=10μm, tranverse magnification ratio =120). Recently, the KAP crystal - plasma distance has been optimized in order to increase the intensity on the film (Johann operating system). In figure1 we give such a spectrum with the space resolution along the collision axis (i.e. the laser beam direction). The microdensitometry of the emission from the compressed central plasma is also reported : the lines are wide and very emissive and a prominent satellite in Lyβ red wing is exhibited at 12.72Å. From LASNEX simulations we estimate the electronic density of the

11.99   12.30   12.72
                12.64

λ(Angströms)

fig.1 F Lyβ and Lyγ emitted from the compressed zone. A prominent molecular satellite is exhibited at 12.72Å

order of 2.10^{23}cm^{-3} and the electronic temperature in the range of 300-800eV. As we will see the accident can be attributed to the formation of the emissive transient F^{8+}- F^{9+} molecule.

2 Formation of ionic transient molecule
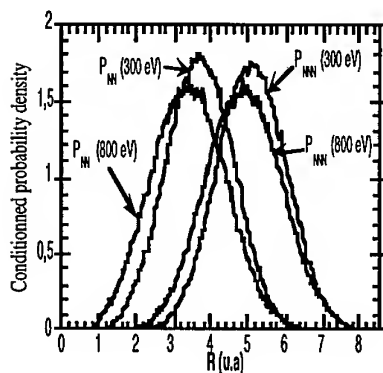
fig.2 Molecular Dynamics simulations for NN and NNN probability densities

Thanks to standard classical Molecular Dynamics (MD) simulations with an electronic screening distance equal to the mean interionic distance R_i, we could assert the validity of the quasimolecular approach for configurations involving small interionic distances. For our conditions (Ne=2.10^{23}cm^{-3}, Te=300 - 800eV) we found 30% configurations for which two ions could be considered as mutual Nerarest Neighbours (NN), the Next Nearest Neighbour (NNN) being excluded from a large forbidden volume surrounding the two NN. The conditional (NN) and (NNN) probability densities, P_{NN}(R) and P_{NNN}(R) respectively,

are given (versus the distance R to a central ion) in figure 2. As we can see, the most probable (NN) interionic distance is close to Ri (~4 a.u. for our conditions).

Moreover P_{NN} and P_{NNN} reveal well separated maxima. These arguments are favorable for a dicenter emission neglecting the interaction with the NNN.

3. Molecular emission code results and comparison with experimental spectra

The emission of one electron diatomic ionic molecule embedded in the plasma has been calculated selfconsistently. By using Born-Oppenheimer assumption, every property of interest depends on the interionic distance. To take account of the ionization potential decreasing process in dense plasmas, a molecular confining volume $\mathcal{V}$ is defined. This volume, limited by the ionic equipotential satisfying the integrated electrical neutrality condition, depends on the mean electronic density Ne and the interionic distance R. A self-consistent field method is proposed to solve the coupled Schrödinger and Poisson equations relative to the bound electron and the free electrons respectively. This method is an improvement of the molecular approach with a uniform electronic density inside the confining volume [6], this last assumption being only valid for high temperatures. The self-consistentcy of the problem is computed by an iterative procedure leading to local properties in the confining volume (the electronic density and the total potential) and to the radiative properties of the dicenter system (the adiabatic electronic energies and the dipolar matrix elements).For the Schrödinger equation, an expansion on the isolated diatomic molecule adiabatic energies and wave functions is justified for Z not too low. The Poisson equation is solved by using a non uniform elliptical mesh and the Dirichlet limit condition on the confining surface (total potential due to nucleus, bound and free electrons equal to zero). Moreover Boltzmann statistics is used for the free electron treatment. We give here the results for F^{8+}- F^{9+} molecule. Concerning the local density we found progressively a uniform plasma or a spherical symmetry around each nucleus when Te or Ne increases, respectively. We get the same spherical symmetry for the equipotentials when Ne or R increases.

In the last part we present F^{8+}- F^{9+} radiative properties in the spectral range of Lyβ line.
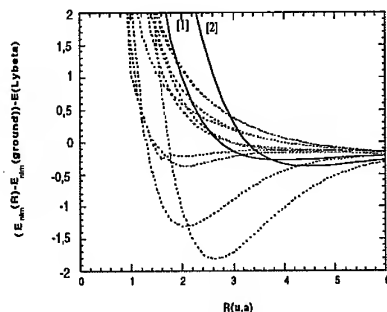
fig.3 Transition energies in F Lyβ spectral range
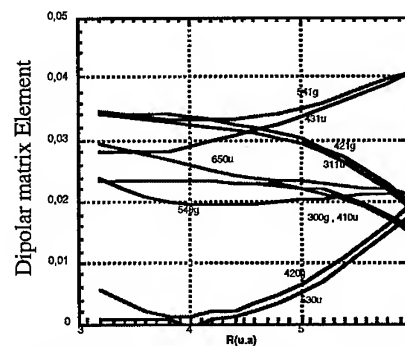
fig.4 Dipolar matrix elements for the molecular transitions in F Lyβ spectral range

416

T_e (eV)/ N_e(cm-3)	9.10^{22}	1.10^{23}	2.10^{23}
300	[1] 12.722 Å [2] 12.772 Å	[1] 12.723 Å [2] 12.771 Å	[1] 12.732 Å [2] 12.770 Å
600	[1] 12.722 Å [2] 12.772 Å	[1] 12.720 Å [2] 12.772 Å	[1] 12.729 Å [2] 12.764 Å

In figure 3 we see that six transition energies exhibit extrema. These extrema involve interionic distances near by the NN probability density maximum only for transitions [1] and [2]. Moreover we remark that the associated dipolar matrix elements (noted 541g and 650u, the upper level spherical numbers, in figure 4 are not negligible whatever R is. All these arguments are favourable for a molecular satellite exhibition. In the table below, we show that the positions of molecular satellite features [1] and [2] do not evolve significantly with Ne and Te.

Thus these features could be exhibited even if the experimental diagnostics involve space and time integrations. In fact molecular satellite [1] at 12,72Å (see fig. 1) is the only one to be exhibited, satellite [2] not being spectrally resolved from helium-like dielectronic satellites uccuring at 12,765Å.

References

[1] S.M.Younger et al, Phys. Rev. Lett. **61**, 962 (1988).

[2] J.D.Dress et al, JQSTR **54**, 237 (1995).

[3] I.Kwon et al, Phys. Rev. E **49**, R4771(1994).

[4] L.Collins et al, Phys.Rev. **52**, 6202 (1995).

[5] D.Salzmann, J.Stein, I.B.Goldberg, R.H.Pratt, Phys.Rev.A **44** (2), 1270 (1991) ; J.Stein, I.B.Goldberg, D.Shalitin and D.Salzmann, Phys.Rev.A **37** (12), 4854 (1988)

[6] P.Malnoult, B.d'État, H.Nguyen, Phys.Rev.A **40**, 1983 (1989)

[7] E.Leboucher-Dalimier, A.Poquerusse, P.Angelo, Phys.Rev.E, **47** (3), R1467 (1993).

E.Lebóucher-Dalimier, P.Angelo, P.Gauthier, A.Poquérusse, AIP, Conference Proceedings 328, Spectral Line Shape **8**, 12th ICSLS, Toronto Canada 1994, ed. by A.D. May, J.R. Drummond, E. Oks.

A STUDY OF DEBRIS CLOUDS FROM LASER INDUCED

SHOCK WAVES

Z. HENIS, B. ARAD, S. ELIEZER, Y. HOROWITZ, A. LUDMISRKY,

S. MAMAN, E. MOSHE, M. WERDIGER

Plasma Physics, Soreq NRC,

Yavne 81800, Israel

Abstract

There is a considerable interest in characterizing debris clouds gener-
ated by shock waves reaching the rear surface of metal targets. When a
shock wave is reflected from the free surface the occurence of a solid to liq-
uid transition will induce a dynamic behaviour such as ejection of debris
and development of instabilities. A study of the debris clouds generated
by laser induced shock waves is presented. Shock waves of order of hun-
dreds of kilobars to more than one megabar are produced in aluminium,
copper and tin targets by a Nd: YAG laser system operting at $1.06 \mu m$, 7
ns, focused to a spot of $200 \mu m$. The diagnostic method includes soft x-
ray shadowgraphy, optical scattering and optical backlighting. The radius
distribution of the ejected particles was in the range $(0.5 - 7).\mu m$ and fits
well to a power scaling law $N(r) \sim r^{-b}$. In the experiments reported here
the Sn samples melt during the sock wave, while the Al and Cu samples
melt during the release following the shock wave.

Introduction.

The reflection of strong shock waves from surfaces can cause either ejection
of material[1-3] from the surface or to the development of hydrodynamic instabil-
ities, such as Rayleigh-Taylor[4,5] instability at material interfaces. The ejected
material moves ahead of the expanding free surface and it might origin from
spall, precipitates or inclusions near the free surface, surface roughness, spa-
tial nonuniformities of the shock profile or hydrodynamic instabilities following
melting of the rear surface.

In this paper a study debris clouds generated by laser induced shock waves
is presented. Laser induced shock waves as a means for studying material prop-
erties at high pressure and temperature was widely used in the last decade[6-9].
The advantage of laser induced shock waves is the short and tunable laser pulse
duration and the simple scaling of the pressure with the intensity.

This time scale τ_f of the surface fragmentation into debris due to spall can be
estimated by L/c, where L is the target thickness and c is the sound velocity. In

418

the experiments here $L \sim 50\mu m$ and $c \sim 5*10^5 cm/s$ and therefore τ_f is the order of 10 ns. The time of growth of the Rayleigh-Taylor instability calculated from the classical theory is $\tau_{RT} \sim (2x/g)^{0.5}$. x is the initial disturbance, of the order of microns and g is the acceleration given by $g \sim u_s/t_L$, where $t_L \sim 2ns$ is the risetime of the laser. Therefore $\tau_{RT} \sim 1ns$. In this paper the surface fragments are measured at asymtotic times of the order of tens ns up to $2\mu s$, i.e. larger than the time scales of these hydrodynamical instabilities. Debris clouds from aluminium, copper and tin targets loaded at pressures of the order of hundreds of kilobars to more than one megabar were analyzed. The diagnostic methods were soft x-ray shadowgraphy to measure the velocity of the debris clouds, optical backlighting to measure the shock velocity and the pressure and optical scattering to detect melting during the shock wave or release and measure the size the debris particles.

Experiments.

The main laser system generating the shock waves is based on a Continuum NY-60 Nd:YAG oscillator followed by glass amplifiers yielding 70 J, 7 ns FWHM pulse focused to a $200\mu m$ spot. The diagnostic channel includes a Continuum NY-81 Nd:YAG oscillator followed by a triple pass glass amplifier. The amplified pulse is converted to green yielding up to 4 J per 5 ns pulse. Further backlighting measurements are done with a cw laser.
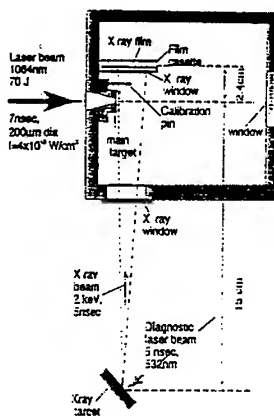
Fig. 1 A schematic representation of the soft x-ray experiment.
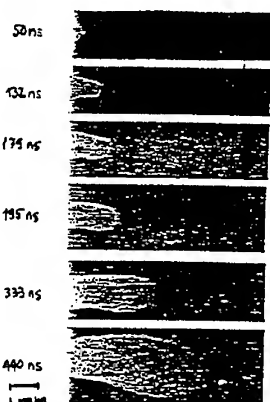
Fig.2 Shadowgraphs of the debris cloud from 90 μm thick aluminium foils.

The experimental setup for x-ray shadowgraphy is shown in fig. 1. The green beam is focused by a F/2 lens onto a zirconium target creating a soft x-ray source. X-ray flashes, taken parallel to the shocked free surface at times in the range $50ns - 2\mu s$, after the main laser shot recorded the debris on a Kodak DEF film. Fig. 2 shows shadowgraphs of $90\mu m$ thick Al targets taken at different times. The time development of the debris cloud is clearly seen. The velocity of the debris clouds determined from the shadowgraphs was $9.28 \pm 0.8 km/s$ for

Al, $3.46 \pm 0.11km/s3.46 \pm 0.11km/s$ for Cu and $3.76 \pm 0.17km/s$ for Sn.

The setup for the scattering experiments is shown in fig. 3. The diagnostic beam colineary with a 10 mW HeNe cw laser is scattered by the debris. The scattered pattern, displayed on a diffusing screen is observed by a cooled CCD camera and the data are recorded by a personal computer. The HeNe is used to measure the opacity of the debris as a function of time. The size of the particles was determined from the angular dependence of the scattered light. The calibration method and the algorithm for calculating the particles radius from the scattering pattern was described elsewhere[10].

Fig. 4 displays the scattered intensity as a function of the angle for a typical experiment. The points represent the experimental data and the curve is the calculated theoretical scattered intensity based on Mie theory. Each data point was obtained by averaging over the polar angle resulting an experimental error $\sim 1\%$. Excellent agreement was observed between the experimental scattered intenstity and the theory. Scattering functions from spherical particles were used in the calculation since as it is shown below the debris are in liquid phase and spherical droplets are expected. In experiments at lower laser intensities when melting is not expected the theoretical scattered intensity did not fit the experimental data. Therefore the above scattering method uses as a diagnostic tool for melting detection.

The radius r of the debris was found in the range $0.5\mu m$ to $7\mu m$ for all the materials studied here. The size distribution of the debris follows the power law

$$N(r) = N_0 r^{-b} \tag{1}$$

N_0 and b are constants. This type of scaling law is found in percolation theories[11]. The experimental values of b are 2.8 for Cu, 3.0 for Al and 3.8 for Sn.

The shock velocity was determined from backlighting measurements[12] based on the decrease of the free surface reflectivity due to the arrival of the shock front at the free surface. The shock pressure P was calculated from the shock velocity using the phenomenological equation of state

$$u_s = c_0 + a.u_p \tag{2}$$

$$P = \rho_0.u_s.u_p \tag{3}$$

u_s and u_p are the shock and the particle velocities accordingly ρ_o is the density of the unshocked material c_0 and a are constants[13]. The pressure in Al was $P = (1.12 \pm 0.33)$ Mbar and $u_p = (3.92 \pm 0.77)km/s$. The free surface velocity $u_{FS} = 2u_p(7.84 \pm 1.55)km/s$. Using these values the ratio f between the velocity of the front of the debris and the velocity of the free surface is $f = 1.1 \pm 0.1$.

The pressure in Sn was determined using the experimental[14] value $f = 1.33$. The pressure obtained in Sn was $P = (0.48 \pm 0.1)$ Mbar. Due to similar

topological structure of the debris clouds of Al and Cu, the pressure $P = 0.89 \pm 0.35$) Mbar in Cu was obtained using $f = 1.1 \pm 0.1$ measured in Al.

In the pressure and temperature domain of parameters involved here melting is expected. The Hugoniot H, the melting curve MV, three shock and the following release paths are shown in fig. 6 to illustrate the possible different responses of the shocked metal. The primed states represent the final temperature attained after release. Material following shock 1 remains solid both during shock compression and relaxation from this state. Material following shock 2 remains solid during the shock wave and may melt during the relaxation. In the shock 3 (threshold for melting during shock wave) the metal goes into the liquid phase under shock compression. The minimun pressure required for melting during the release P_M is the intersection between the Hugoniot and the isentrope that crosses the melting curve at zero pressure. The threshold pressure for melting during the shock wave in Cu, Al and Sn are $1.9 Mbar$[15], $1.3 Mbar$[16], and $0.28 Mbar$[17]. The shock pressure in the experiments with Sn was slightly larger than the melting threshold and therefore the Sn targets melted during the shock. For Al $P_M = o.68 Mbar$[18]. The pressure in Al was in all the experiments larger than P_M therefore the Al have melted during the release. For Cu $P_M = 1.16 Mbar$[19]. This value is equal to the estimated shock pressure within the experimental error therefore it is expected that the Cu samples did also melt during the release.

OPTICAL SCATTERING EXPERIMENTS
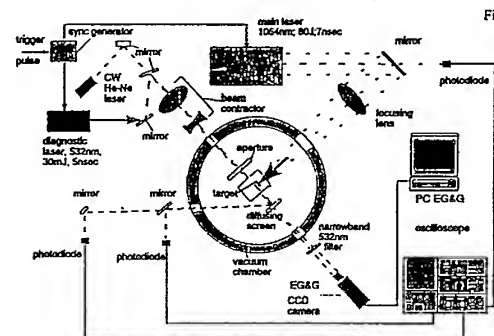
Fig.3 A schematic representation of the scattering experiment.

Fig. 5 The melting curve (MC), the Hugoniot (H) and rarefaction waves in aluminium.

Fig.4 The angular dependence of the scattered light for Al

Conclusion.

An experimental characterization of debris clouds generated by laser induced shock waves in al; Cu and Sn targets is reported. The radius of the debris was found in the range $0.5\mu m$ to $7\mu m$ for all the materials studied here and their size distribution of the debris follows a power law.

This work presents a diagnostic method for melting detection during shock and release waves. Melting detection can shed light on the EOS of materials in the range of parameters corresponding to the isentropic release up to zero pressure.

1. J.R. Asay, L.P. Mix, F.C. Perry, *Appl, Phys. Lett. A*, 29, 254 (1976).
2. P. Andriot, P. Chapron, F. Olive "Shock Waves in Condensed Matter", Menlo Park, USA, American Institute of Physics, New York 1982, p. 505.
3. P. Elias, P. Chapron "Shock Waves in Condensed Matter", Ed. Y.M. Gupta, Plenum Press, New York, 1985.
4. J. Lindl, W.C. Mead *Phys. Rev. Lett*, 34, 1273 (1975).
5. F.C. Perry, L.P. Mix, *Appl. Phys. Lett.*, 27, 194 (1975).
6. S. Eliezer, Y. Gazit, I. Gilath, *J. Appl. Phys.* 68, 356 (1990).
7. I. Gilath et al. *J. Impact Eng.* 14, 279 (1993).
8. F. Cottet, J.P. Rommain, *Phys. Rev. A* 25, 576 (1982).
9. V.E. Fortov, V.V. Kosin, S. Eliezer, *J. Appl. Phys.* 70, 4542 (1992).
10. B. Arad et al., *Rev. Sci. Instr.* 66, 5590 (1995).
11. D. Stauffer "Introduction to Percolation Theory" (Taylor & Francis, London 1985).
12. M. Werdiger, B. Arad, E. Moshe, S. Eliezer, *Quant. Elect.* 25, 153 (1995).
13. K.S. Holland, ed., "T-4 Handbook of Material properties Data Bases", LA-10160-MS (1984).
14. P. Elias, P. Chapron, M. Mondot, "Shock Compression of Condensed Matter-1989", Eds. S.C. Schmidt, J.N. Jonhson, L.W. Davidson (Elsevier Science Publishers B.V. 1990), p. 783.
15. V.E. Fortov, private communication.
16. M. Ross, in "High Pressure Equation of State: Theory and Applications", proceedings of the International School of Physics "Enrico Fermi", Course 113, Eds. S. Eliezer, R.A. Ricci (North Holland, Amsterdam 1991).
17. G.E. Duvall, *Rev. Mod. Phys.* 49, 523 (1977).
18. Z. Henis, S. Eliezer, *Phys. Rev. E* 48, 2094 (1993).
19. A.V. Bushman, G.I. Kanel, A.L. Ni, V.E. Fortov, "Intense Dynamic Loading of Condensed Matter (Taylor & Francis, 1993) p. 158.

MICROFIELD MODELLING IN
STRONGLY COUPLED PLASMAS

I.O. GOLOSNOY
Institute for Mathematical Modelling, Miusskaya sq. 4-A,
Moscow, 125047, Russia
E-mail: golosnoy@imamod.msk.su

The new model of ionic microfield in multicomponent plasma (MSHO) for the case of neutral test particle was constructed. The well-known model APEX is suitable for the case of charged test particle. Merging these two models we obtain the wide-range microfield model.

1   Introduction

Hot, high-density plasmas are produced in many experiments with high-power lasers. The diagnostics of that plasmas are made by spectra methods. The spectra line shapes are an important theoretical tool for this diagnostics.

Ionic microfield distribution in dense plasmas has long been of interest in plasma spectroscopy since spectra line shapes are determined essentially by the influence of fluctuating plasma microfield which acts on plasmas particles. Recently some new methods based on microfield have been obtained for determination of transport properties of dense plasmas. Moreover, investigations fulfilled during the last few years indicate that the thermodynamic properties of plasmas (energy levels occupation, equation of state) depend on plasma microfield too. Therefore it is very important to know the ionic microfield distribution function in a wide range of densities and temperatures.

We are interested in probability density $p(E)$ for microfield intensity E near a test particle with the charge Z_0. N ions and N_e electrons of plasma are immersed in a volume Ω at a temperature T. We assume that ions moving in a uniform neutralizing background of electrons (so-called one component plasmas - OCP). Let us denote $x_k=N_k/N$ for a concentration of ions with charges Z_k and $x_e=N_e/N$ for an electronic concentration. We can define the mean radius of ionic cell R and parameter of nonideality Γ from formulas:

$$(4\pi/3)NR^3=\Omega, \ \Gamma=e^2/(RT).$$

It is now customary to calculate $p(E)$ by means of approximations of the corresponding generating functional $Q(l)$,

$$p(E) = (2\pi/E)\int_0^\infty \sin(lE)Q(l)l\,dl, \qquad (1)$$

where the Fourier transformation of $p(E)$ is

$$Q(l) = <\exp(il\mathbf{E})>. \tag{2}$$

The angular brackets in Eq.2 denote a canonical ensemble average over configurations weighted with a Boltzmann factor, $\mathbf{E}$ denotes the electric field on the test particle due to any configuration.

For calculating the electric microfield distribution function $p(E)$ at a charged ion a convenient model has been proposed by Iglesias and Lebowitz [1] (APEX). However, APEX is less accurate for microfield distribution at a neutral atom ($Z_0=0$) in strongly coupled plasma ($\Gamma>3$). Corrections to APEX for the case $Z_0=0$ (APXC) were presented by Dufty et al [2] and the agreement of APXC with Monte-Carlo calculations for $\Gamma<10$ is quite good. However, it is emphasised by Dufty et al [2] that APXC will not be very accurate for very large $\Gamma>10$. Moreover, APEX and APXC are rather complicated.

2 Microfield model

A simple model for microfield distribution function at a neutral atom in strongly coupled plasma (MSHO) is presented in this paper. MSHO is the modification of simple harmonic oscillators model of Selidovkin [3] (SHO).

$E_0 p(E/E_0)$
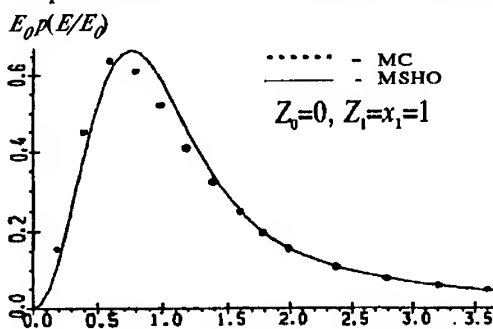
Fig.1. $p(E)$ as a function of E for $\Gamma=10$. $E_0=e/R^2$.

The SHO approximation is valid for the case $Z_0>0$ when $\Gamma>10$. Close collisions are neglected in SHO because the charged ion repels the field particles. But just these collisions form the "tail" of the microfield distribution at a neutral atom. That is why SHO is not valid for the case of $Z_0=0$.

Let us consider the case $Z_0=0$. Divide the matter by the cells. One ion is immersed into the each cell. We assume that ions execute the harmonic oscillations near their equilibrium. The neutral test particle Z_0 is moving free from the matter. In the present model we assume that the electric field on the Z_0 is the sum of two parts. The first part is the field of the centre ion. The second part is the mean field of other ions. This mean field is taken from the following assumptions:

1. It have to provide the harmonic oscillations of Z_k with the frequency from SHO model.

424

2. The sum of the mean field and the field of Z_k is zero at the boundary of the cell. That is why we approximate the mean field by the simple formula:

$$\mathbf{E}_m = -\mathbf{r}\, x_e e / R^3.$$

The cells of ions with different charges Z_k have the different sizes. The radius R_k for Z_k is taken from the electric neutral of the cell:

$$R_k = Z_k^{1/3} x_e^{-1/3} R. \tag{3}$$

So, the sum field in the cell is

$$\mathbf{E}_k = \left[\frac{Z_k(\mathbf{b} - \mathbf{y})}{|\mathbf{b} - \mathbf{y}|^3} - x_e \mathbf{b}\right]\frac{e}{R^2}, \quad 0 \le y, b \le R_k / R. \tag{4}$$

The average in Eq.2 is calculated independently at each cell with taking into account Eq.3 and Eq.4.

Consider the limiting cases. When $b \approx y$, than $E \to \infty$ and $l \to 0$. The main part of microfield is produced by the nearest particle in this case. Then we can consider the relative motion of Z_0 and Z_k and assume $y=0$. The result is:

$$Q(L) = 3\sum_k x_k \int_0^{(Z_k/x_e)^{1/3}} db\, b^2 \frac{\sin\{L(Z_k / b^2 - bx_e)\}}{L(Z_k / b^2 - bx_e)}, \tag{5}$$

where $L = le/R^2$.

If $E << e/R^2$ it means that $L >> 1$. Then the main contribution to $Q(L)$ is given by the region which near the boundary of the cell, because of in this region E_k is near the zero. The probability to locate of the centre ion Z_k near the boundary of the cell is very small. So we can assume that $y << b \approx R_k$. That is why we expand the first part of Eq.4 in a power series of y:

$$1\frac{(\mathbf{b} - \mathbf{y})}{|\mathbf{b} - \mathbf{y}|^3} \approx \frac{(\mathbf{lb})}{b^3} - \mathbf{y}\left\{\frac{1}{b^3} - 3(\mathbf{lb})\frac{\mathbf{b}}{b^5}\right\}. \tag{6}$$

Substitution Eq.4 with expansion Eq.6 into Eq.2 and some manipulations for the limiting case $L >> 1$ result to the following expression:

$$Q(L) = 3\sum_k x_k \int_0^{(Z_k/x_e)^{1/3}} \frac{\sin\{L(Z_k / b^2 - bx_e)\}}{L(Z_k / b^2 - bx_e)}\, \exp\left(-\frac{L^2 Z_k}{2x_e \Gamma b^6}\right) b^2\, db. \tag{7}$$

The investigation of asymptotics for $L << 1$ and $L >> 1$ of Eq.5 and Eq.7 allows to construct the simple approximation (MSHO) which connect the limiting cases:

$$Q(L) = 3\sum_k x_k \exp\left[-\frac{L^2 Z_k}{x_e \Gamma}\right] \int\limits_0^{(Z_k/x_e)^{1/3}} db\, b^2\, \frac{\sin\left\{L(Z_k/b^2 - bx_e)\right\}}{L(Z_k/b^2 - bx_e)}. \tag{8}$$

3 Results

Comparison of $p(E)$ and $Q(l)$ calculations over MC (Dufty *et al* [2], Alastuey *et al* [4]) and MSHO are given in Fig.1,2. Eq.8 gives good results in the case $\Gamma=10$. When Γ decreasing the accuracy of Eq.8 is fell off (Fig.2 for $\Gamma=3.9$). Thus MSHO is suitable for plasmas with $\sum_k Z_k^2 x_k \Gamma>10$ in the case $Z_0=0$. However, APEX is quite good for $Z_0>0$, all Γ and for $Z_0=0$, $\sum_k Z_k^2 x_k \Gamma<10$. Merging two models: MSHO and APEX, we obtain the wide-range microfield model for OCP plasmas.

$E_0 p(E/E_0)$
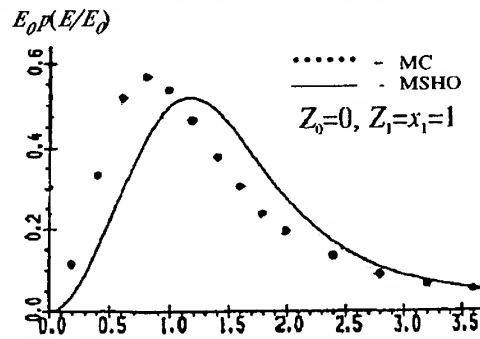
Fig.2. $p(E)$ as a function of E for $\Gamma=3.9$. $E_0=e/R^2$.

References

1. C.A. Iglesias and J.L. Lebowitz, *Phys.Rev.* A **30**, 2001 (1984).
2. J.W. Dufty *et al*, *Phys. Rev.* A **31**, 1681 (1985).
3. A.D. Selidovkin, *Teplofizika visokih temperatur (USSR)*, **6**, 10 (1968).
4. A. Alastuey *et al*, *Phys. Rev.* A **43**, 2673 (1991).

6.- RADIATION PHYSICS

STUDIES OF RADIATION SYMMETRY IN GAS-FILLED HOHLRAUMS

L.V. Powers, S.G. Glendinning, R.L. Berger, D.E. Hinkel,
R.L. Kauffman, W.L. Kruer, O.L. Landen, S.M. Pollaine,
D.B. Ress, T.D. Shepard, L.J. Suter and E.A. Williams
Lawrence Livermore National Laboratory, Livermore CA 94550 USA

N.D. Delamater, A.A. Hauer, E.L. Lindman, G.R. Magelssen and T.J.
Murphy
Los Alamos National Laboratory, Los Alamos NM 87545 USA

B.F. Failor
Physics International, San Leandro CA 94577 USA

A.R. Richard
Centre d'etudes de Limeil-Valenton, Villeneuve-St. Georges FRANCE

Measurements of implosion symmetry in gas-filled
hohlraum targets at the Nova laser facility have shown a
shift from calculations and vacuum experiments equivalent
to a change of ~120 microns in beam position. Direct
imaging of thermal x-ray emission from the hohlraum wall
shows an effective outward shift in the emission pattern in
experiments with standard Nova beam profiles. X-ray
emission patterns from experiments in which a single beam
of Nova is smoothed with a random phase plate suggest
that 10-beam smoothing will produce near-nominal
symmetry in gas hohlraums.

1   Introduction

Extensive experiments have been performed at the Nova laser
facility to characterize radiation and implosion symmetry in hohlraum
targets. Based on extensive measurements of implosion and radiation
symmetry in vacuum and lined hohlraums, a modeling capability has been
developed that quantitatively predicts the symmetry in these target
experiments [1]. Current Nova experiments are applying these
experimental and modeling capabilities to the study of symmetry in gas-
filled hohlraums. These and other Nova experiments in gas plasmas test
physics and modeling issues that potentially affect the NIF target
performance.

2 Comparison of low-Z plasmas in Nova and NIF targets

Current target designs for indirect drive ignition targets for the National Ignition Facility employ gas fill to reduce the expansion of the high-Z hohlraum wall. [2] The gas fills in the Nova experiments were selected to mimic the low-Z underdense plasma in the NIF target. Nova targets attain gas densities similar to NIF designs, but the smaller hohlraum size results in shorter underdense plasma scalelengths. Quantifying the effect of the gas fill on hohlraum and capsule performance measures can, however, test physics issues and modeling techniques relevant to NIF target performance.
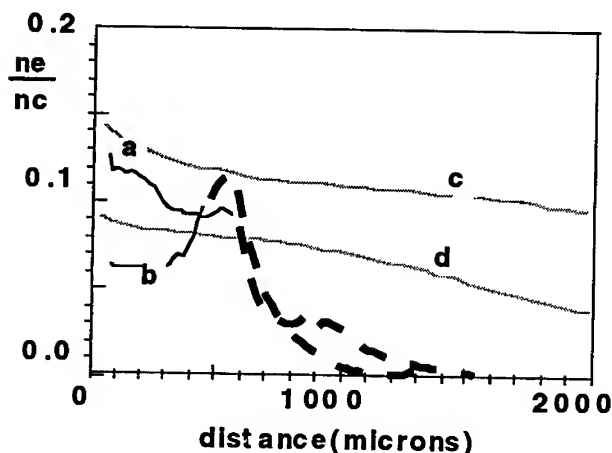
Figure 1: Comparison of low-Z plasma density lineouts along the laser propagation path for Nova propane-filled (a) and methane-filled (b) hohlraums with NIF inner (c) and outer (d) cones. The dashed line indicates material from the containing window.

3 Time-integrated symmetry measurements

Measurements of time-integrated implosion symmetry were performed in hohlraums filled with methane or propane gas at 1 atm pressure, resulting in fill densities of 3% or 7% of critical density for the λ=3520Å wavelength of Nova.[3] The distortion of images of the compressed fuel were recorded for varying axial positions of the laser beams. The capsule performance and shape varied in the manner expected, i.e. the images systematically became more oblate as the beams were positioned further away from the capsule. The recorded capsule shapes, however, were more oblate than calculations predicted, resulting in a descrepancy of ~120 microns in the calculated vs. measured beam position for best symmetry.

3   Measurements of wall emission patterns

Gated images of wall emission patterns have been recorded [4] and compared from vacuum, methane-filled, and propane-filled hohlraums to assess the source of the observed shift in implosion symmetry.   Gated images are recorded through a slot in the hohlraum wall in three x-ray energy bands: 220 eV, 700 eV and gold m-band. This technique provides the unique capability of sampling the portion of the x-ray spectrum that predominantly drives the capsule.   The principal disadvantage is the presence of the diagnostic slot which reduces the hohlraum temperature and potentially modifies the plasma evolution, so that modeling is required to tie these measurements directly to the implosion shape.

With unsmoothed Nova beams, the observed peak of the emission pattern is shifted outward ~100 microns in methane-filled hohlraums during the 1-ns foot of the 2.2 ns shaped laser pulse.   During the peak of the laser pulse, the position of peak emission agrees with calculations but the observed emission pattern is depleted near the hohlraum midplane and enhanced near the hohlraum endcap, resulting in a net shift in the effective symmetry.   The presence of excess energy near the hohlraum endcap can be explained qualitatively by beam deflection in filaments orthogonal to the plasma flow [5].   Viewfactor calculations indicate that this distortion of the emission profile corresponds to a ~5% shift in the flux symmetry at the capsule surface, the equivalent of a ~100 micron shift in the pointing of the laser beam.
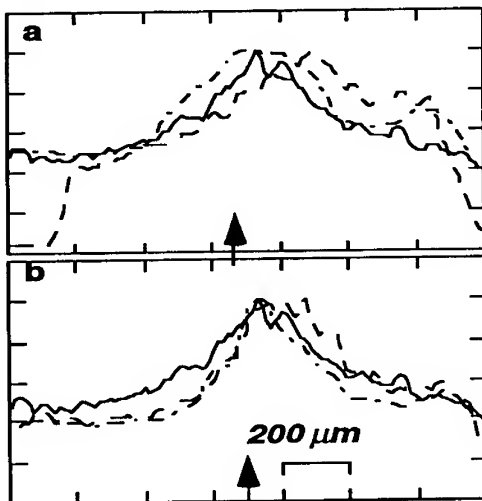
Figure 2: Axial lineouts of thermal (hv~700 eV) x-ray emission pattern for a) unsmoothed and b) RPP-smoothed beams from a vacuum hohlraum (solid line), methane-filled hohlraum (dashed line) and calculation (broken line).   The arrows indicate the initial aim point of the laser.

432

X-ray emission patterns were also obtained from a Nova beam smoothed with a random phase plate. In these experiments, the other beams which heated the hohlraum were unsmoothed. The position of peak emission from the RPP-smoothed beam agreed with calculations within the error bar introduced by Nova's beam pointing uncertainty. The observed emission patterns were still relatively depleted at the hohlraum midplane, consistent with the expected distortion of the emission pattern and reduced energy coupling of the unsmoothed beams. The emission profile near the x-ray spot of the RPP-smoothed beam, however, appears undistorted compared to calculations and vacuum experiments.

4 Conclusions

Observed thermal emission patterns from gas-filled hohlraums are consistent with the observed shift in implosion symmetry. Images of emission patterns from a single RPP-smoothed beam suggest that spatial smoothing will reduce or eliminate the difference between the calculated and measured symmetry. Spatial (KPP) and temporal (SSD) smoothing will be available on all ten Nova beams in the fall of 1996 to establish more quantitatively the smoothing configuration required to obtain nominal symmetry in gas-filled hohlraums.

Acknowledgement

References:

[1] L.J. Suter et al., Phys. Rev. Lett 73, 2328 (1994).
    A.A. Hauer et al., Rev. Sci. Instrum. 66, 672 (1995).
[2] S.W. Haan et al, Phys. Plasmas 2, 2480 (1995).
[3] N.D. Delamater et al., to be published in Phys. Plasmas (June 1996).
[4] D.B. Ress et al., Bull. Am. Phys. Soc. 38, 1885 (1993);
    S.G. Glendinning et al., submitted to Phys. Rev. Lett.
[5] H.A. Rose, Phys. Plasmas 3, 1709 (1996);
    D.E. Hinkel et al., submitted to Phys. Rev. Lett.

STUDY OF A RADIATIVE HEAT WAVE PROPAGATION THROUGH AN X-RAY HEATED PLASTIC FOAM

P. RENAUDIN, J.L. BOURGADE, J. BRUNEAU, S. GARY, E. GUILLY
CEA Limeil-Valenton, 94195 Villeneuve St Georges Cédex, France

K. EIDMANN, G. WINHART
Max-Planck-Institüt für Quantenoptik, 85748 Garching, Germany

The propagation of a radiation heat wave through pure and chlorinated C_8H_8 foam with a density of 45 ± 5 mg/cm^3 was experimentally investigated by space and time resolved absorption spectroscopy in the 30 to 80 Å spectral range. The foams were irradiated by a soft X-ray flux generated by two laser-heated converter gold foils. We present a preliminary analysis of the propagation of the radiation heat wave through the foams including a comparison of the experimental data with predictions of one-dimensional hydrodynamical codes.

1 Introduction

The investigation of heat wave propagation in matter driven by thermal radiation is important to study the role of radiation in plasma hydrodynamics, which is important for Inertial Confinement Fusion and astrophysical plasmas. Since the work of Zel'dovich and Raizer, the behavior of radiatively heated matter is well known theoretically [1]. When the matter is dense enough (i.e. at solid density), the initial propagation of the heat wave is supersonic but is rapidly overtaken by the hydrodynamic motion and the flow becomes ablative. However, a supersonic heat wave can be maintained by lowering the target density. With the use of modern high-power lasers, which can provide thermal X-ray fluxes greater than 10^{13} W/cm^2, several studies have recently been carried out to investigate the interaction and the heating of solid targets by quasi-Planckian soft X-ray pulses. The recent development of low density polymer foams allows to probe the pure nonablative period and to study the radiatively driven supersonic heat wave [2]. Such foams also can be applied in opacity studies because a non-ablative heat wave in foams yields a plasma of well defined density and homogeneous temperature.

Here we report a measurement of the propagation of a radiation driven heat wave in two types of polystyrene foams: a pure C_8H_8 foam and a C_8H_8 foam doped with chlorine. The objective was to measure and compare the speed with which the heat wave propagates in foam with and without chlorine. The principle of our

1 Y. B. Zel'dovich and Y. P. Raizer, *Physics of Shock Waves and High-Temperature Hydrodynamic Phenomena* (Academic, New-York, 1966)
2 T. Afshar-rad et al., Phys. Rev. Letters **73**, 74 (1994) - J. Massen et al., Phys. Rev. E**50**, 5130 (1994)

434

experiment is based on absorption spectroscopy technique. The foam to be studied is irradiated by a quasi-Planckian soft X-ray pulse. An auxiliary plasma ("backlighter") created by a synchronized laser generates an X-ray source which probes the foam perpendicular to the direction of the radiative heat wave propagation.

2. Experimental arrangement

The experiments were performed at the Centre d'Études de Limeil-Valenton with the three-beam Nd:glass PHÉBUS laser facility (λ=0.35 μm, 1.3 ns duration and 10^{15} W/cm^2). Figure 1 shows the experimental configuration. Intense soft x-ray pulses generated from two separate laser-heated gold converters (1200 μm distant and 1 μm thick) irradiated the plastic foam. The backlighter source is a gold plasma located at 3 cm from the foam axis and created by the diagnostic beam with an elongated shape (100*1600 μm^2). The backlighter beam can be delayed, with reference to the two main beams in order to investigate different times in the evolution of the heat wave propagation. A mask (not represented on figure 1) protects the detector from the gold plasma emission generated on the converter foils. The temporal behavior and the absolute flux levels of the soft X-ray pulse produced at the rear side of the gold convertor foil were measured with X-ray diodes. Previous measurements obtained with PHÉBUS in a separate experiment give a rear side X-ray conversion efficiency of 20% for our case [3].
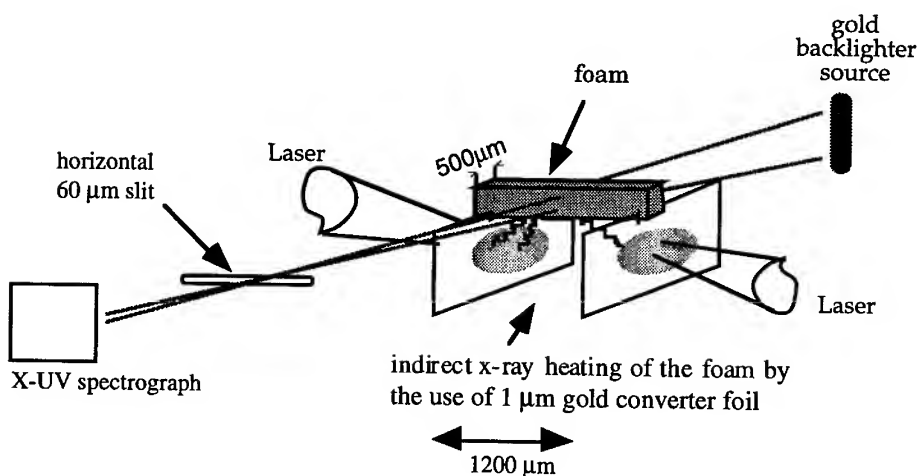
Figure 1: experimental set-up of the target and X-UV spectrograph.

3 D. Babonneau et al., Laser Part. Beams **9**, 527 (1991)

The foam used was a 500*500*1200 μm^3 parallelepiped. Cell sizes in the foam were less than 15 μm in diameter with a high degree of homogeneity through the foam. The foam density was equal to 45±5 mg/cm^3. Two types of foam were irradiated:

- C_8H_8 foam
- C_8H_8 foam doped with chlorine (10 to 14% in mass).

The X-ray radiation originating from the Au backlighter is absorbed by the foam and collected by Spartuvix, a time and space-resolved X-UV spectrograph which used a 2000 l/mm transmission grating together with SiO_2 imaging grazing-incidence mirror coupled to an X-ray framing camera. The spectrometer characteristics of the SiO_2 mirror are 3 Å polishing roughness, 5° grazing angle with a magnification ratio of 1/2. The obtained dispersion of 7 Å/mm allowed analysis of a 30-80 Å bandwidth with a low detection efficiency below the carbon edge at $\lambda = 44$ Å, which is caused by the reflective properties of the grazing incidence mirror. The X-ray probe beam transmitted trough the foam was dispersed by the transmission grating into the +1st and the -1st order, which was recorded on separate cathodes of the X-ray framing camera, respectively. In this way snapshots of the heat wave at two different times (with an exposure time of 300 ps) could be obtained in one laser shot. The spatial resolution along the direction of propagation was obtained with a 60 μm horizontal slit. The magnification was equal to 13.

3. Experimental results and hydrodynamical predictions

At early time, the foam is cold, un-ionized and not transparent in the spectral window of the spectrograph. As the X-ray drive pulse turns on the opacity of the foam is reduced, thus allowing the X-ray probe beam to pass through the target in the region occupied by the heat wave. For a target with an areal mass of (2±0.2) mg/cm^2 and a probe wavelength of 60 Å, the pure carbon foam is calculated to become 20% transparent at an electron temperature of 25-30 eV, using the screened hydrogenic ion models of the SNOP [4] and NOHEL [5] codes. The 20% transmission contour will be taken as being representative of the position of the ionization front.

Simulations were performed using two different 1D lagrangian radiation hydrodynamics codes, MULTI [6] and CHIVAS [7]. Opacities were calculated from tabulated values generated by SNOP and NOHEL, respectively. The X-ray drive was approximated by a Planckian spectrum with a radiation temperature of 110 eV. This value as well as the pulse shape of the X-ray drive was obtained from previous

4 K. Eidmann, Laser Part. Beams 12, 223 (1994)
5 A. Decoster, Rapport des Activités Laser, CEA-LV (1994)
6 R. Ramis et al., Comput. Phys. Commun. 49, 475 (1988)
7 S. Jacquemot and A. Decoster, Laser Part. Beams 9, 517 (1991)

converter studies [3]. A comparison of the measured and predicted propagation of the 20% transmission point of all the data obtained is shown in figure 2. With both hydrocodes (MULTI and CHIVAS) we find good agreement for the propagation of the heat wave front, in particular for the final position at the end of the pulse. According to the simulations the slower propagation of the heat wave in chlorinated foam implies a four times larger Rosseland mean opacity compared to the C_8H_8 foam. This large difference in the Rosseland mean opacity is in agreement with opacity calculations recently performed with the OPAL code [8] and with a modified version of SNOP which runs for mixtures.
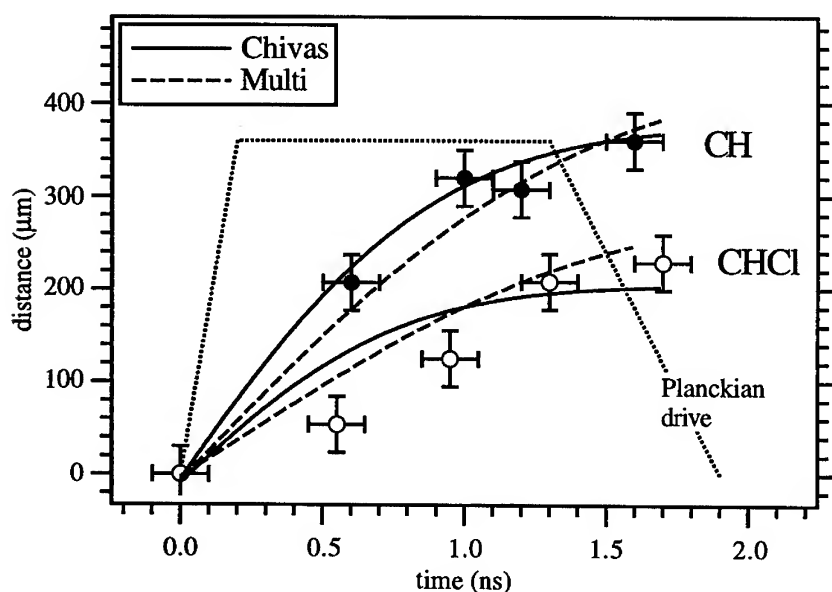
Figure 3: comparison of the observed and calculated propagation of the ionization wave observed in two types of foams at a probe wavelength of 60 Å.

Acknowledgements

8 C.A. Iglesias, private communication. Calculations of the opacity in chlorinated and unchlorinated foam show a four to five times increased Rosseland mean opacity in foam chlorinated with a mass fraction of 10%.

ANALYSIS OF EXPERIMENTS ON ISKRA-5 FACILITY WITH HOHRAUM COVERED BY MATERIALS WITH DIFFERENT Z

S.A. BEL'KOV, A.V. BESSARAB, V.A. GAYDASH, G.V. DOLGOLEVA, N.V. JIDKOV,
V.M. ISGORODIN, G.A. KIRILLOV, G.G. KOCHEMASOV, A.V. KUNIN, D.N. LITVIN,
V.M. MURUGOV, L.S. MKHITARYAN, I.N. NIKITIN, S.I. PETROV, V.A. PINEGIN,
V.T. PUNIN, A.V. RYADOV, N.A. SUSLOV, A.V. SENIK, V.A. TOKAREV

Russian Federal Nuclear Center - Institute of Experimental Physics,
607190, Sarov, Prospect Mira 37, Nizhny Novgorod Region, Russia.

The experimental results, obtained by ISKRA-5 laser facility, and theoretical analysis of the investigations of hohlraum target with X-ray converter layer consists of different Z material are presented. It is shown that for low Z X-ray converter layer fast ions, generated due to nonlinear absorption of the high intensity laser energy, begin to play important role in energy deposition to DT filled central glass shell.

The compression of DT fuel in laser fusion targets is never ideally spherically symmetric. The deviations occur because of the asymmetry of the energy flow at the DT filled capsule or because of the imperfect design of the capsule. The understanding of how various asymmetry factors affect the target compression is a necessary and important element of laser fusion program (see, for example, [1]).

The experiments with indirect drive (hohlraum) targets with a spherical converter box on ISKRA-5 facility demonstrated a relatively stable operation of the targets and reproducibility of the results obtained [2]. They make feasible the studies of asymmetry factors influence on target compression at ISKRA-5 facility. The stability is determined by the choice of the target design, relatively good reproducibility of the laser parameters and physical symmetrization processes inside the box. The calculations show that the radiation field nonuniformity at the central capsule does not exceed $\cong 3\%$.

Still retaining the best studied spherical converter cavity, two types of the experiments are possible to study the effect of a large-scale asymmetry. In the first type the asymmetry is applied to X-rays impacting the target while in the second type the central DT capsule is asymmetric.

We intended to apply the asymmetry to X-rays by coating two of the hemispheres with materials having different atomic numbers (Au-Cd, Au-Cu, Au-Mg, Au-CH). The different Z values result on different efficiencies of X-rays generation on two halves of the sphere and the greater is the difference between the atomic numbers of the coating materials, the greater is the difference in X-rays fluxes.

As the first necessary step, the experiments were carried out where the entire internal sphere surface was coated with a single element (Cd, Cu, Mg) or CH plastic. The hohlraum was represented by a copper box $\varnothing_{box} \sim 2$ mm with 6 entrance laser holes $\varnothing_{hole} = 0.6$ mm. At the center of box a DT gas filled spherical glass shell ~ 280 μm on diameter and the wall thickness $\Delta R_{in} \approx 5 \pm 0.3$ μm was placed. The

438

thickness of the converter layer was chosen such that the layer could not completely vaporize during the pulse time. The laser radiation energy input to the capsule was $E_L \approx 9 \pm 0.2$ kJ with the pulse duration $\tau_{0.5} \approx 0.3$ ns. The wavelength was $\lambda = 1.315$ μm.

The experiments showed that in accordance with the calculations and estimates the "temperature" and total energy of X-ray inside the box were decreasing with the decrease in the atomic number of materials, Z.

Fig.1 presents the measurement results obtained with the multichannel spectrometer based on the X-ray mirrors and crystals for the spectra of X-rays outcoming through the entrance holes in the experiments with different coating materials. Here the markers represent the relative variation of X-rays spectral brightness with the change in Z of materials. The solid curves correspond to similar dependencies obtained with the gas-dynamic SNDP code [3].
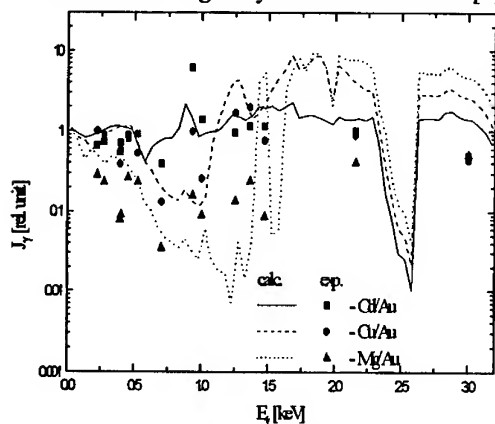
Fig. 1. Theoretical and experimental relative variation of spectral brightness of X-rays outcoming from the entrance holes with the change in Z of materials.

The calculations indicated that the neutron yield decreased with decrease in Z of the converter (more than by 30 times when Au was replaced by Mg).

Fig.2 shows the theoretical dependence of neutron yield on Z of the converter (solid curve). However the experimental decrease of the neutron yield (circles) was much lower.

The calculations and their comparison with the experiments allow to conclude that in addition to X-rays there exist other factor affecting the central target. Since the average effective intensity of the laser radiation at the box wall is $I_L \cong 5 \cdot 10^{14}$ W/cm^2 the role of nonlinear effects of laser-plasma interaction becomes important for the wavelength $\lambda = 1.315$ μm.

The main effect of this nonlinear interaction is generation of suprathermal ("hot") electrons with the average energy about 10 times higher than that of the basis plasma electrons. These electrons exist during laser pulse and if they can arrive to the central target their path lengths in glass are comparable with those of X-rays quanta. However the vacuum gap between the central target and the box wall will insulate the "hot" electrons till the vacuum gap is filled with plasma.

The characteristic closure rate of the gap is $V \sim 10^8$ cm/s. The closure time is $t_c = 8 \cdot 10^{-2}/10^8 = 0.8$ ns. Thus it will occur when the laser pulse terminates.

Another phenomenon of the nonlinear laser-plasma interaction is the acceleration of the, so called, fast ions that mainly receive the energy of "hot" electrons when the laser corona expansion occurs [4]. The characteristic velocity of fast ions

Fig. 2. Theoretical and experimental dependencies of neutron yield on Z of the X-ray converter.

$V_f \sim 5 \cdot 10^8$ cm/s slightly depends on plasma material. For such velocity, the time of fast ions arrival to the central target is $\Delta t \approx 0.2$ ns that is some what later than the X-rays pulse maximum. Thus the fast ions can impact the central target and when the box surface is coated with Mg or CH, the energy contribution to the target can be dominant.

To investigate the role of fast ions in the implosion of the central capsule on ISKRA-5, special experiments were carried out to measure the spectrum of ions from expanding laser corona. To do this, special targets were used without central capsule with additional diagnostic hole with $\varnothing_D = 800$ μm. Ion spectrum was measured with two Faraday caps. One of them was placed on the axis of the diagnostic hole and the other was at the angle of ~13°.

The experiments studied the boxes coated with Au and Mg. Fig.3 presents typical ion spectra measured in experiment. As one see there are two ion components corresponding to different slopes of the distribution function. The steeper dependence dN_i/dv_i up to $v_* \approx 2 \cdot 10^8$ cm/s corresponds to main ions while the part of spectra with the velocities higher than v_* corresponds to fast ions. The form of the spectrum did not depend on the coating material. It confirmed our assumption about the generation mechanism for fast ion. What is interesting is the existence of ions with very high velocity reaching 10^9 cm/s.

Consider the deceleration of the fast ion when it moves through the glass shell. The ion energy at the depth x is determined by the losses resulting from the collisions of the ion on the shell electrons and is described by the relation

$$E_f = E_0(1-\mu)^2, \qquad (1)$$

where

$$\mu = \frac{16\pi}{9\sqrt{3}} \frac{Z_f^2 e^4 N_A^2 \sqrt{m_e} \ln\Lambda_{ei}}{A_f \langle A_{sh}\rangle V_f^0} \int_0^x \frac{\rho_{sh}\langle Z_{sh}\rangle}{T_e^{3/2}} dx \qquad (2)$$

is the path length of the ion in the shell, ρ_{sh}, $\langle Z_{sh}\rangle$, $\langle A_{sh}\rangle$ are the density, average charge and average atomic weight of the shell plasma; V_f is the velocity of the fast ion entering the shell; Z_f, A_f are ion charge and atomic weight; $\ln\Lambda_{ei}$ is coulomb logarithm of the electron collisions; N_A is Avogadro number.

The ion will deposit the energy $\Delta E = E_f(\mu_1) - E_f(\mu_2)$ in the plasma layer from μ_1 through μ_2.

The electron gas of the laser corona in our case has two components: heat component with the density n_c and temperature T_c and "hot" component with the density n_h and temperature T_h. It is well known that the expansion of this plasma involves the flow reconfiguration in region where the densities of thermal and "hot" electrons become equal. For estimations we can count that flow characteristics (density and velocity) change by jump [4]. Introduce the relative fraction of "hot" electrons $\beta = n_h/n_c$ and the ratio of cold and "hot" electrons $h = T_c/T_h$. Then the density of fast ions at the distance $\xi = (R_* - R)/c_s \tilde{t}$ from the jump boundary can be estimated as

$$\rho_f = \rho_* (1+\xi_*) \left(\frac{c_h}{c_s} + \xi_* \right)^{-1} \exp\left(-\frac{\xi c_s}{c_h} \right), \qquad (3)$$

where ρ_* is the plasma density at the jump point, $\xi_* = \ln\left(2\beta^{\frac{1}{1-h}} / (1+\beta) \right)$ is the jump

location, $c_s = \sqrt{ZT_c/M_i}$ and $c_h = \sqrt{ZT_h/M_i}$ - sound speed up and down jump.

In turn, the velocity of fast ions

$$V_f = c_h + c_s (\xi_* + \xi) \qquad (4)$$

To account spherical convergence and deviation diagram of fast ion we multiply (3) by factor $\gamma(R_*/R)^2$.

This model is implemented in SNDP code to evaluate the degree of the effect of fast ions on the implosion dynamics of the central target.

The computational results in terms of this effect are also given in Fig.2 (dashed line). In all computations the parameters β, h and γ were identical: $\beta=0.22$, $h=0.1$, $\gamma=0.05$. It is seen that for the hohl-raum coated with gold and cadmium the effect of the additional energy deposition from fast ions $\Delta E_f \approx 75$-95 J is negligible, while for copper and magnesium coatings the calculated neutron yield increased and actually coincided with the experiment.

Fig. 3. Typical ion spectra in laser corona measured by Faraday caps located at the axis (1) and at the angle of 13° (2) to the axis of the diagnostic hole.

References

1. L.J.Suter, A.A.Hauer, L.V.Powers et.al. *Phys. Rev. Lett.* **73**(17), 2328, (1994).
2. F.M.Abzaev, V.I.Annenkov, V.G.Bezuglov et al. *Letters to ZhETF*, **58**, 28, (1993).
3. S.A.Belkov, G.V.Dolgoleva VANT, ser.:Mat. Mod. Fiz. Proc., #1, 59, (1992).
4. B.Bezzerides, D.W.Forslund, E.L.Lindman. Phys. Fluids, **21**, 2179, (1978).

ENERGY TRANSFER IN LASER PRODUCED PLASMA WITH HIGH X-RAY CONVERSION EFFICIENCY

B. Bazylev[1], V. Tolkach[1], H. Würz[2], G. Romanov[1]

1   Lykov Institute of Heat and Mass Transfer, 220072 Minsk, Belarus
2   Forschungszentrum Karlsruhe, P.O. Box 3640, D-76021 Karlsruhe, Germany

Calculation of radiative energy transfer and x-ray conversion efficiencies in laser produced plasma from multilayer targets was done using the multiray radiation transport equation, using of opacities from CRE with escaping factor correction and taking into account lateral radiation losses from the plasma flame. In this case calculated x-ray conversion efficiencies are in quite good agreement with experimental results obtained at the MISHEN facility.

1.   Introduction

Energy transfer and X-ray conversion efficiencies of plasmas produced by irradiating multilayered planar targets of various configurations with laser beams of power densities up to 10^{14} W/cm^2 were studied experimentally at the MISHEN facility and were numerically modelled [1, 2]. For these calculations 11 group Planck opacities were used obtained from a simplified CRE model without taking into account radiative ionization and excitation. This approach underestimates the plasma emissivity because reabsorption in strong lines increases the population of excited levels and changes the ion concentration. On the other hand the emissivity was overestimated because of the too rough frequency group mesh used. This is demonstrated in Fig. 1 showing emissivities for copper as obtained from the CRE model without and with reabsorption in strong lines for copper [3].

This paper describes results from an updated numerical modelling. For calculation of the radiative energy transfer the multiray integral radiation transport equation with 8 angular directions per hemisphere was used [4]. The influence of the radiation field on the level population and on the ion concentration was taken into account by using the escaping factor concept. Optimized frequency group structures with up to 404 groups were used. Moreover radiation losses through side surfaces of the plasma flame were taken into account.

442

2. Modelling features and optical data

The one dimensional radiation hydrodynamics code used for modelling of the laser beam interaction with different solid multilayered targets is described in [1]. Separate temperatures for the electron and the ion component of the plasma are used. Radiation losses through the side surfaces of the plasma flame may result in a redistribution of the forward and reverse radiative energy flux calculated in 1D geometry. These losses were taken into account in a simplified way assuming constant temperature in the transverse direction. In this case the perpendicular lateral leakage radiation flux $S_\omega(x)$ is given according to

$$S_\omega(x) = \frac{1}{\kappa_\omega} \beta_\omega I^P_\omega (1 - e^{\kappa_\omega L_0}) \tag{1}$$

with β_ω and κ_ω the opacities for emission and absorption I^P_ω the Planck spectrum and L_0 the lateral width of the target plasma. $S_\omega(x)$ enters as loss term in the radiation transport equation and according to eq. (2) the term $E(x_i)$ with

$$E(x_i) = 4 \sum_\omega S_\omega(x_i) \, \Delta x_i \tag{2}$$

enters as loss term into the energy balance equation.

For calculation of optical properties the CRE model was used. The following processes are taken into account: electron excitation and deexcitation, impact ionization, three body recombination, spontaneous emission and photo- and dielectronic recombination. The influence of intrinsic radiation on the plasma emissivity was taken into account by escaping factors. They were calculated for the two different thicknesses of the plasma flame of 0.05 and 0.1 cm. Two opacity sets with optimized 163 and 404 frequency group structure were used in the calculations. Optimization was done with respect to an adequate resolution of the line contours of strong lines and with respect to a reproduction of the main absorption edges.

3. Results and comparison with experiments

For the numerical modelling 2 kinds of multilayered planar targets as shown in Fig. 2 were considered. The targets are illuminated from the side of the copper layer by a laser beam of intensity of $5 \cdot 10^{13}$ W/cm^2 and a

pulse duration of 2.6 ns. In the calculations for the 3 layer target the escaping factor correction of the emissivities was applied for a lateral width of 0.1 cm and 163 and 404 frequency groups were used. For the two-layer target the two lateral widths 0.05 and 0.1 cm for escaping factor correction and 163 frequency groups were used.

The total ablation thickness of the copper layer was about 0.2 µm, thus defining the condition for formation of a reemission layer. In the low Z material mylar a reemission zone is not produced due to the low absorption of the x-ray radiation from the conversion layer. This can be seen from Fig. 3 showing calculated spectral radiation fluxes from the front side. For copper layers of thickness above 0.2 µm radiation in the wavelength region below 20 Å is dominated by copper line radiation from the conversion layer and radiation in the range 20 - 80 Å is copper continuum radiation from the reemission zone [5,6]. For thin copper layers line radiation from oxygen and carbon ions and low intense continuum radiation from these elements can be seen in the wavelength range 20 - 80 Å.

Fig. 4 shows calculated conversion efficiencies as function of copper layer thickness. It is to be seen that 163 group with optimized frequency mesh are sufficient. Between 50 and 70 % of the x-ray radiation is due to copper line radiation between 5 and 20 Å from the conversion and the transition region. The rest is emitted from the reemission region. With escaping factor corrected opacities the calculated x-ray conversion efficiency is in good agreement with the experimental value. Increasing the transverse thickness from 0.05 to 0.1 cm results in an increase of the x-ray emission by a factor of 1.3 in good agreement with the experimental results [1].

The calculations for the 3 layer target show the dominating role of the x-ray radiation from the conversion and the transition region in establishing the reemission zone. The aluminum layer is rather isolated from the copper layer and only radiation can heat it to form the reemission zone. Despite the thin copper layer (<0.1 µm) a plateau in the time dependent radiation flux is formed which clearly indicates formation of a reemission zone in the alu layer. Additionally the conversion efficiency increases noticeably.

4.   Conclusions

Numerical modelling of energy transfer in laser produced plasma was performed by using the multiangle integral radiative transfer equation. Radiation losses from side surfaces were taking into account. Using 163

444

group CRE opacities the conversion efficiency is underestimated on average by a factor of 1,5, using LTE opacities it is overestimated by a factor of 5, using 163 group opacities from CRE plus escaping factor correction resulted in a quite good agreement of measured and calculated conversion efficiencies.

5. References

[1]   N. Burdonski et al., JETP 79 (6) 876, 1994.
[2]   B. Bazylev et al., Laser and Particle Beams 12 (3) 355, 1994.
[3]   V. Tolkach et al., TOPATOM a code for calculation of optical properties, to be published as FZK report.
[4]   B. Bazylev, The 2D S_N and integral radiation transport code TWORAD, to be published as FZK report.
[5]   R. Sigel et al., Phys. Fluids B, 2, 199, 1990.
[6]   K. Eidmann, Laser and Particle Beams, 12, 2, 223, 1994.
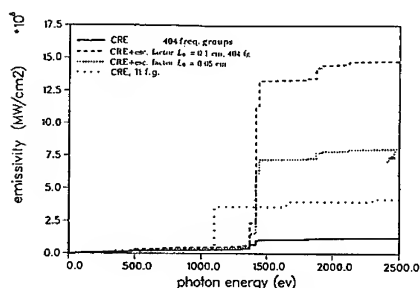
Fig. 1 Comparison of emissivities from CRE and CRE plus escaping factor corrected model for copper plasma of temperature 1 keV and density 0.01 g/cm³.

Fig. 2 Scheme of multilayered planar targets

a) two-layer target with 0.05 - 0.6 µm copper deposited on mylar foil of thickness of 3 µm.

b) three-layer target with 2 µm alu layer and 0.1 µm copper layer

Fig. 3 Calculated spectral radiation fluxes from the front side with and without formation of a reemission layer.
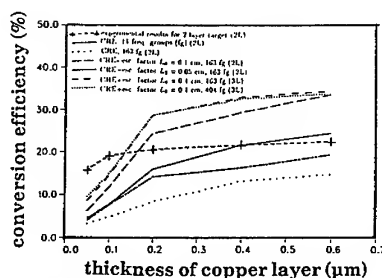
Fig. 4 Comparison of calculated and measured x-ray conversion efficiencies.

PERFORMANCE AND ANALYSIS OF ABSORPTION EXPERIMENTS ON X-RAY HEATED LOW-Z CONSTRAINED SAMPLES

R. W. LEE, R. CAUBLE, T. S. PERRY, P. T. SPRINGER, D. F. FIELDS, D. R. BACH,
F. J. D. SERDUKE,C. A. IGLESIAS, F. J. ROGERS, J. K. NASH, M. H. CHEN,
B. G. WILSON,W. H. GOLDSTEIN, R. A. WARD, J. D. KILKENNY, R. DOYAS,
L. B. DA SILVA, C. A. BACK,

Lawrence Livermore National Laboratory
Livermore, California 94550 USA

S. J. DAVIDSON, J. M. FOSTER, C. C. SMITH

AWE Aldermaston
Reading RG7-4PR, United Kingdom

Results of experiments on the absorption of niobium in a hot, dense plasma are presented. These results represent a major step in the development of absorption techniques necessary for the quantitative characterization of hot, dense matter. A general discussion is presented of the requirements for performing quantitative analysis of absorption spectra. Hydrodynamic simulations are used to illustrate the behavior of tamped x-ray-heated matter and to indicate effects that can arise from the two dimensional aspects of the experiment. The absorption spectrum of a low-$\dot{Z}$ material, in this case aluminum, provides a temperature diagnostic and indicates the advance of the absorption measurement technique to the level of application. The experimental technique is placed in context with a review of other measurements using absorption spectroscopy to probe hot, dense matter.

1 Introduction

Intense lasers can be used to irradiate high-Z targets producing x-ray fluxes that can volumetrically heat materials to substantial temperatures. This x-ray flux produces a state of high energy density matter that can be studied by absorption spectroscopy to yield detailed information.[1] The theoretical and experimental investigation of the x-ray absorption characteristics of these plasmas is an active field of research with applications in astrophysics, inertial fusion, and x-ray laser production.[1-4]

The study of plasma radiative properties requires the simultaneous measurements of the temperature, density, and the absorption, or emission, spectrum. The lack of simultaneity has been a weakness of most absorption measurements. Some experiments have relied on hydrodynamics simulations to infer the plasma temperature and density, while others provide measurements of the temperature, density and absorption spectrum, but on separate experiments.

Here we describe the development of a technique that allows the simultaneous measurements of the temperature, density, and absorption spectrum. This is made possible by two significant modifications of previous experiments. First, the density is obtained by employing a second spectrometer to monitor the sample expansion. Second, a mixture of niobium and aluminum is used, to determine the temperature from the absorption spectrum of aluminum, which occurs in a spectral region distinct from niobium. The temperature can be determined with an error of less than 3% by using detailed spectroscopic models to reproduce the observed aluminum absorption spectrum.[1]

2 Experiment and Results

In this measurement we want to provide benchmark data for LTE opacity codes for a moderate-Z element, niobium. We require, in addition to the absorption spectrum, four pieces of information on the sample itself: 1) the temperature; 2) the density; 3) the sample uniformity; and the 4) degree of deviation from LTE. The sample uniformity and deviation from the LTE state have addressed previously.[1] Here we have improved on past experiments by making temperature and density measurements simultaneous with the absorption measurement. The density measurement is performed with side-on imaging of the sample expansion, while the temperature is inferred from the absorption of the K-shell aluminum co-mixed with the niobium; see Fig. 1. The temperature measurement requires a theoretical model to derive a fundamental character of the sample from the observable, *i.e.*, the spectrum.
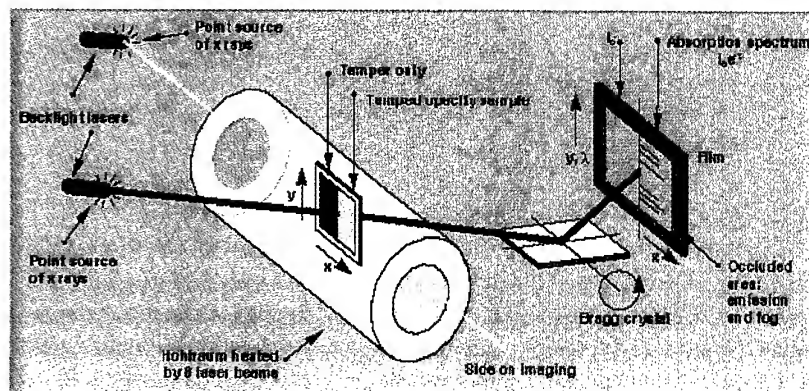
Figure 1: Schematic of the experiment designed to allow quantitative analysis of the absorption spectrum. The key elements are the two backlightts the sandwich target, and two spectrometers.

Sample uniformity is guaranteed by the use of full tamping. The Ni/Al mixture was 3400 Å thick (seen in the direction of the transmission measurement). On both sides of the sample 1500 Å of CH was deposited. In addition, 100-μm-thick foils of CH were attached to n the "ends" of the sample (viewing in the direction of the density measurement). Simulations of the arrangement showed very small temperature and density gradients over the course of the measurement interval, roughly one ns. The heating source was a large gold hohlraum into which eight beams of the Nova laser were focused (the remaining two beams drove the two backlighter fibers). The arrangement is similar to a previous point projection spectroscopy experiment.[5]

Data from the side-on spectrometer showed the sample width from Al absorption features as 4.8 ± 0.4 μm at the time of interest, in agreement with a continuum measurement. Correcting for magnification and source size and given the initial sample areal density, a density of 26 ± 5 mg/cm^3 was obtained.
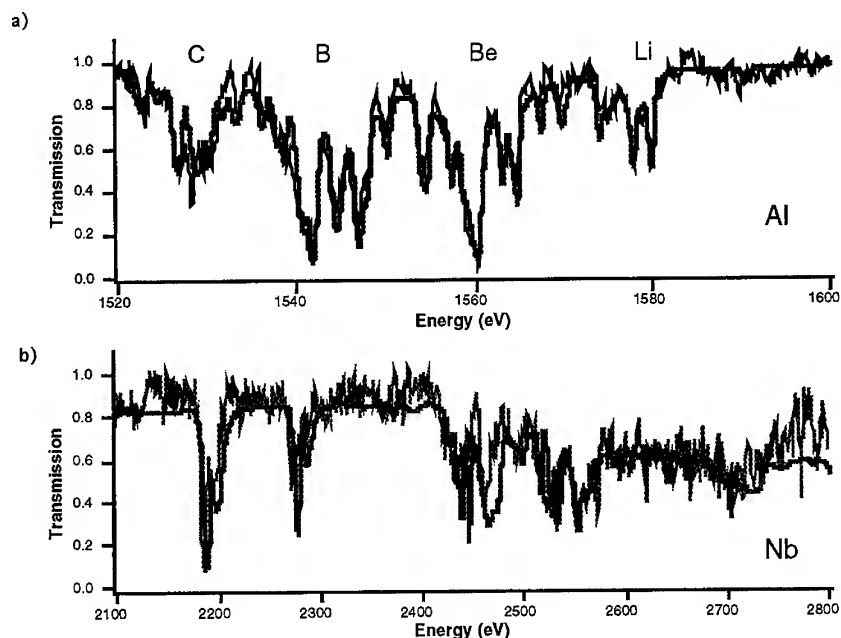
Figure 2: Comparison of the absorption data with calculation shown as transmission versus energy in eV. The calculations are shown as solid lines while the measurements are overlaid as gray lines. In a) the aluminum spectrum was found to match the OPAL opacity code best at a temperature of 48 eV. In b) the STA model was used to calculate the Nb opacity at the temperature and density determined by the experiment.

448

The transmission spectrometer contained two PET crystals, one for Al (2-3 keV range) and one for Nb (1.5-1.6 keV). Fig 2 shows the reduced Al and Nb data. For Al, the opacity code OPAL[6] was used to determine the temperature given the measured density. The theoretical spectrum is sensitive to small changes in temperature but is a weak function density, providing the link between the absorption spectrum and the temperature. In this way the temperature was determined to be 48±2 eV. The weak functional dependence of the transmission on density, which is uncertain to 20%, introduces only 1 eV of the total error. With the temperature accurate to better than ±5% and the density determined to 20%, it is possible to make quantitative comparisons between the experimental results for niobium and the theoretical calculations for the opacity. In Fig 2b, the STA code[7] was used to provide a comparison with the Nb spectrum at 48 eV and 26 mg/cm^3.

The experimental arrangement described above provides a method to quantitatively characterize the state of a hot dense plasma. to within a few percent. In the experiment reported here, sample density and temperature were obtained simultaneously with the transmission measurement. The independent density measurement together with the inferred temperature provide sufficient characterization of the sample to allow for a quantitative comparison between experiment and theoretical models of the niobium transmission spectrum. The method offers substantial improvements over previous methods of evaluating plasma opacities. Individual areas of improvement, such as extraneous signal measurement, measure of the backlight, measurement of the transmission spectrum and reduction of the data will be treated in a future publication.

Acknowledgments

References

1. T. S. Perry *et al.*, *Phys.Rev. Lett.* **67**, 3784 (1992); J. Edwards *et al.*, *EuroPhys. Lett.*, **11**, 631 (1991); P. Stringer *et al.*, *Phys.Rev. Lett.* **69**, 3735 (1992).
2. S. J. Davidson *et al.*, *Phys. Rev. Lett.* **67**, 3255 (1991).
3. L. B. Da Silva *et al.*, *Phys. Rev. Lett.* **69**, 438 (1992).
4. J. Bruneau *et al.*, *Phys. Rev. A.* **44**, R832 (1991).
5. T. S. Perry *et al.*, *J. Spectrosc. Rad. Transf.* **54**, 317 (1995).
6. F. J. Rogers and C. A. Iglesias, *Astrophys. J. Supp.* **79**, 507 (1992).
7. A. Bas-Shalom, J. Oreg and W. H. Goldstein in *Radiative Properties of Hot Dense Matter*, eds. W. H. Goldstein, C. F. Hooper, Jr, J.-C. Gauthier, J. R. Seely and R. W. Lee (World Scientific, Singapore, 1991).

INTEGRATED SIMULATION OF A HOHLRAUM
TARGET FOR ICF

J. RAMIREZ, R.RAMIS
E.T.S.I. Aeronáuticos. Universidad Politécnica. Madrid-28040 SPAIN
J. MEYER-TER-VEHN
Max-Planck-Institut für Quantenoptik. D-8046 Garching, GERMANY

Abstract
A NIF-type hohlraum target is considered in a integrated calculation that uses last revision (4.2) of MULTI2D code. The numerical simulation includes: Lagrangian mesh, tracking of laser beams, inverse Bremsstrahlung absorption, three-dimensional radiation transport, radiation induced hydrodynamics of casing and window panes and radiatively driven capsule implosion. Electron heat conduction (Spitzer with flux limiter), tabulated Equations of State (Sesame) and LTE opacities are also included into the code.

INTRODUCTION
The need of fast enough codes for scanning interesting parameter regions in integrated numerical simulations of ICF targets is clear since years. Consequently, the first (1991) edition of the Two-Dimensional Radiation Hydrodynamic Code MULTI2D [1] has been lately improved with the addition of an electron heat conduction subroutine and the possibility of using material data through tables, with small increase in run time. Although there is still a big step to be done, which is to include non-LTE opacities when relevant, the actual revision of the code offers good semi-quantitative results, particularly on hohlraum dyamics and radiation field symmetrization. In this paper a NIF-type hohlraum target is analyzed and results are presented.

THE TARGET
In summary, the target consist of a central DT-gas sphere (1.74 mm dia.) covered by a first DT-solid layer (0.080 mm thick.) and a second carbon-based ablator layer (0.160 mm thick.), that is located at the center of a cylindrical Au-casing (0.050 mm thick., 6.5 mm o.d. and 10.5 mm length) with curved ends and two (3.25 mm i.d.) laser entrance holes with (0.001 mm thick.) hydrocarbon window panes enclosing a (0.9 mg/cu.cm.) hydrocarbon gas filling.

THE LASER INPUT
About 1.2 MJ are applied to the target by means of four laser cones (two on each entrance hole). The inner cones (26-30 degrees axial angular deflection) take one third of the total energy input and the outer ones (42-64 degrees) the rest of it. Prepulse power is (total) 9 TW from 0 to 10 ns, going then exponencially to 400 TW at 15 ns and remaining constant for another 3 ns more.
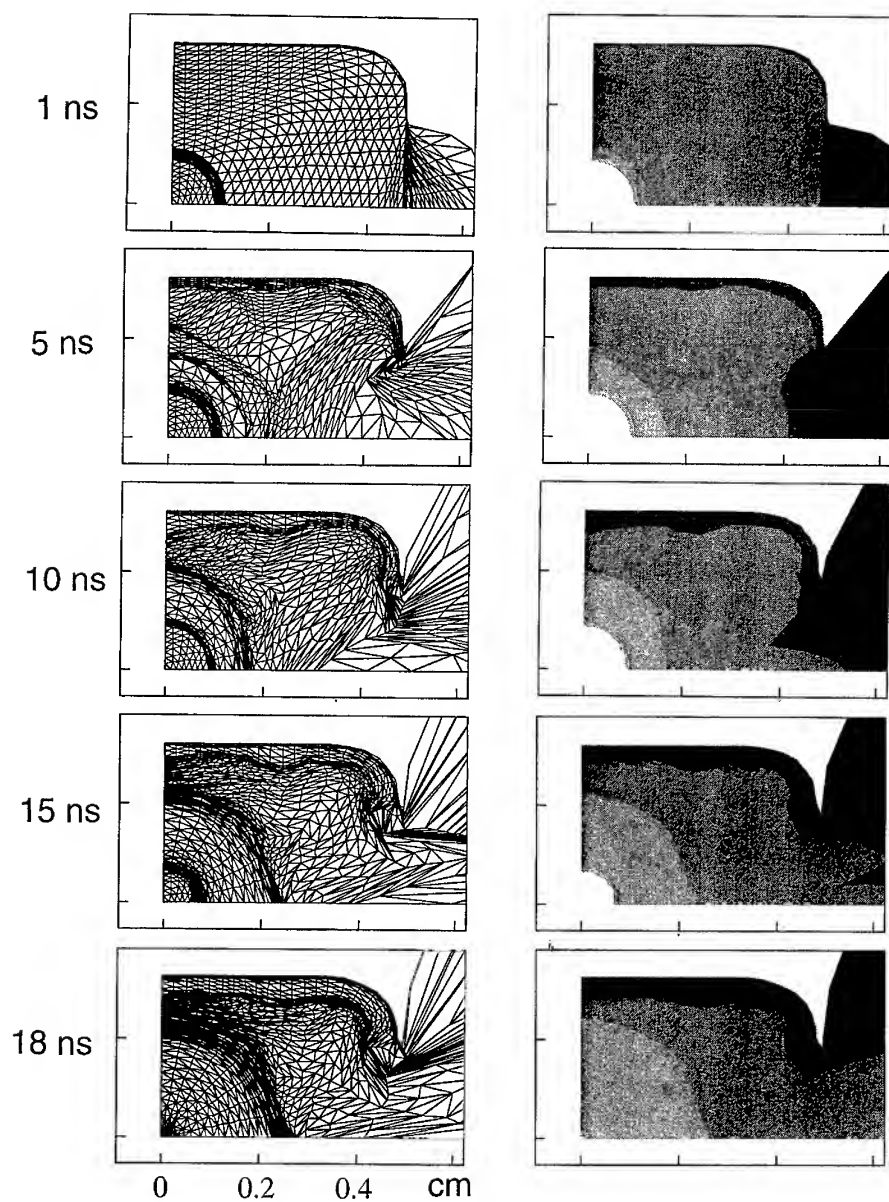
Fig. 1: Mesh and materials at selected times
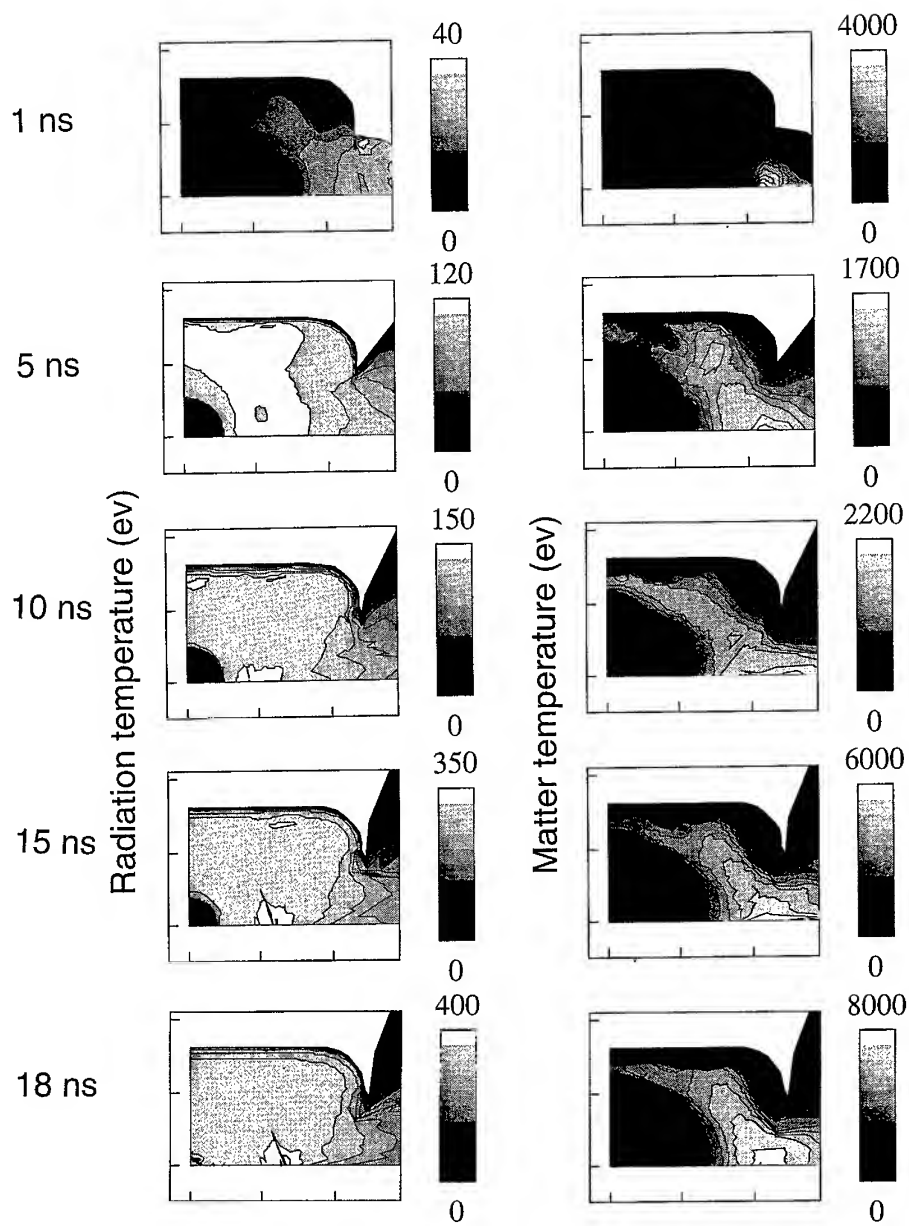
Fig. 2: Radiation (TR) and matter(T) temperatures

452

INDUCED HYDRODYNAMIC OF CASING AND WINDOWS

A quarter cros section of the target (Lagrangian mesh with 2400 cells and materials) is shown in Fig. 1 at selected times 1, 5, 10, 15 and 18 ns. After the first 300 ps the hydrocarbon window blows up and laser beams enter the gas filling. It takes another 600 ps more to get maximun volumetric deposition energy at Au casing. Then, wall heats up, conversion of laser energy into X-rays becomes significant and wall expands. Maximun wall expansion, at outer laser ring and maximun laser input, is about 0.55 mm.

As for the window material, at first it partially moves towards the interior of the target (1-5 ns) but later gas filling forces movement in the oppossite direction.

CAPSULE IMPLOSION

At 9.5 ns the first shock reaches the ablator-solid DT interface while the second (main) one is entering the compressed ablator. Two ns later the capsule thickness has been reduced to one third its original value and DT-gas compression starts. At 17.5 ns DT-gas radius has been reduced around 9 times and the gas heated around 10 kev (hot spot). Finally the solid-DT reaches maximun compression (around 80 times solid initial density) at 18 ns. Fusion physics has not been included in the simulation.

TEMPERATURE PROFILES

Fig. 2 shows isolines for radiation temperature (TR) an matter temperature (T) at selected times 1, 5, 10, 15 and 18 ns. It is interesting to note that it takes several ns to reach above 100 ev TR inside the cavity and that a hot (radiative) point appears at the axis, when the main pulse is active, causing a "pinch" effect that destroys symmetry of compression at later times.

CONCLUSIONS

We have presented a two-dimensional simulation of a hohlraum target based on the newly developed MULTI2D code. Although still of semi-quantitative nature, it provides significant results on hohlraum dynamics and temperature distributions. Particularly, ways to suppress the hot radiative points at the axis should be studied.

REFERENCES

[1] R.Ramis & J.Meyer-ter-vehn, MULTI2D - A Computer Code for Two-Dimensional Radiation Hydrodynamics, Max-Planck-Institut für Quantenoptik, Report MPQ174 (August 1992).

[2] J.Lindl, Physics of Plasmas (November 1995).

[3] Commissariat a l'energie atomique (CEA), Chocs, Numero 13, Avril 1995.

DYNAMICS OF PHOTO-ABLATED CARBON PLASMA IN AN INERT GAS ATMOSPHERE

T.KERDJA, S. ABDELLI, E. H. AMARA*, D. GHOBRINI, M. SI-BACHIR , S. MALEK
Laboratoire d'Interaction Laser-Matière
*Laboratoire des Lasers et Applications
Centre de Développement des Téchnologies Avancées
128, chemin Mohamed Gacem, El-Madania, Alger, Algérie

ABSTRACT.

Time and space-resolved emission spectroscopy measurements were performed to investigate plasma dynamics during laser evaporation of a graphite target in an ambient inert atmosphere. Two stages of expansion are found and are well described, using a viscous drag force model for the first one and a delayed ideal blast wave model for the second. Intense molecular emission is found to occur behind a front separating the plasma with the foreign gas.

INTRODUCTION.

The interaction of the laser ablated plumes with background gases is receiving increased attention due to its importance for film growth by pulsed laser deposition[1] particularly for the deposition of high critical temperature supraconductors, deposition of synthesized metal nitrides and more recently, the fullerene synthesis by ablating a carbon graphite target[2]. Optimization and control of the pulsed laser deposition process require the understanding of the vaporization and the expansion of the ablated material, the plasma playing a key role since it determines the formation of reactive species and high energy ions[3]. Studying the spatial and velocity distribution of the ejected species particularly during initial ejection and expansion can provide a better understanding of these processes.

Here, we present the optical diagnostic of Nd yag laser ablated carbon target in the presence of an ambient gas at low irradiance ($\approx 10^8$ W.cm^{-2}). Spatial and velocity distribution of the ejected species are studied.

EXPERIMENT.

A Q-Swichted Nd Yag laser beam (λ = 1.06 μm , τ = 25 nsec) is focused on a rotating graphite target placed in vacuum chamber. The laser flux density was fixed to 5.10^8 W.cm^{-2}, giving a laser fluence of 4J.cm^{-2} on the target. Either helium or argon environments with pressures ranging from 10^{-1} mbar up to 100 mbar are introduced in the chamber in order to study their influence on the plasma expansion dynamics.The emission spectrum was studied in the 200-600 nm range away and parallel to the target surface (z = 0-12mm). The temporal profiles of CIII* at 451.6 nm, CII* at 426.7 nm, CI* at 247.8nm and the Δv = 0, 1 sequences

of the molecular Swan (C_2*) around 516.5 nm and 473.7 nm are recorded versus the distance from the target surface and the foreign gas.

RESULTS
Lines intensity
Fig. 1 show the spatial dependance of the maximum emission intensity for CI* transition at 247.8 nm in vacuum and helium environment at different pressure.The maximum intensity of CI* transition is located at 0.7 cm and 0.5 cm from the target surface at 5 mbar and 10 mbar of helium respectively. For argon as an ambient gas, the maxima are located at 0.5 cm and 0.4 cm for 0.1 and 0.5 mbar respectively. It can be seen also for both gases that as the pressure of the background is increased, the CI* and CII* transition emission intensities exhibits a sharp profile, with its maximum moving towards the target surface. This sharp profile is highly suggestive of a boundary appearing between the ablated material and the ambient gas. The distance at which it occurs depends on the gas pressure and its nature; at a given pressure, shortest distances are obtained for large atomic mass of the gas[4].

The continuum contribution to the total emission that can be observed in Fig.1 suggests that the emission corresponding to the transitions studied is strongly masked by the continuum emission over a distance of 1mm from the target surface. In comparing the emission in vacuum and in a gas environment, it is possible to clearly distinguish two regions as a function of distance. Up to 3.5mm from the target surface, the emission intensity has the same general behavior in all the environment studied showing a maximum at a distance of 2mm, followed by a decay tail in vacuum.

Temporal evolution
Above some distance, the temporal profile of CII* at 426.7 nm shows a double peak structure which becomes well resolved two pulses as the observation distance is increased. As the distance is furher increased, the maximum intensity of the first peak decreases and vanishes in a few mm. This observation are attribuate to recombination processus. The plasma is stratified into a fast and slow ion components[5]. The faster component of the plume showed free expansion behaviour, while the slow component corresponded to highly collisional regime strongly influenced by the ambient gas. The fast component was rapidly quenched by the increasing ambient gas pressure, and was not detectable above 5 mbar of helium.

Fig. 2 shows the radius of maximum emission intensity attained by CII* transition at different pressures of helium. The initial expansion velocity always remains in accordance with the vacuum expansion velocity, as the pressure is increased, the velocity of the plasma front decreases rapidly and the volume attained in a fixed time is strongly pressure dependent. Experimental data exhibits two stages of

expansion, the first is well fitted using the viscous drag force model, while the second using an ideal blast wave model[6,7]. The radius attained in the first stage, depends strongly on the nature and the pressure of the ambient gas.

Molecular Swan band emission.

In the presence of a background gas, the molecular emission at 517.0 nm corresponding to the well known Swan band emission will dominate the plasma emission. The Swan band arises from transitions between $a^3\pi u$ and $d^3\pi g$ electronic states of the C_2 molecule, in the $\Delta v = -2, -1, 0, 1, 2$ sequences.

The relative intensity of the molecular Swan band emission in helium and argon environment, for different pressures has been represented and show that, as the surrounding gas pressure is increased, the molecular Swan band emission increases and the maximum intensity location moves to the left (target surface), the spatial profile becoming larger and sharper. Helium as an ambient gas gives the highest molecular emission. Fig.3 , represents both the spatial extension of CII* transition at 426.7 nm for two pressures of helium (5 and 10 mbar) and spatial extension of the molecular Swan band emission for the same gas pressures. The maximum emissivity of molecular band emission is located at 0.6 cm, 0.5 cm at 5 and 10 mbar respectively. The same feature is observed in argon environment for 0.1 , 0.5 and 1 mbar. The sharp profile of the spatial extension of both emissivities for CII* transition and CI* transition at 426.7 nm and 247.8 nm respectively , suggests the existence of an alike shock front separating the plasma with the ambient gas. The molecular Swan emission occurs behind this shock front. The temporal profile of the molecular Swan band emission observed occurs on much longer time scale, resulting in a longer signal rise time and a decay time of several hundreds nanoseconds. This suggests that the excitation mechanism takes place via a chemical way or a collisional quenching[8]. The vibrational temperature,determining exchange with heavy particles, was estimated from the emission spectrum of 1-0 sequence of C_2 ($^3\Pi g$-$^3\Pi g$) around 4700Å for different pressures of helium (10, 30and 100mbar) and was found to be between 3000°K and 7000°K.

CONCLUSION.

Spectroscopic diagnostic shows clearly that the presence of ambient atmosphere modifies the plasma expansion dynamics. Above some distance, the plasma is stratified into a fast and slow components, the faster component showed a free expansion behavior, the slow one being strongly influenced by the ambient gas.

Intense molecular Swan band emission dominates the spectrum when an ambient gas surrounds the target. Helium as an ambient gas gives the highest Swan band emissivity. The molecular emission becomes larger and sharper and the emission maximum is correlated with the maximum intensity emission of the CII* specie.

456

REFERENCES.

1. X. D. Wu, et al, Appl. Phys. Lett. 54, 179 (1989)

2. Y. Chai et al, J. Phys. Chem. , 95, 7564 (1991)

3. R. Mitzer et al, App. Surf. Sci. , 69, 180 (1993)

4. J. L. Meunier , IEEE Trans. Plasma. Sci. 18, 904 (1990)

5. S. Abdelli et al, Proc. of 12th International Symposium on Plasma Chemistry, Minneapolis, Minnesota, Aug. 21-25, (1995)

6. A. A. Puretzky et al, Laser Ablation II: Mechanisms and Applications, (ed. by J. C. Miller and D. B. Geohegan, AIP Conference Proceedings, 288 (1993)

7. T. Kerdja et al, to be published in J. Appl.Phys.

8. J. E. M. Goldsmith et al, Appl. Phys. B, 50, 371 (1990)

Fig. 2

Fig. 1

Fig. 3
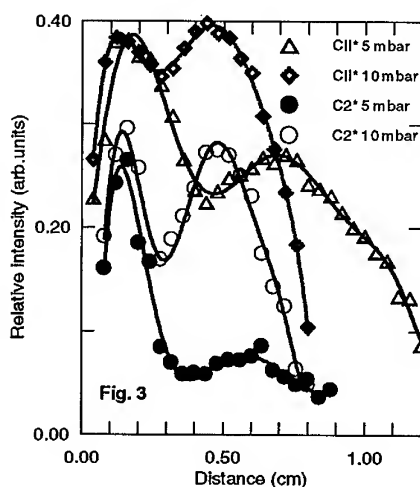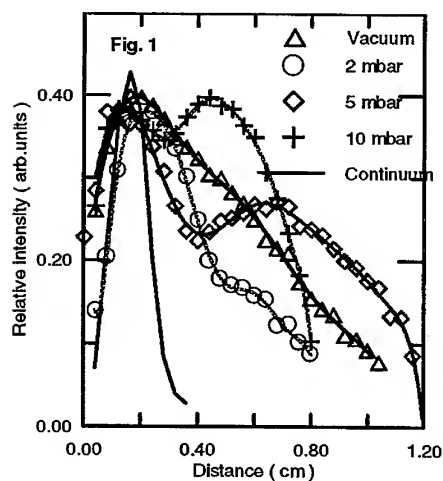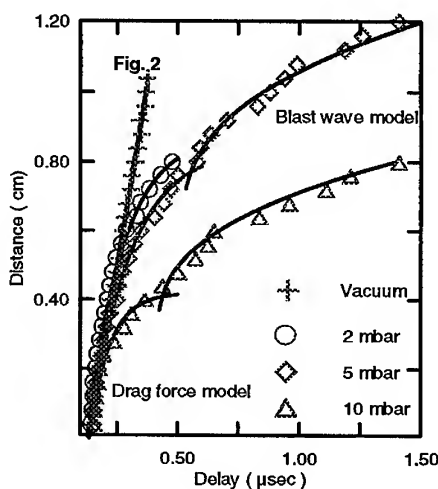
REAR SIDE K-SHELL X-RAY EMISSION
FROM Al FOIL TARGETS

A.MACCHI*, A.GIULIETTI, D.GIULIETTI[†], L.A.GIZZI[¥]
Istituto di Fisica Atomica e Molecolare - CNR, Via del Giardino 7, 56127 Pisa, Italy
*also at Scuola Normale Superiore, Pisa, Italy
†also at Dipartimento di Fisica, Università di Pisa, Italy
¥presently at TESRE-CNR, Bologna, Italy

The K-shell spectra and the intensity of the X-ray emission from the rear side of laser-irradiated Al foils were studied for various target thicknesses. Comparison of front and rear side X-ray intensity gives evidence of high X-ray transmission through the target. The application of rear side emission as a debris-free X-ray source is discussed.

In most of the applications of laser-produced plasmas as soft X-ray sources, the production of debris during target ablation must be carefully controlled, since the debris may damage the sample and the filters used in typical experiments. A He or Ne atmosphere has been introduced in some experiments in order to solve this problem[1]. Also the laser light scattered or reflected from the target may be a nuisance for applications.

The use of the X-ray emission from the rear side of a foil target as a debris-free soft X-ray source has been recently proposed by D.Giulietti et al.[2] and subsequently by Hirose et al.[3]. In these papers it was observed that for an Al foil target, several microns thick, irradiated by a laser pulse of a few nanoseconds duration, laser burnthrough does not occur and thus the target acts as a shield for debris and laser light. On the other hand, anomalously high X-ray transmission through the foil was observed, the X-ray emission intensity from the foil rear side being comparable to the intensity from the front side. Consequently, such technique could result suitable for application purposes.

X-ray transmission through laser-irradiated targets was experimentally investigated also in some papers[4,5,6] mostly devoted to the study of radiative target preheating in laser fusion and of the dense matter equation of state. However, only few authors investigated the X-ray spectrum of the rear side emission, despite the fact that, as discussed below, valuable information on the dynamics of energy transport in the target[7] can be acquired by accurate spectral analysis of such a radiation.

In this paper we analyze K-shell spectra of the rear side emission from laser-irradiated Al foils. The comparison of front and rear side spectra for various target thicknesses gives evidence of ionisation burnthrough and strong increase of the X-ray transmittivity. The X-ray yield of rear side emission is also measured.

The experimental set-up is the same as described in our previous work[2]. A 3 ns, 1.064 μm laser pulse was focused on Al foil targets in a 60 μm focal spot at an intensity of $2 \cdot 10^{13}$ $W\ cm^{-2}$. Front and rear side spectra in the 5-8 Å spectral region were obtained using a Bragg spectrometer equipped with a PET crystal ($2d$=8.742 Å). Each spectrum shown in this paper was taken with a single laser shot.

Fig.1a shows a representative front-side K-shell spectrum from a 6 μm target, consisting of resonance and satellite lines and He-like recombination continuum. For

458

comparison, a rear-side spectrum obtained in the same conditions is shown in fig.1b. The two spectra are quite similar, showing that very efficient X-ray transmission through the 6 μm foil takes place in this spectral window. Fig. 1c shows a rear-side spectrum from a 3 μm target, filtered through a second 3 μm Al foil placed about 1 cm behind the target. Although incomplete on the long wavelength side, this latter spectrum shows strongly attenuated emission lines with respect to the spectrum in fig.1b. Finally a rear side spectrum from a 13 μm target is shown in fig.1d: in this spectrum the lines are weaker with respect to the preceding spectra but they are still clearly distinguishable. In contrast, no lines were distinguished from the background in a rear side spectra from a 6 μm target, filtered through a second 6 μm foil.
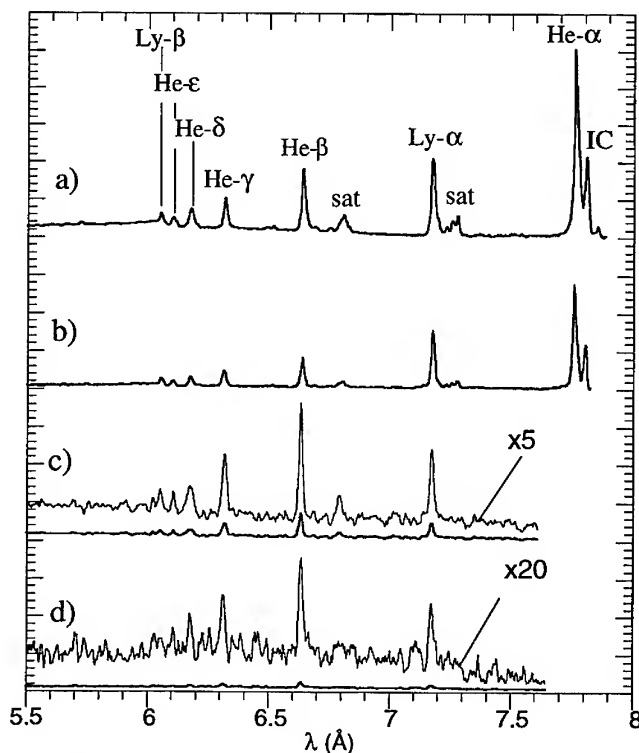
Fig.1: Al K-shell spectra from a) $6\,\mu m$ target front side; b) $6\,\mu m$ target rear side; c) "3+3"μm target rear side; d) $13\,\mu m$ target rear side

Fig.2 shows the ratio between line intensities of the rear-side spectrum 1b and the front-side spectrum 1a. The transmittivity of various thicknesses of "cold" Al is also shown for comparison. From fig.2 it is evident that the transmittivity of the laser-irradiated ("hot") Al foils is definitely higher than the transmittivity of "cold" foils of the same thickness, which is low due to the Al K edge at λ=7.96 Å. It is noticeable that the transmittivity appears considerably higher for the resonance lines than for the dielectronic "satellites" near the He-β and Lyα lines. We believe that this effect is due to the fact that resonance lines are strongly absorbed in the front side coronal plasma, while absorption is negligible for the satellite lines. For this reason the ratio between the intensities of a resonance line and a neighbouring satellite may depend upon the line of view. Thus only the optically thin satellite lines and the Intercombination (IC) line intensities are considered in order to estimate the X-ray transmittivity of the target backside. From fig.2 we find a transmittivity of about 30% at λ≈7 Å. A similar analysis for the 13 μm foil target gives a transmittivity of roughly 5%. Our results can be compared with those of Hirose et al.[3] who analysed rear side L-shell spectra in very similar experimental conditions. From their spectra, a 20% transmittivity can be estimated in the 20-100 Å range for a 7 μm Al target.

In order to estimate the laser ablation depth of the target we used the 1-D lagrangian hydrodynamic code MEDUSA[8], which takes thermal and shock wave energy transport mechanisms into account. According to simulations the ablation depth is expected to be about 3 μm in our experimental conditions and thus it cannot account for the observed foil transmittivity. Furthermore we observe that 1-D simulations are likely to overestimate the ablation depth due to an overestimate of the plasma temperature[2].

Hence the high X-ray transmission must be attributed to a decrease of the Al X-ray absorption in the target backside. Among different processes which may lead to a lower X-ray absorption efficiency, 2-D rarefaction of the target, as suggested by Ng et al.[6], is not expected to play a dominant role in our experimental conditions. In fact, in our case, the
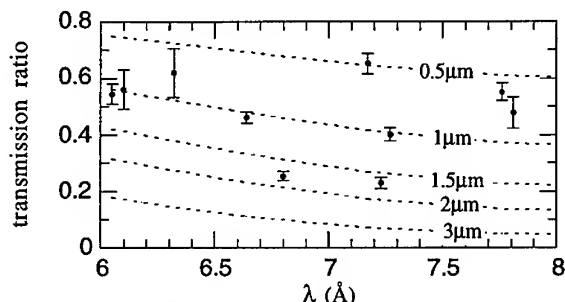
Fig.2: transmission ratio between line intensities of spectra 1b) and 1a). The transmittivity of various Al thicknesses is also reported (dashed lines).

460

laser spot size is much larger than the target thickness and thus expansion of the high density region is expected to exhibit a 1-D behaviour. Suprathermal electron transport is also expected to be negligible since the irradiation intensity is low. Thus, we attributed the anomalously strong X-ray transmission to ionisation burnthrough driven by radiative transport. This explanation was firstly suggested by Duston et al.[7] who simulated experimental conditions very similar to the present ones. In that model the ionisation generated by radiation transport causes the Al photoionisation edges to shift towards shorter wavelengths, thus opening X-ray "transparency windows" which move from the red to the blue side of the spectrum.

According to the ionisation-bunthrough model, from the rear side spectra we can estimate the ionisation in the target backside. In fact, since the transmittivity of the foil target at the IC line wavelength (λ=7.81 Å) is similar to that of a "cold" 1 μm foil (fig.2), at about 1 μm from the target rear face the solid Aluminium must have become "transparent" to this line. Thus, in this region ionisation must have reached the Al^{3+} stage for which the K edge (λ=7.76 Å) lies below the IC line. We have assumed that the transmittivity of ionised Aluminium is obtained from that of neutral Aluminium by simply shifting the absorption edge and then interpolating the mass absorption data between the two edges. If we assume Local-Thermodynamic Equilibrium (LTE) in the dense target, then, according to Saha equation, the rear side temperature corresponding to Al^{3+} ionisation stage is about 25 eV. These results are in reasonable agreement with other experiments[3,9] and simulations[7], although different laser and foil parameters were used.

The time-integrated front and rear side X-ray intensity was measured using an X-ray P-I-N diode. The diode spectral sensitivity had its maximum for $\lambda\approx7$ Å. The spectrally integrated intensity of the X-ray emission from the rear side of the 6 μm and 13 μm targets resulted about 0.1 and 0.02 times the intensity of the front side emission, respectively. According to these values, rear side emission could provide a debris-free X-ray source without a dramatic decrease of the X-ray intensity. Moreover the laser light conversion efficiency into X-rays, which is low for Al, could be increased by coating the Al target front side with a thin layer of some high conversion efficiency material.

References

1. I.C.E.Turcu *et al*, *Phys. Med.* X, 93 (1994)
2. D.Giulietti *et al*, *Il Nuovo Cimento* D **17**, 401 (1995)
3. H.Hirose *et al*, *Phys. Rev. Lett.* **76**, 232 (1996)
4. T.Mochizuki *et al*, *Phys. Rev. A* **36**, 3279 (1987)
5. J.Edwards *et al*, *Europhys. Lett.* **11**, 631 (1990)
6. A.Ng *et al*, *Phys. Fluids* **30**, 186 (1987)
7. D.Duston *et al*, *Phys. Rev. A* **27**, 1441 (1983)
8. J.P.Christiansen *et al*, *J.Comp.Comm.* **7**, 271 (1974); P.A.Rodgers *et al*, RAL report RAL-89-127 (1989)
9. E.A.Mc Lean *et al*, *Phys. Rev. Lett.* **45**, 1246 (1980)

EFFICIENT PRODUCTION OF 2-10KEV XRAYS BY LASER HEATED"UNDERDENSE RADIATORS"

L. J. Suter, R. L. Kauffman, M. S. Maxon,
Lawrence Livermore National Laboratory,
University of California, Livermore, CA 94551 USA
J. F. Davis,
Alme Associates, Alexandria, VA USA

The next generation of high power lasers offers the prospect of creating multi-kilovolt x-rays with >10% efficiency. Such efficiencies are achieved with "underdense radiators", a non-traditional source of laser generated x-rays. Applications of these sources with the proposed National Ignition Facility (NIF) include volume preheating of experiments; bright, multi-keV backlighting; pumps for flourscent imaging of capsule dopants and doppler velocimetry; uniform irradiation of large test objects.

Within the next decade very high power laser facilites may be constructed in Europe and the United States. Two-dimensional (2D) numerical simulations with the Lasnex code [1] indicate that these high power lasers may produce multi-kilovolt x-rays with unprecedented efficiency. For example, consider the two types of sources, shown in figure 1. The source of figure 1a is a column of gas or foam irradiated from one end by a 0.35 micron (blue) laser beam. In simulations using 0.01g/cc of Xe gas irradiated by a 2ns flattop pulse at an intensity of 10^{15}w/cm^2 we find efficiencies into photons of energy >4keV (L-shell Xe and continuum) to be 19% with a 10TW beam. Since a cluster of four "beamlets" of the proposed National Ignition Facility (NIF) [2] will deliver 10TW in the geometry of figure 1a, good efficiency may be achievable with such gas-column sources. Simulations indicate that higher efficiencies and photon energies require more than 10TW. Figure 1b shows a higher power source; a low-Z container, transparent to x-rays of interest, filled with an appropriate Z, low density gas or foam. In simulations using Xe gas at 0.01g/cc, we find near optimal performance for containers 2mm diameter, 1.6mm long with 1mm diameter laser entrance holes. For 2ns pulses, simulated, >4keV efficiencies range from 17% at 20TW to 30% at 60TW.

a)   b)
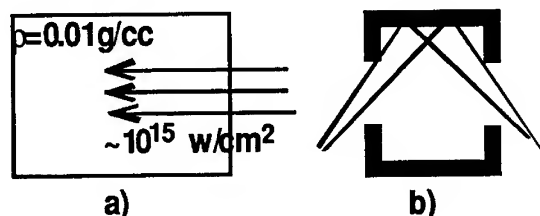
Figure 1- Two types of underdense radiators. a) is a gas column irradiated from one end with a single, large f-number beam. b) a transparent container filled with underdense gas or foam, irradiated with several beams.

as

We have efficient 2-D designs up to ~10keV. Figure 2 summarizes source efficiencies vs. photon energy and compares them with current disc backlighter efficiencies [3]. "Underdense radiators" (so called because the fill density is < critical density) heated by powerful lasers could be far more efficient multi-keV sources than current backlighters.
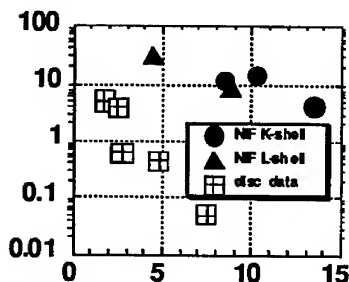
Figure 2- Projected multi-keV efficiencies with sources shown in figure 1b, irradiated at ~60TW, are much higher than current disc efficiencies.
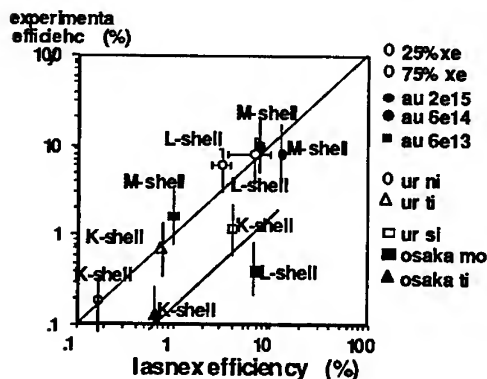
Figure 3 - Comparison of simulated and experimental multi-keV conversion efficiencies from several databases. The xe "gas bags" are the open circles near 10%.

Analysis of Lasnex simulations shows underdense radiators to be much more efficient than discs because of the way the plasma is heated. Compare the underdense source of figure 1a with a disc of the same material heated by the same laser. In underdense material, the heating front can move supersonically (bleaching front). However, a disc's heating front moves subsonically (ablative front). Analysis shows that a bleaching front, as compared to an ablative front, creates far more hot plasma which is denser and, therefore, is more efficient in producing multi-keV x-rays. In particular, we find:

*In producing a given mass of hot plasma, more energy is lost to low photon energy radiation (a parasitic loss) when the heating occurs in a dense ablation front, than when the matter is heated in the uncompressed bleaching front.
*The material in the ablation front rises to higher pressure. This ends up as more kinetic energy per unit of mass heated.

*More kinetic energy causes the hot blow-off behind an ablative heating front to be less dense than behind a bleaching front. Consequently, the blow-off behind the bleaching front produces more of the coronal, multi-keV x-rays per unit mass.

We have tested our ability to predict multi-keV efficiencies against several databases [4,5,6,7]. Figure 3 compares simulated and experimental absolute multi-keV efficiencies. These data include Xe filled "gas bags" specifically shot at Nova to examine multi-keV production by underdense radiators [7]. Except for two low intensity points $(1.4 \times 10^{14} \text{w/cm}^2)$ there is general agreement between experiment and simulations, lending credibility to the projections.

Applications of efficient multi-keV x-ray sources

1-Preheat sources: The preheat temperature, T_e, we can produce in an experimental package a distance d away from the source will be given by

$$\eta_> E_L/(4\pi d^2 \lambda) = (3/2)\rho^*(Z+1)T_e/A^*9.6 \times 10^4$$

Here $\eta_>$ is the multi-keV efficiency; E_L is the laser power; λ is the scale-length over which absorption occurs in the experimental package; ρ, Z and A are the density, atomic number and weight of the experiment we are preheating. Using $\eta_>=30\%$, $E_L=10^6$j, d=1/2cm, ρ=1g/cc, (Z+1)/A=0.33, gives T_e=2eV*cm/λ . Depending on λ, it may be possible to preheat ρ=1 samples to ~5eV up to several 10's of eV. NIF applications for preheat include off-hugoniot equation of state measurements and low-temperature hydrodynamics.

Backlighter sources: Sources like these could serve as the bright, high photon energy, large area backlighters needed for bigger targets. Consider, for example, the 60TW Ge source listed in table 1 scaled up to 100TW (14%>10keV). Viewed from the end of the 2mm diameter cylinder, the >10keV emission/cm^2/sr will be 3.5×10^{13} w/cm^2/sr . This is equivalent to viewing a 10keV hemi-isotropic disc source of 1% efficiency irradiated by 700TW at an intensity of ~2.2×10^{16}w/cm^2.

Pumps for flourescence based diagnosis: Efficient multi-keV sources and high-power lasers may allow us to field flourescence based diagnostics; a qualitatively new way of studying hydrodynamics. The principle is simple. A multi-keV source, at distance d, pumps a dopant in a capsule. In imaging, the number of photons collected from a resolution element r is:

$$\#\text{photons}= (\eta_> P_L/4\pi d^2)r^2(r/\lambda)\eta_F(1/4\pi)\delta\Omega\eta_{det}dt/E_>$$

Here, P_L is the laser power; $E_>$, the source's average photon energy; η_F, the dopant's flourescent efficiency, $\delta\Omega$, η_{det}, dt, the camera's solid angle, efficiency and time resolution. Using r=10mm, P_L=60TW, $\eta_>$=10%, $E_>$=10keV, d=1/2cm,

464

dt=100ps, η_F=0.2 (eg. 8keV Cu-K) gives

#photons=3.2×10^9(10mm/l)$\delta\Omega\eta_{det}$

For a 10mm pinhole at 1cm and the dopant concentration arranged so (r/λ)~0.01 to 0.1, we collect 40-400 photons from each 10mm resolution element. For a curved crystal/Rowland circle system, the number photons could be ~300-3000, at 1% crystal reflectivity.

A compelling possibilty is using flourescence to produce cutaway pictures of capsule mix, similar to those used to visualize mixing in 3-D simulations. At a velocity of 10^7cm/s or more narrowband doppler imaging with a camera of spectral resolving power 1500 or greater could image only one side of the imploding pusher. Related to this, doppler spectroscopy of flourescent lines could measure pusher velocity and, possibly, show the evolution of turbulence, via line broadening, at stagnation. A requirement for this will be an efficient spectrometer which sees only diametrically opposed parts of a doped capsule.

Large fluence-area products with good unifomity: If we require the flux over a test object to be uniform to $\pm$10% the fluence*area product we can generate will be source output times the solid angle we can collect from each source and still get $\pm$10% uniformity. This last term is a strong function of geometry. If all the emission is concentrated at a single point, we can collect only 0.45sr. However, if we produce x-rays in a number of properly distributed sources the useful solid angle increases. With four souces we can collect up to 1.6sr from each source and with 25 sources, 4.5sr. On NIF, the estimated fluence*area products with four sources are: 1-5keV; 50,000j*cm^2; 5-15keV; 14,000j*cm^2. With 25 sources: 1-5keV; 140,000j*cm^2; 5-15keV; 40,000j*cm^2.

1- G. B. Zimmerman and W. L. Kruer, Comments Plasma Phys. Controlled Fusion 2, 51 (1975).
2- J. T. Hunt, K. R. Manes, J. R. Murray, P. A. Renard, R. W. Sawicki, J. B. Trenholme, and W. Williams, "A Design Basis for the National Ignition Facility," Lawrence Livermore National Laboratory, Livermore, CA, UCRL-JC-117399 (1994)
3- R. L. Kauffman, Handbook of Plasma Physics, Vol. 3: Physics of Laser Plasma, p. 123.
4- Kondo, et. al., J. Appl. Phys., 67, 2693, (1990).
5- Yaakobi, et. al., Opt. Commun., 38, 196 (1981).
6- R. L. Kauffman, et. al., Laser Program Annual Report- 1986, Lawrence Livermore National Laboratory, Livermore, CA, UCRL-50021-86
7- R. L. Kauffman, et. al., Laser Program Annual Report- 1996, Lawrence Livermore National Laboratory, Livermore, CA, UCRL-50021-96, vol6, no. 2.

NUMERICAL SIMULATION OF THE X-RAY EMISSION FROM A SOLID ALUMINIUM TARGET IRRADIATED WITH SUB-PS PULSES

K. EIDMANN AND F. PISANI

Max Planck Institut für Quantenoptik, Hans-Kopfermann Str. 1, D-85748 Garching, Germany

We performed a numerical simulation of the x-ray emission from solid aluminium targets irradiated by sub-ps pulses (at $\lambda = 400nm$ and intensities $\leq 10^{17} W/cm^2$) by post-processing the output of a hydrocode in order to solve the time-dependent rate equations. We present results for the conversion efficiency and temporal pulse shape of the dominant He-like ($1s^2 - 1s2p$) and Li-like ($2p - 3d$) resonance lines.

If a sub-ps pulse irradiates a solid target a short-living hot plasma is created which is expected to cool rapidly by efficient heat conduction into the solid and by rapid expansion. The short x-ray pulse emitted in this process may open new applications in the study of very fast processes by means of x rays. An example may be time-resolved x-ray photoelectron spectroscopy. Such applications require clean short x-ray pulses of sufficient high intensity without a long temporal tail.

To get a better quantitative insight we simulated the emission process numerically. For this purpose we calculated the hydrodynamic response of the target by the one-dimensional Lagrangean hydro-code MULTI. To account for the interaction of sub-ps pulses with the target the original version of this code[1] was modified by an electro-magnetic wave solver and an appropriate collision frequency. MULTI is able to treat radiation transport, but only on the basis of steady state radiation models like LTE[2]. Since this approximation is no longer valid for the short pulses considered here, we post-processed the hydrodynamic results of MULTI by means of the FLY code.[a] The time-history of the temperature and the mass density of each Lagrangean cell calculated by MULTI is used as an input for FLY, which solves the time-dependent rate equations and calculates the emitted radiation. Note that the hydrodynamic results are not affected by the details of the radiation physics, because the emission of x rays is only a very small contribution in the energy balance, i.e., post-processing of the radiation physics is a reasonable approximation.

We studied solid aluminium targets irradiated by a laser of the wavelength of $400nm$ which corresponds to a frequency doubled Ti:sapphire laser. For the modest laser intensities $\leq 10^{17} W/cm^2$ and short pulse durations $\leq 150fs$

---

[a]FLY was developed by R.W. Lee of the Lawrence Livermore National Laboratory

considered here effects of light pressure and non-thermal electrons are assumed to be negligible. [3]
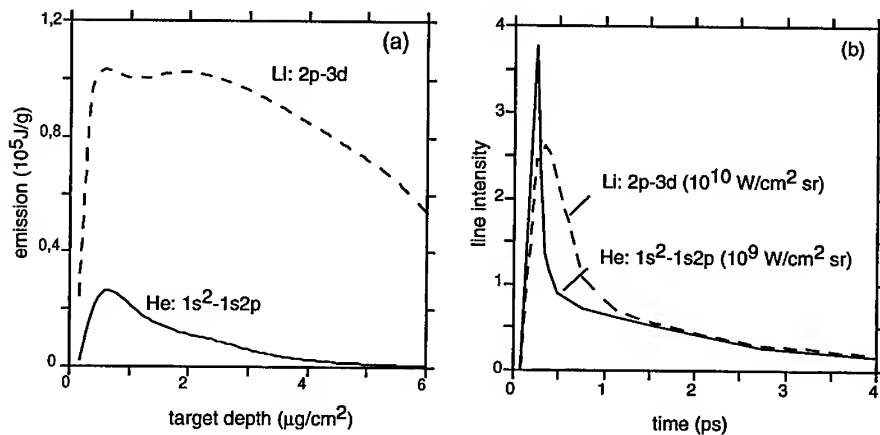
Figure 1: (a) Dependence of the time-integrated line emission on the target depth. Laser is incident from left. (b) Time dependence of emitted x-ray lines. Laser parameter in (a) and (b): $10^{16}W/cm^2$, $150fs$ FWHM.

Results obtained with a $150fs$ (FWHM) pulse (of sine squared pulse shape) at $10^{16}W/cm^2$ are presented in Fig. 1. At this intensity the front layers of the target are heated up to $\approx 300eV$ and the most intense lines are due to the He-like $1s^2 - 1s2p$ and the Li-like $2p - 3d$ transitions. Figure 1a shows the spatial origin of the emission of these lines in the target. The He-like $1s^2 - 1s2p$ line is emitted in a thin hot front layer, whereas the Li-like $2p - 3d$ line is generated in a deeper and colder region of the target.

The temporal shape of the line emission is plotted in Fig. 1b. The emission consists of a short main pulse followed by a slowly decaying tail. It is caused by the slow recombination rate in the expanding plasma. In the case of the He-like $1s^2 - 1s2p$ line the electron collisional interaction between the long living $n = 2$ levels and the radiating $1s2p(^1P)$ level is important, too. We note that the time-dependent solution can be considerably different from the LTE solution. For the conditions of Fig. 1 the LTE solution overestimates the He-like $1s^2 - 1s2p$ line emission by a factor of ≈ 20 and consists only of a short pulse without a long tail, because it follows directly the rapidly decaying temperature.

The total conversion of laser into x-ray energy is given by Table 1. The conversion efficiency is obtained by integrating the emission plotted in Fig. 1a over the target mass (the emitting layer can be considered in good approxima-

Table 1: Conversion η of incident laser energy into x-ray energy radiated into 2π at different incident laser intensities S_l and pulse lengths τ_l. η_{abs} is the fraction of the laser energy absorbed by the plasma.

$S_l(W/cm^2)$	$\tau_l(fs)$	η_{abs}	$\eta(\text{He:}1s^2 - 1s2p)$	$\eta(\text{Li:}2p - 3d)$
3×10^{15}	150	0.23	1.7×10^{-7}	6.6×10^{-5}
1×10^{16}	150	0.15	1.7×10^{-5}	1.7×10^{-4}
5×10^{16}	150	0.07	6.8×10^{-5}	1.5×10^{-4}
1×10^{17}	15	0.13	1.7×10^{-7}	1.7×10^{-7}

tion as optically thin). Due to the increase of the mean ionization the He-like emission increases strongly with laser intensity whereas the Li-like emission has reached saturation at laser intensities of a few $10^{16}W/cm^2$. Besides $150fs$ pulses table 1 exhibits also a result obtained with a pulse width of $15fs$. Lasers delivering such ultra short pulses may be available in the near future. The temporal shape of the emission showed also for this ultra-short laser pulse a large slowly decaying tail on a time scale of a few 100 fs. Table 1 includes values for the absorption of the laser which agree well with data recently measured with 150fs pulses.[4]

Besides single laser pulses we have also studied double pulses for heating the target. In Fig 2 we plotted the result of two 150 fs pulses delayed by 3ps. The laser intensity was $10^{16}W/cm^2$ in both pulses. The second laser pulse creates a hot low density plasma with a temperature of about 1500 eV. The emission from this plasma is strongly enhanced: the total conversion of the He-like $1s^2 - 1s2p$ line is 10^{-4}, i.e. about a factor of 6 larger than the conversion achieved with a single pulse. The x-ray pulse generated by the second pulse has no long tail, but its duration of $0.5ps$ (FWHM) is considerably longer than the laser pulse duration of $150fs$.

The numerical results presented here describe well the trends of experiments. The conversion efficiency given in table 1 is typical for measured data. For example, from the paper of Rousse et al.[5] one can extract a conversion efficiency into 2π of $\approx 3 \times 10^{-5}$ for the He-like $1s^2 - 1s2p$ line (at $S_l = 3 \times 10^{16}W/cm^3$, $\tau_l = 100fs, \lambda = 620nm$). Also the increase of the emission for double pulses has been seen in numerous experiments, see for example.[6] Detailed experimental information about the length and shape of the x-ray pulses suffers from unsufficient temporal resolution which is limited to $2ps$ for x-ray streak cameras.[7] By laser assisted Auger decay a pulse duration of $0.7ps$ has recently been measured in the XUV range,[8] which is similar to the

468
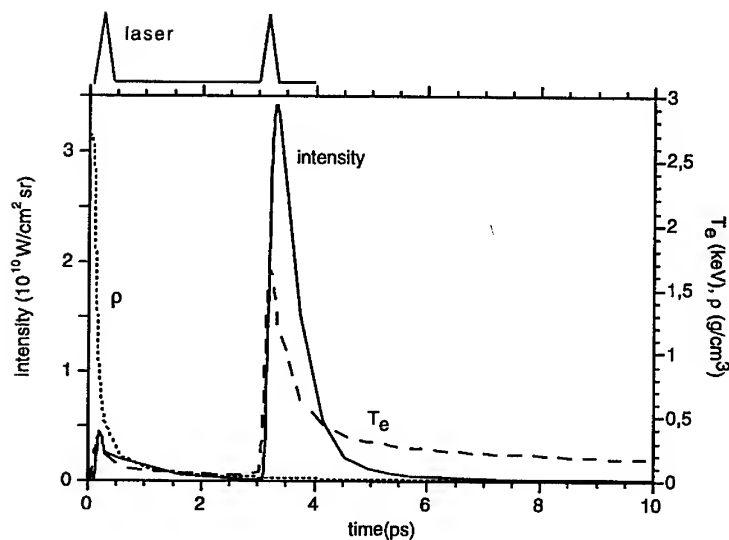
Figure 2: He-like $1s^2 - 1s2p$) line emission for a double pulse (two $150fs$ pulses, both at $10^{16}W/cm^2$, with a delay of $3ps$). In addition the mass density ρ and electron temperature T_e is plotted.

width seen in Fig. 1b for the Li-like $2p - 3d$ line.

Acknowledgments

References

1. R. Ramis et al., Comput. Phys. Commun. 49, 475 (1988).
2. K. Eidmann, Laser and Part. Beams 12, 223 (1994).
3. O. Peyrusse et al., Phys. Rev. Lett. 75, 3862 (1995)
4. D.F. Price et al., Phys. Rev. Lett. 75, 252 (1995)
5. A. Rousse et al., Phys. Rev. E 50, 2200 (1994)
6. U. Teubner et al., Appl. Phys. Lett. 59, 2672 (1991)
7. M.M. Murnane et al., Appl. Phys. Lett. 56, 1948 (1990)
8. J.M. Schins et al., Phys. Rev. Lett. 73, 2180 (1994)

X-RAY GENERATION INSIDE A SPHERICAL HOHLRAUM: "ISKRA-5" EXPERIMENTAL RESULTS AND SIMULATIONS.

S.A. BEL'KOV, A.V. BESSARAB, V.A. GAYDASH, G.V. DOLGOLEVA, N.V. JIDKOV, V.M. ISGORODIN, G.A. KIRILLOV, G.G. KOCHEMASOV, A.V. KUNIN, D.N. LITVIN, V.M. MURUGOV, L.S. MKHITARYAN, S.I. PETROV, V.A. PINEGIN, V.T. PUNIN, A.V. RYADOV, N.A. SUSLOV, A.V. SENIK, V.A. TOKAREV.

Russian Federal Nuclear Center - Institute of Experimental Physics, 607190, Sarov, Prospect Mira 37, Nizhny Novgorod Region, Russia.

The X-rays spectra of the golden spherical box are presented obtained in a series of experiments on ISKRA-5 facility. The total amount of X-rays and spectral characteristics depend both on the cavity diameter and the relative surface area of the laser energy input holes. The numerical simulation of X-ray generation with 1-D radiation gas dynamics SNDP code demonstrates a good agreement between the theoretical and experimental data. The measurements indicate that the energy fraction absorbed by fast ions with the laser energy of ~10 kJ, pulse duration $\cong 0.35$ ns and the cavity diameter of 2 mm achieves about 50% while this fraction is almost negligible for the cavity diameter of 4 mm.

A high-power laser facility ISKRA-5 (VNIIEF) [1] was used to carry out a series of experiments to generate X-ray inside a spherical box with the internal walls covered by a gold layer ~0.5 μm thick. The cavity diameter was 2 or 4 mm. Twelve laser beams with the wavelength 1.315 μm, total energy ~10 kJ and the pulse duration ~0.35 ns were introduced into the cavity through six holes with the diameter of 600 or 400 μm for the 2 mm box and 700 μm for the 4 mm box.

The spectral measurements used:
- the diffraction grid,
- multichannel X-rays crystal and X-rays mirror spectrometer,
- vacuum X-rays diodes spectrometers,
- X-rays streak camera.

This report discusses the results of measurements using the transparent diffraction grid The multichannel spectrometer provide the close results as it can be seen in Fig.1 for one of the shots. The details of the experiment instrumentation and data processing method can be found in [2].

Fig. 1 shows the spectrum shapes obtained from the experiments. An remarkable fact is that the decrease in the relative surface area of the laser energy input holes (LEIH) (compare Fig. 1a and 1b) increases the energy fraction generated in the soft spectrum (0.25<$\hbar\omega$<0.7 keV). This means that when the surface of the entrance laser holes is decreased, the primary laser radiation generated by the hot and low density laser corona (T_e~2.5-4 keV, ρ~ρ_{cr}) is transformed with a high efficiency to the radiation of X-rays corona having a lower temperature and a higher density ($T_e \cong 0.15 \div 0.2$ keV, ρ~0.5÷1 g/cm^3). The increase of the cavity diameter from 2 to 4 mm results in a lower intensity of the laser

a) $\varnothing_{box}$=2 mm, $\varnothing_{hole}$=0.6 mm

b) $\varnothing_{box}$=2 mm, $\varnothing_{hole}$=0.4 mm

c) $\varnothing_{box}$=4 mm, $\varnothing_{hole}$=0.7 mm
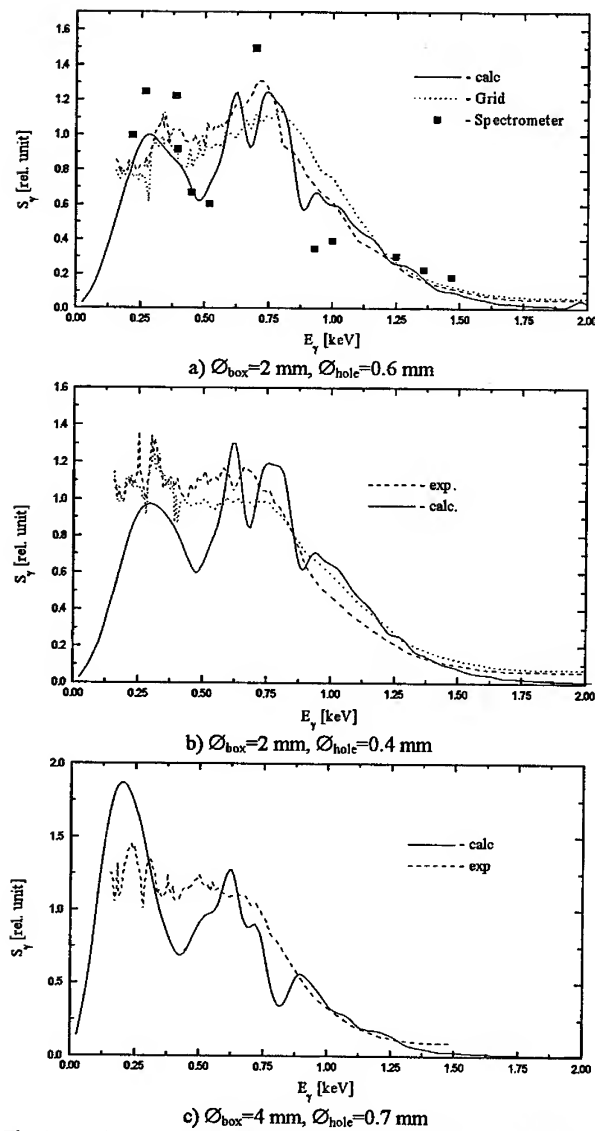
Fig. 1. Calculational and experimental X-rays spectra obtained for different parameters of the converter box.

radiation affecting the cavity wall. As a result, the temperature of the laser corona decreases. It can be seen in Fig. 1c that the energy fraction in the spectrum with $\hbar\omega \geq 0.75$ keV is lower than that in Fig. 1 a,b. In addition the spectrum of X-rays corona becomes softer ($0.25 < \hbar\omega < 0.7$ keV).

The numerical simulations of X-rays generation on these experiments used 1-D radiation gas dynamics SNDP code [3]. The laser radiation absorption was calculated using the invers bremsstrahlung. The opacity and emission capability coefficients in laser and X-rays coronas were calculated with the average ion model.

The laser energy losses through the LEIH were taken into account by introducing the effective absorption coefficient

$$\alpha^* = \frac{\alpha}{1-(1-\alpha)(1-\beta)}$$

where α is the current value of invers bremsstrahlung and $\beta = S_{hole}/S_{box}$ is the relative area of the LEIH.

The losses of X-rays through the LEIH were taken into account by introducing the negative source to the X-rays corona at the depth of about 0.5 of the free path length for each group. The source intensity is proportional to β

The shapes of X-rays spectra thus calculated are also given in Fig. 1. A good agreement between the calculations and experiments is seen. The slot in the computational spectrum with $0.3 < \hbar\omega < 0.6$ keV might be due to that these computations used insufficiently detailed structure of the average ion levels.

As for the X-rays intensity dependence on the relative surface area of the LEIH, Fig. 2 contains for various β the quantity γ/γ_0 where $\gamma = E_\gamma \varnothing_{box}^2 / E_L \varnothing_{hole}^2$; E_γ, E_L is the X-rays energy output from the LEIH and the laser energy inserted into the box, respectively, and $\varnothing_{box}$, $\varnothing_{hole}$ are the box and hole diameters. The quantity γ_0 corresponds to γ for $\varnothing_{box}$=2 mm, $\varnothing_{hole}$=0.6 mm and E_L=9 kJ. The value of E_γ is taken from SND calculations for the calculated curve and from the experimental data for the experimental curve.
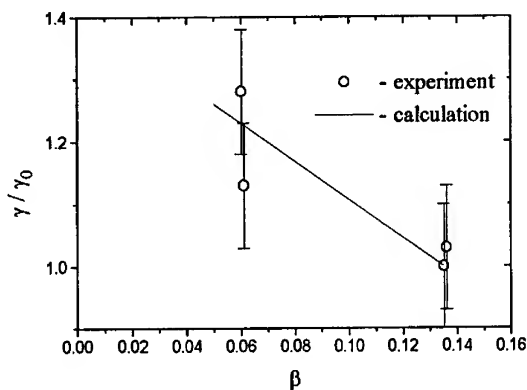
Fig. 2. The relative variation of X-rays energy output through the LEIH with different relative surface areas for the box with $\varnothing_{hole}$=2 mm.

It is seen that the efficiency of the laser radiation conversion to X-rays increases with the decrease of the relative surface area of the LEIH since there are lower losses of light and X-rays through the LEIH.

Fig. 3. present γ/γ_0 as a function of the cavity diameter as given by the experiment and SNDP calculations (curve 1). One can clearly seen the discrepancy in the case $\varnothing_{box}$=4 mm. The fact is that the computations did not take into account in self-consistent way the energy losses due to the generation of fast ions in the case of resonance absorption.
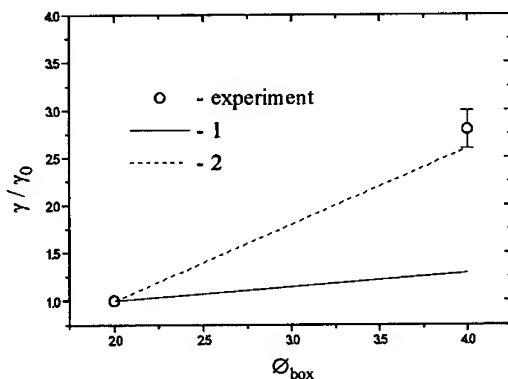
Fig. 3. Relative variation of X-rays energy output from the LEIH for different box diameters.

This absorption is significant when $I\lambda^2 \geq 2 \cdot 10^{14}$ W/cm$^2 \cdot \mu$m^2 where I, λ are the intensity and the wavelength of the laser radiation. The intensity of the laser light affecting the walls of the closed cavity is

$$I \cong \frac{E_L}{\pi\varnothing_{box}^2\tau} \cdot \frac{1}{1-(1-\alpha)(1-\beta)}$$ where τ is the pulse duration. For $\varnothing_{box}$=2 mm, τ=0.35 ns, E_L=9 kJ, $\alpha \cong 0.15$ and β=0.135 $I\lambda^2 \approx 1.3\cdot10^{15}$ W/cm$^2\cdot\mu$m^2 while for $\varnothing_{box}$=4 mm, τ=0.35 ns, E_L=7.5 kJ, $\alpha \approx 0.2$ and β=0.046 $I\lambda^2 \approx 3\cdot10^{14}$ W/cm$^2\cdot\mu$m^2.

Therefore for the box with $\varnothing_{box}$=2 mm, a considerable portion of absorbed energy will be transferred to fast ion and only the remainder will contribute to the formation of the laser corona. For the cavity with $\varnothing_{box}$=4 mm, $I\lambda^2$ is only slightly higher then the fast ions generation threshold and one can expect insignificant energy losses in this case.

In SNDP computation for $\varnothing_{box}$=2 mm and $\varnothing_{hole}$=0.6 mm, E_L varied in the range 9-4.5 kJ and was shown that E_γ/E_L remains unchanged.

Therefore the consideration of energy losses due to the fast ions must decrease the value of γ by $(1-\kappa)$ times where κ is the energy fraction transferred to fast ions. To make the curves on Fig.3 consistent, we must assume that κ=0.5 for $\varnothing_{box}$=2 mm and κ=0 for $\varnothing_{box}$=4 mm (curve 2).

This assumption is confirmed by the measurements of spectrum and the number of fast ions outcoming from the LEIH accomplished in an other series of experiments.

References

1. F.M.Abzaev, V.I.Annenkov, V.G.Bezuglov et al. Letters to ZhETF, 58, 28, 1993.
2. S.A.Belkov, N.V.Zhidkov, N.A.Suslov. The reroduction of X-rays spectrum from the measurements with the difraction lattic in the experiments with indirect exposure targets on ISKRA-5. Reports for ECLIM 24.
3. S.A.Belkov, G.V.Dolgoleva. VANT Ser.: Mat. Mod. Fiz. Proc., #1, 59, 1992.

X RAY RADIATION RATE CALCULATION FOR AN ALUMINIUM LASER PRODUCED PLASMA

E.H. AMARA
Centre de développement des Technologies Avancée
Laboratoire Lasers & Applications
B.P 245 El.Madania , Alger, Algeria

X ray radiation is among the processes that lead to a preheating before the compression phase during laser matter interaction at high laser fluxes. We have obtained in a computer work the rate of radiation of an Aluminium produced plasma by calculating the average charge ,the distribution of ionic species and thus deduced the intensities of emitted bremsstrahlung , recombination and lines radiation. This rate can be used in a hydrodynamic code to take into account the effect of radiations in the energy equation .

1 Principle

Radiations are taken into account in a hydrodynamic simulation code by firstly obtaining the X-ray rate produced as Bremsstrahlung , recombination and lines radiation. In a second step , following figure (1) , we calculate the energy du to
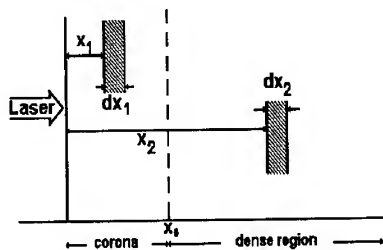
Fig.(1)

radiation given by [1]:

$$\varepsilon(x_2) = 2\pi \int_0^\infty d\omega\, I(\omega)\, \sigma(\omega)\, E_1[\tau(x_0,x_2;\omega)]$$

where

$$I(\omega) = \int_0^{x_0} I(x_1;\omega)\, n(x_1)\, dx_1$$

2 The computer program

In this contribution we calculate the term $I(\omega)$ starting from $I(x_1;\omega)$. The computer program , figure (2) , evaluates the total or partial radiation rate starting from a given ionic density and electronic temperature.

473

atomic data χ_j, $\chi_{j,m}$, $q_{j,m}$, ...

density

temperature

$<z> = f(n_i, T_e)$

potential reduction
$\Delta\chi_j \sim <z>^1$

$z = z+1$

initialisation of sums and products

next excitation state index m j

normalisation factors
of probability term $P_{j,m}$

$N_0 = \dfrac{1}{g_j \exp(\chi_{j,m}/T_e)}$

calculation of $P_{j,m}$

$n_i < 10^{20}$ — yes — $j = m$ — yes — $P_{j,m} = 1$

no — $P_{j,m} = 0$

$n_i < 10^{22}$ — yes — $P_{j,m} = N_0 \exp(\chi_{j,m}/T_e)$

$j = m$ — $P_{j,m} = N_0$

$P_{j,m} = (n_i/10^{20}) N_0 \exp(-\chi_{j,m}/T_e)$

collisional ionisation rate $S_{j,m}$

radiative recombination rate $\alpha_{j,m}$

dielectronic recombination rate $D_{j,m}$

oscillator strength

Einstein coefficients

$S_{z-1} = S_{j,m} P_{j,m}$

$\beta_z \sim S_{z-1}$

$\alpha_z \sim \alpha_{j,m}$

$D_z \sim D_{j,m}$

charge $z = 2, 14$

$\dfrac{N_z}{N_{z-1}} = \dfrac{S_{z-1}}{n_e \beta_z + \alpha_z + D_z}$

deduction of the N_z

calculation of the $<z^2>$

determination of the photon energy range — incrementation $h\nu = h\nu + \Delta h\nu$

calculation of the Bremsstrahlung P_{ff} radiation rate

calculation of the recombination P_{fb} radiation rate

calculation of the lines P_{bb} radiation rate

total radiation $P = P_{ff} + P_{fb} + P_{bb}$

new temperature

new density

Fig.(2) Computer program organisation

The Aluminium ions are at different ionisation states. The X emission from the ionic species differs in intensity and spectral distribution . The population rate of change from a particular level p of an ion j is governed by three processes , populating and depopulating this level . The processes are :

- the ionisations
- the recombinations (radiative α_j , dielectric D_j , three bodies n_e β_j)
- the excitations and deexcitations

The recombination term $R_j = \alpha_j + D_j + n_e \ \beta_j$, corresponding for densities less than 10^{20} cm^{-3} is reduced to $R_j = \alpha_j + D_j$ and place us in the case of coronal equilibrium , wheras for densities greater than 10^{22} cm^{-3} , we are in the case of the three bodies recombination that correspond to the local thermodynamic equilibrium .

3 Results

We have calculated the average charge and the distribution of the ionic species , as functions of the temperature. And thus we have obtained the curves of total radiation including the Bremsstrahlung , recombination and lines radiations.

As an illustration example , figure (3) gives the evolution of the Aluminium average charge for different temperature and an ionic density equal to 10^{22} cm^{-3} . Then on figure (4) we observe the evolution of partial densities of ionic species of the Aluminium for different temperature . We note that the results are in good agreement with those of other authors [2],[3].
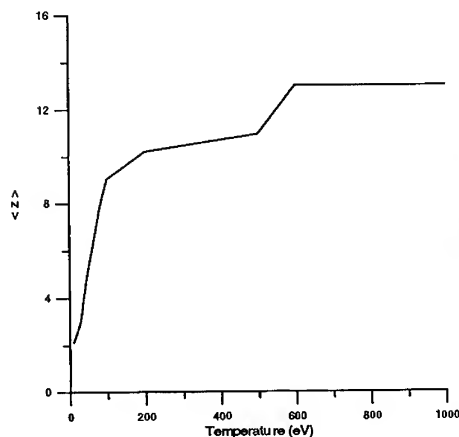
Fig.(3)- Average charge evolution
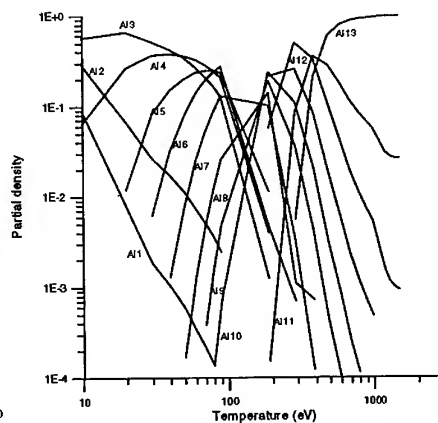
Fig.(4)- Partial densities evolution of the ionic species

476

Figure (5) give the sum of the rate of energies emitted as Bremsstrahlung , recombination and lines radiations for different photon energy hv for an energy range between 175 and 510 eV. The same result is obtained on figure (6) for an energy range from 1600 to 2250 eV.
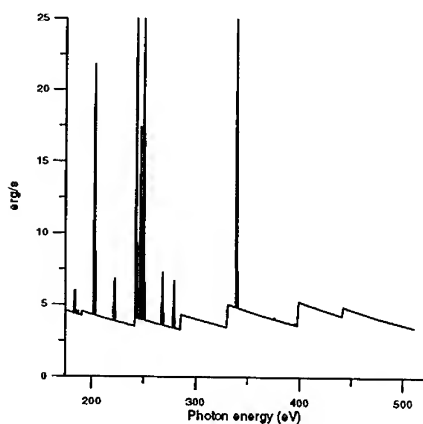
Fig.(5)- Total radiation   Fig.(6)-Total radiation
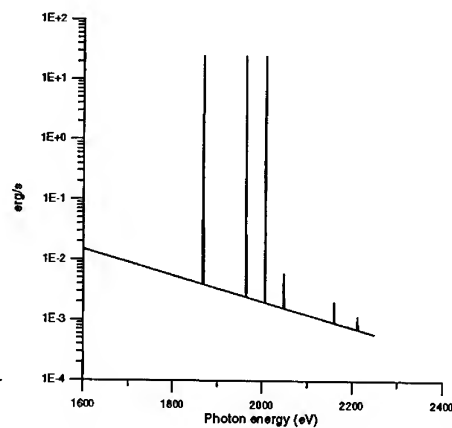
The curves make evident the exp (-x) evolution du to Bremsstrahlung , the recombination phenomenon illustrated by jumps of the radiation rate, and the abrupt jumps are produced when the photon energy correspond to an Aluminium line energy. These results were obtained for an electronic temperature of 300 eV and an ionic density of 10^{22} cm^{-3} .

REFERENCES

[1] D.Salzmann,H.Szichman,A.Krumbein ,C.E.Capjack,Phys. Fluids 20 (2) (1987)
[2] D.Salzmann,A.Krumbein , J. Appl. Phys. 49 (6) (1978)
[3] M.Itoh,T.Yabe,S.Kiyokama , Phys. Rev. A ,V35 (1) (1987)

X-RAY CONVERSION WITH SHAPED
LASER PULSES – RISE TIME EFFECTS

D. BABONNEAU, J.-L. BOCHER, G. FAUCHEUX, D. JURASZEK
Commissariat à l'Energie Atomique
Centre d'études de Limeil - Valenton
94195 Villeneuve Saint-Georges Cedex, France

Time resolved measurements of X-ray emission for various shaped pulses show that too fast rises in the pulses induce significant decreases in the instantaneous X-ray conversion efficiency, while slower rises allow to keep a constant conversion efficiency. This is related to a freeze of the internal energy which cannot be transported to the dense emissive zone : changing of the thermal conduction limitation during the simulation allows to reproduce correct values for the conversion efficiency.

1 Introduction

The time evolution of the radiative temperature in hohlraums is an important point for the success of megajoule laser driven implosions. The relation between this temperature and the laser flux goes through x-ray conversion by the inner cavity surface. We present some time resolved aspects of X-ray conversion on plane gold targets related to the rise time of Phebus laser shaped pulses, and their reproduction by FCI Limeil codes.

2 Experiments

2.1 Set-up

Targets were 20 μm thick gold disks with 2 to 5 mm diameter. The Phebus laser pulses were at 0.35 μm wavelength, with energies around 2.3 kJ, focal spots from 600 μm to 1.2 mm diameter, and two kinds of shaping : one with two steps and a rise time of about 500 ps between the two steps . The contrast between the two levels may be 4 or 10. The other shaping was deduced from the calculation and corresponds to a very much slower rise in 1.5 ns.

Diagnostics allowed to measure time evolution of refracted laser light (laser diodes and calorimeter), time evolution of the X-ray emission (Smart : transmission grating with streak camera), time-integrated spectral X-ray emission (Spart : transmission grating with film, and Demix : broadband spectrometer), space and time evolutions of the X-ray emission around 250 eV and 3 keV (FXD and FMS : hard and soft X-ray streak cameras).

2.2 Results and simulations

Refraction measurements for the **two-step** pulses showed strong instantaneous refraction at the pulse beginning (from 20 to 50 % allowing the laser flux), then a decrease as a function of the time *(fig. 1)*.
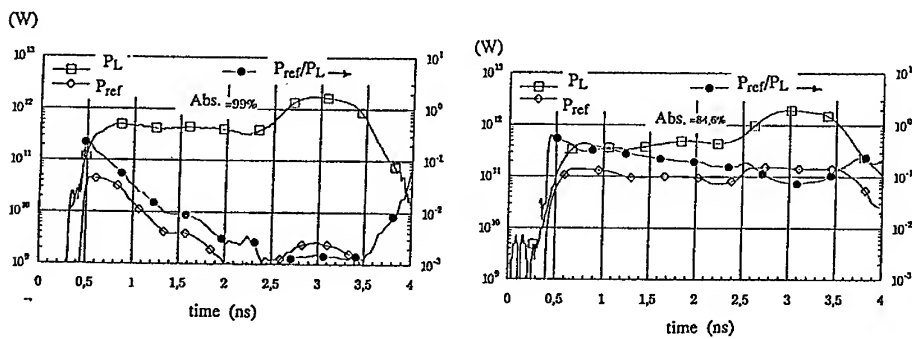
Fig. 1 Time evolutions of the refracted laser power (P_{ref}) and refraction efficiency (P_{ref}/P_L where P_L is the laser power). a- $\Phi^{L\,max} = 1.3 \times 10^{14}$ W/cm^2, b- $\Phi^{L\,max} = 2 \times 10^{15}$ W/cm^2.

For the X-ray instantaneous conversion efficiency (c. e.), the experiments show two features : a slight increase during the first step of the pulse (already observed in Nova experiments for long pulses[1]) and a significant decrease in the main pulse *(fig. 2)*.

Simulations were carried out with FCI1 and FCI2, 1D and 2D hydrodynamical codes with multigroup radiative transfer and non LTE ionization (Radiom model). Calculations confirm the measured behaviour, however the flux limit coefficient which allows to reproduce the c. e. in the low part of the pulse gives a too high value in the main part. An artifice to reproduce the time history of the c. e. is to change the flux limit coefficient during the calculation to have a stronger limitation of the thermal flux in the main pulse (f=0.03) than in the lower part (f=0.2 or 0.3) *(fig. 2)*.

2D simulations reproduce a little better instantaneous c. e. without changing f, but not quite, and give better spectral repartition, due to lateral conduction

---

[1] Ze and al., J. Appl. Phys., **66**, 1935, 1989.

effects which increase soft X-ray emission and limit the thermal axial conduction compared to 1D calculation.
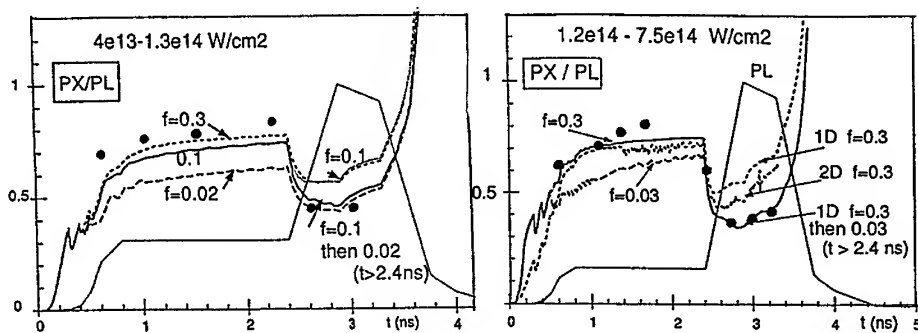
Fig. 2 Instantaneous X-ray conversion efficiencies for two-step pulses.
O experiments; full or dotted lines : simulations (f= flux limit coefficient).

From simulations, we found pulses with a slower rise which product constant conversion efficiencies. Subsequent experiments have been carried out with this sort of progressive pulses, and confirm this predicted evolution. In this case, the agreement between experiments and calculations is obtained without modifying thermal transport along the pulse, with f= 0.1 or 0.05 following the laser flux range *(fig. 3)*. These experiments confirm the hypothesis of the main pulse rising too fast having an influence on the fall of the instantaneous conversion efficiency.
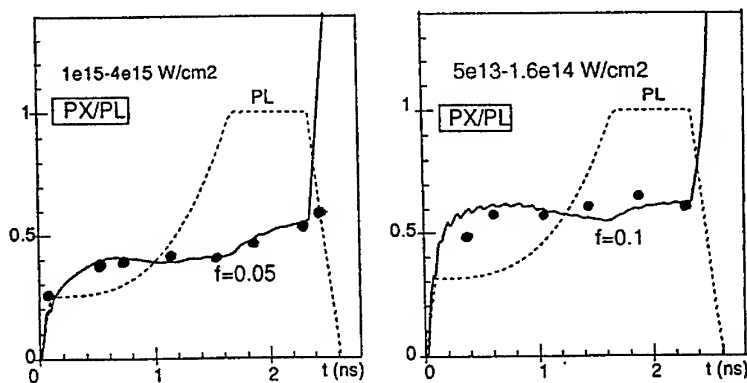
Fig. 3 Instantaneous X-ray conversion efficiencies for progressive pulses.
O experiments; full or dotted lines : simulations (f= flux limit coefficient).

480

All this is related to the problem of energy transport towards the x-ray emissive dense zone, when the pulse is rising too fast during the transition to the laser pulse main part. The figure (fig. 4) shows the comparison between various instantaneous conversion efficiencies of the laser energy in the interaction run. P_L and P_A are the laser incident and absorbed powers, P_X the X-ray emitted power. $P_{int} = d/dt$ (internal energy) and $P_{cin} = d/dt$ (kinetic energy). During the too fast rising pulse part, the instantaneous internal energy conversion efficiency (P_{int}/P_L) suddenly increases, while the instantaneous X-ray c. e. suddenly decreases.
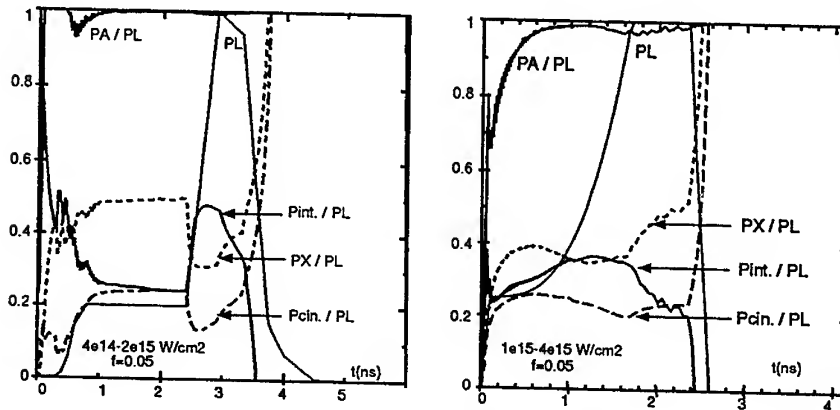
Fig. 4 Comparison of instantaneous conversion efficiencies of the laser energy for two-step and progressive pulses (1D simulations, f= flux limit coefficient).

3   Conclusion

Time resolved measurements, performed with Phebus laser, showed that laser pulse shaping has significant consequence on time evolution of X-ray conversion efficiency, which presents strong falls in the too fast rising parts of laser pulses. The effect exists in the simulations, but is not quite well calculated by hydrodynamical codes in the present conditions (we would need a better treatment of the thermal transport because of gradients steepening such as time dependent zoning, or a kinetic method ?), without changing conduction flux limitation during the pulse. On the contrary, experiments with progressive shapes show stationary conversion efficiencies and are correctly interpreted without transport modification even by a 1D code. Taking into account these stronger than expected variations of conversion efficiency would influence the time evolution of the temperature in the cavities and the megajoule laser pulse shape.

FORMING OF NONEQUILIBRIUM RADIATION AND ITS INFLUENCE ON HYDRODYNAMICS IN THE LASER TARGET

G.Vergunova, V.Rozanov

P.N.Lebedev Physical Institute, Russian Academy of Sciences, 117924 Moscow, Russia, Leninsky , 53

The optical constants determine the radiation spectral composition. Depending on the plasma parameters, the constants may be both equilibrium and nonequilibrium. In a general case the eigen radiation should be considered with account for the radiation effect on the optical constants. Here we discuss such a method. We discuss the influence of the radiation on the formation of the density and temperature profiles.

Under the laser action onto the target there is formed an absorption zone of the radiation; the radiation density in this zone is lower than the critical one, and the temperature is high. From the laser radiation absorption zone the energy inside the target is transported by the electron heat conductivity flux and the radiative wave. Depending on the plasma parameters, the energy flux in the radiative wave may exceed the energy in the heat conductivity wave. The shock wave is the fastest, and it propagates through the cold matter towards the back side of the target.

Thermodynamic conditions may be different, depending on the temperature and density of the plasma. Thermodynamic equilibrium is realised at relatively high densities and low temperatures of the plasma. Note that if there is observed the Thermodynamical equilibrium (LTE) in plasma, then the populations are determined by the following three aspects:

- the rate distribution of free electrons obeys the Maxwell function;

- the plasma ion composition is determined by Saha system of kinetic equations;

- the population of levels is determined by Boltzmann equations.

Under the conditions of local thermodynamical equilibrium the absorption coefficient k_ν' and the radiative capability j_ν' of the plasma are connected by the ratio : $j_\nu'' = k_\nu' I_{\nu p}.$.

In a general case the distribution of the populations may quite strongly differ from the thermodynamical equilibrium. If the plasma density decreases, the rates of the photoprocesses become comparable (or even higher) then the collision rates of the levels population. In the general case the field of the X-ray also influences the rates of the level population, and, thus, the optical constants of the

plasma. The population of each of the levels is determined by the balance of all the population processes, and the solution of the problem becomes very clumsy. It should be noted here that the energy distribution of free electrons is much closer to the Maxwellian, than the level distribution to the Boltzmann and Saha distributions.

Now consider the result of violation of conditions Saha and Boltzmann. Equalise the rates of photorecombination and the triple collision recombination [1,2]

$$R_z = C_{ph.r.} / C_{th.b.r.} N_e \approx (0.2 - 4)\beta^3 T_e^{3.5} \frac{A}{\bar{z}\rho}; \qquad (2)$$

where $C_{ph.r.}$, $C_{th.b.r.}$ are the rates of the photorecombination and the three body collision recombination; A, the matter atomic weight; $\bar{z}$, the average degree of ionisation; ρ, the density of the matter given in g/cm^3; T_e, the electron temperature in keV; $\beta = E_z/T_e$ the hydrogen-like approximation $R_z \sim z^7/N_e$, N_e is the electron density. From this follows, that with the growth of the ionisation multiplicity the range of the equilibrium states ($R_z \ll 1$) is shifted to the high densities. For the laser plasma, containing the elements with high nuclear charge z_n, the degree of ionisation may essentially differ from that obtained in Saha approximation. So, for Si ($z_n=14$) this difference is not significant, and for Au ($z_n=79$) it becomes large.

In the absence of the thermodynamical equilibrium, the photoprocesses are causing a decrease in the average degree of the plasma ionization, as compared to the assumed thermodynamical equilibrium. The distributions of the populations over the levels are different under the assumption of LTE and NLTE. So, the optical coefficients in these two cases are entirely different.

Moreover, in the absence of LTE the plasma radiative capability j_ν'. and the absorption coefficient k_ν' are not connected by the ratio $j_\nu' = k_\nu' I_{\nu p.}$. [3]. For example, if the distribution over the ionisation is not Saha equations, then $j_\nu' = k_\nu' I_{\nu p.} / (1 + R_z)$;

The influence of various optical constants on the radiation is discussed at the example of the calculations modelling the laser interaction with plane Cu targets. The experiments on planar copper foil irradiation have been conducted on the "Mishen" facility [4] under the following irradiation conditions: power density up to $5 \times 10^{13} W/cm^2$, wavelength - 1.054 μm, focal spot diameter ~200 μm. With the help of two X-ray spectrometers - mica crystal spectrometer and transmission grating spectrometer - the X-ray spectra of the produced plasma were measured in the range of 0.1 - 2.5 keV. The X-ray conversion efficiency in the reported experiments was as high as 40-50 % in the above mentioned energy range. The L-spectra of Ne-like copper ions were emitted from the corona region
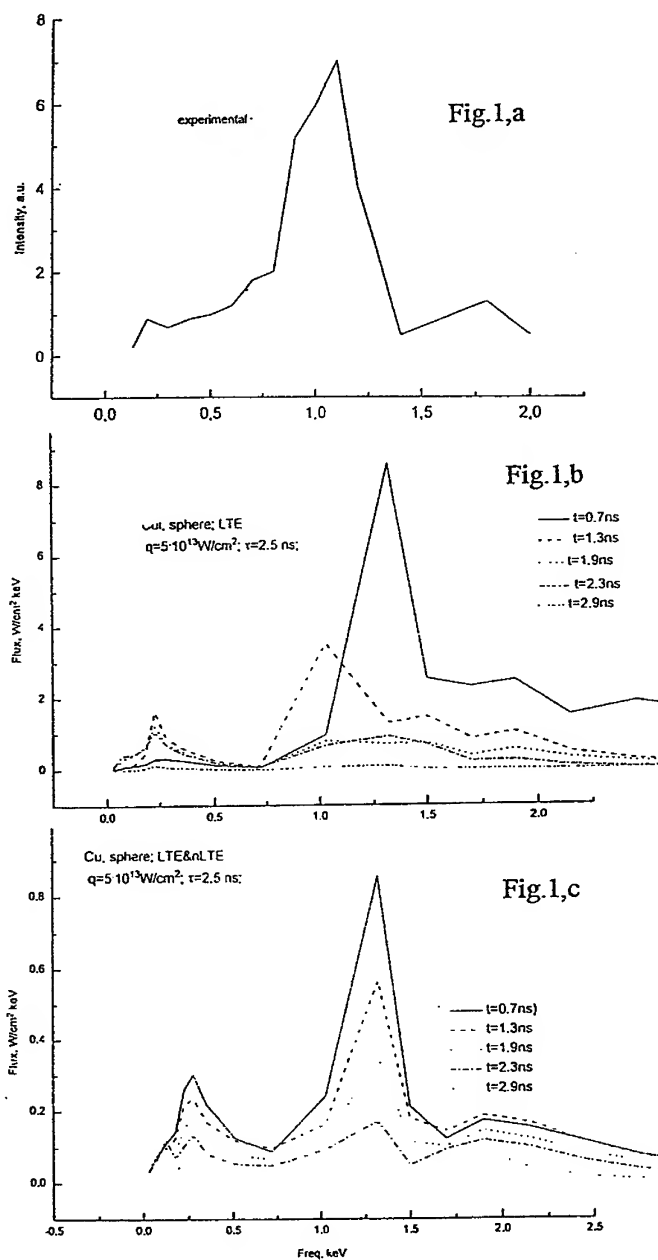
Fig.1. Experimental and calculated spectra.

484

with the temperature of ~500-600 eV and electron density of ~ 10^{21}cm^{-3}. More soft quanta were emitted from both the corona region and from the re-emission zone (average density ~10^{22}cm^{-3}, temperature $\leq$100eV), localised between the critical and ablation surfaces.

Figure 1 illustrates the experimental data which are compared to the calculated spectra that are obtained under assumption of the following optical constants. The radiative capability of the plasma and the absorption coefficients were calculated 1) in the LTE approximation, 2) in the optical transparent matter approximation (NLTE), and 3) in an intermediate case where the optical constants are interpolated between the constants derived in the LTE and the optically transparrent matter approximations with due regard for the self-radiation of the plasma [5]

$$ k = \frac{k_n}{1+\left(\dfrac{k_n}{k_e}-1\right)\dfrac{U}{U_p}} ; \qquad j = \frac{j_n}{1+\left(\dfrac{j_n}{j_e}-1\right)\dfrac{U}{U_p}} ; $$

where 'e'and 'n' radiative emissivity and coefficient of absoption in LTE and NLTE; U_p, , equilibrium density of the radiation; U, X-ray density.

The calculations using the LTE constants (Fig.1.b) yield 60% conversion, and the spectrum of the output radiation does not contradict the experimental data. The emission in the spectral range of 1.24-1.4 keV is yielded from the plasma with $T_e \approx$1 keV and $\rho \approx 10^{-3}$g/cm^3, and in the spectral range of $\approx$ 0.3 keV it is $\rho \approx$(3-5)$\times 10^{-3}$g/cm^3, this temperature is higher than the experimental result. In the calculations using the constants calculated in the optical transparent approximation and in the intermediate layer, the output of the X-ray emission is of 10% (the radiation spectrum is represented in Fig.1.c, for the case 3).. Hydrodynamical profiles are different in these cases.

References.

1. Yu.Afanas'ev, et al. 1982, Trudy FIAN, **134**, p.10-31.

2. G.Vergunova et al. 1990, Trudy FIAN, **203**, pp144-158

3. I.Sobelman, Introduction into the Theory of Atomic Spectra, Moscow, 1977, p.248-260.

4. G.A.Vergunova, V.G.Novikov, V.B.Rozanov. Preprint Lebedev Physics Institute N20, 1992.

5. B.Bazylev et al. JETP,1628-1648, **106**, 1994.

7.- LASER DEVELOPMENTS

AND

X-RAY LASERS

STUDIES OF PHENOMENA INVOLVED IN THE PREPULSE PUMPING OF COLLISIONAL X-RAY LASERS BY OPTICAL INTERFEROMETRY

M. KÁLAL

*Czech Technical University, Department of Physical Electronics, V Holešovičkách 2,
180 00 Prague 8, Czech Republic*

B. RUS, T. MOCEK, J. SKÁLA, B. KRÁLIKOVÁ

Institute of Physics, Department of Gas Lasers, 180 40 Prague 8, Czech Republic

P. ZEITOUN, S. SEBBAN, G. JAMELOT

*Université Paris-Sud, Laboratoire de Spectroscopie Atomique et Ionique, Bât. 350,
91405 Orsay Cedex, France*

A. DEMIR, G.J. TALLENTS

University of Essex, Department of Physics, Colchester CO4 3SQ, U.K.

Interferometry measurements of line plasmas created by the iodine laser PERUN ($\lambda = 1.315\,\mu$m, $\tau \approx 400$ ps FWHM) with intensities equivalent to those generated by low-level prepulses in the collisional excitation soft X-ray lasers (4×10^9 - 1.2×10^{11} Wcm^{-2}) are presented. The interferograms were taken with 4 and 10 ns delays with respect to the peak of the drive laser pulse using the third harmonic of the iodine laser ($\lambda = 438$ nm). Zn (Z=30) and Cu (Z=29) were investigated aiming to account for the appreciable difference of the effect of a weak prepulse in the corresponding J=0-1 soft X-ray lasers, which were recently observed. The results clearly show that the preplasma parameters significantly depend on the target material.

The influence of a weak prepulse on the efficiency of the collisional excitation J=0-1 soft X-ray lasers can now be regarded as a well established fact[1,2]. This phenomenon, however, is not yet sufficiently understood. A big difference of this effect for neighbouring elements (an optimum J=0-1 lasing for a certain combination of prepulse intensity and delay was found in Zn (Z=30) unlike to Cu (Z=29)) belongs to one of its most puzzling features[3]. The computer simulations have so far failed to explain this behaviour.

The experiment on characterization of the prepulse plasmas was carried out at the iodine laser system PERUN at the Institute of Physics in Prague (details of the experimental arrangement were described elsewhere[4]).

A Nomarski interferometer[5] setup was used in a configuration in which the plasma is shone through *down the plasma column axis* (Fig. 1) by a 438 nm 3ω probe beam.

488
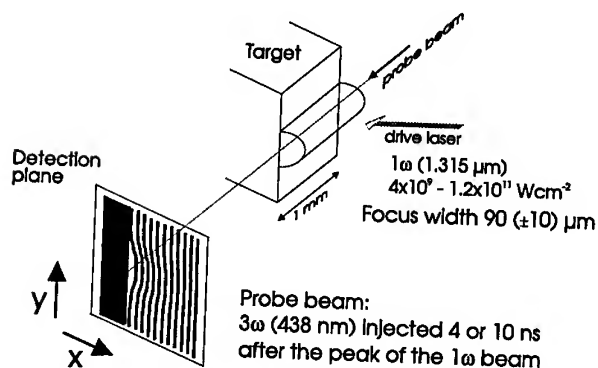
Figure 1: Probe beam path down the plasma column axis.

As shown in Figures 2 and 3 the technique employed made it possible to access electron density up to $\approx 2 \times 10^{19}\,\mathrm{cm}^{-3}$ and to obtain its genuine 2D distribution in the plane perpendicular to the plasma axis (no Abel inversion needed for density unfolding). The surface plasma region where no analysable fringes appear due to refraction/absorption effects is represented in Figs 2 and 3 by the density evaluated from the first distinguishable fringe. It is seen that below $2 \times 10^{10}\,\mathrm{Wcm}^{-2}$ no Cu plasma of appreciable density is created, whilst the opposite is true for Zn. Above this irradiance threshold the density of the Cu plasma in $t = 4\,\mathrm{ns}$ is similar or grater than that of Zn, whilst it appears to decay more quickly that the Zn plasma, as seen from the $t = 10\,\mathrm{ns}$ data. The plasma corona in both cases reveals rather unexpected features, such as the density "jets" and "flanks" surrounding the laser impact region. The major finding is that appreciable differences exists between the two elements even for $10^{11}\,\mathrm{Wcm}^{-2}$ which means that the solid state properties of the target play a substantial role in the plasma evolution. The data equally suggest that for a given element the plasma cannot be brought to mimic the shape of the plasma of another element by merely varying the irradiance, thus giving some insight why the different dependence of J=0-1 output for Zn and Cu with respect to the prepulse intensity has been found for a fixed delay (Ref. 3).

1. G.F. Cairns *et al*, *AIP Conf. Proceedings* **332**, 289 (1995).
2. P. Jaeglé *et al*, *AIP Conf. Proceedings* **332**, 25 (1995).
3. A.G. MacPhee *et al*, *Optics Comm. (submitted)* , May (1996).
4. M. Kalal *et al*, *Proc. SPIE* **2767**, 119 (1996).
5. M. Kalal *et al*, *J. Appl. Phys.* **64**, 3845 (1988).
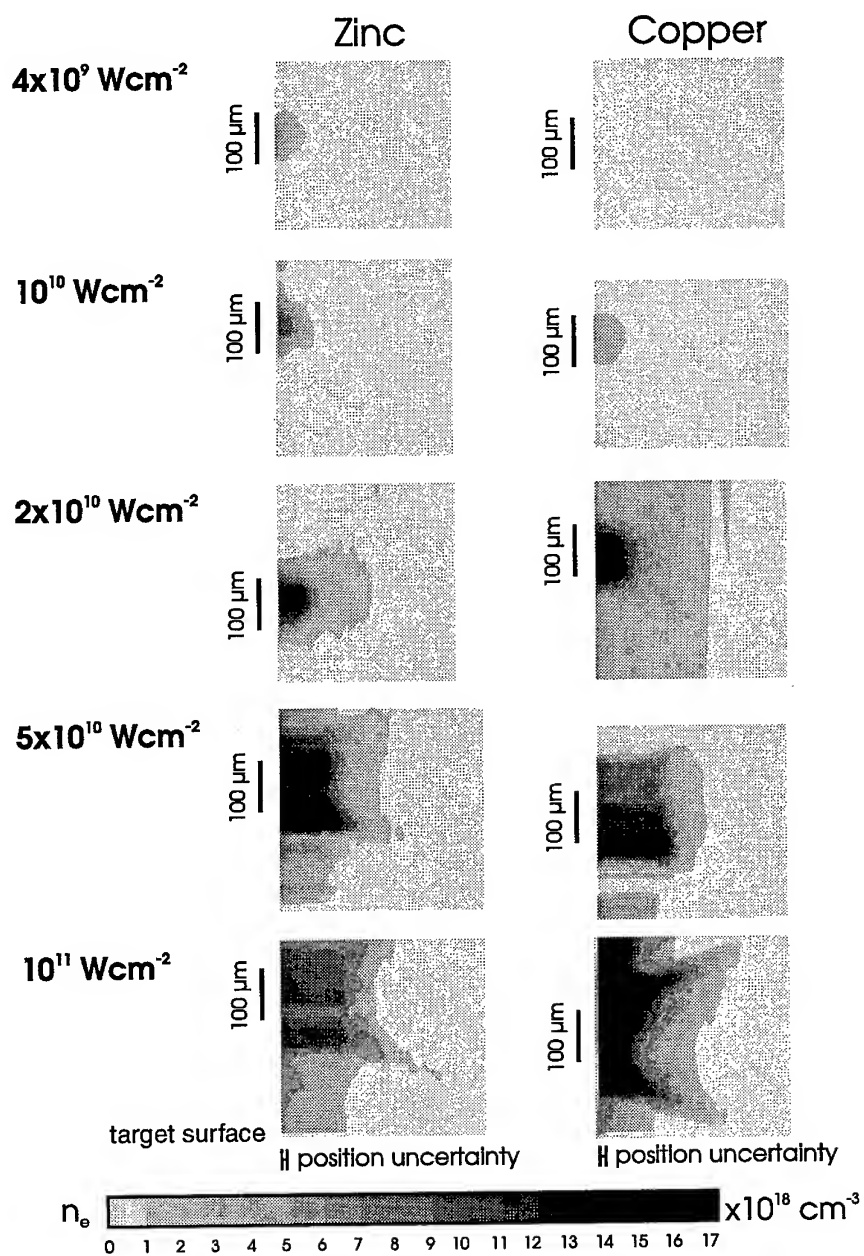
Figure 2. Electron density distribution at t=4 ns after the laser pulse peak.

490

Zinc

Copper

10^{10} Wcm^{-2}

100 μm

100 μm

2x10^{10} Wcm^{-2}

100 μm

100 μm

5x10^{10} Wcm^{-2}

100 μm

100 μm

10^{11} Wcm^{-2}

100 μm

100 μm

target surface

⊩ position uncertainty

⊩ position uncertainty

n$_e$

x10^{18} cm^{-3}

0 1 2 3 4 5 6 7 8 9 10 11 12 13 14 15 16 17
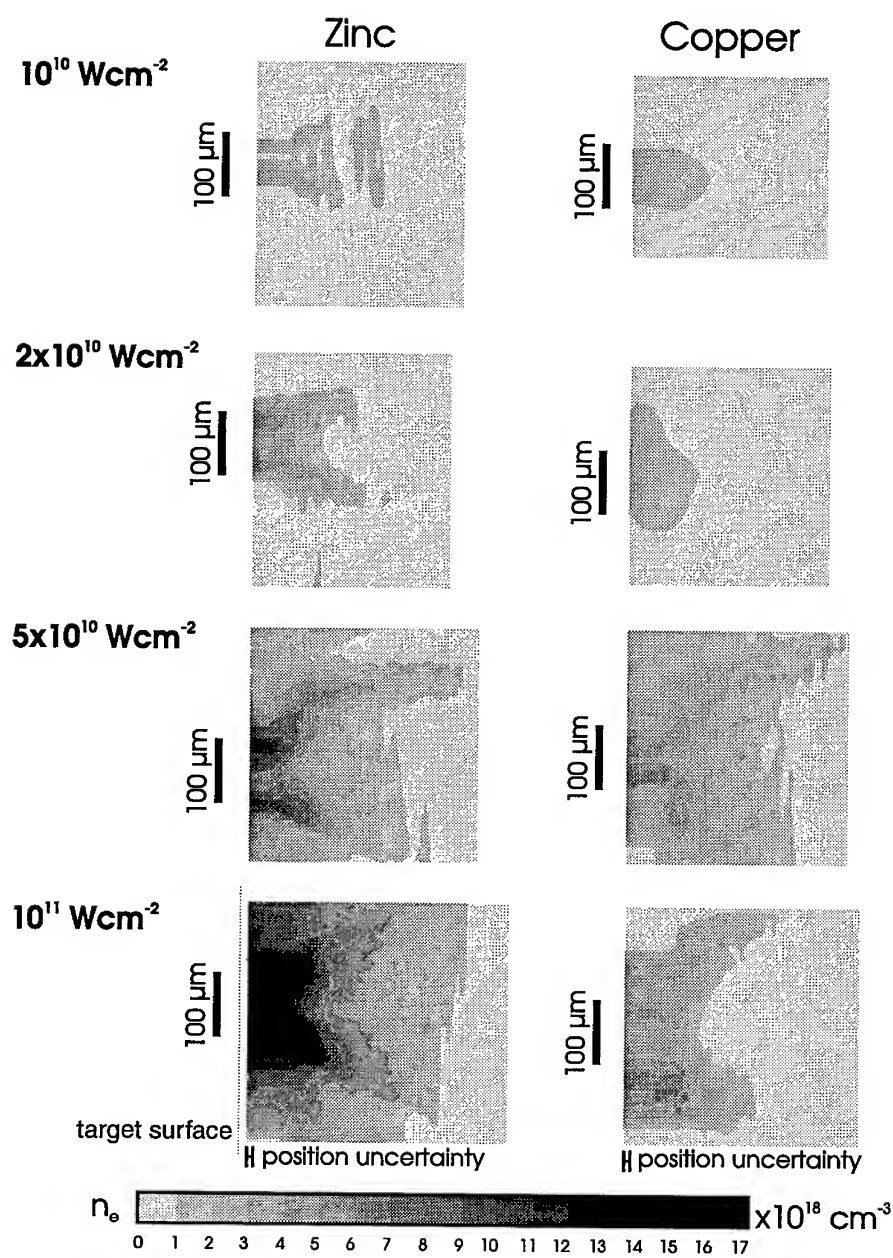
Figure 3. Electron density distribution at t=10 ns after the laser pulse peak.

Channeling of High Intensity Laser Pulse in a Plasma Capillary Channel

Y. Ehrlich, C. Cohen, A. Zigler
Hebrew University, Jerusalem , Israel

J. Krall, P. Sprangle
Naval Research Laboratory, Washington D.C., U.S.A.

An experimental study of optical guiding of a high intensity (above 10^{16} W/cm^2) laser pulse in 1cm long cylindrical plasma channel formed by a slow capillary discharge is presented. Optical guiding of a high intensity pulse in a straight and curved trajectory (radius of curvature = 4.2 cm) is demonstrated for the first time. It is shown experimentally, that the obtained guiding is a linear process and therefore insensitive to the laser intensity in wide range of intensities. Experimental results are in agreement with theoretical estimates and with results from a 2-D numerical simulation code.

Studies of the characteristics of intense laser pulses propagating in plasmas have important implications for such devices as laser driven plasma accelerators, X-ray lasers, harmonic generators and laser fusion drivers.[1-6] However, the plasma volume subjected to the high intensity beam is limited by laser beam diffraction.[7] Optical guiding is one of necessary solutions in order to propagate a laser pulse over distances larger than the vacuum diffraction limited length. Guiding in a preformed plasma channel has been demonstrated previously[7,10] using two laser pulses.

In this paper we report the optical guiding of a high intensity laser pulse over a distances of several Rayleigh length using a plasma channel formed by a slow electrical discharge in a cylindrical capillary . Using this guiding technique, we have obtaining the first demonstration of guiding of a high intensity laser pulse along a curved trajectory. This can have important applications such as possible efficient circular medium for the future X-ray lasers , optical synchrotrons and laser accelerators.

The distance over which guiding is possible appears to be limited only by the capillary length and absorption of the laser by the plasma. Temperature and density of the plasma near the capillary axis can be modified over a wide range[11], independently of guiding conditions (channel absolute depth and width).

The plasma channel is formed by a slow capillary discharge. A typical constricted, ablation dominated capillary discharge configuration consists a 1cm long polypropylene cylinder with a 350μm hole along it. The cylinder is

placed between two electrodes which are connected to the discharge capacitor which stores 0.2 through 0.5 joules and initiated by a triggered spark-gap. The maximum discharge repetition rate is 1.5 Hz. Under conditions where the flow kinetic energy is smaller than the thermal energy , the balance between the power radiated by plasma and the input electrical power defines the plasma temperature T, capillary resistance R., and plasma density ne as functions of the capillary geometry and the current I. This simple approximation yields the following scaling rules: $T=3.3\ I^{0.36}$eV, $n_e = 1.3*10^{20}\ I^{0.91}$ cm^{-3}, and R=1.71 $I^{-0.55}\Omega$, where I is in kA [11]. It was shown that the capillary plasma density and temperature can be simply controlled by varying the electrical parameters of the external circuit[11].

The plasma radial density profile inside the discharge has a density maximum near the walls of the capillary and minimum in the center. For experiments in which the capillary radius was smaller than Rosseland mean free path that controls the radiation losses, the radial electron density profile was found to be parabolic [12]. This feature results from the radial profiles of the pressure and temperature . The pressure across the capillary is expected to be constant, since any disturbance in radial direction will equilibrate with a time scale given by the capillary radius divided by sound speed. This time scale is much shorter than the discharge duration($\sim$ 1μsec) and the flow time along the plasma channel. The temperature is higher at the center and drops near the wall, due to radiation and collisional heat transfer. Therefore, the density is lower at the center and higher near the capillary walls. In the experiments, the axial plasma temperature was $\sim$3eV and the electron density varied within the range $\sim 1*10^{19}$cm^{-3} to $5*10^{19}$cm^{-3}.

For a parabolic plasma channel it can be shown that a Gaussian laser pulse will be matched within the channel with laser spot radius $r_L=(\pi r_e \Delta n)$, where r_e is the classical electron radius. For representative parameters, r_{ch} =150μm and Δn =5x10^{18}cm^{-3}, the matched beam radius is 27 μm. Because the capillary discharge typically produces a large - radius channel, it is capable of transmitting a large range of laser beam width, at one extreme, a laser with $r_L = r_{ch}$ =150 μm can be guided with a density depression of $\Delta n/n < 1\%$. In addition, the capillary can produce a very large density depression ($\Delta n > 10^{19}$ cm^{-3}), such that tightly - focused laser pulses (r$\leq$10μm) can be guided.

The propagation experiments were carried out using a 1cm long cylindrical polypropylene capillary tube with an inner diameter of 350μm . The discharge is initiated by a triggered spark-gap. The experiments were carried out using the Hebrew University Laser System that consists of a Ti-Sapphire oscillator followed by regenerative and double pass amplifiers. The system is capable of delivering a 100femtosecond pulse with energy up to 50mj at 800nm and

repetition rate of 10Hz. Timing electronics, that trigger both the laser and the spark-gap, allow for a variable delay between the initiation of the electrical discharge and the arrival of the laser pulse . The laser was focused on the capillary channel by means an F#=11.5 lens. The laser energy delivered into the capillary and the amount transmitted through was measured by beam splitting and focusing into two calibrated photo-diodes. The laser light transmitted through the plasma channel was collected and reimaged by an optical system onto a CCD camera. The imaged intensities were reduced by inserting thin calibrated neutral density filters. The beam interference in these filters is responsible for the beam profile modulation seen in Figure 1. This figure shows the images of the laser beam at the capillary exit, recorded by the CCD camera with and without the discharge . Laser beam propagation after passing through the capillary channel was studied by recording the images of the transmitted light at various distances from the channel. The distances were varied between 0 to 1cm from the capillary exit . In the case of the straight capillary, the focusing and collecting optics are placed on the same optical axis . In the curved capillary experiments the optical systems were placed at the angle of 7° relative to the channel axis (14° between the two optical systems axes). The curved capillary tube had $350\mu m$ in diameter (identical to the straight capillary) and 4.2cm radius of curvature.

Experimental results show enhanced pulse transmission and substantial reduction of the radius of the transmitted laser light when the capillary is discharged. When the laser light focused by f# = 11.5 lens was transmitted through the capillary without an electrical discharge, the transmission was found to be 25%. This value corresponds to the geometrical opening of the capillary and indicates very low reflection at the capillary walls. The radius of the transmitted laser light at the capillary exit equals the capillary radius ($175\mu m$) equal to the capillary radius. When the pulse is focused into the capillary entrance 250ns after initiation of the electrical discharge, the transmission goes up to 75% and the emerging pulse radius is reduced to $30\mu m$ (Figure 2). Experimental results show a critical sensitivity to alignment (in accordance with [14]) and timing between initiation of the discharge and the arrival of the laser light . The capillary wall ablation was found to be relatively small and a hundred shots did not cause significant widening of the capillary channel. Measurements of the beam diameter were obtained by varying a distance between the capillary exit and the focal plain of the collecting optical system. It was found that the pulse radius didn't vary significantly in the range of 2mm to 7mm away from the capillary exit .

The experimental results of optical guiding in the curved capillary were very sensitive to alignment, particularly the angle of the laser beam with re-

494
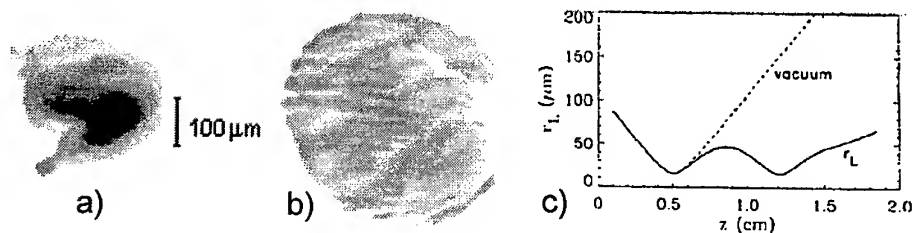
Figure 1: Laser spot image at capillary exit: a. with discharge b. without c. spot size as function of propagation (simulation).

spect to the capillary. With optimal alignment, transmitted intensity increases by a factor of 12, with pulse radius less than 100μm at the capillary exit.

To examine propagation of the laser pulse into, through, and out of the straight channel, simulations were performed using the 2D LEM nonlinear laser code [15]. Fig. 1c shows the laser spot radius r_L plotted versus propagation distance z through the channel, which is located at $0.5 < z < 1.5$cm. In the simulation, the on-axis plasma density is $5.0*10^{18}$ cm^{-3}, $\Delta n = 5.0*10^{18}$ cm^{-8}, and $r_{ch} = 150\mu$m. For comparison, laser propagation in vacuum (no channel) is also shown.

References

[1] See, e.g., *Advanced Accelerator Concepts*, edited by J. Wurtele, AIP Conf. Proc. No. 279 (AIP, New York, 1993).

[2] C.E. Clayton et al . Phys. Rev. Lett. **70**, 37 (1993).

[3] P. Sprangle et. al., Appl. Phys. Lett. **53**, 2146 (1988).

[4] H. Milchberg, C. Durfee, J. Lynch, J. Opt. Soc. Am. B **12**, 731 (1995).

[5] P. Sprangle et. al., Phys. Rev. Lett. **69**, 2200, (1992).

[6] J. Macklin, J. Kmetec, C. Gordon, Phys. Rev. Lett. **70**, 760, (1993).

[7] C. Durfee, J. Lynch, H. Milchberg, Phys. Rev. E **51**, 2368 (1995).

[8] C.E Max, J. Arons and A.B Langdon, Phys. Rev.Lett. **33**, 209 (1974).

[9] G.Z. Sun, E Ott, Y.C.Lee, P. Guzdar, Phys. Fluids **30**, 526 (1987).

[10] C. Durfee, H. Milchberg, Phys. Rev. Lett. **71**, 2409 (1993).

[11] Y. Ehrlich et al, Appl. Phys. Lett. **64**, 3542 (1994).

[12] E. Lithman, M.Sc. Thesis, Hebrew Univ., (1995).

[13] P. Sprangle, E. Esarey, Phys. Fluids B **4**, 2241 (1992).

[14] P. Sprangle, J. Krall, E. Esarey, Phys. Rev. Lett. **73**, 3544 (1994).

[15] J. Krall, E. Esarey, P. Sprangle, Phys. Plas. **1**, 1738 (1994).

Observation of enhanced emission from a stagnant plasma heated by plasma collision

H.YASHIRO, E.TAKAHASHI, Y.MATSUMOTO, T.TOMIE, and Y.OWADANO
Electrotechnical Laboratory, AIST, MITI,
1-1-4 Umezono, Tsukuba, Ibaraki 305, JAPAN

Enhanced spectral line emissions from the stagnated region of symmetrical counter streaming plasmas produced by a KrF laser was observed. This results showed the heating of the plasma by the stagnation. This symmetrical configuration produce the gentle density gradient at this stagnated region. This technique is feasible to decrease the refraction of amplified spontaneous emissions of x-ray lasers by the electron collisional pumping scheme.

1 Introduction

For development of a soft x-ray laser using laser-produced plasma, refraction of amplified spontaneous emissions in the plasma caused by steep density gradient is one of the serious problems. Especially for electron collisional pumping scheme using Ne or Ni-like ion, population inversion is produced at high temperature region near the target surface which is steep density gradient. Then, the amplified spontaneous emissions can be easily refracted to outside of the gain region.

Collision of counter streaming plasmas has been investigated to understand the hydrodynamics of the plasma for the study of inertial confinement fusion especially for the indirect drive scheme.[1,2] If the configuration of the two plasmas are symmetric and two plasmas collide with each other, moderate density gradient will be produced in stagnated region. Moreover, the stagnation caused by the plasma collision raises the plasma electron temperature. If this increase of the electron temperature is sufficient, the stagnant region of the counter streaming plasmas is suitable as the soft x-ray laser medium for the electron collisional pumping scheme.

In this paper we tried to produce gentle density gradient region by the counter streaming plasmas. The enhanced emissions from stagnant plasma by the collision were observed and compared with the one-dimensional hydrodynamic simulation.

2 Experimental arrangement

The experimental setup is illustrated in Fig. 1. The experiment was performed by using a KrF laser system named ASHURA.[3] In this experiment the pulse width was set about 10 ns FWHM (full width at half maximum) and two laser beams were used to produce the two symmetric counter streaming plasmas. Each laser beam was synchronized and irradiated on each target. The x-ray pinhole camera with Al filter was set perpendicular to the direction of the plasma flow to observe the plasmas

496

Top view

KrF laser

Side view

Probe beam

KrF laser

Al

Plasma

Mg

TlAP crystal
spectrograph

Interferometer

Probe beam

Target

Plasma

X-ray pin-hole camera

Interferometer
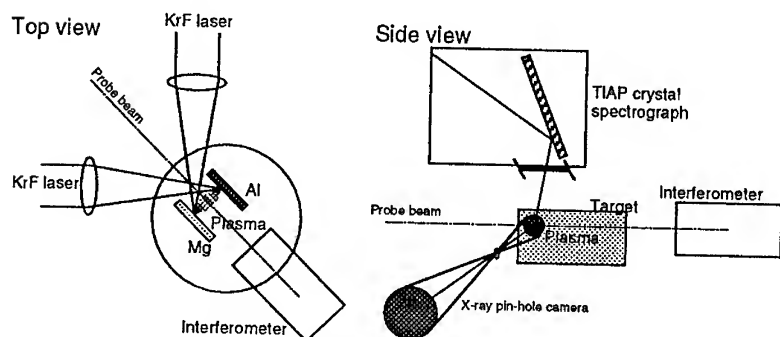
Fig. 1. Schematic diagram of the experimental arrangement.

blow-off from the target. Laser spot diameter was also observed previously by using the same x-ray pinhole camera, and it was about 150 µm. Each laser irradiance on the target was about 1×10^{13} W/cm^2. The distance between two targets was set to be about 1 mm to distinguish the enhanced emission from the stagnant region from the ordinary spontaneous emission near the target surface. Magnesium (z=12) and Aluminum (z=13) slabs were selected as targets to distinguish the spectral lines and to produce the hydrodynamically similar plasmas. A TlAP crystal spectrometry was also used to observe the spectral lines from H-like and He-like Mg and Al ions. An entrance slit equipped with the spectrometry gave the spatial resolution of 60 µm along the plasma expansion direction. Kodak DEF films were used to record the Mg and Al spectral lines. In order to observe the electron density profile, interferogram of the counter streaming plasmas was also taken by using the shortened Stokes probe pulse.[4]

3 Results and discussions

In Fig. 2, the colliding plasma taken by the x-ray pinhole camera is shown. A spectrogram of the colliding plasmas taken by the TlAP crystal spectrometer is shown in Fig. 3 and the spatial profile of the He α spectral lines of Mg and Al ions are shown in Fig. 4. These results show that x-ray emissions decrease as the plasma expand from the target. However, at the center between two targets, all the spectral lines from Mg and Al ions even satellite lines of Mg He α are enhanced. This enhancement of the emissions indicates the raising of the electron

C

C

A

B

1.0 mm

D

280 µm

60 µm

D
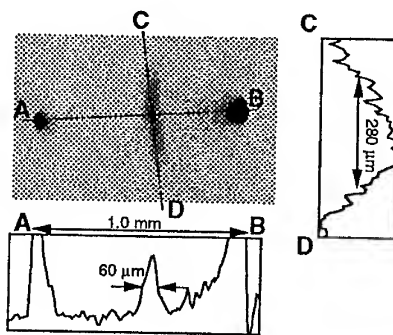
Fig. 2. X-ray pinhole images of the counter streaming plasmas.
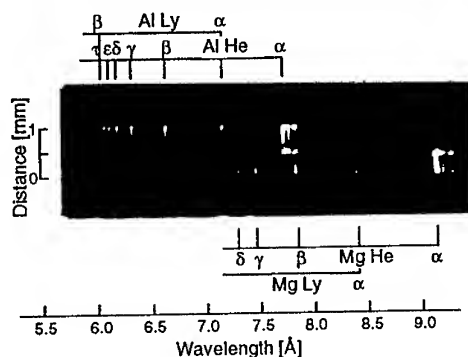
Fig. 3. Space resolved x-ray spectrograph of the counter streaming plasmas.

Fig. 4. Mg and Al He α intentisies as a function of the distance from the targets.

temperature by the stagnation. This peak of the x-ray emission from the stagnant area was very narrow although the plasmas were ejected during the 10 ns pulse irradiation. This result of narrow peak showed that the counter streaming plasmas produced by this configuration were stopped by the other plasma effectively and the motional energy of the plasma was transferred to the thermal energy effectively. However, these results also indicates that the electron temperature at the stagnated region is lower than that around the target surface. Each peak of Mg and Al He α lines was separated about 100 μm as shown in Fig. 4. This disagreement of the peak position is due to short mean free pass of plasmas and little mixing between Mg and Al.

The interferogram of the counter streaming plasmas is shown in Fig. 5. The symmetrical profile of the plasmas and increase of electron density at the center were observed. And the electron density at the stagnant region was evaluated about 10^{19} cm^{-3}.

To understand this enhancement of the spectral lines one-dimensional hydrodynamic model was considered. The target shape was assumed to be a sphere of 50 μm radius to make the expansion similar to the real plasma. We assumed that the plasma was accelerated from the target surface, and at 0.6 mm distance from the surface, all the motional energy of the plasma was transferred to the thermal energy of the plasma. In this
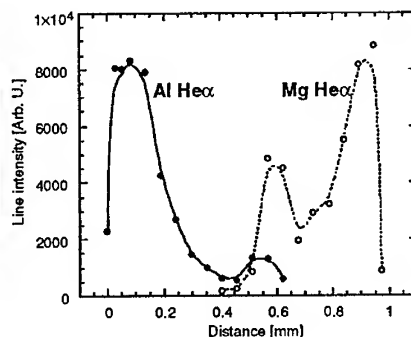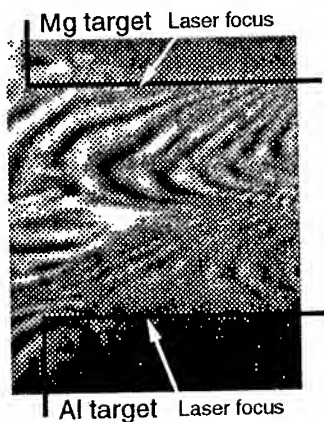
Fig. 5. Interferogram of the symmetrical counter streaming plasmas.

498

simulation the laser irradiance was 3×10^{13} W/cm^2. This numerical result about the electron temperature and density as a function of the distance from the target are shown in Fig. 6. This numerical result of the electron temperature at the stagnant region was twice of the temperature around the surface of the target. However, the experimental result of the spectrogram showed the electron temperature at the stagnant region was lower than the surface of the target. The reason for this difference in the electron temperature is considered to be two-dimensional behavior of real plasmas in the stagnant region. The lateral motion of the real plasma prevents the complete recovery of thermal energy which takes place in one-dimensional simulations. This difference of the electron temperature came from the difference between one-dimensional assumption of the theoretical simulation and the real plasma. However, these experimental and theoretical results indicates the efficient raising of the electron temperature at the stagnant region.

Fig. 6. Theoretical results of one-dimensional hydrodynamic simulation.

4 Summary

In order to produce the low density gradient region of the laser-produced plasma, collision of the counter streaming plasmas was applied. The enhanced x-ray emissions from the stagnant region of the counter streaming plasmas were observed. The electron density increase was observed by the interferometry using Stokes beam. This indicates the effective energy conversion from the motion of the plasma flow to the thermal energy of the plasma at the stagnant region.

References

1. R.A.Bosch et al., *Phys. Fluids* B4, **4**, 979, (1992).
2. M.Dirksmoller et al., *Optics Commun.* **118**, 379, (1995).
3. Y.Owadano et al., *Laser and Particle Beams* **11**, 347, (1992).
4. E.Takahashi et al., *Jpn. J. Appl. Phys.* **34**, L856, (1995).

ULTRAHIGH HARMONIC GENERATION FROM DIATOMIC MOLECULAR IONS

PABLO MORENO, LUIS PLAJA AND LUIS ROSO

Departamento de Física Aplicada, Universidad de Salamanca
E-37008 Salamanca, Spain

We study harmonic spectra from H_2^+ subjected to very intense low-frequency laser pulses. We report the production of harmonic frequencies far beyond the atomic cutoff frequency. These high frequencies are achieved whenever the molecular structure and the electric field parameters provide an appreciable value for the ratio between internuclear distance and the amplitude of oscillation of the ionized electron within the field.

1 Introduction

High-order harmonic generation by gas targets has proved to be a very promising mechanism to achieve coherent radiation sources at large frequencies. So far, the physical origin of the high photon energies in harmonic spectra from atoms has been well understood through the so called *two-step* model. This model predicts photon energies up to $I_p + 3.2U_p$, where I_p is the atomic ionization potential and $U_p = I/4\omega^2$ is the mean kinetic energy of a free electron in the laser field. [1] The same nonlinear dynamical behaviour leading to the production of harmonics is found to happen in any medium submitted to enough intense fields. Notwithstanding, harmonic frequencies beyond the atomic cutoff law have been never reported in the laboratories as well as in numerical experiments. Numerical simulations of the interaction of the ion H_2^+ with intense fields were carried out some years ago [2], and did not reveal any divergence with regard to the atomic law for the harmonic cutoff frequency. The laser parameters were assumed to allow for tunnel ionization of the electron.

We want to demonstrate that under some special but not unrealistic conditions, the harmonic yield from H_2^+ could exhibit peaks with frequencies beyond the prediction of the atomic cutoff law. We will solve one-dimensional time dependent Schrödinger equation for an electron moving in the potential of the molecular ion H_2^+ and a periodic laser field $E(t)$. We assume the field is linearly polarized and the wells are aligned along the direction of polarization, the latter being supported by both experimental and theoretical evidences. The high intensity allows to consider the dynamics restrained to the polarization direction. We will apply the two-step model in order to understand these ultrahigh photon energies in the spectra.

(a)

(b)
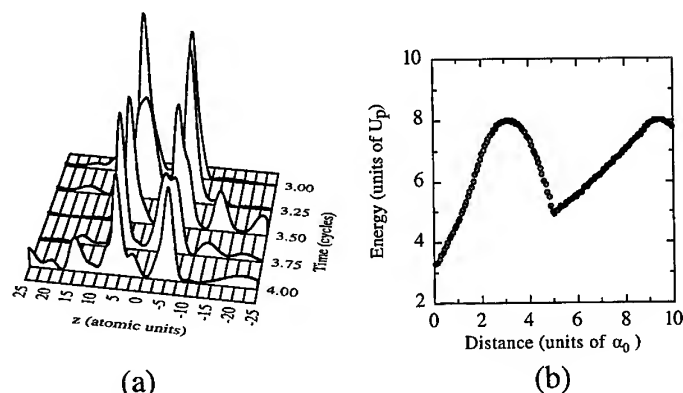
Figure 1: (a) Time evolution of the electronic charge density for one-dimensional H_2^+ with $R = 11$ a.u. in a pulse of peak intensity 1.26×10^{14} W/cm^2 and frequency $\omega = 1.632$ eV. We have plotted the first cycle after a ramp turnon of three cycles; (b) Dependence of the classical kinetic energies of the electron driven by an electric field with distance. The electron is assumed to be released by tunnel effect.

2   Enhancement of the harmonic frequencies in ITI regime

For high intensities of the laser pulse, electrons in molecular systems can undergo a process of inhibition of tunnel effect between the wells. [3] As a result of the large Stark shift of the electronic levels, the electron has a very small probability to cross the internal potential barrier towards the lower well in each half cycle of the field. Therefore, the electronic charge density remains localized in the rising well of the molecular potential. In such conditions, this part of the electron cloud can be detached to the continuum states directly through or over the internal barrier. These processes are called internal tunnel ionization (ITI) and internal barrier suppression ionization (IBSI), respectively. The time evolution of the charge density for a pulse with appropriate intensity and frequency shows the presence of electronic charge density inbetween the wells demonstrating that internal tunnel ionization is happening (Fig. 1a). The presence of peaks in the ionization rate curves from H_2^+ for some internuclear distances for which ITI or IBSI are expected, gives a further confirmation of these ionization procedures. [4]

Electrons detached from atoms or molecules evolve in the continuum states driven by the electric field. This subsequent motion is periodic with an amplitude of oscillation given by $\alpha_0 = \sqrt{I}/\omega^2$, and the exchange of energy between the field and the electron is periodic as well. Thus, the more intense the field the larger α_0 is. For rather small distances we can already consider the influ-
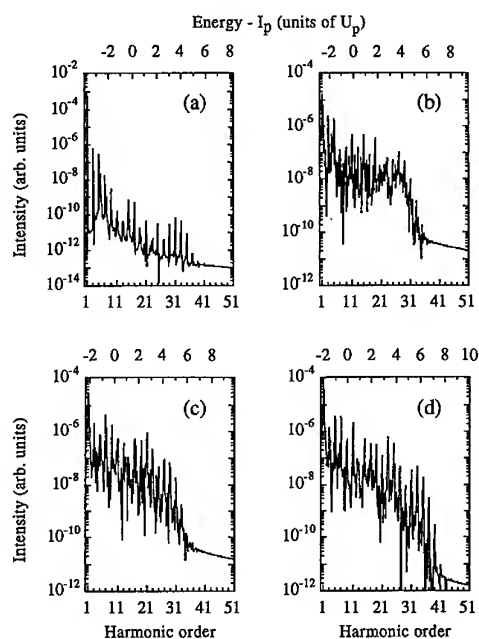
Figure 2: Harmonic spectra from one-dimensional H_2^+ with increasing internuclear distances: (a) 2, (b) 6, (c) 11 and (d) 20 a.u.. The field parameters are the same as in Fig. 1a, and the value of α_0 is about 17 a.u.

ence of the atomic or molecular potential on the ionized electron as negligible. Then, the dynamics of the ionized electron can be understood by means of classical dynamical equations. These equations predict that the electrons can absorb energies from the field up to $8U_p$ as they go far from the cores. We show in Fig. 1b the dependence of these maximum classical energies with the distance. Therefore, we should expect the charge density ionized through the internal barrier to absorb energy from the field as it covers its path between the cores. As this charge density scatters with the partner core it could release its kinetic energy as photons with frequencies up to $I_p + 8U_p$ depending on the internuclear distance R. In Fig. 2 we present a series of harmonic spectra from H_2^+ for increasing internuclear distances, showing the enhancement of the harmonic frequencies, in units of the ponderomotive energy, with the distance between the cores. In addition, the energies are the expected from a classical treatment of the ionized electron. The lower harmonic orders show the *plateau* produced by the charge resonace effect. We have chosen the same values of the

502

peak intensity and frequency of the pulse that in Fig. 1a, thus within internal tunnel ionization regime.

3   Conclusions and discussion

The previous paragraphs lead us to state that the enhancement of the high order *plateau* in the harmonic spectra from H_2^+, in terms of the ponderomotive energy, is closely related to the excursion of the electron in the continuum states, provided it is detached through the internal potential barrier. Therefore, the key parameter is the ratio

$$\frac{R}{\alpha_0} = \frac{R\omega^2}{\sqrt{I}}$$

The absence of such energetic peaks in previous numerical or laboratory experiments could then be explained as a result of the small value of this ratio. In fact, since the main role in this ultrahigh harmonic generation is played by the multiple-well structure of the molecular potential, the effect should be observable in any molecule or cluster under the conditions pointed out before.

The main drawback is to achieve that all the H_2^+ ions have the same internuclear distance at the same time. We can think of preparing them in the same highly excited vibrational states, but this state is inherently quite unstable against dissociation. Otherwise, we can think of keeping dissociation process under control by means of a prepulse, and then submit the ensemble to the ionizing pulse.

Acknowledgments

References

1. For a general review on harmonic generation by atoms, see *Atoms in Intense Laser Fields*, ed. M. Gavrila (Academic Press, Boston, 1992).
2. T. Zuo *et al*, *Phys. Rev.* A **48**, 3837 (1993).
3. F. Grossmann *et al*, *Phys. Rev. Lett.* **67**, 516 (1991).
4. T. Seidemann *et al*, *Phys. Rev. Lett.* **75**, 2819 (1995).

THEORY AND SIMULATION OF FUSION YIELD FROM DEUTERATED TARGETS IRRADIATED BY PICOSECOND LASER

N.N.DEMCHENKO, V.B.ROZANOV

Lebedev Physics Institute, Leninsky prospect, 53, 117924 Moscow, Russia

The direct ion heating effect was considered to explain high ion temperature in plasma produced by picosecond laser. The collisionless mechanisms of ion perturbation damping were taken into account. The code RAPID-SP was modified to calculate the neutron yields. The statement of problem corresponds to the experiments made at Rutherford Appleton Laboratory where the fusion yields from deuterated targets irradiated by picosecond laser were observed. The ion temperature about 100 keV and the neutron yield about 10^8-10^9 have been obtained in the calculations. It was found that the neutrons were produced in the dense part of a target heated by the ion thermal wave.

1 Introduction

The neutron yields of the order of 10^9 from deuterated targets irradiated by picosecond laser were observed in experiment [1]. This result demonstrates the presence in plasma of the high energy ions. The direct ion heating effect [2] can be considered to explain high ion temperature in plasma produced by picosecond laser. The hydrodynamic model was extended for high intensity laser pulse interaction with the target (code RAPID-SP) [3,4].

When high intensity laser pulse ($q\lambda^2 > 10^{15}$ $\mu m^2 W/cm^2$) interacts with the target, the laser flux is transformed mainly into a flux of superthermal electrons [5-7]. The collisional mechanism provides very small fraction of the absorbed flux. The energy of fast electrons is much greater than the thermal energy. The fast electrons are ejected by the field to the energy range significantly exceeding the thermal level. The process is similar to the electron beam propagation in plasma. The diffusion (in velocity space) goes from high to low energy values.

The ponderomotive forces and the related ion nonlinearities play an important role in plasma profile formation for the considered flux densities. The oscillating ponderomotive potential modulates the plasma density and velocity profiles. The dissipation of plasma perturbations leads to the increase of the internal ion and electron energies. There exist such conditions of the laser-plasma interaction when the dissipation is determined mainly by ions.

2 The direct ion heating effect

If the flux density is relatively low, the collisional dissipation of the ion perturbations takes place due to the ion viscosity [2]. The ions are heated in this

case. The rate of heating Q per unit plasma mass can be expressed in the form (linearized approach for homogeneous plasma)

$$Q \equiv \frac{\partial \bar{\varepsilon}_i}{\partial t} = \frac{2\mu k_0^2 u_0^2 G}{\rho_0 c^2 \rho_c^2 c_s^4} q_0 q_1 \tag{1}$$

$$G = \left[(M^2 - 1)^2 + \left(\frac{2\mu k_0 \beta_0 M}{\rho_0 c_s} \right)^2 \right]^{-1}$$

where $\bar{\varepsilon}_i$ is the specific internal ion energy averaged over the oscillation period; $\mu \approx \rho_0 v_{Ti} l_i$, the ion viscosity coefficient; $k_o = \omega / c$, the wave number; ω, the laser frequency; u_0, the velocity with respect to ponderomotive potential maxima; $c_s = \left[(ZT_e + T_i)/m_i \right]^{1/2}$, the sound velocity; $M = u_0 / c_s$, the Mach number; ρ_0, the nonperturbed plasma density; ρ_c, the critical density; q_0 and q_1, the incident and reflected fluxes of laser radiation; β_0, the refractive index. This heating can be considered as the work of the effective friction force between the electromagnetic field beatings and the plasma when the velocity of relative motion equals u_0. The friction force F_i per one ion can be defined by expression

$$F_i = \frac{m_i Q}{u_0} \tag{2}$$

The mean free path of the ions can exceed the ion wavelength with the flux density increase. In this case the wave dissipation occurs due to a collisionless damping on ions and electrons. With the electron inertia neglected, one can write for the longitudinal field in the ion wave [2]

$$E_l = k|P||R| b \sin(kx - \omega_i t + \Delta) \tag{3}$$

where $b = (a_1^2 + a_2^2 + 2a_1 a_2 \cos\delta)^{1/2}$, $a_1 = e/2m_e \omega^2$, $a_2 = T_e \sqrt{G}/8\pi e \rho_c c_s^2$, $k = 2\omega\beta_0/c$, $|P|$ and $|R|$ are the amplitudes of incident and reflected waves ($q_0 = c\beta_0|P|^2/8\pi$, $q_1 = c\beta_0|R|^2/8\pi$), $\omega_i = ku_0$, $tg\delta = 2\mu k_0 \beta_0 M/(M^2 - 1)\rho_0 c_s$, $tg\Delta = a_2 \sin\delta/(a_1 + a_2 \cos\delta)$. As the ion wave is monochromatic, it is necessary to take into account the distribution function deformation in the vicinity of the resonance velocity $v_x = \omega_i/k$. The ion wave damping factors can be written in the form [8,9]

$$\gamma_\alpha = \frac{\gamma_{0\alpha}}{1 + \eta_\alpha} \tag{4}$$

$$\eta_\alpha = \frac{(e_\alpha \varphi_0)^{3/2}}{\lambda v_{p\alpha} T_\alpha m_\alpha^{1/2}} \tag{5}$$

where $\alpha = e, i$ denotes the electron or ion values; λ is the ion wavelength; $\varphi_0 = b|P||R|$, the potential amplitude of a longitudinal field; $v_{pi} = 12\pi Z^4 e^4 n_i \Lambda_i / m_i v_p^3$, $\quad v_p = u_0$ for $u_0 > v_{Ti} = (T_i/m_i)^{1/2}$ and $v_p = v_{Ti}$ for $u_0 < v_{Ti}$; $v_{pe} = 12\pi Z^2 e^4 n_i \Lambda_e / m_e v_{Te}^3$; $\Lambda_{e,i}$, the Coulomb logarithms; $\gamma_{0\alpha}$, Landau damping factors. For a weak field limit ($\eta_{e,i} \ll 1$) we have $\gamma_i / \gamma_e = \gamma_{0i}/\gamma_{0e} = (m_i / Z m_e)^{1/2} s^{3/2} \exp[-\frac{1}{2} M^2 (s+1)]$, where $s = ZT_e/T_i$. The maximum value of γ_i / γ_e at the acoustic resonance ($M=1$) equals $30(A/Z)^{1/2}$ for $s=3$. Consequently, the wide regions of the temperature relations and Mach numbers exist for which the damping due to ions is the basic mechanism of the energy dissipation in the ion wave. For a strong field limit ($\eta_{e,i} \gg 1$) the maximum value of γ_i / γ_e (at $M=1$) equals $7.4(A/Z)^{1/2}$ for $s=2$. If the plasma is the mixture of different ions, the damping is defined by each type of the ions. The summarized damping factor is the broadened function of $Z^* T_e / T_i$ since it is a sum of functions with displaced maxima. Instead of the damping factors γ_α it is possible to consider the effective viscosity coefficients μ_α which result in the same damping factors

$$\mu_\alpha = \frac{2\gamma_\alpha \rho_0}{k^2} \tag{6}$$

This relation permits us to take into account the collisionless mechanisms in the hydrodynamic model.

It should be noted that the linearized theory fails in the vicinity of point $M=1$ for the strong field case. If the theory validity condition [2]

$$(q_0 q_1)^{1/2} / 4c\beta_0 \rho_c c_s^2 \ll (\gamma/\omega)^2 \tag{7}$$

is not satisfied, the high order garmonics are generated. In the strong field case it follows from (4)-(5) that $\gamma_i \to 0$ for $|M| \to 1$. Hence, there exists the region in the vicinity of $|M|=1$ where a stationary flow (in the field beatings frame) is impossible.

506

3 Simulation of neutron yield

The code RAPID-SP enables to simulate the interaction process on the base of hydrodynamic equations with account for the ponderomotive force, effective ion viscosity and the energy transport by ions, thermal and superthermal electrons, and on the base of Maxwell equations for oblique incidence of s- and p-polarized waves. The relativistic increase of the electron mass [10] and density (due to Lorentz contraction in contrast to [10]) are taken into account. Therefore, the plasma frequency is an invariant quantity. The following experimental conditions [1] were considered: massive deutereted polystyrene (C_8D_8) target was irradiated by p-polarised radiation at 30^0 angle of incidence. The laser energy of 20 J and pulse duration of 1.3 psec (at half of maximum) was focused to a 30 μm focal spot.

The density and temperature profiles for the moment of laser flux maximum are shown in Fig. 1. The ion and electron temperatures in underdense plasma have the values of 120 keV and 5 keV, respectively. The plasma density in this region has large perturbations. The flow has a chaotic character due to the strong field and sound point $|M| = 1$ appearance (condition (7) is not fulfilled). The calculated neutron yield equals 7.3×10^8. Neutron yields observed in the experiments have the values 8×10^8 - 4×10^9. The calculated neutron yield is somewhat lower than the experimental one. It is likely that this difference can be diminished by accounting for the beam-like ion energy transport in underdense plasma.

Fig. 1. Density and temperature profiles. Scale factors: ρ_0=1.72 g/cm^3, T_0=139 keV, x_0=139 μm.

References

[1] Fews A.P. et al Annual Report 1994-95 RAL Report TR-95-025 p.30-32

[2] Demchenko N.N. and Rozanov V.B. 1993 JETP 76 997-1001

[3] Demchenko N.N. et al 1990 Fizika Plasmy 16 812-817

[4] Kalashnikov M.P. et al 1994 Phys. Rev. Lett. 73 260-263

[5] Wilks S.C. et al 1992 Phys. Rev. Lett. 69 1383-1386

[6] Brunnel F. 1987 Phys. Rev. Lett. 59 52-55

[7] Gibbon P., Bell A.R. 1992 Phys. Rev. Lett. 68 1535-1538

[8] Sagdeev R.Z. 1964 Problems of Plasma Theory, N4, Ed. by Leontovich M.A. Moscow Atomizdat 20-80

[9] Zakharov V.E., Karpman V.I. 1962 Zh. Eksp. Teor. Fiz. 43 490-499

[10] Kaw P. and Dawson J. 1970 Phys. Fluids 13 472-481

Interaction of intense ultra-short laser pulses with solid targets

V.V.Kostin, N.E.Andreev, V.E.Fortov

High Energy Density Research Center OIVT RAS,
IVTAN, 127412, Moscow, Izhorskaya 13/19, Russia,

The interaction of an intense (10^{15} $<I<10^{17}$ W/cm^2) subpicosecond (0.1$<$t$<$0.5 ps) normally incident laser pulses with solid targets is investigated. Target material heating, redistribution of the absorbed energy in the target, plasma creation and shock wave generation are investigated.

1 Introduction

Recent developments in the generation of high power femtosecond laser pulses offer new possibilities in the studies of ultra fast phenomena. The interaction of power radiation with target substance is accompanied by ionization of matter in laser field, heating of the electron component of the produced plasma, electron-ion energy exchange, energy transport from the heated region via the electron thermal conductivity and radiation processes, and also by formation of a plasma corona and hydrodynamic flows of a matter. Presented work is aimed to the investigation of the following physical phenomena: laser irradiation absorption, target material heating and cooling, plasma expansion and influence of these phenomena on a shock wave generation in the irradiated matter.

The interaction of an intense ultra-short normally incident laser pulses with the solid targets is investigated for the laser irradiation wavelength equals to 0.35 mkm and pulse parameters mentioned above. In contrast to longer pulses, a femtosecond pulse deposits its energy in the target surface before significant hydrodynamic motion orthogonal to the surface occurs [1]. The irradiated region is not only strongly heated, but is also pressured into the Gbar regime because it is heated at a constant volume [1,2]. Light photons are absorbed by the electron component of the target matter. Energy exchange between electron and ion components of the matter takes place due to electron-ion relaxation. Energy evolution of the heated plasma is defined by the following mechanisms: electron and radiative thermoconductivity, electron-ion energy exchange, ionization and recombination processes and plasma expansion. Pressured area is created by the following mechanisms: ablation pressure, ponderomotive force, electron and ion components of the target material heating.

508

Investigation of solid targets-ultra-short intense laser pulses interaction was carried out with the help of one-D numerical simulation. Study of the interaction of radiation with a target can be significantly simplified when the characteristic times of the processes mentioned correspond to the different time scales.

2 Research Method

Light photons are absorbed by the electron component of the target matter. Laser pulse parameters described above allow to consider the laser energy deposition by the normal high and low frequency skin-effect theories [2].

The interaction of ultra-short intense normally incident laser pulses with the solid target is investigated with the help of 1-D Lagrange computer code, which allows to take into account: laser irradiation absorption and ponderomotive force action, electron-ion energy relaxation, ionization of the heated matter and thermoconductivity of both types- radiative and electron, elastoplastic properties and destruction of the target material [2]. The radiative relaxation may be omitted at the early stages of the plasma heating. The time of the matter heating to the temperatures when the produced plasma can be treated as an ideal gas is of the order or less then 10 Fs for considered pulse intensities [2]. Since the total pulse duration is much longer then this estimated time the target material was described in limits of ideal gas approximation (thermophysical properties and equation of state). The laser field absorption was calculated on the real electron density profile determined by the hydrodynamic motion of the laser plasma [2]. Equations of electrodynamics wave propagation, thermoconductivity and conservation of mass, momentum and energy were solved in complex to obtain the electron and ion temperature profiles in the target and the distribution of plasma density and pressure.

Radiative heat transfer was treated in limits of multigroup approximation with the Rosseland and Plank opasity coefficient obtained by means of a average atom model. It allows to describe the energy heat transfer inside of the target and outside emission by the heated plasmas [3]. Electron thermoconductivity was described by the classical Spitzer theory.

3 Results discussion

A large part of radiation is reflected from the target surface and a smaller part penetrates the target substance to the depth of the skin-layer where it is absorbed either due to the electron-ion collisions (the classical skin-effect) or due to the electron reflection from the plasma-vacuum boundary (the anomalous skin-effect).

Electron component of the target is heated by the light photons energy absorption.

Electron temperature decreasing occurs due to the thermal wave propagation, plasma expansion, radiative heat transfer and energy exchange with ion component. The heated plasma expansion during the pulse action is very small and the energy looses by this mechanism is negligible. For example, for pulse intensities $I=10^{17}$ W/cm^2 and duration $\tau=100$ fs the maximum of the electron temperature (equals to 900 eV) is changed due to this reason on value order of 10 eV and heated plasmas expands to the value of the order of 40 nm when the heated region depth is 200 nm and skin-layer depth equals to 10 nm. Later descussed results are obtained for the same pulse parameters: intensity $I=10^{17}$ W/cm^2 and duration 100 fs.

Electron-ion energy relaxation leads to the energy reduction on a value of the order of 15 eV for the same pulse parameters during the pulse action. Maximum of the ion component temperature at the end of laser pulse equals to the 80 eV.

Radiative heat transfer leads to exchange of the energy distribution in the target matter: due to energy transmission from more heated regions to a cool areas. It defines the more effectively expansion of the plasmas, since the expanded plasma is cooled. This mechanism of the energy evolution leads to decreasing of maximal electron temperature (inside of the plasma) on a value of the order of 40 eV. It may be explained not only by the direct energy heat transfer but due to growth of looses by plasma expansion too.

The main mechanism defining the energy evolution in the target is the electron thermoconductivity. As it was mentioned above due to this reason the heated region size grows approximately in ten times during the pulse action. Hence, the electron thermoconductivity influents on the energy balance in the matter much more then any other.

The pressured area is formed by the following mechanisms: due to plasma motion (ablation pressure), electron and ion components heating and ponderomotive force action. At the early stages of the target heating the pressured area corresponds to the thermal wave in the target material. The main mechanism of the pressured area formation in this case is the heating of the electron component. Growth of the ion component temperature of the target material increases the lattice pressure. At the early stages the front of high pressured area and its profile corresponds to the heated region. Then the front of compressed area begins to outstrip the thermal wave due to difference in the propagation velocities. The profile begins to change its form.

Shock wave was observed for time of about 0.5 *ps* after the start of laser pulse for the pulse parameters, mentioned above: it depends mainly on the pulse intensity and pulse duration. It has a "classical" strength front surface and a "tail". The increase of both pulse duration and beam energy flux leads to decrease of the time of the shock wave formation, but it is not a proportional connection. Under these conditions pressure reaches the values of the order of Gbar range (Fig. 1).

510

The light emission by the heated plasma has a wavelength in the region of soft X-ray mainly.

4 Summary

Obtained results allow to draw a conclusion that the energy evolution is defined by the different mechanisms, such as the plasma expansion, heating of the matter by the electron and radiative thermoconductivity and electron-ion energy relaxation. Electron thermoconductivity is more essential mechanism of the energy exchange (cooling of the heated plasma). Shock wave generation for these ultra-short pulse durations has another character then for longer pulses. Compressive areas form by the substance heating mainly. Shock wave generates after the pulse action and its initiation is connected with the difference in the propagation velocities of thermal and compressive waves. Obtained values of a pressure for these conditions reaches 1.5 Gbar.
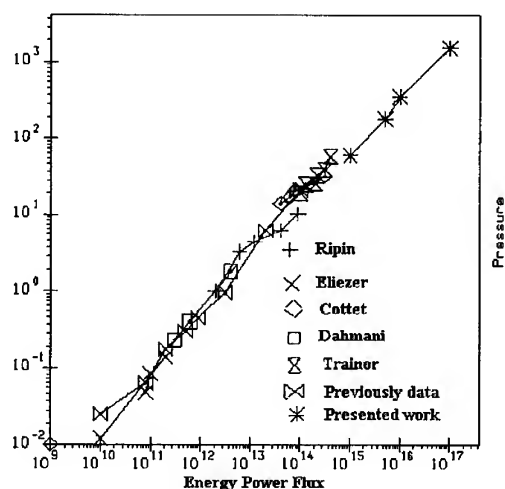
Fig.1 Pressure vs Energy Power Flux

5 References

[1] Wang X.Y., Downer M.C. // OPTIC LETTERS, v.17, 20, 1450-1452 (1992)

[2] Andreev N.E., Fortov V.E., Kostin V.V. et all // Plasma Phys. Rep. (Rus. J. Physica Plasmy) 21, 7, 1-8 (1995)

[3] Kostin V.V., Borisov R.B. et all // Rus. J. Physica Plasmy (to be published)

[4] Wilks S.C., Kruer W.L., Tabak M., Langdon A.B. // Physical Rev. Lett., 69, 9, 1383-1386 (1992)·

NUMERICAL MODELLING OF THE OPTICAL FIELD IONIZED NITROGEN RECOMBINANT XUV SCHEME

N. S. KIM[a,b,c], A. DJAOUI[a], M. H. KEY[a], J. S. WARK[b], D. NEELY[a], S. G. PRESTON[b], M. ZEPF[b], C. G. SMITH[b], and A. A. OFFENBERGER[d]

[a]Rutherford Appleton Laboratory, Chilton, Didcot, Oxon OX11 0QX, U.K.

[b]Department of Physics, Clarendon Laboratory, University of Oxford, Parks Road, Oxford, OX1 3PU, U.K.

[c]Kumho Information and Telecommunication Laboratory, 572 Sangam-dong, Kwangsan-ku, Kwangju, 506-303, Korea

[d]Department of Electrical Engineering, University of Alberta, Edmonton, Alberta, T6G 2G7, Canada

We have used a 1-D numerical model in cylindrical symmetry to describe the emission of resonance radiation from Li-like nitrogen ions in a recombinant optical field ionized plasma. These calculations are specific to the conditions of an experiment undertaken with the SPRITE KrF CPA laser system. This experiment showed a nonlinear increase in intensity of the resonance line ($3d_{5/2}$ - $2p_{3/2}$ at 24.7 nm) with increasing pressure in a gas jet target. The length of the irradiated plasma was 1 mm. The numerical modelling reproduces the increase of observed intensity with gas pressure, but it indicates that the resonance emission is optically thick and that there is no XUV laser gain. We conclude from this work that although short pulse UV irradiation has been predicted to be an optimum driver for this class of x-ray laser, it is nevertheless difficult to achieve conditions leading to gain and that the prognosis for this approach is not as good as may have been previously presumed.

1   Introduction

Since possibility of a gain from a nonequilibrium hydrogen plasma[1] and a ground-state x-ray lasing by optical field ionization (OFI)[2] had been proposed long time ago, many research groups performed theoretical and experimental studies to realize the x-ray lasers produced by OFI[3-6]. The OFI x-ray lasers can be obtained during recombination up to upper-laser level following OFI induced by a high-intensity short-pulse lasers. It is essential for laser from excited to ground level that the recombination must be faster than the time scale of the radiative and collisional filling of the lower-laser (ground) level[7]. So one of main lasing conditions is to get a low electron temperature to induce sufficiently fast recombination and the electron temperature should be much less than ionization potential. This lasing

512

down to ground state has a merit of large lasing transition energy which gives wavelength range of several to tens nanometers but very complete emptying of the ground state during ionization is required. For the ground-state lasing by OFI, small-signal gain[3] and efficiency[4] were calculated recently and amplified spontaneous emission on L_α line in H-like Li at 13.5 nm[5] was firstly observed in 1993. After then subsequent simulations and experiments have been performed by many laboratories but the measured gain-length products are relatively smaller than 5 which is known as criteria for x-ray lasing[8].

As a feasibility study for the OFI x-ray laser an extremely ultraviolet (XUV) emission from Li-like nitrogen ions was recently measured at Rutherford Appleton Laboratory when nitrogen ion density is changed[9,10]. In this experiment SPRITE KrF excimer laser was used to drive OFI x-ray laser at 24.7 nm which was $3d_{5/2}$ - $2p_{3/2}$ resonance line from Li-like nitrogen ions. The driving laser parameters are pulse duration of 350 fs, wavelength of 248 nm, and intensity at target of 5×10^{16} W/cm^2. This numerical modelling was performed to get more idea for this experiment since there was no direct evidence of x-ray gain.

2 Optical scheme and simulation code for modelling of OFI x-ray laser produced from Li-like nitrogen ions

In this modelling driving laser for OFI x-ray laser is assumed to have gaussian profile in space and time and to be a KrF excimer laser with same parameters which was used in Refs. 9 and 10. This laser is focused axially into a nitrogen gas jet target and focal spot size is 20 μm.

KrF LASER
(350fs, 5.0x10^{16}W/cm^2)
Focal Diameter=20 μm
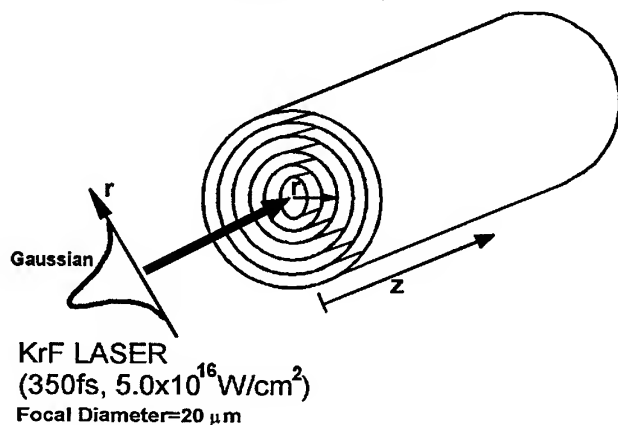
Fig.1: Optical scheme for the axial irradiation of pumping laser

This optical scheme is shown in Fig.1. Axial and radial direction are denoted by z and r, respectively. This modelling is using a one-dimensional hydrodynamic model in cylindrical and includes tunnel ionization, nonlinear inverse bremsstrahlung, radial heat conduction (MED104)[11].

An average atom model

was used to calculate the average ionization stage and ground and excited state ion densities. Nitrogen ion density is changed from 1.0×10^{18} to 1.0×10^{19} cm^{-3}.

3 Simulation results by MED104 code

To get an idea for a gain, emission intensities from Li-like nitrogen ions were calculated for both plasma lengths of 1 μm and 1 mm where 1 μm plasma length was used as a case of optically thin plasma. After multiplying the emission intensity from plasma with 1 μm length by 1000, it was compared with one from plasma with 1 mm length. In Fig.2 experimental and simulation results are plotted with changing nitrogen ion density. Vertical axis is expressed by logarithmic scale. This experimental results are adopted from Ref. 10 as a purpose of comparison. The emission intensity from the plasma with 1 mm length in Fig. 2(d) is two-order less than one from the plasma with 1 μm length by 1000 in Fig. 2(a). Curves in Fig. 2(b) and Fig. 2(c) are experimental results fitted to each simulation result.
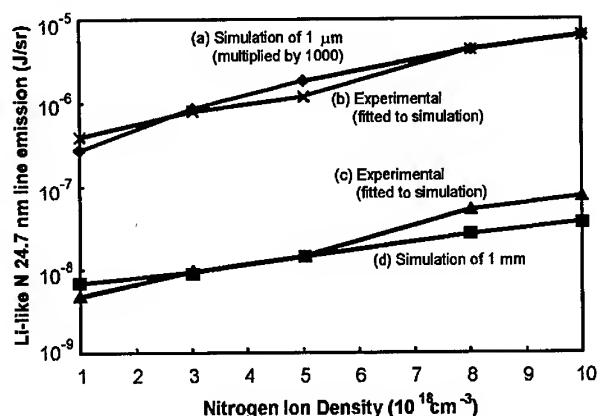
Fig. 2: 24.7 nm line emission from the Li-like nitrogen ions with changing the ion density.

From this results it is shown that the plasma source with 1 mm length is too optically thick to produce x-ray lasing since there is strong absorption. However We can see similar nonlinear increase of intensity with ion density between experimental and simulation results for both plasma lengths.

To understand origin of strong absorption spatial gain profile was also calculated for several time steps (refer Fig. 3). Here nitrogen ion density of 10^{19} cm^{-3} was used and time steps were 0.5, 5, 10, 15, 20 ps. We can see that there is strong absorption region and it is propagated outwardly as time goes on.

514
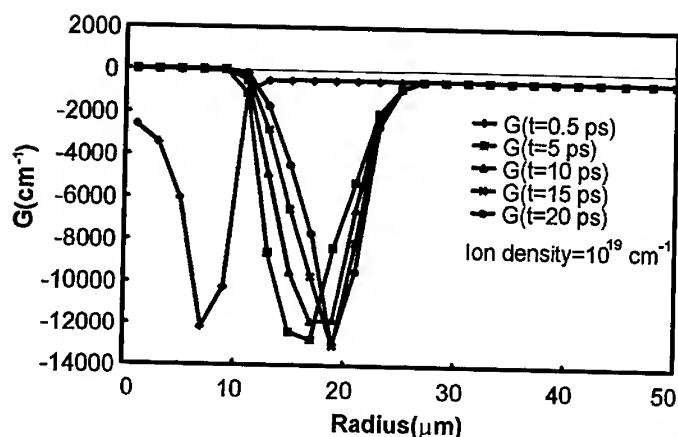
Fig. 3: Spatial profiles of the x-ray gain from the Li-like nitrogen ions for several time steps

4 Summary

We calculated the x-ray emission from the Li-like nitrogen plasma produced by the OFI which is known as good scheme for table-top x-ray lasers. Although this simulation could make similar nonlinear behavior as the experiment in Refs. 9 and 10, it does not suggest that there is any evidence of XUV laser gain. Therefore we conclude from this study that it is not easy to achieve conditions leading to gain with short-pulse UV driving laser.

References

1) L. I. Gudzenko et al., Sov. Phys. JETP **18**, 998 (1964)
2) J. Peyraud et al., J. Appl. Phys. **43**, 2993 (1972)
3) N. H. Burnett et al., IEEE J. Quantum Electron. **26**, 1797 (1990)
4) D. C. Eder et al., Phys. Rev. A **45**, 6761 (1992)
5) Y. Nagata et al., Phys. Rev. Lett. **71**, 3774 (1993)
6) D. C. Eder et al., Phys. Plasmas **1**, 1744 (1994)
7) D. C. Eder et al., AIP Conf. Proc. **332**, 87 (1994)
8) R. C. Elton, X-Ray Lasers (Academic, New York, 1990)
9) S. G. Preston et al., RAL Annual Report RAL-TR-95-025 (1995)
10) A. A. Offenberger, Proc. of the Workshop on Ulltrashort Pulse Excimer Lasers and their Applications, Streatley-on-Thames, 18 Sept. 1995, p.1.82
11) A. Djaoui et al., Phys. Rev. E **50**, 4961 (1994)

AN INTENSE PULSED X-RAY SOURCE FOR LASER PRODUCED PLASMA STUDIES

S. S. ELLWI, T. A. HALL and A. D. BADGER
Physics Department, University of Essex, Colchester, Essex
CO4 3SQ UK

An investigation of a new electron beam x-ray source using a laser produced plasma as the cathode is described which uses an alloy of (Fe, Ni, Co) anode - aluminium target cathode combination. A pulsed Nd YAG (λ=1.06µm), 1ns pulse length was used to irradiate the target and create the plasma. This plasma is used as the cathode of a diode to which a high voltage is applied so as to accelerate any free electrons to the anode. The x-ray spectrum of the source was investigated using a crystal spectrometer with a LiF crystal (2d= 0.4nm) coupled to a CCD photodiode array . Two x-ray photodiodes and an oscilloscope were used to record the time history of the x-ray pulse and an x-ray pinhole camera and DEF film were used to study the spatial emission region. The spectrum was found to be characteristic of Iron, Copper and nickel k_α and K_β- line emission superimposed on a weak continuum. The form was dependent upon the voltage applied to the anode and the separation between the anode and the cathode.

1 Introduction

The conventional x-ray tube produces x-rays by accelerating electrons from a thermionic or field emission cathode onto an anode where line and continuum radiation are emitted. Such tubes have many desirable features, such as monochromaticity (of the line radiation) and the ability to produce hard x-rays. In principle it is possible for such a tube to emit very short pulses of x-rays, but the intensity of these pulses is limited by the electron current that can be drawn from a thermionic cathode. This results in a peak x-ray power $\sim 10^6$ less than that of a laser produced plasma in the soft x-ray region, making single shot nanosecond/picosecond x-ray studies impractical using a conventional tube. An explosive electron emission (EEE) tube, in which the electron source is a plasma produced by explosion of the cathode microedges under a high applied voltage is one way in which the limitation of electron current can be overcome. However, the lower threshold voltage for stable electron emission by explosion is $\sim$ 50 keV and this device is limited to the production of higher energy x-rays. [1]

The limitation on the electron current can also be overcome by using a laser produced plasma as the cathode which has an effective temperature of several millions of degrees Kelvin. Potentially, very large currents can be drawn from such cathodes which can be produced using small, pulsed lasers with output energies of a few millijoules. An x-ray source using such a cathode has the further advantage that it is easily synchronisable to an external event.

2 Experiment

The laser that was used in these experiments consisted of a single longitudinal, single transverse mode, Q-switched Nd YAG oscillator (λ = 1.06 µm) of pulse

516

duration ~20 ns followed by a fast Pockels cell pulse slicer which can select a 1 - 5 ns duration pulse. [2] This pulse is amplified by a single Nd YAG amplifier to produce pulse energies up to a few millijoules. This laser pulse is then focused onto the aluminium cathode of the x-ray source using a simple $f/4$ plano - convex lens.

Electrons are drawn out from the plasma by the applied electric field and are accelerated towards the anode. The sharp point on the anode tip results in a crude focusing of the electrons which, when the they strike the anode, result in both bremsstrahlung and K_α and K_β radiation being emitted. For any given anode material, the conversion efficiency and properties of the x-rays produced are dependant upon three parameters : the anode material, the anode-cathode separation, L and anode voltage V_a.

The LiF crystal spectrometer with a 256x1024 array Andor Technology single stage cooled CCD detector was used to record the spectra. The x-ray emission on a single shot was more than sufficient to produce a high quality spectrum and it was necessary to introduce 12.5μm aluminium foil filtering in front of the spectrometer to reduce the signal to an acceptable level. The transmission of the filter at the K_α lines is approximately 60%.

3 Results and Discussion
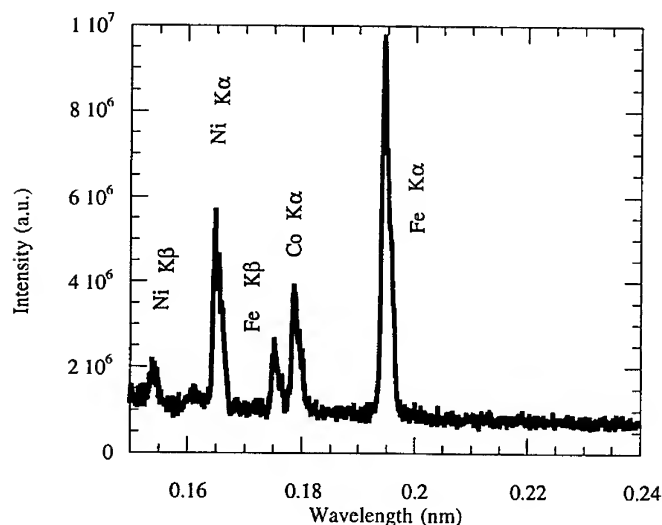
Figure 1   Corrected spectrum obtained using Lif crystal spectrometer with CCD detector at anode potential 30 kV and anode cathode separation 0f 0.9mm.

Figure 1 shows a corrected spectrum obtained with an anode potential of 30 kV and anode - cathode separation of 0.9mm.

A simple one dimensional model has been developed to describe the operation of the x-ray source. Although certain aspects of the source are clearly two or three dimensional, the justification for considering only a one dimensional, model is that the operation of the x-ray source is dominated by the emission of electrons. This can be justified as follows; the region of emission is characterised by the Debye length in the longitudinal (x) direction and the focal spot diameter in the y and z directions and since the Debye length is generally much smaller than the focal spot diameter, a one dimensional approach is a reasonable approximation.

The laser pulse produces a plasma on the surface of the cathode and this plasma expands away from the surface. [3] This expansion is described by a self similar model and the electron density and Debye length have the following spatial and temporal profiles

$$n_e = n_0 \, e^{(-\alpha/C_s t)} \qquad\qquad 1$$

$$\lambda_d = (\varepsilon_0 k_B \, T_e/n_e e^2)^{1/2} \qquad\qquad 2$$

where n_0 is the electron density ($\sim 10^{21} cm^{-3}$), C_s is the ion sound speed, k_B is a Boltzmann's constant and T_e is the electron temperature.

Using these forms we define a " plasma electric field", E_s, as being that electric field that would be created if all of the electrons in a slab of thickness λ_d were moved through a distance λ_d keeping the ions fixed.

This field is given by

$$E_s = \frac{e n_e \lambda_d}{\varepsilon_o} \qquad\qquad 3$$

We make the assumption that the point of emission of the electrons from the plasma is where the applied electric field, E_x, is equal to the space charge electric field , E_s. The position in space where this condition is met will vary in time.

Since at the electron emission point we assume that all the electrons are accelerated by the applied field, then the current density of the electrons across this point can be determined from the sum of the thermal flux and the flow velocities;

$$J_{em} = e n_e U = (\frac{e n_e C_s}{4} + e n_e \frac{x}{t}) \, |_{x = x_e} \qquad\qquad 4$$

where J_{em} is the diode current density (A cm^{-2}), U is the plasma flow velocity, C_s is

518

the ion sound speed, e the electronic charge, x is the plasma expansion position from the cathode and t is the plasma expansion time. Electrons emission will occur when x is equal to x_e .

The production of characteristic x-ray emission cannot occur until the incident electron has sufficient energy to produce the relevant ionisation, e.g. 1s ionisation for K shell emission. The intensity of a particular line will therefore depend both on the ionisation cross section and the probability of fluorescent decay. The intensity of K-shell emission in the threshold region obeys the empirical relationship [4].

$$I = 1.58 J_{em} (V_a - V_k)^r \qquad\qquad 5$$

where r=1.7, V_a is the electron energy in electron volts and V_k is the energy required to produce a hole. Thus higher accelerating voltages lead to higher signals. In order to have a value for the x-ray flux I, in terms of photons/cm^2, J_{em} in equation 4 was calculated and integrated over the time of the discharge, τ.

4   Conclusion

This x-ray source offers a method for the production of short, intense pulses of moderate energy x-rays with a very low laser energy input (a few mJ). The x-ray spectrum of the source is characteristic of the K- line emission of the anode material and depends upon the separation of the point of irradiation by the laser beam on the target and the anode tip as well as the applied voltage and the arrangement of the electrical circuit.

References

1-Dmitriev M., "X-Ray Probes", 1989 (unpublished)
2-Fabrikesi E; PhD Thesis "Laser Physics" , Physics Department, Essex University, 1981
3-Chen, Francis F., *Plasma Physics and Controlled Fusion* 1989 (New York)
4-Williams F, *Introduction to x-ray spectroscopy* , 1987 (London)

EXPERIMENTAL INVESTIGATION OF
POPULATION INVERSION FORMATION PROCESS
IN 10ps KrF LASER PRODUCED RECOMBINING PLASMAS

E.MIURA, T.TOMIE, I.OKUDA and Y.OWADANO

Electrotechnical Laboratory
1-1-4 Umezono, Tsukuba, Ibaraki, 305 JAPAN

Irradiation conditions required for achieving population inversion in 10ps KrF laser produced recombining plasmas were experimentally investigated. To realize higher ionization state, suppressing an ASE (amplified spontaneous emission) prepulse accompanying a 10ps pulse was effective. Small spot size irradiation gave rapid expansion of the plasma, when the ASE prepulse was suppressed.

1 Introduction

Recombination pumping scheme is a promising method for achieving highly efficient short wavelength X-ray lasers. While there have been many reports on gain observation[1], there have been few reports on observation of large gain length product.[2,3] To obtain short wavelength X-ray lasers, the production of an initially high density plasma and the following rapid cooling of the plasma are required. Therefore, a short-wavelength short-pulse pumping laser is necessary. We focused on a 10ps KrF laser as a pumping laser and have so far reported an amplification of 10ps pulses up to a few joules[4] and experiments to observe an amplification of F Hα line.[5]

As mentioned above, because the process for forming population inversion is complicated in the recombination scheme, in order to achieve large population inversion effectively, it is crucially important to understand details of the process and to find optimum irradiation conditions. In this paper, we report results of experiments to find irradiation conditions required for achieving population inversion in 10ps KrF laser produced recombining plasmas.

2 Experimental Condition

A few joules energy pulses of 10ps duration have been obtained from the KrF laser system "ASHURA" composed of one discharge amplifier and two e-beam pumped amplifiers.[4] The 10ps pulse was focused on Ge and Al slab targets with a spherical(f=100cm) or an aspherical(f=25cm) lens. The maximum intensities were 3×10^{15}W/cm^2 and 1×10^{16}W/cm^2, respectively. When a 10ps pulse was amplified, an amplified spontaneous emission(ASE) of 20ns duration accompanied the 10ps pulse. When the ASE prepulse was focused with a spherical lens, the intensity was 3×10^{10}W/cm^2. The level of the ASE prepulse was suppressed by using a saturable absorber dye. When the ASE prepulse was suppressed, the maximum intensity ratio of the 10ps pulse to the ASE prepulse was 10^8. Spatially integrated X-ray spectra between 5Å

520

and 10Å were recorded on a Kodak DEF film with a TlAP crystal at 60 degrees direction from the laser incidence direction.   High resolution X-ray spectra spatially resolved along the plasma expansion direction were also observed with a large dispersion PET crystal.

3   Effective Ionization Method

When a pumping laser pulse is as short as 10ps, it may be difficult to achieve required ionization state owing to the short period available for the ionization. To find optimum conditions for realizing higher ionization state, we investigated dependence of ionization balance on irradiation conditions.

Figures 1 and 2 show the laser intensity dependence of relative conversion efficiencies from laser energy to intensity of 4d-2p lines from F-like and Ne-like Ge ions, respectively. In Figs.1 and 2, closed and open circles represent data for suppressing and non-suppressing ASE, respectively. The laser intensity was varied by changing the laser spot diameter keeping the laser energy constant. As seen in Fig.1, in the high intensity region above $5 \times 10^{14} W/cm^2$, the conversion efficiency was nearly equal in both cases. In the low intensity region below $5 \times 10^{14} W/cm^2$, the conversion efficiency was higher, when the ASE prepulse was suppressed. As seen in Fig.2, in the intensity region below $1.5 \times 10^{14} W/cm^2$, the conversion efficiency was also higher, when the ASE prepulse was suppressed. These results show that the higher ionization state was realized by suppressing an ASE prepulse, and above results are interpreted as follows.
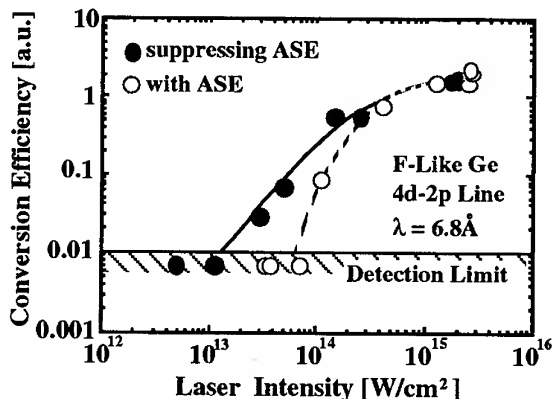
Fig.1   Laser intensity dependence of relative conversion efficiency from laser energy to intensity of 4d-2p line (λ=6.8Å) from F-like Ge ions.
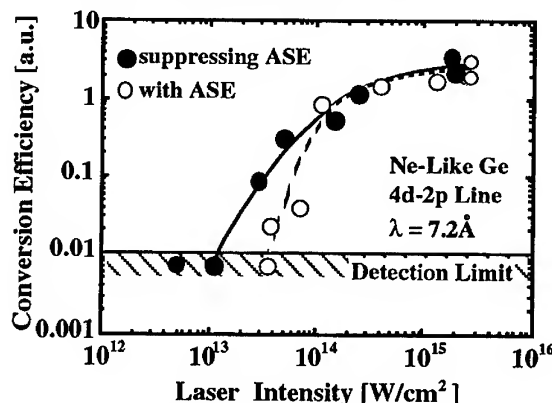
Fig.2 Laser intensity dependence of relative conversion efficiency from laser energy to intensity of 4d-2p line (λ=7.2Å) from Ne-like Ge ions.

Because ionization time[6] is proportional to the inverse of electron density, higher electron density plasma is necessary to realize effective ionization. When a 10ps pulse is accompanied with an ASE prepulse, the 10ps pulse will be absorbed in a long scale length preformed plasma produced by the prepulse. The electron density of this plasma will be slightly lower than the critical density of KrF laser. On the other hand, when the ASE prepulse was suppressed, the density profile. of the plasma will be very steep and the energy deposited near the critical density region will be conducted to higher density region. Therefore, the 10ps pulse can interact with higher electron density plasma, and efficient ionization can be expected, when the prepulse is suppressed. Generation of higher electron density than the critical density by suppressing an ASE prepulse has been experimentally observed, and supported by a numerical simulation.[7] Our experimental results shown in Figs.1 and 2 are consistent with the above expectations.

4 Rapid Expansion of Plasma

To obtain large population inversion, rapid expansion of an initially high density plasma is necessary. Because the initial density of KrF laser produced plasma is high, it may be difficult for electron density and temperature to reach gain generation region especially for long wavelength X-ray lasers. We investigated irradiation conditions required for achieving rapid expansion of plasmas.

Electron density can be estimated from deviation of low-lying levels from local thermal equilibrium(LTE)[8]. In a recombining phase, when electron density is high and LTE condition is realized, populations of low-lying levels are determined by collisional processes from high-lying levels. When the electron density becomes lower, the rates of collisional processes supplying population to lower levels decrease, and the populations of low-lying levels decrease. Therefore, the intensity ratios of lines from high-lying levels to those from low-lying levels become larger in lower electron density region. In the following analysis, we used the intensity ratio of Heγ line to Heβ line from He-like Al ions.

Figure 3 shows spatial
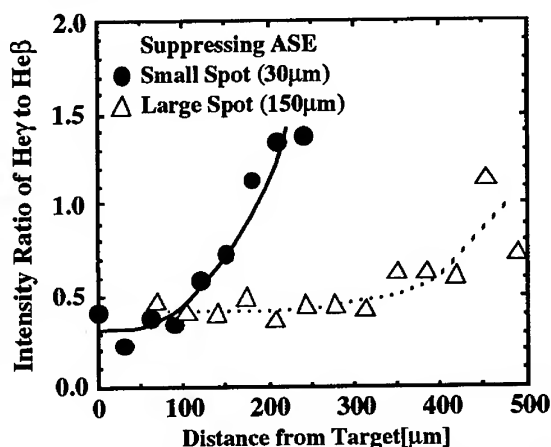
Fig.3   Spatial distributions of intensity ratio of Heγ line to Heβ line for large and small   spot size irradiation. An ASE prepulse was suppressed in both cases.   Laser intensities were $3 \times 10^{15} W/cm^2$ and $1 \times 10^{16} W/cm^2$ for large and small spot irradiation, respectively.

522

distributions of the intensity ratio of Heγ line to Heβ line, when an ASE prepulse was suppressed. In Fig.3, closed circles and open triangles represent data for small(30μm) and large(150μm) spot size irradiation, respectively. As seen in Fig.3, more rapid expansion was achieved, when a spot size was smaller, as expected. Figure 4 shows the observed data, when an ASE prepulse was not suppressed. The initial electron density was lower than that in the case of suppressing an ASE prepulse. Clear decrease in electron density was not noticed in this case, although spot size was small. This slow expansion may have be due to large volume of the plasma preformed by the prepulse. Thus, the suppression of prepulse and small spot size irradiation are crucially important for achieving rapid expansion of plasma.
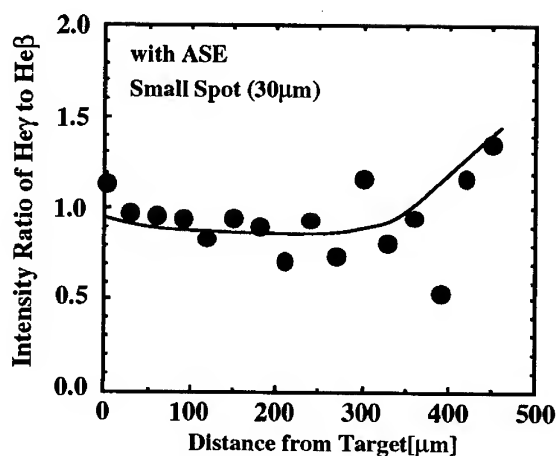
Fig.4 Spatial distributions of intensity ratio of Heγ line to Heβ line for small spot size irradiation without suppressing an ASE prepulse.

5 Summary

Irradiation conditions required for achieving population inversion in 10ps KrF laser produced recombining plasmas were experimentally investigated. It was found that suppressing a prepulse was effective to realize higher ionization state, because a higher electron density plasma was generated by suppressing the prepulse. It was also found that small spot size irradiation gave rapid expansion of plasma. Moreover, suppression of the prepulse was found to be important for rapid expansion of plasma.

References
   1. For example C.Chenais-Popovics *et al., Phys.Rev.Lett.* **59** 2161(1987)
   2. S.Suckewer *et al., Phys.Rev.Lett.* **55** 1753(1985)
   3. J.Zhang *et al., Phys.Rev.Lett.* **74** 1335(1995)
   4. T.Tomie *et al., Laser and Part. Beams* **8** 299(1990)
   5. T.Tomie *et al., AIP Proc.* **332** 171(1994)
   6. R.H.Huddlestone and S.L.Leonard, *Plasma Diagnostics Techniques*, (Academic Press, New York, 1965)
   7. T.Tomie *et al., Proc. SPIE* **1551** 213(1991)
   8. H.R.Griem, *Plasma Spectroscopy*, (McGraw-Hill, New York, 1964)

CHARACTERISATION OF THE VULCAN Nd:GLASS LASER FOR MULTI-TERAWATT OPERATION

C. N. DANSON, N. BRADWELL, L. J. BARZANTI, J. COLLIER, A. DAMERELL,
C. B. EDWARDS, C. JOHNSON, M. H. KEY, D. NEELY, M. NIGHTINGALE,
D. A. PEPLER, I. N. ROSS, P. RYVES, C. STEPHENS, N. THOMPSON,
M. TRENTELMAN, E. WOLFRUM, F. N. WALSH AND R. WYATT
Rutherford Appleton Laboratory, Chilton, Didcot, Oxon OX11 0QX, U.K.

Chirped Pulse Amplification (CPA) [1] as implemented on VULCAN [2] is capable of delivering 30 J to target with pulselengths in the sub-picosecond regime. Results from various experiments [3],[4] have indicated that intensities of 10^{18} - 10^{19} W cm^{-2} have been achieved on target. However, a detailed characterisation of the beam's focal spot intensity distribution was necessary to confirm these results.

1 Introduction

The transmission of energy through a well defined pin-hole provides a useful technique for characterising the intensity distribution obtained at the focal plane of a short pulse high intensity laser system. One of the main limitations when using pin-hole transmission measurements is the effect of 'pinhole closure'. This occurs when a plasma which can refract or reflect the drive beam is formed at the edges of the pin-hole and has sufficient time to expand and either partially or completely fills the pin-hole before the laser pulse has passed through. The spatial and temporal evolution of pinhole closure is very much dependant on the f-number of the focusing optic and the pinhole diameter. For a plasma the lateral expansion velocity may be in the 10^5 - 10^8 cms^{-1} region which gives a motion of ~10 microns in the timescale of the interaction. Therefore, only when the focal spot and thus the pin-hole radius is a few times 10 microns will pin-hole closure become important. The magnitude of the effect lessens at higher f-numbers due to the larger focal spot sizes having lower intensities and the larger pinhole diameters required. Thus using a longer focal length optic reduces the effects of pinhole closure and also facilitates ease of alignment.

2 Experiment

For these experiments a Nd:YLF APM oscillator [2] operating at 2-3 ps and at 1053 nm was used. The ultra-short pulse is stretched, amplified to ~40 J and then apodised to 75 mm x 110 mm to avoid clipping on the large aperture compression gratings. After compression the pulse is focused using a 3 m focal length off axis

524

parabola (OAP) and energy measured at the exit port of the interaction chamber. A 5% leakage from the turning mirror in the chamber supplies signal to the laser pulse diagnostics: a single shot autocorrelator; spectrometer; and an equivalent plane monitor (EPM). Initial null shots showed that 60% of the energy entering the target area was incident on the target plane.

The EPM consists of a 9.6 m focal length lens and two etalons producing a 2d array of spots each representing a different plane in the focusing beam including the focal plane. The array is incident on an 8 bit CCD and the spots are analysed by evaluating the radial energy distribution. Two active pinhole cameras with intensified CCDs were used to check the alignment on a shot to shot basis. Shots were taken with energies ranging from 10 J to 20 J on target.

3 Results

The percentage of incident energy transmitted through pinholes of varying diameter measured on high energy (10 - 30 J) shots are shown on figure 1. The two circular data points shown on figure 1 represent the amount of energy stopped by a circular disk of diameter D placed at the focal plane. Pinhole closure reduces the amount of energy transmitted through a pinhole and increases the amount of energy stopped by a central disk, generally indicating a lower and upper bound to the transmission respectively. The horizontal axis on figure 1 has been normalised to units of the
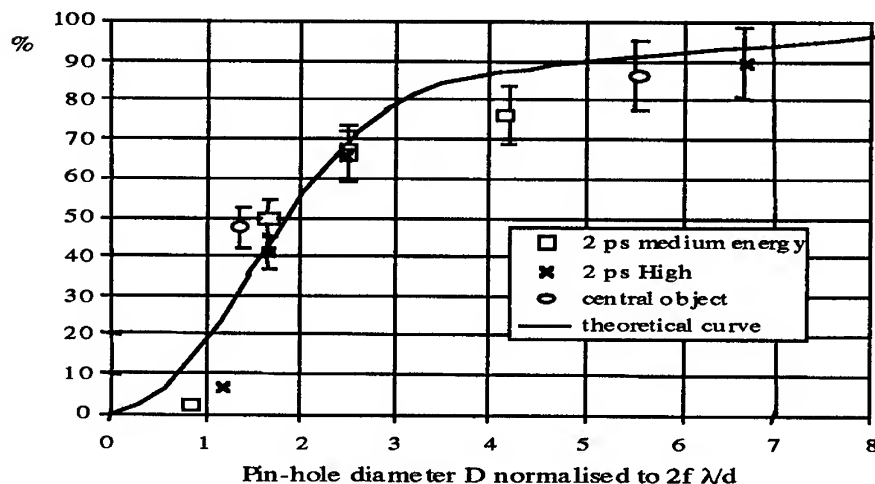
Figure 1. Energy transmission results for the VULCAN CPA beam.
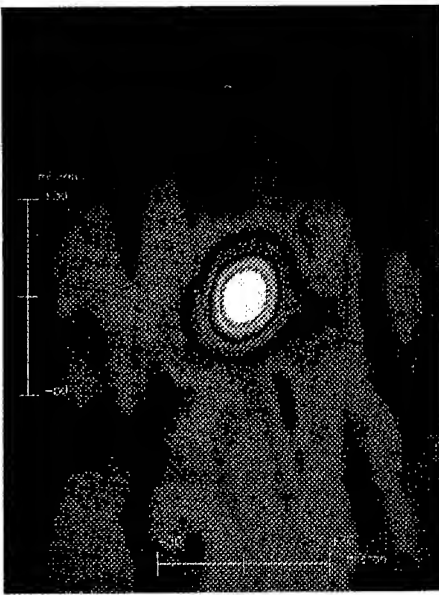
Figure 2: A typical output from the Equivalent Plane Monitor for minimised system B-integral. The scale shown corresponds to the spatial size at the target focal plane.

Figure 3: Output from the EPM for a high energy shot with B-integral = 14.4 showing significant focal spot degradation.

beam diffraction limit ($D_n = 2f\lambda/d \approx 60$ µm) defined as the distance between the first minima in the diffraction pattern for a rectangular beam. The beam diameter d is taken as the average size in the horizontal and vertical directions for the rectangular beam d = 0.1 m.

A theoretical transmission curve T(D) was initially generated by integrating the transmission through a circle of diameter D placed at the focus of a 3 m focal length perfect optic illuminated by a uniform rectangular beam. Using the generated curve, a fit to the data was obtained using the curve T(mD) where m represents the number of times that the focal intensity distribution exceeds that of a diffraction limited beam. The fit T(mD) where m = 3.5 (shown by the solid line on figure 1) generally shows a good fit to the experimental results. However, at both D < 1.2 and D > 5 some discrepancy exists. At D > 5 measurement are ~4% lower than the fit, since plasma closure effects are negligible in this region, these results indicate that this small fraction of the incident energy is being diffracted significantly further out into the wings of the intensity distribution.

526

The ratio of the energy contained within an equivalent pinhole diameter measured using the EPM data, to the transmitted energy through a pin-hole is close to 1 as would be expected for diameters D many times larger than the diffraction limit. This ratio increases dramatically to ~10 when the pin-hole diameters in question are close to ~1 indicating significant plasma closure effects.

The effect of B-integral on the beam was examined by placing up to 5 cm of optical quality glass in the recompressed CPA beam at full energy. The EPM data from low energy (< 0.1 J) shots demonstrated that the glass had a negligible effect on the transmitted laser beam focal intensity distribution. Intensity contour maps from the EPM for a total system B-integral of 1 and 14.4 are shown in figures 2 and 3 respectively. The intensity contour map on figure 2 demonstrates the high quality of the VULCAN CPA beam operating under typical conditions. The contour map shown in figure 3 at a B-integral of 14.4 shows some degradation of the intensity distribution but, the beam is still only 5 times the diffraction limit. This is a surprisingly good result and is mainly attributable to the high degree of intensity uniformity across the near field of the VULCAN CPA beam.

The beam uniformity was examined by exposing a high speed IR film in the near field. About a third of the beam size was densitometered with a step size of 50 μm. The rms deviation σ_{beam} is calculated from the calibrated intensities yielding a relative roughness of the beam of 6.6%.

4   Conclusions

A characterisation experiment of the VULCAN CPA beam was investigated to determine the focusability, the beam uniformity and the effects of B-integral on focusability. The beam was shown to be ~3.5 times diffraction limited. It has been observed that despite a high B-integral the beam was still 5 times diffraction limited demonstrating that VULCAN CPA has good uniformity across the beam. When these results are extrapolated to subpicosecond operation using f3 focusing optics, i.e. normal operating conditions, it indicates an intensity on target of ~10^{19} W cm^{-2}.

References

[1]   D. Strickland and G. Mourou, Ops Comm, Vol 56, No. 3, pp 219-22, 1985
[2]   C N Danson et al, Ops Comm, Vol. 103, No. 5,6, pp 392-397, Dec 1993
[3]   J. Zhang et al, Accepted to Phys Rev A
[4]   A. Modena et al, Nature Vol. 377 p. 606, 19th October 1995

PULSE TRAIN MODE RAMAN LASER PUMPING FOR A SOLID-STATE ACTIVE MEDIUM

A.BURTSEV, A.BORODKIN, N.BYKOVSKY, Yu.SENATSKY

P.N.Lebedev Physical Institute of the Russian Academy of Sciences, Leninsky Prospect, 53, Moscow, 117924, Russia

A feasibility of a solid state laser driver pumping by Nd -lasers with flashlamps is examined. At the pulse train mode operation Nd-laser 1.06 μm radiation may be effectively transformed by SRS to the absorption bands of several rare-earth and transition-metal activator ions in crystals. 0.94 and 1.33 μm free running Nd^{3+}:garnet lasers are to be useful for Yb^{3+}:YAG and Co^{2+}:MgF_2 active media pumping. Stored energy efficiencies of 2-4% are expected under Nd-laser pumping of driver's amplifier modules.

A considerable study is being given now to solid state active media and pumping sources for a laser-driver of the future thermonuclear reactor based on laser fusion. Not very high requirements imposed on the driver within the framework of the "hybrid reactor" concept give grounds for searching of lasers which are suitable for an average-power operation with the pulse repetition rate v of several Hz, the efficiency η of several percents and the energy of the typical laser beamline of 10^4 J [1]. Under these conditions one may consider for the pumping of a solid state active medium not only semiconductor laser diodes, but also systems with flashlamps. Flashlamps pumped Nd-lasers are of special interest for such an application as this type of lasers is now one of the most commonly used and efficient sources of powerful radiation in the near IR region. Nd-laser pumping of Yb^{3+}-Er^{3+}: glass, Ni^{2+}, Co^{2+}:MgF_2 and some other media is known for a long time [2]. A sensitiser of Er^{3+}, Tm^{3+}, Ho^{3+} - doped laser crystals based on Cr^{4+} ions which absorbs at the wavelength λ_0=1.06 μm was produced recently [3]. The efficiency of Nd^{3+}:garnet lasers reaches now $\eta_{FR} \approx 10\%$ at the 1.06 μm free-running (FR) operation and $\eta_{FR} \approx 3$ % at the λ_1=1.33 μm [4].In this work we want to discuss several new aspects of Nd-lasers application as pumping sources connected with the transformation of the pump radiation wavelength.

Giant pulse train mode (PTM) operation of a Nd-laser occurs in a rather simple way by a bleachable filter Q-switching of the laser cavity. For the average power Nd^{3+}:YAG lasers the efficiency of the PTM regime is 0.8-0.9η_{FR} [5]. In the spectral region from 1 to 1.5 μm there are the absorption bands of some of the rare-earth ions and of the several transition-metal ions in crystals which were considered

to be used in high power lasers [6]. The PTM Nd-laser 1.06 μm radiation may be transformed into the noted spectral region in the processes of stimulated Raman scattering (SRS). The highest conversion efficiency (up to 70-90 %) may be attained in the SRS by rotational levels of diatomic molecules in gases such as N_2, H_2 [7]. The requirements to the Raman radiation parameters (beam divergence, time and spectral contents) for pumping of a bulk solid-state material must not be severe. For example, Fig.1 illustrates $Co^{2+}:MgF_2$ absorption band [2] which overlaps with the wavelengths of a cascade of Stokes components (s1-s5) of 1.06 μm radiation under SRS of a Nd-laser in hydrogen (Stokes shift 587 cm^{-1}). Note, that Ho^{3+} and $Tm^{3+}:YAG$ absorption bands overlap also with the 1-st and 2-nd Stokes components of this scattering. $^4F_{3/2} - {}^4I_{9/2}$ laser transitions of Nd^{3+} ions in glasses and crystals with the wavelength λ_2 in the 0.91-0.95 μm region were operated by flashlamps pumping at room and reduced temperatures [8]. From spectroscopic data, the FR efficiency of Nd-laser at λ_2 must be comparable with η_{FR} at λ_1. After improvements in cooling and pumping systems and in the cavity design Nd-laser efficiencies over 3% are believed for λ_1 and λ_2 operation. This perspective gives ground for study of the $Nd^{3+}:YAG$ and $Nd^{3+}:YSGG$ laser 0.94 μm FR pumping of $Yb^{3+}:YAG$ active medium which is now one of the promising candidates to the laser-driver [6]. A 1.33 μm Nd -laser FR pumping is to be useful for $Co^{2+}:MgF_2$ (Fig.1). A 1.315 μm iodine laser pumping for this crystal was proposed by P.Kryukov.

Table 1 contains some laser and spectroscopic data [2,6,9] of three rare-earth ion-doped YAG and $Co^{2+}:MgF_2$ crystals which are of interest in case of Nd-laser PTM Raman or FR pumping. With this data the numerical modeling of the selective pumping of slab laser elements in the 'active mirror' geometry (Fig.2) [6] was carried out under the following assumptions: the pump pulse duration, t_{pump}=200 μs; slab aperture, 5x5 cm^2; thickness, d cm; the number of slabs N; slab average temperature, 300°K (for $Co^{2+}:MgF_2$ - 100°.K). Table 2 illustrates typical results of numerical modeling for rather moderate ratios J^{pump}/J^{pump}_{sat} of the pump fluences to saturation fluences. From these data stored energy efficiencies under Nd^{3+}-laser pumping are $\eta_{st} \approx 50$-75%, the highest η_{st} being for $Yb^{3+}:YAG$ due to its small quantum defect. Stored energy densities ε of 3-4 J/cm^3 and laser saturation fluences $J^{las}_{sat} \approx 10$ J/cm^2 for Yb^{3+} and Ho^{3+}: YAG crystals allow one to use these active media in the driver for the efficient regenerative amplification of short (10^{-8}-10^{-9} s) light pulses. For $Tm^{3+}:YAG$ and $Co^{2+}:MgF_2$ crystals J^{las}_{sat} are much higher than a typical optical damage threshold of laser components (≈ 20 J/cm^2). The efficient extraction of the stored energy for these materials is possible by powerful light pulses of longer duration (10^{-7}s) with a subsequent compression. A very wide (≈ 1000nm) fluorescence line of $Co^{2+}:MgF_2$ crystal is of interest also for femtosecond pulse amplification. Only 1-3°C temperature difference across the slab thickness at ν=1 Hz was calculated for all active media samples. The total efficiencies estimated

for Nd-laser PTM Raman and FR pumping for all crystals are 2-3%. In case of Co^{2+}:MgF_2 pumping by a combination of a 1.06 μm laser line and s1-s3 Stokes components with properly arranged intensities the efficiencies over 4% are anticipated.

A 1 kJ Nd^{3+}:glass laser system for modeling experiments in selective pumping is under construction on the base of the "Delfin" laser facility.

References

1.   N.Basov. "Nuclear Reactor with a Laser Thermonuclear Source of Neutrons". Proc. of the IAEA Tech. Committee Meeting on Drivers for ICF, Paris, France, Nov. 14- 18, pp.13-28 (1995).

2.   P.Moulton 'An Investigation of the Co:MgF_2 Laser System', IEEE J. of Quant. Electr. vol.QE-21, 10, pp.1582 -1595, (1985).

3.   E.Zharikov, S.Kalitin, Yu.Papin et al. 'Cr^{4+} Ions as a New Efficient Sensitiser of Laser Materials for the Wavelength Range 1.5-3 μm, Activated with Er^{3+}, Tm^{3+}. Ho^{3+} Dy^{3+} Ions', Kvantovaya Elektr., 21, 11, pp.1035-1037, (1994)

4.   I.Shcherbakov et al. 'Characteristic properties of thermal and lasing regimes of optically dense active media', M. "Nauka", Trudy IOFAN, 26, pp.107-124 (1990).

5.   T.Basiev, A.Kravetz, A.Fedin 'Q-switching with LiF:F_2^- Crystals in a Technological Pulse Periodic Pumped YAG:Nd Laser', Kvant.Elektr. 20, 6, pp.594-596, (1993).

6.   Ch.Orth and S.Payne 'System Study of Diode-Pumped Solid-State Laser Driver for Inertial Fusion Energy', in 1st Ann. Int. Conf. Solid State Lasers for Application to ICF, M.Andre, H.Powell edit. Proc. SPIE 2633, pp.264- 271, (1995)

7.   N.G.Basov, A.Z.Grasyuk, Yu.I.Karev et al. "A Raman Hydrogen Laser for Efficient Coherent Summation of Nanosecond Light Pulses". Kvant. Elektr., 6, 6, pp.1329-1331, (1979).

8.   R.Wallace and S.Harris 'Oscillation and Doubling of the 0.946 μm Line in Nd^{3+}:YAG' Appl. Phys. Letters 15, 4, pp.11-112, (1969)

9.   S.Payne, L.Chase, L.Smith et al. 'Infrared Cross-Section Measurements for Crystals Doped with Er^{3+}, Tm^{3+} and Ho^{3+} ', IEEE J. of Quant. Electr. v.28, 11, pp. 2619-2630, (1992)

Table 1

Laser crystal	λ_{pump} μm	σ_{pump} $\times 10^{-21}$ cm^2	τ ms	J^{pump}_{sat} J/cm^2	λ_{las} μm	σ_{las} $\times 10^{-21}$ cm^2	J^{las}_{sat} J/cm^2
Ho^{3+}:YAG	1.13	5.3	7.8	33	2.098	9.8	9.7
Tm^{3+}:YAG	1.22	4.5	10.5	36	2.011	2.2	43
Co^{2+}:MgF_2	1.33	3.6	1.0	42	1.95	1.5	68
Yb^{3+}:YAG	0.938	6.0	1.2	35	1.03	18	10.7

Table 2

Laser crystal	C $\times 10^{20}$ cm^{-3}	d cm	N	t_{pump}/τ	J^{pump}/J^{pump}_{sat}	η_{st} %	ε J/cm^3
Ho^{3+}:YAG	0.9	1.1	4	0.026	1.0	46	3.6
Tm^{3+}:YAG	3.2	0.5	3	0.02	1.5	50	18
Co^{2+}:MgF_2	2.2	0.9	5	0.20	2.5	60	15
Yb^{3+}:YAG	0.4	1.7	6	0.17	1.7	75	4.3
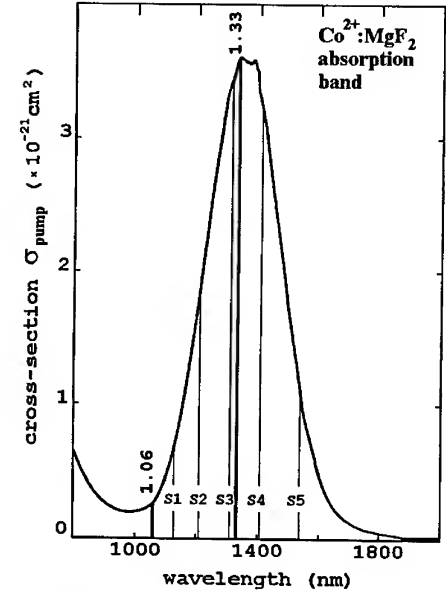
Figure 1
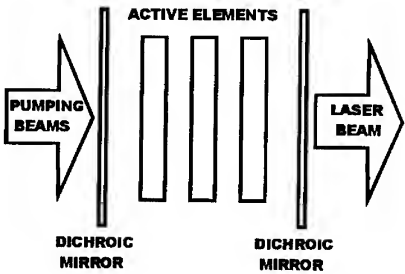
Figure 2

SOFT-X-RAY LASING AT 28.5 NM IN NEON-LIKE CHROMIUM

J. E. BALMER, A. R. PRÄG, and F. LÖWENTHAL
Institute of Applied Physics, University of Berne
Sidlerstr. 5, CH-3012 Berne, Switzerland

Intense 3p - 3s, J = 0 - 1 soft x-ray lasing at 28.5 nm in neon-like chromium has been observed experimentally using the table-top Nd:glass laser of the University of Berne as the pump source. 2.4 cm long chromium slab targets were irradiated with 100-J/500-ps pulses at the fundamental wavelength of 1.054 μm. The prepulse technique was applied using a defined prepulse 5 ns before the main pulse and with a prepulse-to-main pulse intensity ratio of 0.7%. At a pump energy of 90 J, corresponding to a pump irradiance of approximately 10 TW/cm^2, a gain coefficient g = 2.3 ± 0.3 cm^{-1} was measured.

Since the first demonstration of soft-x-ray lasing in collisionally pumped neon-like selenium at wavelengths near 21 nm [1,2] the possibility of scaling to shorter wavelengths as well as the development of table-top x-ray lasers driven at pump energies well below the kilojoule level has been a major issue. Important progress in this direction was made through the introduction of the prepulse technique in which a low-energy prepulse irradiates the target a few nanoseconds before the main driving pulse. Nilsen et al. [3] recently reported on 3p - 3s, J = 0 - 1 lasing in neon-like chromium (Z = 24) at the wavelength of 28.5 nm, applying the prepulse technique and using a delay of 7 ns between the prepulse and the main pulse, a prepulse-to-main pulse energy ratio of 0.5%, and a drive laser energy of 1.1 kJ (pulse duration 600 ps). Li et al. [4] demonstrated lasing in neon-like calcium at a wavelength of 38.3 nm with a pump irradiance of 5 TW/cm^2 and Präg et al. [5] achieved lasing in neon-like titanium at the wavelength of 32.6 nm at an irradiance as low as 2.5 TW/cm^2.

In this work we report on an experimental demonstration of 3p - 3s, J = 0 - 1 soft x-ray lasing at 28.5 nm in neon-like chromium using a compact drive laser. Applying the prepulse technique at a fixed prepulse-to-main pulse energy ratio of 0.7%, we demonstrate that lasing at 28.5 nm can be observed at a pump energy as low as 90 J, corresponding to an irradiance of 10 TW/cm^2. This represents, to our knowledge, the lowest pump irradiance for which soft x-ray lasing at a wavelength shorter than 30 nm in a neon-like ion has been reported to date. The experiments were performed using a table-top Nd:glass laser capable of delivering up to 120 J at 1054 nm with a pulse duration of 500 ps (FWHM).

A line focus 2.5-cm long and approximately 80-μm wide is produced by using an aplanatic doublet with a focal length of 500 mm combined with a cylindrical lens with a focal length of -1700 mm. All the surfaces of the focusing optics are

532

antireflection-coated and have a clear aperture diameter of 100 mm. The beam diameter is 85 mm. A defined prepulse of 0.7% at a constant delay of 5 ns is produced with the aid of an antireflection-coated beamsplitter in the beam path of the double-passed 90-mm amplifier. The spatial coincidence of the prepulse and the main pulse was adjusted to better than 10 μm, given by the resolution of the CCD camera used for the adjustment. The energy of the main pulse was varied between 60 J and 100 J by varying the gain in the preamplifier rod. The laser irradiated 2.4-cm long polished chromium slab targets with the line focus overfilling the target on both sides for maximum uniformity [6].

The principal diagnostics used was a time-integrating, space-resolving spectrometer. The spectrometer used a 1200-grooves/mm, concave (radius of curvature: 5649 mm), Harada-type reflection grating [7] and a 40-mm diameter P20 phosphor screen coupled to a cooled CCD camera having a pixel size of 25 μm x 25 μm. The spectrometer looked axially onto one end of the plasma column with the spatial resolution in the direction perpendicular to the target surface. The one-dimensional spatial resolution of better than 25 μm was realized by using a spherical gold mirror with a radius-of-curvature of 2 m, adjusted at a grazing-incidence angle of 5.5°. The mirror forms an image of the plasma column on the phosphor screen with a magnification of 3. The grating disperses the incident radiation perpendicularly to the direction of the spatial resolution. The wavelength coverage was 12 nm with a spectral resolution of ~0.2 nm.
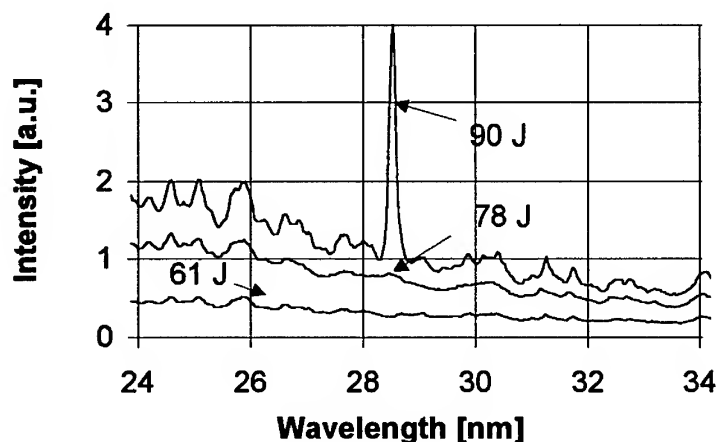
Fig. 1. Spectral intensity for various pump energies

The measurements were performed with the fixed prepulse-to-main pulse energy ratio of 0.7% and without a prepulse. Without an intentional prepulse, lasing on the 3p - 3s, J = 0 - 1 line at 28.5 nm in neon-like chromium was not observed. Figure 1 shows scans of the space-resolved spectra for a 2.4-cm long chromium target irradiated at main pulse energy between 60 and 90 J. The 28.5-nm line is seen to dominate the spectrum at a pump energy of 90 J, corresponding to an irradiance of 10 TW/cm^2, whereas it is not observed at a pump energy of 61 J. Figure 2 shows the scaling of the laser line intensity with increasing target length for pump energy of 90±5 J. A fit to the Linford formula yields a value for the gain coefficient of approximately 2.3±0.3 cm^{-1}.

In summary, we have experimentally demonstrated J = 0 - 1 soft x-ray lasing at 28.5 nm in neon-like chromium. The prepulse technique was applied with a constant delay time of 5 ns between the 0.7% prepulse and the main pulse. Lasing was observed for drive laser energies above 90 J, corresponding to a pump irradiance of 10 TW/cm^2. To our knowledge this is the lowest pump laser energy reported to date for a neon-like soft x-ray laser at a wavelength shorter than 30 nm. Further reduction of the drive laser energy may be possible, for example, by variation of the delay time between the prepulse and the main pulse and/or by using a series of pump laser pulses of shorter duration (multiple-pulse technique).
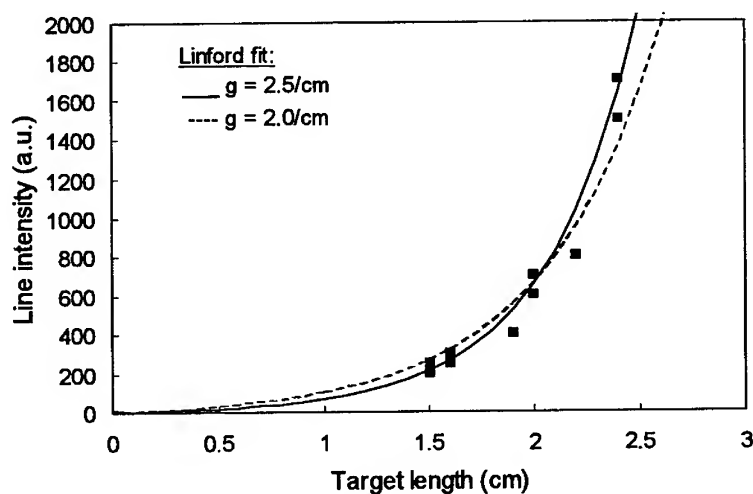
Fig. 2. 28.5-nm line intensity vs. target length. Solid and dashed lines are the Linford curves for g = 2.5 and 2.0 cm^{-1}, respectively.

534

References:

[1]   D. L. Matthews et al., Phys. Rev. Lett. **54**, 110 (1985);

[2]   T. N. Lee, E. A. McLean, and R. C. Elton, Phys. Rev. Lett. **59**, 1185 (1987)

[3]   J. Nilsen, B. J. MacGowan, L. B. Da Silva, and J. C. Moreno, Phys. Rev. A **48**, 4682 (1993);

[4]   Y. Li, G. Pretzler, and E. E. Fill, Phys. Rev. A **52**, R3433 (1995)

[5]   A. R. Präg, A. Glinz, J. E. Balmer, Y. Li, E. E. Fill: *"Prepulse dependence of J=0-1 lasing at 32.6 nm in neon-like titanium"*, Appl. Phys. B (in print)

[6]   A. Glinz, J. E. Balmer, Opt. Commun. **111**, 285 (1994)

[7]   T. Kita, T. Harada, N. Nakano, and H. Kuroda, Appl. Opt. **22**, 512 (1983)

DEVELOPMENT OF HIGH-POWER EXIMER γ-PUMPED LASERS SYSTEMS INTENDED FOR INVESTIGATION THE PHYSICS OF THERMONUCLEAR TARGETS WITHIN THE ENERGY RANGE 0.1-1 MJ

E.K. Bonyushkin, R.I. Il'kayev, A.P.Morovov, A.L..Pavlovskii.,
B.V. Lazhintsev

*Russian Federal Nuclear Center - All-Russia Scientific Research
Institute of Experimental Physics,
Arzamas-16*

S. Yu. Gus'kov, V.B. Rozanov
*Lebedev Physical Institute of Russian Academy of Science,
Moscow*

I.B. Zmitrenko
*Institute of Mathematic Simulation of Russian Academy of Science,
Moscow*

Results of experimental and calculation and theoretical investigations on eximer laser pumping by γ-radiation powerful source is presented. Based on the results of investigations there are proposed laser systems for study of thermonuclear targets compression physics.

In our earlier reports [1,2] we informed about basic possibility use for researches of inertial thermonuclear fusion and plasma physics research of high powerful gas lasers, pumped by γ-radiation of a small (less than 1 kiloton) nuclear explosion. As a pumping source the nuclear explosion possesses a number of unique peculiarities essential for laser thermonuclear fusion problem. This is its small dimensions defining the pumping high space and time symmetry; high γ-radiation density providing the pumping high specific power $(10 - 100\ MeV/cm^3)$; this is the pumping high specific power of laser gas medium $(0.3 - 1.5)\ J/cm^2$, as well as high degree of pumping uniformity at $E_\gamma > 1$ MeV. These peculiarities are easily realized using the longitudinal laser pumping in one-pass "running wave" mode with synchronous

propagation along active volume of medium excitation area by γ-radiation and laser pulse generation front. The medium excitation mechanism, at that, is consisted of γ-radiation Compton-scattering and energy transmission to secondary electrons in recombination-nonequilibrium plasma.

Gamma-pumped lasers have the advantages: their laser radiation pulses one can use without any conversion of their time and spectral characteristics. Duration and time structure of laser pulse at the use "running wave" mode with the longitudinal pumping is definitively determinate by γ-pulse, and if γ-pulse duration is rather small, it is necessary to form laser pulse with use of nonlinear optics elements, in addition. The possibility of direct pumping of short-wave eximer lasers exclude of the initial laser radiation spectral conversion and there occurs the possibility to produce systems with the laser radiation wavelength of large range. We shall explain these possibilities in detail lower.

Experimental and calculation-theoretical researches performed in VNIIEF were justified and formed the basis of our later proposals. Much attention is given to eximer and radiation-chemical lasers, in optimal way corresponding optimally the condition of the pumping by short γ-pulse in the "running wave" mode. This is eximer UV-laser on XeF^* molecule (λ=0.351 μm) and radiation-chemical IR-laser on XeF^* molecule ($\lambda \approx 3$ μm) [3-6].

Operation mixtures composition optimization and estimation of their spectral radiation characteristics were performed in laboratory investigations with excitation the small of active media by electrons of high current electron accelerators. Simultaneously with these investigations there were made calculation and theoretical estimations of the expected characteristics of eximer UV-lasers with γ-ray pulse pumping (operating mixture $Ne + Xe + NF_3$, radiation molecule XeF^*, λ=0.351 μm). On the basis of consideration the kinetics of the main plasma-chemical reactions in terms of laser radiation generation and transfer there considered a mathematical model of problem within the limits of two-temperature approximation and one-dimensional geometry. The mode of unipass laser with longitudinal pumping in the form of "running wave" is foreseen. One of the calculation purpose is the estimation of optimal composition of gas mixture of different levels and pumping rate by γ-radiation. It is shown that the laser radiation pulse in a sufficiently extended system repeats the pumping pulse at coaxial radiation propagation. At noncoaxial laser and γ-radiation propagation (within the small angles limits) some laser radiation pulse duration rise takes place (fig. 1). The preliminary calculation estimation have been done and for radiation-chemical HF-laser [5]. Fig. 2 shows the ratio of laser pulse amplitude, propagating in the direction of γ-pulse pumping and in

the opposite direction ("forward-back" ratio) the ratio peculiar for the "running wave" mode. As it seen in the figure even at the distance of some tens centimeters from the laser initial part (from the side of γ-radiation source) the laser pulse value propagating "back" is some orders less than the pulse value, propagating together with the pumping pulse. As a result, that laser radiation propagation in γ-radiation direction occur in amplifying medium during the hole time of γ and laser radiation along the laser, while the reverse pulse propagates in practically inert medium. Nonstable relaxation character of laser pulse back front at the outset of γ-pulse pumping propagation in laser medium and, thus, at the outset of laser amplification and shaping is connected with spectral transmissions influence in the pulse amplification onset mode. In the process of the further laser radiation amplifying (that is at laser and γ-radiation running along active medium and the saturation effect achievement) the role of side effects disappears.

On the basis of calculational and experimental (laboratory) data a programme of investigation on nuclear explosion was scheduled and some designes for such investigations were carried out. A great part of experiments has been performed with the cylindrical geometry lasers small scale models. Laser cuvette systems during laboratory assemblage are shown in fig. 10,11. Energy, time and space characteristics of laser radiation were researched in experiments. A serious attention is paid to the problem of the pulse space formation, that is to receipt of its satisfactory divergence, reasonable for investigations of inertial thermonuclear fusion. There are some schemes of formation in conformity with "running wave" mode: "geometric shaper", the master oscillator-amplifier system, "cone amplifier-shaper" [1,4]. The use of "cone amplifier-shaper" in the "running wave" mode with short γ-pulse pumping allows simultaneously to solve the divergence and contrast problem in the laser source single scheme. As for our assessments laser energy up to 70-90 kJ receipt is possible in cone laser, made as one independent module. Let's give some number illustrating the researches results in lasers scale models as an example:

1. Eximer UV-laser:
operating mixture $Ne : Xe : NF_3 = (1000{:}30{:}7)$, p=5...6 atm;
λ=0.351 μm
radiation energy - 6 kJ
efficiency - up to 4%
non focused energy density - up to 8 J/cm^2
pulse duration < 8 ns
specific energy release - up to 28 J/l

2. Radiation-chemical IR-laser

operating mixture $SF_6 : H_2 = (9:1)$, p=2 atm, $\lambda \approx 3$ μm
radiation energy - 70 kJ
efficiency - up to 6%
non focused energy density - up to 8 J/cm^2
pulse duration < 8 ns
specifical energy release - up to 40 J/l

The results received in experiments testify the convincing possibilities of gas lasers with pumping by nuclear explosion γ-radiation with their use in research of inertial thermonuclear fusion.

If the nuclear explosion is the pumping source, it is possible to create multichannel laser systems with one-, two- and multilateral radiation introduction for thermonuclear targets compression in $10^5 - 10^6 J$ range of laser energy.

One of the main peculiarities of such systems one should consider the possibility of receipt of the given time characteristics of laser pulse. The pulse time symmetry of multichannel system is defined only by the accuracy of the space arrangement of modules relative to the pumping source and target*. This important factor allows at the use of some module to realize shaping the pulse in time, while the modules use with the different laser energy allows to make the shaping range rather substantial.

Nowadays there is published a number of works (e.g. [7]), testifying to the great advantage in shaping of thermonuclear target G at the transition into the earlier given shape of laser pulse, e.g. shape [7]

$$P(t) = P_0 \cdot \left\{ \frac{1}{(t - t_0)^2} - \frac{1}{t_0^2} \right\}, \ 0 \le t \le \tau < t_0 \ t_0 = 1.125 \cdot \tau, \tau = 6 \text{ ns}$$

Fig. 3 and 4 show possibility of laser pulse shaping. The shape of given in fig. 3 pulse is selected by means of 4 modules radiation, in fig. 4 - of 5 modules. Their relative energy contribution of each module, shapes and duration, their maxima arrangement. As it seen from fig. 3 already four modules allow to make the pulse shape satisfying the given one within 5-10% limits on the laser energy; five modules make the resulting laser pulse practically coinciding with the given. It should be in radiation of

---

*) The word "module" should be understood as one laser, and word "channel" - either one or several modules radiation of which is directed in one point (one part of the target surface).

the latter in mentioned that overwhelming part of laser energy (>80%) is contained the time module. The energy of the last but one module is in 6-7 times less, the latter modules are lacking power, small laser with rather modest requirements to their design peculiarities and load parameters of the optical elements (lens, mirrors).

The possibility of the direct pumping of short wave eximer lasers favors the substantial simplification of the optical schemes of considered systems.. On the one hand this circumstances exclude of necessity of laser radiation spectral transformation, but on the other hand opens wide possibilities of laser pulse shaping on the wave length. Such shaping possibility is defined by a set of eximer molecules; using in the modules of multichannel systems: XeF^* ($\lambda = 351$ nm), $XeCl^*$ ($\lambda=308$ nm), $XeBr^*$ ($\lambda=282$ nm), KrF^* ($\lambda=248$ nm), $KrCl^*$ ($\lambda=222$ nm), ArF^* ($\lambda=198$ nm), Xe_2^- ($\lambda=172$ nm).

A rather interesting and perspective there occurs the simultaneous shaping of laser pulse on time and length of wave, when laser pulse rises on amplitude (fig. 3,4) the radiation wave length shortens.

To the great advantage of γ-pumping laser systems one should consider the possibility of their radiation high contrast achievement (up to 10^7). It is defined by physical scheme peculiarity - γ-radiation pulse source plus unipass laser of "running wave" with longitudinal pumping. In particular, if using the conical amplifier shaper, pre radiation is practically absent, while possible background γ-radiation may be done wittingly lower the generation threshold.

The thermonuclear targets compression on the direct-drive laser fusion scheme requires the high degree of uniformity of energy distribution on laser beam cross section. This characteristic is provided in our case by uniform in cross section of laser pumping by γ-radiation following from just geometry of the longitudinal pumping. Some nonuniformity may arise only due to the edge effects, originating near gas-wall boundary, namely, due to Compton-effect on the wall material. This effect is lowered up to the level not exceeding 3-5% by removal the laser wall from the "force" arrangement bearing gas pressure and carrying all mechanical loads (fig. 5). The arrangement of proper laser volume is made as thin and light as possible (aluminium, plastic, paper) while it doesn't carry any mechanical loads besides its own weight. Such constructions were used during the researches performance in VNIIEF. If under experiment conditions on the direct-drive laser fusion scheme the additional lowering of nonuniformity, at the account of the edge effect (that is <3-5%) is necessary, it may be achieved at the account of the use of physical dependence of pumping power (fig. 6). For this pumping of the most energy released part of the laser may take place to the right from the maximum of curve K=f(W) in fig. 6. Some basic elements may

540

be proposed as an example of gas laser use with pumping by nuclear explosion γ-radiation. Cone amplifier-shaper is used as laser modules in this schemes.

1. Scheme with two-channel radiation input (fig. 7). Two groups of modules serves as laser energy sources (there are 1-5 modules in each group); their energy is focused to the target from the opposite sides by elliptical mirrors. Such scheme may be used for example for the target of "hohlraum" type.

2. Scheme with six-channel radiation input with the use of lenses and mirrors (fig. 8). Lasers radiation is focused in six points of the target surface arranged symmetrically according the method of cube side centers. This scheme may be used analogously for "laser hot bed" target [8]. In each six laser channels there may be used 4-5 modules with the aim of laser pulse shaping on the wave length or on time [fig. 9].

3. Basic scheme with 4 modules with laser pulse in time shaping (fig. 6 view from above). So, the total diagram with six-sided input of energy contains 24 modules. Such system is calculated on the total energy, incorporated in the target 200-400 kJ.

Preliminary estimation showed that the experiment cost (with the use of the nuclear explosion as a source of laser and target pumping) can be of 4-6 millions. dollars depending on the complexity of the general scheme applied.

REFERENCES

1. E.K. Bonyushkin, R.I. Il'kaev, A.I. Pavlovski, A.P. Morovov, N.G. Basov. About testing experiment with targets for gain 1 based on using of the powerful pulsed laser pumped by γ-radiation of the underground nuclear explosion. Proceedings of the 23 European Conference, Oxford, 19-23 Sept. 1994, p. 89-91.

2. E.K. Bonyushkin, R.I. Il'kaev, A.P. Morovov, A.I. Pavlovski, B.V. Lazhintsev. Ignition experiment design based on γ-pumped gas lasers. Abstracts of 12th International Conference on Laser Interaction and related Plasma Phenomena, Osaca Japan, April 24-28. 1995.

3. B.V. Alekhin, E.K Bonyushkin, V.V. Varaksin, B.V. Lazhintsev, A.E. Lachtikov, A.P. Morovov, V.A. Nor-Arevyan, A.I Pavlovski, R.O. Orlov, V.G. Rogachev.. Running wave eximer laser pumped by γ-radiation. Abstracts of the Branch Conference "Physics of nuclear exited plasma and problems of nuclear pumped lasers", v. 3, p. 272, 1992.

4. B.V. Alekhin, E.K Bonyushkin, V.V. Varaksin, B.V. Lazhintsev, A.E. Lachtikov, A.P. Morovov, V.A. Nor-Arevyan, A.I Pavlovski, R.O. Orlov, V.G. Rogachev, V.B.

Shlyakhovoj. Research of laser radiation shaper pumped by γ-radiation of nuclear explosion. Proceedings of the Second International Conference "Physics of nuclear-exited plasma and nuclear pumped lasers problems" (NPL-94), v. 1, p. 338, Arzamas-16, 1995..

5. A.I. Pavlovski, E.K Bonyushkin, V.V. Varaksin, G.S. Vinyarski, A.E. Lachtikov, G.M. Mischenko, A.P. Morovov, V.D. Urlin.. Research of pulsed chemical γ-ray pumped HF-laser. DAN, 1993, v. 331, N 3, p. 299.

6 A.I. Pavlovski, E.K Bonyushkin, V.V. Varaksin, G.S. Vinyarski, A.E. Lachtikov, G.M. Mischenko, A.P. Morovov, V.D. Urlin..Characteristics research of poweful HF-laser exited by γ-radiation of the nuclear explosion. Proceedings of the Second International Conference "Physics of nuclear-exited plasma and nuclear pumped lasers problems" (NPL-94), v. 2, p. 214, Arzamas-16, 1995..

7. Z.Yu. Gus'kov, V.B. Rozanov, N.V. Zmitrenko. Pulse shaping influence on the targets near break-even point. Proceedings of the 23 European Conference, Oxford, 19-23 Sept, 1994, p. 281-284.

8. Z.Yu. Gus'kov, V.B. Rozanov, N.V. Zmitrenko. ICF target with distributed absorption of laser energy. Proceedings of the 23 European Conference, Oxford, 19-23 Sept, 1994, p. 275-279.

DYNAMICS OF AMPLIFIED SPONTANEOUS EMISSION
IN X-RAY LASER WITH RANDOM OPTICAL INHOMOGENEITIES

F.A.STARIKOV

Russian Federal Nuclear Centre - Institute of Experimental Physics (VNIIEF)
Sarov (Arzamas-16), Nizhni Novgorod reg. 607190, Russia

The amplified spontaneous emission (ASE) dynamics in x-ray laser with small-scale fluctuations of the dielectric permittivity $\tilde{\varepsilon}$ is studied. The ASE scattering by $\tilde{\varepsilon}$ is found to reduce the ASE spatial coherence degree and coherent power. With an increase in the laser length the coherence length tends to a constant value. At the weak regular refraction the ASE scattering by $\tilde{\varepsilon}$ decreases the gain observed. At the strong regular defocusing refraction the effect of $\tilde{\varepsilon}$ on ASE has the "latent" character: an essential fall in the high coherence degree is accompanied by a small decrease in the axial intensity and small broadening of the ASE beam as a whole.

1. Introduction

The effect of regular large-scale inhomogeneity of dielectric permittivity ε on the x-ray laser radiation has been fairly well studied. The optical micro-inhomogeneities also exist in the plasma as a result of the various instabilities [1]. These inhomogeneities, treated as random ones, can affect the gain and propagation of x-ray radiation [2]. The account for $\tilde{\varepsilon}$ in the ASE calculations could be made by method based on parabolic equation for the radiation field amplitude. However in case of the stochasticity of the radiation source and parameters of the medium it would require an enormous number of computations followed by the ensemble averaging that is time-consuming. We use the method based on paraxial equation for the transverse correlation function (TCF) of the field amplitude [3]. It is convenient when the ASE transverse coherence length is much less than the beam width. In present paper the single-pass ASE is studied with allowance for the regular transverse inhomogeneity of ε and its micron-scale fluctuations $\tilde{\varepsilon}$.

2. The TCF-method

The equation for the TCF $B \equiv \langle A(\mathbf{r}_1;z)A^*(\mathbf{r}_2;z) \rangle$, where $A(\mathbf{r};z)$ is the slowly varying field complex amplitude and the corner brackets mean the statistical averaging, at the single-pass amplification has the form [3,2]:

$$\left[\frac{\partial}{\partial z} + \frac{i}{k}\frac{\partial^2}{\partial \mathbf{r}\partial \mathbf{r}'} + \frac{ik}{2}[\bar{\varepsilon}(\mathbf{r}_1;z) - \bar{\varepsilon}(\mathbf{r}_2;z)] - \frac{\alpha(\mathbf{r}_1;z)/2}{1 + B(\mathbf{r}_1,0;z)/J_{sat}(\mathbf{r}_1;z)} - \right.$$
$$\left. - \frac{\alpha(\mathbf{r}_2;z)/2}{1 + B(\mathbf{r}_2,0;z)/J_{sat}(\mathbf{r}_2;z)} + \frac{\pi k^2}{4}H_\varepsilon(\mathbf{r},\mathbf{r}';z) \right] B(\mathbf{r},\mathbf{r}';z) = b_{sour}(\mathbf{r},\mathbf{r}';z), \quad (1)$$

where $\mathbf{r}_1$, $\mathbf{r}_2$ are the transverse radius-vectors; $\mathbf{r}'=\mathbf{r}_1-\mathbf{r}_2$, $\mathbf{r}=(\mathbf{r}_1+\mathbf{r}_2)/2$. Eq.(1) embodies: the diffraction; refraction on regular profile $\bar{\varepsilon}$; regular amplification with the

542

small gain coefficient α and saturation (J_{sat} is the saturation intensity); the radiation source b_{sour} in volume of the medium; scattering by the permittivity fluctuations $\tilde{\varepsilon}$ in the Markov approximation (the term $H_{\varepsilon}(\mathbf{r},\mathbf{r}';z)=(2/\pi)^{1/2}\sigma^2(\mathbf{r},z)l_{\parallel}(\mathbf{r},z)\{1-\exp[-r'^2/2l_{\perp}^2(\mathbf{r},z)]\}$ at the Gaussian spatial spectrum of $\tilde{\varepsilon}$, where σ^2, $l_{\perp}$ and $l_{\parallel}$ are the variance, transverse and longitudinal correlation lengths of $\tilde{\varepsilon}$, respectively [2]). Inside the gain medium ($|\mathbf{r}_{1,2}|\leq a$) the defocusing profile $\bar{\varepsilon}(\mathbf{r})=1-\Delta\varepsilon+r^2/z_r^2$, where $z_r=a/\Delta\varepsilon^{1/2}$ is refraction length. Outside the gain medium ($|\mathbf{r}_{1,2}|>a$) $\alpha=0$, $\tilde{\varepsilon}=0$, $\bar{\varepsilon}=1$.

The ASE parameters depend on the ratio between the $\tilde{\varepsilon}$ scattering length $z_{sc}=[6(2/\pi)^{1/2}(al_{\perp})^2/\sigma^2l_{\parallel}]^{1/3}$ [4] and z_r. At high values of $\exp(\alpha z)$ and $\exp(\alpha z_r)$, the transversely unlimited homogeneous gain and the statistically homogeneous fluctuations $\tilde{\varepsilon}$ Eq.(1) has the analytical solution [5].

3. The case of weak regular refraction

When $z_{sc}<z_r$, the ASE scattering by $\tilde{\varepsilon}$ decreases the gain observed at $z\geq z_{sc}$, i.e., axial radiant intensity $q(0)\sim\exp(\alpha z-\kappa_{sc}z)$ at unsaturated gain. The behaviour of $\kappa_{sc}(\sigma)$ depends on $d\equiv kal_{\perp}/z_{sc}$. For the plane (2D) medium with the flat gain at $d^3\geq 1$ we have $\kappa_{sc}\approx 1/z_{sc}$ [4] then $\kappa_{sc}\sim\sigma^{2/3}$ (for 3D medium κ_{sc} will increase most likely twofold). When $d^3\ll 1$, $\kappa_{sc}\approx 3d^2/z_{sc}\sim\sigma^2$ [6] and, thus, κ_{sc} is independent on $l_{\perp}$ and a.

The ASE scattering by $\tilde{\varepsilon}$ decreases the ASE spatial coherence at the laser output and the coherent power including the case of the large Fresnel numbers [5, 6]. The transverse coherence length L_c is defined from the decrease of the modulus of coherence factor to a certain value h. With increasing z L_c tends to the constant value $L_c^{max}\approx[(1-h)/2]^{1/2}\lambda z^{max}/\pi a$, where $z^{max}\approx(2/3)^{1/3}z_{sc}$ at $6d^2/(1-h)\gg 1$ and $z^{max}\approx 2(1-h)z_{sc}/9d^2$ at $3d^3/(1-h)^{3/2}\ll 1$. $L_c^{max}<l_{\perp}$ at large values of d^3 and $L_c^{max}\gg l_{\perp}$ at small values of d^3. The plots of divergence angle θ_{div}, containing 90% of ASE power, as function of z are shown in Fig.1 at $l_{\varepsilon}=l_{\perp}=l_{\parallel}$. The fall in divergence with increasing z due to the gain spatial filtering is replaced by the tendency to constant value $\theta_{div}\approx 2\theta_{sc}$, where $\theta_{sc}=a/z_{sc}$ is the characteristic scattering angle [4]. Gain saturation increases the divergence and diminishes L_c. At deep saturation the off-axis peak forms in the radiant intensity q distribution [4], the maximum q being observed at $\theta\approx\theta_{sc}$.
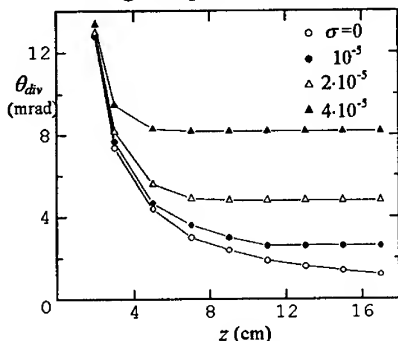
The influence of $\tilde{\varepsilon}$ on ASE may be approximately neglected at the laser length $z\leq z^{max}$. The variance of the plasma electron density σ_{Ne} is given in Table 1 for $z=z^{max}=5$ cm and the various values of λ, a, l_{ε}, where the relationship $\varepsilon=1-4\pi e^2 N_e/m_e\omega$ is used.

Fig.1. Plots of θ_{div} (z) for $\lambda=21$ nm, $a=150$ μm, $\alpha=4$ cm^{-1}, $\Delta\varepsilon=0$, $l_{\varepsilon}=1$ μm and various σ.

Table 1

λ, nm	10				20			
a, μm	25		100		25		100	
l_ε, μm	1	10	1	10	1	10	1	10
σ_{Ne}, 10^{21}cm^{-3}	.04	.14	.1	.56	>.03	.04	.04	.14

For $N_e=10^{21}$ cm^{-3} an effect of $\tilde{\varepsilon}$ can be possible at the N_e fluctuations on the level of a few percent. There are several interesting experimental data. In the Ne-like Se exploding foil x-ray laser ($\lambda\approx21$ nm) [7] the ASE angular divergence parallel to the foil, where $\bar{\varepsilon}$ profile is steep and refraction in near-axis region is small, is considerable larger than the expected value $\theta_g=2a/z$. In the Ne-like Y x-ray laser ($\lambda\approx15.5$ nm) [8] the divergence parallel to the target is larger than θ_g and independent on z. These data can be interpreted with the help of presented results.

4. The case of strong regular refraction

The ASE dynamics in x-ray lasers [7,8] in the plane perpendicular to the target is affected by regular refraction since the $\bar{\varepsilon}$ profile is sufficiently smooth due to the predominant plasma expanding in this direction during x-ray lasing. The refraction in the defocusing gain medium is said to highly improve the ASE coherence with increasing z [9]. Nevertheless, the experimental far-field measurements in an off-axis region, where the radiant intensity is maximal, give a small coherence and no significant z-variation of coherence degree in the direction perpendicular to the foil for the Ne-like Se x-ray laser [10]. But it has been found [11] that the familiar heavy growth with an increase in z is inherent in L_c of ASE emerging through the laser end, whereas L_c of ASE emerging through the laser side surface is relatively short and weakly depends on z in the limiting cases of unsaturated and saturated gain. This fact can help to interpret the experiment since the side ASE gives a main contribution to the off-axis maximum peak of q at gain saturation.

The smaller-than-anticipated coherence [10] can also arise from the presence of $\tilde{\varepsilon}$. At $z_{sc}>z_r$ the ASE scattering by $\tilde{\varepsilon}$ decreases the high coherence and diminishes the coherent power [6]. At the flat gain L_c is restricted by the value $L_c^{max}\approx(\chi/3)^{1/2}\lambda z_{sc}/\pi a$ at $d^2>\chi$ and $L_c^{max}\approx2^{1/2}l_\perp\exp[\chi/3d^2-C/2]$ at $d^2<\chi/2$, where $\chi=(z_{sc}/z_r)\ln(1/h)$, $C\approx0.58$ is the Euler constant. In the former case $L_c^{max}<l_\perp$ whereas in the latter case $L_c^{max}>>l_\perp$. The analysis shows that at $z_{sc}>z_r$ the ASE scattering by $\tilde{\varepsilon}$ is not analogous to the linear absorption unlike the refraction-free case. The fluctuations $\tilde{\varepsilon}$ have, in a sense, a "latent" effect on the ASE: the high coherence is destroyed but the axial radiant intensity does not vary [6]. Fig.2 contains the plots of q and L_c in the far field as the functions of the angle θ, obtained for 2D medium at saturated gain with rounded profile $\alpha=\alpha[1-(x/a)^2]$. A perceptible fall of L_c of the end ASE (at $\theta\leq0.8\Delta\varepsilon^{1/2}$) is observed. The sharp difference in L_c between the end and side ASE disappears. The broadening of ASE beam as a whole is relatively weak. Only an off-axis peak in the q distribution is smeared more appreciably. The fluctuations $\tilde{\varepsilon}$ weakly affect the ASE coherence at the certain conditions [6]. The

rough estimate gives that at the maximum $N_e=10^{21}$ cm^{-3} the complete coherence is feasible if the level of the N_e fluctuations does not exceed a few percent of N_e.

5. Conclusions

The ASE scattering by permittivity fluctuations $\tilde{\varepsilon}$ is found to impair the ASE angular and coherence properties. The coherence length growth and divergence decrease are restricted with increasing in z. At weak regular refraction ($z_{sc}<z_r$) the ASE scattering by

Fig.2. Plots of q (——) and L_c in far field (- - -) vs. θ at $\lambda=21$nm, $a=150\mu$m, $z=4$cm, $\alpha_0=4$cm^{-1}, $\Delta\varepsilon=10^{-4}$, $l_\varepsilon=1.4$ μm, $\sigma=0$ (1); $4\cdot10^{-5}$ (2) and saturated gain; $l_{cr}=\lambda Z\cosh(z/z_r)/4a$, Z is the distance from the output to the far field.

$\tilde{\varepsilon}$ is analogous to linear absorption and decreases the gain observed. At strong regular refraction ($z_{sc}>z_r$) the essential fall in coherence degree is accompanied by the relatively small decrease in the ASE axial intensity and weak broadening of ASE beam as a whole. In many interesting cases the effect of $\tilde{\varepsilon}$ on ASE can be neglected at the plasma electron density irregularity that does not exceed $\sim(1\div10)$ percent of its maximal mean value.

Acknowledgments

References

[1] Rosen M D, *Phys.Fluids B* **2**, 1461-1466 (1990).

[2] Starikov F A, Urlin V D, *Sov. J. Quant.Electron.* **21**, 393-396 (1991).

[3] Starikov F A, *VANT Ser. Teor. Prikl. Fiz.*, No.4,14-23 (1989).

[4] Starikov F A, *Quant.Electron.* **23**, 412-416 (1993).

[5] Starikov F A, *Proc.2nd Int.Conf."Physics of Nuclear-Induced Plasmas and Problems of Nuclear-Pumped Lasers"*, (Arzamas-16, 1994), 260-270 (1995).

[6] Starikov F A, *Proc.SPIE* **2796**, in print; *Quant.Electron.* **26**, No.3 (1996).

[7] Matthews D et al., *J.Opt.Soc.Am.B* **4**, 575-587 (1987).

[8] Ratowsky R P et al., *ICF Quart.Rep.*UCRL-LR 105821-94-2 (LLNL, Livermore, CA), **4** (2), 63-69 (1994).

[9] London R A,Strauss M,Rosen M D, *Phys.Rev.Lett.* **65**, 563-566 (1990).

[10] Trebes J E et al, *Phys.Rev.Letts* **68**, 588-591 (1992).

[11] Starikov F A, *Quant.Electron.* **24**, 320-326 (1994).

AMPLIFIED SPONTANEOUS EMISSION AT GAIN SATURATION: TWO INVESTIGATION APPROACHES

V.K.LADAGIN, F.A.STARIKOV, V.A.VOLKOV

Russian Federal Nuclear Centre - Institute of Experimental Physics (VNIIEF)
Sarov (Arzamas-16), Nizhni Novgorod reg. 607190, Russia

The amplified spontaneous emission (ASE) is studied with the help of solving the parabolic equation (PE) for the field amplitude by the Monte-Carlo technique and solving the equation for the transverse correlation function (TCF). The TCF-method is more advantageous than the PE-method in the case of ASE with incomplete spatial coherence. When the ASE intensity is close to saturation intensity, the statistical linearization of the equation for TCF leads to a certain overestimation of the absolute values of ASE mean intensity whereas the radiant intensity profile shape is not deformed.

1. Introduction

The theoretical description of x-ray laser includes the dynamics of the amplified spontaneous emission (ASE). One of the approaches is the direct numerical solving of parabolic equation (PE) for the radiation field complex amplitude [1,2]. However at the radiation stochastic source the PE-method requires an enormous number of computations of the equation (trials) followed by the ensemble averaging. To avoid this ensemble averaging, we use the method based on the equation for the transverse correlation function (TCF) of the field amplitude [3]. If the ASE coherence length is much less than the beam width (that usually occurs in experiments), the TCF-method enables to obtain the numerical result with the much less consumption of computer time in comparison with PE-method. This is conditioned by the absence of the ensemble averaging and by the smaller number of the transverse mesh points. A special feature of TCF-method is in the approximate character of the equation for TCF at gain saturation that causes the ASE parameters to be rather different from the statistically mean ones [4]. In present paper the ASE parameters, obtained by the TCF-method and by the method of statistical trials (Monte Carlo) of PE, are compared.

2. Main assumptions

The PE for the slowly varying complex amplitude A of quasi-monochromatic radiation field in the case of single-pass amplification has the form:

$$\left[\frac{\partial}{\partial z} + \frac{i}{2k}\frac{\partial^2}{\partial \mathbf{r}^2} + \frac{ik}{2}\varepsilon(\mathbf{r},z) - \frac{\alpha(\mathbf{r},z)/2}{1 + J(\mathbf{r},z)/J_{sat}(\mathbf{r},z)} \right] A(\mathbf{r},z) = S(\mathbf{r},z), \qquad (1)$$

where $\mathbf{r}$ is the transverse vector, z is the longitudinal co-ordinate. Eq.(1) embodies the diffraction, refraction due to the permittivity profile ε, regular amplification with the small gain coefficient α and the possibility of saturation in the steady-state approximation of two-level medium $(J(\mathbf{r},z)=|A(\mathbf{r},z)|^2$ is the flux density, J_{sat} is the

saturation flux density), the radiation source S in volume of the medium, delta-correlated in space. We consider the case when J in the denominator of nonlinear term of (1) is the instantaneous flux density. Thus, the amplified radiation is assumed to be narrowband, coherence time τ_c being more greater than the radiation relaxation time.

From (1) one can derive the equation for TCF $B(r,r';z)=<A(r_1;z)A^*(r_2;z)>$, where $r'=r_1-r_2$, $r=(r_1+r_2)/2$ and the corner brackets mean the statistical averaging. To average the nonlinear terms of the equation, the method of statistical linearization is applied. It consists in the replacement of fluctuating $J(r_{1,2},z)$ in the denominators of nonlinear terms with the means $\beta B(r_{1,2},0;z)$, where $B(r,0;z)$ is the density flux in the TCF-method. Then we obtain [3]:

$$
\left[\frac{\partial}{\partial z} + \frac{i}{k}\frac{\partial^2}{\partial r \partial r'} + \frac{ik}{2}[\varepsilon(r_1;z) - \varepsilon(r_2;z)] - \frac{\alpha(r_1;z)/2}{1 + \beta B(r_1,0;z)/J_{sat}(r_1;z)} \right.
$$
$$
\left. - \frac{\alpha(r_2;z)/2}{1 + \beta B(r_2,0;z)/J_{sat}(r_2;z)} \right] B = Q\delta(r_1 - r_2).
$$

(2)

ASE parameters obtained from (2) must be close to the mean ones due to proper choice of β. Specifically, the radiant intensities, determined by two methods, $q_B(\theta)= \lambda^{-2}\iint B(r,r';z)\exp(ik_\perp r')drdr'$ and $<q(\theta)>=\lambda^{-2}<|\int A(r,z)\exp(ik_\perp r')dr|^2>$, must coincide.

When gain saturation is weak, the statistics of A is of the Gaussian type, the rms deviation of J from $<J>$ being equal to $<J>$. In spite of deep fluctuations of J, the denominators of nonlinear terms in (1), (2) differ from unity weakly. When saturation begins to influence, the relative level of the J fluctuations begins to decrease against $<J>$, the quantity of $[<J^2>/<J>^2-1]^{1/2}$ falls off [4]. At deep saturation $[<J^2>/<J>^2-1]^{1/2}<<1$, therefore the replacement of fluctuating fluxes J in the denominators of nonlinear terms of (1) with the means, i.e. $\beta=1$, is justified. The maximum difference of the solutions of (2) from the mean quantities is at $<J>\approx J_{sat}$. The relative overestimation of the ASE mean flux density reaches about 20% if the only amplitude fluctuations of the source field are taken into account [4].

3. Numerical results

When the results of the TCF-method and the PE-method were matched in [4], the phase fluctuations of the source field were ignored, although they result in the great angular divergence of the spontaneous emission. Now we conduct the comparison of the ASE mean angular characteristics obtained from the one-fold solving of (4) at $\beta=1$ and, repeated many times, solving of exact Eq.(1) with averaging of the results over an ensemble. The algorithms of the numerical solving of (1) and (4) are described in [3] and [5], respectively. The transverse half-size of 2D gain medium is $a=150$ µm, its length $z=5$ cm, $\lambda=21$ nm. Inside the gain medium ($|x_{1,2}|\leq a$) α

548
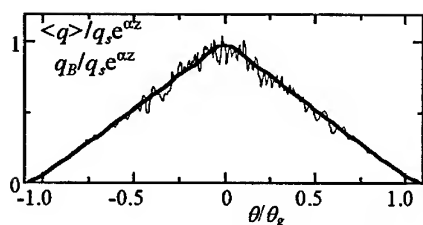
Fig.1. Plots of $<q(\theta)>$ (—) for N_r=300 and $q_B(\theta)$ (—) at unsaturated gain and with no refraction.

is flat and α=4 cm^{-1}. The defocusing profile of ε has the form $\varepsilon(x)=1-\Delta\varepsilon+x^2/z_r^2$, where $z_r=a/\Delta\varepsilon^{1/2}$ is the refraction length. Outside the gain medium α=0, ε=1. The delta-correlated source in the volume at high values of exp(αz) and exp(αz_r) is replaced with the source in the z=0 plane. The boundary condition for (1) $A(x,0)$ is in accord with $B(x,x';0)$ [6].

The difference in the results that would be obtained by the two methods can result from the approximate character of (2) as well as from the possible errors of calculations in each of the methods. Therefore a comparison is worth carrying out first at unsaturated gain (J_{sat}=∞) when the results must coincide. In Fig.1 the ASE angular distributions are shown for unsaturated gain and with no refraction (θ_g=2a/z=6 mrad). The Monte-Carlo method at N_r=300 trials gives the $<q>$ distribution that weakly fluctuates about the q_B profile, coinciding with the analytical distribution. Thus the errors of calculations in each of the methods are negligible.

The calculations at saturated gain are conducted for such J_{sat} that at the laser output $<J>\approx J_{sat}$. So, the approximate character of (2) must show itself the most highly [4]. In Figs 2 and 3 the ASE angular distributions are given in the absence ($\Delta\varepsilon$=0) and presence ($\Delta\varepsilon$=10^{-4}) of refraction. The deep fluctuations of q are in single trial. In refraction-free case on the beam periphery the modulation period of q is

Fig.3. Plots of $<q(\theta)>$ (—) for N_r=1 (a), 300 (b) trials and $q_B(\theta)$ (—) at gain saturation and with no refraction.

Fig.4. Plots of $<q(\theta)>$ (—) for N_r=1 (a), 300 (b) trials and $q_B(\theta)$ (—) at gain saturation and with refraction.

larger because of the higher coherence degree [7]. In the refraction case the coherence degree is higher in the near-axis region of beam where the ASE, emerging through the laser end, dominates. The ASE, emerging through the laser side surface, gives a main contribution to the off-axis peaks of $<q>$ at refraction angle $\theta_r=(\Delta\varepsilon)^{1/2}=10$ mrad and has the more low coherence [7]. It is seen the TCF-method overestimates the absolute values of $<q>$ by ~30%. At the same time the TCF-method does not deform the $<q>$ profile. At less or more deep saturation the error in the determination of $<q>$ by the TCF-method decreases. In refraction-free case a calculation in the TCF-method takes the computer time one-tenth as much as a trial in the Monte-Carlo method. To obtain the rather reliable results by the Monte-Carlo method, it is needed to average at least over (10÷100) trials in an ensemble. It is also interesting to compare two methods in the 3D case. Such calculations by the TCF-method are practicable and carried out for the axially symmetrical medium [3], whereas the 3D calculations by PE-method are absent since they would require an impractically large number of the mesh points [2].

4. Conclusions

The ASE in the x-ray laser with refraction is investigated by solving PE for the field amplitude by the Monte-Carlo technique and solving the equation for TCF in 2D medium. In the case of ASE with low spatial coherence the TCF-method gives the results more quickly in comparison with PE-method. At gain saturation the statistical linearization of the equation for TCF leads to a certain overestimation of the absolute values of the ASE mean intensity but does not deform the radiant intensity profile shape. The maximum relative overestimation occurs, when the flux density is close to the saturation density, and constitutes about 30%.

References

[1] Borovskii A V, Galkin A L, Korobkin V V,
    Sov.J.Quant.Electron. **18**, 915-919 (1988).
[2] Feit M D, Fleck J A, Jr, *J.Opt.Soc.Am. B* **7**, 2048-2060 (1990).
[3] Starikov F A, *VANT Ser. Teor. Prikl. Fiz.*, No.4, 14-23 (1989);
    No.2, 33-38 (1990).
[4] Starikov F A, *ibid*, No.3, 20-24 (1989).
[5] Ladagin V K, *VANT Ser.Met.Progr.Chisl.Resh.Zad.Mat.Fiz.*, No.1, 19 (1985).
[6] Kandidov V P, Ledenev V I, *Vestnik MGU, ser. Fiz.Astr.*, **23**, 3-8 (1982).
[7] Starikov F A, *Quant.Electron.* **24**, 320-326 (1994).

IMPROVEMENT OF THE SPACE-TIME INTENSITY DISTRIBUTION OF THE PULSED IODINE PHOTODISSOCIATION LASER PERUN

B.Králiková J.Skála P.Straka K.Rohlena
Institute of Physics, Acad. Sci. Czech Rep.,
Prague 8, Na Slovance 2, 180 40 Czech Republic

Abstract

A radial delay of the laser pulse intensity distribution over the radius of the iodine laser system Perun causing a pulse deformation and effectively prolonging the laser pulse in the focus was removed by applying image relaying in the start up phase of the pulse.

1 Introduction

Current status of the iodine high-power laser system PERUN (output energy 40 J, attainable power density $10^{15} W cm^{-2}$, with the possibility of an efficient conversion in the 2nd and 3rd harmonics, a good stability of laser parameters and the repetition time 10 to 15 minutes) offers a possibility of routine target experiments with a participation of external users. A part of the programme is aimed at the interaction experiments based on the laser beam splitting in two pulses reaching the target at different times i.e. the second beam interacts with the plasma generated by the first one. These experiments strictly require a radially uniform space-time distribution of the intensity (STID) due to the demand on a precise tuning of the delay (fractions of nanosecond). That is why effort is devoted to a determination of the STID in the system. It has been found that the propagation speed of the laser pulse shows a radial dependence; the local pulse FWHM vary from 300 to 400 ps, but the in overall (radially integrated) pulse FWHM is from 700 to 1000

ps. This leads not only to an uncertainty in the pulse timing, but also the interaction time is prolonged and the power density in the focus is diminished. The spatial inhomogeneity itself is currently improved in many ways (spatial filtering or apodizing), but these methods cannot influence the time behaviour of the pulse. Inhomogeneities of the STID were treated by the authors of paper [1], who were trying to explain the difference between the output pulse duration in the system ISKRA determined experimentally and theoretically . They pointed out that the spatial inhomogeneities of the input beam and of the inversion population density can cause time delays of the pulse along its cross-section. The reason is that the local propagation speed of the laser beam is affected both by the input pulse intensity and by the local coefficient of amplification. Since a number of differences between the systems PERUN and ISKRA exists (e.g. radial distribution of the inverse population, laser medium) it is hardly possible to apply the results of [1] directly.

2 Experimental setup and results

The system PERUN consists of an quasi-semiconfocal resonator and four amplifiers (A1-A4). With respect to the above mentioned dependence of the STID on the input intensity we decided as a first step to apply image relying to a section of the optical path between the first (A1) and second amplifier (A2). The original and the upgraded optical schemes are given in fig. 1. In the the present version the aperture D1 in front of A1 is relayed to the diafragm just in front of A2. The STID was measured with a streak camera placed at the output of the last amplifier. The pulse at a given radius is reduced while passing through the laser chain, which is similar for both the arrangements, but the radially integrated pulse durations differ substantially. With the new arrangement the value of the total pulse length is close to the local one. The degree of
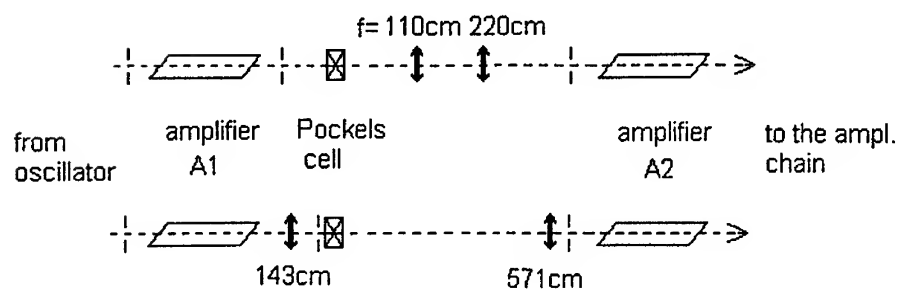
Figure 1: Original and upgraded scheme of the iodine photodissociation system Perun

rectification of the radial distributions depends on the position of the oscillator beam with respect to the aperture in front of the A1 amplifier. In fig. 2 the radial distributions of the laser intensity taken directly in front of the third amplifier A3 for both the optical schemes are given. A pronounced radial distribution in the original arrangement is clearly visible.

3   Discussion and conclusions

Due to a relatively low pressure of the working medium it can be supposed that the inverse population density profile is proportional to that of the pumping UV radiation measured in empty amplifiers. Our experimental results [4] suggest that the UV pump profile is fairly flat and thus there is no need to worry about the influence of the inverse population on the propagation velocity. The results confirmed the conclusion of [1] that the local propagation velocity
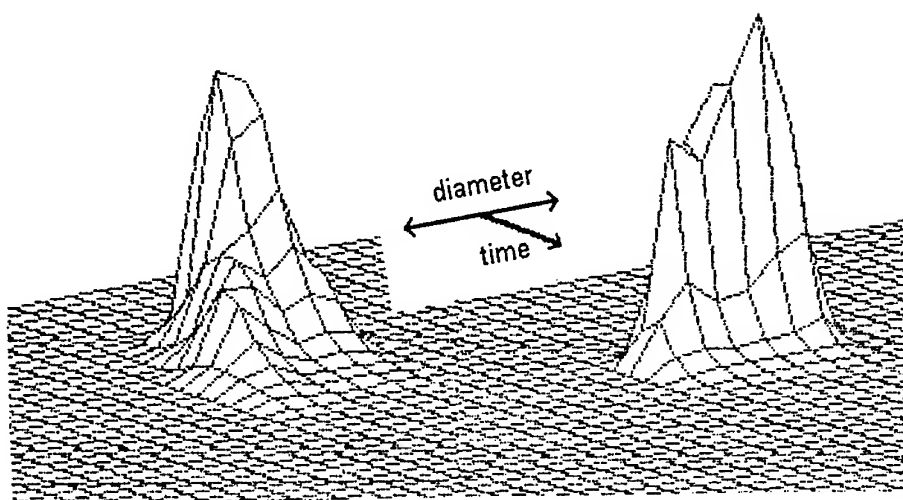
Figure 2: Space - time distribution of the laser pulse intensity before and after the modification of the laser system

of the beam through the amplifiers is strongly dependent on the intensity of the input pulse as it is distributed over the radius. The image relaying is cutting out just the central part of the profile, which then remains flat while propagating down the laser chain. Another improvement of the STID might be achieved by a similar image relying between the second and the third amplifier.

1. E.E.Fill, Optics Communic. 49/4 (1984) 362; G.Brederlow et al., IEEE QE-16/2 (1980) 122.

2. Laser Annual Report-1975, Lawrence Livermore Laboratory, Ed. K.L.Cummings, pp.72, 226.

3. I.N.Voronitch et al., Izv.Ak.Nauk USSR, Ser.Fiz. 54/10 (1990) 2016.

4. J.Skála, B.Králiková, M.Chvojka, Proc. 3rd Int. Wokshop on Iodine Lasers and Applications, Bechyně Castle 1992, SPIE Vol. 1980 p.49.

BEAM COMBINATION CHARACTERISTICS IN PARALLEL AMPLIFICATION USING SEPARATE STIMULATED BRILLOUIN SCATTERING PHASE CONJUGATION MIRRORS

HONG JIN KONG, YUN SUP SHIN, JAE OH BYUN, HYUN SU KIM,
KI YOUNG UM, JONG RAK PARK, JAE YONG LEE, KI HO HAN
AND HEE SU PARK

*Department of Physics, Korea Advanced Institute of Science and Technology, 373-1
Kuseong-dong Yuseong-gu Taejon, Korea*

Beam combination experimental setup with two beam lines using 1 cm^2 area square wedge sets, one Nd^{3+}:glass rod for active medium and two FC-72 cells with purification up to 0.2 μm for phase conjugate mirror(PCM) is constructed and two pass amplified output patterns with minimized diffraction lines are presented.

1. Introduction

To overcome the traditional limits[1] of solid state laser to achieve high power with good beam quality, many scientists have tried the beam combination method using stimulated Brillouin scattering(SBS) materials for PCM[2~6] during the past three decades. The reason for using PCM's instead of full mirrors is to compensate aberrations induced by inhomogeneities of the laser medium and, so that, to reduce beam divergence, can resulting in an improved intensity distribution in the near field, etc.[1] By this method, one can achieve high power beyond traditional limits. Also, to get the more efficient output energy, it has been reported that through the purification of the SBS materials the reflectivity of PCM can be increased without reaching breakdown.[7]

In establishing the beam combination setup, many researchers use beam splitters for the laser beam division(intensity splitting method).[1,5] There is another method to divide the laser beam; the wavefront splitting method, using a set of wedges. With the use of wedges of square shape, there are several advantages compared with beam splitters. First, the available cross section of the input laser beams can be used more effectively with square shapes and have various applications like lithography, annealing, machinery manufacturing, etc. Second, with the use of beam splitters, the recombined beam which is composed of two or more beams with different phases can interfere to cancel each other, so there is an inevitable energy loss of a factor of two at the beam splitter. Third, the system using beam splitters has fundamental limitation to expand the beam combination system repeatedly.

In this paper, for the basic realization of SBS master oscillator power amplifier(MOPA) beam combination system using square-shape-wedge and to
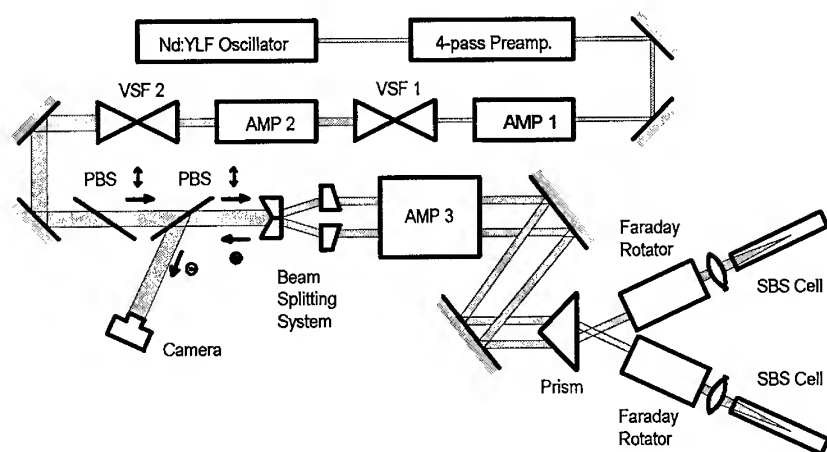
Fig. 1. Schematic diagram of basic beam combination experimental setup. 4-pass amp and AMP 1, 2, 3 are Nd^{3+}:glass.

observe the characteristics of spatial profiles of reflected and recombined laser beams, we construct the simple scheme of the two beam line system. To minimize possible differences of two beam path characteristics, we use the Nd^{3+}:glass laser rod(40 mm diameter) for the two pass gain medium of both beam line. We also use two separate SBS media to observe the spatial profiles of reflected and recombined beams which have random phase to each other. With this simple setup, greatly reduced near field diffraction fringes in the recombined beam are presented.

2. Experimental Setup

The experimental setup consists of laser source, beam splitting optics, two pass amplifier with PCM's and detection system.(Fig. 1) We use parts of Sinmyung I laser system[8] (Nd^{3+}:YLF master oscillator, 4-pass pre-amplifier and main Amp. 1 & 2) for the source of the laser beam. Gain media of amplifiers are Nd^{3+}:glass(1.054 μm) and the laser beam after 2nd vacuum spatial filter(VSF 2) has 40 mm diameter, 150 mJ energy and 6 ns pulsewidth in FWHM.

For the beam splitting optics, we use square shape wedge sets with BK7 material. One set consists of 4 wedges(1 cm^2 area, 15° deflection angle) and we use 2 wedges to make the divided beams parallel. After the wedges, beam size is 8 mm × 8 mm and separated 5 mm to each other.

Amp. 3 of Sinmyung laser(Nd^{3+}:glass, 40 mm diameter) is used as a two

556

(1)   (2)

Fig. 2. Burning patterns of reflected beams. (1)PCM, (2)ordinary Mirror

PCM, phase=0   mirror, phase=0

PCM, phase=π   mirror, phase=π

(1)   (2)
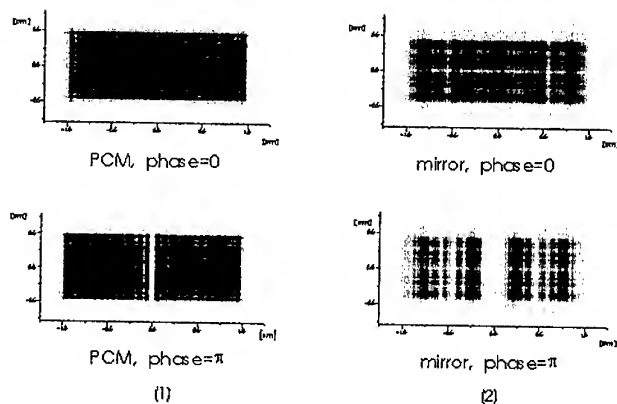
Fig. 3. Simulations of spatial diffraction patterns. (1)PCM reflected, (2)ordinary mirror reflected.

pass active medium which introduces thermal distortion. Faraday rotators and thin film polarization beam splitters(PBS) are used to extract and detect the two passed output beam. FC-72(C_6F_{14}) which results in good SBS reflectivity [9] is used for SBS material. Each FC-72 material in the SBS cell is purified up to 0.2 μm filtration to improve the SBS reflectivity without breakdown.

3. Results & Conclusion

In constructing the beam combination system using square shape wedges and to make a high power laser, the spatial profile uniformity of each amplification step is important. If there were spikes from diffraction patterns or distortions, the efficiency of amplification would be decreased and optical components might be damaged. PCM introduced in the system can solve these problems. Figure 2 is the burn patterns of the output beam after two pass amplification; (1)reflected from PCM's, (2)reflected from ordinary full

557

mirrors with 40 mJ input energy at each mirror. The beam reflected and recombined from ordinary mirrors has distinguishable diffraction patterns. On the other hand, that of PCM reflected is very smooth and there are a few vague diffraction lines. The distance of two pass between the wedge system and PCM's is long(5 m) compared with the wedge size. Therefore, strong diffraction must appear without the phase conjugation effect. The smoothened spatial pattern from the PCM-reflected beam proves that the SBS materials of our experiment, FC-72, have good phase conjugate property. The space(0.8 mm) between two square shape images can be explained by the random phase difference between the PCM reflected beams. Fig. 3 is the simulation of diffraction pattern 50 cm after square shape aperture with 10 μm thickness gap (1)reflected from PCM's, (2)reflected from ordinary full mirrors. For the random phase case, the simulation predicts 1 mm space between images even when the PCM's are used. Simulation and experimental results are similar to each other. For the same phase case, the simulation predicts very narrow space. The space may be minimized by phase locking methods. When we compare the experimental results with simulation, experimental result pattern is smoother than the simulation pattern. We can consider the reason as the high frequency filtering effect[1] at the focal point inside the SBS medium. From the above reasons, we can observe fairly good spatial profiles when the PCM's are introduced.

In conclusion, we aimed to observe the basic characteristics of square shape wedge introduced SBS beam combination system which has two pass MOPA structure for the pre-step of constructing the practical high power SBS laser system. Square shape output beams with minimum diffraction patterns are observed and compared with ordinary mirror reflected patterns. PCM's compensate not only thermal distortion of the active medium but also diffraction patterns of square shape wedges. To improve the spatial pattern and to make narrow the space between the reflected images, several techniques are needed such as light guide in the SBS medium[1], phase locking of focused beams[10], optical contact of wedges, etc.

References

[1] D. A. Rockwell, IEEE J. QE 24(6), 1124 (1988)
[2] R. H. Moyer, et al., J. Opt. Soc. Am. B. 5(12), 2473 (1988)
[3] N. G. Basov, et al., Sov. J. Quantum Electron. 9, 237 (1979)
[4] N. G. Basov, et al., Sov. J. Quantum Electron. 11, 1335 (1981)
[5] D. L. Carroll, et al., J. Opt. Soc. Am. B. 9(12), 2214 (1992)
[6] M. Valley, et al., J. Opt. Soc. Am. B. 3(7), 1492 (1986)
[7] H. J. Eichler, et al., Opt. Comm. 89, 260 (1992)
[8] H. J. Kong, et al., Laser Interaction with Matter, 321 (1994)
[9] Private communication with ILE, Osaka Univ., Japan.
[10] T. R. Loree, et al., Opt. Lett. 12, 178 (1987)

PROGRESS IN IODINE LASER FOR PLASMA AND HIGH INTENSITY INTERACTIONS

S.M.KULIKOV, Y.V. DOLGOPOLOV, A.M.DUDOV, V.A.EROSHENKO,
G.G.KOCHEMASOV, S.N.PEVNY, N.N.RUKAVISHNIKOV, A.B.SMIRNOV,
S.P.SMYSHLYAEV, S.A.SUKHAREV, A.F.SHKAPA

Russian Federal Nuclear Center (VNIIEF),
Sarov 607190, Nizhni Novgorod Region, Russia
Fax: (831) 30 54565; Phone: (831) 30 56893, e-mail: kulikov_2566@spd.rfnc.nnov.su

Results on development of a source of laser radiation focused in the wavelength size spot for obtaining quasistationary ($\tau \sim 10^{-9}$ - 10^{-10} s) fields with intensity of 10^{20} 10^{21} W/cm^2 and for research of atoms behavior in such fields are presented.

Introduction

At present for producing superhigh intensities ($\sim 10^{21}$ W/cm^2) laser pulses in the femtosecond range ($\sim 10^{-13}$ s) are used as a rule. We offer a radically different way - generating of superhigh intensities in relatively long nanosecond pulses ($\sim 10^{-9}$- 10^{-10} s). What does it give us? First of all, the capability appears to research the substance behavior in quasi stationary fields (as compared to the typical relaxation atomic times). Secondly, the capability appears to observe the process but not only its results. Thirdly, in this case we deal with practically monochromatic radiation.

1. Laser setup

In powerful laser facilities the accumulation of aberrations takes place during amplification of a pulse. For this reason the laser spot size on target is usually much greater than the radiation wavelength and makes up to 20 - 100 λ. We suggest to use a laser facility with phase conjugation for compensation of aberrations and for focusing of radiation into a wavelength size spot. Layout which explains the operation of this system is shown in Fig.1. The facility is based on a High Explosive Iodine Laser ($\lambda = 1,315$ μm). The master oscillator[1] radiation passes through the modulator, forming a pulse with a duration of ~ 2 - 20 ns, and then beam enters a vacuum chamber and is focused into a λ - size spot by a microobjective. A parabolic mirror (D/F$\approx$1) of 30 cm diameter forms an input beam to the high explosive amplifier[2]. After amplification the radiation is reflected backwards by the phase conjugation device (SBS mirror). The amplified Stokes radiation is collected by the parabolic mirror and some fraction of it (depending on phase conjugation fidelity) is focused in a λ - size volume.
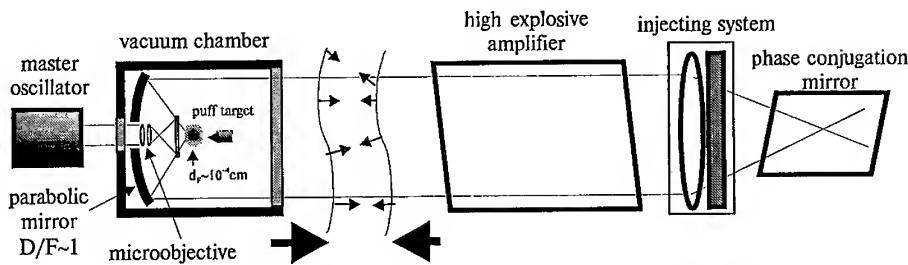
Fig.1. Principal scheme of the laser facility for obtaining superstrong light fields

2. Phase conjugation and compensation of aberration

The main sources of wave front aberrations in the laser system considered above as well as characteristic values defining the wave front aberrations are presented in Table 1 (where: C_n - structure constant for atmospheric refractive index fluctuations).

Table 1

Factor affecting wavefront quality	Temporal dependance	Our experimental conditions
Optics figure errors	Static	1-2λ (d = 100mm)
Aberrations	Static	1-3λ
Lenses misalighment decenter tilt	Static	±3mm $\pm5°$
Pump induced effect	μs	$L\Delta n \approx 10^{-4}(1\text{-}e^{-t/\tau})$, $\tau \approx 1\mu s$
Turbulence	ms	$500m, C_n^2 \sim 10^{-15}$ cm$^{-2/3}$

To guarantee high quality compensation of these aberrations, the SBS mirror is provided with an injecting system including kinoform raster and selector of the phase conjugated components for enhancing the phase conjugation fidelity[3]. Optimal compositions of multicomponent gaseous media for SBS which minimize the influence of competitive processes (SRS, thermal and
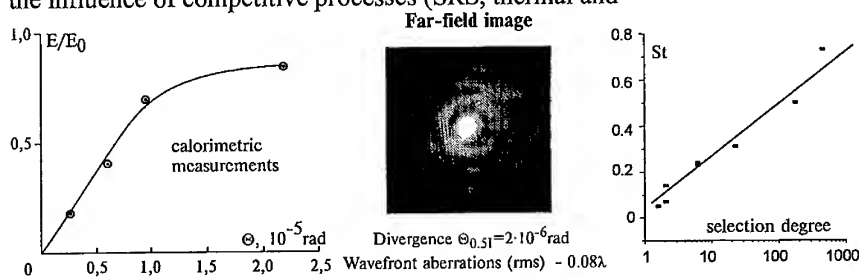
Fig.2. Far field energy angular distribution and Strehl ratio vs selection degree.
striction distortion and optical breakdown) have been determined. The following characteristics of SBS media have been achieved: parameter $gW_{cr} = 480$ s/cm (g is

the SBS gain, W_{cr} is the critical energy of self-action process), breakdown threshold $\sim 10^{12}$ W/cm^2.

Experiments carried out have shown that for beams of a diameter up to 10 - 50 cm it is possible to obtain Strehl number of St $\approx$ 0.4-0.7 (see Fig 2) when the degree of selection of the phase conjugated component is $\eta \sim 500$ (the selection degree is the ratio of the full energy reflected from the SBS mirror to that passed through the angular selector).

3. Development of λ - size reference radiation source.

The considered scheme of radiation focusing into microvolumes assumes the availability of a reference radiation source of the size $\sim \lambda$. The diffraction limited beam (of 6 mm diameter) was focused by the eight-component microobjective with focal length f = 4.4 mm. A laser spot with Airy distribution has been formed in the focal plane. There was about 77% of total energy in the central core of a 1 µm diameter (see Fig. 3). Damage of the microobjective lenses was not observed for pulses of 25ns duration and the energies of up to 10 mJ (I $\sim$ 2 MW/cm^2).

Energy distribution of the focal spot

Focal spot image
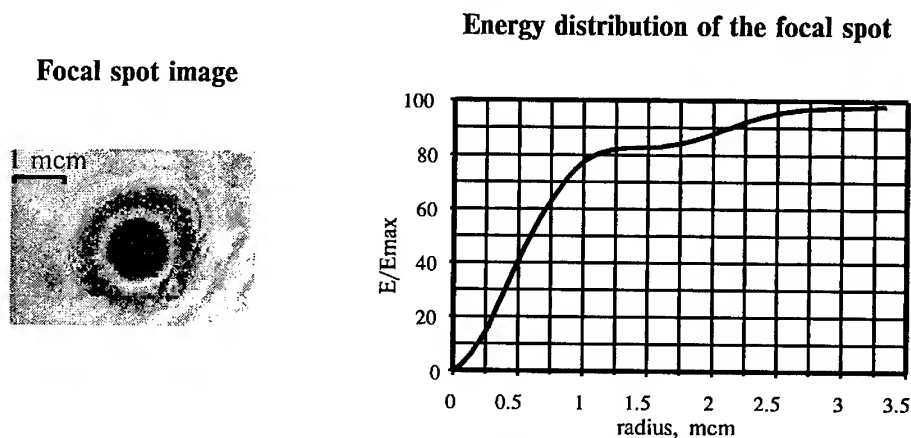
Fig. 3. Focusing of reference radiation into microvolume

4. Generation of 0.1-1 ns pulses in a laser with phase conjugation

For iodine laser the pulse duration of 100ps seems to be achievable at an energy density of > 1 J/cm^2. The other requirement which is very important for the pulse shortening process is that of a specific pulse front profile. Numerical simulations of the laser pulse reflection by the SBS mirror and further amplification for input pulses of 2 - 20 ns have been fulfilled. For the 20ns pump pulse the duration of Stokes pulse was $\sim$ 0.6ns at an SBS reflection coefficient of 75%. This pulse width increased

during amplification up to ~1.6ns. For the 2ns pump pulse strong Stokes pulse compression was observed in the calculations. The Stokes pulse duration was ~80ps. The output Stokes pulse duration was about 130 ps after amplification.
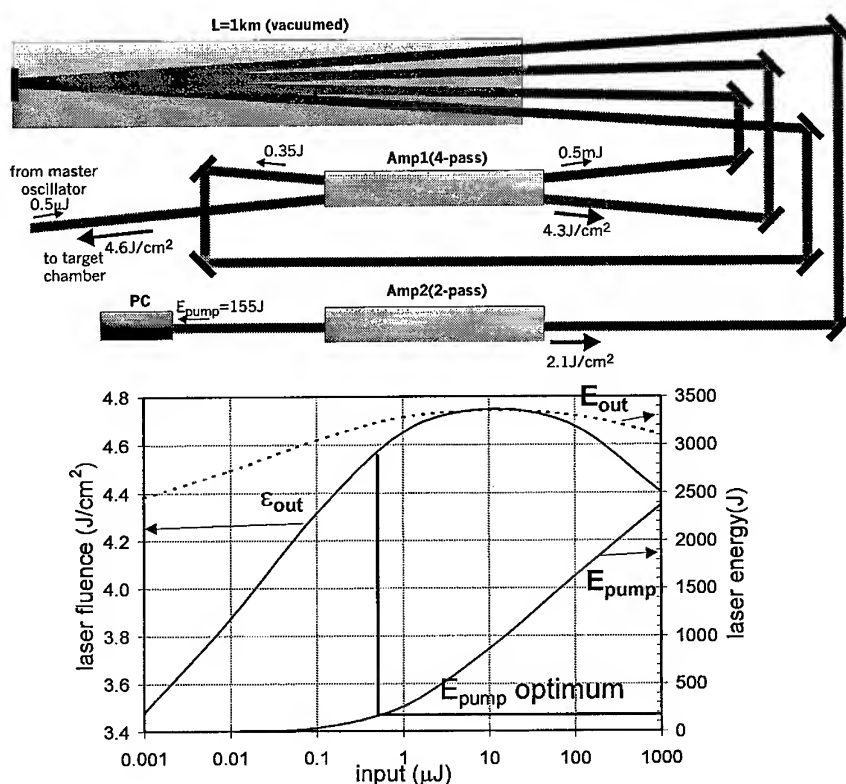
Fig.4. Layout of laser amplifier and energy calculation results.

For obtaining high energy densities ($\varepsilon > 1$ J/cm^2) at weak input signals from a λ-size source ($\varepsilon_{in} \sim 10^{-9}$ J/cm^2) it is necessary to have a small signal gain coefficient up to 10^{10}. In order to eliminate self-excitation of amplifiers it is suggested to use a vacuum pipeline of 1 km length for optical decoupling the amplifying cascades (Fig.4). In that case the distance between laser cascades will be about 2 km. So the stability of the laser channel with respect to self-excitation will be increased because of space filtering of noise radiation on a long path and because of a large (10 - 30 μs) delay time for a parasitic feedback. Simulation shows that in such a scheme an output pulse energy density of up to $\varepsilon_{out} \sim 4.5$ J/cm^2 can be achieved. The radiation energy and power will be $E \sim 3$ kJ, $P \sim 20$ TW respectively

562

at a beam aperture of ≈ 30 cm and a pulse duration of ~ 130 ps. With an objective of D/F $=1$ and Strehl number of St $\approx 0{,}7$ it is possible to achieve an intensity of: $I_F \approx \dfrac{\varepsilon_{out} D^4}{\lambda^2 F^2 \tau_L}$ St $= 1.10^{21}$ W/cm^2

Conclusion.

Design study on experimental results confirms that the concept of laser facility with focusing of radiation into extreme small volumes can be realized. This work was supported by ISTC under the project # 111.

Referencies

1. A.M.Dudov, G.A.Kirillov, S.M.Kulikov, et al, "Single axial mode iodine laser with gain modulation by magnetic field of pump lamps", *Izv.AN SSSR, serial fisicheskya*, vol.52, 327, 1988.
2. Y.V.Dolgopolov, G.A.Kirillov, G.G.Kochemasov, S.M.Kulikov, S.N.Pevny, "High power nanosecond pulse iodine laser provided with SBS mirror", in *Proceeding of the SPIE Conference on "Gas and Metal Vapor Lasers and Applications"*, v.**1412**, p.267-2731, 1991.
3. Y.V.Dolgopolov, A.M.Dudov, G.A.Kirillov, *et al*, "High power iodine laser with high quality phase conjugation", *Izv.AN SSSR, serja fizicheskaja*, vol. 58, pp. 35-40, 1994.

Demonstration of Amplification for Li-like-Oxygen in z-pinch recombining plasma

E. Eberl, T. Wagner, Y. Griffaton, S. Jelinek, D.H.H. Hoffmann
Physikalisches Institut I, Universität Erlangen-Nürnberg, 91058 Erlangen, Germany

This paper is reviewing the amplification of XUV radiation at 519.7 Å and 498.5 Å with a gain-length product of 2.5 and 2.2 for the 4f-3d and 4d-3p transition in an oxygen z-pinch plasma. Time resolved measurements of the O VI (519.7 Å) transition were performed and the dependence of the line intensity on the discharge current and initial gas pressure is reported.

Introduction

The first successful demonstration of collisionally excited and recombination pumped soft-x-ray lasers in plasmas generated by powerful laser drivers was achieved more than ten years ago [1,2]. Such progress has been made in reducing the wavelength and increasing the power of the laser transitions. The large pump lasers used in this kind of soft-x-ray laser experiments are only available at a few laser facilities in the world. Today the development of compact soft x-ray lasers with higher efficiency and repetition rate is an important task of the x-ray laser research. Approaches are the evacuated [3,4,5] and gas filled [6,7] capillary discharges.

As an alternative with enhanced reproducibility and increased repetition rate we proposed the use of a cylindrical plasma, generated in the core of an ultra-fast, small diameter z-pinch discharge [8]. The ion species results from the initial gas filling instead of the wall material. The pinch dynamics and the contraction velocity as well as the ion density and the plasma temperature can be controlled by the initial gas pressure. Recent experiments performed at the University of Erlangen-Nürnberg accomplished the first demonstration of x-ray amplification in a fast, small diameter pinch discharge-created plasma. The pump mechanism is based on collisional recombination, which is important for hydrogenic and lithium-like ions.

Gain-length products of gl = 2.5 and gl = 2.2 were measured in the 519.7 Å and 498.5 Å of Li-like oxygen in a 90 mm long plasma column generated by a fast z-pinch discharge [9]. We summarize these results and present new measurements of the development of the laser line intensity as a function of time.

Measurements results

The experiments to investigate the amplification in Li-like oxygen were conducted utilizing the fast z-pinch discharge setup shown schematically in figure 1. The oxygen plasma column is produced in a cylindrical z-pinch, driven by a high voltage pulse generator. It consists of a 3-stage Marx generator (3 x 50 nF) and a coaxial pulse forming line filled with deionized water as dielectric. The water pulse line is discharged through a spark gap switch, pressurized with N_2, into a 14 mm diameter pinch tube filled with preionized gas. The amplitude of the applied current pulse was about 40 kA accompanied by a dI/dt of 1.5 x 10^{12} A/s and 160 ns pulse duration. The preionization of the working gas in the discharge tube is essential for reliable
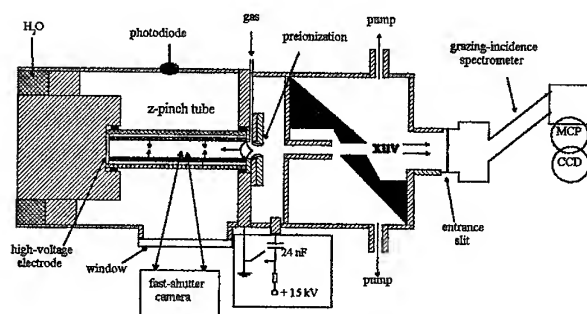
Fig. 1: Schematic drawing of the experimental setup with the used diagnostic tools. The z-pinch tube terminates the coaxial pulse forming line and the axial emitted XUV-radiation is observed with a grazing incidence spectrometer.

and homogenous plasma cylinders. The high rate of current rise leads to a fast compression of the plasma towards the symmetry axis. A shock front is formed due to the high compression velocity (10^7 cm/s) which also propagates towards the z-axis. The shock front is collapsing on the axis and is producing plasma cylinders of less than 0.5 mm diameter and 30 to 90 mm in length.

A system composed by a 1.5 m grazing incidence spectrometer with a 600 lines/mm grating at an angle of 86 degree was used to analyse the radiation axially emitted by the plasma column through the hollow grounded electrode. During the different phases of the pinch plasma evolution the emitted radiation was observed by a gated multi channel plate, MCP (time resolution: 5 ns), coupled with a slow scan CCD-camera for discharge tube lengths of 30, 44 and 90 mm. The spectral resolution of the detection system in the range of 500 Å is 0.5 Å. In these experiments special care was taken in maintaining constant the characteristics of the excitation, defined by the amplitude and period of the current pulse. The first observation of amplification in O VI at 519.7 Å was realized in oxygen gas at a pressure near 20 Pa. A differential pumping system was used to pump the working gas through the discharge tube continuously . The current amplitude was 40 kA at a current rise of $1.5 * 10^{12}$ A/s.

In figure 2 three spectra are shown for discharge tube lengths of 30, 44 and 90 mm. The time (t = 198 ±2 ns) which the spectra were taken corresponds to 45 ns after maximum compression of the z-pinch plasma. The intensities of the 519.7 Å and 498.5 Å transition of Li-like oxygen were observed to rise as the plasma length was increased from 30 to 90 mm. In the first spectrum, corresponding to a 30 mm long as well as the surrounding lines 508.0 Å, 525.8 Å (O III) and 554.0 Å (O IV) were observed and the intensities of the specific lines were comparable to each other. In the spectrum corresponding to the 44 mm long discharge tube, the intensity of the 519.7 Å (O VI) line surmounts those of all neighbouring lines. In the case of the 90 mm long plasma column, the 519.7 Å line and the 498.5 Å line totally dominate the spectrum. The intensities of the laser lines show a exponential rise with increasing plasma length, shown in figure 3. The best fit of the measured data to the Linford
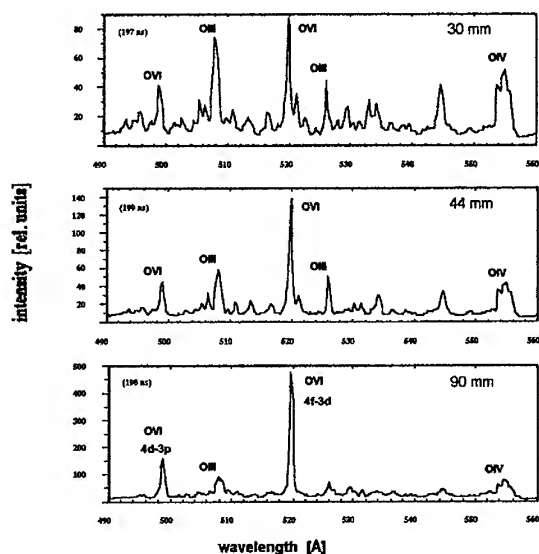
Fig. 2: Time resolved spectra of the axial emission in the neighbourhood of 519.7 Å for different discharge tube lengths. The discharges were performed with 40 kA current pulse in a pressure of 20 Pa oxygen.
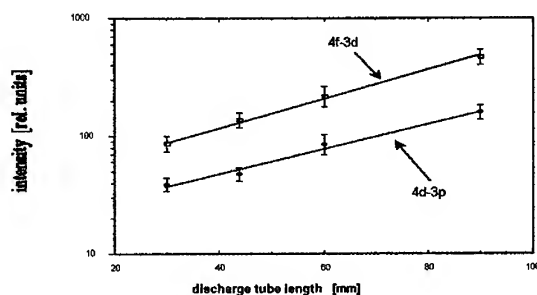
Fig. 3 Intensities of the 4f-3d an 4d-3p lines of lithium-like oxygen O VI as a function of the discharge tube length.

formula [10] gives a gain coefficient of 0.28 cm^{-1} and 0.24 cm^{-1} for the 4f-3d-and 4d-3p-transition, corresponding to a gain-length product of 2.5 and 2.2 for the 90 mm plasma column.

Time resolved measurements of the O VI lasing line (519.7 Å) were performed with a fast photomultiplier tube (PMT). The time resolution of the detection system was < 2 ns. The observed spectral range was about 0.8 Å corresponding to a slit width of 250 μm. In the recombination phase the width of the amplified lasing line is about $\Delta\lambda \approx 0.6$ Å (FWHM). Figure 4 shows the measured time history of the O VI line

intensity at discharge conditions, when amplification occurs. During the different pinch phases we were able to observe the XUV-emission intensity at the wavelength of 519.7 Å. The first intensity peak about 155 ns relative to the current pulse corresponds to the maximum compression of the plasma. After the pinch the cooling of the plasma column starts and the intensity of lasing line decreases. When the proper plasma conditions for electron collisional recombination are reached the intensity of the O VI line shows a sharp increase. The second intensity peak of the lasing line is about 30 ns after the pinch and the FWHM time duration of the laser pulse is approximately 5 ns.
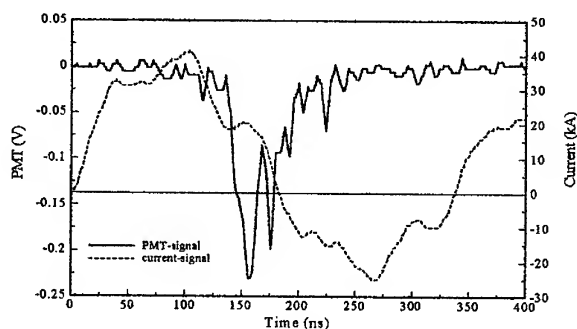
Fig. 4: Time resolved measurements of the O VI (519.7 Å) line intensity with a fast photomultiplier tube (solid line), corresponding to a 40 kA current (dashed line) discharge through 14 mm diameter, 90 mm long plasma column filled with 20 Pa of oxygen.

Conclusion

XUV amplification was observed in a shock wave generated oxygen plasma by using a fast, compact z-pinch discharge as a driver. For different plasma lengths the intensity of the lasing line was measured time resolved and a gain-length product of 2.5 (4f-3d) and 2.2 (4d-3p) was obtained. The O VI lasing line (519.7 Å) was observed by a fast photomultiplier tube (PMT) coupled with a plastic scintillator. In the expansion phase the laser activity due to the recombination leads to a gain peak with a duration of about 5 ns.

References
[1] Mathews D.L. et al., 1985 Phys. Rev. Lett., **54**, 110
[2] Suckewer S.et al., 1985 Phys. Rev. Lett., **55**, 1753
[3] Rocca J. J., Beethe D.C., Marconi M.C., 1988 Opt. Lett. **13**, 565
[4] Steden C., Kunze H.-J., 1990 Phys. Lett. A, **151**, 534
[5] Shin H.-J., Kim D.-E., Lee T.-N., 1994 Phys. Rev. E, **50**, 1376
[6] Rocca J. J. et al., 1994 Phys. Rev. Lett., **73**, 2192
[7] Rocca J. J.et al., 1995 Phys. Plasmas, Vol. 2, **6**, 2547
[8] Hartmann W. et al., 1991 Appl. Phys. Lett., **58**, 2619
[9] Wagner T. et al., 1996 Phys. Rev. Lett. **22**, 3124
[10] Linford G. J. et al., 1974 Appl. Optics, **13**, 379

MEASUREMENT OF LOCAL GAIN AND ELECTRON DENSITY IN AN YTTRIUM X-RAY LASER AMPLIFIER

R. CAUBLE, L. B. DA SILVA, T. BARBEE, JR, P. CELLIERS, C. DECKER,
R. A. LONDON, J. C. MORENO, J. E. TREBES, A. S. WAN AND F. WEBER

Lawrence Livermore National Laboratory
Livermore, California 94550 USA

X-ray lasers have measured average gains significantly less than calculated and a persistently low level of spatial coherence. We have used an x-ray laser both as an injected signal to a short x-ray laser amplifier and as an interferometer beam to measure two dimensional local gain and density profiles of the x-ray laser plasma with near-1-mm resolution. The measured local gain is in agreement with atomic models, but it gain is unexpectedly spatially inhomogeneous. This inhomogeneity explains the low level of spatial coherence observed and helps explain the disparity between observed and simulated gains.

1 Introduction

Laboratory-poduced x-ray lasers (XRLs) have been shown to be powerful tools in the diagnosis of large, high density plasmas.[1,2] XRLs feature short wavelength, short pulse duration, high brightness and suffcient longitudinal coherence to employ them as backlighters or interferometry sources in the diagnosis of dense, fast-moving plasmas typical of laser-irradiated solids.

Much x-ray laser research effort has centered on the persistent inability to be able to model observed gain and spatial coherence properties; simulations over-estimate both features. Additionally, research has been directed toward enhancing XRL brightness and coherence.[3] Enhanced brightness has been achieved through improved target and experimental design, but the XRL remains spatially incoherent.[4]

Predictions of XRL performance start with a calculation of the local laser gain found from an atomic model with level populations determined by expected conditions in the XRL plasma. For the Ne-like Y XRL which we investigate here (a 3p-3s transition in neon-like yttrium at 155 Å[5]), where the expected density is ~ 10^{21} cm^{-3} and the temperature is near 1 keV, the calculated local gain is in the range of 10-20 cm^{-1}. Laser line trapping and radiation propagation with refraction, accounted for in full two-dimensional, time dependent hydrodynamic simulations, lower the average calculated gain to 10-11 cm^{-1} for few-cm-long XRLs. However, the average measured gain for the yttrium laser is still lower, ~ 5.3 cm^{-1}.[5]

The accuracy of the atomic kinetics calculations has been here addressed here by using the XRL beam from a long, 3 cm, target to probe a short, 2 mm, XRL target which is driven in the same manner as the longer target. The short target acts as a one-pass amplifier of the incident probe from which the gain in the amplifier

can be measured.[6] Since the amplifier is so short, there is negligible refraction of the lasing line. We have obtained the local gain profile with very high spatial resolution (1.3 μm). Also, we have performed the gain measurements using in an interferometer which employs the XRL allowing us to simultaneously measure the electron density profile. Both experimental features are necessary to conclude why measured XRL gain and coherence fall below predictions.

2 Experiment and Results

In order to make the gain measurement and at the same time measure the electron density profile of the short amplifier, we used the XRL interferometer setup[2] shown in Fig. 1. Multilayer mirrors and beamsplitters provided a narrow bandpass (155±4 Å). The signal was recorded on a 1024x1024 element CCD camera; the short, ~ 75 ps duration of the XRL pulse effectively gated the image. Additional filters around the CCD eliminated stray optical light. While the XRL target was driven with one beam of Nova, the amplifier was driven with another line focused Nova beam time-delayed for arrival of the XRL beam.

Fig. 2a is an image of only the self-emission of a 2 mm yttrium target (no XRL backlighter and thus no interferometry). The view is end-on to the foil, which is sitting at zero on the vertical scale and is irradiated from above by a 120 μm line focus along the line-of-sight. All that is visible is unstructured emission. The maximum number of counts per pixel is about 600 above background.
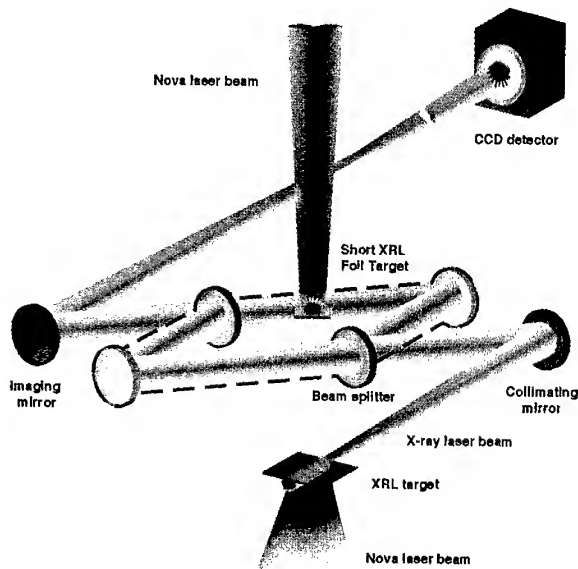
Figure 1: Experimental setup for x-ray laser interferometry.

Fig. 2b is an image of an yttrium foil the same length as depicted in Fig. 2a under the same drive conditions except that the foil is backlit by an yttrium XRL so that the foil plasma acts as an XRL amplifier. The data show strong amplification; the number of counts throughout most of the plasma is 10000 to 40000 above background. The local gain can be found from $I = I_0 e^{gL} + I_0 + I_S$, where I is the amplified intensity, I_0 the incident intensity (equal to one-half the recorded background since the background is delivered through two arms of the interferometer), I_S, is the self-emission value taken from Fig. 2a, g is the gain and L is the amplification pathlength, 2 mm. The local gain was found to be 10 - 15 cm^{-1} in the central plasma, in general agreement with atomic models. The area of significant gain is limited to about 150 μm across the spot (horizontally) and from about -50 μm to about + 125 μm vertically.

The actual cause of the small-scale structure in the local gain, which is repeatable, is unknown, but we believe that it is the result of temperature fluctuations in the plasma. We believe that these temperature fluctuations are due to nonuniformities in the driving beam. As long as the driving beam is static over the time of peak gain, it is possible that such channels would not dissipate during the amplifying interval (~ 75 ps). Although laser-plasma instabilities, such as thermal self-focusing, can also give rise to small-scale filaments of high temperature plasma, this is an unlikely cause of the observed structure since we do not observe the density fluctuations associated with this mechanism.

The nonuniform structure also has a bearing on XRL coherence. As we have observed, the region of amplification in the XRL plasma is highly inhomogeneous. Since much of the gain is generated in small isolated regions, the spatial coherence of the XRL cannot be improved without smoothing the temperature field in the plasma. If the isolated gain structure is caused by modulations in the driving laser, smoothing of the beam may alleviate the pockets and improve the spatial coherence of the x-ray laser.

In conclusion, we have employed an yttrium x-ray laser to perform end-on 155 Å interferometry of short laser-exploded yttrium foils. We were able to measured the two dimensional local gain and electron density profiles of the x-ray laser plasma with near-1-μm resolution. The average measured local gain is in agreement with atomic models, but the gain profile is unexpectedly inhomogeneous. Intense gain occurs in regions of ~ 10 μm due, we believe, to modulations in the driving laser beam. This nonuniformity in gain may explain the disparity between measured and simulated gains for few-cm-long XRLs. In addition, it also explains the low level of spatial coherence observed.
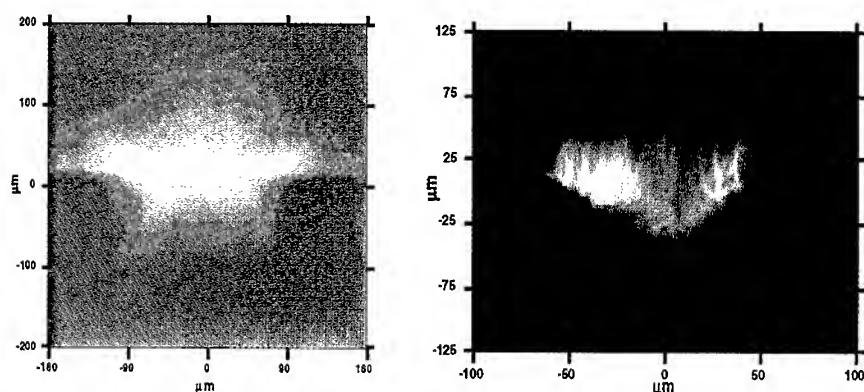
Fig. 2a: Image of self-emission of a 2-mm-long yttrium foil driven by a Nova line focus laser beam. There is no x-ray laser backlighter. Fig. 2b: Interferogram of a 2-mm-long yttrium foil driven by a Nova line focus laser beam (from above). The light regions are areas of intense local amplification of the backlighting yttrium x-ray laser. The plot is local gain along the lineout indicated on the image. The position of the lineout is noted by the bars on either side of the image.

Acknowledgments

References

1. D. Ress *et al.*, *Science* **265**, 514 (1994); R. Cauble *et al.*, *Phys. Rev. Lett.* **74**, 3816 (1995); D. H. Kalantar *et al.*, B. A. Remington, F. Weber and S. V. Weber, *Phys. Rev. Lett.* **76**, 3574 (1996).
2. L. B. Da Silva *et al.*, *Phys. Rev. Lett.* **74**, 3991 (1995).
3. R. Kodama *et al.*, *Phys. Rev. Lett.* **73**, 3215 (1994); C. L. S. Lewis *et al.*, *Opt. Commun.* **91**, 71 (1992).
4. J. E. Trebes, *et al*, *Phys. Rev. Lett.* **68**, 588 (1992).
5. G. M. Shimkaveg *et al.*, *Proc. Soc. Photo-Opt. Instrum. Eng.* **1551**, 84 (1992); L. B. Da Silva *et al.*, *Opt. Lett.* **18**, 1174 (1993).
6. C. H. Skinner, *Opt. Lett.* **16**, 1266 (1991).

8.- SHORT PULSE INTERACTIONS

SPACE- AND TIME-RESOLVED MEASUREMENTS OF ULTRA SHORT PULSE LASER-PRODUCED PLASMA DENSITY GRADIENTS

J.-C. GAUTHIER, J.-P. GEINDRE, P. AUDEBERT

Laboratoire pour l'Utilisation des Lasers Intenses,
Ecole Polytechnique, 91128 Palaiseau, France

C. QUOIX, G. HAMONIAUX, A. MYSYROWICZ

Laboratoire d'Optique Appliquée,
Ecole Supérieure des Techniques Avancées, 91120 Palaiseau, France

We have studied the variations of the electron density gradient scale length of plasmas produced by sub-picosecond and picosecond laser pulses at irradiances below $10^{16} W/cm^2$ by measuring the phase shift of a $100 fs$ probe pulse by spectral interferometry. Results for S- and P-polarised probe light are in very good agreement with hydrodynamic simulations.

1 Introduction

Plasmas produced by focusing an intense sub-picosecond laser pulse on a solid target have unique properties. For relatively low laser irradiance ($I <$ $10^{14} W/cm^2$) and ultra-short laser pulses ($\approx 200 fs$), laser energy deposition occurs over a very small thickness (comparable to the skin depth) near the target surface, at an electron density close to solid density. Because it starts after the laser pulse, hydrodynamic expansion depends only on the initial conditions. This kind of plasma, of relatively low electron temperature ($\approx 10 - 100 eV$), is perfectly suited to study collisional absorption. At higher irradiances and longer laser pulses ($1 - 2 ps$), the laser heats the plasma during the hydrodynamic expansion. In this work, we have investigated these two interaction regimes by measuring the phase shift of a probe laser pulse with S and P polarisation [1] by spectral interferometry in the frequency domain [2]. The transition between these two regimes was obtained by varying the laser irradiance ($10^{13} W/cm^2 - 10^{16} W/cm^2$) and the laser pulse duration ($0.2 - 0.75 - 2.5 ps$).

2 Experimental results and hydrodynamic simulations

We have used a Ti:sapphire laser providing a $800 nm$ laser pulse with energies up to $30 mJ$ at $10 Hz$. Two different grating compressors were used to vary independently the duration of the laser-producing pump and probe pulses. The pump pulse was focused onto the target at $3.5°$ incidence by a $40 cm$ focal

574

length fused silica lens. Apertures were inserted in the laser beam path to vary the laser irradiance. The $100fs$ probe pulse was frequency-doubled to $400nm$; it was passed through a Michelson interferometer to produce a pair of collinear probe pulses separated by $3.5ps$. The probe pulses were focused on target with an angle of incidence of $45°$ with respect to the target normal; the probe focal diameter was $\sim 200\mu m$ (FWHM) to encompass largely the pump focal spot.

Results presented here have been obtained with a dielectric (fused silica) target. A more complete description of the experimental system and of our implementation of the frequency domain interferometric technique can be found in References 1 and 2.
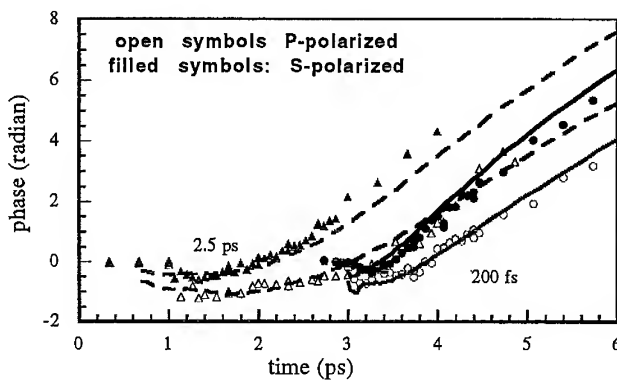
Figure 1: *Phase shift as a function of time for a laser fluence of $96J/cm^2$. Triangles: 2.5ps, circles: 0.2ps. Full symbols: S-polarisation, open symbols: P-polarisation. Solid and dashed lines show FILM simulation results for 0.2ps and 2.5ps pulse duration, respectively.*

We have shown previously [1] that the phase shift of a probe pulse propagating in a plasma is made of three contributions: i) the Doppler phase shift due to the motion of the reflecting plasma surface, ii) the phase shift due to the laser propagation in the underdense plasma, and iii) the phase shift jump upon reflection. The last contribution depends strongly on the polarisation of the laser with respect to the plane of incidence and on the electron density gradient scale length [1]. To simulate the behavior of the phase of the reflected probe pulse, we have studied the temperature and density evolution in the heated fused silica target using the one-dimensional hydrodynamic code FILM, which has been extended to evaluate laser absorption by solving the Maxwell equations in a steep gradient plasma [3].

Figure 1 shows the measured and calculated phase shift as a function of time for an incident fluence of $96J/cm^2$, two pulse durations (0.2 and 2.5ps), and S and P laser polarisations. The maximum of the laser pulse is located at 3.2ps for both pulse durations. At very short times, the absolute phase is null, as expected for a dielectric target. The phase shift variation is first negative. The negative phase minimum is more pronounced for P polarisation. Then, the phase shift varies almost linearly. The time period during which the phase is negative corresponds to the probe pulse reflection on a highly collisional plasma (normal skin effect [4]). We note that the period of time where the phase is negative is comparable to the pulse duration for short laser pulses. For longer pulse durations, the phase minimum occurs only during the early rising edge of the pump pulse. At intermediate times, the gradient scale length increases and the phase jump upon reflection is different for the two laser polarisations. Resonance absorption increases negatively the phase shift for P polarisation [1]. At late times, the phase shift is dominated by the Doppler effect which does not depend on the pump pulse duration.

Figure 2 shows the variations of the S-polarised phase shift as a function of time for different pulse durations and laser irradiances. We note a very good agreement between the experimental results and the FILM simulations. For 0.2ps pump pulse duration, collisional absorption processes (which correspond to the negative period of the phase shift) dominate during the laser pulse and hydrodynamic expansion occurs only after the end of the pulse. For 2.5ps pump pulse duration, laser heating is longer and smoother and hydrodynamic expansion happens before the end of the pulse. At the higher irradiance, the initial evolution of the phase is well described by the simulations. However, the measured expansion at late times is slower than predicted. For 2.5ps duration, a sharp negative phase jump of about one radian is observed during the rising edge of the pulse. The corresponding laser fluence, obtained by integrating in time the laser irradiance up to the phase jump time, is $\approx 2.4 - 3.2J/cm^2$. This can be attributed to the breakdown of the dielectric [5].

3 Conclusion

We have studied the phase shift of a 100fs probe pulse after reflection on the density gradient of sub-picosecond and picosecond laser-produced plasmas at irradiances below $10^{16}W/cm^2$. Results are in good agreement with hydrodynamic simulations using the FILM code. The analysis of the data is underway to extract the electron density gradient scale length from the difference between the phase shift measured with S- and P-polarised probe light.

576
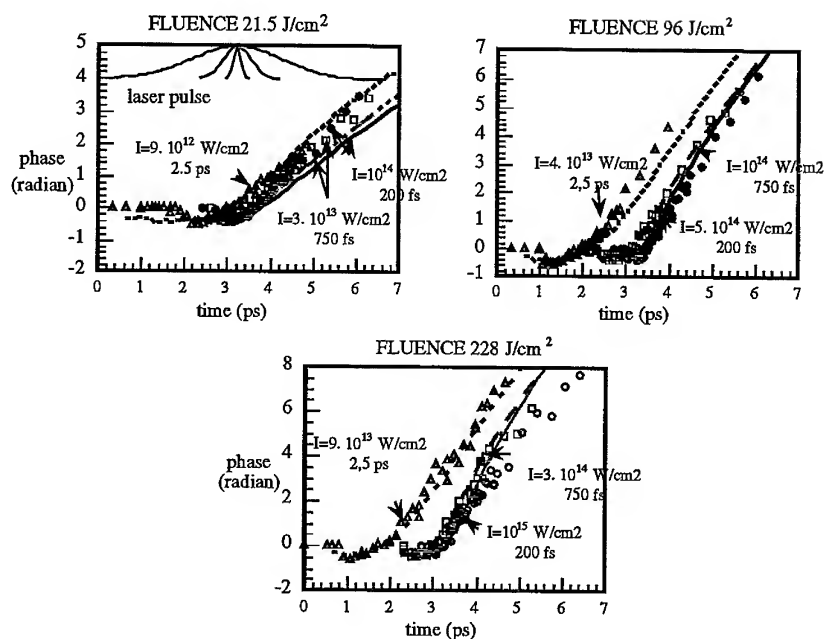
Figure 2: *Phase shift as a function of time for a laser fluence of* 21.5, 96 *and* 228J/cm^2 *and S-polarisation. Circles:* 0.2ps, *squares:* 0.75ps, *triangles:* 2.5ps. *Solid, dashed, and dotted lines show FILM simulation results for* 0.2ps, 0.75ps, *and* 2.5ps *pulse duration, respectively.*

Acknowledgments

References

1. P. Blanc *et al, Journal Opt. Soc. Am.* B **13**, 118 (1996).
2. J.P. Geindre *et al, Optics Lett.* **19**, 1997 (1994).
3. F. Falliès, PhD Thesis, University of Paris-Sud, Orsay (1994).
4. F. Cornolti *et al, Las. Part. Beams* **9**, 474 (1991).
5. B.C. Stuart *et al, Phys. Rev.* B **53**, 4 (1996).

HARMONIC GENERATION FROM A VACUUM-PLASMA INTERFACE.
AN ALTERNATIVE SOURCE FOR XUV RADIATION

G. D. TSAKIRIS, S. KOHLWEYER

Max-Planck-Institut für Quantenoptik, Hans-Kopfermann-Str. 1,
D-85748 Garching, Germany

The experimental observations of harmonic generation by short, intense laser pulses interacting with solid surfaces are interpreted in terms of a simple model in which the interaction of the EM-wave with plasma-bound electrons is considered. It is shown that the mixing of the oscillations in the parallel direction with those perpendicular to the surface is responsible for the anharmonic motion of the electrons and the resulting harmonic emission.

At laser intensities of $10^{18}W/cm^2$ or greater, a host of new phenomena are expected to occur in the field of laser-plasma interaction. One of the most interesting aspects in this context is the generation of high order harmonic radiation in the interaction of high-power laser pulses with solid targets. The highly nonlinear behavior of an overdense plasma possessing steep density gradients was first demonstrated in nanosecond experiments using a CO_2 laser[1,2] With the advent of the modern high power laser systems operating at a wavelength of roughly a factor ten shorter but at the same time delivering pulses yielding focused intensities by a factor 100 to 1000 higher than the CO_2 laser system, the question that naturally arose was whether one would be also able to efficiently produce high orders of harmonics. The big advantage in this case is that the resulting harmonic radiation has an absolute wavelength also shorter by a factor of ten. Moreover, the whole arrangement would be of tabletop size compared to the large scale facility used for the CO_2 experiments. Three experiments[3-5] have recently demonstrated the feasibility of harmonic generation in intense laser pulse interaction with solid targets using lasers operating at wavelengths close to $1\mu m$, pulse durations between $130fs$ to $2.5ps$ and focused intensities from $10^{17}W/cm^2$ up to $10^{19}W/cm^2$. In the most recent experiment[5] up to 75th harmonic of the $1053nm$ laser light, i.e. coherent radiation at $14.0nm$ wavelength, was observed with conversion efficiencies ranging from 10^{-4} to 10^{-6}. Obviously, this method appears to be very promising in the quest for a source of coherent radiation in the wavelength range between the K-edges of oxygen at $2.3nm$ and carbon at $4.4nm$, in the so-called *water window*. The scheme is very attractive because the plasma medium not only exhibits strong nonlinearities but, unlike the process of high harmonic generation from gases[6]

(a)

$n(z)$

$\vec{A}_i(z,t)$

$\vec{A}_r(z,t)$

$\omega_p^2 \sim n_e$

$\vec{A}_r(z,t)$

$F_i \sim \exp\left(\dfrac{z}{\delta}\right)$

$F_D \sim \dfrac{\partial A^2}{\partial z} \sim f\lambda^2$

Z

F_R

λ_D

$2Z$

Z

F_R

λ_D

$F_R = -m\omega_p^2 \cdot z$

(b)

$I = 10^{18}\ W/cm^2,\ \alpha = 0 = 45^\circ,\ n_p/n_c = 10,\ \tau = 50\,fs,\ \lambda = 800\ nm$
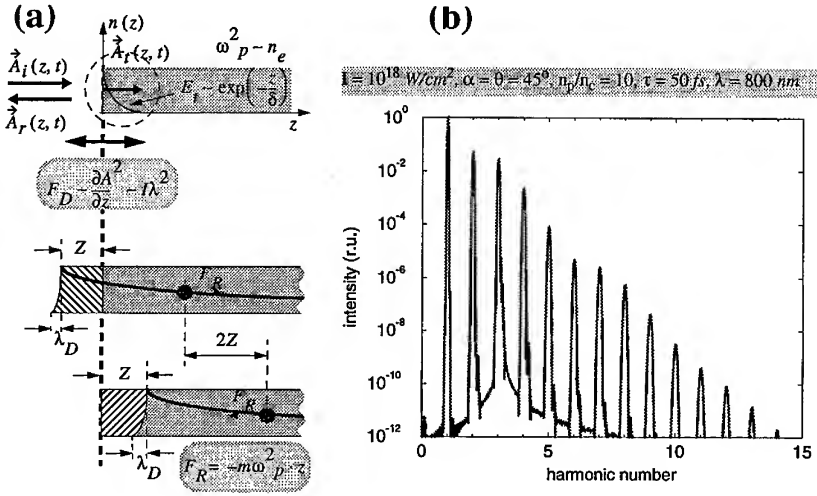
Figure 1: (a) Schematic showing the basic assumptions involved in the model. (b) The harmonic spectrum calculated by the model for the indicated values of the different parameters.

can also withstand arbitrarily high fields.

Most of the theoretical investigations for the interpretation of the experimental results have been performed with the help of sophisticated particle-in-cell (PIC) simulation codes.[7-10] To make the underlying physics more transparent, we have developed a simple model for the generation of harmonic radiation on plasma-vacuum interface based on certain simplifications. We consider a short (50 fs FWHM) laser pulse impinging on a solid surface. It is assumed that the material becomes fully ionized right at the beginning of the laser pulse. The plasma formed consists of heavy ions that do not have time to expand during the laser-plasma interaction and of electrons bound to the immobile ions by electrostatic forces. Thus, most of the subsequent interaction is that of an EM-wave with an overdense plasma possessing steplike density profile. The situation is schematically depicted in Fig. 1a. The incident laser pulse is reflected off this overdense plasma while an evanescent component penetrates to a distance δ approximately equal to the skin depth for the plasma frequency $\omega_p^2 = 4\pi e^2 n_e/m$, i.e., $\delta \approx c/\omega_p$. The electrons are subjected to a driving force due to the transmitted EM-wave which results in an oscillatory motion with components parallel (in the x- y-direction) and perpendicular (z-direction) to the plasma-vacuum interface. Assuming perpendicular incidence along the z-axis (see Fig. 1a), the laser pulse can be described in terms of the transmitted
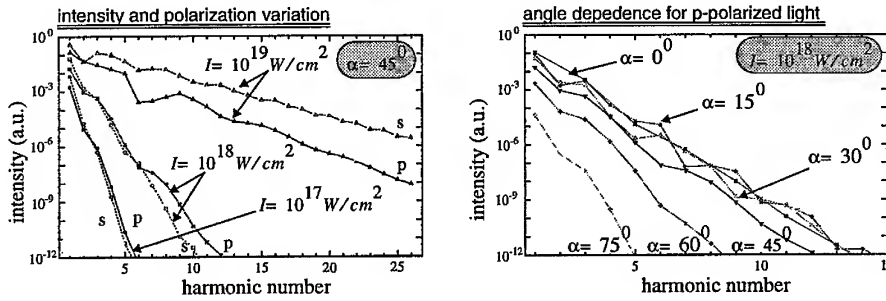
Figure 2: Variation of the harmonic yield for different intensities and for s- and p-polarization. Also, angle dependence for p-polarized light. The rest of the parameters used in the calculation are $n_e/n_c = 10, \tau = 50fs$ and $\lambda = 800nm$.

part of the vector potential as $\vec{A}_t(\vec{r},t) = A_{0,t} P(\eta) \cos(\omega t - \phi_t) e^{-\frac{z}{\delta}} \vec{e}_x$. Here, $P(\eta)$ with $\eta = \omega t - kz$ is the pulse form, and ϕ_t is the phase of the transmitted wave with respect to the incident wave which depends on the plasma density. The total force acting on the electrons at the interface inside a skin depth is then:

$$\vec{F}_T = \frac{d\vec{p}}{dt} = -m\omega_p^2 z\vec{e}_z + q(\vec{E}_t + \vec{v} \times \vec{B}_t) \tag{1}$$

The first term on the right in this equation is recognized as the plasma restoring force $\vec{F}_R$ due to the charge separation while the last two terms represent the driving Lorentz force $\vec{F}_L$ due to the evanescent part of the pulse. The electric and magnetic fields are connected to the vector potential through the known relations $\vec{E}_t = -\partial_t \vec{A}_t$ and $\vec{B}_t = \nabla \times \vec{A}_t$, respectively. A perturbative solution of Eq. 1 yields to the first order the following result:

$$\frac{d\vec{p}_{(1)}}{dt} + m\omega_p^2 z\vec{e}_z = \frac{q^2 A_{0,t}^2}{4m}\left(1 + \cos(2\omega t - 2\phi_t)\right) \nabla\left(P(\eta)e^{-\frac{z}{\delta}}\right)^2 \tag{2}$$

As it can be easily seen, the motion of the electron in the perpendicular direction to the interface is that of a driven harmonic oscillator with eigenfrequency ω_p and driving frequency 2ω. The driving force consists of a constant and an oscillatory term with both terms proportional to $A_{0,t}^2 \sim I\lambda^2$. The driving force time-averaged over a laser period, during which $P(\eta) \approx const$, yields the well known expression for the ponderomotive force. Continuation of the perturbative expansion to higher orders introduces consecutively higher frequencies, i.e., terms exhibiting $\cos(3\omega)$, $\cos(4\omega)$, $\cos(5\omega)$ ... time dependence.

580

This analysis shows that the origin of harmonic emission is the nonlinear mixing of the transverse and the longitudinal electron oscillations, which for high intensities become more and more anharmonic. It should be pointed out here that the $\vec{v} \times \vec{B}$ term in the Lorentz force is responsible for this mixing.

We have numerically solved the fully relativistic equation of motion (Eq. 1) to obtain the trajectories of the electrons in the EM-wave of the incident pulse. Subsequently, using the standard expression for the emission from accelerated charges [11] the spectrum was calculated. An example of this calculation is shown in Fig. 1b. A parametric study of the harmonic yield under different conditions reveals that (a) there is a strong increase of harmonic intensity and harmonic number with laser intensity, (b) for large incident angles the harmonic production decreases, (c) the polarization of the incident laser light has an influence on the harmonic production only for relativistic intensities. Most of these results are summarized in Fig. 2.

In conclusion, the simple model presented here provides considerable insight in the origin of harmonic generation. Most of the results are in qualitative agreement with PIC simulations.[9,10] However, for intensities $I > 10^{18} W/cm^2$ and large incident angle the model indicates efficient harmonic production for both polarizations (see Fig. 2), which is in disagreement with PIC results. This is attributed to more complicated motion of the electrons [10] due to effects that are not included in this model.

Acknowledgments

References

1. R. L. Carman *et al., Phys. Rev. Lett.* **46**, 29 (1981).
2. R. L. Carman *et al., Phys. Rev. A* **24**, 2649 (1981).
3. S. Kohlweyer *et al., Opt. Comm.* **117**, 431 (1995).
4. D. von der Linde *et al., Phys. Rev. A* **52**, R25 (1995).
5. P. A. Norreys *et al., Phys. Rev. Lett.* **76**, 1832 (1996).
6. A. L'Huillier *et al.,* J. Phys. B: At. Mol. Opt. Phys. **24**, 3315 (1991).
7. S. C. Wilks *et al.,* IEEE Trans. Plasma Sci. **21**, 120 (1993).
8. S. V. Bulanov *et al., Phys. Plasmas* **1**,745 (1994).
9. P. Gibbon, *Phys. Rev. Lett.* **76**, 50 (1996).
10. R. Lichters *et al.,* to be published in *Phys. Plasmas* 1996.
11. J. D. Jackson, *Classical Electrodynamics*, John Wiley & Sons, N.Y., 1962.

UNDERDENSE PLASMAS FROM THIN FILMS: PRODUCTION, INTERFEROMETRIC CHARACTERISATION AND SHORT-PULSE INTERACTION STUDIES

M.BORGHESI[1], A.GIULIETTI, D.GIULIETTI[2], L.GIZZI[3], A.MACCHI[4], D.NEELY[5], O.WILLI[1]

Istituto di Fisica Atomica e Molecolare (IFAM-CNR), Pisa (Italy)
[1] *The Blackett Laboratory, Imperial College of Science, Medicine and Technology, London (UK)*
[2] *also at Dipartimento di Fisica, Universita' degli Studi , Pisa (Italy)*
[3] *presently at TESRE-CNR, Bologna (Italy)*
[4] *also at Scuola Normale Superiore, Pisa (Italy)*
[5] *Central Laser Facility, Rutherford Appleton Laboratory, Chilton (UK)*

Plasmas produced by laser irradiation of Al foils have been characterised via interferometry with picosecond resolution. The progress achieved in the characterisation with respect to a previous experiment performed by our group is reported, together with a preliminary study of the propagation of a short pulse through these plasmas.

1. Introduction

The study of laser interaction with long scale, underdense plasmas, crucial for ICF applications, requires suitable plasmas to be produced in a controllable way. A well established and flexible method consists in exploding a thin target by irradiating it with laser pulses. Both diagnostic development and target design are fundamental issues, in view of a detailed characterisation of plasmas produced with this technique. In particular, due to the growing interest in short pulse interaction, the development of diagnostics able to resolve physical phenomena on picosecond and subpicosecond temporal scale is strongly required.

The production and characterisation of plasmas produced by symmetrical laser irradiation of thin targets was the object of a previous experimental study by our group [1] performed at the Rutherford Appleton Laboratory (RAL), Chilton (UK) in 1992. In that experiment, the plasmas were characterised via interferometry with temporal resolution of 100 ps. This limited the readability of the interferograms, since the visibility of the fringes vanished in the inner region of the plasma, where the density variation during 100 ps was large enough to smear out the fringe pattern. A complete density map could be obtained only at late stages of the plasma evolution (typically after 4 ns from the peak of the pulse). We report here about the progress in the production and characterisation of plasmas produced from thin foils

582

achieved in a recent experiment also performed at RAL.

2. Experimental arrangement

The plasma was produced by four 600 ps, 1.053 µm heating beams of the Vulcan laser, in the configuration reported in [1]. The heating beams were superimposed on target in two opposite pairs in a 650-µm FWHM focal spot for an irradiance on each side below 10^{14} W/cm^2. The targets used were Al disks, with a diameter of 800 µm and a thickness of 0.4 µm. A Chirped-Pulse Amplified (CPA) pulse (1 ps duration and energy up to 10 J) was used as the interaction pulse and was focused onto the preformed plasmas, with variable delay, at irradiances below 10^{17} W/cm^2.

A portion of the pulse was frequency doubled to 0.53 µm, and used as a transverse optical probe. A modified Nomarski interferometer[2] was used to measure the density profile of the preformed plasma and also to detect density modification induced by the short pulse. The short pulse energy transmitted through the plasma was monitored by a calorimeter.

3. Interferometric characterisation

The use of a short pulse optical probe marked a notable progress in the interferometric characterisation of the plasma. Interferograms taken 2.2 ns after the peak of the heating beams are shown in fig.1.

The progress obtained is evident from comparison with interferograms obtained with the 100 ps probe[1]. In that case, even at later times, the visibility of the fringes was lost over a considerably wider region: in interferograms taken 3 ns after the plasma production, the density was not measurable over a region 400 µm wide. With the picosecond probe, it was possible to measure the density profile almost over the length of the whole plasma as early as 2 ns. The density profile was obtained from the interferogram using a Fourier transform method for the phase extraction[3], and subsequent Abel inversion of the phase distribution.

4. Target design

The Al dots were alternatively coated on plastic foils or held by four tiny arms in the shape of a X. The interferograms of fig.1 refer to plasmas produced from these two different type of targets. Plasmas produced from X-shaped targets appear to be potentially more suitable for interferometric studies of the interaction. In fig. 1b) the interference fringes are visible virtually over the length of the whole plasma. On
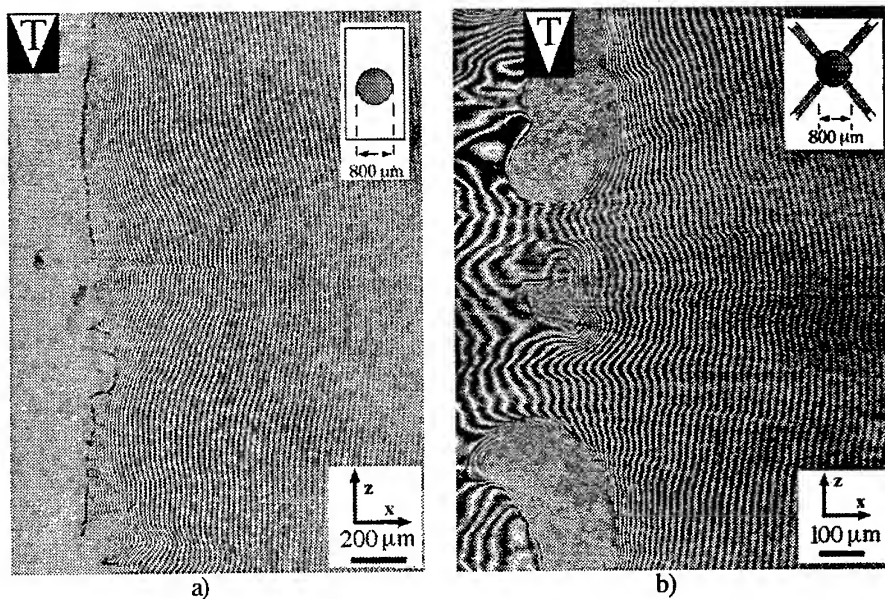
Fig.1 Interferograms taken 2.2 ns after the peak of the heating beams. In the right top corner, the type of target from which the plasma has been produced is represented. The original target position is indicated by the "T" wedge.

the contrary, in fig.1 a) a part of the interferogram is obscured by the shadow of the dense, slowly expanding plasma created on the plastic substrate, in the line of sight of the probe, by the low energy wings of the laser spot. On the other hand, while the cylindrical symmetry of plasmas produced from the targets of fig.1a) is confirmed by the good agreement between the experimental density profile and hydrocode predictions, the plasma produced on the small arms of an X-shaped target introduces a non negligible perturbation to the whole plasma symmetry and, consequently, difficulties in the determining the plasma density.

5. Short pulse interaction with the preformed plasmas

Finally, the propagation of a ps pulse at irradiances below 10^{17} W/cm^2 through the characterised plasmas has been studied. Density modifications induced by the short pulse in the preformed plasma, likely due to residual ionization of the Al plasma, were observed via interferometry. The transmitted energy fraction of the short interaction pulse was measured as a function of both interaction and heating intensity. In the investigated intensity range the short pulse transmission through the plasma appears to be substantially not related to the energy of the short pulse itself, while it depends from the heating intensity through a sort of threshold

584
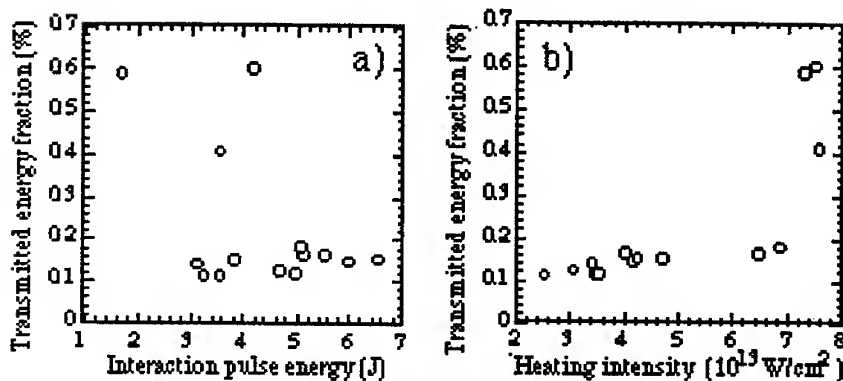
Fig.2: Transmitted energy fraction of the short interaction pulse vs. a) interaction pulse energy and b) heating beams energy.

mechanism (see fig.3). In other words, the hydrodynamic evolution of the preformed plasma appears to play an essential role in determining the conditions of the propagation process.

6. Conclusion

Long scale, underdense plasmas suitable for interaction studies were produced by uniform laser irradiation from opposite sides of thin targets. The use of a picosecond pulse probe led to relevant progresses in the density mapping of the plasma with respect to previous results obtained with a lower temporal resolution. Different target design were experimented and their relatives merits compared. The propagation of a short pulse through the plasma appeared to strongly depend upon the preformed plasma density conditions.

Acknowledgements:

References:

1. L.A.Gizzi et al, Phys. Rev. E **49**, 5628 (1994)
2.. R.Benattar, C.Popovics, R.Sigel, Rev. Sci. Instruments **50**, 1583 (1979)
3. M.Takeda, H.Ia, S.Kobayashi, J.Opt.Soc.Am. **72**, 156 (1982)

COLLECTIVE EFFECTS OF LASER POWERFUL SUPER SHORT PULSES ENERGY TRANSFORMATION

VADIM S. BELIAEV

Central Research Institute of Machine Building of Russian Space Agency
Pionerskaya 4, Kaliningrad, Moscow Region, 141070, Russia

In frames of reasonable simplification the model of intensive ultra short pulse laser radiation interaction with matter has been built with regard to the effect of the produced plasmas with atoms. The role of collective processes at the laser radiation interaction with matter in parameters range at $J > 10^{17}$ W/cm² and duration $\tau < 100$ fsec increases and becomes defining. It has been shown that with nowadays laser radiation parameters this radiation effects on atomic and nuclear structures by means of their interaction with electromagnetic fields of laser produced plasma and this interaction is being accompanied by strong action at nucleus.

The results of collective processes research on the basis of the analytical model construction of the interaction with matter of the laser radiation in parameters range at $J > 10^{17}$ W/cm² and duration $\tau < 100$ fsec was presented in referenses [1,2].

The full picture of intensive super short laser radiation interaction with matter may be built only with regard to created plasmas effect on atomic structures with their electron shells and nuclei.

With this in mind the collective processes at 5 stages of femtosecond laser plasmas development were considered:

1. Laser plasmas interaction with free electrons; plasmas instabilities development in skin-layer scale ($\sim 10^{-5}$ cm).

2. The process of tunnel ionization, ionization explosion, electron continuum creation, the consideration of the accompanying processes in 10^{-8} cm scale.

3. The process of created super strong fields action on electrons shells, the stratification of shells, pinch-effect with shells compression up to the scales of Compton's wavelength $\sim 10^{-11}$ cm.

4. Laser radiation transformed action on nucleus through their electrons shells. The phenomenon has the scale of the order of Fermi (10^{-13} cm).

5. The collective process of synchronous nuclear excitation action on laser produced plasmas.

The model of laser radiation interaction with matter is constructed on the basis of analytical solution of the self-consistent equations system and is used for the following phenomena description: for electromagnetic field - Maxwell's equations; for electron plasmas states - Vlasov's equation; for ionizing process - Keldysh's equation.

The basic set of equations includes all the effects of nonstationary ionization that can be described in a self-consistent manner using the electron distribution function. Let us consider two important effects that are completely determined by the distribution function: anisotropy of electron heating and anisotropy of ionization. Anisotropy of heating is mainly assosiated with the appearance of

the component P_{ij} of the electron-pressure tensor. As shown in [3], such components of the electron-pressure tensor are responsible for efficient conversion of the laser-pulse energy into microwave radiation and spontaneous generation of quasi-static magnetic fields in a medium with a Weibel instability. However, when the flux of the laser pulse is greater than 10^{17} W/cm^2 and duration of the laser pulse less than 100 fsec, the ionization rate due to tunneling effects lies within the range of $(10^{15} - 10^{18})$ sec^{-1}. In other words, the ionization rate is one or two orders of magnitude greater than the plasmas

frequency of a solid-state plasma, $\omega_o = \sqrt{n_o e^2/m\varepsilon_o} = (10^{15} - 10^{16})$ sec^{-1}. Under these conditions, we should take into consideration the collective effects assosiated with the anisotropy of tunneling ionization. For such a situation, the linear theory of instability of laser action on a medium predicts the excitation of a broad spectrum (from 10^{15} to 10^{18} sec^{-1}) of electromagnetic oscillations in a solid-state plasma due to instabilities. Because of the short time of laser action and the high ionization rate, the electron distribution function in such a medium becomes substantially anisotropic and unequilibrium.

At the initial phase of the intensive super short pulse radiation action upon matter in skin-layer a large scale vortical electron structure with the electric field exceeding interatomic strength and with free electrons current with relative concentration of the order of 10^{21} 1/cm^3 is induced. It is shown that at such conditions the process of anisotropy atoms ionization and anisotropy electrons heating takes place in the plane which is perpendicular to the laser beam with the process frequencies of the order of plasmas. This stage may be called as "induced" and it is characterized by the energy accumulation in the electron component. At this the spontaneously generated magnetic fields due to Weibel's instabilities development are maintained during the whole time of the pulse action and are of quasi-stationary character. The amplitude of the magnetic fields achieves the value of the order of 10 MGs.

This value is determined by component P_{XX} of the electron-pressure tensor

$$B_o = \mu_o H = \mu_o \left(2P_{XX}/\mu_o\right)^{1/2} > 10 \text{ MGs for initial intensity } J > 10^{17} \text{ W/cm}^2.$$

The development of the high frequency potential and vortical instabilities at the leading edge of the laser pulse at the conditions of high ionization frequency leads towards the small electrons group collective acceleration with high tempo which is more than 10 MeV/fces.

This value is determined by value of tunnel frequency ν_i $d\varepsilon_o/dt \cong mc^2 \nu_i \left(N_a/n\right)$ for fast particles with concentration $n << N_a$ (N_a - concentration of atoms).

Among all various properties and structures of femtosecond laser plasmas in this case we are interested in such plasmas ability to generate super strong electric and magnetic fields which act directly on atoms and first of all on electrons shells through which the action on the nucleus is realized. The special

role in vortical fields generation may play relavistic plasmas small scale turbulence.

At the second stage the structural rebuilding of the atomic electrons shells in super strong electromagnetic fields of ultra short duration leads towards atomic electrons binding energy transformation into the electron continuum vortical energy at the expense of low ionization cost. Second stage is liable for electron continuum creation ($\Delta\omega \sim 10^3$ sec^{-1}) with energy density $\sim 10^8$ J/cm^3, solitons creation and induced transparency appearing [1].

The collective processes at the microscopic level with nonhomogeneity atomic scales and the fields intensities of the order of interatomic are considerable here. 10^{17} W/cm^2 is the threshold intensity of the falling laser radiation for these processes development. The structural rebuilding of electrons shells occurs in the self-consistent field, which includes the static component of the nuclei atomic fields and the stochastic one, occurring at plasmas instabilities development during the ionization decay of atom outer shells. The vortical component of the stochastic field at the development of the microscopic turbulence with the fields nonhomogeneity of the order of atomic size contains the high amplitudes of the magnetic fields exceeding the value of 10 MGs. This corresponds to high frequency pressure upon electron shells of the order of 10^8 atm exceeding the inner atomic pressure.

At such magnetic fields at the third stage the process of spin stratification of atomic electrons according their energy is effective. The electrons with spin orientation opposite the magnetic field receives the energy $h\Omega$, where h - is the Planck constant, Ω - is the hyrofrequency of electrons in magnetic field; the electrons having the spin orientation along magnetic field give their energy to the wave. The first group of electrons overcome the potential barrier moreover the probability of this tunnel process increases greatly at the expense of the strong electric field and the electrons becomes "quazifree". The second group "falls" at the lower levels, compressing (condensing) the lower lying shells. "The ionization explosion" of the atomic electrons outer shells occurs at the time of the tunnel ionization of the order of $10^{-16} \div 10^{-17}$ sec at the expense of the atomic inner structure rebuilding that is lower energy levels condensation with energy transmission at the expense of spin interaction. It should be mentioned that the process of such type have been already considered in the theory of wave collapses when as a result of collapse in some long dissipation area of small size localized in all dimensions is created. This effect was called "the vortex (crater) effect" and the effect of "nucleation". This process leads towards atoms collective cooling with condensation of electrons upon low energy levels.

At the fourth stage lower electrons shells packing stimulates the process of K-capture type and the nucleus excitation up to its distraction with energy liberation. The nuclei with great quadrupolar momentum are promising in this respect. The plasmas spectrum analysis appearing at the terawatt laser action

(about 10^{16} W/cm²) upon the tantalum target showed the presence of the atoms lines of the VI row of the periodical elements system.

There is an analogy of this stage in classical consideration as well, when for the super strong fields creation a directed explosion is used. In our case these conditions are realised due to the magnetic field "interfrostedness" into the ideal conductive electrons shells. In this case the "ionized explosion" connected with tunnel ionization processes undertake the role of the explosion products.

Thanks to magnetic flux conservation at electrons shells compression strong magnetic field achieving the value of 10^{11} Gs is created near the nucleus at the distance which is of the order of Compton wavelength. This magnitude corresponds to the amplitude of magnetic field on Bohr's orbit and is about 10^9 Gs when energy of magnetic interaction with electron μB exceeds the energy of ionization $\mu B > \hbar^2/8mr_B$.

At fifth stage the nuclei group synchronous excitation during tunnel ionization times ($< 10^{-17}$ sec) leads towards the collective process of nuclei excitations energies action upon the created laser plasmas. The excited nuclei may come into the ground state by means of direct excitation or decay energy transmission to electrons group (inner conversion collective process). In this case appearing electron pressure anisotropy exceeds the value of 10^{17} J/m³ which corresponds to the induced fields strength is more than 10^4 MGs. The small electrons group acceleration tempo is defined by the formula and may achieve the value of 1GeV/fsec. $d\varepsilon/dt = N_a v_i E_{nucl}/n_e$ for $E_{nuc} \approx 8$ MeV/nucleon.

The conducted researches open the series of works on electromagnetic stimulation of the collective atomic and nuclear processes in laser produced plasmas.

References.

1. Arefyev V.I., Beliaev V.S., Specific Features of the Propagation of a High-Power Ultrashort Laser Pulse in a Solid-State Plasma, *Laser Physics*, **5**, No 4, 1995, p.1-12.
2. V.Beliaev, Collective Effects of Ionizing Radiation Powerful Super Short Pulses Energy Transformation, *Proceedings of the International Conference on Lasers'95, Dec. 1995, Charleston, South California, USA.*
3. Silin V.P. at al., 1990, *Zh.Tekh. Mat. Fiz.*, **82**, 18.

APPLICABILITY OF THE QUIVERING MOTION IN A LASER FIELD TO NUCLEAR FUSION

LUIS ROSO

Departamento de Física Aplicada, Universidad de Salamanca,
E-37008 Salamanca, Spain.

The quivering motion of a classical charged particle - an atomic nucleus- inside a Terawatt - Petawatt laser pulse is studied. Under these intensities the motion of the particle corresponds to a drift velocity -depending on the initial conditions- and a quiver oscillation. This oscillation represents a fast and periodic acceleration and slow down of the particle. At these frontier intensities, the kinetic energy of the nucleus due to this quivering is high enough to trigger fusion reactions. The proposed system works for the deuteron-triton fusion reaction, but is more appropriated for other reactions like the, ecologically clean, proton-boron 11 reaction.

The intensity of the laser pulses has been improving over the past decade. This has been basically due to what is called chirped pulse amplification, a technique to expand, amplify and compress the laser pulse, getting a subpicosecond pulse with a peak power of the order of the terawatt [1]. These laser pulses represent a very high concentration of energy. We want to show here how these lasers can be used to accelerate nuclei, as a result of the quiver motion of a charged particle in an electric field, to energies that are relevant for nuclear reactions. In particular, if a plasma with two different nuclear species is studied, we suggest the possibility of laser-induced collisions resulting from their differential accelerations. For several pairs of nuclei these collisions can be energetic enough to overcome Coulomb repulsion, giving then a possible nuclear fusion.

Let us consider two different nuclei of masses m_1 and m_2 and electric charges eZ_1 and eZ_2 that move inside a laser field. The simple classical equations giving the motion of both nuclei are,

$$m_1\,\vec{a}_1(t) = e^2 Z_1 Z_2 \frac{\vec{r}_1 - \vec{r}_2}{|\vec{r}_1 - \vec{r}_2|^3} + eZ_1\,\vec{E}(\vec{r}_1,t)$$

$$m_2\,\vec{a}_2(t) = e^2 Z_1 Z_2 \frac{\vec{r}_2 - \vec{r}_1}{|\vec{r}_1 - \vec{r}_2|^3} + eZ_2\,\vec{E}(\vec{r}_2,t)$$

590

where $\vec{r}_1(t)$ and $\vec{r}_2(t)$ indicate the positions of both nuclei, and $\vec{a}_1(t)$ and $\vec{a}_2(t)$, their respective accelerations, in the laboratory frame. The first term indicates the nuclei repulsion, and the second the interaction with the laser electric field. Magnetic effects have not been considered.

We are considering a laser field, therefore its wavelength is of the order of the micron. Being this length much higher than the distance between nuclei, if we start from liquid densities, it is reasonable to consider that the electric field is $\vec{E}(\vec{r}_1,t) = \vec{E}(\vec{r}_2,t) = \vec{E}(t)$. This can be regarded as the dipole, or long wavelength approximation.

The time dependence of the field is $\vec{E}(t) = \vec{E}_0(t)\,cos(\omega_L t)$. The field amplitude $\vec{E}_0(t)$ is slowly varying in time, and it accounts for the switch on and off of the pulse. To study the dynamics of the collision between both nuclei it is worth changing to an intrinsic coordinate frame in place of the laboratory frame. Introducing the relative coordinate $\vec{r} = \vec{r}_2 - \vec{r}_1$ it is easy to show that the relative acceleration is given by,

$$\vec{a}(t) = e^2 Z_1 Z_2 \frac{1}{\mu} \frac{\vec{r}}{r^3} + e\,\frac{m_1 Z_2 - m_2 Z_1}{m_1 + m_2}\,\frac{1}{\mu}\,\vec{E}_0\,sin(\omega_L t)$$

with $\mu = m_1 m_2/(m_1 + m_2)$ being the reduced mass. We observe that the laser introduces a relative acceleration between both particles provided that $m_1 Z_2 - m_2 Z_1$ does not cancel. It indicates that the proposed mechanism does not work for deuterium-deuterium collisions. We need therefore to consider nuclei with very different Z/m ratios.

This clearly shows that the relative motion is given by the effective amplitude,

$$\vec{E}_0^{eff} \equiv \frac{m_1 Z_2 - m_2 Z_1}{m_1 + m_2}\,\vec{E}_0$$

This effective amplitude is the laser field amplitude times a factor proportional to the dipole of the two nuclei system. Since we are interested in collisions able to trigger fusion reactions, we need energies in the keV-MeV range. This suggest that the oscillatory motions of the particles in the laser field have large amplitudes. Then it is a reasonable approximation, for a preliminary study, to eliminate the Coulomb internuclear repulsion in the relative acceleration classical equation.

Therefore we only calculate the oscillations in the field. With this approximation we can analytically obtain the kinetic energies at the collision. This calculation is extremely simple and allows a very close approximation for the collision energies.

We have studied this classical motion equation. The quiver motion is given by

$$\vec{a}(t) = -\frac{e}{\mu} \vec{E}_0^{eff} sin(\omega_L t)$$

$$\vec{v}(t) = \frac{e}{\mu} \frac{\vec{E}_0^{eff}}{\omega_L} cos(\omega_L t)$$

It is easy to show that the energy of the collision, $T = \mu v^2/2$, can be as high as

$$T_{max} = \left(\frac{m_1 Z_2 - m_2 Z_1}{m_1 + m_2}\right)^2 \frac{e^2}{2\mu} \frac{E_0^2}{\omega_L^2}$$

The computation of solutions of the classical motion equation gives trajectories that, depending on the initial conditions, either are divergent from the beginning or give two particles that approach each other initially, then collide and finally escape. We have computed many of these trajectories for different initial conditions, calculating in each case the minimum distance between both nuclei r_{min}. This minimum distance is easily related to the kinetic energy, T, of the collision by the simple relation, $T = e^2 Z_1 Z_2/r_{min}$. The collision energies and minimum internuclear distances for different intensities are shown in Table 1. It corresponds to $\hbar\omega_L = 1\,eV$, and only to the quiver motion.

	10^{19} W/cm^2	10^{20} W/cm^2	10^{21} W/cm^2	10^{22} W/cm^2	
D + T	0.05 keV	0.5 keV	5 keV	50 keV	T_{max}
	25000 fm	2500 fm	250 fm	25 fm	r_{min}
p + ^{7}Li	1 keV	10 keV	100 keV	1 MeV	T_{max}
	1400 fm	140 fm	14 fm	1.4 fm	r_{min}
p + ^{11}B	1.1 keV	11 keV	110 keV	1.1 MeV	T_{max}
	1200 fm	120 fm	12.0 fm	1.2 fm	r_{min}

Table 1.- Collision energies and minimum internuclear distances for three different nuclear reactions, and different intensities. This Table corresponds to $1eV$ photons, and only to the quiver motion.

592

In conclusion we have suggested the possibility of nuclear collisions induced by an intense laser pulse. For the most intense today available laser we are close to enter a regime of collision energies relevant for nuclear fusion. Therefore we want to finish suggesting a new possibility to obtain fusion in a different way from laser inertial confinement. The idea is to use this quiver motion to induce energetic collisions, and because it is a non-thermal motion of a oscillatory nature, confinement maybe is not as important as in the purely thermal case.

These ideas apply to the deuterium-tritium reaction, but they work for many other cases. In particular it is specially promising the case of a proton colliding with heavier nuclei with almost the same number of protons and neutrons. For example the proton-lithium 7 reaction need further study. The best candidate may be the ecologically clean proton-boron 11 reaction.

These naïve equations indicate that the lower the frequency the higher the quiver energy. Clearly the first objection to the use of long wavelength lasers is the propagation inside the plasma. Probably the best solution is to try to ionize completely the reactants and then try to trap the resulting nuclei inside a laser beam, for example. It is also possible to explore low density situations with a very large reaction volume to avoid plasma propagation problems, but then the Lawson criteria seem difficult to accomplish.

Reference

1. For an updated outline of the present situation of the chirped pulse amplification lasers see, for example, "High-Field Interactions and Short Wavelength Generation", vol. 16, 1994 OSA Technical Digest Series (Optical Society of America, Washington DC, 1994), and the related feature issues on the Journal Optical Society of America B, vol 13, January and February 1996.

Short Pulse Laser Harmonics from Overdense Plasma Surfaces Driven at Relativistic Intensities

R. Lichters* and J. Meyer-ter-Vehn

Max–Planck–Institut für Quantenoptik, 85748 Garching, Germany

Abstract

The generation of harmonics by interaction of an ultrashort laser pulse with the boundary of a plane overdense plasma layer is studied at intensities $I\lambda^2 = 10^{16} \ldots 5 \times 10^{19} \mathrm{Wcm}^{-2}\mu\mathrm{m}^2$ by fully relativistic one-dimensional particle–in–cell (PIC) simulations. Harmonic emission increases with intensity; simulations reveal harmonic orders up to the 100th with conversion effieciency $\eta_{100} \approx 10^{-7}$. Short density ramps at the plasma surface lead to enhanced harmonic emission in connection with excitation of plasma waves in the ramp region. A cutoff of the harmonic spectrum at the bulk plasma frequency can be observed. Also, for short density ramps, emission at twice the bulk plasma frequency occurs which is explained by kinetic effects.

The progress in making ultra-short (10–100 fs) laser pulses with intensities $I\lambda_0^2 = 10^{17}\mathrm{Wcm}^{-2}\mu\mathrm{m}^2$ and above[1] has opened new possibilities to investigate relativistic laser-plasma interaction and generation of high harmonics. First experiments looking for harmonics from solid surfaces irradiated by ultrashort laser pulses have been reported recently[2,3,4]. Calculations of relativistic laser plasma interaction at overdense plasma boundaries have been performed by a number of groups[5,6,7,8]. The interaction of short laser pulses with steplike overdense plasma surfaces has recently been studied in detail by $1D3V$ PIC simulations and a cold relativistic plasma fluid model[8]. It was shown that the generation of harmonics can be understood in the framework of a simple relativistic fluid model as reflection from the oscillating surface, taking full account of retardation. Here, we extend the work of[8] (1) to higher intensity and (2) investigate the influence of a density scale length $L > 0$ at the plasma surface on harmonic emission by $1D3V$ PIC simulations. This is important for the interpretation of experiments, since prepulses and laser pedestal create a layer of ablating plasma before the main pulse hits the surface.

For a steplike density profile, the harmonic intensities increase when lowering the plasma density and when rising the laser intensity into the relativistic regime $a_0 > 1$; here, the dimensionless amplitude $a_0 = eA_0/mc$ of the vector potential of the laser pulse is related to the laser intensity I and wavelength λ_0 by $a_0^2 = I\lambda_0^2 / (1.37 \times 10^{18} cm^{-2}\mu m^2)$ for linearly polarized light; e and m are charge and rest mass of the electron, and c is the velocity of light in vacuum. An illustrative PIC simulation result is given in Fig. 1 (a). It shows

a power spectrum of light reflected from a steplike plasma profile of density $n/n_c = 27.5625$, where $n_c = \omega_0^2\, m\varepsilon_0/e^2$ is the critical density. The laser pulse with amplitude $a_0 = 6$ is p-polarized and obliquely incident under $\alpha = 45°$. The spectrum shows harmonics above noise level up to the 100th with the ratio $\eta \approx 10^{-7}$ of the power of the 100th harmonic to the power of the incident pulse. Fig. 1 (b) shows a summary of several simulations; the intensity of selected harmonics is plotted vs. the amplitude of the incident laser pulse. Apparently, the harmonic intensities increase dramatically when the laser amplitude enters the relativistic regime $a_0 > 1$. It is also indicated, that low order harmonics saturate at $a_0 \gg 1$.
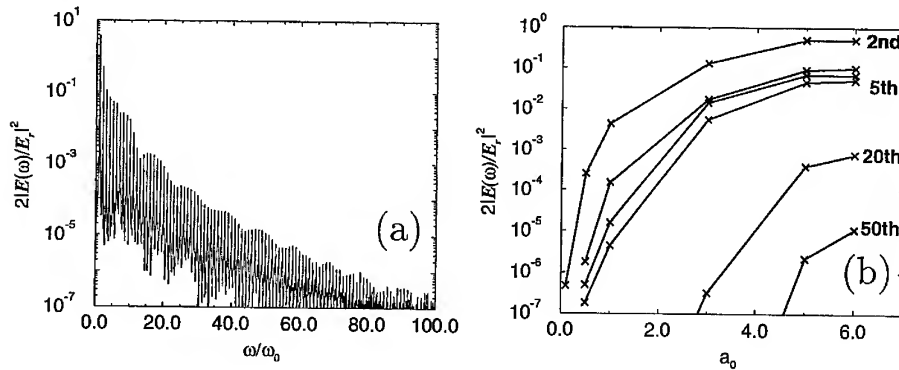
Figure 1: PIC simulations for steplike plasma profiles with density $n/n_c = 27.5625$; pulse duration $T = 30\tau$, where τ is the laser cycle time, $\sin^2$-shaped rising and falling pulse edges of ten cycles duration; angle of incidence $\alpha = 45°$ and p-polarization. (a) Power spectrum of reflected light, time averaged over the pulse duration. The incident laser amplitude is $a_0 = 6$. (b) Selected harmonics' intensities for varying incident intensities.

In the following, we study the influence of short linear density ramps at the plasma surface on harmonic generation. Fig. 2 (a) shows a power spectrum of reflected light for a p-polarized laser pulse of amplitude $a_0 = 0.5$ interacting at $\alpha = 30°$ with plasma of bulk density $n/n_c = 27.5625$ and density ramp length $L = 0.2\lambda_0$. The bulk plasma frequency is $\omega_p = 5.25\omega_0$. The harmonics up to the fifth are strongly enhanced compared to the case of $L = 0$, and a sharp cutoff is observed between the fifth and the sixth harmonic. When the ramp length L is further increased, the striking cutoff vanishes, the harmonic intensities reach a maximum at $L \gtrsim \lambda_0$ and decrease again slowly. This is demonstrated in Fig. 2 (b).

Fig. 3 shows electron density snapshots vs. coordinate x and time t during four laser cycles for the simulation that corresponds to Fig. 2 (a), $L = 0.2\lambda_0$. It shows that the p-polarized obliquely incident laser pulse generates plasma
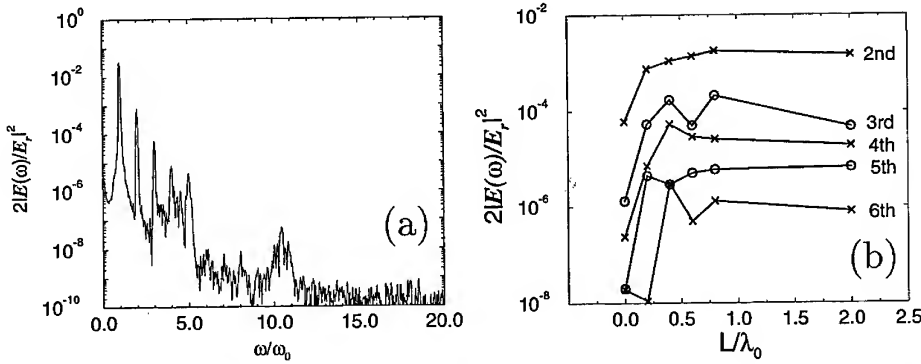
Figure 2: PIC simulations for plasma profiles with bulk density $n/n_c = 27.5625$ and varying density ramp length L; pulse amplitude $a_0 = 0.5$, pulse shape $\sin^2(\pi t/T)$, where $T = 30\tau$; angle of incidence $\alpha = 30°$; p-polarization. (a) Power spectrum of reflected light. The density ramp length is $L = 0.2\lambda_0$. (b) Selected harmonics' intensities vs. L/λ_0.

waves in the ramp region which run towards the vacuum. At positions, where the local plasma frequency equals harmonics of the laser frequency, plasma oscillations of this frequency are resonantly excited. Near the bulk density, oscillations at $5\omega_0$ are excited, and roughly in the middle of the ramp, the excitation of oscillations at $4\omega_0$ is observed ($\omega_p(x) \propto \sqrt{x}$, when $n(x) \propto x$). The resonant layers act as sources for harmonic radiation. The resonances occur only for harmonics up to the bulk plasma frequency, here the 5th harmonic, which can explain the sharp cutoff observed in Fig. 2 (a). The fact that this effect occurs only at short ramps $L < \lambda_0$ could be used as a diagnostic for the density scale length of laser produced plasmas in experiments.

Fig. 3 shows besides plasma waves in the ramp region waves inside the bulk plasma with phasevelocity pointing into the bulk. The origin of these waves are bunches of electrons extracted from and reinjected into the plasma once per laser cycle[9], the black color-coded low density plasma in Fig. 3. The bunches can be shown to excite plasma waves with phase velocities equal to the maximum velocity of the bunches. These waves in turn lead to radiation at harmonics of the plasma frequency, which can be demonstrated using the wave equations for the cold relativistic plasma fluid derived in[8],

$$\left(\partial_x^2 - \frac{1}{c^2}\,\partial_t^2\right) a = \left(\frac{\omega_p}{c}\right)^2 \left[n\,\frac{\sqrt{1-\beta_x^2}\cdot(a - \hat{\mathbf{y}}\,\tan\alpha)}{\sqrt{1 + (a\cos\alpha)^2 - a_y\sin 2\alpha}} + \hat{\mathbf{y}}\,\tan\alpha\right].\quad (1)$$

Nonlinear plasma waves inside the bulk contribute source terms oscillating at harmonics of ω_p to the RHS of Eq. 1. The lowest harmonic which is able to propagate through the plasma to be detected in the vacuum region outside the

596
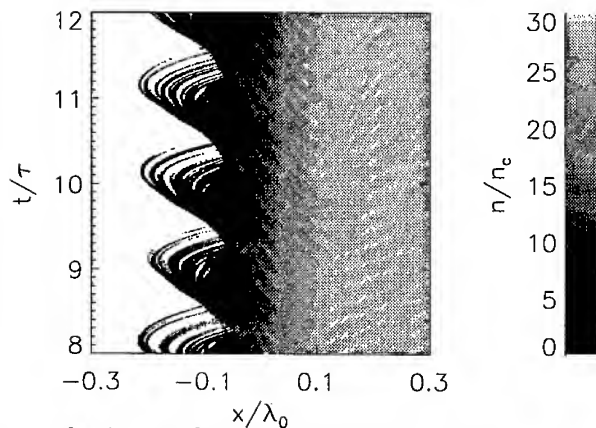
Figure 3: Electron density snapshots vs. coordinate x and time t for four laser cycles. The p–polarized laser pulse with amplitude $a_0 = 0.5$ and 30 periods duration is obliquely incident under $\alpha = 30°$; the bulk plasma density is $n/n_c = 27.5625$ and $L = 0.4\lambda_0$.

plasma, $\omega = 2\omega_p$, is observed in Fig. 2 (a).

In conclusion, we have presented simulations revealing high harmonic orders up to the 100th with conversion efficiency $\eta_{100} \approx 10^{-7}$. We have shown that short density ramps at the plasma surface enhance the harmonic intensities. The generation of radiation at twice the bulk plasma frequency by interaction of short laser pulses with overdense plasma has been reported for the first time.

[*] E-mail: lichters@mpq.mpg.de
1. M.D. Perry, G. Mourou, Science 264, 917 (1994).
2. S. Kohlweyer, G.D. Tsakiris, C.-G. Wahlström, C. Tillman, I. Mercer, Opt. Comm. 117, 431 (1995).
3. D. von der Linde, T. Engers, G. Jenke, P. Agostini, G. Grillon, E. Nibbering, A. Mysyrowitz, A. Antonetti, Phys. Rev. A 52 (1), R 25 (1995).
4. P.A. Norreys, M. Zepf, S. Moustaizis, A.P. Fews, J. Zhang, P. Lee, M. Bakarezos, C.N. Danson, A. Dyson, P. Gibbon, P. Loukakos, D. Neely, F.N. Walsh, J.S. Wark, A.E. Dangor, Phys. Rev. Lett. 76 (11), 1832 (1996).
5. S.C. Wilks, W.L. Kruer, W.B. Mori, IEEE Trans. Plasma Sci. 21 (1), 120 (1993).
6. S.V. Bulanov, N.M. Naumova, F. Pegoraro, Phys. Plasmas 1 (3), 745 (1994).
7. P. Gibbon, Phys. Rev. Lett. 76 (1), 50 (1996).
8. R. Lichters, J. Meyer-ter-Vehn, A. Pukhov, submitted to Phys. Plasmas (1996).
9. F. Brunel, Phys. Rev. Lett. 59 (1), 52 (1987).

Fast Ignitor Physics:
Relativistic Magnetic Self-Channeling

A. Pukhov* and J. Meyer-ter-Vehn

Max-Planck-Institut für Quantenoptik, Garching-bei-München, Germany

Abstract

We present 3D PIC simulations for laser pulses with relativistic intensity propagating in slightly underdense plasma. We observe the formation of magnetized light channels which merge into a single channel with a width of 1 - 2 wavelengths due to magnetic interaction. A representative case is discussed in which the intensity on axis increases from initially $1.2 \times 10^{19} \mathrm{W/cm^2}$ to $2.0 \times 10^{20} \mathrm{W/cm^2}$. A key feature is the strong current of relativistic electrons in the direction of light propagation that generates magnetic fields up to 100 MG. Also, ion acceleration and plasma cavitation are discussed.

The Fast Ignitor[1] is a new concept for ignition of precompressed fusion targets involving picosecond laser pulses at relativistic intesities. It may become important also in the context of beam fusion. In this concept a superintense ($I > 10^{18} \mathrm{W/cm^2}$) laser pulse has to drill a channel through overdense plasma to reach the target core. However, the critical surface is preceeded by a long region of underdense plasma, where the laser beam can experience strong relativistic self-focusing and filamentation.

A laser beam propagating in underdense plasma with a plasma frequency ω_p smaller than the laser frequency ω undergoes relativistic self-focusing as soon as its total power P exceeds the critical value

$$P_{cr} \approx 17 \left(\omega/\omega_p\right)^2 \ GW; \qquad (1)$$

this has been established both theoretically[2] and experimentally[3]. The self-focusing is due to the relativistic mass increase of plasma electrons and the ponderomotive expulsion of electrons from the pulse region. Both effects lead to a local decrease of plasma frequency and an increase in refractive index. The medium then acts as a positive lens. An analysis in terms of the envelope and paraxial approximation[4] shows that, depending on laser pulse and plasma parameters, either self-focusing of the whole pulse or pulse filamentation occurs.

The present paper describes laser light propagation far above threshold (1) and deals with additional effects that become dominant when the dimensionless amplitude $a = eA/mc^2$ of the vector potential A enters the relativistic regime, $a > 1$; here, e and m are charge and rest mass of the electron, and

c is the velocity of light. It was shown in 3D [5] and in 2D3V [6,7] PIC simulations, that the radiation then drives strong currents of relativistic electrons in the direction of light propagation, magnetizing the plasma. The generated quasistatic magnetic field is $B_\perp^s = (en_e)2\pi r$ at distance r from the beam axis. The field $B_\perp^s$ may become as strong as the magnetic field of the light wave itself, which is $B = aB_0$ in units of $B_0 = mc\omega/e$. For light of wavelength $\lambda = 2\pi c/\omega = 1\mu m$, one obtains $B_0 = 107.1$ MG. In units of B_0, the quasistatic magnetic field is

$$B_\perp^s/B_0 = (n_e/n_c)\pi r/\lambda \tag{2}$$

and is of order B_0 when n_e approaches the critical density $n_c = \pi mc^2/(e\lambda)^2$. We also notice that the cyclotron frequency ω_c corresponding to $B_\perp^s$ satisfies $\omega_c/\omega = B_\perp^s/B_0$ and may become resonant with the light frequency. This may lead to magnetic focusing in addition to the other focusing mechanisms.

The present work treats this striking phenomenon by 3D3V PIC simulations with the code LPlas3D. The code was run on the high-performance RISC workstation IBM RS6000 7015/R24 with 1 GB main memory. A typical run needs about 50h CPU time.

A representative case with an incident intensity of 1.24×10^{19}W/cm^2, corresponding to $a = 3$ ($\lambda = 1\mu m$), is shown in Fig. 1. It confirms the formation of a single propagation channel with considerably enhanced concentration of light on the axis. The incident beam propagates through an unstable filamentory stage and finally collapses into a single channel with a width of $1 - 2\lambda$.

The Fig.2 presents the longitudinal cuts through the plasma volume of the instantaneous intensity $I = c\left(E^2 + B^2\right)/8\pi$ on the left column, and the low-frequency (quasistatic) part of the magnetic field component averaged over 1.5 laser periods on the right column. The positions of the cuts are: $X_I = 12\lambda$, $X_{II} = 18\lambda$, $X_{III} = 27\lambda$, $X_{IV} = 36\lambda$, the time of the snapshot is $t = 320fs$. It is seen as the filamentation of the laser pulse evolves sequentially through stages of strong fluctuations, cut I, ring and central filament, cut II, pure ring, cut III, to the single central filament eventually, cut IV. This beam contraction is attributed to the magnetic field that pinches the electron current; the light channels follow the currents, guided by the refractive index modified by the fast electrons. The axial currents amount to $\approx 0.5en_0c$ and generate peak magnetic fields between 50 - 100 MG. The corresponding quasistatic magnetic field having a good toroidal form at the beginning, cut I, becomes more and more elongated in the vertical direction, cut IV. This is due to the preferable electron scattering in the pulse polarization direction, that is vertical.

An important feature is plasma cavitation. It is seen in the ion density plotted in Fig. 3 for time $t = 500fs$. The expulsion of electrons from the

region of high beam intensity generates an electrostatic field which accelerates the ions in radial direction. We find ion energies up to 3 MeV in the simulation. An outgoing collisionless shock is observed. In the region of tightest focusing, the ion density on axis is almost zero. The cross-section of the ion channel is about circular. Such channel formation in plasma has been seen in 2D PIC simulations, see e.g. [7,8]; in 3D geometry, the effect becomes more prominent.

Both linear and circular polarization lead to single channel formation. Linear polarization has the effect that the distributions of J_x and $B_\perp^s$ at the positions of tight focusing are elongated in the direction of polarization. We find that the electrons are accelerated mainly in the plane of polarization in forward direction, but with a certain angular spread relative to the beam axis. Their distribution in energy resembles a thermal spectrum with a temperature between 3 - 5 MeV.
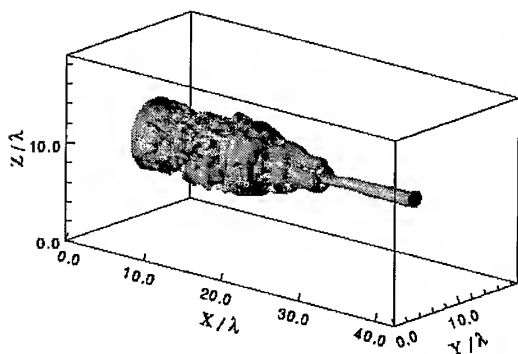
Fig. 1. Perspective view of the self-focusing pulse. The plotted surface corresponds to 0.67 $<I_{max}>$ in each (Y,Z) plane.
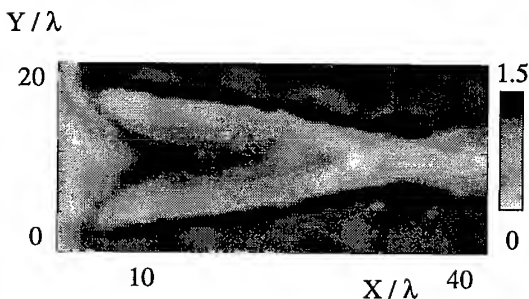
Fig. 3. Ion density n_i/n_0.
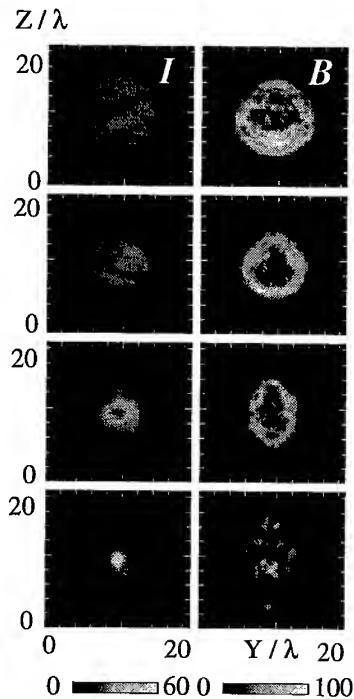
Fig. 2. Transverse cuts of intensity $I \times 10^{19}$, W/cm^2 (left column) and quasistatic magnetic field B, $MGauss$ (right column).

The results reported here call for experimental verification. The fast electrons emerging from the target in the direction of laser propagation and also the quasistatic magnetic fields of order 100 MG provide characteristic signatures to look for. The electrons are emitted into a certain angle in forward direction, for linearly polarized light in the plane of polarization and axially symmetric for circular polarization. Also, the simulations show that the B^s-field is frozen in the plasma and survives after the driving pulse has passed. We expect that it will decay due to collisions during some 100 ps and that it can be detected experimentally, e.g., by means of Faraday rotation.

In conclusion, we have presented the first three-dimensional PIC simulations of laser pulse propagation in near-critical plasma at relativistic intensities. The outstanding feature is the coalescence of magnetized light filaments into a single light channel with a diameter of 1-2 wavelengths due to magnetic interaction. In real 3D geometry, the light intensity on the axis is enhanced by more than one order of magnitude. Plasma cavitation is found along the channel. Hole boring into overdense plasma is a key feature for fast ignition of fuel targets in the context of inertial confinement fusion [1].

Acknowledgements

[*] E-mail: pukhov@mpq.mpg.de
1. M. Tabak *et al.*, Phys. Plasmas **1**, 1626 (1994).
2. C. E. Max, J. Arons, and A. B. Langdon, Phys.Rev. Lett. **33**, 209 (1974); G.Sun *et al.*, Phys. Fluids **30**, 526 (1987); P. Sprangle *et al.*, IEEE Trans. Plasma Sci. **PS-15**, 145 (1983); G.Schmidt and W. Horton, Comments Plasma Phys. & Contr. Fusion **9**, 85 (1985); A. B. Borisov *et al.*, Phys. Rev. **A45**, 5830 (1992).
3. A. B. Borisov *et al.*, Phys. Rev. Lett. **68**, 2309 (1992); P. Monot *et al.*, Phys. Rev. Lett. **74**, 2953 (1995).
4. A. B. Borisov *et al.*, Plasma Phys. Contr. Fusion, **37**, 569 (1995).
5. A. Pukhov and J. Meyer-ter-Vehn, Phys. Rev. Lett. **76**, 3975 (1996).
6. S. Bulanov, F. Pegoraro, and A. Pukhov, P. R. L. **74**, 710 (1995).
7. G. A. Askar'yan *et al.*, JETP Lett. **60**, 251 (1994).
8. S. C. Wilks *et al.*, Phys. Rev. Lett. **69**, 1383 (1992).
9. W. B. Mori *et al.*, Phys. Rev. Lett. **60**, 1298 (1988).

IRRADIANCE SCALING OF HARMONICS FROM SOLID TARGETS

M. ZEPF, M. CASTRO-COLIN, D. CHAMBERS, S.G. PRESTON, J.S. WARK,
J. ZHANG
Clarendon Laboratory, Department of Physics, University of Oxford, Oxford OX1 3PU,
UK

C.N. DANSON, D. NEELY, P.A. NORREYS
Rutherford Appleton Laboratory, Chilton, Didcot, Oxon OX11 0QX, UK

A. DYSON, A.E. DANGOR, P.LEE
Imperial College of Science, Technology and Medicine, London SW7 2AZ, UK

M. BAKAREZOS, P. LOUKAKOS, S. MOUSTAIZIS
IESL/FORTH, University of Crete, P.O. Box 1527, 711 10 Heraklion, Crete, Greece

A.P. FEWS
H.H. Wills Physics Laboratory, University of Bristol, Bristol BS8 1TL, UK

P. GIBBON
Max Plank Gesellschaft, Research Unit " X-ray Optics", University of Jena, Jena,
Germany

The scaling of conversion efficiency of harmonics created during the interaction of a 2.5 ps, 1053 nm laser pulse with a solid target has been recorded for irradiances up to $10^{19} Wcm^2 \mu m^2$. Extrapolation of the data suggests conversion efficiencies of 10^{-4} into the 100th harmonic might be attainable at irradiances $< 3 \; 10^{19} \; Wcm^{-2}\mu m^2$. The source brightness is estimated to be $10^{13} \; Wcm^{-2}sr^{-1}$ at 220 Å for $10^{19} \; Wcm^{-2}\mu m^2$, rivalling that of collisional XUV lasers.

There is currently great interest in the production of coherent XUV radiation by the process of XUV lasers and, more recently, high harmonic generation using high power picosecond laser radiation. Several groups have had considerable success in generating high odd-order harmonics from gases [1,2] , with harmonic wavelengths as short as 67 Å being observed [3]. The high harmonics are produced due to the extreme non-linearity of the atomic polarisability in the intense laser field, with the symmetric nature of the atomic potential dictating that only odd-order harmonics are observed.

In addition to harmonic generation from gaseous targets, there has recently been a renewal in interest in generating high order harmonic radiation from high-power laser interactions with solids [4-6]. Such high harmonics were first observed in nanosecond experiments using CO_2 lasers where harmonics up to the 46th order were observed. The long laser wavelength (10.6 μm) ensured significant ponderomotive steepening of the plasma density profile [7]. Both odd and even order harmonics are generated via the relativistic current associated with the electrons being dragged back-and-forth across this asymmetric density step. Recently Gibbon

601

has performed PIC-code simulations of laser-solid harmonic generation for sub-picosecond pulses [8] He concludes that for $I\lambda^2 > 10^{19}$ Wcm$^{-2}\mu$m^2 and modest shelf densities of $N_e/N_{critical} = 10$, up to 60 harmonics can be generated with power conversion efficiencies of 10^{-6} Importantly, Gibbon's simulations predict that the harmonic order is simply determined by $I\lambda^2$, thus short wavelength lasers should produce shorter absolute wavelengths for a given value of $I\lambda^2$.

These predictions have recently been investigated by several groups [5,6]. More recently the authors observed 75th harmonic from the 1.053 μm laser and reported very good agreement with PIC simulations (figure 1a) in the intensity range from 5 x 10^{17} Wcm^{-2} to 10^{19} Wcm^{-2} [9,10]. The conversion efficiencies into these high orders are greater than 10^{-6}, which compares well with other methods of generating coherent XUV emission [2].
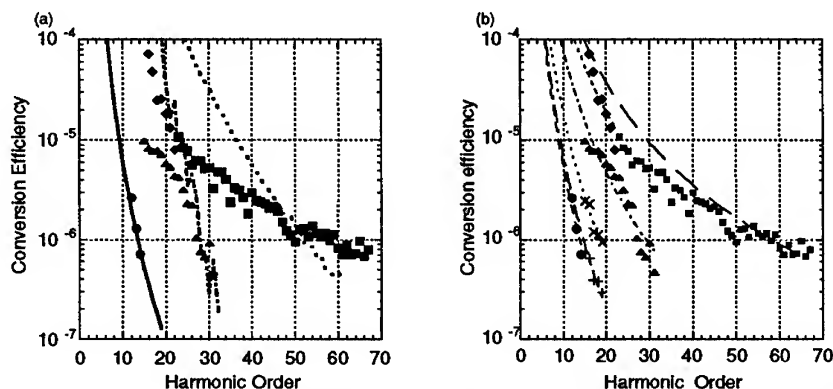
Figure 1 Conversion efficiencies (assuming isotropic emission) against harmonic order for various irradiances. squares 10^{19} Wcm$^{-2}\mu$m^2; diamonds 6.3 10^{18}Wcm$^{-2}\mu$m^2; triangles 5.5 10^{18}Wcm$^{-2}\mu$m^2; diagonal crosses 3 10^{18}Wcm$^{-2}\mu$m^2; horizontal crosses 2.5 10^{18}Wcm$^{-2}\mu$m^2 and circles 4.7 10^{17}Wcm$^{-2}\mu$m^2. Curve fits are (a) theoretical calculations of the absolute conversion efficiency for 5 10^{17}Wcm$^{-2}\mu$m^2(solid line), 5 10^{18} Wcm$^{-2}\mu$m^2 (dot-dashed line) and 10^{19}Wcm$^{-2}\mu$m^2 (dotted line) and (b) best power law fits from equation (1).

The experimental results reported here are from experiments carried out at the VULCAN laser facility at the Rutherford Appleton Laboratory [11]. The laser produced pulses of 2.5 ps duration and energies of around 20 J on target. The contrast of the laser pulse was measured to be better than 10^{-6}:1 . A single shot autocorrelator measured the pulse length for each shot. The laser was focused onto the target by an f/4.2 off-axis parabolic mirror and the targets were optically polished glass slabs with a CH overcoat.

As can be seen in figure 1b the conversion efficiency increases strongly with increasing irradiance. A simple scaling law was proposed [9] to fit the observed conversion efficiency into higher orders (12th- 68th) observed experimentally;

$$E_{Harmonic} = E_{Laser} \left(\frac{\omega_{Harmonic}}{\omega_{Laser}} \right)^{-x} \tag{1}$$

and are shown as fits to the experimental data in figure 1b.

So far no numerical calculations or experimental data has been published investigating the scaling of the conversion efficiency of harmonics from solid targets at irradiances above 10^{19} Wcm$^{-2}\mu$m^2. Figure 2 shows the dependence of the fitting coefficient x from equation (1) on irradiance. The trend in the data available suggests that using higher irradiances could lead to even higher conversion efficiencies for high order harmonics. The two line fits in figure 2 are extrapolations of the experimental data and show that very high conversion efficiencies can be expected using irradiances of > 10^{19}Wcm$^{-2}\mu$m^2. The upper curve has been chosen to converge to x=2, the lower curve to x=0, which corresponds to the asymptotic limits predicted by an extremely simple electron-trajectory model in the non-relativistic and relativistic regimes respectively. This simple model neglects the effects of saturation and space charge. A value of x=2 would correspond to a conversion efficiency of 10^{-4} for the 100th harmonic which has a wavelength of 100 Å for 1μm laser and 24.8 Å for a KrF laser. Modelling is currently under way to ascertain the high intensity limit of the electron trajectories in order to provide an upper bound on the possible conversion efficiency.
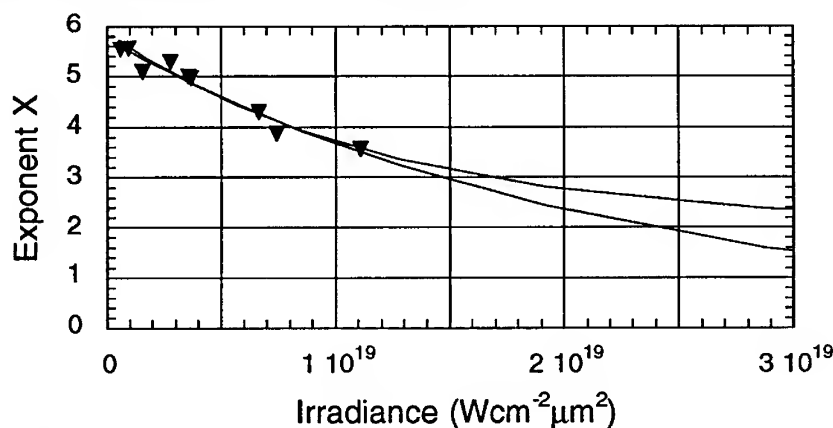
Figure 2 Dependence of the fitting parameter x from equation (1) on irradiance. The two curve fits are extrapolations using an exponential fit to the data. The upper fit converges to x=2, the lower to x=0.

The harmonic emission was observed to have a significantly larger angular distribution than the cone angle of the laser beam. XUV harmonics were observed over an angle of 31.5° with no observable change in intensity. For this measurement the target was rotated while the spectrometer and the laser remained fixed. This observation was confirmed by a single shot measurement of the angular distribution

604

of the third harmonic which was found to be constant over 103°. The source size for the 45th - 50th harmonics was measured to be $< 6\mu m^2$ [12] (this was the resolution limit) at full width half maximum using an XUV imaging system. It is therefore possible to place a lower bound of $10^{13} Wcm^{-2}sr^{-1}$ on the brightness of the source at 10^{19} $Wcm^{-2}\mu m^2$.

It is worth mentioning at this point that the angular distribution is probably very sensitive to the exact nature of the interaction, particularly the pre-pulse levels of the interaction pulse. Intuitively one would expect the harmonic radiation to be contained in the cone angle of the incident laser beam in the specular direction, because the component of the wavevector parallel to the critical density surface should be conserved. A possible explanation for this discrepancy is the Rayleigh Taylor like critical surface rippling predicted by the PIC simulations of Wilks *et al.*[13]. This interpretation is corroborated by the invariance of the conversion efficiency relative to s and p polarisation. This is contrary to theoretical predictions, but can be understood if the interaction surface is assumed to be random, making the definition of a surface orientation, and subsequently a specular angle, impossible. This problem could be overcome by the use of pre-pulse free lasers, leading to a narrower angular distribution and a significantly higher brightness.

In conclusion we have shown that harmonics generated from solid targets are a very promising new source of short pulse, coherent XUV radiation. The scaling law presented in this publication suggests that it should be possible to produce XUV radiation very efficiently and with a brightness similar to that of an XUV laser.

Acknowledgements

References

1. A. L'Huillier *et al.*,Phys. Rev. Lett. **66**, 2200 (1991).
2. T. Ditmire *et al.*, Phys. Rev A. **51**, R902 (1995).
3. S.G. Preston *et al.*, Phys. Rev A. **53**, 31 (1996).
4. S.C. Wilks *et al.*, IEEE Trans. Plasma Sci. **21**, 120 (1993).
5. S. Kohlweyer *et al.*, Opt. Comm. **117**, 431 (1995).
6. D. von der Linde *et al.*, Phys. Rev. A. **52**, R25 (1995).
7. R.L. Carman *et al.*, Phys. Rev. Lett. **46**, 29 (1981).
8. P. Gibbon, Phys. Rev. Lett. **76**, 50 (1996).
9. P.A. Norreys *et al.*, Phys. Rev. Lett **76**, 1832 (1996).
10. J. Zhang *et al.*, Phys. Rev. A. (accepted, to be published July 1996).
11. C.N. Danson *et al.*, Optics Comm. **103**, 392 (1993).
12. D.Chambers *et al.*, to be published.
13. S.C. Wilks *et al.*, Phys. Rev. Lett. **69**,1383 (1992).

a-Si:H THIN FILM PATTERNING BY GREEN FREQUENCY-DOUBLED Nd-YLF LASER IN PHOTOVOLTAIC MODULES FABRICATION

S. AVAGLIANO, M.L. ADDONIZIO, E. TERZINI
ENEA - Centro Ricerche, Via del Vecchio Macello, I - 80055 Portici, Napoli, Italy.

Thin films of a-Si:H and a-Si:H/metal deposited on SnO2/glass substrate have been patterned by a Q-switched diode-pumped, frequency-doubled Nd-YLF laser.
A more effective a-Si:H removal, due to laser induced stress detachment associated to the pressure of the evolving vapour, has been observed. a-Si:H/metal removal is only obtained when a compact and strongly adhesive metal is deposited on semiconductor film. To minimize the debris falling back and film re-deposition (self-ablation), a free evolution and removal of the laser plume are required. No laser induced crystallization of amorphous film has been evidenced.

1.0 Introduction

The laser scribing process is a key technology for the high performance hydrogenated amorphous silicon (a-Si:H) integrated modules fabrication [1].

Currently, the photovoltaic device consists of a multilayer thin film structure: TCO/p(a-SiC:B)-i(a-Si:H)-n(a-Si:P)/Metal deposited on glass. For series connected single and/or tandem modules, three laser scribing steps are needed: the transparent conductor oxide (TCO) [2], the active pin-a-Si:H cell and back metal scribes. The selective removal of each layer is quite difficult due to their conflicting optical and thermal properties.

The back-contact (Ag, ZnO, Al based multilayers) is the most crucial laser patterning step [1] which, if incorrectly performed, affects the modules performance by shunt creation between front and back contacts. Shunt effect is much more critical for the pin/pin tandem cells due to their higher open-circuit voltage.

We have analyzed the scribe quality as a function of the beam-material interaction effects (laser debris, vapour plume, a:Si crystallisation) and of the structural/mechanical properties of the back-metal. Countermeasures to avoid undesired effects are reported.

2.0 Experimental

Thin film layers, deposited on TCO [3], have been scribed by a green light (λ=523 nm) emitted by an AO Q-switched Nd-YLF laser equipped with Second Harmonic Generator (SHG) and operating in TEMoo mode. All the scribes have been done with the beam passing through the glass (back-scribing) [2] moving on a x-y motorized stage (fig.1).

The laser is pumped by two diode laser arrays with emission wavelength selected and
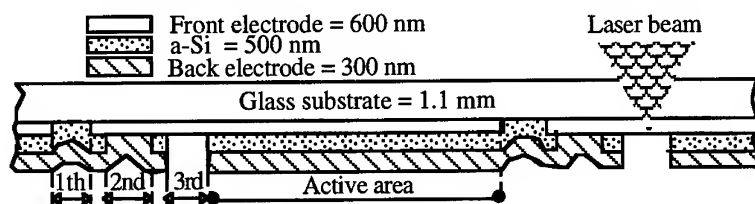
Fig.1 Back-scribing schematic picture with enlarged sectional views of the electrode coupling region.

temperature tuned (shift is about 0.3 nm/°C) to match an absorption band of Nd-YLF crystal around 800 nm. SHG crystal is outside the resonator between the output mirror and the beam-expander. Fig.2 reports the measured laser characteristics.

Optical and scanning electron microscopy (SEM), electron probe microanalysis (EPMA), X-ray and Tencor profilometer have been utilized for morphological, compositional, structural and dimensional analysis of the scribed regions.
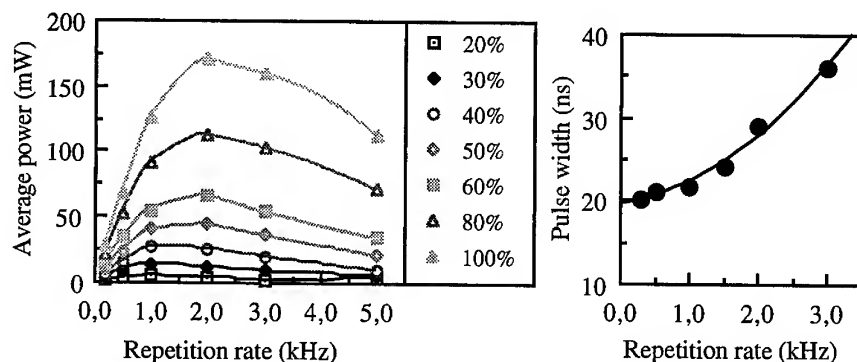
Fig.1 Average laser power (at different diode pumping power) and pulse width versus Q-switch frequency.

3.0 Results and Discussion

The high a-Si:H absorption coefficient ($\approx 10^5$ cm^{-1}) and its low reflectivity ($\approx 25\%$) at 523 nm, allows a good laser-beam/material coupling. In addition the low melting temperature (≈ 1000 °C) and the low thermal diffusivity (≈ 0.1 cm^2/s) [4] don't require high irradiance and limit the heat dispersion. The low values of both optical absorption depth (few tens of nanometer) and the heat diffusion length (≈ 900 nm) limit in a narrow zone the laser induced processes. The low absorption/diffusion length ratio results in a superficial heat generation (surface heating). Furthermore a-Si:H has a non-direct energy gap of about 1.75 eV. At laser photon energy of 2.37 eV there is, however, an interband direct transition, which does not require phonon assistance to occur. Consequently we expect a negligible temperature dependence of laser radiation absorption process.

Two series of scribing results on a-Si:H are summarized in the fig 3. In each series,
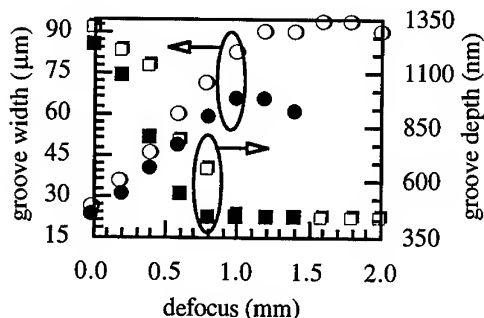
Fig.3 Grooves width and depth versus defocus distance (lens focal point-working plane relative position) at 14 mW (■, ●) and 28 mW (□, O) of average laser power (1 kHz, 50 mm/s). For each power it is possible to get good quality grooves (high selectivity and no swelling) having different widths. The TCO, substantially transparent at laser wavelength, can show an heat affected zone only near the focus region ($\approx 10^8$W/cm^2) due to heat transfer from a-Si.

the groove width increases with the defocus up to a maximum, which shifts toward larger defocus values when higher powers are used. At higher defocus the power density decreases causing a reduction of groove width with a defective material removal.

The fig.4 evidences sharp edges and "mechanic-like" cracks around the groove with no presence of melted-resolidified and built-up matter. The shape groove and the short interaction-time (21 ns) allow to infer that the a-Si removal mechanism is due to laser induced stress detachment associated to the a-Si evolving vapour and related pressure. The absorbed light leads, starting from the groove centre, the material in a vapour status, while the film backside is still in the solid state (surface evaporation). The associated vapour pressure produces the blow-up of the remaining material in form of large particles within a circular zone which is larger than that where the vaporization occurs.

Fig. 4 Optical microscope image of a-Si scribe.

Fig. 5 SEM image of an a-Si/Ag/Al film unremoval.

SEM observation of the groove walls and X-ray diffraction performed on 2×1 cm^2 sample area containing more than 50 scribe lines 20 μm apart, didn't evidence micro-crystalline silicon. The best results have been obtained with laser power density sets at minimum value ($\approx 4 \times 10^7$W/cm^2), that involve the absence of laser induced plasma (regime of normal evaporation) and small volumes of laser-plume.

The 3rd scribing step removes the back contact and the underlying a-Si:H jointly. Large longitudinal metal fractures (due to the tangential stress twice higher than axial stress), see fig.5, have been observed when very soft metal covers the structure. The vapour escapes from this fracture line and doesn't produce the material removal. All the attempts to obtain a completly open groove, without bridge creation between adjacent cells, failed when evaporated Ag was used as back-contact. A complete removal has been obtained when the sputtering conditions for a compact and strongly adhesive metal and/or ZnO/metal have been selected. Then we conclude that the quality of this scribing step depends on the structural/mechanical properties of the back contact.
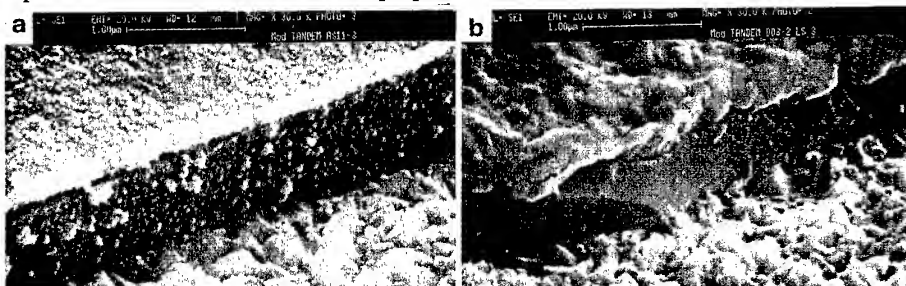
Fig. 6 (a) The condensing vapour plume shunting the cell. (b) A clean scribe with a-Si unaffected.

608

In the fig.6a it can be seen that the condensing laser plume together with droplets of sub micrometer size uniformly cover the groove. Fig.6b shows a clean scribe obtained in the same operating conditions but allowing the vapour-plume free evolution and enhancing its removal by using a vacuum suction apparatus.

However tongues of material sticking on the scribe wall (electrical shunting paths), see fig.7, can be still found even in the optimized scribing conditions. They are due to the laser near-gaussian intensity profile and to the back contact high thermal diffusivity. The lower temperature reached on the groove edges only produces the metal softening and a stretching phenomenon verifies during the a-Si/Me detachment.
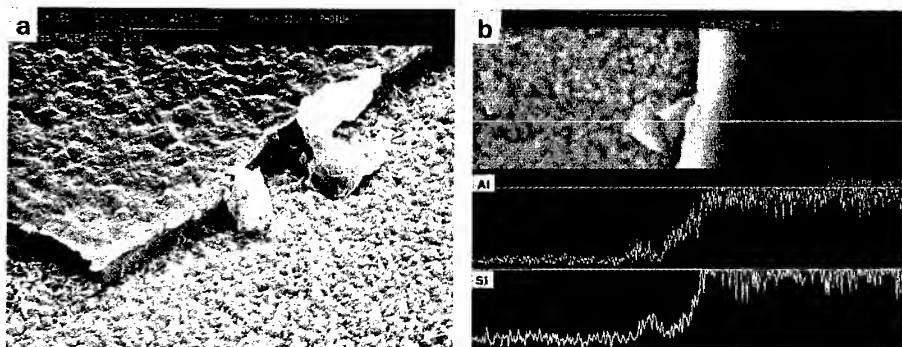
Fig. 7 (a) Tongues of Si/metal negatively affect the grooves quality. (b) Compositional profile of the material tongue. The line scan profile shows the presence of Al and Si.

4.0 Conclusions

The knowledge of the laser-induced physical phenomena leads to an improvement of the laser scribing technology with an enhancement on the a-Si modules performance.

The free evolution and removal of the laser plume has been indicated as a fundamental point for quality scribing. The lowest power density for groove formation has to be used to avoid debris falling. Shunts creation has to be ascribed to structural/mechanical properties of the back electrode and to a-Si/Metal material tongues, while no crystallisation has been observed on the groove walls. Modules with efficiency of 8.5 % on 900 cm^2 area have been realized after cutting down the shunts occurrence.

Efficiency can be still improved by: 1) shaping and homogenizing the beam as a "flat-top" intensity profile that produces an uniform removal with high edge definition; 2) modifying the flow fabrication process with the substitution of the 2nd laser scribing with a step of laser welding. This allows the metal deposition after the junction realization avoiding extra-handling and hence shunts due to both airborne and laser debris.

References

[1] Y. Ichikawa et al., Proc. 11th E.C. PVSEC, Montreaux (1992), 203.
[2] S. Avagliano et al., Proc. 12th E.C.PVSEC, Amsterdam (1994), 1218.
[3] E. Terzini et al., a-Si Symposium MRS, S. Francisco (1996) to be published.
[4] S. Kiyama et al., JJSPE, 56-8 (1990), 1500

HARMONIC EMISSION FROM SHORT-PULSE LASER INTERACTIONS WITH OVERDENSE PLASMA TARGETS

T. J. M. BOYD and R. ONDARZA R.[†]

Physics Department, University of Essex,
Wivenhoe Park, Colchester CO4 3SQ, UK.

The generation of harmonic orders emitted by reflection from the interaction of p-polarized light waves with an overdense plasma characterized by a steep density gradient is analysed. The electron dynamics is described by linearizing the relativistic cold fluid equations and by expressing the density perturbation at the plasma-vacuum interface in terms of the radiation field. A perturbation procedure is then adopted to solve the wave equation within a skin depth into the plasma. Particle-in-cell simulations have been carried out to test the model used. In the simulations ions were treated as an ambient neutralizing immobile background. It is shown that the power emitted for the third harmonic scales as $a_0^4 (\omega_0/\omega_p)^2$ where a_0 represents the normalized amplitude of the radiation field and ω_0 and ω_p are the laser and plasma frequency respectively. The emission exhibits a distinct resonance at densities four times critical. For the fifth harmonic two resonances are predicted by the theoretical model and confirmed by simulations. Scalings for the conversion power efficiencies for the different harmonic orders as a function of the intensity and the wavelength of the laser have also been obtained from the simulations.

1 Introduction

Experiments on the interaction of high intensity laser light with dense plasma targets have led to renewed interest in the generation of high harmonics of the frequency of the incident light. Strong harmonic production from target plasmas was first reported by Carman *et al.* [1] with up to 46 harmonics detected from targets irradiated by $10.6\,\mu m$ light. This emission was attributed to nonlinear resonant absorption with the plasma wave coupling to the radiation field in the steep density gradient and generating harmonics. The highest harmonic was consequently interpreted as corresponding to the upper shelf density of the steepened profile. The natural cut-off implied by this mechanism appeared to be borne out by PIC simulations though these numerical experiments suffered from relatively poor space and time resolution making it difficult to resolve harmonics above the first 10 or so.

Recent PIC simulations by Gibbon [2] at higher irradiances and with shelf densities no more than $10\,n_c$ where n_c is the critical density show no evidence of a cut-off, with about 68 harmonics detected. A number of experiments has confirmed harmonic generation from the interaction of intense laser pulses of

duration some hundreds of femtoseconds to a few picoseconds with solid targets [3,4]. The first of these reported harmonics up to the 7th from Al targets irradiated at intensities of $10^{17}\,W\,cm^{-2}$ while the second recorded harmonics up to the 68th from experiments at intensities up to $10^{19}\,W\,cm^{-2}$.

The work described here does not address harmonic generation at such high intensities and the analysis carried out corresponds more closely to that of the experiments of Kohlweyer *et al.* [3]. The electron response to the fields of the light wave is mildly relativistic rather than ultrarelativistic. The model is further restricted to light incident normal to the plasma surface and on a plasma with a density ranging from moderately to highly overdense. For normal incidence the form of the source in the wave equation is such that only odd harmonics are present in the spectrum. The electron dynamics is described by the relativistic cold fluid equations and a perturbation analysis leads to expressions for the power radiated in the 3rd and 5th harmonics. The results obtained are compared with 1D particle-in-cell simulations with immobile ions. Scaling of the conversion efficiencies for harmonic orders up to the 11th as a function of intensity has been found from the simulations. Third harmonic generation produced by reflection of light waves normally incident on overdense plasmas has been studied by Wilks *et al.* [5] who calculated the third power conversion efficiency, discussed below.

2 Formulation of the problem

The full set of relativistic fluid equations that describe the interaction of an electromagnetic plane wave with a nonthermal plasma, with ions considered as a neutralizing immobile background is given by

$$\frac{\partial n}{\partial t} + \frac{\partial (n\,v_z)}{\partial z} = 0$$
$$\frac{\partial p_z}{\partial t} = e\,\frac{\partial \phi}{\partial z} - m_0\,c^2\frac{\partial \gamma}{\partial z} \qquad (1)$$
$$\Box^2\,a_\perp = k_p^2\,\frac{n}{n_0}\,\frac{a_\perp}{\gamma}$$

where $k_p = w_p/c$ and $\gamma = \sqrt{1 + a_\perp^2}$. The electron plasma frequency is w_p , m_0 is the electron rest mass, n_0 is the ambient ion background density and $a_\perp$ is the normalized amplitude of the external radiation field.

In order to obtain the power emitted for each harmonic of the incident light wave we decompose the vector potential as a sum $a_\perp = a_0 + \epsilon\,a_3 + \epsilon^2\,a_5 + O\left(\epsilon^3\right)$ where a_0 represents the fundamental wave and a_3 and a_5 the third and the fifth harmonics respectively; ϵ is a measure of the strength of each mode and

is used as a formal perturbation expansion parameter. Introducing this form for $a_\perp$ in the last equation of (1) and separating the different orders we obtain

$$
\begin{aligned}
\left(\Box^2 - k_p^2\right) a_0 &= 0 \\
\left(\Box^2 - k_p^2\right) a_3 &= k_p^2 \left(\frac{\delta n}{n_0} a_0 - \frac{1}{2} a_0^3\right) \\
\left(\Box^2 - k_p^2\right) a_5 &= k_p^2 \left\{\frac{3}{2} a_0^2 \left(\frac{a_0^3}{4} - a_3\right) + \frac{\delta n}{n_0}\left(a_3 - \frac{a_0^3}{2}\right)\right\}
\end{aligned}
\tag{2}
$$

where the density deviations from the equilibrium configuration has been expressed as $n = n_0 + \epsilon\,\delta n$. To close the last system of equations it is necessary to express the electron density in terms of the vector potential. By doing so, we linearize the continuity equation and neglect variations of n_0. We choose the solution to the first equation in (2) as $a = a_0\, e^{-z/\delta}\cos(\omega_0 t)$, where $\delta^2 = c^2/(\omega_p^2 - \omega_0^2)$ is the skin depth in the plasma and $\omega_p > \omega_0$. Introducing the electron density at first approximation into the expression for a_3 we have

$$
\left(\Box^2 - \frac{\omega_p^2}{c^2}\right) a_3 = \frac{\omega_p^2}{c^2} a_0^3\, e^{-3\,z/\delta}\,\cos\psi\left\{\left(1 - \alpha^2\right)\left(1 + \frac{\cos 2\psi}{1 - 4\,\alpha^2}\right) - \frac{\cos^2\psi}{2}\right\}
\tag{3}
$$

where $\alpha = \omega_0/\omega_p$ and $\psi = \omega_0 t$. We solve (3) by means of a Bogoliubov-Krylov procedure [6] and substitute for $a_0 \to 2\,(\omega_0/\omega_p)\,a_0$, in keeping with anomalous skin effect theory [7,8] to arrive at the final expressions that give the ratio of the power of the third and fifth harmonics to the fundamental

$$
\frac{P_3}{P_1} = \left(\frac{9}{8}\right)^2 a_0^4 \left(\frac{\omega_0}{\omega_p}\right)^2 \frac{1}{\left(1 - 4\frac{\omega_0^2}{\omega_p^2}\right)^2}
\tag{4}
$$

For the third harmonic a fourth power scaling for (ω_0/ω_p) has been found by Wilks $et\ al.$ [5] for the case when $(a_0\,\omega_0/\omega_p) \ll 1$. Figure 1a,b shows the conversion efficiencies for the reflected third and fifth harmonic light waves and are compared with expressions (4) and (5).

$$
\begin{aligned}
\frac{P_5}{P_1} &= \left(\frac{5}{12}\right)^2 \left(\frac{\omega_0}{\omega_p}\right)^8 a_0^8 \left[\frac{3}{8} + \frac{1}{(4\,\alpha^2 - 1)}\left\{\left(\frac{\omega_p}{\omega_0}\right)^2 \frac{(3 + 24\,\alpha^2)}{32\,(4\,\alpha^2 - 1)} + \right.\right. \\
&\quad \left.\left. + \left(1 - \alpha^2\right) + \frac{27}{16}\left(\frac{\omega_p}{\omega_0}\right)^2 \frac{(1 - \alpha^2)}{(16\,\alpha^2 - 1)}\right\}\right]
\end{aligned}
\tag{5}
$$
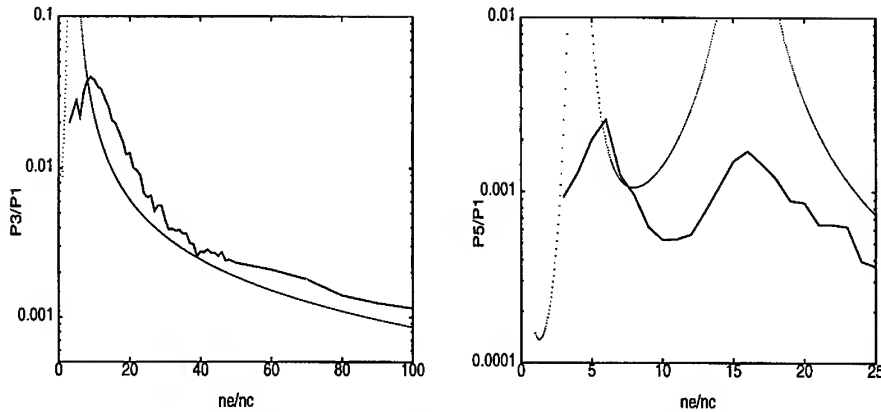
Figure 1: *Power of the third and fifth harmonics as a function of the electron plasma density,* $\lambda = 0.248\,\mu m, T_e = 1\,keV, a_0 = 0.5.$ *Solid lines for a) third harmonic and b) fifth harmonic, dotted lines for the analytical approximation.*

3 Conclusion

The analysis presented here shows that emission at the third harmonic reflected from an overdense plasma is proportional to $a_0^4 \left(\omega_0/\omega_p\right)^2$ for mildly relativistic laser-solid interactions and exhibits a resonance at a density $4\,n_c$. Fifth harmonic emission also shows a resonance at this density and a further resonance at $16\,n_c$. With any perturbation expansion, confidence in the result diminishes as the order rises and we have not analysed P_7/P_1 but simulations show the pattern of resonant density emission persisting, with the number of resonances increasing with order.

Acknowledgements

References

[1] R. L. Carman, C. K. Rhodes, and R. F. Benjamin, *Phys. Rev. A* **24**, *2649 (1981)*.
[2] P. Gibbon, *Phys. Rev. Lett.* **76**, *50 (1996)*.
[3] S. Kohlweyer *et al.*, *Optics Comm.* **117**, *431 (1995)*.
[4] P. A. Norreys *et al.*, *Phys. Rev. Lett.* **76**, *1832 (1996)*.
[5] S. C. Wilks, W. L. Kruer, and W. B. Mori, *IEEE Trans. on Plasma Sci.* **21**, *120 (1993)*.
[6] N. Krylov and N. Bogoliubov, *Int. to Nonlin. Mech., Princeton Univ. Press, N. J. (1947)*.
[7] W. Rozmus and V. T. Tikhonchuk, *Phys. Rev. A* **42**, *7401 (1990)*.
[8] E. G. Gamaliy and R. Dragila, *Phys. Rev. A* **42**, *929 (1990)*.

MAXIMUM ION ENERGY AND HOT ELECTRON TEMPERATURE MEASUREMENTS FOR PICOSECOND SOLID TARGET INTERACTIONS BETWEEN 10^{17} Wcm^{-2} AND 10^{19} Wcm^{-2}

P.A.NORREYS and C.N.DANSON
Central Laser Facility, Rutherford Appleton Laboratory, Chilton, Didcot, Oxon
OX11 0QX, United Kingdom.

A.P.FEWS,
H.H.Wills Phsyics Laboratory, University of Bristol, Tyndall Ave, Bristol, Untied
Kingdom.

F.N.BEG, A.R.BELL, A.E.DANGOR, , P.LEE, and M.TATARAKIS
Imperial College of Science, Technology & Medicine, Prince Consort Road,
London SW7 2AZ, United Kingdom

M.E.GLINSKY and B.A.HAMMEL.
Lawrence Livermore National Laboratory, Livermore, California, United States of
America

The maximum ion energy associated with the isothermal plasma expansion in high intensity 1053nm picosecond laser pulse interactions with solids has been measured by CR-39 ion detectors. The hot electron temperatures have been measured by K alpha x-ray spectroscopy.

We report here on a series of experiments that were conducted on the CPA beam line of Nd:glass laser VULCAN. The laser operates at a wavelength of 1053nm or 1054nm. It delivers upto 25J onto target with pulse durations in the range 700 fsec - 2.5 psec. The targets, placed at 30 degrees to the target normal, consisted of massive glass slabs overcoated with plastic(CH) and Cu or CH 'lollipop' targets of 270 or 540 μm diameter. An f/4.2 off axis parabola focused the radiation onto target. The contrast ratio was measured to be 10^{-6}. Energy pinhole transmission measurements indicate a x3.5 diffraction limited focal spot.

The energetic ion emission (associated with the fast electron driven isothermal plasma expansion) was recorded by CR-39 plastic nuclear track detectors. CR-39 records charged nuclear particles as tracks which are etched into the surface of the detector after exposure. A separate etch track is produced by each incident ion and the dimensions and depth of penetration of the track enables the energy and atomic number of the ions to be uniquely determined. CR-39 detectors are sensitive to ions with energies $\geq$ 100 keV/nucleon. The detectors were covered in an array of upto

12 Mylar filters which increased in thickness by 2.5 μm and 8 steps of Al of thickness   25 μm. Each step is sensitive to a different energy interval, giving an energy resolution of 0.1MeV in the range 0.1 - 6.0 MeV. In addition, a aluminium wedge of thickness 0.20mm at one end and 1.1 mm at the other was used to measure ions with energies upto 14MeV. In all shots, one piece of CR-39 was placed in the normal incidence direction, either on the chamber wall at a distance of 55cm or at the end of an extension tube 2.5m from the chamber centre.

The energetic ion emission associated with the fast electron driven plasma expansion were predominantly from protons. The ion spectra in most of the shots show an exponential decreasing profile with increasing ion energy, followed by a sharp cut-off.   This can be attributed to charge separation which   limits the ion velocities by forming a non-neutral electrostatic sheath which truncates the exponential density profile.
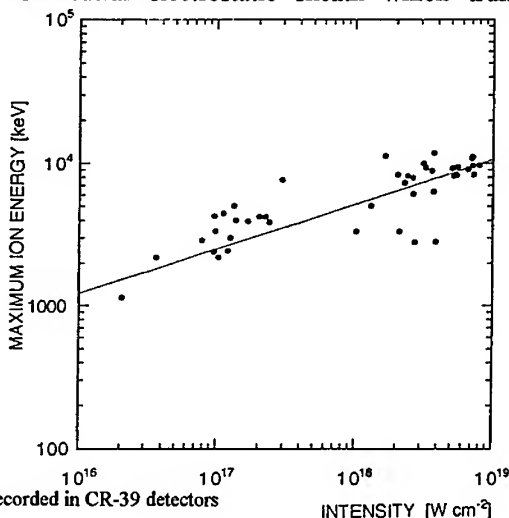
Figure 1. Maximum ion energies recorded in CR-39 detectors

Figure 1 shows the maximum ion energies plotted against incident irradiance. These scale as:

$$E_{max} = 1.2(\pm 0.3) \times 10^{-2} I^{0.313 \pm 0.03} keV$$

This scaling is in quantitative agreement with that reported by Tan, McCall and Williams [1] for longer pulse duration high irradiance experiments, who proved that the maximum ion energies were proportional to the hot electron temperature.

The characteristic temperature of the energetic electrons that generated in the interaction can be characterised by measuring the K_α x-ray emission that the energetic electrons induce when they pass through multi-layer targets.

Measurement of the relative K_α x-ray fluorescent emission from two or more layers can yield an estimate of the number and energy of the electrons, taking into account: (a) electron energy loss in the materials, (b) K shell ionisation cross sections, (c) the number of K_α photons produced by an electron of a particular energy (d) the x-ray mass absorption coefficients of the materials in the target [2].

The targets consisted of: 25μm Pd on 72μm Sn, 47μm Pd on 72μm Sn, 25μm Mo on 25μm Sn and 12μm Mo on 25 μm Sn with the laser irradiating the Pd or Mo side of the metallic sandwich targets. These medium Z materials were chosen so that the number and energy of the photons detected from each layer lay within the dynamic range of the instrument, and the K shell binding energies were high enough to minimise K_α fluorescence induced from the plasma x-ray emission but were not above the usable range of the detector.

A 16-bit x-ray CCD (Reticon RA1024J with 10^6 13.5μm×13.5μm pixels with 4.5μm thick depletion layer) was used for obtaining the x-ray spectra. The CCD was used in a single hit mode, i.e. where the collection efficiency of the CCD is chosen such that the probability that two photons interacting with one pixel is small. In this mode the value V_p read out from each pixel is directly proportional to the energy of the x-ray photon E_p. After the CCD is exposed, an image, composed of multiple single hits, is captured and stored on a computer. A histogram is then constructed of the number of hits against V_p and, to a first approximation, this histogram gives the x-ray spectrum.

To obtain an estimate of the number and energy of the electrons, K shell ionisation cross sections given by

$$s_k = 7.92 \times 10^{-14} \frac{\ln(U_k)}{E_k^2 U_k} \quad cm^2$$

(U_k is the ratio of the electron energy E to the K shell binding energy E_k) which used Spencer's fast electron energy deposition model for electron traversing cold material, x-ray mass absorption coefficients and Krause's data on the number of K_α photons produced for a given electron energy. The targets were modelled as a series of thin planar targets. An electron at energy E_o is propagated through the targets and the total K_α emission is calculated for the detector placed at an angle 35 degrees to the target normal. The response function of the detector is the probability that a photon interacts with a pixel and this can be obtained from the mass absorption co-efficients of silicon with the thicknesses of the dead and the depletion layers in the CCD chip together with the transmission of the 100 μm thick In filter. The detector was calibrated using a 4.1 mCi Cd source for a 180 second exposure. This source decays to Ag by electron capture and the silver emits K shell radiation in the ratio 83.4% at 22 keV and 16.4% at 25 keV. The detector energy

response function was found to be linear with $E_p = 0.0818(v_p -3.01)$ keV for photon energies between 17.5 keV $< E_p <$ 28.5 keV.

Figure 2(a) shows a plot of the calculated ratio of the number of the K_α photons from the first and second layers plotted against electron temperature (i.e. the electrons have a Maxwellian distribution) and the experimentally determined ratios for the different sandwich target materials irradiated. The experimental points lie within the range 70 - 200 keV. Figure 2(b) shows the electron tempearture plotted against incident laser energy. Using the nominal x3.5 diffraction limited operation of the VULCAN laser, this puts the intensity on target in the range 1.1×10^{18} - 7.0×10^{18} Wcm^{-2}. However, the maximum ion energies for these shots were, on average, lower than the scaling established in figure 1, and suggesting that the intensities on target were in the range 1×10^{17}Wcm^{-2} - 6×10^{17} Wcm^{-2}.

(a)   (b)
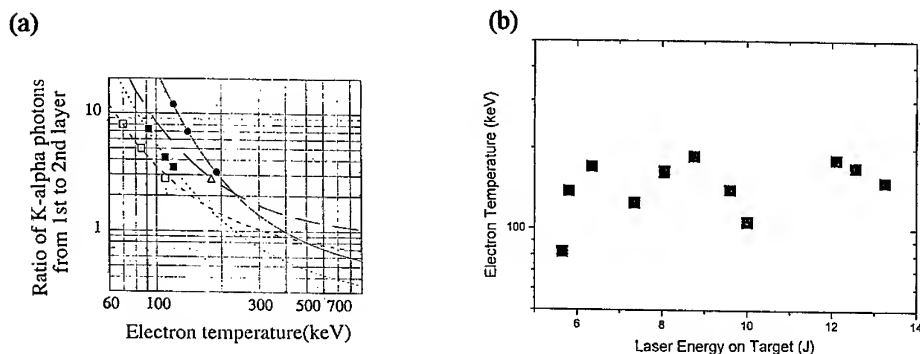
Figure 2(a) ratio of K alpha signals recorded in the two metallic layers and (b) the electron temperature plotted against incident laser energy.

These two sets of measurements are consistent either with a profile-steepened resonance absorption process where the hot electron temperature T_{hot} scales as $T_{hot} \propto (I\lambda^2)^{1/3}$ [4], or where the electron temperature is of the order of the ponderomotive potential and $T_{hot} \propto (I\lambda^2)^{1/2}$ [5]. The data certainly rule out models which predict $T_{hot} \propto (I\lambda^2)^{1.0}$ scalings.

[1] T.H.Tan, G.H.McCall and A.H.Williams. Phys. Fluids 27, 296 (1984).

[2] P.Lee.   PhD thesis, University of London (1996).

[3] B.Luther-Davies, A.Perry and K.A.Nugent Phys Rev A 35, 4306 (1987).

[4] D.W.Forslund, W.Kindel, K.Lee, E.I.Lindman and R.L.Morse. Phys. Rev. A 11, 679 (1976).

[5]. S.C.Wilks Phys. Fluids B 5, 2603 (1993).

SPECTRAL MODIFICATION IN ULTRA-SHORT PULSES INDUCED BY IONIZATION FRONTS AND RELATIVISTIC PLASMA WAVES

A. BENDIB[*+], A. TAHRAOUI[*], K. KALACHE[*+]

*Laboratoire de Physique des Milieux Ionisés, Institut de Physique, U. S. T. H. B., El Alia, Bab Ezzouar, BP 32, Alger, Algerie.

+Laboratoire de l'Interaction Laser - Matière, C. D. T. A., BP 1017, Algérie.

◆Département des Sciences Fondamentales, E. N. P., BP 182, El Harrach, Algérie.

P. CHESSA and P. MORA

Centre de Physique Théorique, Ecole Polytechnique,91128 Palaiseau,Cedex France.

The weak spectral modification in short-pulses due to the field-induced ionization and relativistic plasma wake fields has been studied under the 1D approximation. Analytic models and a more quantitative simulation are presented. It has been shown that the laser spectrum is blueshifted for moderate laser intensities ($<10^{16}$ W/cm^2) and redshifted for ultra-high laser intensities($>10^{17}$ W/cm^2). The model results are shown to be in very good agreement with the numerical simulations.

I. INTRODUCTION

This work deals which several aspects of spectral modification in ultra-short pulses ($\tau_L \leq 1$ps, $I \sim 10^{18}$ W/cm^2) by ionization front and plasma waves. For moderate laser intensities ($\leq 10^{16}$ W/cm^2) and low gas pressures (~ 1 atm), tunnelling ionization of atoms, may occur. It can cause a rapid increase in the electron density, which results in a spectral modification of the laser pulse. On the other hand, for very high laser pulse intensities ($> 10^{17}$ W/cm^2), the field-induced ionization is no longer efficient. Nevertheless, for such ultra-intense laser pulses, the ponderomotive and relativistic effects may drive an intense electron wakefield wich may modify the spectral properties of the laser pulse.

II. SPECTRAL MODIFICATION DUE TO THE IONIZATION FRONT

A. Analytic model

We use the 1D-Vlasov equation for electron with an additional source term

$$\frac{\partial f_k(\vec{v},z,t)}{\partial t} + \vec{v}.\frac{\partial f_k(\vec{v},z,t)}{\partial \vec{r}} - \frac{e}{m}(\vec{E}+\vec{v}\wedge\vec{B}).\frac{\partial f_k(\vec{v},z,t)}{\partial \vec{v}} = \left(R_k(z,t)n_{k-1} - R_{k+1}(z,t)n_k\right)\delta(\vec{v}), \quad (1)$$

where n_k ($\vec{r}$,t) is the space-time-dependent electron density of the kth degree of ionization. The source term on the R.H.S. of Eq. (1) corresponds to the process where the electrons are created at rest, through the tunnelling-ionization

mechanism. The kth ionization rate R_k is averaged over an optical cycle[1].Taking the appropriate moment of Eq. (1), we obtain,

$$\frac{dn_k}{d\xi} - \frac{R_{k+1}(\xi)}{c}n_k(\xi) = \frac{R_k(\xi)}{c}n_{k-1}(\xi), \qquad (2)$$

For moderate laser intensities, the ponderomotive force has been neglected. Equation (2) has to be completed with the wave equation,

$$\left(\frac{2}{c}\frac{\partial}{\partial\xi} - \frac{1}{c^2}\frac{\partial}{\partial\tau}\right)\frac{\partial\vec{E}(\xi,\tau)}{\partial\tau} = k_p^2(\xi)\vec{E}(\xi,\tau). \qquad (3)$$

where, $\tau = t$, $\xi = z - ct$, $k_p(\xi)$ is the plasma wavenumber and $n = \sum\limits_{i=1}^{k_{max}} in_i$ is the electron density computed until the final degree of ionization k_{max}. For solving these equations, we use the slowly varying amplitude and the tenuous plasma approximation,

$$\vec{E}(\xi,\tau) = E_L(\xi,0)\left(\cos\left(k_0\xi - \frac{\omega_p^2(\xi)}{2\omega_0}\tau\right)\hat{u}_x - \sigma\sin\left(k_0\xi - \frac{\omega_p^2(\xi)}{2\omega_0}\tau\right)\hat{u}_y\right), \qquad (4)$$

where $\sigma = 0$ or 1, for a linearly and a circularly polarized pulse respectively. We give in Fig. 1 the electron density profile $n(\xi)$, the initial pulse profile $I(\xi)$ and the spectral density $I(\lambda)$ of the laser pulse propagating through an hydrogen gas, for interaction lengths, $\Delta z = 400$ µm. We note that the laser pulse spectrum is blueshifted. Although the spectral blueshift increases with increasing laser intensity due to the increase of the density gradient, a saturation may occur. This can be explained by the relative position of laser pulse with respect to the electron density. Indeed, as the laser intensity increases, the density gradient is more important ,whereas the ionization front extent is more reduced, resulting in a spectral shift saturation.

Fig. 1

B. Numerical simulation

In order to validate the approximations used in our model, we compare the results in Figs. 1 to a 1D numerical simulation. For this, we have implemented a code for the resolution of the wave equation coupled with continuity and electron motion equations valid for hydrogen gas or for any gas being ionized once by the pulse
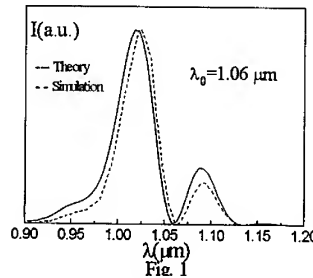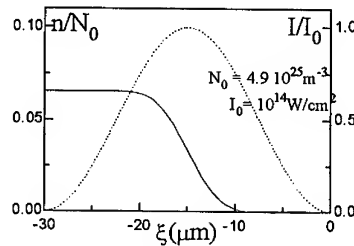
field. Since the wave equation is directly solved and no assumption is made upon pulse envelop, we can use the instantaneous ionization rate . By comparison with the model presented in section II.A, we drop here two approximations. The first one is the fixed envelop approximation. The second is related to the current derivative in wave equation: the approximation of slow electron density creation is no more necessary and the term $- en \partial n \vec{v} / \partial t$ is kept. The results are reported in Fig. 1, where we have simulated the same conditions given in Sec. II.A. Although the differences between the model results and the simulations, increase when pulse intensity or interaction length are increased, the main features stay unchanged and the model behaves very satisfactory.

III. SPECTRAL MODIFICATION BY PLASMA WAVES

A. Analytic model.

Using the cold-relativistic model[2] , the wave equations for the normalized vector potential $\vec{a} = e\vec{A} / mc$ and the normalized scalar potential $\Phi = e\phi / mc^2$ read,

$$\frac{\partial}{\partial \tau}\left(\frac{\partial \vec{a}}{\partial \tau} - 2c\frac{\partial \vec{a}}{\partial \xi}\right) = -\Omega_p^2(\xi)\vec{a}, \quad (5)$$

$$\frac{d^2\Phi}{d\xi^2} = \frac{1}{2}\frac{\omega_p^2}{c^2}\left(\frac{1+a^2}{(1+\Phi)^2} - 1\right), \quad (6)$$

where, $\Omega_p^2(\xi) = \dfrac{\omega_p^2(\xi)}{1+\Phi}$, is the

relativistic plasma frequency. For solving Eq. (11), we use, as in Sec. II.A, the slowly varying amplitude approximation, obtaining,

Fig 2

$$\vec{a}(\xi,\tau) = a_0 \sin(\pi\xi/L)\left(\cos\left(k_0\xi + \frac{\omega_p^2}{2\omega_0}\left(\frac{\Phi}{1+\Phi}\right)\tau\right)\hat{u}_x - \sigma\sin\left(k_0\xi + \frac{\omega_p^2}{2\omega_0}\left(\frac{\Phi}{1+\Phi}\right)\tau\right)\hat{u}_y\right), \quad (7)$$

The numerical results are displayed in Fig. 2. We can observe that the intense-short pulse spectrum $I(\lambda)$ is redshifted. This is due to that in the pulse extent, the gradient of the source term $\Omega_p^2(\xi)$ of Eq. (5) is mainly positive.
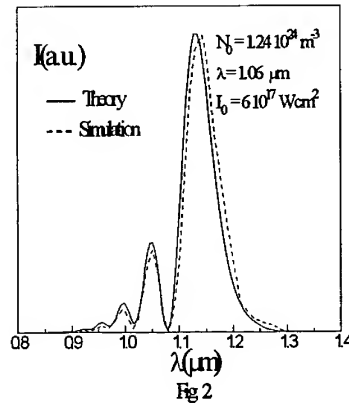
B. Numerical simulation

We have performed the same calculation by means of a more complete simulation code. This time we drop the self-phase-modulation scheme, so the pulse shape is free to change. Some approximations have been done on the envelope equation, based on the time scale separation for very underdense plasmas $\left|\bar{a}^{-1}\partial\bar{a}/\partial\tau\right| \ll \max\left(\omega_p, T^{-1}\right) \ll \omega_0$. For instance, the wave equation can be reduced by dropping the $\partial^2\bar{a}/\partial\tau^2$ term due to the second inequality[3]. In this case the wave is, for instance, insensitive to the forward stimulated Raman scattering[3]. In order to integrate the wave equation, the slowly varying parameter $\Omega_p^2(\xi)$ must be computed by electron motion. To this purpose we integrate the lagrangian equation of electron motion across the pulse. Besides the laser plasma interaction, this code consider the gas ionization too. At each time τ and each position ξ the cycle averaged tunnel ionization rate was calculated. The number of electron was increased following the ionization probability. So each part of the pulse interacts with the previously created plasma and eventually carries on the ionization process. We have applied this simulation code to the same physical situation presented in Sec. III. A and the resulting final spectrum is reported in Fig. 2 . The agreement with the previous model is excellent.

IV CONCLUSION

A simple ionization and relativistic models which describe the pulse interaction propagating through a neutral gas for moderate and ultra-high laser intensity , are proposed. These models was used to predict the spectral modification in the ultra-short laser pulse. The agreement with the simulation are particulary good.. For an ultra-short laser pulse propagating through a neutral gas, it results a blueshift spectrum for moderate laser intensity ($\leq 10^{16}$ W/cm^2), due to the ionization process and a redshift spectrum for ultra-high laser intensity ($> 10^{17}$ W/cm^2), due to the combined action of the relativistic and the ponderomotive effects. For an intermediate regime, one can expect a broadning of the laser spectrum

REFERENCES

[1] S. C. Rae and K. Burnett, Phys. Rev. A 46, 1084 (1992).
[2] P. Sprangle, E. Esarey, and A. Ting, Phys. Rev. Lett. 64, 2011 (1990).
[3] P. Mora and T. M. Jr Antonsen, Phys. Rev. E53, 2068 (1996).

RESONANCE ABSORPTION AND FAST ELECTRONS IN SHORT-PULSE LASER-TARGET INTERACTIONS

J. LIMPOUCH, L. DRSKA, M. TAGVIASHVILI

Faculty of Nuclear Science and Physical Engineering, Czech Technical University, Břehová 7, 115 19 Prague, Czech Republic

A.A. ANDREEV

Institute of Laser Physics, Vavilov State Optical Institute, Skt. Petersburg, Russia

Absorption of ultrashort-pulse laser obliquely incident on solid aluminium target is investigated with a non-LTE hydrodynamics model. The spectrum and energy of fast electrons generated by resonance absorption are calculated in a self-consistent way. Fast electrons penetrate into the target and deposit their energy in the dense material, forming a precursor of thermal wave.

1 Introduction

Interactions of intense subpicosecond laser pulses with solid targets are now widely studied, both experimentally and theoretically. Various types of plasma description, including PIC, Vlasov, Fokker-Planck and hydrodynamics, are used in numerical simulations of the interactions.

In this paper we investigate the interaction of an ultrashort-pulse laser with a planar aluminium target, with the focus of the research directed to the role of resonance absorption and fast electrons in the behaviour of the evolving plasma. This study is partly parallel to the paper of Davis et al.[1], but a consistent description of resonance absorption enables us to evaluate the fraction of energy absorbed locally via collisions in the expanding plasma and the energy and spectrum of fast electrons accelerated via Landau damping of plasma wave, that are transported and absorbed in the dense target material.

2 Physical model

The dynamics of plasma is described via one fluid two temperature Lagrangian hydrocode with electron and ion thermal conductivity, both natural and artificial ion viscosity and ponderomotive force impact on plasma motion. Very fine spatial grid with typically 500 cells is used to model in detail the shape of density profile in the expanding plasma so that the laser fields may be calculated properly. The ionic populations in plasma are calculated via set of atomic rate equations for populations of charge states. The coefficients of radiative and three body recombination are summed over a set of final energy levels. When

622

the rate of collisional ionization is calculated, thermal equilibrium of excitation levels inside one charge state is assumed. The energy loss by bremsstrahlung and recombination radiation is taken into account.

Laser absorption and electromagnetic fields are calculated for p-polarized laser radiation by numerical solving Maxwell equations in hot plasma, taking into account spatial dispersion. The boundary conditions are: no transverse and longitudinal waves incident from overdense region, given incident laser intensity and no longitudinal wave incident from vacuum.

The collision frequency by Lee and More[2] is used to find collisional part of laser absorption. Landau damping of the longitudinal plasma wave through the acceleration of resonance electrons is precisely described by an integral operator[3]. However, so as to avoid solving of integro-differential equation in each time step, complex β^2 approximation[3] is applied for Landau damping in the hydrocode

$$\beta^2 = \frac{k_B T_e}{m c^2} \frac{1}{1 - i\nu_l} \qquad \nu_l = \frac{1}{4} \left(\frac{n_c}{n} - 1 \right)$$

The description of Landau damping by integral operator was used for verification of the approximation in a few model cases.

The Cherenkov acceleration of electrons by plasma wave damping is treated in each time step via stationary electron diffusion in the velocity space. The averaged diffusion coefficient $D(v)$ is calculated in the model of electron acceleration by resonant Fourier component F_k of longitudinal electric field. As they are practically no components F_k oriented to overdense plasma, only electrons travelling to plasma vacuum boundary are accelerated.

When reflected from the plasma vacuum boundary, fast electrons accelerate ions. The spectrum of fast ions can be found from electron spectrum[4]. The transport of electrons into the target is described simply as continuous slowing down. The fast electron stopping power is written in Bethe-Bloch form[1]. The fast electron energy is thus transformed to thermal energy included in the hydrocode and leads to a precursor of the thermal wave. Small part of this energy, lost to K_α radiation, is neglected.

3 Results and conclusions

An ultrashort pulse (100 or 400 fs FWHM Gaussian with no prepulse) was assumed to be obliquely incident at 45° on plane Al target. The peak power, taken normally to the target, was varied between 10^{15} and 10^{17} W/cm^2.

The profiles of laser fields are shown in fig.1 together with the density profile for the highest studied intensity and 400 fs pulse. The figure clearly
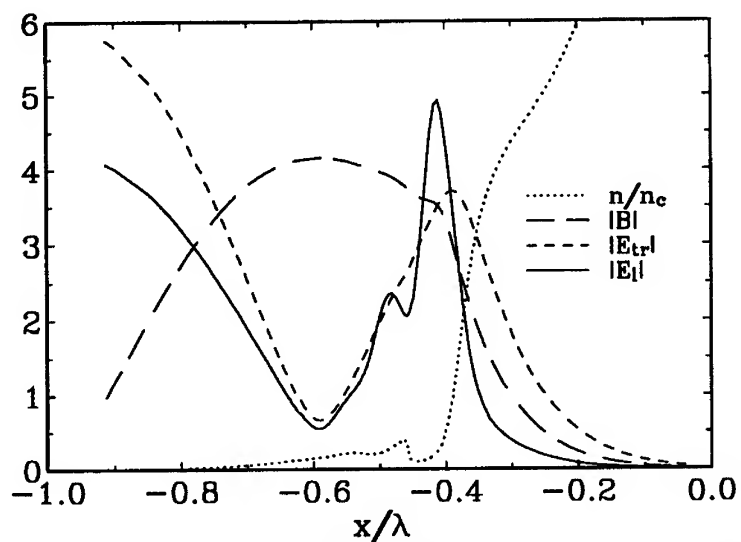
Fig.1 Density profile and electromagnetic fields at the maximum intensity 10^{17} W/cm^2 on target of 400 fs FWHM pulse of laser with $\lambda = 0.256\mu$m and angle of incidence 45°.
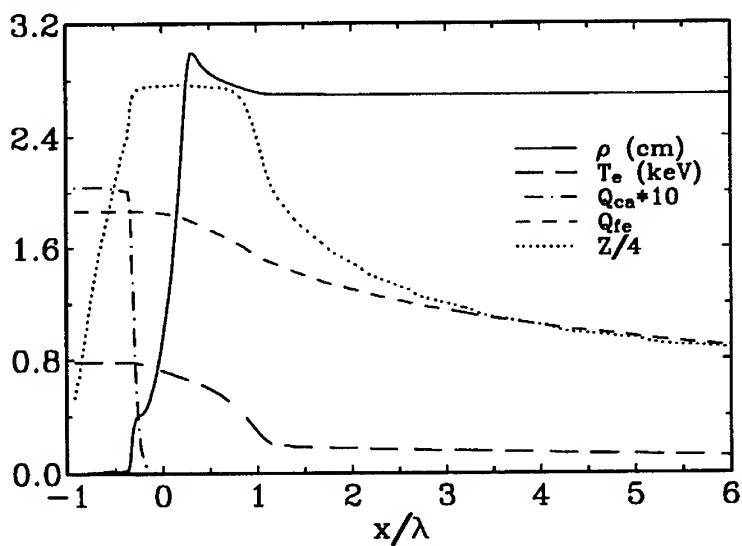
Fig.2 Global profiles at the conditions of fig.1. Q_{ca} is the part of energy flux absorbed by collisions, Q_{fe} is the energy flux by fast electrons.

demonstrates an enormous steepening of density profile in combination with practical depletion of subcritical region. The density profile modification leads to decrease of absorption to 32 % at the pulse maximum. The absorption by Landau damping is by an order more effective than the collisional absorption. The temporal profile of absorption efficiency tends to have minimum at laser pulse maximum and reveals some variations due to changing density profiles. The overall absorption efficiency was 36 % in this case, from which only 1/9 was absorbed by collisions. For lower intensities the depletion of subcritical region is not observed, and spatial density oscillations are formed for 400 fs pulses. The absorption efficiencies are then generally higher.

Global profiles of density, temperature and average ion charge are plotted in fig.2 for the conditions of fig.1. The sharp decrease of energy flux Q_{ca} just behind critical surface depicts the area, where collisional absorption, mainly due to transverse electric field, is active. The slow decrease of energy flux Q_{fe} by fast electrons (up to 100 keV) leads to preheating of the target. The thermal wave precursor reaches the end of simulation box at 1.54 μm approximately 150 fs before the pulse maximum (at 0.6 of maximum intensity). At lower intensities fast electron penetration capability is considerably lower, thermal wave precursor is sometimes not observed, however, the heat wave front moves ahead of the shock wave.

Thy dynamic evolution of plasma produced by an ultrashort-pulse laser has be characterized in the framework of hydrodynamics model. The energy and spectrum of fast electrons has been calculated in a self-consistent manner. The impact of fast electrons on target dynamics has been shown. The results are very sensitive to the stopping power and thus a more advanced treatment of fast electron transport may improve the simulation results significantly.

Acknowledgments

References

1. J. Davis *et al.*, *Laser and Particle Beams* **13**, 3 (1995).
2. Y.T. Lee and R.M. More, Phys. Fluids **27**, 1273 (1984).
3. N.E. Andreev, *DSc Thesis*, Lebedev Physical Institute, Moscow 1978.
4. A.B. Gurevich and A.P. Mescherkin, *ZhETP* **80**, 1810 (1981).

INTERACTION OF THE TRAIN OF THE PICOSECOND LASER PULSES WITH SOLID TARGET

B.A.BRYUNETKIN
State Research Center of Russia "VNIIFTRI",
Mendeleevo, Moscow Region, 141570, Russia

V.S.BELIAEV, A.S.KURILOV, A.P.MATAFONOV, V.I.VINOGRADOV
Russian Space Agency,
Central Research Institute of Machine Building
Kaliningrad, Moscow Region, 141070, Russia

A.I.MAGUNOV
General Physics Institute
Vavilova St. 38, Moscow, 117924, Russia

G.I.VERGUNOVA
P.V.Lebedev Physical Institute,
Leninsky Prospect 53, Moscow, 117924, Russia

Here we present an experimental and theoretically study of the influence of the picosecond prepulse train on the process of the laser-target interaction. Time-integrated X-ray spectra of the magnesium plasmas were recorded with the help of the crystal spectrometer equipped with a spherical bent mica crystal. HD-calculations and kinetic modeling were used for the evaluation of the plasma parameters and simulation of the experimental spectra.

1. Introduction.

Investigation of the interaction of the pico- and femtosecond laser pulses with solid target are carried out very intensively at present time (see, for instance [1]). The analysis of the X-ray line emission of highly charged ions is very powerful tool for these purposes [2,3]. Here we present the study of the influence of the picosecond prepulse train on the process of the laser-target interaction.

2. Experimental setup.

The experiments were carried out on the CPA Nd-glass laser facility "NEODIM" at TSNIIMASH. The scheme of the laser installation is shown in Fig.1. The parameters of the main picosecond pulse are following: the energy of $0.3 \div 0.7$ J, pulse duration of 1.0 psec full width at half maximum (FWHM) at the fundament wavelength 1.06 mkm. The train of prepulses has contain five picks with linear growing in intensity from the first to the last one, where are going with repetition delay $\sim$ 15 nsec. The ratio of the sum of the prepulse energies was about 10^{-3} to the main pulse energy. The laser beam was focused upon flat solid target, made from Mg at the angle of 45° from the target

Fig.1. Laser facility "NEODIM".

1 - Nd-glass rod
2 - diaphragm
3 - polaraiser
4 - mirror
5 - Pockels cell
6 - negative feedback operation unit
7 - synchronization unit
8 - high-voltage pulse unit
9 - high reflection spherical mirror
10 - dye cell with high-reflection mirror
11 - quartz plate
12 - holographic diffraction gratings
13 - telescope
14 - high-reflection mirror
15 - spatial filter lens
16 - fast photodiode
17 - spatial filter
18 - Fresnel prism
19 - 15 mm by 300 mm rod amplifier
20 - 30 mm by 320 mm rod amplifier
21 - $2\omega_0$ KDP crystal

A - master oscillator
B - stretcher
C - regenerative amplifier
D - Nd-glass amplifier
E - compressor

normal. The focal spot diameter was about 100 mkm so that an incident laser intensity of up to $5 \cdot 10^{15}$ W/cm^2 was achieved.

Time integrated X-ray emission of the magnesium plasma have been registered with the help of four-channel pinhole camera (filter cut off energy ~ 0.8 KeV) and high-resolution spectrometer equipped with spherical shape mica crystal [4]. Be-filter with the thickness of 7 mkm was used to protect the X-ray film RAR-2495.

3. Experimental results and discussion.

The evaluation of the pinhole images of plasmas allowed us to establish the size of the X-ray source about 100 ± 20 mkm. The densitogram of the experimental spectrum near the resonance line of the He-like MgXI-ion is shown in the Fig.2 (We use traditional notation for Li-like satellite transitions [5]). Simple estimations, using of well known methods of the X-ray spectroscopy [6] are shown that the average in time and space parameters of plasma are: $N_e \approx (3 \div 4) \cdot 10^{19}$ cm^{-3}, $T_e \approx 120 \div 150$ eV. Since we expect more high parameters, in particular concerning the electron temperature, the numerical simulation of the laser target interaction were provided.

The numerical code "RADIAN" was used, which included absorption of the laser radiation, a two-temperature radiative gas dynamics, the energy transfer by the electron heat conductivity. The radiation was calculated in the multi-group approximation. The basic results of calculation are shown in the

Fig. 2. Experimental spectrum.

Fig.3. The main qualitative conclusion are following. Before the arrival of the main picosecond pulse the plasma temperature is very low - about 1 eV, the density drops from 10^{21} cm^{-3} up to 10^{18} in the distance of ~ 4 mkm from critical surface. During the action of the main pulse (10^{15} W/cm^2) the temperature in this region dramatically grows (up to ~ 750 eV), but the density practically have not changes. In the moment of the time ~ 6 psec after the main pulse the temperature drops up to of 300 eV, the density profile is stable.

We not be able to fit the experimental spectra, using a hole set of plasma parameters in time and space. We can propose, that the disagreement between numerical calculation and experiment is a result of the time- and space averaging of the experimental spectra, and the time-resolved measurement will be needed.

Fig.3. Numerical simulation of the laser pulse train interaction with magnesium target:
- at the moment of maximum of the main pulse;
- at the 6 psec after main pulse.

628

4. Conclusion.

In conclusion, we mean, that the experimental situation discussed above, can be very interesting for some applications, for instance, the train of the low-level psec-prepulses in combination with the main psec-pulse can be used to drive a collisional X-ray laser scheme, analogous scheme was recently demonstrated in [7].

References.

1. High-Field Interaction and Short-Wavelength Generation, Feature Editors: H. Milchberg, R. Freaman, JOSA, **13**, № 1,2 (1996).
2. B.A. Bryunetkin et al., JQSRT, **53**, 45 (1995).
3. F.B. Rosmej, B.A. Bryunetkin et al., J. Pyts. B: At. Mol. Opt. Phts., **29**, L299 (1996).
4. B.A. Bryunetkin et al., Laser and Particle Beams, **10**, 839 (1992).
5. A.H. Gabriel, Mon. Not. R. Astron. Soc., **160**, 99 (1972).
6. V.A. Boiko et al., J. Sov. Laser Res., **6**, 85, (1985).
7. P.V. Nickles et al., Proc. SPIE, **2523**, (1995).

SKIN EFFECT IN SUBPICOSECOND LASER PLASMAS

A.A ANDREEV[1], K.YU. PLATONOV[1], J.-C. GAUTHIER[2]

[1] *Institute for Laser Physics, SC "Vavilov State Optical Institute",*
12 Birzhevaya line, St Petersburg 199034, Russia

[2] *Laboratoire pour l'Utilisation des Lasers Intenses,*
Ecole Polytechnique, 91128 Palaiseau, France

The absorption coefficient of ultrafast, high intensity laser pulses is calculated for plasmas with an anisotropic electron distribution function and a finite electron density gradient scale length in the limiting cases of normal and anomalous skin effects. For anisotropic electron distribution functions, the important effect is the increase of the laser absorption coefficient for large transverse to longitudinal electron temperature ratios.

1 Introduction

In recent years, investigations of the interaction processes of ultrashort ($\tau_p < 1ps$), high intensity ($I\lambda^2 > 10^{16}W/cm^2\mu m^2$) laser pulses [1] with solid targets have been performed intensively [2,3]. During the interaction, a dense ($n_e > 10^{22}cm^{-3}$), hot ($\approx keV$) plasma is produced by laser absorption at the surface of the target; the laser deposition thickness is comparable to the skin depth ($\approx 10nm$). In previous works [4,5], the theory of the skin effect for such plasmas was developed within the approximation of an abrupt boundary between the plasma and vacuum. Recently, numerical simulations [6] have shown the considerable influence of plasma inhomogeneity on laser absorption. The plasma inhomogeneity always exists in an experiment because of the presence of a prepulse, even if the scale of the density inhomogeneity is $L << \lambda$, where λ is the wavelength of laser radiation. The theory of the skin effect in one-dimensional inhomogeneous plasmas with an isotropic temperature distribution was formulated for the first time in Reference 7. The present work generalizes the theory of the skin effect in a one-dimensional inhomogeneous plasma to the case of an anisotropic electron distribution function and to the case of oblique incidence of a linearly polarized laser wave. The magnetic field of the wave, that was not taken into account in Ref.7, will play an important role for plasma anisotropy and oblique incidence. Calculation of the skin effect will be performed within the framework of the perturbation theory. This limits the electric field strength E in the plasma by the condition $v_e = \frac{eE}{m\omega} < v_T = \sqrt{\frac{T_e}{m}}$, where v_E is the oscillation velocity of an electron in the laser field, v_T is the thermal velocity, and ω the laser frequency.

We consider the oblique incidence (with an angle θ with respect to the normal Oz of the target plane) of a linearly polarized laser wave on a plasma which is inhomogeneous along the z axis. We start from the set of kinetic equations for electrons (ions are immobile) and Maxwell equations. The solution of the kinetic equation is obtained by using the standard methods of perturbation theory [4]. Calculating the current density, we obtain, similarly to Ref.7, a linear differential equation that determines the electric field in the plasma.

2 Analytical results for S- and P-polarized light

First, we consider the case of S polarization:

$$\frac{d^2 E_y}{dz^2} - \frac{\omega^2}{c^2} E_y =$$

$$-\frac{4\pi i\omega e^2}{mc^2}\{\int_z^\infty dz' \int_0^\infty dp_z W^{-1/2} e^{-\Phi(z';z^*)} 2\cosh(\Phi(z;z^*))$$

$$[E_y(z') + \hat{B}_1(z')]f_M(z';p_z) + \int_{-\infty}^z dz' \int_{p_1}^\infty dp_z W^{-1/2} e^{-\Phi(z;z^*)}$$

$$2[\cosh(\Phi(z';z^*))E_y(z') - \sinh(\Phi(z';z^*))\hat{B}_1(z')]f_M(z';p_z)\}$$

where $\Phi(z;z_1;z_2) = \int_{z_1}^{z_2}(-i\omega + \nu)X^{-1/2}(z,z'')dz''$ is a phase term; $W = 2\cos^2\theta/m\{p_z^2/2m + e\cos\theta[\phi(z) - \phi(z')]\}$; $X(z,z'') = 2\cos\theta/m\{p_z^2\cos\theta/2m + e[\phi(z) - \phi(z'')]\}$; $\hat{B}_1(z) = ip_z\cos\theta/m\omega\frac{\partial E_y}{\partial z}\frac{T_\perp - T_\parallel}{T_\parallel}$; $\Delta = \frac{T_\perp - T_\parallel}{T_\parallel}$; and $p_1 = \{2em\cos^3\theta[\phi(z') - \phi(z)]\}^{1/2}$.

One of the potentials that gives an analytical solution is the linear potential. It corresponds to an exponential electron density gradient: $e\phi\cos^2\theta/T_\parallel = -z/L$, $L_n = L\cos\theta$. We consider the solution of the preceding equation in the limiting case $|\alpha| = L\omega/v_{T_\parallel}\sqrt{1 + \nu^2/\omega^2} >> 1$ (normal skin effect) and obtain the resulting formula for the absorption coefficient η in the form of a single integral:

$$\eta = \frac{A}{\kappa\sqrt{\pi}}\sinh 2\kappa\pi \int_{-\infty}^\infty d\xi e^\xi Re\{\frac{1}{\sqrt{G}}e^{-\alpha^2/4G}\}\{Im\Gamma(1 + 2i\kappa)K_{2i\kappa}(2e^{\xi/2})\}^2$$

where $G = \sqrt{A/\alpha e^\xi} - \kappa^2$ and $K_\nu(x)$ is the MacDonald function.

This gives with the help of the saddle point method:

$$\eta = \sqrt{2}\pi A^{5/4}\alpha^{1/4}e^{-3\alpha^{5/4}A^{-1/4}}\sinh(2\pi k)/k.$$

Here $A = L^3/l_{sa}^3$, $l_{sa} = (c^2 v_T/\omega_p^2 \omega)^{1/3}$, $k = \omega L/c$, $\omega_p^2 = 4\pi e^2 n^{(0)}/m$ and $n^{(0)}$ is the maximum electron density. In the case of the anomalous skin effect $|\alpha| \ll 1$ the phases Φ in the electric field equation are small and can be omitted. Using the technique of functional equations as in Ref.7, we obtain the absorption coefficient $\eta = 1 - |R|^2$ where the reflection coefficient from the plasma takes the form:

$$R = \frac{1 + \omega L/c[-\pi/2 + i(\log \pi A/\sqrt{2} + \tilde{\gamma}\tilde{C})]}{1 - \omega L/c[-\pi/2 + i(\log \pi A/\sqrt{2} + \tilde{\gamma}\tilde{C})]}$$

Here $\tilde{C} = 0.577$, $\tilde{\gamma} = 2.75 - 0.1 v_{T_\parallel} \Delta/\omega L$.
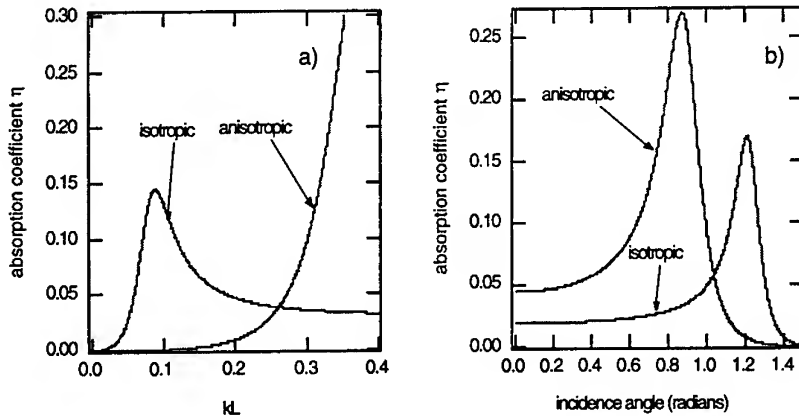
Figure 1: a: absorption coefficient as a function of the reduced scalelength for S polarisation. b: absorption coefficient as a function of the incidence angle for P polarisation. Parameters: $v_T/c = 0.1$, $\omega_p^2/\omega^2 = 60$, $kL_n = 0.3$.

The reflection coefficient is close to unity for the assumed relations $\lambda \gg L \gg l_{sa}$. The temperature anisotropy is significant for $v_{T_\parallel} T_\perp/\omega L T_\parallel \gg 1$. In this case, wave absorption stongly increases. Fig.1a shows the absorption coefficient η calculated as a function of the scale of plasma inhomogeneity kL. It is seen that $\eta(kL)$ has a local maximum. These results are in agreement with numerical calculations [6]. Thus, analytical calculations show that for a S-polarized wave in the limiting cases of normal and anomalous skin effects ($\alpha \gg 1$ and $\alpha \ll 1$) the absorption is weak, but it increases when $\alpha \to 1$.

632

One can expect that at $L \approx v_{T_\parallel}/\omega$ and $\omega c/\omega_p v_{T_\parallel} \approx 1$ the absorption will be maximum for the case of inhomogeneous plasmas with a finite density gradient scale length L because in this case $L \sim l_{sa} \sim l_d$ (where l_d is the dispersion length) and electrons lose all their energy in the skin layer.

For the case of P-polarized light, the equation to be solved for the electic field E_x is slightly more complicated due to the resonance absortion effect which couples E_x to the longitudinal E_z field. Using the same approximations than for the case of S polarization, we get the results shown in Fig.1b where we have plotted the absorption coefficient as a function of the incidence angle with respect to normal.

3   Conclusions

In the present work we have derived an integro-differential equation for the calculation of the electromagnetic field in a plasma, taking into account temperature anisotropy and one-dimensional spatial inhomogeneity. Relations between the wavelength, the scale of the density inhomogeneity, and the depth of the skin layer can be arbitrary. A new feature of our calculations is the accounting of the magnetic field of the wave in the kinetic equations. In the case of an anisotropic electron distribution function, the important effect is the increase of the laser absorption coefficient for large transverse to longitudinal electron temperature ratios.

Acknowledgments

References

1. G. Mourou and D. Umstadter, *Phys. Fluids* B **4**, 2315 (1992).
2. J.C. Kieffer *et al*, *J. Quant. Elec.* **25**, 2640 (1989); M.M. Murnane *et al*, *Science* **251**, 531 (1991); B. Luter-Davis *et al*, *Kvantovaya Elektronika* **19**, 317 (1992); J.C. Kieffer *et al*, *Phys. Fluids* B **5**, 2330 (1992).
3. R. Mancini *et al*, *J.Phys. B At. Mol. Opt. Phys.* **27**, 1671 (1994); P. Audebert *et al*, *J. Phys. B: Atom. Optical Mol. Phys.* **27**, 3303 (1994).
4. W. Rosmus and V. Tikhonchuk *Phys. Rev.* A **42**, 7401 (1990).
5. A.A. Andreev *et al*, *Zhurn. Eksp. Teor. Fiz.* **101**, 1303 (1992).
6. T. Y. Briang-Yang *et al*, *Phys. Plasma* **2**, 3146 (1995).
7. M.A. Liberman *et al*, *Zhurn. Eksp. Teor. Fiz.* **62**, 1737 (1972).

PROPAGATION OF A SHORT LASER PULSE IN PREFORMED PLASMAS AT RELATIVISTIC INTENSITIES

M.BORGHESI, A.J.MACKINNON, L.BARRINGER, L.A.GIZZI*, C.MEYER, O.WILLI

The Blackett Laboratory, Imperial College of Science, Technology and Medicine, London SW7 2BZ, UK

* *TESRE-CNR, Bologna, Italy*

The propagation of a ps pulse at intensities above 10^{18} W/cm^2 through preformed plasma has been experimentally studied using the Vulcan laser in CPA operation mode at the Rutherford Appleton Laboratory, Chilton (UK) Relativistic channelling of the pulse over many Raleigh lengths appeared to be a typical feature of the propagation through a near critical underdense plasma, and was detected through spatially resolved second harmonic emission. A study of the possibility of propagation at densities above critical has been also carried out.

1. Introduction

The study of the propagation of an ultra-intense laser pulse through a plasma is of great relevance for a number of applications, namely particle acceleration via plasma waves[1], x-ray laser studies[2], and the Fast Ignitor scheme for ICF[3]. For intensities in the relativistic regime, phenomena such as relativistic self-focusing and self-guiding of the pulse are expected to take place[4]. A relativistic effect also predicted[5] is overdense penetration of a laser pulse at relativistic intensity, due to the increase of effective critical density seen by the pulse.

An experimental study of the propagation of a picosecond laser pulse at relativistic intensities through preformed plasmas is presented here.

2. Experimental arrangement

The experiment was performed at the Rutherford Appleton Laboratory using the Vulcan laser in the CPA operation mode. The targets used were plastic foils. Their thicknesses varied in the range 0.1-0.5 mm. The plasma was preformed by a 400 ps pulse, frequency doubled in a KDP crystal to λ=0.527 μm and focused onto target in a spot of around 200-300 mm in diameter, at irradiances below 10^{13} W/cm^2. Typical operating parameters for the interaction pulse were 10-20 J on target in a pulse duration of 1-3 ps, focused in a spot of 10-20 μm in diameter. Consequently, intensities above 10^{18} W/cm^2 were obtained. Both heating and interaction beams were focused onto target by an f/5 Off-Axis Parabolic mirror (OAP). The delay between heating and interaction pulses could be varied, thus allowing interaction with the plasma at different stages of its evolution.

The plasma was diagnosed with a temporally independent probe pulse, of wavelength 0.527 μm and pulse duration of few picoseconds. A Nomarsky modified interferometer[6] allowed 2-D, time resolved density maps of the preformed plasma to be obtained. Schlieren photography[7] with a sensitivity of 5 mrad, was used to observe the effects of the interaction on the plasma. Polarimetric[7] measurements were also performed, using a Raman-shifted probe, in order to detect magnetic fields generated during the interaction. Two Streak Cameras (SC), set respectively to collect green and infrared light, were used to observe, with resolution of few picoseconds, the temporal evolution of the transmitted radiation. Spectra of the backscattered radiation were obtained with a grating spectrometer using a 1200 lines/mm grating (linear dispersion 15 A/mm).

3. Experimental results

3.1 Interaction with underdense plasmas

In Fig.2, a Schlieren image of the plasma is shown, taken 30 ps after the interaction with a preformed plasma of peak density $5 \; 10^{20}$ el./c.c. The focal spot in vacuum was 20 μm in diameter, giving an average irradiance of $3.2 \; 10^{18}$ W/cm^2. The density distribution 30 ps after the interaction is imaged, with picosecond temporal resolution.

A narrow second harmonic emission filament is visible in the centre of the plasma. This feature, present in a high number of experimental observations, is time-integrated and corresponds to radiation emitted during the interaction. It can therefore be interpreted as a signature of the spatial extent of the interaction beam in the plasma and, consequently, as evidence of self-channelling of the pulse. The diameter of the channel is about 5 mm, and its length is 130 μm, i.e. more than 6 times the Rayleigh length corresponding to a 5 μm size.

Self-channelling of an intense short pulse in near critical underdense plasma has been recently predicted by 3-D PIC simulations[8]. The simulations show that during the interaction large magnetic fields are generated by currents of fast electrons moving in the direction of laser propagation. These fields can become large enough to pinch the fast electron current and confine the laser radiation into a narrow channel.

The results obtained with the other diagnostics seem to confirm the scenario described above. Second harmonic spectra of the backscattered radiation showed a pronounced red shifted broadening, consistent with Self Phase Modulation undergone by the pulse while propagating through the cavitating channel[9].

Preliminary measurements of the magnetic fields generated during the interaction were also performed, with a polarimetric technique. From the
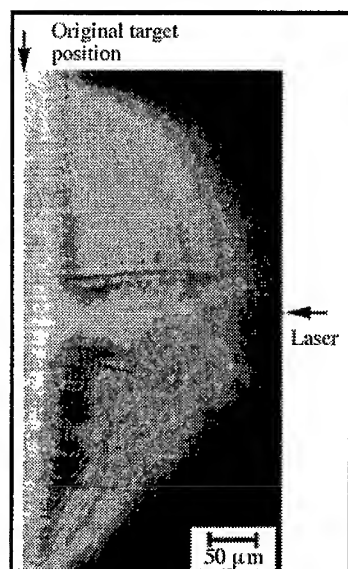
Fig. 2. Time-resolved Schlieren image taken 30 ps after the interaction of a 1 ps, 1.054 μm pulse at irradiance 3.5 10^{18} W/cm^2 with the preformed plasma of Fig. 1. The narrow channel feature visible in the centre of the plasma is due to time integrated second harmonic emission.
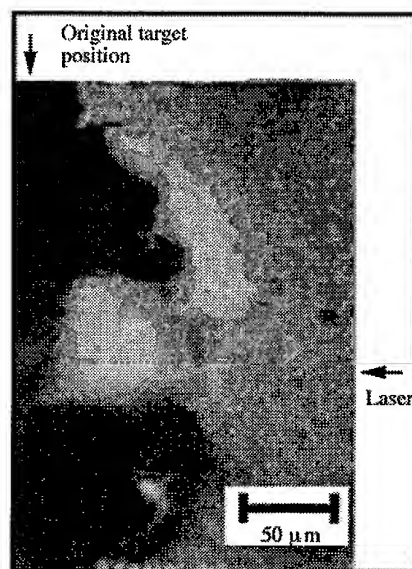
Fig. 3. Polarigram taken during the short pulse interaction with a preformed plasma in the same conditions of fig.1. The presence of magnetic fields is indicated by dark and bright patterns in correspondence of local variation in the probe polarisation, induced by Faraday rotation.

measurements, the presence of two different type of toroidal magnetic fields is suggested. The first (with an amplitude of a fraction of a MG), detected on the outer edge of the plasma, on the laser side, has direction consistent with $\nabla n \times \nabla T$ generation mechanisms[10]. The direction of the second, more intense field (about 2 MG), closely surrounding the laser axis, is consistent with field generation from fast electrons comoving with the laser pulse, as predicted by 3-D PIC simulations. Further investigations are however necessary to confirm this assumption.

3.2 Interaction with overdense plasmas

The interaction with an overdense plasma was also studied. The temporal evolution of the radiation transmitted through the plasma was observed with optical Streak Cameras. On the SC set to detect green radiation, both transmitted heating beam and second harmonic from the IR CPA pulse could be observed. Information on the temporal evolution of the plasma could be obtained from the data, and matched to 1-D simulations of the plasma evolution. The plasma density at the instant of the interaction could be inferred. In one experimental observation, the hydrocode

636

predictions suggest that the pulse, at an intensity of $3 \cdot 10^{18}$ W/cm^2, propagated through a plasma of peak density $2 \cdot 10^{21}$ cm^{-3} ($2n_c$ for $\lambda=1$ μm). However, due to the limited number of data available, this has to be considered more a study of feasibility than a conclusive experimental study.

4. Conclusion

The interaction of short pulses at relativistic intensities with preformed plasmas has been experimentally studied in different plasma conditions. The propagation in near critical underdense plasmas appeared to be characterised by strong self channelling of the pulse, as predicted by 3D PIC simulations. A preliminary study of the possibility of overdense propagation has also been performed.

Acknowledgements

References:

1. W.Tajima and J.Dawson, Phys.Rev.Lett. **43**, 267 (1979)
2. D.C.Eder, P.Amendt, S.C.Wilks,Phys.Rev.A **45**, 6761 (1992)
3. M.Tabak et al, Phys. Plasmas **1**, 1626 (1994)
4. P.Sprangle, E.Esarey, Phys.Fluids B **4**,2241 (1992)
5. P.Kaw, J.Dawson, Phys. Fluids **13**, 472 (1970)
6 R.Benattar, C.Popovics, R.Sigel, Rev. Sci. Instruments **50**, 1583 (1979)
7. O.Willi, in *Laser Plasma Interaction 4*, Proceedings of the XXXV SUSSP, St Andrews (1988)
8. A.Pukhov and J.Meyer-ter-Vehn, Phys. Rev. Lett. **76**, 3975 (1996)
9. D.Giulietti et al, Opt. Comm. **106**, 52 (1994)
10. J.A.Stamper, Laser & Part.Beams **9**,841 (1991)

THE SELF-FOCUSING OF INTENSE LASER BEAMS IN INHOMOGENEOUS PLASMAS

Z. M. SHENG[a] and J. MEYER-TER-VEHN

Max-Planck-Institut für Quantenoptik, Hans-Kopfermann-Str.1,
D-85748 Garching, F. R. Germany

Abstract

The evolution equations for a circularly polarized laser beam are given, accounting for the magnetic field generation through inverse Faraday effect. The stationary self-focusing modes of intense laser beams in inhomogeneous plasmas are studied.

1 Introduction

It is well-known that the laser beam can be self-focused due to the effects of both relativistic-electron-mass increase and transverse ponderomotive force in the laser field [1]. However, the studies on self-focusing of laser beams are still not complete for the case of circularly polarized light wave. As early as in 70's, the excitation of a magnetic field by a circularly polarized electromagnetic wave in plasma, known as inverse Faraday effect, was found experimently [2,3]. The produced magnetic field can be as large as tens mega-gauss or even larger when the incident light wave is at relativistic intensities. Because the magnetic field tends to prevent electrons from being driven out of high intensity region by the ponderomotive force, it can largely modify the propagation of intense light beams. Recently, a self-consistent study of self-focusing for circularly-polarized laser beams was given accounting for the magnetic field generation in homogeneous ambient plasma [4]. In the work presented here, we extend the above study to inhomogeneous ambient plasmas. In the interaction of an intense laser pulse with gaseous media, the plasma produced either by the prepulse or the leading edge of the laser pulse has an electron density maximum on the axis ignoring the hydrodynamic evolution [5]. Generally, this kind of density profile is not beneficial for the self-focusing of the pulse. We show that, at low light power, two different trapping modes can occur where the peak intensity of one mode is displaced from the axis; But at high light power, only one trapped fundamental mode is found.

638

2 Basic Equations

For a circularly polarized laser beam propagating in a plasma with transverse inhomogeneity with an electric field component

$$\mathbf{E_L} = \frac{1}{2}E_0(\hat{e}_x + i\lambda\hat{e}_y)\exp(ikz - i\omega t + i\psi_0) + C.C., \tag{1}$$

where $E_0(x, y, z, t)$ is the real amplitude slowly varying in time and space as compared to the exponential term, λ is either equal to 1 or -1, corresponding to the right or left-circular polarization, respectively. A magnetic field is produced by the inverse Faraday effect, which, in the cylindrically symmetric geometry, can be calculated self-consistently by

$$\mathbf{B_s} = -\frac{2\pi\lambda ec}{\omega}\left(\frac{\eta^2 n_s|a|^2}{\gamma^2} - \int_r^{+\infty}\frac{\eta|a|^2}{\gamma}\frac{d}{dr}\left(\frac{\eta n_s}{\gamma}\right)dr\right)\hat{e}_z, \tag{2}$$

where $a = eE_0\exp(i\psi_0)/m\omega c$, n_s is slowly varying electron density, the relativistic factor $\gamma = (1 + \eta^2|a|^2)^{1/2}$ with $\eta = (1 - \lambda\omega_c/\omega\gamma)^{-1}$ and $\omega_c = eB_s/mc$. On the right-hand side of Eq.(2), the first term is concerned with the circular motion of single electrons which contributes a magnetic dipole moment and the second term comes from the plasma current due to the inhomogeneity of both the plasma density and laser intensity. The equations governing the evolution of the laser beam are

$$\nabla^2\mathbf{a_L} \quad - \quad \frac{1}{c^2}\frac{\partial^2\mathbf{a_L}}{\partial t^2} = \frac{\eta k_p^2}{\gamma}N_s\mathbf{a_L}, \tag{3}$$

$$N_s \quad = \quad \mathrm{Max}\left(0, f(\mathbf{r}) + k_p^{-2}\nabla_\perp^2\phi\right), \tag{4}$$

$$\nabla_\perp\phi \quad = \quad \frac{\eta}{2\gamma}\left(\nabla_\perp|a|^2 + \frac{\lambda\omega_c}{\omega}\nabla_\perp(\frac{\eta}{\gamma}|a|^2)\right), \tag{5}$$

where $\mathbf{a_L} = e\mathbf{E_L}/m\omega c$, $\phi = e\Phi/mc^2$, $k_p = \omega_p/c$ with $\omega_p^2 = 4\pi n_0 e^2/m$, $N_s = n_s/n_0$, and the ion density is assumed in the form of $n_{i0} = n_0 f(\mathbf{r})$. Substituting $\mathbf{a_L} = a/2(\hat{e}_x + i\lambda\hat{e}_y)\exp(ikz - i\omega t)$ into Eq.(3), assuming $z' = z - v_g t$ and normalizing $\xi = k_p^2 z'/k$ and $\rho_\perp = k_p\mathbf{r}_\perp$, we obtain the evolution equation for the circularly polarized laser beam in plasma,

$$\left(\nabla_\perp^2 + 2i\frac{\partial}{\partial\xi} + \sigma\right)a = \frac{\eta N_s}{\gamma}a, \tag{6}$$

where $\nabla_\perp^2 = d/d\rho(\rho d/d\rho)/\rho$, the dispersion relation $\omega^2 = k^2 c^2 + \sigma\omega_p^2$ for laser beams has been used, $v_g = d\omega/dk$ is the group velocity, $\sigma \leq 1$ is a constant eigenvalue meanful only for the stationary solution of Eq.(6) and depending on the light power of the eigenmode. The higher the power of the trapped eigenmode, the smaller the σ value.

3 Stationary solutions in inhomogeneous plasmas

The stationary equation is

$$\frac{1}{\rho}\frac{d}{d\rho}\left(\rho\frac{da}{d\rho}\right) + \sigma a = \frac{\eta N_s}{\gamma}a, \tag{7}$$

which is similar to the one given by Sun et al. [1] except for the different forms of N_s, γ and η. Here, we take a to be real. Equations (7) is solved together with Eqs.(2), (4) and (5) with the boundary conditions: $a(\rho)|_{\rho\to\infty} = 0$, $da/d\rho|_{\rho=0} = 0$ $N_s|_{\rho\to\infty} = 1$, and $\omega_c/\omega|_{\rho\to\infty} = 0$. They are solved numerically by the shooting method. We use the asymptotic solution of Eq.(7) at some large radius ρ_∞ as a starting point for numerically integrating inward. The asymptotic solution is the modified Bessel function $a(\rho) \sim C_\infty(\kappa\rho)^{-1/2}\exp(-\kappa\rho)$ for $\rho \to \infty$ and $\kappa^2 = 1 - \sigma$. We choose $f(\rho)$ in the following form

$$f(\rho) = \begin{cases} \exp(-(\rho/\rho_n)^4), & \rho \le \rho_n/2 \\ 0.9394, & \rho > \rho_n/2 \end{cases}$$

Obviously, stationary trapped modes are available only when $\sigma < 0.9394$. Otherwise, the solutions do not decay exponentially. Figure 1(a) shows the
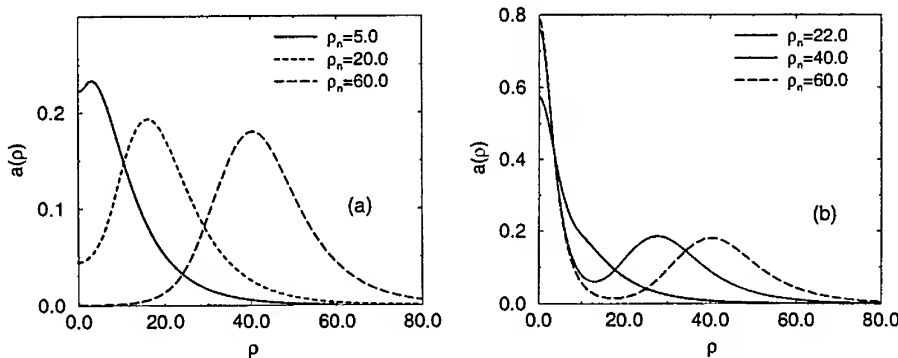
Figure 1: Two self-focusing modes in inhomogeneous plasmas with different ρ_n values for $\sigma = 0.93$ and $\omega_p^2/\omega^2 = 0.5$. (a) Amplitude profile of one mode; (b) Amplitude profile of another mode. The corresponding electron density and magnetic field are not shown here.

amplitude profile of the trapped mode for some values of ρ_n for $\sigma = 0.93$. At this σ value, the main focusing mechanism is the relativistic electron-mass increase for this case. Due to the inhomogeneous plasma density profile, the peak amplitude of the laser beam is shifted from the central region. Both the normalized trapping power and the radius increase with the ρ_n value. Meanwhile, when ρ_n increases to some value about 22.0, new trapped mode is found

as shown in Fig.1(b). For this mode, the effect of the electron displacement plays an important role. Obviously, the relation between these two modes is not similar to that between the first and second eigenmodes in homogeneous plasma discussed by Borisov, et al.[1] The existence of these two modes at the same σ value may be attributed to the complicated coupling between the focusing effect of relativistic electron-mass increase and the electron displacement, and the defocusing effect in inhomogeneous plasma for this case.

When σ reduces enough (the corresponding light power increases), only one trapped mode is found. The peak amplitude is located at $\rho = 0$. The effect of the electron displacement or cavitaion by the ponderomotive force is dominant, and the trapped mode is simply the result of a balance mainly between the focusing effect of electron cavitation and defocusing effect of dispersive spreading in this case. Figure 2(a) and 2(b) show the normalized trapping power and radius of the self-trapped eigenmode, which are defined as $P = \int_0^\infty |a(\rho)|^2 \rho d\rho$ and $\rho_a = (\int_0^\infty |a(\rho)|^2 \rho^3 d\rho / P)^{1/2}$, respectively, as a function of ρ_n for $\sigma = 0.9$ and 0.6. For $\sigma = 0.6$, the trapping power changes very little when ρ_n increase, and the radius almost does not change. It shows that the effect of electron cavitation is dominant in the self-focusing of the laser beams in this case.
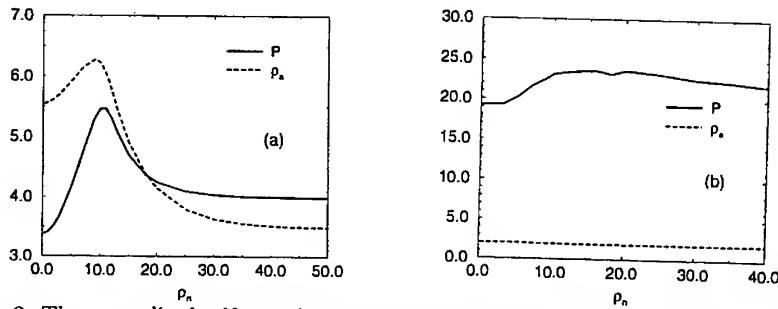
Figure 2: The normalized self-trapping power and radius as a function of the parameter ρ_n for the plasma inhomogeneity for $\sigma = 0.9$ (a) and 0.6 (b) when $\omega_p^2/\omega^2 = 0.5$.

1. For example, C. E. Max, et al., Phys. Rev. Lett. **33**, 209 (1974); G. Z. Sun, et al., Phys. Fluids **30**, 526 (1987); A. B. Borisov, et al., Phys. Rev. A **45**, 5830 (1992).

2. J. Deschamps, et al., Phys. Rev. Lett. **25**, 1330 (1970).

3. A. D. Steiger and C. H. Woods, Phys. Rev. A **5**, 1467 (1972); A. Sh. Abdullaev et al., Sov. Phys. JETP **54**, 493 (1981); E. Kolka, et al., Laser Particle beams **13**, 83 (1995).

4. Z. M. Sheng and J. Meyer-ter-Vehn, to be published.

5. For example, A. J. Mackinnon, et al., Phys. Rev. Lett. **76**, 1473 (1996).

MAGNETIC FIELD ADVECTION MECHANISM IN THE LASER-TARGET OVERDENSE PLASMA

T. J. M. BOYD and A. TATARINOV.

Physics Department, University of Essex,
Wivenhoe Park, Colchester CO4 3SQ, UK.

A phenomenological model has been applied to examine the penetration of intense magnetic fields in plasmas with densities between 4 and 10 times critical density, irradiated at laser intensities between 10^{18} and 10^{20} W cm^{-2}. The role of highly relativistic electrons produced in interactions in the underdense plasma in the advection of the magnetic field into the overdense plasma is critical. The model used to describe the evolution of the magnetic field is an electron magnetohydrodynamic (EMH) approximation, valid over short time scales. A magnetic field generated at the interface of the overdense plasma by the incident light coupled with the solenoidal field associated with the flux of fast electrons, propagates with velocity $\alpha v_e/4$, where α is the fraction of fast electrons and v_e their velocity. For electrons of relativistic velocities and α up to 10%, the magnetic field can penetrate a depth of a few laser wavelengths in times of the order of a picosecond.

1 Introduction

Strong localized magnetic fields are known to be generated in non-uniformly irradiated targets, driven by a thermoelectric $\nabla N \times \nabla T$ source first identified by Biermann as a generator of magnetic fields in stars. While its role in astrophysics is now discounted other than as a seed for dynamo action, thermoelectrically generated magnetic fields have been diagnosed and characterized in laser target plasmas, at intensities of typically a few megagauss [1,2]. At such levels, self-generated magnetic fields are capable of affecting aspects of the interaction physics though in no sense do they dominate the dynamics [3]. For uniformly illuminated targets the strength of the source is much diminished though magnetic fields may still arise from nonuniform structures in the coronal plasma like filaments or jets.

Present preoccupation with short pulse high intensity laser plasma interactions has led to a re-awakening of interest in magnetic field generation in target plasmas. In particular PIC simulations by Wilks et al [4] pointed to evidence of strong magnetic fields present in the target plasma. These fields have not yet been observed but the limited characterization available from simulations suggests some differences from the fields generated in the coronal plasma. Not only are the fields in a typical simulation (for intensities of around 10^{19}W cm^{-2} and with plasma densities up to several times the critical density)

markedly larger than any observed in the coronal plasma but they exhibit the opposite polarity and significantly persist well into the overdense plasma to a depth of several wavelengths. Similar characteristics have been seen in recent simulations by Dyson and Boyd [5] with a circularly polarized driver. These results show an expected spatially dependent polarity and in addition a strong B_z field attributable to the inverse Faraday effect.

Magnetic fields on the scale seen in the simulations, if confirmed experimentally, are capable of affecting the interaction physics and the suprathermal electron transport in particular. This is an issue of some interest in the context of the fast-igniter concept proposed by Tabak [6], which depends on the suprathermal electron flux produced through the interaction of intense laser light with the underdense plasma to propagate to the compressed high density core and ignite the fuel.

The present paper is concerned not with the generation of intense magnetic fields but with the penetration of these fields into the superdense plasma. An attempt was made by Sudan [7] to explain the presence of large magnetic fields in high intensity laser plasma interactions but this work found fields only within a fraction of a classical skin depth and failed to explain the field penetration that is a feature of the simulations. The work presented here is based on a simple model that incorporates in a phenomenological way the flux of suprathermal electrons injected into the overdense plasma and examines their role in the penetration of a field at the boundary into the supercritical region.

2 Cold electron fluid model

The model used to describe the evolution of the magnetic field is one based on the electron MHD equations [8] and valid over short times and small scalelengths. By short we mean that times of interest are shorter than those characteristic of ion motion but at the same time long enough for the displacement current to be disregarded. The model plasma is cold i.e. electron thermal velocities are much less than flow or field velocities. Since we are interested principally in target plasmas in which strong magnetic fields are present we may impose an ordering $r_{Li} \gg L \gg r_{Le}$ where r_{Li}, r_{Le} denote the ion and electron Larmor radii. By analogy with conventional MHD it is useful to define an electron Alfvén velocity $v_{Ae} = B/(4\pi N_e m_e)^{1/2}$. A further criterion for the applicability of electron MHD may then be expressed by $v_A \ll j/Ne \ll v_{Ae}$ where v_A is the conventional Alfvén velocity.

The current driven by the flux of suprathermal electrons induces a return current, but over sufficiently short time scales the conductivity of the cold over-

dense plasma is too low for these to balance. There is in consequence a net electron current. An evolution equation for the magnetic field is obtained from a generalized Ohm's Law and two time-dependent Maxwell equations (neglecting displacement current). The magnetic field is made up of two components. One of these is a field $\mathbf{B_0}$ attributable to the laser at the plasma critical surface. The other derives from the current driven by the flux of suprathermal electrons. We assume that this electron flux from the underdense plasma takes the form of a cylindrical beam of radius r. Then the field components B_0, B_θ satisfy the model equations

$$B_{0\,t} + \frac{\varepsilon^2}{r}(B_\theta B_0)_z - \kappa^2 B_{0\,zz} - \varepsilon^2 B_{0\,zzt} = 0 \qquad (1)$$

$$B_{\theta\,t} + \frac{\varepsilon^2}{r}(B_\theta^2)_z - \kappa^2 B_{\theta\,zz} - \varepsilon^2 B_{\theta\,zzt} = 0 \qquad (2)$$

where the variables are normalized as $t \to t\omega$, $r \to r\omega/c$, $B \to eB/(m\omega c)$, $\kappa^2 = \omega/(4\pi\sigma)$, $\varepsilon^2 = \omega^2/\omega_p^2$, $\omega_p^2 = 4\pi e^2 N/m$.

This model consists of two nonlinear Korteveg-de Vries-Burgers - like equations, the first of which couples the surface field B_0 and the solenoidal field, while the second is naturally independent of B_0. Solving (2) allows the advection velocity of the B_0 field by the electrons to be determined. The nature of the solutions to equations (1) and (2) depends on the relative dominance of coefficients of the various terms.

3 Discussion

Various propagation characteristics are shown in Figs.1-4. When the relative population of suprathermal electrons is small enough to be neglected, diffusion and dispersion dominate and the field decays exponentially (Fig.1). This corresponds to the limit investigated by Sudan [9] albeit using a different model. Once the advective term begins to contribute, the form of the wave front is defined by the relative contribution of the diffusion and dispersion terms. The monotonic profile (Fig.2) corresponds to strong diffusion while the oscillating (soliton-like) structure evolves (Fig.3) when the diffusion is weak relative to dispersion.

We have studied for a range of parameters the non-linear effect of magnetic field penetration into overdense laser-produced plasma. For times over which the ion motion may be neglected, and in the case of small dissipative resistivity, the nonlinear $\mathbf{j} \times \mathbf{B}$ term plays the dominant role in advecting the field into the transcritical region. The surface magnetic field induced by the laser penetrates the overdense plasma through the agency of the net current deriving from the

644
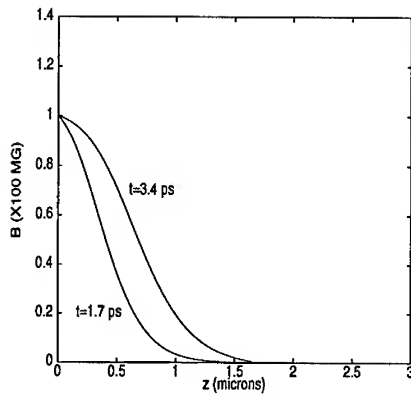
Fig.1: $\varepsilon^2 = 0.25$, $\kappa^2 = 0.001$, $\alpha = 0.001$
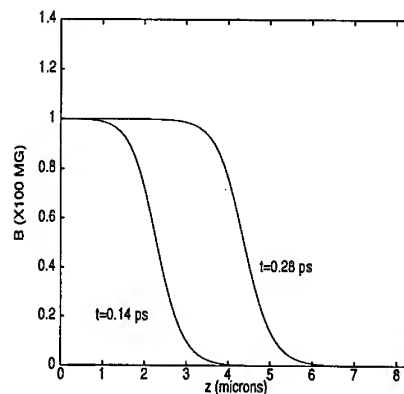
Fig.2: $\varepsilon^2 = 0.25$, $\kappa^2 = 0.1$, $\alpha = 0.1$
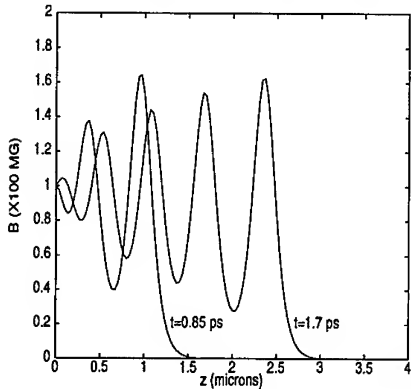
Fig.3: $\varepsilon^2 = 0.25$, $\kappa^2 = 0.0001$, $\alpha = 0.01$
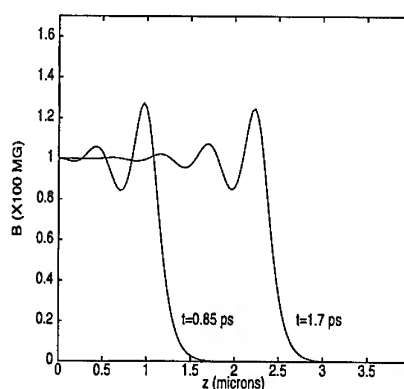
Fig.4: $\varepsilon^2 = 0.25$, $\kappa^2 = 0.001$, $\alpha = 0.01$

Figs.1-4. Advection of surface magnetic field into the overdense plasma.

flux of suprathermal electrons which persists over times of the order of the pulse.

References

[1] J. A. Stamper, E. A. McLean and B. H. Ripin, *Phys. Rev. Lett.* **40**, *1177 (1978)*.

[2] A. Raven, O. Willi, *Phys. Rev. Lett.* **41**, *554 (1978)*.

[3] H. C. Barr, T. J. M. Boyd *et al. Phys. Rev. Lett.* **53**, *462 (1984)*.

[4] S. C. Wilks, W. L. Kruer, M. Tabak, A. B. Langdon *Phys. Rev. Lett.* **69**, *9, 1383 (1993)*.

[5] T. J. M. Boyd and A. Dyson (to appear, 1996)

[6] M. Tabak *et al. Phys. Plasmas* **1**, *5, 1626 (1994)*.

[7] R. N. Sudan, *Phys. Rev. Lett.* **70**, *20, 3075, (1993)*.

[8] A. V. Gordeev, A. S. Kingsep, L. I. Rudakov, *Phys. Rep.* **243**, *215, (1994)*.

STIMULATED RAMAN SCATTERING FROM RELATIVISTICALLY INTENSE LASER PULSES IN PLASMA

H.C. BARR, T.J.M. BOYD, S.J. BERWICK, S.F. ALI, and F.I. GORDON

Physics Department, University of Essex,
Colchester, England CO4 3SQ

Stimulated forwards scattering generated within intense subpicosecond linearly polarized laser pulses propagating in underdense plasma is analyzed using a relativistic fluid model. The pulse is unstable to a hybrid of stimulated Raman forwards scattering (SRFS) and the relativistic modulational instability (RMI), the latter inhibiting the former at high intensity. Linearly polarized pulses couple an infinite hierarchy of fluctuations; it is shown that the instability growth is accurately modelled as a 6-wave interaction with higher order couplings negligible due to the destructive interference between SRFS and RMI. The hybrid SRFS/RMI instability is at its most potent at intensities of $10^{18} - 10^{19}$ Wcm^{-2} for $1\mu m$ wavelength laser light. At higher intensities, growth is reduced due to the relativistic electron mass increase. This also causes the forwards scattered emission to be trapped within the pulse. Significant blue shifts result when the scattered light decouples from the laser pulse.

1 Introduction

Stimulated Raman forwards scattering (SRFS) is a basic instability in laser-plasma interactions which can lead to the break-up of laser pulses. It is also used beneficially in plasma-based accelerator schemes to generate large amplitude plasma wake fields which can accelerate electrons to relativistic energies. A linearly polarized electromagnetic wave (ω_0, k_0) will couple a hierarchy of fluctuations at $(\omega + n\omega_0, k + nk_0)$, where n is an integer. At low intensities such that $q = eA_0/mc^2 \ll 1$, where A_0 is the vector potential of the laser, Raman forwards scattering is well approximated as a 4-wave instability comprising a plasma wave $(n = 0)$ and Stokes and anti-Stokes emission lines $(n = \pm 1)$. The latter also couple directly through a modulation at $(2\omega_0, 2k_0)$ of the relativistic factor in the electron quiver velocity. This is the relativistic modulational instability (RMI), a weaker yet distinct branch at low intensities. As the intensity rises, the two instabilities merge. We investigate here how they interfere, how many modes are active in determining the instability growth and the effect of the relativistic electron mass increase induced by the intense laser light [1,2,3].

2 Formulation

We consider direct forwards scattering from an underdense plasma modelled by the 1D covariant fluid equations, analyzed in the pulse group velocity frame. The vector potential a is given by

$$\ddot{a} - a'' + \frac{\omega_{p0}^2}{\gamma} \frac{n}{n_0} a = 0$$

where dots are time derivatives, primes space derivatives in the propagation direction (x), n_0 is the ambient electron (ion) density assumed constant, n is the electron density, ω_{p0} is the plasma frequency and γ the relativistic mass increase. Times are normalized to ω_0^{-1}, lengths to c/ω_0, densities to the laser critical density n_c, and $a = eA/mc^2$ where A is the vector potential. Fluctuations in n (γ) give rise to SRFS (RMI). The electrostatic response is described by

$$\dot{p}_x = (\phi - \gamma)'$$

$$\dot{n} + (n p_x / \gamma)' = 0$$

$$\phi'' = n - n_0$$

where $\gamma = (1 + p_x^2 + a^2)^{1/2}$, p_x is the electron fluid momentum and ϕ is the potential. Kinetic pressure is negligible here. An instability analysis [4] yields the following difference equation for the scattered light vector potential $A_s(k,\omega)$:

$$\begin{aligned}
&\left[1 + \lambda\big(f_+(k,\omega) + f_-(k,\omega)\big)\right] A_s(k,\omega) \\
&\quad - \lambda f_-(k,\omega) A_s(k_{-2}, \omega_{-2}) - \lambda f_+(k,\omega) A_s(k_{+2}, \omega_{+2}) = 0
\end{aligned}$$

where $k_n = k + n k_0$, $\omega_n = \omega + n \omega_0$ and

$$f_\pm(k,\omega) = \left(1 - k_\pm^2 c^2 / \epsilon_p(k_{\pm 1}, \omega_{\pm 1})\right) / \epsilon_s(k,\omega)$$

$$\epsilon_s(k,\omega) = \omega^2 - \omega_{pr}^2 - k^2 c^2, \qquad \epsilon_p(k,\omega) = \omega^2 - \omega_{pr}^2$$

$$\gamma_a = (1 + q^2/2)^{1/2}, \qquad \omega_{pr}^2 = \omega_{p0}^2 / \gamma_a, \qquad \lambda = q^2 \omega_{pr}^2 / 4\gamma_a^2 \omega_0^2$$

Mode coupling is determined by the coupling parameter λ, which maximizes at $q = 2$, and $f_\pm$. The constant γ_a is the relativistic mass increase due to the laser driver which reduces the plasma frequency, ω_{pr}, and saturates the electron quiver velocity q/γ_a when $q \gg 1$. The first term in the functions $f_\pm$ derives from the RMI coupling, the second from the SRFS coupling. Although the above system is solved in the pulse frame for the complex eigenfrequencies, we plot the pulse frame growth rate ν_g relative to laboratory time.
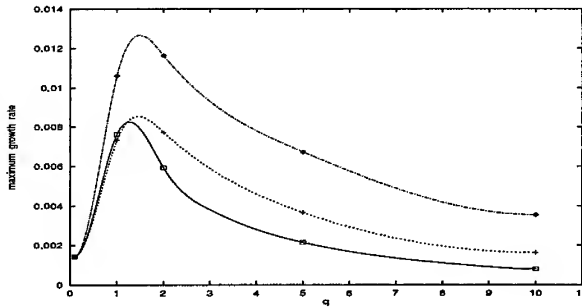
Figure 1: *Pulse frame maximum growth rate ν_{gmax}/ω_o vs q. Exact and 6-wave SRFS/RMI (—), 4-wave SRFS/RMI (- - -) and 4-wave SRFS (- · -).*

3 Results

Figure 1 shows a plot of the maximum growth rate ν_{gmax} versus q including coupling to all orders for a density $n = 0.1n_c$. It shows a strong maximum at $q = 1-2$. For comparison, we include the results obtained when the analysis is limited to a 4-wave interaction and including or excluding the effects of the RMI instability. The four modes are the laser driver at (ω_0, k_0), a plasma wave at $(\omega \approx \omega_{pr}, k \approx \omega_{pr}/c)$, and the Stokes and anti-Stokes emission at the sum and difference frequencies/wavenumbers. The RMI influence can only be neglected in the $q \ll 1$ limit. For $q \approx 1$ the interference of the RMI markedly reduces the SRFS growth although the instability is still well-approximated as a 4-wave interaction. At this and greater intensities the instability is strongly coupled in the sense that $\nu \sim \omega_{pr}$. Figure 2(a) shows the spectrum of unstable modes for q=1. At still higher intensities, a 6-wave interaction closely approximates the exact solution, where it is necessary to include the next pair of electrostatic fluctuations at $(\omega \pm 2\omega_o, k \pm 2k_o)$. It is also seen that $f_\pm(k_{2n}, \omega_{2n}) \to 0$ for $|n| \geq 1$. This means that the RMI and SRFS coupling are exactly out of phase. Only the 'central' plasma mode differs in that $k^2 c^2 / \epsilon_p(k,\omega) \to 1 - i$ compared with a value 1 for all other plasma modes. Figure 2(b) shows the complete spectrum for q=10 (10^{20} W cm^{-2} for $1\mu m$ light). The intervention of the RMI severely restricts the spectrum of unstable SRFS modes and alters the resonance conditions for maximum growth; curiously, the effect of the RMI/SRFS interaction is to lock the maximum growth conditions at $(\omega \approx \omega_{pr}, k \approx \omega_{pr}/c)$, exactly the values for low intensity SRFS. Neither instability individually would have optimum growth at this frequency/wavenumber. When the electron quiver velocity saturates ($q \gg 1$) the growth rate $\nu_g \approx \omega_{pr}^3/2$.
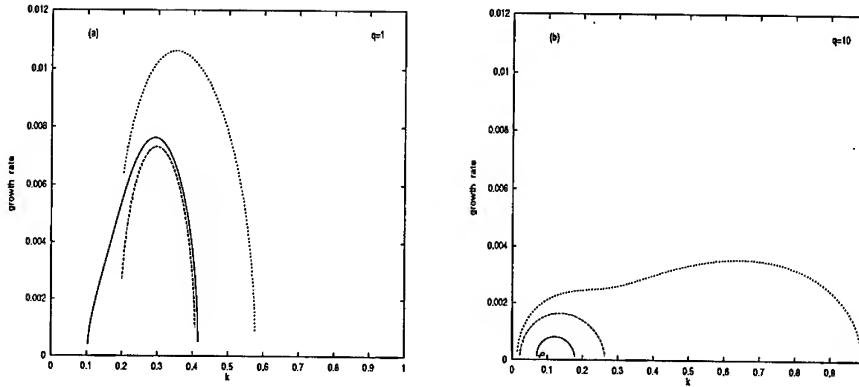
Figure 2: *Pulse frame growth rate ν_g/ω_o vs wavenumber k for (a) q=1 and (b) q=10. Exact and 6-wave SRFS/RMI (—), 4-wave SRFS/RMI (- - -) and 4-wave SRFS (· · ·).*

The scattered frequencies, through the interaction of SRFS and RMI, are therefore locked at $\omega_s = \omega_0 \pm \omega_{pr}$. Such radiation is trapped within the pulse. This is clear from the pulse frame analysis where the emission is generated at frequencies near to its critical density and the plasma external to the pulse appears overdense. However, as the beam diffracts and spreads, the intensity will reduce; in the pulse frame this appears as a time-dependent increase in the plasma frequency ω_{pr} which will upshift the emission frequency to that corresponding to ω_{p0} while leaving the wavelength unchanged. Lorentz-transforming this back to the laboratory frame gives an upshift in both Stokes and anti-Stokes emission by a factor $\approx \gamma_a^{1/2}$.

In conclusion, we have shown that forwards scattering at ultra-high intensities is a 6-wave hybrid of the SRFS and RMI instabilities. Optimum growth is locked at the resonance conditions appropriate to low intensity SRFS although the instability is strongly coupled and growth determined by the relativistic plasma frequency and not the saturated electron quiver velocity. We have compared the above pulse frame growth rates with Vlasov code simulations up to intensities $q = 1$ and found reasonable agreement.

4 References

[1] C.J. McKinstrie and R. Bingham, *Phys.Fluids B* **4**,2626 (1992).
[2] S. Guerin, G. Laval, P. Mora, J.C. Adam, A. Heron, *Phys.Plasmas* **2**,2807 (1995).
[3] W.B. Mori, C.D. Decker, D.E. Hinkel, T. Katsouleas, *Phys.Rev.Lett.*, **72**,1482 (1994).
[4] H.C. Barr, T.J.M. Boyd, F.I. Gordon, S.J. Berwick, *Laser and Part.Beams* **13**,525 (1995).

ULTRASHORT PULSE LASER-PRODUCED PLASMA X-RAYS FROM SILICA TARGETS: A PARAMETRIC STUDY

S. BASTIANI, P. AUDEBERT, J.P. GEINDRE, J.C. GAUTHIER
Laboratoire pour l'Utilisation des Lasers Intenses, CNRS, Ecole Polytechnique,
91128 Palaiseau cedex, France

We have studied the X-rays emission above 1.5 keV from femtosecond laser-produced plasmas. The variation of the silicon Kα line intensity with the incidence angle and laser intensity has been analysed. We have observed the existence of a laser intensity threshold marking the transition between two different regimes of laser energy absorption. Hydrodynamical simulations using the FILM code have been used to analyse the data.

1 Introduction

Plasma production by high-intensity, ultrashort laser pulse irradiation of solid targets allows the study of very short X-ray emission (less than a picosecond) [1-3]. Absorbed laser energy generates a plasma of size comparable to the skin depth (≈ 100Å) and with a lifetime of the same order of laser pulse duration. Due to the strong gradients and the high intensity, at the end of the laser pulse a rapid quenching of the plasma X-rays emission is expected by hydrodynamic expansion and thermal conduction in the target bulk. During the laser pulse, non-linear laser-plasma interactions produce suprathermal ·electrons [4,5] that generate Kα line emission. The plasma absorbs the laser energy by collisional and resonance absorption; the balance between them is determined by the electronic density and by the density gradient shape in the absorbing region. It is possible to affect the size of the absorbing region in different ways: producing a preformed plasma [6]; using a spatially modulated surface as target [7,8]; varying the experimental parameters (incidence angle and so on) [9,10]. In order to deeply understand the variation of the laser energy absorption, we have studied the silicon X-ray spectra as a function of the incidence angle with respect to the target normal as well as a function of laser intensity and duration.

2 Experimental set-up

A CPA Ti:Sapphire laser ($\lambda \approx 800 nm$) delivering $120 fs$ duration, $60 mJ$ energy, $10 Hz$ repetition rate pulses was focused by a f/16 lens on SiO$_2$ targets. This allows a maximum intensity of $6 \cdot 10^{16}$ W/cm^2 and, thanks to a specially designed doublet stretcher [11] to compensate for phase errors of third and fourth order, with an intensity contrast ratio of 10^{-8}, as measured by third order autocorrelation. We have studied the time-integrated Kα emission by means of a Von Hamos spectrograph (PET crystal) coupled with a cooled X-rays sensitive CCD. To minimise the background on the CCD image (high energy electron-induced X-ray fluorescence

from the crystal) we have shielded the interaction region with $1cm$ thickness lead foils and fitted the entrance port of the spectrograph with a permanent magnet producing a static magnetic field of $5000G$ parallel to the detector plane. We varied the laser incidence angle between 5 and 75 degrees and the laser pulse duration (by slightly detuning the grating pair of the compressor stage) between $120fs$ and $1.5ps$. We also varied the laser energy impinging on the target putting different apertures on the beam.

3   Some experimental results and interpretation

3.1 $K\alpha$ intensity

The results obtained for the $K\alpha$ line intensity are reported in Fig. 1 for the different pulse durations used ($120fs$, $400fs$ and $1.5ps$).
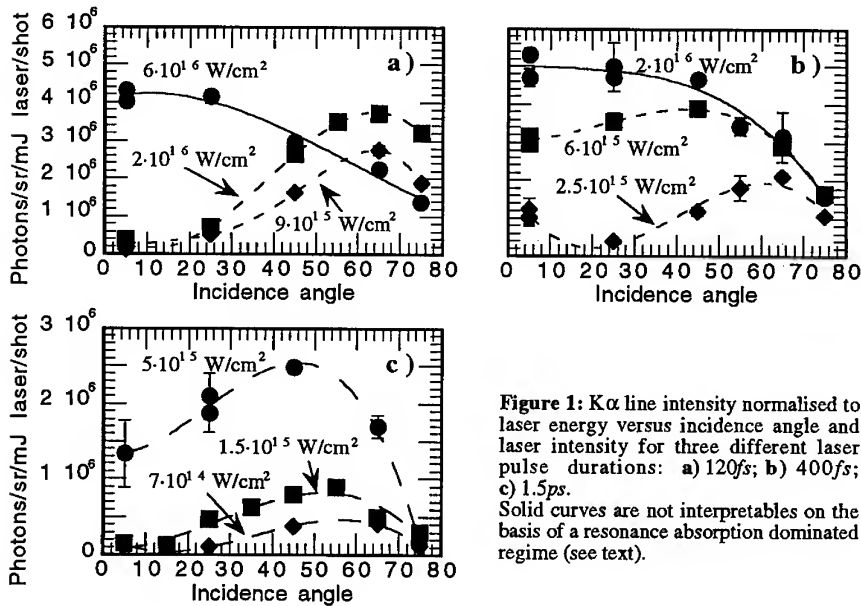
Figure 1: $K\alpha$ line intensity normalised to laser energy versus incidence angle and laser intensity for three different laser pulse durations: **a)** $120fs$; **b)** $400fs$; **c)** $1.5ps$.
Solid curves are not interpretables on the basis of a resonance absorption dominated regime (see text).

These results show the presence of a laser intensity threshold between a behaviour explainable by the resonance absorption (dashed lines) and a more complex one (solid lines). We have performed simulations with the hydrodynamical code FILM to interpretate the experimental results. In Fig. 2 we report the absorption fraction as a function of incidence angle for different pulse durations and intensities. The thin lines represent the resonance absorption fraction and the solid lines the total absorption fraction. From these graphs we can observe that the resonance

absorption is characterised by an increase of the maximum emission angle for decreasing laser intensity (I_L) as well as decreasing pulse duration.
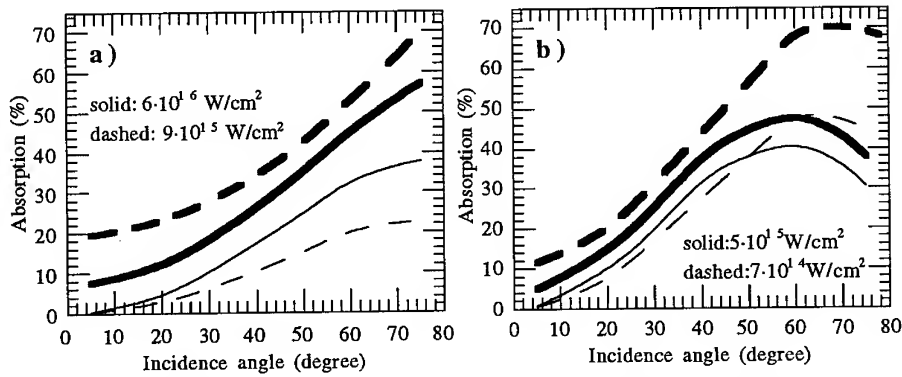
Figure 2: a) absorption percentage versus incidence angle for 120fs laser pulse duration; **b)** absorption percentage versus incidence angle for 1.5ps laser pulse duration. The thin lines are relative to the resonance absorption and the thiks lines to the total absorption.

This increase is due to the decrease of the density scale length. In fact, the simulations have shown that the maximum emission angle is well represented by the W.K.B. approximation: $\vartheta_{opt} \approx \arcsin\left(0.8 / \left(k_o L\right)^{1/3}\right)$, where L is the density gradient scale length. The density scale lengths obtained are, respectively, $L/\lambda \approx 0.01$ for the $I_L = 6 \cdot 10^{16}$ W/cm^2, 120fs pulse duration case and $L/\lambda \approx 0.05$ for the $I_L = 5 \cdot 10^{15}$ W/cm^2, 1.5ps pulse duration case. This behaviour can be observed in our experimental results for I_L below 10^{16} W/cm^2. Above this value, the Kα intensity behaviour seems more complex and is not yet well explained. The simulations obtained with the 1-D hydrodynamic code FILM have shown a density steepening in proximity of the critical density for increasing I_L. It is caused by the ponderomotive force and can introduce some instabilities in the n_c region.

3.2 Kα conversion efficiency

In Fig. 3a we report the Kα line intensity versus laser energy flux. For every experimental point, we have reported in Fig. 3b the measured hard X-rays energy, ranging from about 3 to some tens keV. From these graphs, we can recognise the optimal conditions for the Kα production. The maximum Kα conversion efficiency is obtained for nearly normal incidence and maximum laser energy flux, but with a corresponding maximum hard X-rays emission (❶ in Fig. 3). By the way, for nearly grazing incidence and intermediate laser energy flux, the conversion efficiency is nearly as high as in the former case, but the hard X-ray energy is remarkably less (❷ in Fig. 3). From the point of view of the applications this interaction condition is obviously preferable.
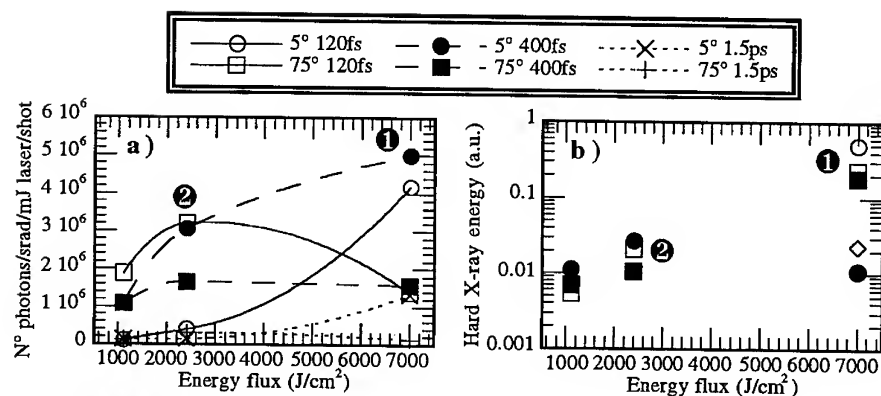
652

Figure 3: a) $K\alpha$ conversion efficiency versus laser energy flux for different incidence angles and laser pulse durations; **b)** measured hard X-rays energy corresponding to data in a).

4 Conclusions

We have analysed the laser energy absorption in the ultrashort pulse duration regime through the X-rays conversion efficiency. We have shown the presence of two different absorption regimes, depending on laser intensity. The measured maximum conversion efficiency of the laser energy is $9 \cdot 10^{-4}\%$ for the $K\alpha$ and 18% for the hard X-rays. In the "optimal" condition (❷ in Fig. 3), they are respectively of $6 \cdot 10^{-4}\%$ and 8%. Presently we are developing PIC simulations to characterise the energy of the suprathermal electrons produced in the various interaction conditions.

References

[1]   P. Audebert *et al*, *Europhys. Lett.* **19**, 189 (1992)

[2]   R.C. Mancini *et al*, *J. Phys. B: At. Mol. Opt. Phys.* **27**, 1671 (1994)

[3]   M. Murnane *et al*, *Science* **251**, 531 (1991)

[4]   F. Falliès, Thèse de Doctorat de l'Université Paris VI, Paris (1994)

[5]   A. Rousse, Thèse de Doctorat de l'Université Paris XI, Paris, (1994)

[6]   J.C. Gauthier *et al* in *Laser Interaction with Atoms, Solids and Plasmas*, NATO ASI Series B: Physics, Vol. **237**, p. 357 (Plenum, New York, 1994)

[7]   M. Murnane and H.C. Kaypten, *Appl. Phys. Lett.* **62**, 1068 (1993)

[8]   J.C. Gauthier *et al*, *SPIE Proceedings* **2523**, 242 (1995)

[9]   A. Rousse *et al*, *Phys. Rev. E* **50**, 2200 (1994)

[10] U. Teubner *et al*, *Phys. Plasmas* **2**, 972 (1995)

[11] A. Sullivan and W.E. White, *Opt. Letters* **20**, 192 (1995)

Harmonic Generation from a Subps UV (KrF) Laser Plasma

I.B.Földes, J.S.Bakos, N.A.Moustafa, G.Veres
KFKI-Research Institute for Particle and Nuclear Physics
H-1525 Budapest,Hungary

Z.Bakonyi, T.Nagy and S.Szatmári
JATE University, Department of Experimental Physics
H-6720 Szeged, Hungary

Harmonic generation of the ultraviolet KrF laser beam is investigated at an intensity of $5 \cdot 10^{15} W/cm^2$. Intense second and third harmonic generation of the beam in the surface plasma was observed both for p- and s-polarized radiation.

1   Introduction

Ultrashort laser pulses seem to be efficient drivers for generating high harmonics of radiation, thus providing coherent sources of VUV radiation. Besides of harmonic generation in neutral gases there are two basic methods for generating this radiation in plasmas. The first is to generate harmonics in low temperature preformed plasmas[1] by using the nonlinearities of weak ionization states. The second method is to generate high harmonics in the almost steplike density profile of plasmas on solid surfaces. Up to the 13th harmonics was generated by this method using a near IR laser beam[2], and high harmonics were generated by a visible light source, too[3]. A recent experiment with a 1 μm laser of 10^{19} W/cm^2 intensity resulted harmonics up-to the 75th from solid surfaces[4]. Our purpose was to investigate this process by an ultrashort UV laser pulse with different polarizations in order to get more insight into the harmonic generating mechanism.

2   Experiment

In our experiment a table-top excimer-dye hybrid laser system[5] was used. In such systems an excimer-laser-pumped pulsed dye laser system is used for short pulse generation in the visible range. After frequency doubling the pulse is amplified in a three-pass excimer UV amplifier. The laser system delivers pulses of 600 fs duration up to 15 mJ energy at 248 nm. In order to determine the focused intensities the size of the focal spot was measured for different beam diameters. The diffraction properties of the beam were close to the theoretical limit. In the case of maximal beam aperture the beam was 1.5 times diffraction

654

limited. Thus we focussed the beam by a simple lens of 33 cm, obtaining a focal spot diameter of ~ 20 μm in our target experiments, resulting in $5 \cdot 10^{15}$ W/cm^2 intensity.

In order to control the contrast of the beam the laser intensity was compared with the ASE intensity in the focus. The energy density of the pulse was ~ 4000 times larger than that of the ASE. Since the pulse duration of the signal (700 fs on target) is much shorter than that of the ASE (15 ns) the intensity contrast is better than 10^7.

Experiments were carried out on aluminum, polystyrene (CH) and bare glass targets using both s- and p-polarized laser beams. The polarization contrast was better than 25:1. The target was aligned at 45° of incidence, each shot could hit a fresh surface element. A toroidal holographic grating of 550 lines/mm collected the specularly reflected light and the emitted VUV radiation from 25 to 130 nm. Similarly to the method applied by von der Linde et al.[2] we used a beam block at the center of the incident beam in order to suppress the fundamental beam. An aperture blocked the fundamental beam before the grating. The detector was an MCP with a phosphor screen. The visible light of the screen was imaged onto a CCD detector.

3   Results

Second harmonic (2ω) generation was observed for each type of target and - surprisingly - for each polarization. It could be observed as a function of intensity in an order of magnitude range showing a roughly square law dependence on the fundamental intensity. Fig.1 shows the experimental data for a pure glass target heated by p-polarized beam. The solid line is a fitted parabola.
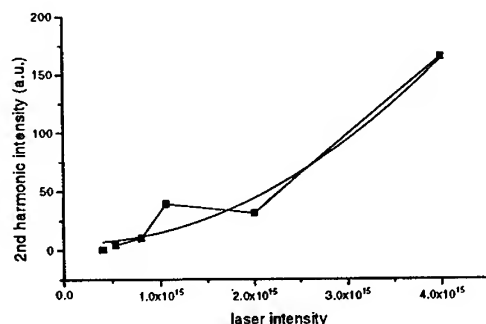

Figure 1: The intensity of the second harmonic signal in glass vs. laser intensity (p-polarized). The smooth curve is a fitted parabola.

655

The second harmonic signal was more intense, than the third harmonic (3ω) radiation which was observed for both polarizations, too. The third harmonic signal is clearly demonstrated e.g. in Fig.2 on a CH target for s-polarized light at different intensities. Observable 3ω signal required 2-3 times higher intensities than 2ω. It can be clearly seen that a 50% attenuation of the beam reduces the signal to the noise level, thus the intensity dependence cannot well be measured.
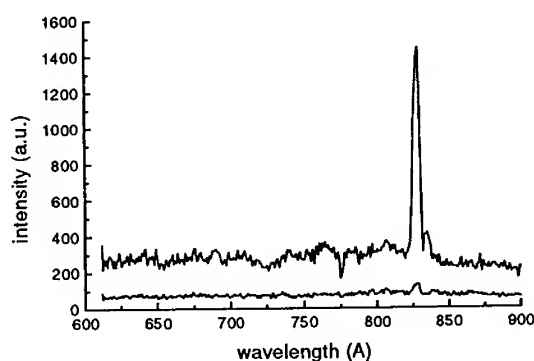

Figure 2: Third harmonic signal on CH target at two different laser intensities ($5 \cdot 10^{15}$ and $2.5 \cdot 10^{15} W/cm^2$, s-polarized)

In the case of an Al target it is difficult to separate the 3ω signal from the Al IV lines as seen in Fig.3. However, the 3p-4s lines of Al IV are expected to be week, therefore the existence of 3ω radiation is very probable. The situation is similar for an eventual 5ω signal for carbon which is in the vicinity of CIII features. As the intensity in our experiments was significantly lower than in the previous ones [2-4], the absence of higher harmonic signals is in agreement with the expectations.

The observed signals both for 2ω and 3ω radiation was practically independent of the beam polarization. This is in sharp contrast to previous observations in solid surface plasmas by visible radiation [2,3] in which cases harmonic generation was dominantly an effect for p-polarized light. The early experimental observations of harmonics with a low intensity IR laser [6], in which case the anharmonicity was generated inside the solid material also strongly preferred p-polarized light. It must be mentioned however, that the focussing stability and consequently the intensity had significant shot to shot variation in our experiments, therefore a more accurate comparison of intensity thresholds must be carried out in future experiments. The eventual independence from polarization of the beam is in agreement with observations of Norreys et al [4].
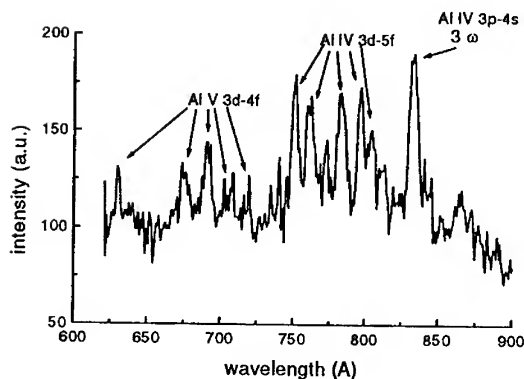
Figure 3: Spectrum between 600 and 900 Å on Al target

The difference from the latter experiment is that our experiments assure us, that our laser was free from prepulse. Thus we are convinced that the harmonics originate from the steep density gradient. The similarity of results for both polarization points to a necessary revisiting of explanations of harmonic generation in solid surface plasmas.

4 Acknowledgments

5 References

1. Y. Akiyama et al., *Phys. Rev. Lett.* **69**, 2176 (1992).
2. D. von der Linde et al., *Phys. Rev. A* **52**, R25 (1995).
3. S. Kohlweyer et al., *Opt. Commun.* **117**, 431 (1995).
4. P. A. Norreys et al., *Phys. Rev. Lett.* **76**, 1832 (1996).
5. S. Szatmári, *Appl. Phys. B* **58**, 211 (1994).
6. Gy. Farkas et al., *Phys. Rev. A* **46**, R3605 (1992).

HIGH EXPLOSIVE IODINE LASER FOR FAST IGNITION CONCEPT

S.A.SUKHAREV, G.A.KIRILLOV, G.G.KOCHEMASOV, S.M.KULIKOV,
N.V.MASLOV, S.N.PEVNY

Russian Federal Nuclear Center - Institute of Experimental Physics (VNIIEF)
607200, Arzamas-16, Nizhni Novgorod Region, Russia
Fax: (831) 30 54565; Phone: (831) 30 56646, e-mail:sukharev_2566@spd.rfnc.nnov.su

Introduction

The fast ignition concept, discussed in a number of papers [1], offers the possibility of producing significantly higher gains with much less driver energy than by the conventional approach. It foresees three phases of laser influence to the target: (1) A capsule is imploded as in conventional approach to form a high-density DT core; (2) A hole is drilled through the coronal plasma with ponderomotive force of laser radiation which brings the critical surface nearer to high-density core; (3) The core is ignited by the ignition laser at high $I\lambda^2$.

We have proposed the driver scheme to fast ignition concept based on high explosive (HE) iodine laser module, developing at Arzamas-16, having phase conjugation device, controlled pulse shape and up to 70 kJ energy in single beam [2,3].

1. Main principles of laser design for fast ignition concept [1]

Capsule implosion (phase 1). To obtain a cold-type target implosion it is enough to reach the following parameters of fuel: $\rho R = 0.4$ g/cm^2; $T \approx 0.5$ keV; $\rho = 150$ g/cm^3. For this it is necessary to enclose the energy of $E_{DT}=4\pi(\rho R)^3 C_V T/3\rho^2 \approx 0.7$ kJ at $C_V = 11.5 \cdot 10^7$ J/g$\cdot$keV, or laser energy of about 20 kJ at the absorption coefficient of ~3% and pulsewidth of some nanoseconds.

Hole boring (phase 2). According to existing notions plasma "pushing" process requires 100-200 ps of time and is defined by the value $I\lambda^2$ where I is laser intensity on a target and λ is wavelength. For hole boring this parameter should be within the range of $I\lambda^2 \sim 10^{18}$-10^{20}W$\cdot\mu$m/cm^2. The value of $I\lambda^2$ which one can provide on a target is determined by laser energy E, pulse duration τ and laser spot size d on the target. At $\tau = 150$ ps and rather large spot of 90 μm it is possible to reach $I\lambda^2 \approx 10^{19}$ W$\cdot\mu$m^2/cm^2 on a target at the laser energy of $E_2 = 50$ kJ, which is well provided by one HE iodine laser module.

Core ignition (phase 3). To heat the fuel up to 10 кeV it is necessary to enclose an energy $E_3 = 3 \cdot 10^8/\rho^2$, which corresponds to $E_3 \approx 15$ кJ for $\rho = 150$ g/cm^3. Duration of an ignition pulse should be of ~20 ps, that is long enough to heat the fuel up to the fusion temperature but shorter than the fuel disassembly time. To obtain such a laser pulse we propose to use one module of HE iodine laser and to apply stimulated Ra-

man scattering (SRS) pulse compression. The energy efficiency of SRS compression is limited by energy losses on media excitation ($\eta=1-\Omega/\omega_p$, where Ω, ω_p are the frequencies of media phonons and pump photons accordingly). For iodine laser and rotational SRS in compressed SF_6 with Stokes shift $\Delta\nu = 775$ cm^{-1} the limit efficiency is $\eta\sim0.9$. In experiments [4] a successful pulse compression from 350 ps up to 3-5 ps with energy efficiency of 50-60% was demonstrated.

2. Shock pumped iodine laser [2,3,5]

The laser scheme considered above is based on experimental and theoretical investigations of HE iodine laser with phase conjugation performed in Arzamas-16. The basis of laser is two-cascade amplifier with 1.3 m total aperture. The main results obtained on such a laser in the scheme with SBS mirror are submitted on Fig.1, as well as a pump geometry and a beam near-field image.
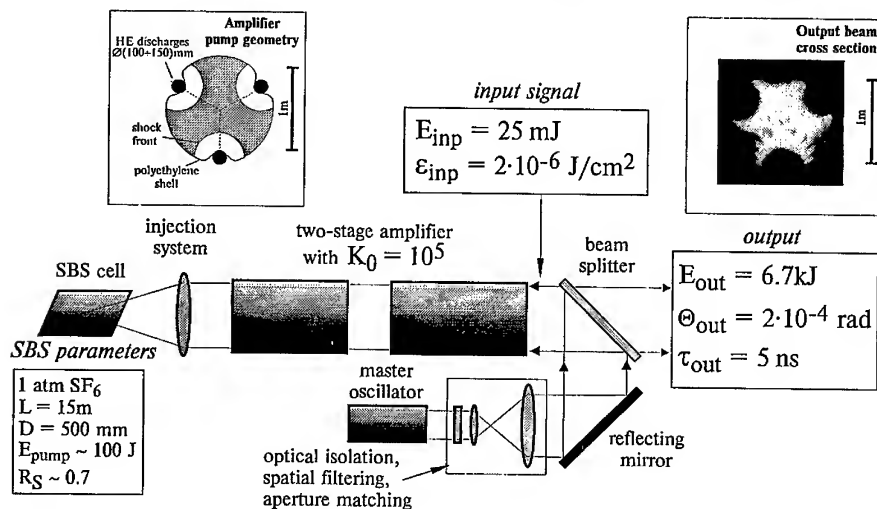
Fig.1. Double-pass amplification scheme with SBS mirror (HE iodine laser, VNIIEF experiments)

Experimental investigations on population inversion accumulation process in the shock pumped iodine laser have been carried out. The relative inversion up to 85% is obtained which practically agrees with calculationally expected one

Theoretical and experimental investigations of phase conjugation for high energy beams of large diameter (0.1-1m) have been fulfilled. Strehl number of ~0.73 and self-pointing accuracy not worse than $\sim1\cdot10^{-6}$ rad have been obtained in experiments for the beams with divergence $\theta_{0.5J}\approx2\cdot10^{-6}$rad at energy level ~0.5kJ.

Investigations of pulse spatial-temporal structure formation in large-aperture (≥0.5m) iodine lasers have been carried out. 2D calculations of this process practi-

cally agree with experiments, so we can produce in experiments both long (~1 ns) and short (100-150 ps) pulses.

Based on these results the project of HE iodine laser with ~10 MJ energy (International Microfusion Facility - IMF) for high gain ICF experiments was proposed and substantiated in 1993-94 by VNIIEF and LLNL [2,3]. This is a multichannel laser facility based on two-pass HE iodine laser having phase conjugation device, controlled pulse shape and 70 kJ energy in single beam.

The laser module design is shown on Fig.2. The amplifier designed as a polyethylene film tube of ~200 m length. Laser medium are pumped by explosive lamps, located in two active zones of 5 m length separated from each other by a distance of ~100 m. The laser medium must be separated from the pump source medium by the special filter, which cuts off the harmful band of hard UV radiation with $\lambda < 0.18$ μm. Then according to the calculations, tested in experiments, it is possible to produce the output energy at the level of ~ 70 kJ. In this case the gain of the weak signal should be held at the level of 10^6-10^7 (in experiments we have already operated with gains of order 10^5-10^6).

Amplifier channel layout

Output energy

Multi-beam mode with pulse tailoring
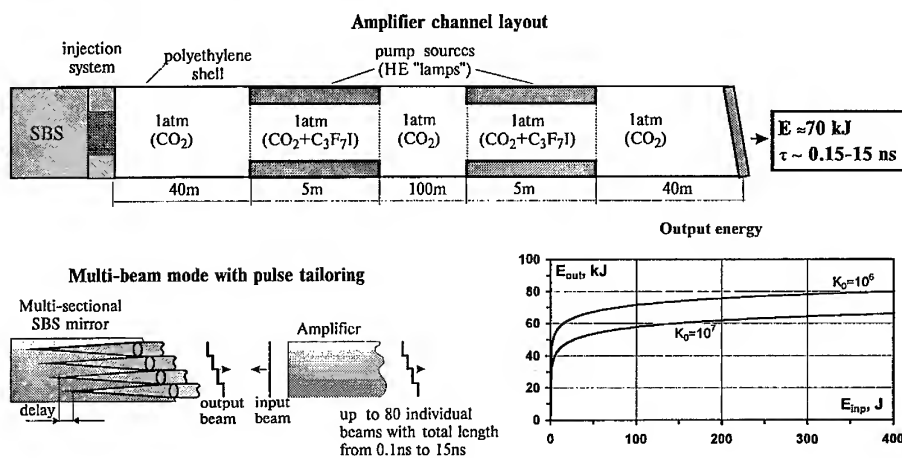
Fig.2. Laser module conceptual design

The key element of the laser channel is the multisectional SBS mirror with the high quality phase conjugation. It is the array of 1,3 m total diameter, which consists of 80 independent SBS mirrors each having input aperture of 13 cm. Changing the pulse time delay between the independent SBS mirror pulses, we can form pulses at the target practically of any shape and the pulsewidth from ~0.15 ns to ~15 ns. We have experimentally tested the pulse coincidence accuracy at 2-sectional SBS mirror and obtained the value of ≤ 40 ps.

660

3. General arrangement of laser system

Thus, the general configuration of a laser system for experiments in a fast ignition mode may be as presented on Fig.3. For such system only 4 modules of HE iodine laser will be required totally: two modules are needed for the first phase (capsule implosion), one module for the second phase (hole boring) and one module else for the third stage (core ignition). The laser beams at 2-nd and 3-rd phases should incident onto a target along the same optical axis. It can be executed with the help of selective (on wavelength) mirror thanks to Stokes shift at SRS.

Fig.3. General arrangement of HE iodine laser system for fast ignition

Conclusion

Above proposal represents the possible application of HE iodine laser in forth-coming experiments on thermonuclear ignition and burning. The feasibility of this project essentially depends on feas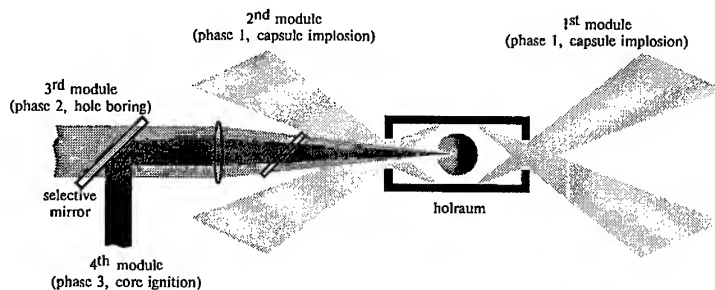ibility of a fast ignition concept as a whole. The key is hole boring which requires more detailed investigations. In addition, the special activity should be devoted to SRS compression for laser pulses of ~ 10 ps duration and of ~ 30 kJ energy. These questions can be investigated in partly at Arzamas-16 in collaboration with LLNL within the framework of the ISTC project #111.

Referencies

1. M.Tabak, J.M.Hammer, M.E.Glinsky, W.L.Kruer, et al, *"Ignition and High Gain with Ultrapowerful Lasers"*, LLNL, ICF Quarterly Report, vol.4, no.3, April-June 1994, pp.90-100
2. S.G.Garanin, G.A.Kirillov, G.G.Kochemasov, S.M.Kulikov, S.N.Pevny, S.P.Smyshlyaev, S.A.Sukharev and I.N.Voronich, *"Examination of iodine laser facility based on shock wave pumping for target irradiation experiments"*, Report under the Contract No.B239720 for LLNL, 1993
3. R.I.Ilkaev, G.A.Kirillov, G.G.Kochemasov, S.M.Kulikov, V.N.Mikhailov, S.N.Pevny, L.D.Rjabev, S.A.Sukharev, E.V.George, W.J.Hogan and E.M.Campbell, *"IGNIS - A High Gain Test Facility"*, IAEA Technical Committee Meeting on Drivers for ICF, Paris, France, 14-18 November 1994
4. V.A.Gorbunov, V.B.Ivanov, S.B.Paperny and V.R.Startzev, Izvestiya Akademii Nauk SSSR seriya fizicheskaya, v.48, p.1580, 1984
5. S.A.Sukharev, *"The High Power Iodine Laser Fusion System ISKRA-4M Generating 1 kJ at 2w Based on Eight Beam Irradiation Scheme"*, IAEA Technical Committee Meeting on Drivers for ICF, Osaka, Japan, April 15-19, 1991

FEMTOSECOND LASER DRIVEN SHOCK WAVES

A. D. BADGER, R. EVANS[a], F. FALLIÈS[b], T. A. HALL and M. H. MAHDIEH
Department of Physics, University of Essex, Wivenhoe Park, Colchester, Essex, CO4 3SQ England.

P. AUDEBERT, J-C. GAUTHIER and J-P. GEINDRE
Laboratoire pour l'Utilisation des Lasers Intenses, Ecole Polytechnique, 91128 Palaiseau, France.

A. DJAOUI
Central Laser Facility, Rutherford Appleton Laboratory, Chilton, Didcot, Oxfordshire, OX11 0QX.

A. ANTONETTI and A. MYSYROWICZ
Laboratoire d'Optique Appliquée (L.O.A.), ENSTA Centre de l'Yvette, 91120 Palaiseau, France.

Results of the observation of shock waves at an Al/fused silica interface are presented. The shock waves were driven by $400nm$, $2mJ$, $\sim150fs$ pulses from a frequency doubled $10Hz$ CPA Ti:Sapphire laser. The observations were made using frequency domain interferometry, in which changes in the phase and reflectivity of a pair of probe pulses can be recorded simultaneously. Changes in the phase of the probe pulse result from changes in the electron temperature and density at the reflecting point, as well as its motion; changes in the reflectivity are dominated by changes in the electron temperature. A modified version of the hydrodynamic code MEDUSA, which included an electromagnetic wave solver to correctly model the absorption of ultra-short laser pulses was used to simulate the experiments. A postprocessor based on the wave solver was used to compute the probe pulse phase and reflectivity changes. These were found to be sensitive to the equation of state chosen. There is a moderate agreement between the form of the experimental results and the simulation predictions. However, neither the Thomas-Fermi or SESAME equations of state can provide an adequate explanation for the detailed differences. We conclude that these differences are due to non-equilibrium effects.

1 Introduction

The study of matter under extremes of density and temperature has long been of interest[1]. Shock waves driven by long laser pulses have been used to generate such conditions[2]. Celliers and Ng[3] have found evidence for non-equilibrium effects using nanosecond laser pulses and silicon targets. Observations with increased temporal resolution are now possible with Chirped Pulse Amplification (CPA) techniques. Vu et al.[4,5] reported time resolved probing of electron thermal transport with a 100fs laser pulse and the ionisation in a shock wave driven by a 700fs laser pulse. Our arrangement is similar, but our results are very different. This paper describes

---

[a] Present address: Laboratoire d'Optique Appliquée, ENSTA Centre de l'Yvette,91120 Palaiseau, France.
[b] Present address: Applied Physics Group, School of Physics and Space Research, Birmingham University, Edgbaston, Birmingham, B15 2TT England.

the results of the optical probing of shock waves driven by femtosecond laser pulses, using frequency domain interferometry[6,7], in which observations are made by recording the changes in phase and reflectivity of a pair of collinear femtosecond probe pulses separated in time, with a high spatial and temporal resolution[8,9].

2   Experiment

The plasma was produced by a $400nm$, $150fs$, $2mJ$ (pump) laser pulse. This was focused onto the target by an $f/4$ Bowen telescope, producing a $5\mu m$ (FWHM) focal spot. The pump pulse was created by frequency doubling the $800nm$ pulse from a $10Hz$ CPA Ti:Sapphire laser in a KDP crystal with ~10% conversion efficiency. The pulse was expected to be stretched slightly to ~$150fs$, but to have a very low prepulse level. A pair of collinear probe pulses, separated by $2.5ps$ were produced by passing an $800nm$, $130fs$, $10\mu J$ probe pulse through a Michelson interferometer.

The targets were evaporated Al layers of various thicknesses on $2mm$ thick fused silica substrates. Each one had a thin (100Å) tracer layer which was used to obtain the pump-probe pulse timing. The pump-probe delay was altered using a computer controlled timing slide. The s- or p-polarised probe pulses were incident on the rear of the target at $45°$ in vacuum. The probe beam was partially defocused to a spot of ~$100\mu m$ (FWHM) so as to cover the region affected by the pump pulse and not to produce any optical breakdown or damage itself. The reflected probe was imaged onto the slit of a $0.25m$ Jobin Yvon grating spectrograph with ~$100\times$ magnification. The spectrograph output was digitised by a PC and CCD camera.

3   Results

Figure 1 shows the temporal phase shift variation, for a p-polarised probe reflected from 2300Å of Al irradiated at $1\times10^{15}Wcm^{-2}$. Negative phase corresponds to a blue shift of the probe. Time zero is given by the first phase change of the tracer layer.

The experiment has been modelled using a modified version of the 1D Lagrangian hydrodynamic code MEDUSA[10]. This includes an electromagnetic wave solver[11] and the TKN conductivity model[12] to accurately model the absorption of ultra-short laser pulses and the Thomas-Fermi or SESAME[12] equations of state (EOS). A post-processor, based on the wave solver was used to model the propagation of the probe pulse. The simulation results for an incident irradiance of $5\times10^{14}Wcm^{-2}$, which gives the best fit to the experimental results are also shown in figure 1. This implies that the absorbed irradiance was not as expected.

4   Discussion

Three contributions to the phase change are possible: changes in (1) the reflecting
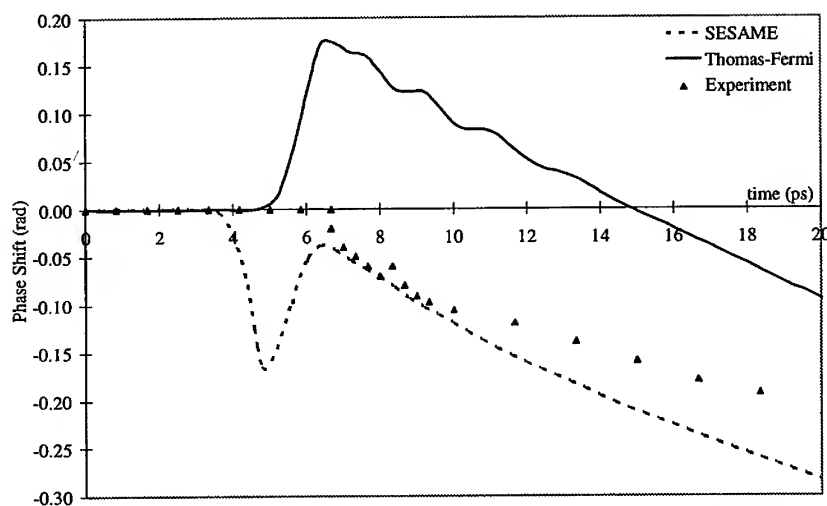
Figure 1. Temporal variation of the phase shift for a p-polarised probe reflected from a 2300Å Al layer. The experimental irradiace was $1\times10^{15}Wcm^{-2}$. $5\times10^{14}Wcm^{-2}$ was used for the simulations.

surface optical properties, (2) the reflecting surface motion and (3) the refractive index of the material between the reflecting surface and the observer. S- and p-polarised phase shift measurements have shown only a small difference at early times after the shock arrival indicating that the density scale length of the Al plasma at the interface is small[8]. The third case can be neglected under these conditions. The phase shift due to the motion of the reflecting surface can easily be calculated. The simple case of a mirror moving at a velocity u, through a medium of refractive index n, the Doppler shift for an observer viewing at an angle θ gives

$$\frac{d\Phi}{dt} = 2\omega_0\left(\frac{u}{c}\right)n\cos\theta \tag{1}$$

where ω_0 is the frequency of the probe light, $d\Phi/dt$ is the rate of change of phase (i.e. Doppler shift) of the probe pulse.

The steady decrease in phase beyond 6ps is due to the Doppler motion of the reflecting Al layer at the interface, not a reflection from the shock front which propagates into the fused silica. Simulation results show a moderate agreement at these times. But, simulations using both EOS forms show early phase features while zero phase is recorded experimentally. From 3-6ps, the phase predicted by using the SESAME EOS shows a rapidly increasing negative trend. This arises from a change in the optical properties of the reflecting Al layer due to an increase in the electron temperature. This is countered by a positive swing which starts at ~4ps and is due to an increase in the electron density at the reflecting surface. The Thomas-Fermi EOS simulation shows a similar trend, but the initial negative phase

664

is less pronounced. The difference between the two EOS models arises because of the different predictions of the ionisation state in the reflecting layer.

Before $6ps$, the zero phase in the experiment indicates that the layer is not being heated. The first detectable change in reflectivity occurs $\sim 1.5ps$ after the first phase change[14], reinforcing this. The shock velocity can be found from an accurate knowledge of the pump-probe pulse timings and the first detected phase change.

5   Conclusions

By using frequency domain interferometry we have measured both the particle and shock velocities at an Al/fused silica interface. These are in reasonable agreement with predictions from hydrodynamic simulations. The simulated phase is sensitive to the EOS used, particularly at early times (3-$6ps$), i.e. when the shock breaks out of the Al. MEDUSA does not model non-equilibrium effects and this may explain the differences between the simulation and the experiment at these early times.

Acknowledgements

References

1. Hall T. A., in NATO-ASI Conference '*Laser Interaction with Atoms, Solids and Plasmas*', ed. More R M (Plenum, New York 1994).
2. Löwer Th. *et al.*, *Phys. Rev. Lett.* **72** 3186 (1994).
3. Celliers P. and Ng A., *Phys. Rev. E* **47** 3547 (1993).
4. Vu B-T. V. *et al.*, *Optics Letters* **18** 723 (1993).
5. Vu B-T. V. *et al.*, *Phys. Rev. Lett.* **72** 3823 (1994).
6. Tokunaga E. *et al.*, *Optics Letters* **17** 1131 (1992).
7. Geindre J.P. *et al.*, *Optics Letters* **19** 1997 (1994).
8. Audebert P. *et al.*, *Phys. Rev. Lett.* **73** 1990 (1994).
9. Blanc P. *et al.*, *J. Opt. Soc. Am.* **13** 118 (1996).
10. Djaoui A. and Rose S. J., *J. Phys. B: At. Mol. Phys.* **25** 2745 (1992).
11. Falliès F., Private communication (1995).
12. Lee Y. T. and More R. M., *Phys. Fluids* **27** 1273 (1984).
13. Holian K., *Los Alamos National Laboratory Report LA-10160-MS* (1984).
14. Hall T. A. *et al.*, in preparation.

FEMTOSECOND OPTICAL PROBE MEASUREMENTS OF THE PROPAGATION OF TERAWATT LASER PULSES IN UNDERDENSE GAS TARGETS

R. FEDOSEJEVS[a], X.F. WANG[b] and G. D. TSAKIRIS
Max Planck Institut für Quantenoptik, Hans-Kopfermann Str. 1,
D-85740 Garching, Germany

Optical investigations are reported of the interaction of $0.3TW, 250fs$ Ti:sapphire laser pulses with underdense plasmas created from high density gas jet targets. Shadowgraphy using a 2ω probe pulse, images of the transmitted radiation and images of 1ω and 2ω sidescattered radiation are reported for nitrogen and hydrogen. Nitrogen demonstrates ionization induced refraction which is modelled with a simple numerical gaussian beam model while hydrogen demonstrates the onset of channeling expected at the critical power for relativistic self focussing.

As an ultra-short laser pulses penetrates into a gas target at high intensites the gas ionizes via tunnel ionization[1] in the rising edge of the pulse creating an electron density gradient which refracts the radiation outwards[2-5]. The onset of refraction can be reduced by the use of pulsed gas jet targets which allow high intensities to be achieved at the entrance to the gas interaction region. Also, plateau ionization states can be achieved above certain intensities if full ionization occurs such as for H^+ at intenisties $> 10^{14}W/cm^2$. It is then possible for part of the laser pulse to propagate within this plateau region without dominant refraction effects. As the power in the laser pulse exceeds a critical power given by $P_C = 17n_c/n_eGW$, where n_e is the elctron density and $n_c = m_e\omega_L{}^2/4\pi e^2$ is the critical density, the onset of relativistic self focussing of the laser pulse is also predicted[6] and has been reported in pulsed hydrogen gas targets at low densities using high intensities[7]. Thus the propagation of a laser pulse at ultra high intesities in gas targts involves a complex balance of a number of time dependent processes.

We report here experiments on the propagation of high intensity laser pulses into high density gas targets at electron densities of 0.01 to 0.2 n_c and at power levels up to the critical power for relativistic self focussing. The experiments were carried out using a TW Ti:sapphire laser system generating 250fs pulses at 790nm with an energy of 80mJ at the target. These pulses were focussed using a 90° off axis parabola to a focal spot with a peak intensity of

---

[a]on leave from the Department of Electrical Engineering, University of Alberta, Edmonton, Canada

[b]on leave from the Shanghai Institute of Optics and Fine Mechanics, Shanghai, P.R. China

$3 \times 10^{17} W/cm^2$ and a 50% energy containing diameter of $20\mu m$. The target consisted of a pulsed $500\mu m$ diameter free expansion nozzle[8]. A synchronised probe pulse was obtained by reflecting 4% of the main pulse from a beam splitter and frequency doubling to 395nm wavelength. This probe pulse was employed for time resolved transverse shadowgraphy of the gas jet interaction by imaging onto a CCD camera. Using the same imaging system the 1ω and 2ω scattering and emission were observed from the side of the plasma.
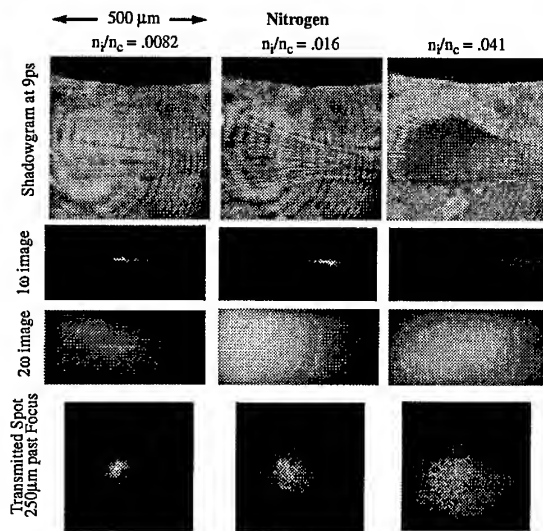

Figure 1: Images from a nitrogen plasma for peak ion densities of .0082, .016 and .041 n_c from left to right respectively. The top row shows shadowgrams taken with a delay of 9ps, the second and third rows show the images obtained from the side through 12nm and 33nm bandwidth filters centered at 790nm (1ω) and 400nm (2ω) respectively, and the last row shows the transmitted radiation imaged at a point $250\mu m$ past the focal position

The refraction of the laser pulse propagating through the gas jet is clearly visible in shadowgrams taken at a time of $9ps$ after arrival of the laser pulse for various pressures of nitrogen gas as shown in Fig.1 together with transmitted and scattered light images. The laser beam enters from the right hand side of the images with its vacuum focus near the middle of the image and the peak of the gas density located $115\mu m$ further left. As can be seen in Fig.1 the emission at 1ω becomes weaker, broadens and shifts towards the incoming laser with higher density, indicative of the refraction of the laser beam. The emission at 2ω appears near the vacuum focus at lower pressures but disappears in the plasma emission at higher pressures. The self emission of the plasma observed

in the 2ω image also shifts towards the laser at higher pressures.

In order to compare the refraction to that expected from the ionized electron density profile a refraction model for gaussian beams[9] has been extended to include a non-uniform density profile corresponding to that of the gas jet. The equation for the propagation of the rays is solved numerically. In this model a power law relation is used for the ionization state of the gas as a function of intensity, based on the barrier ionization model. The predicted trajectories of the beam radius calculated from this model are shown in Fig. 2 for two densities of the gas jet overlayed on the shadowgram images for these densities. It is expected that the observed shadowgrams should correspond to the outer ionization contour, $Z = 1$, predicted by the model. As can be seen the predicted refraction agrees qualitatively with the images. However, the measured refraction is stronger than that calculated here. This may arise in part from refraction from individual ionizing filaments created from non-uniformities in the laser beam. Such small filaments have signifcantly smaller radii and thus much higher electron density gradients than that of the whole beam which is used in the above calculation.
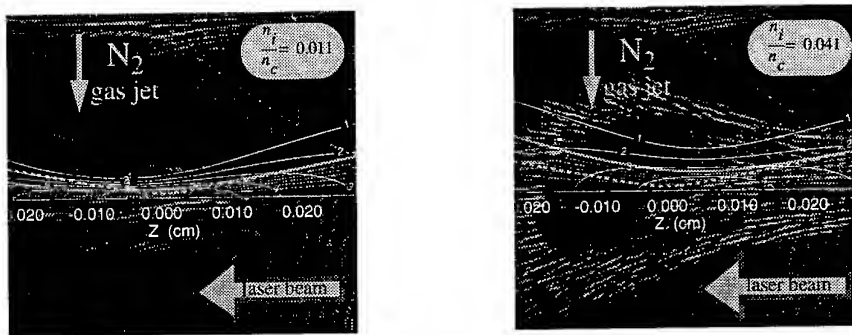
Figure 2: Model calculations for nitrogen plasma for ion densities of 0.011 and $0.041n_c$ overlayed on shadowgrams taken at the same densities. The solid and dashed thick curves give the beamwaist trajectory in the plasma and vacuum respectively. The thin numbered curves show the ionization contours labeled by ionization state.

Different results are obtained when hydrogen is used as the gas target and the conditions approach those required for relativistic self focussing, $P_C = 0.3TW$ for $n_e = 0.06n_c$. In this case, as shown in the shadowgram image given in Fig. 3 a channeling of the radiation is observed along the laser axis through the gas jet target. In addition, the transmitted radiation image $250\mu m$ past focus, shown in Fig.3, shows hot spots at high densities, around those required to give the critical power for relativistic self focussing. Such hot spots are

668

quite different than the smooth refracted images abtained for similar electron densities of nitrogen, helium or argon an example of which is shown in Fig. 1. We expect that the low ionization threshold for hydrogen allows the creation of a more uniform starting plasma and thus allows the self focussing to begin as the conditions approach those required for relativistic self focussing.
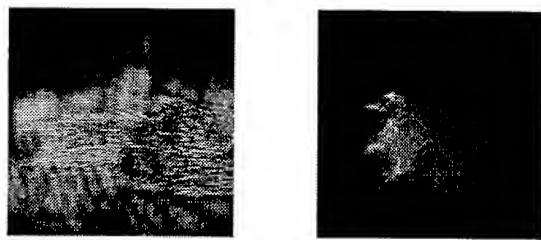

Figure 3: Shadowgram taken at a time of $1.3ps$ (left) and transmitted spot image (right) for hydrogen plasma at a peak ion density of $0.16n_c$. The left image is $520\mu m$ across and the right image is $420\mu m$ across

In summary, we have presented results on the propagation through high density gas targets at high intensities approaching the critical power for relativistic self focussing. While most gases show refraction as expected from the non-uniform ionization electron density profiles, hydrogen shows the onset of some self focussing behaviour at these power levels. A simple refraction model has been employed to predict the ionization induced refraction behaviour.

Acknowledgments

References

1. M.V. Ammosov *et al.*, *Sov. Phys. JETP* **64**, 1191 (1986)
2. R. Rankin *et al.*, *Optics Lett.* **16**, 835 (1991)
3. Y.M. Li *et al.*, *Optics Comm.* **93**, 366 (1992)
4. S.C. Rae *et al.*, *Optics Comm.* **97**, 25 (1993)
5. A.J. Mackinnon *et al.*, *Phys. Rev. Lett.* **76**, 1473 (1996)
6. G.Z. Sun *et al.*, *Phys. Fluids* **30**, 526 (1987)
7. P. Monot *et al.*, *Phys. Rev. Lett.* **74**, 2953 (1995)
8. Y.M. Li *et al.*, *Meas. Sci. Technol.* **5**, 1197 (1994)
9. E.E. Fill *et al.*, *J. Opt. Soc. Am. B* **11**, 2241 (1994)

A HIGH EFFICIENCY SOFT X-RAY AND OPTICAL SPECTROMETER DESIGN

D. NEELY, P. NORREYS

Rutherford Appleton Laboratory, Chilton, Didcot, Oxon OX11 0QX, U.K.

M. ZEPF

Department of Physics, Clarendon Laboratory, University of Oxford, Parks Road, Oxford, OX1 3PU, U.K.

The production of harmonic radiation from high intensity laser gas/solid interactions is presently an area of active interest world-wide. We report the novel design of a high efficiency spectrometer capable of detecting emission from 5 to 1100 nm on a single shot basis which was used experimentally in a solid target harmonic experiment. The spectrometer uses two in-line gratings to separately disperse the optical and soft X-ray emission onto two independent detectors. The optimum operating angle for the flat-field soft X-ray grating, for a given spectral range was determined using a ray tracing routine which located a detector plane where the spectral and spatial resolution were limited only by the resolution of the micro-channel plate detector. The spectrometer was operated primarily in an imaging slitless mode with a solid angle collection of 30 μ sterrad. The ultra violet, optical and infra-red spectrum was obtained by placing a planar grating to intercept the undiffracted zero-order component reflected from the first grating.

1 Introduction

X-ray emission spectroscopy is an essential diagnostic to measure the efficiency with which harmonics[i] of the drive laser wavelength can be produced or the gain coefficient of a soft X-ray laser transition[ii]. Typically, on experiments carried out on the VULCAN high power laser, a soft X-ray spectrometer[iii] incorporating a 1200 lines/mm aperiodically ruled flat-field grating[iv] is used to examine emission in the 2 ↔ 30 nm region. Normally, either film (ILFORD Q-plates) or a streak camera is used to record the signal.

To facilitate new investigations an increase in detection sensitivity and spectral range was required. The improvements implemented to this end were:-

(1)   incorporating a variable focal length imaging cylindrical pre-mirror to increase the flux density at the detector plane. The 300 nm gold overcoated 160 mm long BK7 glass mirror had an RMS surface roughness < 1 nm and was operated at a glancing angle of 4° to maintain high soft X-ray throughput at low magnifications ~3. Using a variable mirror greatly increased the locational flexibility of the system;

(2)   using a micro-channel plate (MCP) permanently maintained under high vacuum as the detector in the 5-100 nm region. MCP's are more sensitive detectors than film;

670

(3)   the addition of a limited aperture filter between the grating and the soft X-ray detector, which efficiently discriminates against fluorescent and scattered emission within the spectrometer giving significantly reduced background;

(4)   placing a planar grating to intercept the undiffracted zero-order component reflected from the first grating and adding a second detector plane. This gives spectral coverage in the 1100-150 nm region simultaneously with soft X-ray exposures, both sampling of the same angular emission cone from the source.

Figure 1 shows a schematic diagram of the final instrument.
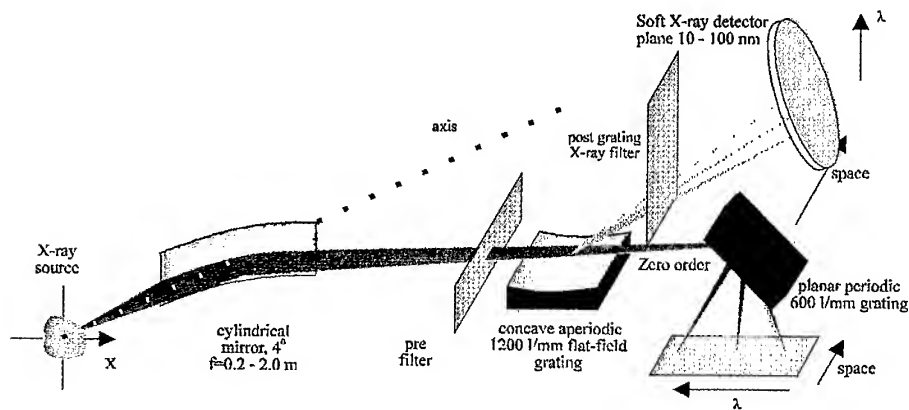

Figure 1 Schematic diagram of extended range imaging spectrometer.

To obtain maximum sensitivity it is necessary to simultaneously obtain optimum spatial and spectral resolution. Since the imaging mirror's surface is orthogonal to the grating surface the spatial imaging of the mirror and spectral imaging/ dispersion of the grating can be considered separately and combined at the final design stage. The solution to the imaging problem is a circular image plane I(λ) centred about the flat-field grating, of radius r = |MI| - |MG| where M is the mirror and G is the grating . Therefore, when r has been determined for a given source distance S and grating glancing angle g, the adjustable focal length imaging mirror can be set so that its imaging plane coincides with the grating's.

The spectral imaging properties of this grating were investigated using a geometrical ray tracing program which solved equation (1). Where ρ is the groove density[v], R the grating radius = 5649 mm, λ is the wavelength being examined, n the grating unit normal, m the order, and θ_{out} the output angle, ρ_0 = 1200 lines/ mm, b_2 = -20, b_3 = 455.8 and b_4 = -11840 and the grating surface is 50 mm long.

$$Sin^{-1}\left[\hat{\underline{n}} \wedge \hat{\underline{s}} - m\lambda\rho\right] = \theta_{out} \quad \text{where} \quad \rho = \rho_O\left[1 + \frac{2b_2}{R}x + \frac{3b_3}{R^2}x^2 + \frac{4b_4}{R^3}x^3\right]^{-1} \qquad (1)$$

The ray tracing program followed a bundle of 51 and located the optimum spectral resolution plane for each wavelength. Figure 2 shows these planes for a source distance of 0.62 m (the value used experimentally) for a range of glancing angles onto the grating. In figure 3 the grating to detector distance I is plotted as a function of wavelength for the detector planes shown in figure 2. As stated earlier, the ideal detector plane solution has a constant value of I. Using an MCP detector it can be shown that a relaxation of this condition (~ 4 % of I) occurs due to the limited resolution p $\approx$ 200 μm of the MCP. Figure 3 clearly shows that this is achievable, with settings having deviations less than 2 % existing. The graph also shows that the average value of I is a slowly varying function of g. The optimum value of g to give a minimum deviation in I for a given source distance S is plotted in figure 4. Operating the spectrometer along this curve maintains I at 245.5±0.3 mm over a wide range of source distances 0.15 < S < 1 m.

To achieve optimal spatial and spectral resolution for the zero order optical radiation reflected from the first grating and dispersed by the second planar grating
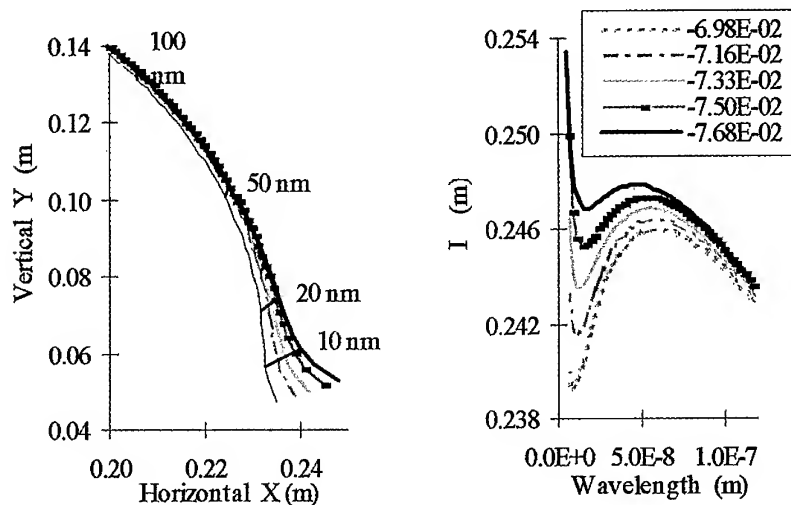

Figure 2 Focal planes for a 1200 lines/mm flat-field grating and a source to grating distance of 0.62 m.

Figure 3 Focal plane distance I for a source to grating distance of 0.62 m. The Key gives the glancing angle g in rads.
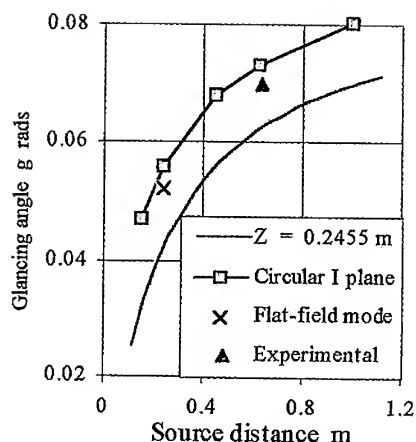
672

Figure 4 Graph showing glancing angle for flat-field grating to achieve circular focal plane at different source distances.
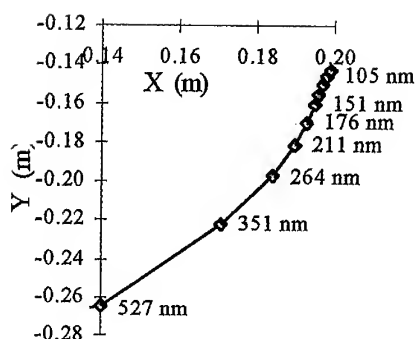

Figure 5. Optical detector plane for first order of a 500 l/mm (200 nm blaze) grating at 52 degrees situated 185 mm behind the flat-field grating.

it is desirable to have the zero order image distance Z almost equal to I. Also plotted in figure 4 is the required glancing angle to achieve Z = I = 0.2455 m. Clearly, it is not possible to obtain optimal spatial and spectral resolution in the optical region using a planar grating when the flat-field grating is optimised for the soft X-ray region. Figure 5 shows the optimal spectral resolution plane for planar 600 lines/mm grating. Placing the detector in this plane will give maximum spectral resolution but the orthogonal spatial plane will be out of focus. This will lead to a loss in sensitivity. However, since the harmonic production efficiency is significantly higher in the optical region than in the XUV, sensitivity here is not a major limitation. Throughputs of 20% in the optical were achieved and in the soft X-ray region the throughput increased from ~1% @ 100 nm to 10% @ 100 nm. Analysis of the spectra obtained is presently underway and will be reported in more detail later. A typical spectra obtained using this instrument is shown in [1]. Thanks to S. Moustaizis for his encouragement and helpful discussions.

References

[i] P. A. Norreys et al, Efficient Extreme UV Harmonics Generated from Picosecond Laser Pulse Interactions with Solid Targets. Phys. Rev. Lett, Vol 76, No 11, p1832-1835 (1996)

[ii] D. Neely et al, Optics Communications, 87, 231-236 (1992)

[iii] RAL flat-field drawing number SL-6700-321-02-A

[iv] Hitachi Part No. 001-0437 blank size30x50x10 mm Blaze angle 87 degrees.

[v] T. Kitta, T. Harada, N. Nakano and H. Kuroda. Applied Optics, 22, 4 (1983) p512-513.

THE SIMULATION OF HIGH-BRIGHTNESS, HARD X-RAY SOURCE BASED ON HIGH-INTENSITY INTERACTION OF ULTRA-SHORT LASER PULSES WITH HIGH-Z TARGET.

V.A.LYKOV, V.E.CHERNYAKOV, Ya.Z.KANDIEV,
I.A.LITVINENKO, V.G.NIKOLAEV

Russian Federal Nuclear Center - VNIITF
PO box 245 Snezhinsk (Chelyabinsk-70), 456770, Russia.
E-mail: lyk@nine.ch70.chel.su

The results of numerical simulations of fast electrons interaction with matter, calculated yield and angular distribution of bremsstrahlung and fluorescence K-α X-ray radiation and generation of electromagnetic fields, carried out by ERA, PM2D and PRIZMA code for state of experiments on interaction of ultra-short laser pulses with high-Z targets at intensity of 10^{16} -10^{18} W/cm^2 are presented. Spherical targets with conical hollows and conical targets of high-Z matter are proposed for experiments with picosecond lasers to increase the brightness of hard X-ray source.

1 Introduction

The promising trend in development of high brightness X-ray source is the implementation of high intense, short-pulse laser's technique. Tightly focused radiation of ultra-shot pulses from terawatt laser on high-Z target leads to hard bremsstrahlung and characteristic K-L and M-L X-ray radiation [1-3]. Medical research requires X-ray sources with energies in range of 20-80 keV and minimum source size [4].

The paper presents both the results of calculations of thin layer heating caused by fast electrons taking into account of self-generated electrical fields, performed by 1D-ERA code [5] and the results of PM2D code simulation of electron motion and generated electromagnetic fields at the interaction of ultra-short laser pulses of high intensity with flat targets.

The calculations of fluorescence yield and bremsstrahlung X-ray for experiment's state published in paper [1] were performed by PRIZMA code [6] using Monte-Carlo methods.

There are also presented estimations and results of 2D-calculations on proofing possible significant increase of X-ray source brightness if intensive short laser pulses were focused into conical targets and spherical targets with conical hollows.

2   THE 1D-ERA CODE CALCULATIONS OF FAST ELECTRONS INTERACTION WITH MATTER.

The interaction of laser radiation with matter results in the generation of fast electrons with effective temperature of $T_f = 100$ keV at laser intensity of $q_l \approx 10^{18}$ W/cm^2 on targets [1-3].

Penetrating in the target matter fast electrons heat it and may cause saturation yield of unshifted component of fluorescence line of K-α radiation [7]. The additional energy loss of fast electrons in the target due to self-generated electrical fields and Joule heat of the target by inverse currents may serve as other processes leading to unshifted K-α X-ray saturation. The yield of bremsstrahlung and unshifted K-α X-ray with account of target heating by the inverse currents may be decreased in $1 + S$ times, where the value $S = Q_j/Q_{st}$ is the ratio of Joule to collision target heat by fast electrons.

The calculations of target heating by fast electrons were performed by the ERA code in which fast electrons transfer model [8] in Fokker-Plank approximation with account of self-generated electrical fields is realized. The formula, interpolating calculations for Coulomb logarithm within zero-temperature and fully ionized matter with the weight equal to the matter ionization degree was added to this model. Interpolation formulas for equation of state (EOS) and Fe-ionization degree, published in paper [9] were used in these calculations. The interpolation formula, based on paper [10] data was used for electrical conductivity.

The unidirectional energy flow of fast electrons with the assumption of their isotropic angular distribution and Maxwell energy distribution of fast electrons with the temperature of T_f(keV)=$100(q_l/10^{18}$ W/cm^2 $)^{1/3}$ was used in these calculations. The time dependence of laser intensity (q_l) on the target in the form of isosceles triangle with 0.5 ps FWHM and the peak value of q_l=$5 \cdot 10^{17}$ W/cm^2 was used. The calculations were carried out for conversion efficiency (A_f) of laser radiation to fast electrons equal to A_f=0.12 and A_f=0.5.

The 1D-ERA code calculations give the values of S=0.12 for fast electron intensity $q_f \approx A_f q_l \approx 6 \cdot 10^{16}$ W/cm^2 and S=0.29 for $q_f \approx 2.5 \cdot 10^{17}$ W/cm^2. The electrical fields of $E = 25$ MV/cm, the temperature of T=$100 \div 200$ eV and the pressure of P=$100 \div 500$ Mbar may occur in the target as it follows from performed calculations. The additional experimental data on the electrical conductivity for the range of temperatures mentioned above and solid densities of the target are required for achieving higher accuracy of calculations.

3 THE RESULTS OF THE PM-2D CODE CALCULATIONS OF ELECTROMAGENETIC FIELDS.

The calculations of fast electrons motion and self- generated electrical fields outside flat target were performed by the 2-dimensional PM2D code. The PM2D code makes it possible to simulate relativistic electrons motion by PIC method with account of self-generated electric fields, calculated by Poisson equation and self-generated magnetic fields, calculated by Bio-Savare equation.

The results of calculations for cylindrical geometry (z, r) are presented on Fig. 1,2. The disk surface source with diameter of 20 μm for fast electrons with isotropic angular and Maxwell energy distribution with temperature of $T_f(\text{keV}) = 100(q_l/10^{18} \text{ W/cm}^2)^{1/3}$ was used in this calculation. The time dependence of laser intensity (q_l) on the target in the form of isosceles triangle with 1 ps FWHM and the peak value of $q_l = 10^{16}$ W/cm^2 was used. The conversion efficiency of laser radiation to fast electrons was assumed to be equal $A_f = 0.15$.
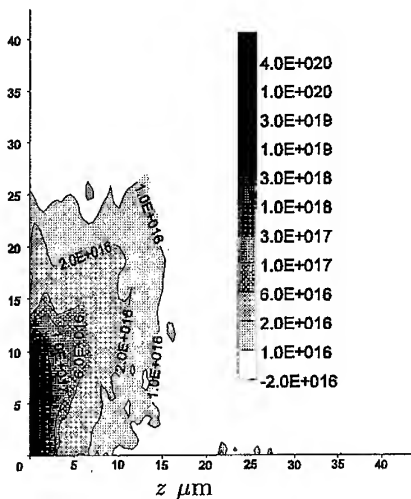

Fig.1

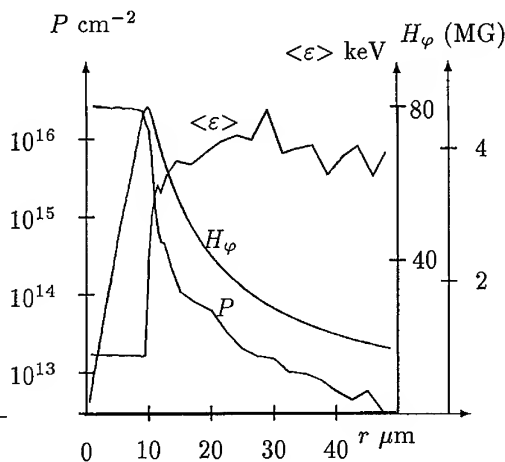Fig.2

Fig.1. The fast electrons density outside the target at moment t=0.5ps.

Fig.2. The amplitude of magnetic field (H_φ) at moment t=0.5ps, the flow (P) and mean energies $(<\varepsilon>)$ of the electrons through the target surface versus radii.

As it follows from the estimations and calculations performed by the PM2D

code without account of ion emission from the target surface, the electromagnetic field returns fast electrons to the region with the dimension about of $\lambda_d \approx 1\mu$m from source. The fast electrons density is maximum inside this volume and steeply decreases outside this volume. Maximum values of the electrical and magnetic fields outside the fast electrons source volume nevertheless may achieve values of $E \approx 1 \div 10$ MV/cm and $H \approx 1 \div 5$ MG consequently.

4 THE RESULTS OF THE PRIZMA CODE CALCULATIONS OF X-RAY YIELD AND ANGULAR DISTRIBUTION.

The experimental data on the laser interaction with matter obtained at Janus facility (Nd-laser, $\lambda = 1053$ nm, 500 fs, 1.5 TW) was published in paper [1]. The high-Z slabs (Zn, Ge, Mo, Sn) were irradiated at normal incidence to the laser axis. Maximum conversion efficiency (K) of laser radiation to K-α X-rays was measured for Mo target (E = 17.5 keV). The measurements performed at 15° from the target normal and give the value of $K_{\exp} = 3.7 \cdot 10^{-5}$ (calculated to the total solid angle of 4π) at laser intensity of $q_l = 5 \cdot 10^{16} \div 5 \cdot 10^{17}$ W/cm^2.

The simulations of electrons interaction with slabs, the generation and the transfer of bremsstrahlung and fluorescence K-α X-rays were performed by the PRIZMA code [6] using Monte-Carlo methods for states of experiments [1]. The following physical processes were simulated in the computations: elastic and nonelastic electrons scattering, the δ-electrons birth, the bremsstrahlung and fluorescence X-ray generation and transfer.

The 2-D PRIZMA code calculations of bremsstrahlung and fluorescence K-α X-ray induced by fast electrons of the disk source with diameter of 20 μm were performed. The isotropic source of fast electrons with Maxwell energy distribution and temperature (T_f) at the outer surface of Mo target with the thickness of $\Delta = 25$ μm was used in these calculations.

The calculated fluorescence X-ray yield (Y) and efficiency conversion (K_c) of laser energy into K-α X-rays per one electron of source are presented in Table 1. The efficiency conversion (K_c) includes correction on the anisotropy of K-α X-rays in the direction of measurements. The value of K_c weakly depends on temperature T_f in the range of $25 \div 100$ keV and the experimental data of $K_{\exp} = 3.7 \cdot 10^{-5}$ obtained in paper [1], allows us to make the estimation of laser energy quota (A_f) transferred to fast electrons and it is shown in Table 1 also. The value $A_f = K_{\exp}/K_c$ was about of 3% in experiments [1] performed with Mo-slabs at intensity $q_l = 5 \cdot 10^{16} \div 5 \cdot 10^{17}$ W/cm^2 as it follows from PRIZMA-code calculations. The fast electrons intensity $(q_f = A_f \cdot q_l)$, obtained in the experiments [1], probably has value of $q_f < 2 \cdot 10^{16}$ W/cm^2 so the correction factor on Joule heating of target, seems to be insignificant.

Table 1.

T_f (keV)	25	50	100
Y (%)	0.14	0.38	0.74
K_c (%)	0.09	0.12	0.13
A_f (%)	4.1	3.1	2.9

The increase of efficiency conversion (K) may be achieved by increasing laser energy quota that is transferred to fast electrons by resonance absorption of laser radiation. This effect was apparently observed in the experiments using pre-pulse, the increased ASE and grated targets [2]. The experiments with picosecond laser radiation entranced into hollow spherical shell also result in increasing of conversion efficiency [2]. However the value of shining surface and the brightness of X-ray source may increase not so significantly. Moreover such hard X-ray source would have poorly defined and instable angular and brightness parameters.

Focusing of high-intensity short laser pulses into: 1) conical targets and 2) spherical targets with conical hollows may appear to be the other possible trend of increasing brightness and quality of hard X-ray radiation source.

The 2-D PRIZMA code calculations were performed for two cases: 1) the conical Mo target ($2\alpha=90°$) with the wall thickness of 20 μm and 2) Mo-sphere 50 μm in diameter with conical hollow ($2\alpha=90°$). The results of calculations performed in assumption that laser light could be focused into focal spot with diameter of 20 μm and the fast electrons temperature could be of about 100 keV are presented in Table 2 for statistic dispersion of about 4%.

Table 2. The angular distribution of K-α yield ($\frac{dY}{d\Omega} \cdot 10^4$) reduced to point source of unit electron power.

| $\mu=\cos\theta$ | -1 | -0.8 | -0.6 | -0.4 | -0.2 | 0 | 0.2 | 0.4 | 0.6 | 0.8 |
	-0.8	-0.6	-0.4	-0.2	0	0.2	0.4	0.6	0.8	1
case 1	7.4	6.0	5.3	4.8	5.2	5.7	6.1	6.0	6.3	6.8
case 2	6.4	5.5	5.3	5.3	5.3	5.4	5.5	5.2	5.3	5.3

The resonance absorption of laser radiation on conical surface of the target wall would lead to the increase of the factor A_f up to 50% and conversion efficiency of laser energy into K-α X-ray could increase up to 0.05%.

678

References

1. J.Dunn, B.K.F.Young, A.K.Hankla *et al.* "Study of Supra- thermal Electrons and K-alpha X-rays from High Intensity 500 fs Laser-Produced Plasmas". Report at 12th International Conference on LI&RPP. Book of Abstracts, 170, (Osaka Japan, April 24-28,1995).

2. A.Rousse,J.P.Geindre,P.Audebert,*et al.* "Radiative pumping generated by a hot electron K-alpha X-ray source in femtosecond laser-produced plasmas experiments". Report at 12th International Conference on LI&RPP. Book of Abstracts,51, (Osaka Japan, April 24-28,1995).

3. P.V.Nickles, M.Schnuerer, M.Kalachnikov *et al.* "Absorption, hot electrons and hard X-ray emission from laser produced plasma at $I \leq 10^{18}$ W/cm^2". Report at 12th International Conference on LI&RPP. Book of Abstracts,231, (Osaka Japan,April 24-28,1995).

4. K.Herrlin, *et al.*, *Radiology*, **189**, 65, (1993).

5. V.A.Lykov, N.G.Karlykhanov, V.E.Chernyakov,A.A.Chikulaev. Laser Interaction with Matter. Proceedings of 23rd European Conference. IOP Conference Series Number **140**, 21, (IOP Publishing,Bristol and Philadelphia, 1995).

6. Ya.Kandiev, V.Plokhoi. *Voprosy Atommoj Nauki i Tekhiki. Metodiki i Programmy*, **2**, 70, (Moscow, 1993).

7. J.D.Hares,J.D.Kilkenny,M.H.Key *et al. Phys.Rev.Lett.*,**42**,1216,(1979).

8. Lykov V.A., Shirokovskaya O.S. *Voprosy Atommoj Nauki i Tekhiki. Metodiki i Programmy*, **3**, 73, (Moscow, 1988).

9. M.Eliseev and G.E.Klinishov. *Preprint IAM USSR*, **48**, (Moscow,1980).

10. Y.T.Lee and R.M.More, *Phys. Fluids*, **27**, 1273,(1984).

NONLINEAR COLLISIONLESS INTERACTION
OF ULTRASHORT LASER PULSES AND EXPLANATION
OF THE UMSTADTER EXPERIMENT

H. HORA*, R. HÖPFL

European Network (J.M. Martinez-Val, Polyt. Univ. Madrid) at
Anwenderzentrum, Hermann-Geib-Str. 18, 93053 Regensburg, Germany
*Perman. Address: Dept. Theor.Physics, Univ. NSW, Sydney 2052, Australia
At present Guest Prof., Inst. Laser Engin., Osaka Univ., Suita Osaka 565, Japan

J.M. MARTINEZ-VAL, S. ELIEZER, M..PIERA

ETS Ingen. Industr., Jose, Gutierrez Abascal 2, 28006 Madrid/Spain

B.W. BOREHAM**, P.R. BOLTON

Lawrence Livermore, National Laboratories, Lievermore, Cf. 94550, USA
**On leave from Centr. Queensld. Univ., Rockhampton, 4700, Australia

W. SCHEID, and T. HÄUSER

Institut f. Theoret. Physik, Univ. 35392,Giessen, Germany

The advent of very intense laser pulses of 20 fs to ps duration permits an application of the collisionless nonlinear force acceleration of plasma blocks to the conical fusion reactor scheme. A further field is the elaboration of the high limit of the 111the and higher harmonics generation based on photon density relations to the fine structure constant. A further result is the quantitve explanation of the 10^8 electrons of up to 30 MeV electrons and their beam properties measured by Umstadter by a free wave accelerator scheme.

1 Nonlinear Force Acceleration of Plasma Layers

The finally derived complete nonlinear force of laser plasma interaction (Hora 1969, 1985, 1991) to study the acceleration of plasma was most interesting for such short times of the ps range at laser intensities above 10^{14} W/cm^2 for neodymium glass lasers. The real time computations for (nonlinear) collisional plasma could be carried out with the geniune two fluid model up to 40 ps for neodymium glass laser intensities of 10^{16} W/cm^2 showing the stochastic pulsation (stuttering) (Maddever et al 1990) as measured with a stuttering time of 6 to 30 ps (Hora, et al. 1992). where the stuttering can be avoided by beam smoothing (Kato, Mima et al 1984) as calculated. The first push of each of the nonlinear force driven plasma accelerations happened within few ps.

Following the numerical evaluations as described before (Hora, 1991, Chapter

679

10.5) we find the following formula for the ion energy ε_i in the (mainly collisionless) accelerated deuterium plasma layers (ablated and compressed) depending on the neodymium glass laser intensity I

(1) $\varepsilon_i = 416(I/10^{16}W/cm^2)^{1/2}\,eV$

This nonlinear force pushing of thick plasma layers to about 10 keV energy can be used for high efficiency (50% or more) driving plasma layers without much heating in the bi-conical compression process as elaborated before (Martinez-Val et al 1993) where the wall losses are strongly reduced due to the very high speed (more than Mach 500) of the DT layers.

2 Photon Density and Higher Harmonics Generation

Based on the measurement of the lateral emission of electron from a laser beam (Boreham et al 1979) together with further observations, a correspondence principle of laser interaction was derived (Hora et al 1987). The intensity I* of a laser of frequency ω where the average elongation and the average momentum of the quivering electron has a product of $h/2\pi$, corresponds to a photon density

(2) $n_{ph} = m\omega^2/(4\pi e^2) = n_{cc}$

which curiously is equal to the electron density n_{cc} in a plasma at Langmuir cut-off. Relating the photon density D per wave length cube one arrives at a relation of the purely classical electron cut-off density with Planck's quantum constant h and the relativistic fine structure constant α. We noted further (Boreham et al 1996, 1996a) that the number of the highest harmonics H produced in the fs laser pulses of relativistic intensities is given by

(3) $H = (D/4)^{1/5}$

This agrees with measurements where the cut-off H is 111 (Macklin et al 1993) and 135 (L'Huiller et al 1993).

3 Free Wave Acceleration and the Umstadter Experiment

The free wave acceleration of electrons by Lasers (Hora, 1988; Evans 1988) seems to provide a complete theoretical explanation of the recent laser accelerator experiment described by Umstadter (1996). The scheme of the free wave laser acceleration was aimed to look into straightforward mechanisms where plasma and

its highly complex properties are not involved. The first step was to provide conditions (Hora, 1988) where the electrons are being trapped into the intensity minima of a laser interference field by the nonlinear force and are accelerated when these minima are moved. Since there was some concern whether this is possible at all, a detailed numerical study with the necessary higher order solution of the motion of the electrons in the intensity minima and subsequent acceleration of the wave field clearly proved this mechanism (Cicchitelli et al 1990).

The second step was to evaluate the energy an electron receives within half a cycle of the laser wave. The relativistic motion can then be solved analytically in closed form (Scheid et al 1989, Häuser et al 1994). If a linear parised plasma wave propagates in the x-direction with the electric field oscillating into the y-direction, the Lorentz factor γ and the distances x and y the electron is moved are

$$(4) \qquad \gamma = 1 + 2\delta^2/k^2; \quad x = 3\delta^2\,\lambda^3/(32\pi^2) \quad y = -/\delta\lambda^2/(4\pi); \quad z = 0$$

where λ is the wave length and $\delta = (eE_0)/(mc^2)$ using the mass m and charge e of the electron and the amplitude E_0 of the laser electric field. Expressed by the laser power P, the Lorentz factor is

$$(5) \qquad \gamma = 1 + (2^{5/2}eP^{1/2})/(mc^{5/2}\pi) = 1 + (P/2.7\times10^9\,W)^{1/2}$$

After this gain the electron (within the phase symmetric plane wave) looses then this energy again within the following half cycle of the wave (Scheid et al 1989), returning to the initial value in the y-direction and being shifted by 2x, showing then no net gain at all . If the electron should keep the gained energy, the second half cycle would have to be removed by a rectifying of the laser beam. Alternatively the electron can be moved into a sidewise cut wave (beam) and has to leave the beam after a half cycle before being slowed down.

The same mechanism can be followed up numerically for a more realistic case (Häuser et al 1994): If a laser wave packet (sometimes called a pancake of photons) of some femtosecond duration is hitting a resting electron, its exact motion can be followed up. The fully phase-symmetric wave without any rectification and a Gaussian lateral intensity decay moves the electrons first sidewise by the transversal electric filed component and then axially due to the Lorentz force. Because of the laterally varying intensity, the electron receives a net energy gain (Häuser et al 1994) after the (phase symmetric) laser pulse has passed. This indeed depends on the co-ordinates which the electron has at the beginning with respect to the beam centre. The laser beam is described exactly as the complete Maxwellian solution including then the (earlier not treted) longitudinal field components necessarily to be added to the usual transversal components (Cicchitelli et al 1990a). The maximum net energy ε_{max} such an accelerated electron can gain is - derived from higher order numerical results including the longitudinal field - 57.5%

682

of the energy ε_0 given for the plane wave solution (5). This is the free wave accelerator as published since 1991 in full agreement (apart from the longitudinal field effect) with the independently derived results of Woodworth, Kreisler and Kerman (1996).

For the case of the experiment of Umstadter (1996) with a peak power of 25 TW we arrive from Eq. (5) at

(6)　$\gamma = 97.225;$　or　$\varepsilon_0 = 49.7\,\text{McV}$　or　$\varepsilon_{max} = 28.6\,\text{MeV}$

This value is in rather good agreement with the measured 30 MeV (Umstadeter 1996) . It is interesting to note that this result was achieved only if the longitudinal laser field (Cicchitelli et al 1990a) was included.

A further interesting agreement of the calculations with the measurements is the angle of the electron emission. As shown (Umstadter 1996), the diameter of the pulse of the 10^8 electrons of 30 MeV energy is about 2 cm at 8 cm distance from the interaction area corresponding to a beam aperture of $\alpha = 14.2^{\text{o}}$. Our calculation based on the half-wave acceleration model taking $\tan(\alpha/2)=y/x$ from Eq. (4) for higher order approximation arrives at an angle of 10.9^{o} which value may be increased for the realistic photon pancake case.

As a consequence of this calculation we predict that the similar experiment with the 2 PW laser (P erry et al 1994) at Livermore will produce 300 MeV ions where because of the larger value y in Eq. (4), 10^9 or even more electrons should be accelerated. The angle α shoud be about three times smaller.

Discussions about this topic with Professors K. Mima, Y. Kato, Y. Kitagawa, and T. Yamanaka are gratefully acknowledged.

Boreham, B.W., and Hora,H., 1979, Phys. Rev. Lett. 42, 776
Boreham, B.W., H. Hora, and P.R. Bolton, 1996, AIP Proceedings, *Laser Interaction and Related Plasma Phenomena,* S. Nakai, and G.H. Miley eds, (AIP, New York) p. 1223
Boreham,B.W., et al, 1996, Opt. Comm. (in print)
Cicchitelli, L. and H. Hora 1990, IEEE J. Qant. El. 26, 1833
Cicchitelli, H. Hora, and R. Postle, 1990a Phys. Rev. A41, 3727
Evans. R., 1988, Nature 333, 296
Häuser T., Scheid, W., and Hora, H., 1994, Phys. Lett. A186, 189
Hora, H., 1969, Phys. Fluids 12, 182
Hora. H., 1985, Phys. Fluids 29, 3706
Hora, H., and Handel, P., 1987, *Advances in Electronics and Electron Physics* P. Hawkes ed. (Acad. Press, New York) Vol. 69, p. 55
Hora, H., 1988, Nature 333, 337
Hora, H., 1991, *Plasmas at High Temperature and Density* (Springer, Heidelberg)
Hora, H., and Aydin, M., 1992, Phys. Rev. A45, 6123
Kato, Y., Mima K., et al 1984, Phys. Rev. Lett, 53, 215
L'Huiller, A., et al 1993, Phys. Rev. Lett. 70, 774
Macklin, J.J., et al 1993, Phys. Rev. Lett. 70, 766
Maddever, R.A.M., Luther-Davies, B., and Dragila, R. 1990, Phys. Rev. A41, 2154
Martinez-Val. J.-M., Piera, M., and Miley, G.II., 1993, Fusion Technol. 23, 218
Perry M.D., and Mourou. G. 1994. Science 264, 917
Scheid, W. and H.ora, H., 1 1989. Laser and Particle Beams 7, 315
Umstadter, R., 1996, Laser Focus 32 (No.2), 101
Woodworth, J.G., Kreisler M.N., and A.K. Kerman, *The future of Accelerator Physics:the Tamura Symposium,* AIP Conf. Proceed., T. Tajima ed., (Am. Inst. Phys., New York) p. 378